HIGH RESOLUTION TEM IMAGING OF CDTE

A DISSERTATION

SUBMITTED TO THE DEPARTMENT OF MATERIALS SCIENCE

& ENGINEERING

AND THE COMMITTEE ON GRADUATE STUDIES

OF STANFORD UNIVERSITY

IN PARTIAL FULFILLMENT OF THE REQUIREMENTS

FOR THE DEGREE OF

DOCTOR OF PHILOSOPHY

TSUTOMU T. YAMASHITA

JUNE 2015

© 2015 by Tsutomu Yamashita. All Rights Reserved.
Re-distributed by Stanford University under license with the author.

This work is licensed under a Creative Commons Attribution-Noncommercial 3.0 United States License.
http://creativecommons.org/licenses/by-nc/3.0/us/

This dissertation is online at: http://purl.stanford.edu/nw538jc4688

I certify that I have read this dissertation and that, in my opinion, it is fully adequate in scope and quality as a dissertation for the degree of Doctor of Philosophy.

Robert Sinclair, Primary Adviser

I certify that I have read this dissertation and that, in my opinion, it is fully adequate in scope and quality as a dissertation for the degree of Doctor of Philosophy.

William Nix

I certify that I have read this dissertation and that, in my opinion, it is fully adequate in scope and quality as a dissertation for the degree of Doctor of Philosophy.

Fernando Ponce

Approved for the Stanford University Committee on Graduate Studies.

Patricia J. Gumport, Vice Provost for Graduate Education

This signature page was generated electronically upon submission of this dissertation in electronic format. An original signed hard copy of the signature page is on file in University Archives.

Abstract

The thesis covers several distinctly different topics that I worked on while at Stanford from 1979 to 1984. Chapter 1 covers application of high resolution transmission electron microscopy (HRTEM) techniques applied for the analysis of CdTe and CdS materials. In addition, lattice defects found in these materials were characterized by the HRTEM method. Video recording of defect motion in CdTe was taken, and the images were analyzed to determine the type of defects that were observed. Image processing also was applied to the video recording to enhance the contrast in the images. This work done many years ago was followed up with a new HRTEM analysis of CdTe using a modern aberration-corrected microscope to study the capability of these new microscopes applied to the imaging of CdTe. The latest simulation software was used to compare the experimental images to simulated images. This new study is covered in Chapter 2. Chapter 3 covers the HRTEM analysis of the CdS/CdTe solar cell heterojunction interface. This was the original intention for developing the HRTEM technique on CdTe. An attempt was made to correlate some of the findings to the observed electrical characteristics of the heterojunction solar cells. On a similar topic, defects in GaAs films grown by molecular beam epitaxy (MBE) on GaAs substrate grown by the liquid encapsulated Czochralrsky method (LEC) were studied and this work is described in Chapter 4. This work was conducted at the Hewlett-Packard Laboratory during the 1981-1983 timeframe when I was an intern there. Many of the same techniques described for the work on CdS/CdTe were used to try to understand the defect formation mechanism in MBE-grown GaAs films. One interesting side note to this work was the characterization of GaAs whiskers during MBE growth of GaAs films on GaAs substrate. By using high resolution TEM and X-ray diffraction, it was determined that the whiskers were hexagonal phase GaAs, which is very unusual for GaAs. Recently, there has been considerable interest in GaAs whisker growth and they have some interesting applications.

Chapter 5 covers TEM analysis of magnetic thin films based on sputtered CoRe, CoPt and CoCr alloys. This was the subject of my first research project at Stanford. The work on magnetic thin film media was in collaboration with Tu Chen at the Xerox Palo Alto Research Center (PARC), and the intent was to characterize the microstructure of sputtered thin film and relate it to its magnetic properties and the deposition condition. A variety of conventional TEM techniques was applied to the investigation of the films, along with X-ray diffraction analysis. Many groundbreaking discoveries were made by Tu Chen at Xerox concerning the thin film magnetic media, and how their microstructure affects the limits of magnetic recording. It was a rare privilege to participate in some of his work during my career at Stanford. I made the study of magnetic thin film media my lifelong career while being employed at Komag Inc. from 1984 to 2007 and at Western Digital Corporation from 2007 to 2012. I had an ongoing collaboration with Professor Robert Sinclair on the study of microstructural development in magnetic thin films using TEM from 1984 to 2012. Some of the materials cited on CoCr-based magnetic thin films were conducted during these periods of collaboration between Komag Inc. and Stanford University. As an addendum, a description of zirconia-based overcoat development done at Komag is described. This was a continuation of the work on zirconia solid electrolyte that I did in collaboration with Farhad Moghadam and the late Professor Stevenson at Stanford. Sputtered zirconia film was used successfully as a protective overcoat for magnetic thin film disks.

HRTEM of CdTe and CdS covers image simulation based on Bloch Wave formulation developed by Pirouz Pirouz and computed images are compared to the experimental images obtained from the Philips EM400 model TEM. HRTEM is an interference image that comes from a phase shift introduced by the specimen itself and the spherical aberration and defocus of the objective lens in the microscope. A direct comparison between the image and the structure is not possible without controlling all of the key parameters of the microscope, and computed images are necessary to verify the relationship between the actual structure and the HRTEM images. Great advances have been made in electron microscopy since then. Spherical aberration of the electron

microscope can now be corrected and resolution of the microscope has reached 0.05 nm. A Titan 80-300 TEM equipped with an aberration corrector is used to image CdTe, again, using the latest HRTEM methods to obtain atomic resolution images. Experimental images are then compared against the computed images to determine the conditions that are necessary to obtain a correspondence between the structure and the image. Special care and setup is still necessary in order to obtain atomic resolution images; those parameters are discussed in Chapter 2.

A second aspect of the high-resolution imaging technique developed in this work is dynamic imaging of lattice defects in CdTe, imaged in the [110] orientation. Due to a high density of defects that are inadvertently introduced into the CdTe specimen by ion milling during sample preparation, many common lattice defects such as dislocations and stacking faults are imaged. Interesting dislocation reactions, which were theorized as far back as 1957 by Shockley, actually have been observed in-situ in the TEM. Stacking faults terminated by partial dislocations were annealed out of the crystal lattice by electron beam heating inside the TEM and such motion of defects was recorded by a video recorder.

CdTe material is used in solar cells due to its ideal bandgap, which is a close match to the energy of solar radiation. Today, the CdS/CdTe heterojunction is used extensively for thin film solar cells owing to its high efficiency and simple manufacturing method, making it a cost effective solution for solar power generation. Some background information on CdS/CdTe heterojunction solar cells is presented and high resolution lattice images of the interface are shown and described in detail. CdS and CdTe can form an epitaxial relationship in a variety of ways, and they are analyzed by TEM and X-ray methods. There is some general relationship between the junction performance and the CdS/CdTe interface, which can be made and this is summarized in this work.

Work that was similar to the analysis of the CdS/CdTe heterojunction interface concerns the defect characterization of MBE-GaAs film deposited on LEC-grown GaAs substrate. This structure has important commercial applications in many high-

speed devices and for optoelectronic components. This work begins with X-ray topography characterization and TEM studies of defects in the LEC GaAs substrates, followed by study of the interface between the MBE GaAs and the LEC GaAs substrates. A high density of defects originates at the interface of these two materials. Additional study was conducted on AlAs/GaAs interface grown on top of the MBE GaAs. One of the significant problems with MBE GaAs is the formation of defects that originate on the LEC substrates during the growth of the film. These defects were a significant problem, particularly the type called the *oval defects* named for their particular shape. An attempt was made to characterize them and surmise their origin. On the last side note to this work, a description of the discovery of the hexagonal phase of GaAs is made. In typical GaAs-based devices, a pure GaAs film is deposited on top of a GaAs wafer by MBE so that a more perfect layer of GaAs can be formed on which other layers are deposited, such as GaAlAs for example. In an accident where the GaAs was inadvertently grown at less than the ideal ~ 530^{o}C substrate temperature, a high level of GaAs whisker growth is initiated. Whisker growth is often a nuisance in device fabrication, and the mechanism that leads to such growth is of technical interest in preventing them. Under some conditions, the growth rate of whiskers is quite remarkable, leading to some amazing structures. The growth of the whiskers is fed by surface diffusion, and the growth occurs at a very high rate. The whisker growth in GaAs was a nuisance that required some understanding of what they are, how they originate, and how to reduce their occurrence. In analyzing the GaAs whiskers, it was discovered that they always originate at surface defects on GaAs, and that they have a hexagonal crystal structure that is heavily faulted. They always grow along the $<111>_{A}$ direction. The whiskers are generally more resistive than the surrounding GaAs film because they tend to charge-up during microscopy. At the time of this investigation, hexagonal GaAs has only been reported in high-pressure studies, and it is quite unusual to see this phase created by conventional means. Hexagonal phase GaAs whiskers have now been reported and studied for the past 10 years or so because interest has emerged in making devices out of them.

Magnetic thin films were in development throughout the 1970s as the next material to replace the Fe-oxide in use then. Both sputtered and plated Co-based thin films were in consideration. One of the key factors in consideration was how high a coercivity (Hc) the film could achieve. Several factors were in play, such as the magnetic anisotropy of the film, grain structure and phase, and degree of isolation the grains have with each other. To achieve the highest anisotropy, the rare earth elements such as Pt, Sm, Re, Ru were in consideration to be alloyed to the cobalt, but due to the cost of these additive elements, sputtered media did not achieve widespread acceptance initially. The films that we investigated first were CoRe alloy films provided by Tu Chen at Xerox. One of the first critical questions asked was whether the film contained a significant amount of the face-centered cubic (FCC) phase or not. Conventionally, this would have been answered by such techniques as analyzing the electron diffraction pattern for the presence of the FCC phase. However, this turned out to be quite difficult because the FCC phase diffraction rings were in close proximity to the HCP phase diffraction rings. A technique such as selected area dark field imaging would not yield useful results. For this purpose, a 2½-D imaging method refined by Michal and Sinclair was employed to determine the location of the FCC phase and its prevalence or abundance in the film. It was shown that a small amount of FCC phase does exist in the film, and that it is likely to be in the highly faulted region within the HCP matrix. One thing that became certain was that the FCC phase needs to be avoided as much as possible as its presence clearly reduces coercivity, Hc. One remedy was to add alloying elements that increased the stacking fault energy in cobalt so that the HCP phase was enhanced and stabilized. This resulted in films with higher coercivity.

Work on CoRe shifted to CoPt alloys at Komag Inc., as Pt provides higher Hc potential and it is more readily available compared to Re. Work that went into making CoPt-X alloys successful for thin film media application is described using many of the key principles that were developed at Xerox PARC by Tu Chen. Control of preferred orientation in these films through nitrogen addition and nucleation control during sputtering are described in detail. In addition, the idea of isolating the grains in the film in order to reduce noise and inter-particle magnetic exchange was fully practiced, first

with the use of high sputtering pressure and later by addition of immiscible oxide phases into the target in order to force such segregants into the grain boundaries.

CoCr magnetic thin films were first proposed by S. Iwasaki as ideal material for perpendicular magnetic recording in 1979. A very high amount of Cr addition was suggested, in the 20 atomic% range, which is near the solubility limit of the Cr in Cobalt. Despite the fact that such a high amount of Cr should reduce the net magnetization of the film, the actual magnetization of the film is higher than expected based on the Co-Cr binary phase diagram. The initial investigation of CoCr system in collaboration with Tu Chen at Xerox dealt with understanding whether the phase diagram is correct or not and whether this film deposited at relatively high substrate temperature shows any evidence of segregation at the grain boundaries. Using the available energy dispersive X-ray spectroscopy (EDS) system at the time which was attached to the TEM, clear indication of Cr segregation at the grain boundaries was observed, particularly at the triple junction between the grains for highly annealed specimens. An obscure phase diagram from a Russian source was discovered, which suggests that under long annealing times a separate phase does indeed form for this alloy system. Work continued on this alloy system by many workers for several years. CoCr alloy with Ta addition was discovered to have excellent magnetic properties when used in combination with Cr underlayer to form a longitudinal media structure. A more sophisticated EDS method was employed on this alloy system to provide much more clear-cut evidence for Cr segregation, and that Ta plays a role in the enhancement of segregation, while Ta itself is not affected and remains largely unsegregated. A key feature of the alloy is that high temperatures as high as 250-300^{o} C are required during deposition to achieve useful Cr segregation.

The idea of segregation in thin film media playing a major role in enhancing the magnetic properties, hence, the areal density capability, was long advanced by Tu Chen. Grain isolation further promotes exchange decoupling between the grains, which is an important factor in keeping the transition zone between recorded bits narrow. This was a key concept that was demonstrated by Tu Chen at Xerox PARC in the late 1970s to early 1980s. The CoCrTa/Cr-based thin film system came to dominate the longitudinal

recording media by 2000, and the work that had gone into it from the early days of CoCr investigations played a critical role in understanding how this alloy system works. The importance of grain separation through grain boundary isolation continues to play an important role in thin film media design used in hard disk drives today. Perpendicular magnetic recording media that are used in hard disk drives (HDD) today all use oxide phase segregation that was pioneered by Komag for use in CoPt-based magnetic alloys.

As a side note, a sputtered form of stabilized zirconia made directly from yttria-stabilized zirconia was investigated for potential use in thin film media used in hard disk drives as an overcoat to protect the media. RF magnetron sputtering technique was developed to sputter the target and microstructural and diffraction analysis of the film indicated that the film is crystalline, and it forms the cubic zirconia phase. This film was commercialized as an overcoat on thin film media, and had some success in providing excellent tribologial coating to them. Being a dense and durable material, it also provided excellent corrosion protection as well as superb tribological coatings for wear-protection. By employing the phase diagram, it is known that solubility of oxides such as alumina (Al_2O_3) is quite low in zirconia. By creating alloyed targets of zirconia with alumina, the sputtered film with approximately 5 % alumina becomes completely amorphous and this film found a useful application as protective coating on magneto-optic (MO) recording media. MO media is made from TbFeCo magnetic film, which is particularly prone to corrosion. By sandwiching the ZrO_2-Al_2O_3 coating above and below the sensitive TbFeCo, the film provided significant protection against corrosion. It also served as an anti-reflective coating due to its excellent optical properties. Media made with this coating continue to operate even 20 years after they were made.

Therefore, this work demonstrates that characterization using advanced TEM methods is highly advantageous in developing practical material device systems ranging from semiconductor-based solar cells to metallic magnetic recording media.

Acknowledgments

I like to thank Professor Robert Sinclair for his years of support in this work and for his encouragement to come back after many years to complete this thesis. Professor Sinclair was my undergraduate and co-term master's advisor at Stanford as well. Others to whom I owe many thanks are my mentors, collaborators, and supporters for my efforts during my graduate life and many have become my lifelong friends.

Robert Sinclair
Richard A. Bube
William D. Nix
Dave Stevenson
Eric Pop
Shan X. Wang
Stig Hagström
Fernando Ponce
Birgit Jacobson
Tu Chen
Bruce Charlan
Robert M. White
Pirouz Pirouz
Farhad Moghadam
Alan Fahrenbruch
Gary Michal
Jan Werthen
Ko Nishimura
Tom Anthony
John Bravman
Jim Wittig
Subhash Shinde
Robert Burmeister
John Carruthers
Doug Collins
J. N. Miller
S. J. Eglash
Geoffrey Woolhouse
Tom Cass
Bob Smith
G. Elliot
Greg Anderson
C. W. Wei
Gerardo Bertero
Rajiv Ranjan
Lai-Hing Chan
Tom Nolan
Kai Tang
Unoh Kang
Ai Leen Koh
Ann Marshall
Joon Suk Park
Steven Madsen
Roy Kim

I am especially indebted to Xerox Palo Alto Research Center (PARC) for providing me the first project under Professor Sinclair to work on thin film magnetic media. I was assigned to Tu Chen to work on his cobalt-based films and he became my lifelong mentor at Komag where I went to work. This project was supported by the late Stig Hagström who was the PARC lab director at the time, and Robert M. White who was Tu Chen's manager. Stig Hagström became the chair of the Stanford Materials Science Department for many years, and Robert (Bob) White served as undersecretary at the Department of Commerce, then an IEEE Magnetic Society chair and Professor at Carnegie Mellon and at Stanford. I was also fortunate to work as an intern at HP Labs in Palo Alto, where I met Tom Cass and Bob Smith who had developed a very sophisticated and important method for preparing TEM specimens and created the dimpler tool for this purpose. I had the use of HP headquarters' computer center for image simulation work, and the use of their TEM sample making facility and their newly installed JEOL 200CX microscope.

Of all the co-workers, I am particularly indebted to Fernando Ponce who was my co-worker and a true friend in working on the HRTEM technique, and he introduced me to so many new ideas. Without him, the work on HRTEM could not have been accomplished. Other students such as Tom Anthony, Ko Nishimura, and Jan Werthen along with the research associate, Alan Farenbruch in Professor Bube's group also helped me greatly with their advice and support on the working of solar cells.

Professor Bube supported me from his DOE program on the investigation of CdTe material for many years. We gratefully acknowledge support from the Basic Energy Sciences Division of the Department of Energy, the National Science Foundation (equipment grant), and the Alfred P. Sloan Foundation (RS).

DEDICATION

I wish to dedicate this dissertation to my parents, Michio and Noriko Yamashita. They have provided me constant support for my endeavors to pursue science as a career path despite all the obstacles throughout my life.

TABLE OF CONTENTS

LIST OF TABLES

LIST OF FIGURES

CHAPTER 2: Page

Page

CHAPTER 3:

Page

Chapter 1: High Resolution TEM Imaging of CdTe and CdS

1.1 Background for High Resolution TEM (HRTEM) Technique

The transmission electron microscope (TEM) by virtue of using electrons has the intrinsic capability of imaging very small features. Electron microscopy is based on two fundamental discoveries, first by de Broglie postulating the wave-particle duality of matter in 1924 [1-1], and second by Busch in 1926 [1-2] that a solenoid acting on electrons acts similarly to a convex lens with light rays. Max Knoll and Ernst Ruska constructed the first prototype electron microscope in 1931 [1-3], which was the first demonstration of its principle. In the same year, Reinhold Rudenberg of Siemens-Schuckertwerke applied for a patent [1-4]. Ruska and his team proceeded to develop the first TEM and demonstrated its capability in 1933. Siemens delivered the first commercial TEM in 1939 at I.G. Farben-Werke in Munich. After World War II, Ruska continued to develop the tool at Siemens, and the first TEM with 100,000X magnification was developed there. All modern TEM's today owe their basic design to Ruska, who won the 1986 Nobel Prize in Physics for its development. The prize was shared with Gerd Binnig and Heinrich Rohrer for their invention of the scanning tunneling microscope [1-5].

By the early 1970s, the point resolution of the state-of-the-art TEM reached 0.3 nm, and it became possible to study various semiconductor materials and devices with near atomic resolution. The high-resolution TEM technique (HRTEM) became sufficiently well-developed both theoretically and experimentally, so that it can be applied to the study of various material issues related to the semiconductor materials and to the important devices that were made from them. In this thesis, the HRTEM technique is applied to the study of CdTe, an important photovoltaic material used as the absorber material in thin film solar cells. The HRTEM technique attempts to use the ultimate resolving power of the TEM by using the high coherence of the electrons to form near-atomic resolution images of the structure in projection. The relationship between the image and the actual atomic structure of the specimen is often not straight

forward, and the technique require some care in the setup of the TEM imaging condition and knowledge of some microscope parameters which are normally not necessary in conventional TEM work. Additionally, HRTEM often requires image simulations to interpret the image. These special aspects of the technique will be discussed further as they are applied to the study of the CdTe material.

The basic construction of a modern TEM is illustrated in figure 1-1. The latest models (in 2015) incorporate a highly coherent field emission filament for the source, which requires a very high vacuum for its operation. The objective lens design has advanced greatly over the years, and addition of an aberration-free lens system allows adjustment of the microscope spherical aberration coefficient (C_s) to obtain a very high resolution and the ability to adjust the contrast of the high-resolution images. The information limit of current aberration-corrected TEM is at 0.05 nm [1-6]. Chromatic aberration is also improved with energy filters to provide a more monochromatic electron source. Photographic plates have been replaced by an imaging system, which provides vastly superior image recording and convenience, with added advanced image processing to manipulate, analyze, and enhance the images. TEM is usually equipped with an electron energy loss spectrometer (EELS) and an energy dispersive X-ray spectrometer (EDS) to provide point-by-point chemical analysis at sub-nanometer resolution. Scanning TEM (STEM) features combined with EELS and EDS have made the TEM a versatile analytical instrument capable of providing a vast amount of information regarding the specimen being analyzed.

A resolution of an optical imaging system is defined by the diffraction limit, with Airy disk diameter given by Abbe's equation:

$$d = \frac{0.61\,\lambda}{n \sin \alpha} \approx \frac{0.61\,\lambda}{\alpha} \qquad \text{(Eqn. 1-1)}$$

d = resolution (minimum resolvable distance)

n = refractive index of the medium

α = aperture angle

λ = wavelength of the energy source

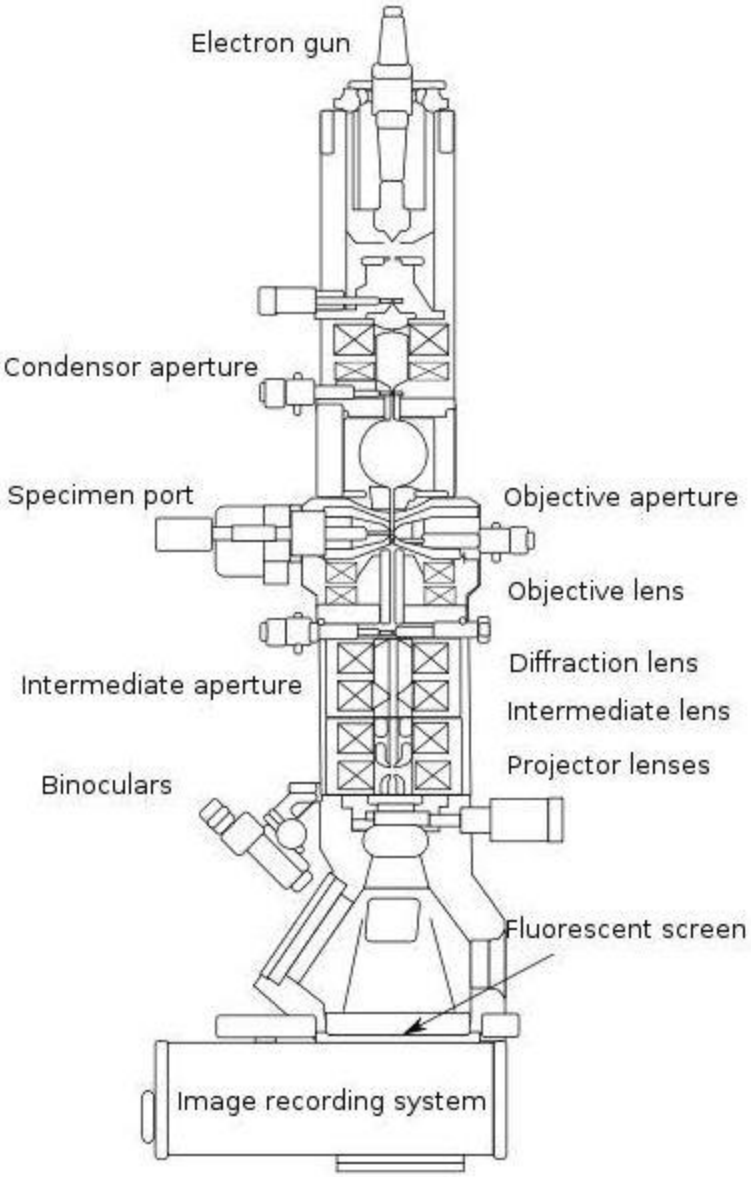

Figure 1-1: Schematic drawing of a typical TEM column, indicating the main components. (From Wikipedia commons, CC BY-SA 3.0)

http://commons.wikimedia.org/wiki/File%3AScheme_TEM_en.svg

For electrons, the angle α is small and n=1, so that the bottom term can be replaced by α . Through the de Broglie equation, the wavelength of an electron is given by

$$\lambda_e = \frac{h}{\sqrt{2\, m_o eV\left(1+\frac{eV}{2m_o C^2}\right)}} \qquad \text{(Eqn. 1-2)}$$

h is Planck's constant, m_o is the rest mass of an electron, and V is the energy of the accelerated electron, with relativistic correction incorporated into the equation.

h = 6.626 x10^{-34} m^2kg/s (J.s)
m_o = 9.109 x10^{-31} kg
e = 1.602 x 10^{-19} C
c = 2.998 x 10^8 m/s
V = accelerating voltage

Electron wavelengths for various accelerating voltages are tabulated below in Table 1-1.

Accelerating Voltage	v/c	λ (pm)
1 V	0.0019784	1226.4
100 V	0.006256	122.63
1 keV	0.062469	38.763
10 keV	0.019194	12.204
100 keV	0.54822	3.7013
200 keV	0.69531	2.5078
300 keV	0.77653	1.9687
1 MeV	0.81352	0.87189

Table 1-1: Electron wavelength for various accelerating voltage and ratio of electron velocity to speed of light (v/c) is also tabulated.

Even though the wavelengths of electrons at typical operating voltages for TEM are very small, the achievable resolution of the TEM is not as good as it could be due to spherical and chromatic aberrations that come from the electromagnetic lenses. Spherical aberration occurs because the outer ring of the electron lens always focuses the electron beam more strongly than the inner zone. Chromatic aberration mainly comes from the energy spread that is inherent in the electron source itself. Electrons that are slightly lower in energy are focused more strongly than the higher energy ones are, for example. Consequently, the resolution capability of a conventional TEM is much worse than it could be compared to the equivalent optical analog. For example, the point resolution is ~100 x λ_e for the TEM and in optical microscopy, the figure is ~0.5 x λ. Consequently, even by increasing the operating voltage of the microscope, the gain in resolution that could come from a smaller wavelength is not realized due to larger spherical aberration that comes with the stronger lenses in a higher voltage microscope. Smaller λ_e gives smaller beam divergence α, but the conventional resolutions in 1 MeV vs. 300 keV microscopes are similar. In addition, some of the more interesting materials to study are those with lower atomic numbers and they are much more susceptible to radiation damage. Such material requires lower accelerating voltages and much gain has come from improvement in aberration correction. Scherzer described the resolution limit of a TEM in the presence of a spherical aberration in his seminal work in 1936 [1-7].

In HRTEM, the image contrast comes from interference of the various scattered electron waves. The specific type of imaging to be described here is called *multi-beam imaging* because the TEM objective aperture is large enough to allow multiple diffraction beams to pass and the image is formed by recombining them. Unlike the situation where only the transmitted beam is used for bright field imaging, there is no absolute focus point where the image is the sharpest. Instead, the focus itself becomes a variable for obtaining images that may represent the projection of the specimen structure. This is because HRTEM depends on phase contrast, and the image in effect is a 2D interference pattern. Phase contrast images can be difficult to interpret because many factors contribute to the phase shifts between different scattered beams. For

example, they are dependent upon specimen thickness, orientation, scattering factor (e.g., atomic mass), and astigmatism. Additionally, the nature of the electron microscope itself contributes to the phase shift. When multiple beams are allowed through the objective aperture, the beams scattered to higher angles are brought to focus at a different point due to the inherent spherical aberration of the electromagnetic lens. Electrons that are at a higher angle of scattering are always brought to focus more strongly than those at the center, and slight phase shifts are introduced which are a function of the spherical aberration coefficient and diffraction angle. Microscope defocus also introduces additional phase shifts.

When the sample to be imaged is very thin, and amplitude variations do not contribute to the images, this situation is called the *weak phase object approximation*. HRTEM has the capability to image the projected interior of the specimen, and provide information on local structure of the sample, unlike the case of X-ray diffraction, which provides averaged diffraction information over a large area of the sample. Therefore, HRTEM can provide localized information about atomic arrangements in materials. In conventional TEM (CTEM), the contrast comes mostly from diffraction.

Mathematically, the imaging process in the TEM can be described by the use of the Fourier Transforms as it is used in electrical engineering for the analysis of waveforms and actions of filters in modifying the spectrum of waveforms as described in a standard textbook on Fourier transforms such as that by Bracewell [1-8]. For example, the electrical waveform represented by V (*t*) has a spectrum defined by S (*f*) which is a Fourier transform of V (*t*).

$$S(f) = \int_{-\infty}^{\infty} V(t) e^{-i2\pi/t}\, dt \qquad \text{(Eqn. 1-3)}$$

$$V(t) = \int_{-\infty}^{\infty} S(f) e^{i2\pi/t}\, df \qquad \text{(Eqn. 1-4)}$$

An electrical filter that acts on the waveform can be described by a frequency dependent complex quantity T(*f*), which is called the transfer factor of the filter. When

an input waveform V_1 (t) is applied to the filter and in order to calculate the output waveform $V_2(t)$, one analyzes $V_1(t)$ into its spectrum and multiplies each spectral component by the corresponding transfer factor to obtain the spectrum of $V_2(t)$. This is expressed as:

$$S_2(f) = T(f)\, S_1(f) \qquad \text{(Eqn. 1-5)}$$

$$V_2(t) = \int_{-\infty}^{\infty} T(f) S_1(f) e^{i2\pi/t}\, df \qquad \text{(Eqn. 1-6)}$$

Multiplication of transforms is equivalent to the convolution of the original functions; therefore ,V_2 (t*)* can be obtained directly from $V_1(t)$ by:

$$V_2(t) = I(t) \oplus V_1(t) \qquad \text{(Eqn. 1-7)}$$

Where $\oplus$ signifies convolution and I(*t)* is the Fourier transform of the filter transfer factor, T(*f*).

Since the electrons that travel through the column in the TEM can be described as a wave function, the mathematics that are used in the treatment of electrical signals and the actions of filters and antennas on the waveform can also be used to model the behavior of the electrons in the TEM. Desired output is the waveform (function) of the electron that has passed through the specimen and focused by the lenses on the screen. Many reference materials describe the mathematics of the imaging process for the HRTEM [1-9, 1-10]. The initial electron wave function that enters the sample interacts with the potential of the sample and is scattered. Only the elastically and forward scattered electrons are collected. The exit wave function of the electrons from the sample is not quite simple, and strongly depends upon the thickness of the sample and its scattering ability. Interaction of the electrons and the atomic potential give rise to the exit wave function under the sample. At the back focal plane of the objective lens where the diffraction pattern forms, the wave function can be expressed as a Fourier

transform of the exit wave function. Mathematically, the diffraction pattern is the same as the spectrum of the waveform in equation 1-3. The microscope parameters such as spherical aberration and focus conditions can be incorporated into a transfer function, which is multiplied with the Fourier, transform of the exit wave function. This is equivalent to the transfer factor T(f) in equation 1-5. Therefore, the objective lens is treated similarly to a "filter" in an electrical circuit. The resulting product then can be inverse Fourier transformed to obtain the wave function at the image plane. A more detailed description of the mathematics behind the image formation in HRTEM is given elsewhere [1-11].

When the exit wave passes through the imaging system of the microscope, it undergoes additional phase changes. The recorded image is not a direct representation of the crystallographic structure of the specimen. The exit wave and the image wave have a highly non-linear relationship and the image wave is affected by the aberrations of the objective lens and the defocus. The phase contrast transfer function or CTF describes the phase change that the microscope imposes on the exit wave function. The CTF is an important parameter in HRTEM technique that must be measured and manipulated in order to obtain useful images. Therefore, some attention is now given to its characteristics and measurement of parameters that contribute to the function. The CTF following the convention used by Williams and Carter [1-12] and described by Spence [1-13], for spatial frequency k, is given by:

$$CTF(k) = A(k)\, E(k)\, 2sin(\chi(k)) \qquad \text{(Eqn. 1-8)}$$

Where $A(k)$ is the aperture function, $E(k)$ is the envelope function that attenuates the higher spatial frequencies, and $\chi(k)$ is a function of the aberration of the electron optical system. The sinusoidal term, $sin(\chi(k))$ will determine the sign that the components of spatial frequency k will have, which in turn determines the contrast in the image. If only the spherical aberration is considered to a third order and defocus Δf ,

χ is rotationally symmetric about the optic axis, and thus, depends on modulus $k = |k|$, given by:

$$\chi(k) = \frac{\pi}{2} C_s \lambda^3 k^4 + \pi \Delta f \lambda K2 + \ldots\ldots \quad \text{(Eqn. 1-9)}$$

C_s is the spherical aberration coefficient,

λ is the wavelength of the electron,

There are other terms left out of the $\chi(k)$, which is a series. They are usually not considered in the discussion of the CTF function.

The defocus in a TEM can be adjusted with high precision, and unlike its optical analog, the defocus in HRTEM can actually simplify the interpretability of the images. The envelope function $E(k)$ can incorporate many factors and it is this function that effectively limits the resolution of the images by damping higher order spatial frequencies. $E(k)$ can be expressed as a product of various factors:

$$E(k) = S(k)\ E_{co}(k)\ E_d(k)\ E_{va}(k)\ E_D(k) \quad \text{(Eqn. 1-10)}$$

$S(k)$ - angular spread of the electron source

$E_{co}(k)$ - chromatic aberration

$E_d(k)$ - specimen drift

$E_{va}(k)$ -specimen vibration

$E_D(k)$ –detector variation

$S(k)$ and $E_{co}(k)$ usually dominate and these two terms are given by:

$$S(k) = exp\left[-\left(\frac{\pi\alpha}{\lambda}\right)^2 (C_s\lambda^3 k^3 + \Delta f \lambda k)^2\right] \quad \text{(Eqn. 1-11)}$$

$$E_c(k) = exp\left[-\frac{1}{2}(\pi\lambda\delta)^2 k^4\right] \quad \text{(Eqn. 1-12)}$$

$$\delta = C_c \sqrt{4(\frac{\Delta I_{Obj}}{I_{Obj}})^2 + (\frac{\Delta E}{E_{acc}})^2 + (\frac{\Delta V_{acc}}{V_{acc}})^2} \qquad \text{(Eqn. 1-13)}$$

α is the beam divergence for the electron beam illuminating the sample. C_c is the chromatic aberration constant. $\Delta I_{obj}/I_{obj}$ and $\Delta V_{acc}/V_{acc}$ are the instabilities in the objective lens current and the accelerating voltage. $\Delta E/E_{acc}$ represents the energy spread of the electrons from the filament source. $E_S(k)$ is usually called the spatial envelope function and $E_{CO}(k)$ is called the *temporal* envelope function.

In 1949, Scherzer [1-14] found that optimum defocus for obtaining a wide band where low spatial frequencies are transferred to the image with similar phase is given by:

$$\Delta f_{Scherzer} = -\sqrt{\frac{4}{3} C_s \lambda} \qquad \text{(Eqn. 1-14)}$$

This defocus condition is called the *Scherzer defocus,* and it defines the point resolution of the microscope where the CTF crosses the abscissa for the first time. It is obtained by taking a derivative of eqn. 1-9 and solving for the flat part of the CTF. The term $\sqrt{\frac{4}{3}}$ in the literature is often rounded to 1.2 and can often lead to slight differences in quoted values for the Scherzer defocus for the same microscope. The optimal resolution at Scherzer defocus is then given by:

$$d_{res(Scherzer)} = 0.66\, \lambda^{\frac{3}{4}} C_s^{\frac{1}{4}} \qquad \text{(Eqn. 1-15)}$$

An example of the CTF (without the envelope function) is shown in figure 1-2 for Philips EM400 TEM operating at 120 kV with Cs = 1.1 mm at Scherzer defocus of

-70.1 nm. As can be seen, CTF has a broad pass band at Scherzer defocus, and $d_{res(Scherzer)}$ for this microscope is 0.298 nm (3.356 nm^{-1}).

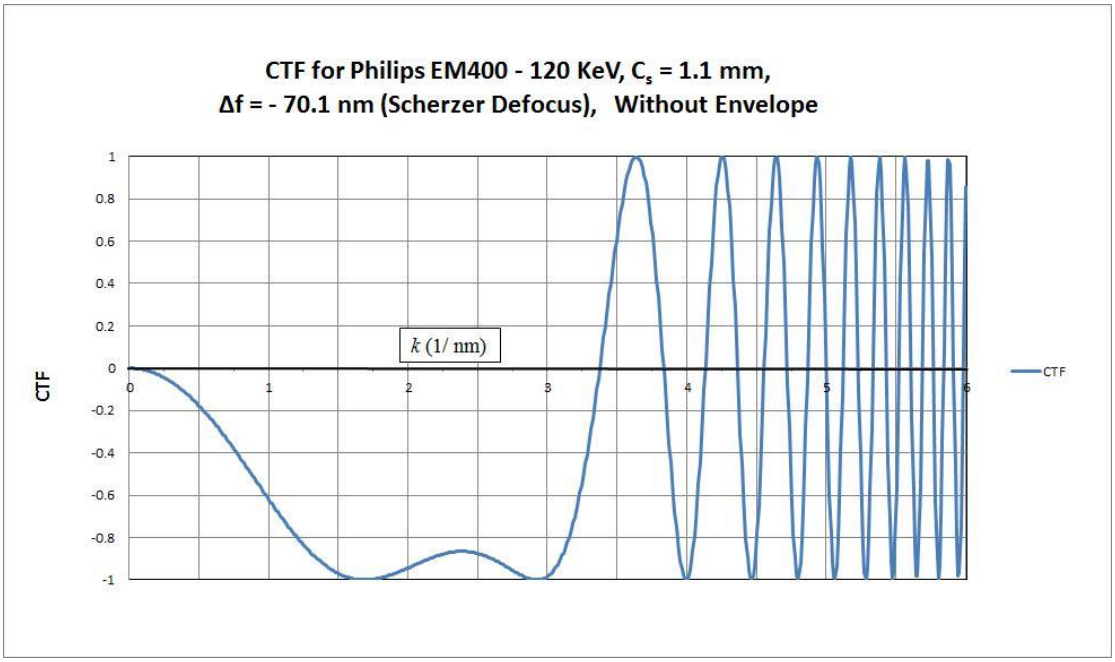

Figure 1-2: CTF for Philip EM400 microscope operating at 120 kV with C_s = 1.1 mm at Scherzer defocus, Δf = - 70.1 nm. The x-axis is *k*, the reciprocal space in units of nm^{-1}.

The effect of equations 1-11 and 1-12 is to attenuate the CTF at higher *k* values, and it means that the higher order beams will not contribute to the image contrast. The CTF function with the spatial and temporal envelopes for the Scherzer defocus condition is plotted in figure 1-3. δ value of 4.0 nm was used from eqn. 1.9 and the value used for $(\frac{\Delta I_{obj}}{I_{obj}})^2$ and $(\frac{\Delta E}{E_{acc}})^2$ terms were ~1.5 x 10^{-6} (1.5 ppm) and the last term was ignored. The manufacturer (Philips) provided these values. It can be seen that beam divergence plays a major role in attenuating the CTF. The 4.0 nm value used for δ is probably larger than it is in actual practice, since instabilities over the very short exposure times of the negatives (or even shorter for electronic imaging systems) are

considerably better than the numbers typically quoted by the instrument manufacturers, which are often measured over much longer time intervals. From figure 1-3, it can be seen that spacing information beyond the flat part of CTF will be transferred with relatively large fluctuations in phase, which depends sensitively on defocus. In addition, the beam divergence of 0.3 mrads is much smaller than in practice for a typical LaB_6 filament used at the time of this work. In current microscopes with very high brightness field emission source and very sensitive image sensors, the 0.3 mrads beam divergence is quite realistic and the envelope can be extended much farther in k space than in the past. It should be also noted that for beams within the flat part of the CTF in the Scherzer defocus condition, the negative value for the CTF implies that the image (of atoms) would appear black on bright background on the screen.

For the aberration-corrected TEM, optimal setting for the HRTEM imaging is different than in conventional TEM with fixed C_s. The C_s value can be adjusted in an aberration-corrected TEM, including zero and negative values, and the optimal defocus setting and the resolution will change depending upon the C_s value that is selected. The choice depends partly on the material that is to be imaged. However, the CTF equation still applies. The selection C_s value to use in an aberration-corrected TEM will be discussed in more detail in Chapter 2. The following discussion of CTF applies to conventional TEM with relatively large, fixed C_s values.

Direct lattice imaging of elemental semiconductor materials, such as silicon and germanium, by HRTEM has been used to develop the technique from the earliest impetus to obtain a higher resolution from the TEM. The reasons are several. Semiconductor materials are commercially important, and there are critical issues with the material and processes used on them that required the highest resolution possible. At the same time, semiconductor materials had idal lattice spacing to test and challenge the ultimate resolution capability of the microscopes in that period, which was in the range of 0.2 to 0.3 nm in the late 1970s. A third factor was the availability of large single-crystal wafers from which specimens could be readily produced with the right low index orientation to image the lattice. A high level of perfection in the crystalline structure also provided large areas where the specimen can be imaged. In addition, the

specimens were stable under the high intensity electron beam, and not easily degraded during imaging [1-15, 1-16, and 1-17]. Extension to II-VI and III-V compound semiconductors was an interesting expansion of these works because of the similarity in physical properties, structure and lattice spacing of many of these materials to those of elemental semiconductors. The presence of two different atoms adds interesting complexities to the images. For example, GaAs had been imaged by Hashimoto et al. in 1978 [1-18] and Olsen et al. in 1980 [1-19].

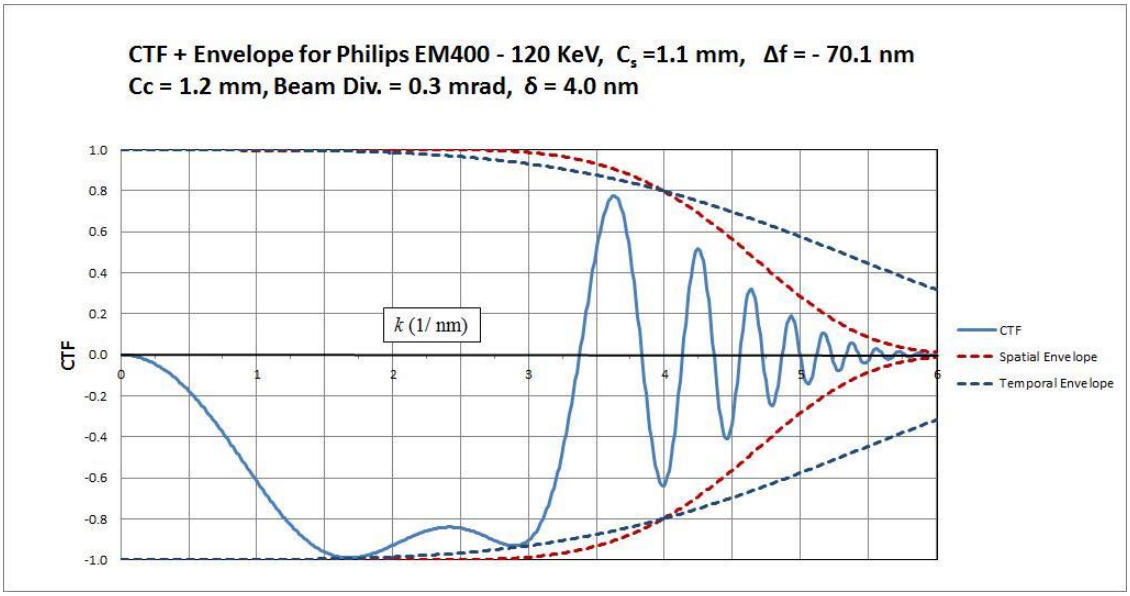

Figure 1-3: CTF with spatial and temporal envelopes included for Scherzer defocus condition. Beam divergence is 0.3 mrads, and δ from equation 1-13 at 4.0 nm.

A CTF at Δf = -130.0 nm defocus, and beam divergence of 1.0 mrad, and other conditions kept the same as in figure 1-3, is plotted in figure 1-4 to illustrate the effects of adjusting the defocus on the CTF. One of the easily noticed effects of defocus change on the HRTEM image is the cyclical change in contrast of the image spots from dark spots to bright spots for the position of the atoms, and this is due to the phase shift of the primary, low index diffracted beams, from negative to positive value by the CTF.

The CTF can transfer different diffracted beams with varying phases to the image. This action complicates the image contrast so that it can become difficult to interpret the images. Higher order diffracted beams can be selectively passed through at condition other than at Scherzer defocus to contribute to the image, which can further complicate the image contrast. Therefore, image simulation is often necessary to determine whether the image will show a useful contrast that can be related to the actual structure of the crystal being imaged. Note that for simple structures with a small number of diffracted beams, the CTF can be tuned to optimize their contribution to the image, by appropriate adjustment of defocus, beam divergence, and the selection of the objective aperture size by the TEM operator.

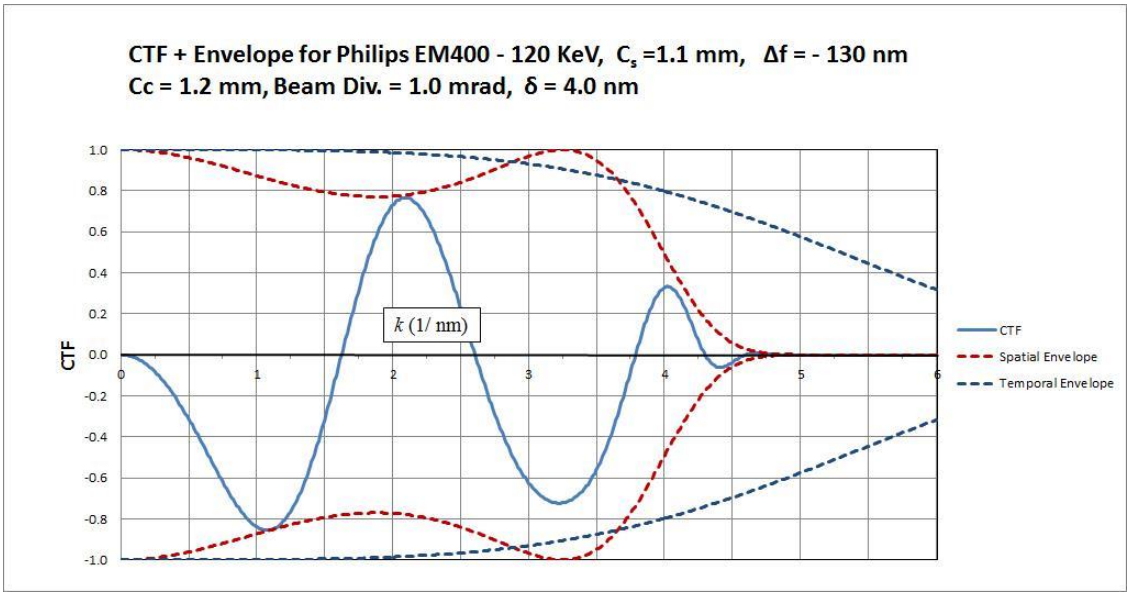

Figure 1-4: CTF for Δf = -130 nm with all other factors kept the same as in figure 1-3.

The [011] orientation is often the most interesting one to image using HRTEM for both single and compound semiconductors since it has relatively large atomic spacing and each atomic species all lie parallel to each other with a large separation between them. Silicon for example, has a separation of 0.136 nm, GaAs has 0.141nm, and CdTe has 0.162 nm separation between the closest atoms in this projection. In the

case of II-VI and III-V compound semiconductors, the two different atoms in the lattice lie on their own columns in the [011] projection. In addition, two sets of {111} planes are imaged in an end-on projection and this allows for direct imaging of typical lattice defects in these materials. These semiconductors that are used in a highly ordered crystalline form normally have very few lattice defects, but their presence affects their electrical and photonic properties; therefore, they are interesting in their own right as something to be studied.

1.2 Image Simulations

Computer simulation of HRTEM images is an important part of the technique because of the aforementioned difficulties in directly interpreting the experimental images and correlating them to the actual projected structure of the crystal. The phases of various diffracted beams are modified through the imaging process by the CTF, so that image characteristics change according to the settings of the microscope, such as the defocus condition. In addition, the dynamical interaction of the electrons with the atomic potential of the specimen must be considered, and this interaction varies as a function of specimen thickness. There are two methods for calculating this dynamical interaction, first is the Bloch-wave and the second is the multi-slice formulation. Detailed mathematical descriptions of image simulation methods are beyond the scope of this thesis, and they are easily available in many textbooks and papers on this subject. Hirsh, Howie, Nicholson, Pashley and Whelan [1-9] describe the many-beam dynamical theory of electron diffraction in their electron microscopy textbook. Another book, *Experimental High-Resolution Electron Microscopy* by Spence is also a good source of information on the practical application of HRTEM and mathematics used in the image simulations (Chapter 5, page 103) [1-10]. In this thesis, both Bloch-wave and multi-slice image simulations are used to compare the experimental images to the simulated images. The Bloch-wave image simulation program was written by P. Pirouz [1-20]. The team at Arizona State University (ASU) wrote the multi-slice simulation program based on the work by Goodman and Moodie [1-21]. Both of these programs

were written in FORTRAN code and ran on a mainframe computer. More modern image simulation also based on multi-slice formulation written by Kilaas[1-22] also was used. This program ran on a Mac computer.

1.3 Optical Diffractogram Analysis

The use of optical diffractograms is quite important for the measurement of various microscope parameters relevant to HRTEM. Therefore, this topic is covered separately here at the outset. In a modern TEM, the optical diffractogram easily is obtained digitally from the image and it has become an indispensable tool for microscope operation and analysis of the image. By using the amorphous material that is often present on TEM specimens, optical diffractogram rings provide the means to independently measure the C_s value and defocus conditions of the microscope. In fact, this same method is used to calibrate the lenses used in the aberration-corrected microscope. A lookup table is created based on a series of optical diffractograms taken at various lens current settings, and the lens current is adjusted iteratively to obtain the desired C_s value.

The C_s and Δf defocus for a particular imaging condition are obtained by analyzing the high-resolution image from an amorphous material, with internal calibration to obtain the microscope camera constant. Typically, a through focus series is taken of an amorphous carbon film with accurately adjusted stigmation. The optical diffractogram must be obtained from the image and the resulting ring patterns are measured to obtain a fit to eqn. 1-9 as outlined below. The optical diffractogram is a representation of the contrast transfer function, and contains within it the information from eqn. 1-9, and some indication of the envelope function as well. The symmetry of the optical diffractogram also shows the condition of the astigmatism correction and other information such as specimen drift. The diffractogram method to obtain C_s and Δf was originally published by Krivanek [1-23].

From eqn. 1-9, following conditions can be obtained:

$sin\ (\ \chi(k)\ ) = 1$, when $\chi(k) = \pm \frac{n\pi}{2}$ n = odd (bright ring)

$sin\ (\ \chi(k)\ ) = 0$, when $\chi(k) = \pm \frac{n\pi}{2}$ n = even (dark ring)

This situation arises in the optical diffractograms taken from a *weak phase object* such as a thin amorphous carbon film because only those spatial frequencies that are phase shifted close to $n\pi$ (n is odd) will be imaged with full contrast, and those with n even will not be imaged at all [1-24]. The amorphous film is chosen since such material contains the broadest range of spatial frequencies. The micrograph of the amorphous film should be taken without the objective aperture in an exact axial illumination, and care taken to reduce the beam divergence as much as possible. The optical diffractogram of the amorphous film then is a good representation of the contrast transfer function used to obtain the image. The bright rings represent the location of the spatial frequencies where the CTF allowed the information to be passed through, and the dark rings represent the spatial frequencies that was not transferred to the image.

By rearranging equation 1-9,

$\frac{n}{k^2} = (C_s \lambda^3)\ k^2 + (2\ \Delta f\ \lambda)$ into the form $y = m\ x + b$ (Eqn. 1-16)

By assigning sequential n = odd values to the bright rings and n = even values to the dark rings, and obtaining the value of k from the internal calibration standard, one can plot $\frac{n}{k^2}$ against k^2, and the slope of the curve will be $C_s\ \lambda^3$ and the y-axis intercept will be $2\Delta f\lambda$. The optical bench used for generating the diffractorgram is shown in figure 1-5. This system used a He-Ne laser with a beam expander to select the area on the TEM negative to obtain the diffractogram. A projection screen is used to image the optical diffractogram, and once the desired pattern is obtained, a camera was placed at the exact same location as the screen to obtain high quality images, which can

be used to make the measurement of the ring positions. A Polaroid film pack was often used to obtain the diffractograms that can be quickly analyzed, but this often did not produce images with high enough contrast and precision. A 35mm single lens reflex (SLR) camera without the lens was then used to record the images directly onto a high contrast black and white negative. Then the film had to be processed and prints made from the negatives in order to analyze the optical diffractogram images.The entire process was quite laborious and time-consuming, especially compared to the current digital method.

Experimental data taken on a Philips EM400 at 120 keV with manufacturer specified C_s of 1.1mm is plotted in figure 1-6. Three data points are shown. An amorphous carbon film was used, and HRTEM images were taken at several defocus conditions without the objective aperture. Some care had to be taken to reduce beam divergence as much as possible by expanding the imaging electron beam. Relatively long exposure times had to be used, but still short enough to avoid specimen drift. Another set of HRTEM images was taken of silicon [011] so that lattice images were obtained at the same objective lens current setting and the same magnification. This image was used to calibrate the camera length of the diffractometer.

Table 1-2 tabulates the calculated C_s and Δf obtained from the curve fitting of the data to equation 1-16. Correlation factor (R^2) for the linear fit of the data points is also shown in the table. It can be seen that one of the correlation factors is not very good (e.g. data 2 with R^2 = 72.5%). Deviation from linearity comes mainly from the low *n* values, and this is because the exact location of the ring position for low values of *n* is somewhat more difficult to define from the micrographs. However, the analysis provides C_s values that are relatively close to the manufacturer-specified value of 1.1mm. Also included in Table 1-2 and in figure 1-6 is the data from Krivanek's paper [1-23] as a comparison. The data points were measured from the optical diffractogram shown in his paper. Krivanek's microscope had C_s of 1.8 mm (JEM 100B TEM), and the value measured from the optical diffractogram was very close to this value at 1.79 mm. An additional comment about the diffractogram analysis is that relatively large

negative defocus settings must be used in order to generate enough data points in the curve fitting. Only in a large defocus setting, can one obtain a sufficient numbers of rings in the optical diffractograms. For the graph of n/k^2 vs. k^2 in figure 1-6, the negative values of n/k^2 represent regions with underfocus (negative Δf values). Consequently, the value of n assigned to the rings must be negative in the case of underfocus, and positive for overfocus. The contour lines drawn on the graph represent various values of n as indicated in the figure.

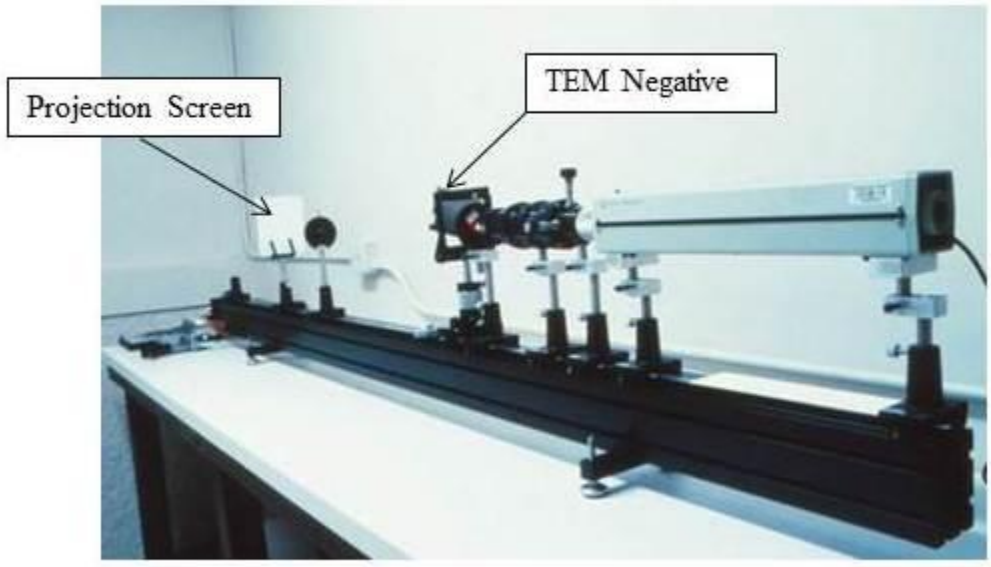

Figure 1-5: The optical bench set-up at Stanford for obtaining diffractograms from the TEM negatives.

The diffractogram analysis as outlined above using an optical bench is difficult to perform in practice. The negatives from the amorphous carbon film must be exposed with just the right contrast. A proper alignment of the optical bench to avoid spurious reflections from a multiple set of lenses is difficult to achieve. In addition, the beam divergence must be set to low as possible in the TEM, in order to obtain sufficient

number of rings in the diffractogram. This reduces the illumination brightness so that long exposure times are required and specimen drift can occur during the exposure. However, the key advantage of taking the optical diffractogram is that astigmatism and specimen drift can be detected in the image. An example of a diffractogram from a well-exposed negative is shown in figure 1-7. The diffractogram was taken using a SLR camera and rinted from a high contrast negative. There is a slight astigmatism evident in the rings, based on a slight asymmetry in the shape of the rings. The entire process of obtaining optical diffractograms from a negative was time-consuming and unfortunately after-the-fact for issues such as astigmatism corrections. In a modern TEM in the last twenty years, the use of negatives have largely disappeared with the use of high resolution video camera and an image acquisition system mounted on the TEM. Fast Fourier Transforms (FFT) can be performed digitally on the image as it is being acquired so that very accurate astigmatism corrections are applied in real time. In fact, the digital FFT feature has become an indispensable tool for correctly stigmating the microscope, and to calibrate the microscope C_s settings in the case of an aberration-corrected TEM.

It should be noted that in order to obtain a higher contrast in the optical diffractograms, it is better to use a material with higher atomic number, such as amorphous Ge, for example, compared to using an amorphous carbon film. The higher atomic number elements and materials have larger electron scattering, and this leads to higher contrast in the optical diffractograms.

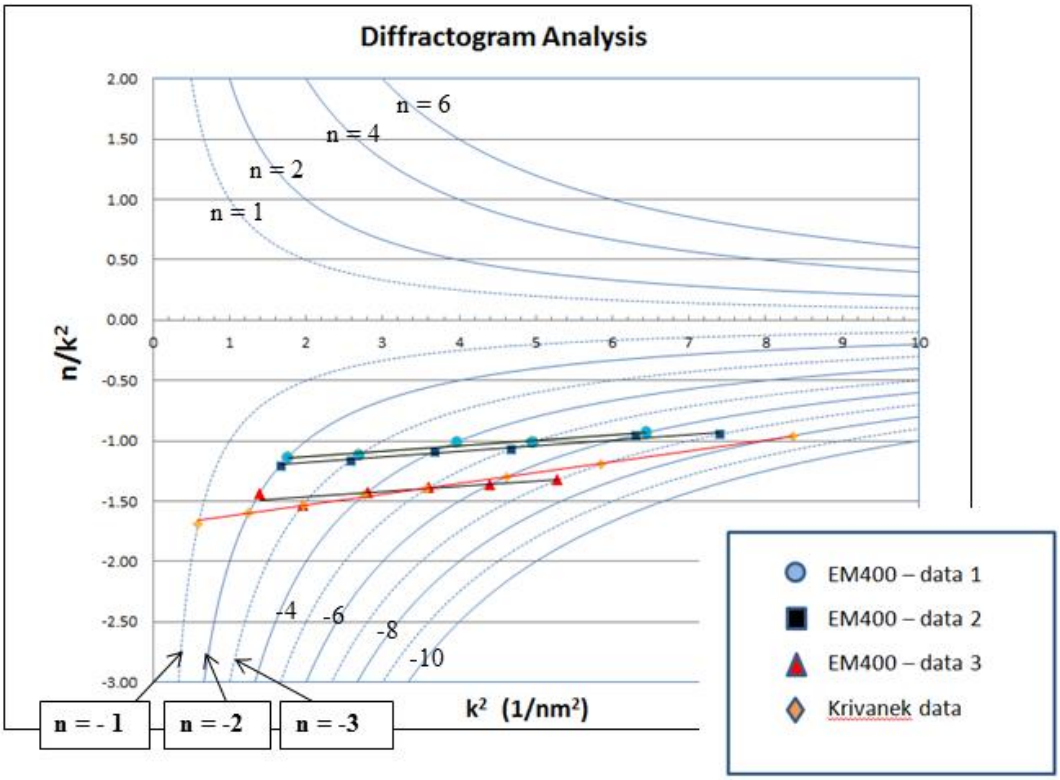

Figure 1-6: Plot of k^2 vs. n/k^2 to determine C_s and Δf from the optical diffractograms. Several data points are shown, including the data derived from Krivanek [1-23].

	C_s (mm)	Δf (nm)	R^2
Data 1	1.18	-182	0.947
Data 2	1.10	-231	0.725
Data 3	1.27	-191	0.971
Krivanek's Data	1.79	-232	0.997

Table 1-2: Tabulation of C_s and Δf calculated from the curve fit of optical diffractogram data shown in figure 1-6. Krivanek data was taken from ref. [1-23], measured from the optical diffractogram shown in the reference. Krivanek data was taken with a JEM 100B microscope at 100 kV.

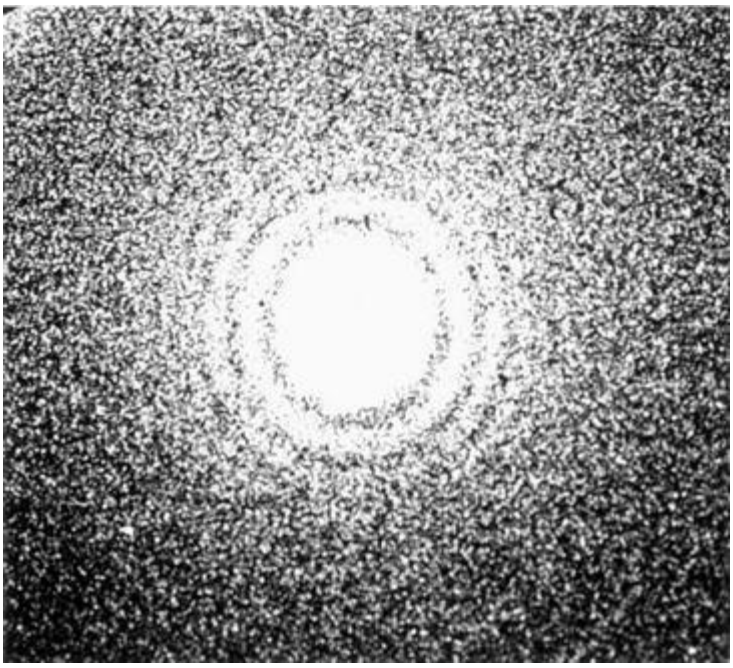

Figure 1-7: Optical diffractogram of an amorphous carbon film, taken on an optical bench shown in figure 1-5. There is a slight astigmatism evident in the image, as indicated by a slight asymmetry in the ring shape from the exact circularity.

1.4 Key Summaries Regarding HRTEM

It is important to emphasize that a HRTEM lattice image obtained by passing many diffracted beams through the objective aperture is in essence, an interference image. It would not be accurate to call the bright or dark spots that form in the image as atoms or sets of atoms because only in some restricted situations does the image have a direct one to one correspondence with the position of the atoms in the specimen. However, typically the highest contrast images that are obtained in a typical HRTEM have symmetry features that mimic the projection of the lattice, even for the defects that are in the specimen. Therefore, the interference image still provide useful information about the sample. Multiple diffracted beams that are allowed through the objective aperture in the back focal plane of the microscope recombine and interfere

with each other in a complex manner depending upon their angle from the transmitted beam. Thus, the image obtained is a result of complex interactions between the beams with the specimen itself and the aberrations of the microscope. For those beams that are allowed through the objective aperture, the spherical aberration coefficient and the microscope defocus influence each beam differently depending upon their reciprocal space vector. The CTF can provide some indication of which beams will contribute and by how much to the image. Amplitudes of the beams are also important to the contrast, because each beam is affected differently as it travels through the thickness of the specimen. However, the image simulations must be performed to be certain that one will obtain image characteristics that represent the actual atomic structure in the specimen.

A set of conditions useful for obtaining interpretable HRTEM images is listed below. Although it is not necessary to follow each item, they are useful when more detailed analysis of the HRTEM image is necessary, for example, when image simulation becomes necessary. The input to the simulation requires precise knowledge of the microscope operating parameters and the specimen condition.

1. Specimens must be thin (they are weak phase objects) so that images are obtained in the specimen before the occurrence of the first extinction thickness fringe.

2. Use TEM with a small C_s value and small λ (e.g., use higher voltages).

3. TEM should be well aligned and both electronically and mechanically stable.

4. Specimens must be precisely oriented in a low index zone axis for easier interpretation.

5. Astigmatic corrections must be done precisely, preferably using optical diffractograms.

6. Record through-focus series images with well-calibrated defocus steps.

7. Take optical diffractograms of amorphous material to verify C_s and defocus settings.

8. Minimize the beam divergence to maximize the contribution to the image from higher order reflections, and measure the value.

9. Compare experimental images with computer simulations of the images.

1.5 Notation Convention Used for Planes and Directions

The standard convention for naming planes and directions is used in this thesis through their Miller indices.This is not often followed rigorously by many references cited in this thesis and it may cause some confusion when their notation is used as is from the references. Therefore, where it is appropriate or possible to do so, the notations will be converted to the standard format. The standard convention for planes and directions are as follows:

(hkl) refers to a specific crystallographic plane.
[hkl] refers to a specific crystallographic direction.
{hkl} refers to generic crystallographic plane that have many equivalents.
<hkl> refers to generic crystallographic direction that have many equivalents.

By definition, a zone axis will always be a direction, either using either brackets [ ] when a specific direction must be given in order to discuss specific reflection in the zone axis, or other directions and planes that are referenced to the specific zone axis. The indices within a < > sign is used to refer to a generic direction. The wafer orientation notation generally uses < > to refer to a generic direction, not to the surface. Therefore, the same convention is used in this thesis.

1.6 Material Properties

1.6.1 CdTe Material Properties

CdTe is a crystalline II-VI semiconductor often used as an infrared optical window and a main absorber layer in a solar cell. It has a direct bandgap of 1.44 eV, and its photonic response is ideally suited to the solar spectrum for use in a solar cell applications. Typical properties of CdTe are listed in table 1-3 based on a data by Zanio [1-25]. Cadmium and cadmium compounds are highly toxic and potentially carcinogenic. Exposure affects the respiratory tract, kidneys, and liver. Ingestion may cause nausea, salivation, vomiting, and diarrhea. Ingestion or inhalation of cadmium/cadmium compounds may be fatal. Tellurium is converted in the body to dimethyl telluride, which imparts a garlic-like odor to the breath and sweat. Heavy exposure may result in headache, drowsiness, metallic taste, loss of appetite, nausea, tremors, convulsions, and respiratory arrest. CdTe is toxic if ingested and improperly handled. In its CdTe compound form, it is less toxic than elemental cadmium; however, the toxicity is not related directly to the presence of cadmium. The compound itself is toxic due to the potential of causing cell membrane, mitochondria, and cell nucleus damage. Although the compound has now been used extensively in solar cell panels, it is with the understanding that the CdTe is protected within the cell structure and that panels can be recycled safely once their useful life is over. A recent report on CdTe by Raugei and Fthenakis [1-26] finds that large-scale use of CdTe PV modules does not present any risks to health and the environment, and recycling the solar cell modules at the end of their useful life completely resolves any environmental concerns. The same report adds that modules do not produce any pollutants during use, and offer great environmental benefits by displacing the use of hydrocarbon fuels. There are very strict regulations regarding cadmium in products in most places in the world, and there are government and industrial limits on the amount of cadmium that can be in their products. However, some exceptions appear to be made for the use of CdTe in solar panels that are installed in large commercial PV farms. First Solar Inc. is now one of the largest commercial producers of solar cell panels based on CdTe thin films, and they claim to have installed the equivalent of 10 GW of panels worldwide. They have a

recycling program to extract CdTe from the used panels [1-27]. Another reason for recycling is to recover the precious tellurium which there are only limited supply.

CdTe can be alloyed with mercury to make very effective infrared detector materials (HgCdTe), and alloyed with Zn to make solid state X-ray and gamma ray detectors. HgCdTe is widely used in the military and in scientific instrumentations where high performance infrared detection is needed [1-28]. Single-crystal CdTe can be grown by high-pressure Bridgman method (HPVB) and by high-pressure vertical zone melting method (HPVZM). HPVB is the most typical method employed in growing single-crystal CdTe. Although doping can create p and n-type CdTe, stoichiometry adjustments can also produce the same effect. Excess Cd creates n-type while excess Te creates p-type material. The p-type CdTe can be obtained by phosphorus doping. CdTe has a high absorption coefficient of $2x10^5$ to $2x10^4$/cm from 400 to 800 nm wavelength, and short wavelength photons up to the bandgap are absorbed near the surface, making it ideally suited for thin film solar application. Up to 99% of the photons E > Eg are absorbed within 2 μm of the film thickness. In comparison, only 30% of the photons are absorbed by silicon even at a thickness of 10 μm from the surface.

A simple solar cell structure with a transparent oxide to form a heterojunction cell with p-type CdTe was investigated extensively. Materials such as ITO (In_2O_3: Sn), ZnO, and SnO_2 have been used as transparent windows and to form a junction. Cells made by evaporation of n-type CdS film on single-crystal p-type CdTe were first produced by Muller et al. in the mid-1960s [1-29]. The Stanford group under Bube et al. produced high efficiency structure based on CdS/CdTe heterojunction and using an ITO transparent electrode to produce a cell with an efficiency of 7.9% [1-30]. A thin film CdS/CdTe heterojunction with high efficiency was pioneered by Chu et al. using closed space sublimation method (CSS) to grow CdTe thin film, and they produced a CdS/CdTe heterojunction cell with 15% efficiency [1-31]. The method that they pioneered is now used by First Solar Inc. to make their solar cell products.

Molecular Formula	CdTe
Crystal Structure	zincblende (cubic) F $\bar{4}$ 3m
Lattice Spacing	0.648 nm at 300^{o}K
Density	5.86 g/cm^{3}
Bandgap	1.44 eV @300^{o}K, direct bandgap
Refractive Index	2.649 @ $n_{10.0}$
	2.610 @ $n_{20.0}$
Absorbance μ (λ), cm-1 (10 μm)	0.167
Electron Affinity	4.28 eV
Electron Effective Mass	0.1 m_e
Hole Effective Mass	0.4 m_e
Low-Frequency Dielectric Constant	10.2
Electron Mobility (Intrinsic)	1100 cm^{2}/V.s
Hole Mobility (Intrinsic)	80 cm^{2}/V.s
Melting point	1041^{o} C
Boiling Point (Evaporation Start)	1050^{o} C
Thermal Expansion Coefficient	5.9x10^{-6} /K at 293^{o} K
Thermal Conductivity	6.2 W/m·K at 293^{o} K
Specific Heat Capacity	210 J/kg·K at 293^{o} K
Young's Modulus	52 GPa
Poisson Ratio	0.41

Table 1-3: List of properties for CdTe. (From Zanio [1-25] and partly from Wikipedia)

CdTe has a zincblende crystal structure (zinc sulfide), also called sphalerite with the space group of F$\bar{4}$3m. It closely resembles the cubic structure of diamond, silicon, and germanium. Many semiconductor materials are tetrahedrally coordinated, and compounds with the sphalerite structure include many III-V and II-VI compound semiconductors such as GaAs, InP, AlAs, ZnSe, and InSb. A ball and stick model of ZnS with the sphalerite structure is shown in figure 1-8.

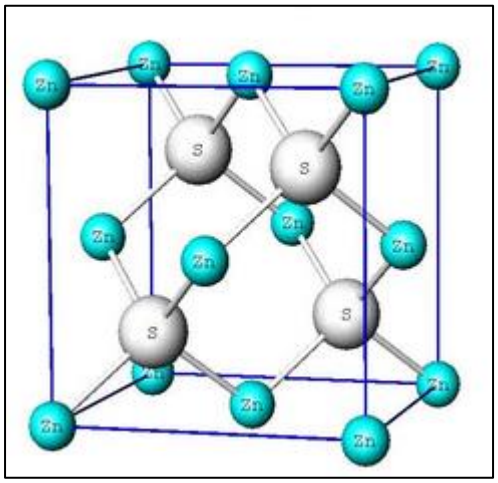

Figure 1-8: Structure model of ZnS cubic sphalerite structure.

The unit cell contains four molecules (Zn-S pairs) and they occupy the following positions in the cell.

Zn: (0, 0, 0), (0, ½, ½), (½, 0. ½), (½, ½. 0)

S: (¾, ¼, ¼), (¼, ¾, ¼), (¼, ¼, ¾), (¾, ¾, ¾)

The structure is an interlocking FCC crystal lattice. The Zn and S positions can be interchanged without affecting the symmetry.

For the CdTe, the projections in <001> and <011> orientations are shown in figure 1-9 and figure 1-10.

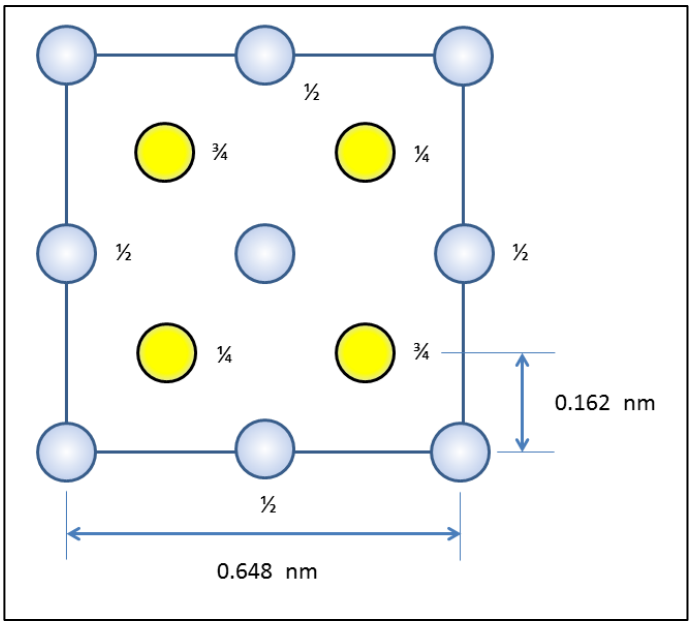

Figure 1-9: CdTe in the <001> projection. The fractions indicate the position of atoms in the z-direction (out of the paper).

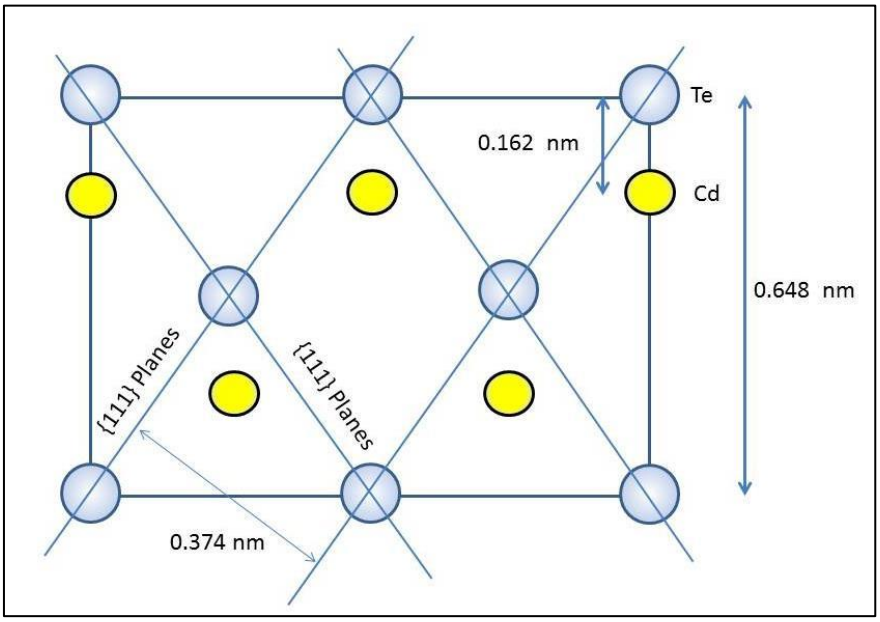

Figure 1-10: CdTe in the <011> projection, which is the most suitable orientation for HRTEM imaging. All of the atoms of each species lie on top of each other, and two sets of {111} planes can be imaged in an end-on projection.

For HRTEM imaging, the <011> projection is the most interesting and useful, because each atomic specie lies on top of each other in separate columns, and the projection contains two {111} planes in an end-on projection. The {111} planes are the close-packed planes in diamond and sphalerite structures, and these planes are the ones containing planar defects such as stacking faults. Terminating the stacking faults are a pair of partial dislocations, which could be imaged end-on in the <110> orientation. Therefore, the <110> orientation is the most popular to use for semiconductor materials such as silicon, germanium, III-V and II-VI compounds with a cubic structure. A comprehensive tabulation of basic properties of CdTe have been compiled by Zanio [1-25] and by Triboulet and Siffert [1-32].

1.6.2 CdS Material Properties

CdS occurs naturally and exists in two forms, as rare minerals greenockite and hawleyite. It is more prevalent as an impurity in sphalerite and wurtzite, and they are the main sources of cadmium. The crystal structure can be either hexagonal with the wurtzite structure or cubic with the sphalerite structure. The hexagonal wurtzite structure is considered more stable, but both hexagonal and cubic forms exist in nature. The most common use of CdS has been for yellow pigment, but owing to the toxicity and being a carcinogen, it is now largely banned from common use. Cadmium yellow is largely CdS and it gained popularity in the late 1800s by painters such as Van Gogh. His famous paintings of sunflowers use cadmium yellow pigments. CdS is now used in solar cell application as the buffer layer for both copper-indium-gallium-selenide (CIGS) cells and CdS/CdTe heterojunction cells. CdS is intrinsically n-type due to the deficiency of sulfur. Vacancies have a high affinity for electrons, and electron conductivity is relatively high, making it useful as a window material in CdTe solar cells. Basic properties of CdS are outlined in Table 1-4, based on the data by Ray [1-33].

Molecular Formula	CdS
Crystal Structure	Hexagonal (Wurtzite) $P6_3mc$ and cubic sphalerite
Lattice Spacing (Hexagonal)	a = 0.414 nm, c = 0.671 nm at 300 ^{o} K,
Lattice Spacing (Cubic)	a = 0.581 nm
Molecular Weight	144.46 g/mole
Density	4.92 g/cm^3
Melting Point	1750^{o}C (10 MPa)
Boiling Point	980^{o}C (sublimes)
Bandgap	2.42 eV @300 ^{o}K, direct bandgap
Refractive Index	2.5
Electron Affinity	4.5 eV
Electron Effective Mass	0.15 – 0.17 m_e
Electron Mobility	400 cm^2/V.s
Hole Mobility (Intrinsic)	80 cm^2/V.s
Thermal Conductivity	40.1 W/mK at 293^o K
Specific Heat Capacity	0.47 J/gK at 293 ^{o} K
Thermal Expansion Coefficient	a1 = 6.26 x 10^{-6} /K at 293 ^{o} K a3 =3.5 x 10^{-6} /K at 293 ^{o} K
Young's Modulus	45 GPa
Poisson Ratio	0.38

Table 1-4: Basic properties of CdS (after Ray [1-33]).

CdS has the wurtzite structure, and the prototypical material is (ZnFe)S with the space group of $P6_3mc$. Other compounds with the same wurtzite structure include AgI, ZnO, CdSe, α-SiC, GaN, AlN and BN. A ball and stick model of wurtzite is shown in figure 1-11.

The position of the atoms in a unit cell are as follows:

Cd: (0, 0, 0), (1/3, 2/3, ½)

S: (0, 0, u) (1/3, 2/3, u+1/2)

$u \approx 3/8$ under ideal $c/a_o = 1.633$

CdS $c/a_o = 1.623$

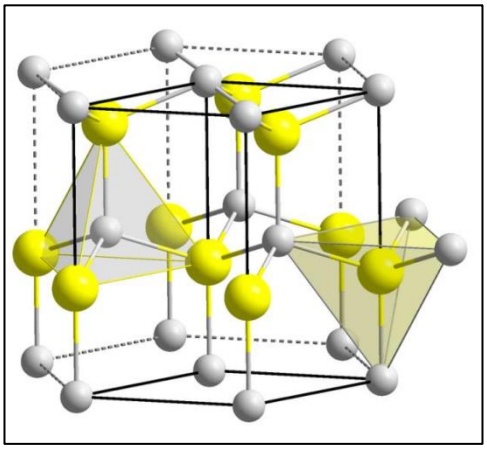

Figure 1-11: Structure of Wurtzite (ZnFe)S. Yellow balls represent the sulfur atoms.

Figure 1-12a shows the unit cell atom placements, viewed from the [0001] direction. Fractional numbers indicate the positions of S atoms in the z-direction (out of the paper). Figure 12b shows the projection of the structure along the $[2\bar{1}\bar{1}0]$ orientation which is the most useful orientation for HRTEM imaging because all of the atoms lie on top of each other with their own respective atomic species, and the basal planes are imaged on an end-on projection. The $[2\bar{1}\bar{1}0]$ orientation is equivalent to the <011> orientation in the cubic sphalerite structure.

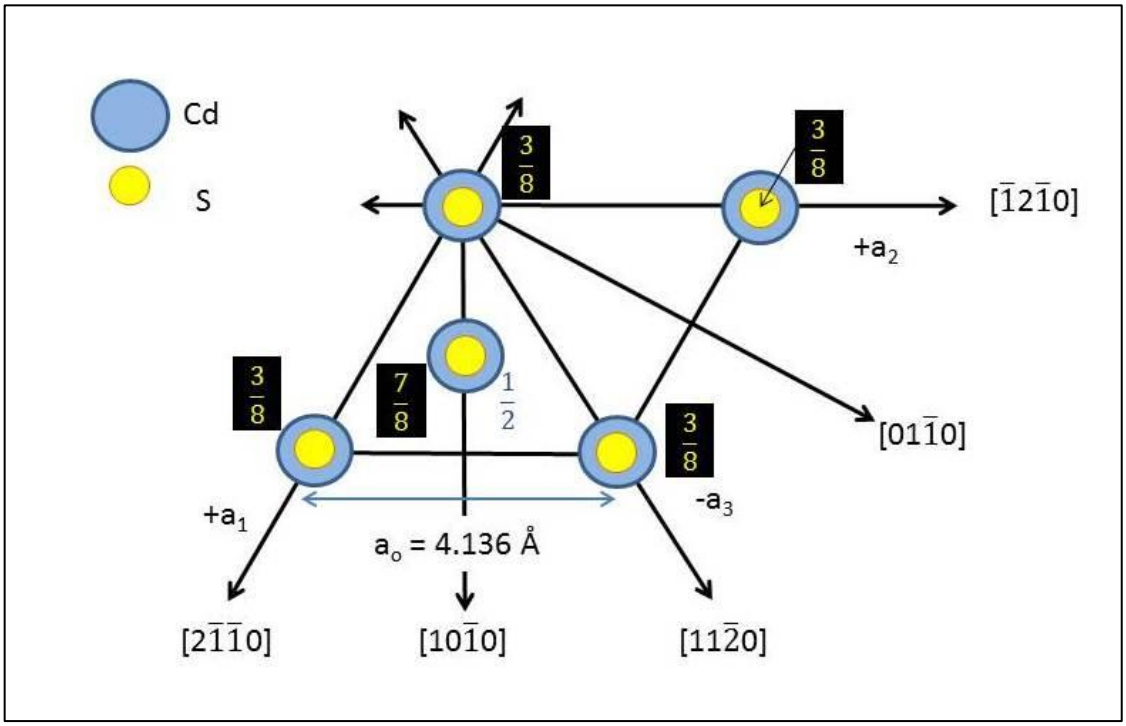

Figure 1-12a**:** Projection of wurtzite structure in the [0001] orientation with the Cd atoms placed on the corners, using the Miller-Bravais notation.

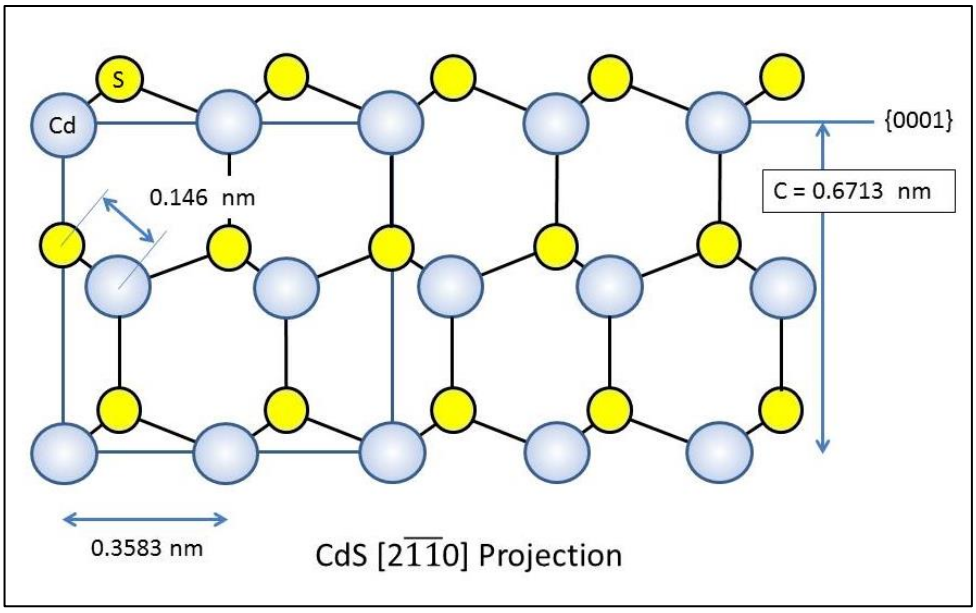

Figure 1-12b**:** Projection of CdS in [2$\bar{1}\bar{1}$0] orientation and the unit cell (the box drawn on the left). There are six equivalent directions for [2$\bar{1}\bar{1}$0].

1.7 TEM Specimen Preparation Methods

Preparing electron transparent specimen has always presented difficulties for TEM analysis. TEM specimens from CdTe, CdS, and heterojunction interfaces were also difficult to make, and a great deal of effort was expended in developing practical techniques for specimen preparation. Other materials discussed in this work such as thin film magnetic media often used the same methods developed for the TEM specimen preparation for semiconductor materials, and the specific procedures used in each case are also outlined here. Bulk CdTe and CdS single-crystal materials were made by the Bridgman technique. CdTe was produced at the Center for Materials Research, Stanford University, using a modified Bridgman method, and doped with phosphorus to approximately $10^{17}/cm^3$ carrier density for p-type conductivity [1-34]. A crystal boule was typically 2.5 cm in diameter and approximately 5 cm in length. Major difficulties lay in the fact that the boule consisted of polycrystalline grains that were usually 5 to 10 mm in size. The ~1mm thick wafers were usually sliced from the boule using a wire saw, then square pieces ~5 x 8 mm were cut from the wafer. A SiC slurry usually was used on the wire saw, made by South Bay Technology, Inc. [1-35]. Usually, no particular attention was paid to the crystalline orientation of the square samples unless a specific orientation was desired. The square pieces were then polished and small solar cell devices were fabricated on top, often, by depositing CdS and indium tin oxide (ITO) films. Even though the devices were very small, it was sufficient to measure everything that was needed to study the electrical and photonic behavior. The CdTe material was quite expensive and not many solar cell specimens were prepared. Those that were made had considerable amount of time and effort invested into various electrical and photonic measurements.

A typical CdTe wafer cut from a boule is shown in figure 1-13. Grains of different sizes are clearly visible. This particular wafer was mechanically polished then chemically etched using a bromine-in-methanol (Br:MeOH) solution to delineate the grains. For device fabrication, the wafer was typically polished mechanically using a fine alumina slurry followed by successively finer diamond paste down to 0.25 μm. This was followed by chemical polishing using a 5% (by volume) Br:MeOH solution.

A fine grade polishing pad can be used in combination with Br:MeOH solution to bring the wafer to a mirror polish. Both the bromine and a Br:MeOH soluttion are highly toxic and corrosive. Bromine easily evaporates in its pure liquid form and in methanol solution. Therefore, these liquids must be always handled inside a fume hood while wearing protective gloves and a face shield. Only a small volume of Br:MeOH solution was prepared at a time, usually less than 100 ml. at a time to be used immediately.

The polished wafer surface was examined by X-ray diffraction after polishing, typically with the Laue method to determine the orientation of the grains in the wafer. In practice, this was quite difficult as the grains were usually not oriented in a convenient low index orientation. The objective was to obtain a grain with the [011] orientation for HRTEM imaging. An expedient method was to break a small piece of the wafer to expose the cleavage surface which is the {011} plane in CdTe. A 3 mm diameter disk could be cut-out from the wafer based on the cleavage plane using a combination of wire saw and an ultrasonic cutter. Once the 3mm disk is obtained, it can be lapped down to 100 – 200 μm thickness using successively smaller alumina slurry and diamond paste, finishing with 0.25 μm or smaller diamond paste to obtain the mirror-like surface. CdTe is very brittle and delicate compared to other semiconductor materials such as silicon and GaAs.TEM specimen cannot be mechanically lapped much thinner than ~100 μm before falling apart.

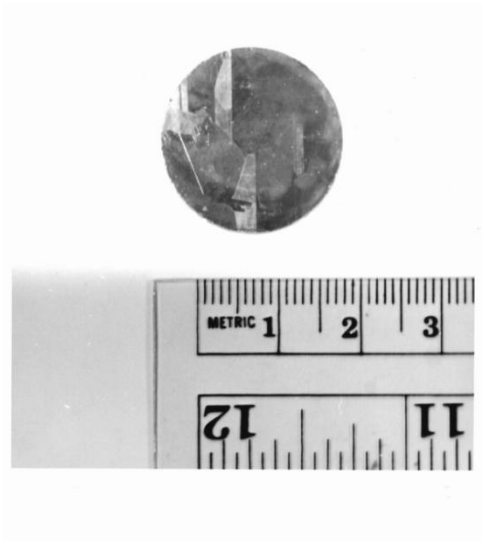

Figure 1-13:Typical CdTe wafer sliced from a boule. The crystal is made by Bridgman method. Grains of different orientations are clearly visible.

An electron transparent specimen was obtained by ion-milling for many hours. The typical condition for ion-milling was 3 to 5 kV at an angle of 15° to 20° until a hole was obtained at the center of the specimen, followed by a few minutes at 2 kV to remove any damaged layer. Early work used an Technics MIM-VI ion-milling tool [1-36]. Typical argon pressure was 10 mTorr, and ion current of 10 μA. For some of the later specimens, Gatan Dual Ion Mill model 600 was used [1-37]. This tool was one of most successful ion-milling tool to be developed specifically for TEM specimen preparation. Its success was due to its ease of use and easy maintenance, and higher through-put with its dual chambers.

To prepare a CdS TEM specimen from a bulk crystal, the cleavage planes in CdS, which is along the $\{1\bar{1}00\}$ planes, must be identified first. The $\{1\bar{1}00\}$ planes are the prism planes in the hexagonal structure. The orientation of interest for the HRTEM imaging of CdS is the $[11\bar{2}0]$. Bisecting the two prism planes are the $\{11\bar{2}0\}$ type planes. CdS is mechanically stronger compared to the CdTe, and the TEM specimen can be thinned down to ~ 50 μm before ion-milling. Consequently, the ion-milling time was much shorter compared to the CdTe specimen.

The key bottleneck to many TEM specimen preparation is the ion-milling time. With usually only one ion-mill tool available to service each TEM, the through-put of the TEM analysis itself is often dependent on the ion-milling time. The biggest factor then, for ion-milling thru-put is how thin the specimen can be made before ion-milling. For a delicate material such as CdTe, inability to thin the TEM specimen much below 100 μm before ion-milling was a serious issue in ability to look at many specimens. A mechanical thinning tool called a *dimpler* became one of the most important and useful tool to be developed for preparing TEM specimen. With the dimpler, it because possible to thin the specimen to 50 μm or less, even for a delicate material such as CdTe. For more mechanically robust material such as Si and GaAs, it was possible to go to thickness of ~10 μm. This was possible because the dimpler thinned only the center of the TEM specimen, keeping a thicker outer rim for greater mechanical stability. The dimpler achieves this geometry by using a thin rotating wheel which ground or polished the center of the TEM specimen while the TEM specimen itself

rotated while attached to a specimen stage. Small strips of polishing pad were cut and glued to the dimpler wheel using a cyanoacrylate glue. Successively finer abrasives were used to polish down the center of the specimen. The *dimpling* of the center of the TEM specimen was how it got its name. This tool greatly reduced the ion-milling time required to obtain electron transparent specimen, thereby increasing the through-put of the specimens through the TEM. Additionally, it became possible to prepare cross section specimen with good mechanical integrity, so that it became an indispensable tool for preparation of semiconductor material where imaging the devices often required a cross sectional view.

At Stanford, a mechanical dimpler was constructed based on an original model that was developed at Hewlett-Packard (HP) Laboratories by Tom Cass and Bob Smith in the mid to late 1970s. The term *dimpler* was the name that they had coined, and later the term itself was trademarked by the VCR group when the HP design was commercialized by the VCR group [1-38]. HP Laboratories provided a copy of their tool to NASA-Ames laboratory, and we copied the basic function of this tool for Stanford [1-39]. At a later time, HP Laboratories' dimpler also was used for specimen preparation, especially for the cross section TEM samples described in Chapters 3 and 4. HP's dimpler was made with greater precision, and it was able to thin the specimen much farther than the Stanford version. Tom Cass and Bob Smith at the HP Laboratories can be credited with the original design for the dimpler, and devising the specimen preparation method around this tool. Many of us took advantage of their expertise and experience in the preparation of semiconductor materials and cross section samples. Figure 1-14 shows the schematic of the construction of the dimpler tool at Stanford. A set of pulleys rotate a grinding wheel attached to a rotor (18). The specimen is glued to a small turntable (14). The specimen stage can be moved in the x-y directions (4 and 13) to center the grinding wheel over the TEM specimen. A counter-balance at the end of the arm can be adjusted to change the load of the arm to the specimen. The grinding wheel speed and turn table rotation speed can be adjusted to achieve a desired grinding rate. A close-up of the grinding wheel and turntable is shown in figure 1-15. A binocular was placed over the turntable to track the progress of

the grinding steps as shown in figure 1-15. Additionally, the turntable can be placed on an optical microscope stage and the thickness of the dimple in the specimen can be monitored much more precisely, to within a few micrometers using the focusing micrometer on the optical microscope.

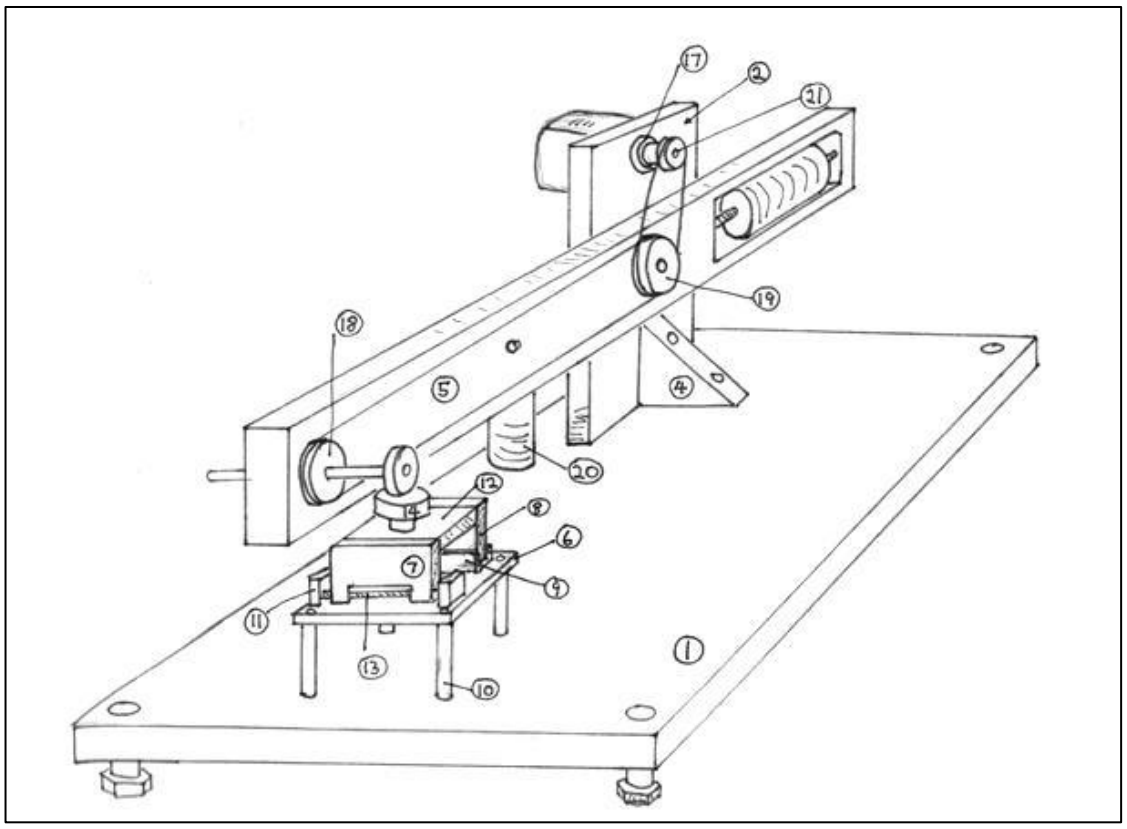

Figure 1-14: An illustration of the first Stanford dimpler constructed for TEM specimen preparation.

The following illustrations show the methods used to make various types of TEM specimens using the dimpler. Figure 1-16 illustrates how a 3mm diameter CdTe disk was created from the CdTe wafer. During dimpling, extreme care has to be made to not to punch through the sample as this would invariably destroy the center of the sample and ruin the specimen. CdTe parts are extremely brittle and fragile compared to other semiconductor materials. Therefore, it required extra caution in specimen preparation. Another indicator of dimpled thickness was that when the region becomes

very thin, it becomes slightly translucent so that the microscope illumination could be seen as dull red light as it reflected off the stainless dimpler mount. This worked well for a material such as silicon, but CdTe was usually too fragile to push the thickness to this stage, which for silicon was usually few microns.

Figure 1-15: Left, a close-up detail of the dimpler grinding wheel and the turntable. Right photo shows the microscope used to monitor the progress of dimpling the specimen.

Another method that was used was to cut a round or square piece of cleaved or wire-cut part from the bulk crystal with the [011] orientation, and the specimen was jet thinned using 2% Br:MeOH solution. This method can be performed manually using a fine nozzle directed to the center of the specimen with the edges protected with black wax. This was quite effective and fast in preparing specimens from a single-crystal. Ion-milling at approximately 4 keV at 15° for a few hours was sufficient to obtain an electron transparent sample. This type of specimen preparation method was used for dynamic imaging of defects as described in Section 1.10.

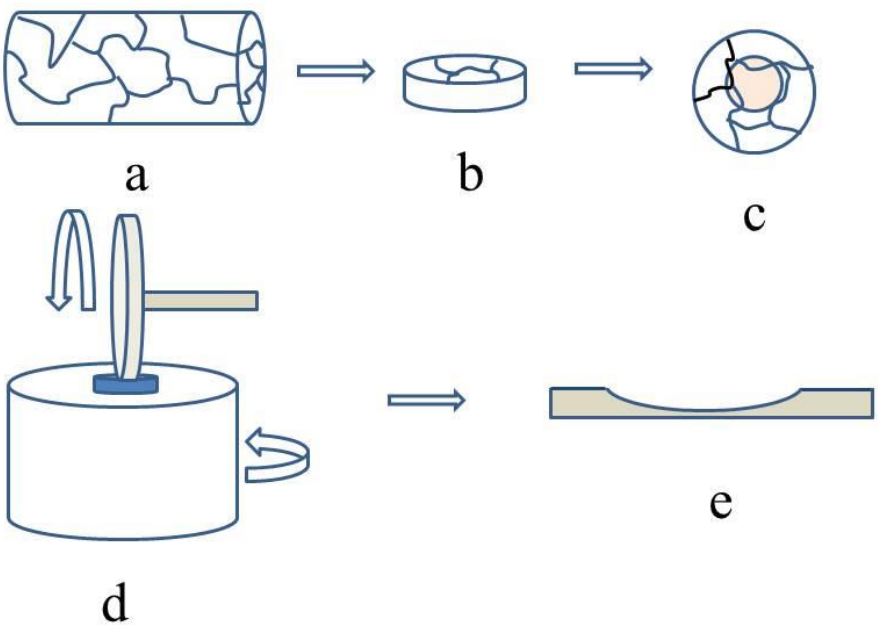

Figure 1-16: Method for extracting a crystallographically oriented TEM specimen from a CdTe boule. **a**) Polycrystalline CdTe boule, about 2 cm dia. x 5cm. **b**) A wafer is cut by wire-saw containing one grain that is oriented close to the desired [011] face based on the cleavage plane. Usually the cleavage plane is determined by chipping a small piece from a large grain from the boule. **c**) Coring a 3mm diameter disk from the wafer containing the grain with the right orientation. **d**) A 3mm disk is mounted to the dimpler specimen stage after thinning to ~ 200-300 μm by hand. The dimpler is used to thin the center until it is approximately 30 – 50 μm thick. **e**) Final geometry of the TEM specimen after dimpling. The sample is then ion-milled at the center to electron transparency. Dimpling was sometimes done from both sides of the specimen to maintain a thicker rim.

Another method to prepare a bulk specimen was to encapusulate a small piece with the proper crystallographic orientation in a bakelite thermosetting plastic. At Stanford, the crystal was imbedded into an 1 inch diameter cast, typically used for metallographic specimen mounting. This was then thinned down by hand to approximately 1-2 mm in thickness using a polishing wheel with alumina abrasive paper, then an ultrasonic drill was used to cut a 3mm disk containing the CdTe grain. One problem with this method was that the large pressure used for the Bakelite thermosetting often cracked the irregularly shaped CdTe piece. The remedy was to use a finely ground Bakelite poweder. Once a 3 mm disk was made, the same method as illustrated in figure 1-16 was used to dimple the center. The advantage of this method was that only a small piece of CdTe would be sufficient to make the TEM sample. At HP Laboratories, the facility had a specially designed 3 mm specimen mounting jig so that subsequent thinning was quite fast using a polishing pad. The encapsulating method is shown in figure 1-17.

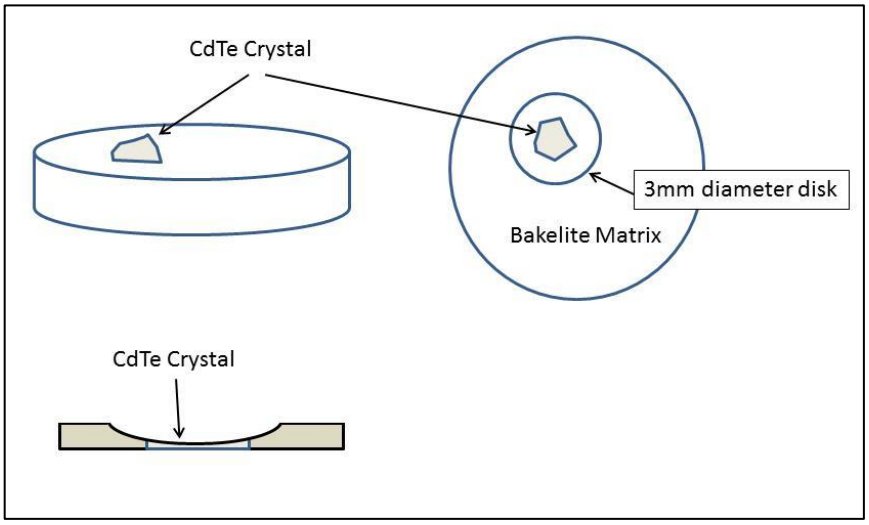

Figure 1-17: Specimen preparation method by encapsulating a small oriented grain inside a Bakelite matrix. A 3 mm disk is cored from the larger matrix, then thinned to 200-300 microns. The part is then dimpled at the center down to ~50 microns.

The cross section TEM sample preparation method is described next. This technique was pioneered at HP Laboratories and most of the details for this type of specimen preparation were worked out by the researchers there. Now, the method is widely used by many microscopists all over the world. It is especially well-suited for semiconductor applications and for thin film analysis where the films need to be examined in cross section. The specimen is first cut into small bars, usually using a small diamond saw, then the bars are glued face-to-face using the epoxy bond. Sometimes a crystal bond is used, other times cyanoacrylate glue. Usually the top surface of the film on the substrate needs to be protected or encapsulated to prevent over-etching during ion-milling. A thick layer of either a metal or inert material is deposited on top of the film. After gluing the pieces face-to-face, the part is then thinned mechanically by hand. If the joined bar is thick enough, then a 3 mm diameter disc can be cored out directly from the joined bars. Alternatively, a "dummy" bars of silicon strips can be glued to both side of the pieces containing the interface, so that a 3mm disk can be cut from the assembled pieces. A mechanical coring tool can be used or the ultrasonic cutter to core the 3 mm disk. If the bars are too small, then the they have to be cut small enough so that they can fit inside a 3mm diameter encapsulating medium such as Bakelite as described previously. Once the two glued bars are encapsulated, the same process, as described before, is used to mechanically thin the parts, followed by dimpling and ion-milling to obtain electron transparent sample. Ion-milling for CdTe specimens was the same as described previously. The process is illustrated in figure 1-18. This approach was later described in a simple fashion by Bravman and Sinclair [1-40] which became a useful reference for many researchers.

As it was the case with the crystalline piece embedded inside the Bakelite, the two joined bars are very fragile and utmost care must be taken while mechanically thinning the sample, and subsequent dimpling. The latter is usually stopped within ~50 μm thickness in order to prevent the bars from cracking and falling apart in the case of CdTe specimens. Often the glue joining the two bars would fail when thinned too much. Other materials such as silicon, GaAs, and hard disk media for example, can stand up much better during dimpling so that one can push the center thickness down to a few

microns. One of the useful slurries to use at the last step was a Syton® solution [1-41], which is a colloidal suspension of extremely small SiO_2 particles suspended in an aqueous alkaline solution. This slurry has a moderate chemical etchning effect together with the mechanical polishing action from the SiO_2 particles that are only a few nanometers in size. The silica particle size in the Syton® solution can be varied. We used a particle size of 2.5 nm.

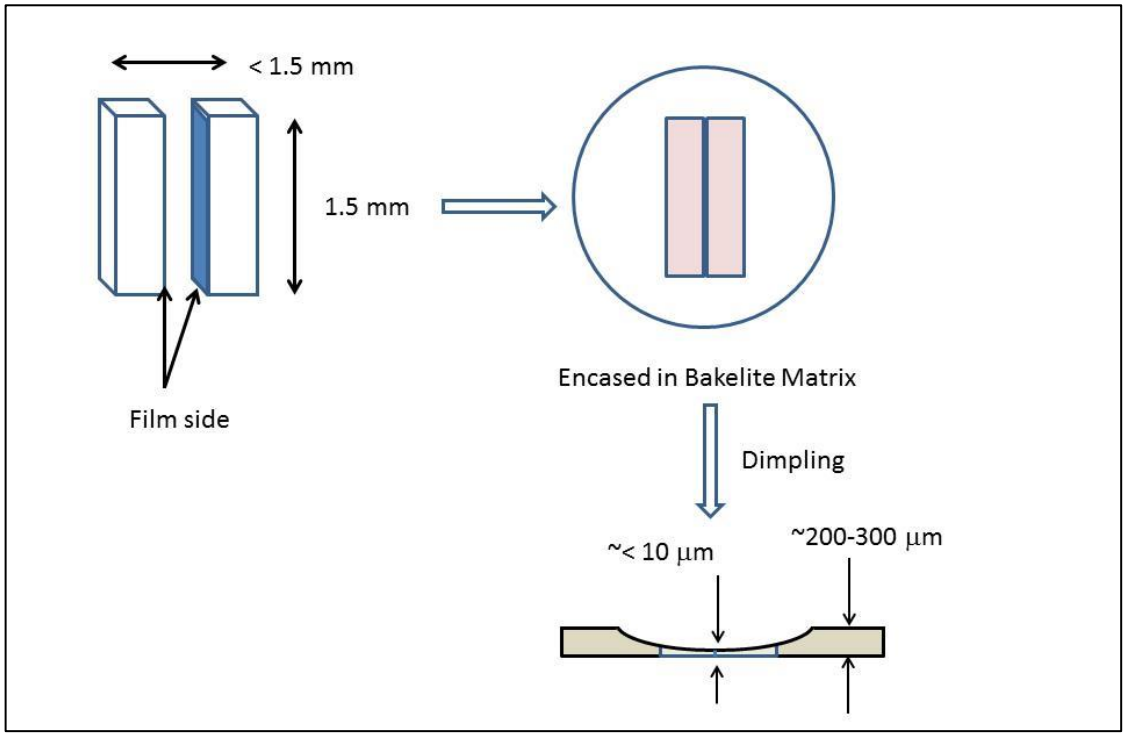

Figure 1-18: Cross section TEM sample preparation method using an encapsulation method. The film sides are glued face-to-face, and encased in a Bakelite matrix. The sample is then mechanically thinned to ~200 - 300 μm, followed by dimpling the center. Finally the specimen is ion-milled to electron transparency.

This chemo-mechanical polishing process using a Syton® solution was extremely effective in obtaining a very gentle, slow and well-controlled polishing rate in the final step of dimpling. A narrow strip of felt pad was glued with high precision

onto the metal wheel surface to gently polish the specimen surface. This technique was also developed at HP Laboratories by Tom Cass and Bob Smith. The Syton® and similar solutions are also used in polishing the semiconductor wafers in a chemo-mechanical planarization (CMP) process, and for polishing the hard disk aluminum substrate surfaces. An atomically smooth surface can be obtained using this material. The advantage of making the dimpled center as thin as possible is to reduce the ion-milling time, which is slow and expensive. When the increase in TEM throughput is factored, the dimpler provides tremendous value in a TEM facility. A photograph of cross section TEM specimen after ion-milling is shown in figure 1-19. Bakelite encapusulation was used on this specimen. The two bars are slightly offset from each other, but the holes where the electron transparent areas are located are quite large after ion-milling. Without dimpling, TEM specimens would often require several days of ion-milling with frequent checking of the sample to judge the progress. Additionally, the failure rate for TEM specimens without the dimpling was high, with more than half of the attempts ending in failure. With dimpling, the success rate improved dramatically to ~80% or more. For cross section specimens, specimen preparation without the use of the dimpler would have been nearly impossible.

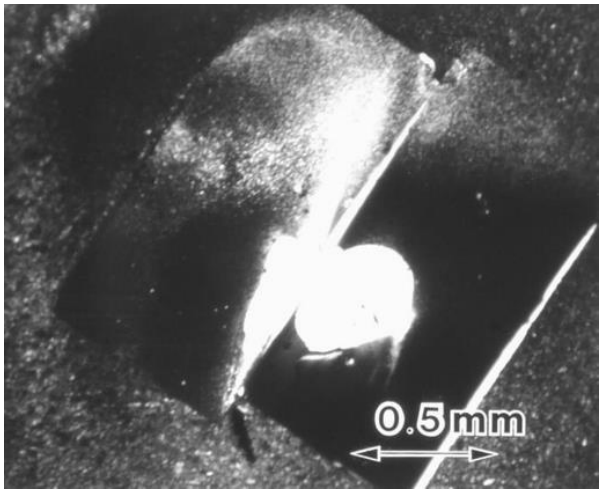

Figure 1-19: Photograph of a cross section TEM specimen of CdS CdTe/ interface. The white region in the center is a hole formed after ion-milling.

One of the problems with using Bakelite to encapsulate the cross section bars as shown in figures 1-18 and 1-19 was that the specimen sometimes charged-up during

TEM examination due to poor electrical conductivity of the Bakelite encapsulant. This was alleviated by evaporating a thin layer of gold or carbon film on the specimen. The specimen bars with electron transparent holes can be easily protected from getting coated by placing a thin and narrow paper strip across the TEM specimen so that the bars are not coated. After this procedure, the TEM specimen is cleaned again for several minutes in the ion-mill tool to make sure that any contaminants from the evaporation process are cleaned-up around the specimen hole.

A critical choice in ion-milling with Ar ions was the energy to use for the milling. CdTe and CdS are prone to ion-beam damage, and the sample has to be cooled with liquid nitrogen and a lower kV used for the milling. Between 3 to 6 kV was typical for the ion-beam milling tool, but often a lower energy such as 2 to 3 kV was used for CdTe, especially at the finishing stage. Initially, higher power was used to rapidly thin the sample. Finishing was done for up to several hours at 2 kV to reduce beam damage. It turns out that even at 2 kV, the specimens were being damaged. This was realized much later. A shallow angle at approximately 10° was used to obtain a large area of electron transparent region. However, higher angles of 15 to 20° were usually used in the initial ion-milling. The shallower angle was thought to reduce damage. Much of ion-milling technique had to be developed by trial and error as this method had not been used done before. There are many problems that can develop, such as back sputtering that can contaminate the specimen, and beam damage which at times is difficult to recognize when looking at a specimen for the first time. After ion-milling, the specimen also can be quite reactive, and it can oxidize or build up a contamination very quickly. Usually, the TEM specimen had to be imaged almost immediately following ion-milling to avoid these effects. For HRTEM, the specimen surface must be completely free of foreign contaminants and oxidation. Usually, the contamination, especially the amorphous variety, is easy to recognize at the specimen edge with its characteristic appearance.

A commercial Dimpler® tool was introduced by Vince Carlino of VCR group in the mid 1980s and hundreds were sold, with a license from HP Laboratories and Tom Cass. Gatan also delivered a compact and simplified tool called the Dimple Grinder [1-

37] which also became very popular and continues to be sold. Both tools use the same grinding/polishing concept that was originally developed at HP Laboratories. Figure 1-20 shows the VCR and Gatan versions of the dimpler tool.

Thin film media used for magnetic recording was usually sputtered on to a microscope slide coated with a few tens of nanometer thick evaporated carbon (graphite) film. It had been verified earlier that the film deposited on a graphite coating behaved identically to the one deposited directly on a glass slide by magnetometry, using a vibrating sample magnetometer (VSM). Therefore, it was assured that the film should be the same whether sputtered on a glass slide directly or on an evaporated carbon. For the films deposited on a coated graphite, applying a thin layer of collodion solution on the slide would cause the coated film to delaminate in large sheet of many millimeters in size. Collodion is basically a nitrocellulose dissolved in ether. When applied on the film deposited on graphite, the ether dries out quickly, leaving a thin layer of cellulose on the surface, which imparts high stress on the film. The stress easily delaminates the film from the graphite surface. Once the film delaminated, it is a simple matter to pick it up, sandwich it between a folding copper grid and dissolve the nitrocellulose film with acetone. The sample is then ready for TEM examination immediately. For cross section imaging of films, the method described earlier with two bars glued together was used. In this case, an extensive amount of dimpling was required followed by ion-milling. Metal films are much more susceptible to argon ion-beam damage compared to the typical semiconductor material. Therefore, greater care (lower keV) was needed to thin the sample. Alternatively, the specimen was much more amenable to mechanical polishing so that cross section samples can be pushed to very low thickness before ion-milling.

Recently, using focused ion-beam (FIB) tools to cut out a small sliver of the sample directly from devices and wafers has become much more prevalent and a more convenient way of making TEM specimens. This is much faster and easier than preparing 3 mm disks, which must be prepared, dimpled and ion-milled, even though the FIB tool often costs more than $2M each. For creating an oriented sample of CdTe, for example, it is sufficient to have a very small area with the known crystallographic

direction of the crystal. Then a small piece can be carved from the area and attached to a specially designed grid by the ion beam. Although the FIB tool is very expensive, the speed at which a high quality TEM sample can be prepared has truly revolutionalized the TEM analysis. A combination of the automated FIB tool with automated TEM made by the Field Emission Inc. (FEI) are used in the manufacturing of magnetic recording heads used in the hard disk drive (HDD). The automated TEM is used to measure critical dimensions of the device to control manufacturing processes with amazing efficiency and precision. The key elements in magnetic recording heads are cut out using the FIB tool, and TEM samples are automatically prepared and put into a carousel that is designed to be loaded into the automated TEM. Using a very sophisticated program and mechanical manipulators, the TEM makes automated line-width measuremnets on the parts to monitor the manufacturing control and tolerances on the recording head. Hundreds of parts per day are measured in this manner around the clock in the recording head factory. The TEM analysis and specimen making technology have truly advanced greatly within the last 10 years.

Figure 1-20: Left, a commercial Dimpler® tool built by the VCR group [1-38] by Vince Carlino who licensed the design from HP Laboratories and Tom Cass. Right, a Gatan Dimple Grinder [1-37] with a simple and compact design.

1.8 HRTEM of CdTe and CdS

1.8.1 CdTe in <110> Orientation

In the late 1970s to early 1980s, the HRTEM imaging of semiconductor materials received considerable attention, as lattice resolution was required in order to understand the various defects and interfacial issues that had been affecting their electrical and photonic properties and performance. In this context, achieving the best possible resolution from the TEM, given the limitations that come from various microscope parameters, was receiving attention as lattice parameters of important semiconductor materials were close to the limit of the capabilities of TEM at that time. Major symposia were being held to discuss the theory and experimental aspect of HRTEM, a good e**x**ample was the Nobel Symposium on *Direct Imaging of Atoms in Crystals and Molecules*, held at Lidingö, Sweden in 1979 [1-42]. The Materials Research Society (MRS) held regular symposia on defects in semiconductors for many years [1-43]. This work on CdTe in the <110> orientation was intended to determine the limits of the capability of the TEM in order to obtain the highest resolution possible. Some result already had been reported on silicon by Izui et at. [1-16] and on GaAs by Hashimoto et al. [1-18] and by Olsen et al. [1-19].

The projection of the CdTe structure in <110> orientation was shown in figure 1-10. The smallest spacing between Cd and Te columns is separated by 0.162 nm in this orientation. Two sets of {111} planes are imaged end-on, each {111} plane separated by 0.374 nm. The microscope used in this work was a Philips EM400 transmission electron microscope equipped with a high-resolution stage with nominal value for the spherical aberration coefficient (C_s) of 1.1 mm and the chromatic aberration coefficient (C_c) of 1.2 mm at 120 kV. The microscope used a LaB_6 filament. The specimen stage had no tilting capabilities. Thus, the specimens had to be made in the exact orientation. Any deviation from the desired zone axis (e.g., [110] zone) had to be made up by wedging the specimen with a thin aluminum foil. The process took many iterations to achieve a desired orientation for the specimen.

The condenser aperture size used for lattice imaging was 200 μm, corresponding to an illumination semi-angle of 2.1 mrads with the fully focused beam. Thirty-nine beams with the lowest CdTe d-spacing reflection of {440} (d = 0.114 nm) were admitted by the objective aperture, and the magnification was 800,000X. Under typical microscope operating conditions, multi-beam images with image spots corresponding to the unresolved atomic column pairs (0.37 nm apart) were easily visible on the screen through the binoculars. Through-focus image series, usually consisting of nine plates, were taken at either 5 or 10 nm defocus steps, with exposure times of approximately 1 second for the Kodak 4463 film. For this particular study, optical diffractometer analysis of the negative according to Krivanek [1-23] did not yield any useful results because the specimen did not contain much amorphous material to form a diffractogram. The method could have provided an independent measurement of C_s and microscope defocus Δf for the images. Approximate values of Δf were obtained by calibrating the through-focus series with respect to the condition for Fresnel fringe disappearance (i.e. minimum contrast condition), which occurs approximately 30 nm underfocus for the present microscope according to Heinemann [1-44]. The value of C_s is a function of specimen height in the column (objective lens focusing current). In our analysis, C_s was assumed to be approimately constant (1.1 mm), since our present microscope has no capability for adjusting specimen height and most specimens were expected to occupy the same position in the column every time.

An experimental lattice image of CdTe near the edge of the specimen is shown in figure 1-21. The region in the center, bounded by a fault, is a micro-twin (Σ=3) which extends several microns into the crystal. Numerous defects of various types were observed in most of the specimens that were examined. The inset in the figure is the diffraction pattern from the same area, with the image of the objective aperture showing the number of beams admitted through the objective aperture to form the image. In addition, the diffraction pattern has been properly oriented with the image, and the small faint diffraction spots come from the twinned region. The twinned region is too narrow to produce significant amplitude in the diffraction intensity.

A set of through-focus micrographs of the region near the edge of the crystal is shown in figure 1-22. The defocus values indicated in the figure are approximate values. Within the twinned region of the crystal (image (b) and (c) in figure 1-22), the individual spots, with similar separation of the columns of cadmium and tellurium atoms, appear to have been resolved. In addition, a slight systematic intensity difference can be observed between the resolved columns. Close examination of the images shows that the image is not a correct representation of the projected structure. The spacing between the closely spaced spots is larger than it should be relative to the other dimensions of the unit cell. The distance between the Cd and Te atoms is separated by 0.23 nm instead of the correct value of 0.16 nm. An extreme close-up image from figure 1-21 is shown in figure 1-23 to illustrate the point. A similar elongation has been observed in high-resolution images of silicon by Izui et al. and in GaAs and AuAl by Hashimoto et al. [1-16, 1-18]. The thickness of the crystal at the region of "atomic resolution" is estimated to be between 3 - 8 nm. This estimate is based on the assumption of a wedge-shaped crystal and the observation of Pendellösung thickness contour (indicated by an arrow in figure 1-21), which occurs between the thicknesses of 10 - 13 nm, according to the multi-beam image calculations.

In the thicker regions of the crystal, the image departs from the correct symmetry, and in some places, disappears altogether. However, at certain thicknesses, an image with the apparent high resolution reappears. This is shown in figure 1-24 and in the inset photograph. The twinned region is the same as shown in figure 1-21, but located further into the specimen. The apparent resolution is even better than in fig. 1-23, but this is because the spots are even farther separated, by approximately 0.28 nm, instead of the proper 0.162 nm. A through-focus series of the same area indicates that this type of image can be obtained over much greater range of defocus than in the thin area. Unfortunately, Δf and the specimen thickness, which are needed for image matching calculations, could not be determined accurately for the region of interest. The thickness of the region in question is probably approximately 20-30 nm, estimated from its relative position with respect to the crystal edge. High-visibility lattice images

from even thicker crystals are unlikely because of inelastic scattering effects according to Pirouz [1-45].

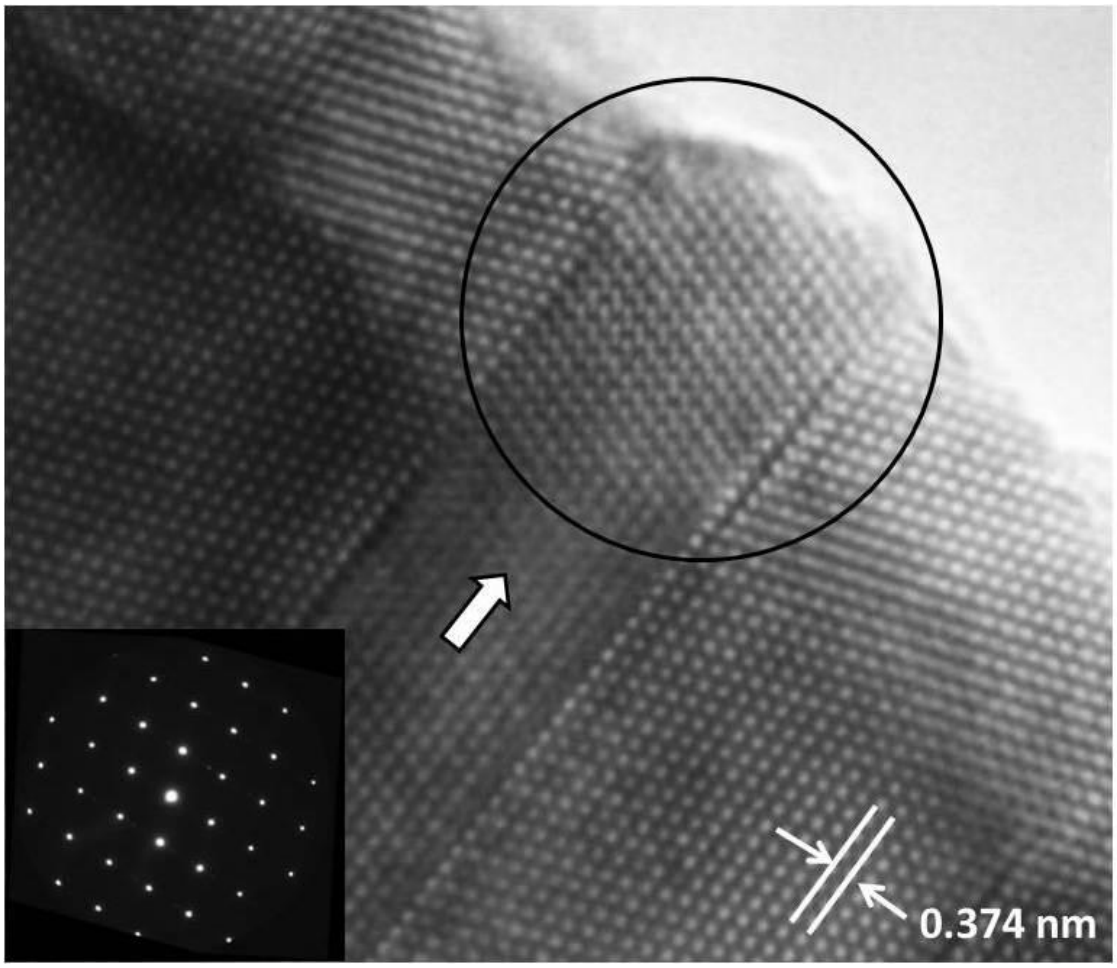

Figure 1-21: A lattice image of CdTe in the <011> orientation, showing the region of apparent high image resolution near the edge of the specimen, circled in black. The edge of the specimen is seen in the upper right corner. The arrow indicates the position of the Pendellösung extinction contour in the twinned region. The diffraction pattern, with the outline of the objective aperture used in our observation, is inset.

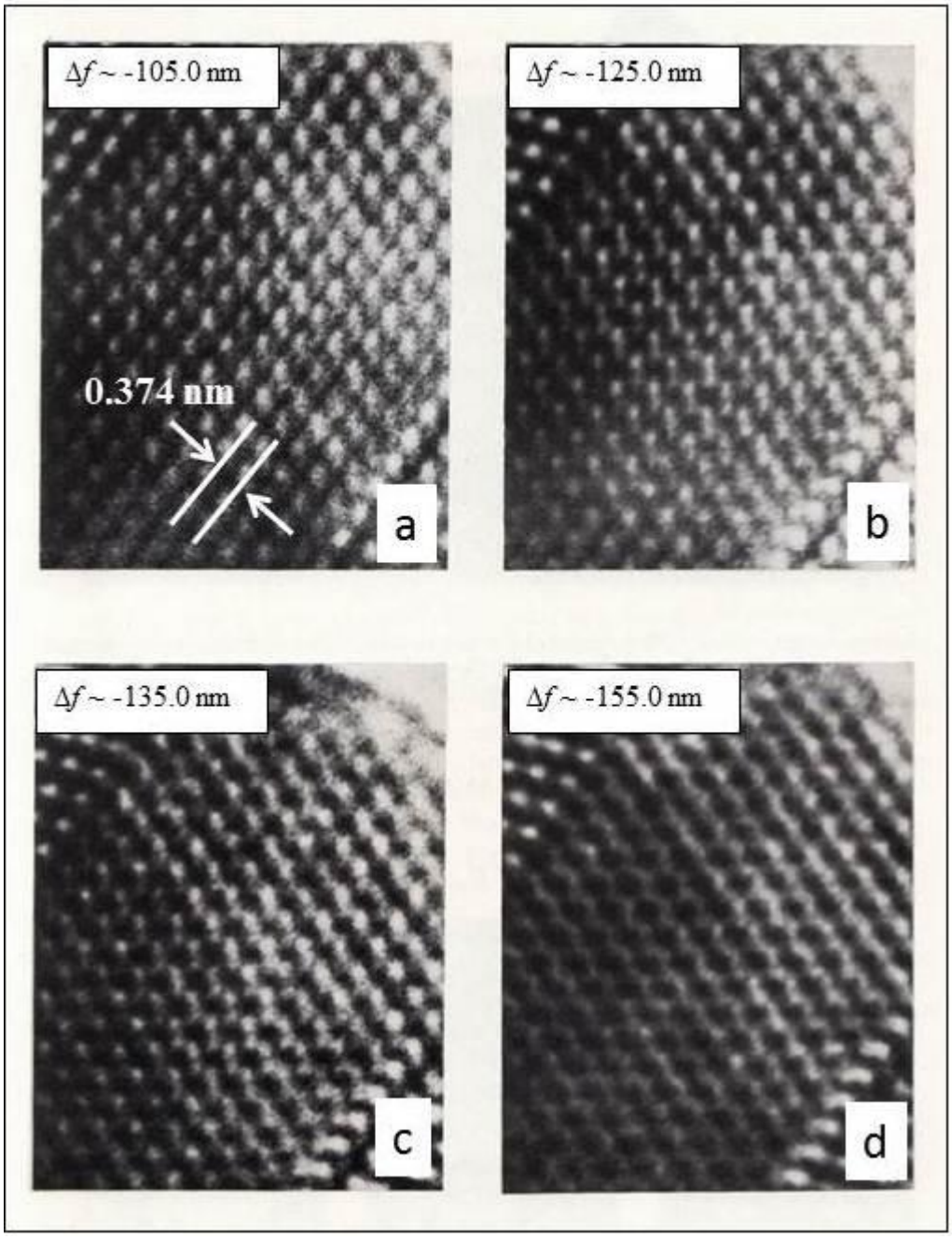

Figure 1-22. A through-focus series of micrographs of the region near the edge of the crystal in figure 1-21, with the estimated defocus values indicated in the figure. The spot resolution and intensity difference are especially clear in (b) and (c).

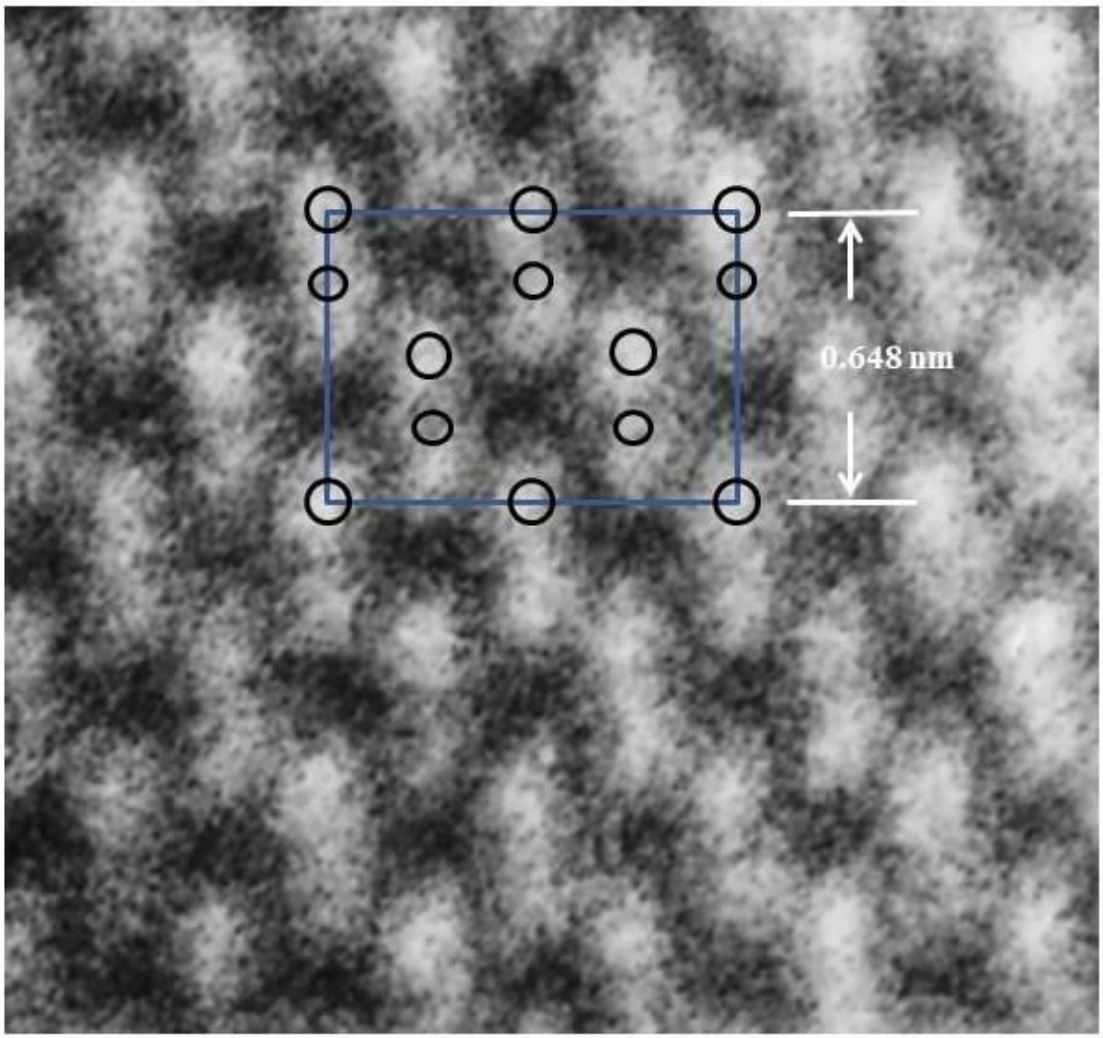

Figure 1-23: Enlarged image from figure 1-22, with the structure of CdTe <011> superimposed on the image. The actual position of the atoms are indicated in circles. It clearly can be seen that one of the image spot positions is elongated in the vertical direction for the actual experimental image.

The CTF for the Philips EM400 microscope is shown in figure 1-25 with the envelope functions included in the figure. The Scherzer defocus condition for the microscope is at Δf = - 70.1 nm using equation 1-14. The beam divergence, α is 2.1 mrads and the temporal coherence value, δ = 4.0 nm for the microscope. The chromatic aberration coefficient is 1.2 mm. Additionally, the Scherzer resolution would be 0.298

nm using equation 1-15. It would appear that the envelope from the beam divergence would attenuate any contribution from the beams beyond the (200) reflections at 0.324 nm, but image simulations were carried out to determine whether more insight can be obtained from the exercise. Various reflections from the CdTe in the [011] zone axis are listed in Table 1-5.

To determine the actual effect of various microscope parameters on the image, a large number of image calculations, based on Pirouz [1-45] for a non-centrosymmetric crystal, were performed. A total of 129 beams were taken into account in the calculation of Bloch-wave vectors and amplitudes. Although truncation in the calculation is inevitable, previous experience by Pirouz in similar situations has indicated that 129 beams are enough for the calculation. An important consideration in the calculation was the computing cost associated with generating each image. These calculations were conducted at the time using mainframe computers at the Stanford computing center. CPU time was quite expensive then, but today the comparable calculations can be performed in seconds using personal computers. The most time-consuming part of the present image calculations is the diagonalization of an N-by-N matrix to give the Bloch-wave amplitudes, the computing time increasing dramatically with the number of beams, N. For non-centrosymmetric crystals, 129 beams can be reduced to only 70 beams by symmetry considerations according to Pirouz [1-45]. The 129 beams goes out to (6,6,6) reflections at g = 16.044 nm^{-1}. In the calculated images, bright regions correspond to regions of high electron density (i.e. positive contrast). The intensities were divided into 10 levels of gray and converted into an overprinting routine on a line printer.

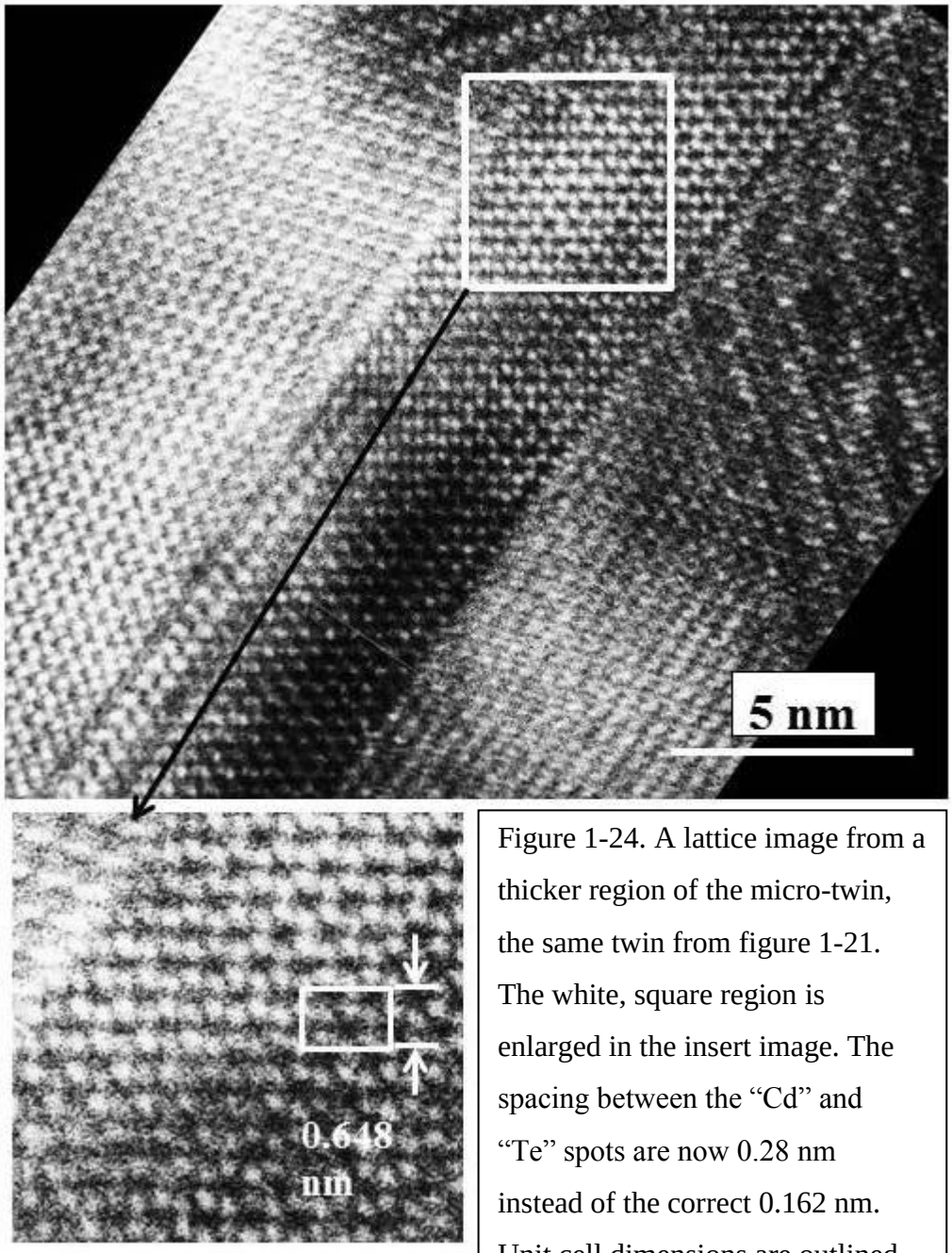

Figure 1-24. A lattice image from a thicker region of the micro-twin, the same twin from figure 1-21. The white, square region is enlarged in the insert image. The spacing between the “Cd” and “Te” spots are now 0.28 nm instead of the correct 0.162 nm. Unit cell dimensions are outlined in white in the photograph.

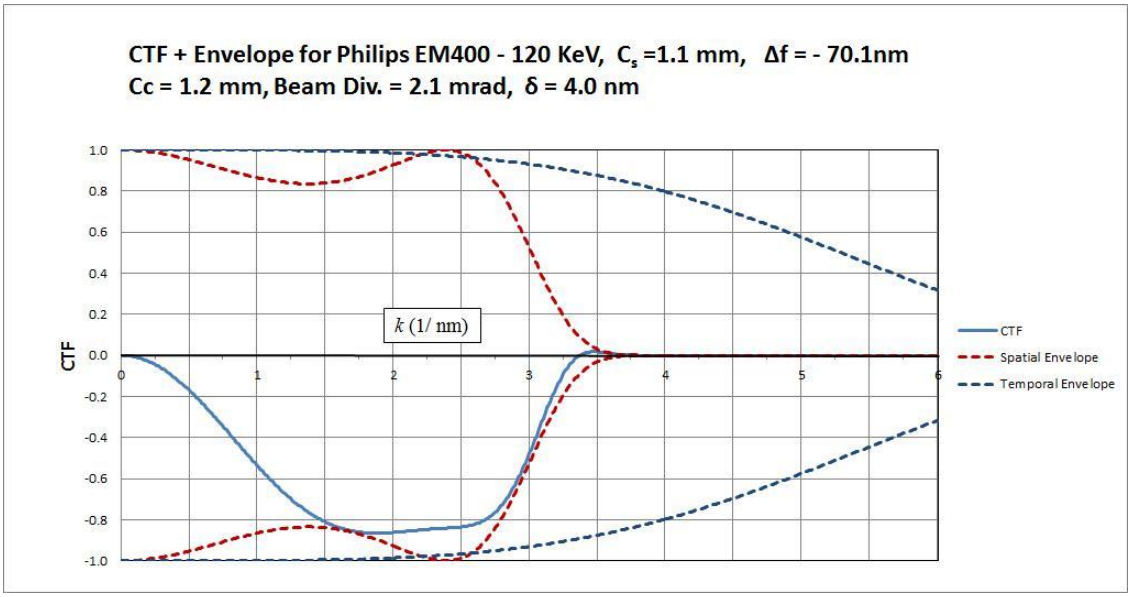

Figure 1-25: CTF for EM400 microscope with the envelope included, at the Scherzer defocus of - 70.1 nm. It can be seen that the beam divergence contribution dominates and the reflections beyond 3.356 nm^{-1} will not contribute to the image. This corresponds to the lattice spacing of 0.298 nm or smaller.

An experimentally obtained image that resembles the projection of the potential distribution (PPD) is desirable. The PPD along the beam direction is given by $V_p(\bar{\boldsymbol{r}})$, which can be expressed as a Fourier series expansion of the crystal potential [1-46]:

$$V_p(\bar{\boldsymbol{r}}) = \frac{h^2}{2me}\sum_g U_g \exp(2\pi i \mathbf{g}\boldsymbol{r}), \qquad \text{(Eqn. 1-17)}$$

U_g is the Fourier coefficient of potential calculated from the atomic scattering factors for electrons by Doyle and Turner [1-47], and $\boldsymbol{r}$ is a two-dimensional vector in the plane perpendicular to the beam direction. An experimental image that appears similar to the PPD may be obtained for a very thin crystal ($t << 1/\Delta\gamma^{jl}$) and a constant value of the CTF for all reflecting vectors, **g** contained within the objective aperture. Under these idealized conditions, the Bloch-wave formulation can be shown to reduce to the

PPD form by Pirouz [1-48], which is equivalent to the weak-phase object approximation. Such an image can be called the *PPD-type* image. The PPD-type image can give a first-order estimate of the influence on image formation of different atomic species in the structure and the effect of different number of beams contributing to the image. The term $\Delta\gamma^{jl}$ comes from the Bloch-wave formulation for dynamical electron scattering [1-9], and it is the difference in the diagonal matrix of eigenvalues for *j* and *l* branches of the Bloch-waves. The main importance in this discussion is that $1/\Delta\gamma^{jl}$ is the extinction thickness or ξ_g where the image contrast is expected to become minimized.

				a_o =	0.6483 nm	
h	k	l	d (nm)	1/d (nm^{-1})	# Reflections	total
0	0	0			1	1
1	1	1	0.374	2.672	4	5
2	0	0	0.324	3.085	2	7
0	2	2	0.229	4.363	2	9
3	1	1	0.195	5.116	4	13
2	2	2	0.187	5.343	4	17
4	0	0	0.162	6.170	2	19
1	3	3	0.149	6.724	4	23
4	2	2	0.132	7.557	4	27
3	3	3	0.125	8.015	4	31
5	1	1	0.125	8.015	4	35
0	4	4	0.115	8.726	2	37
2	4	4	0.108	9.255	4	41
6	0	0	0.108	9.255	2	43
5	3	3	0.099	10.115	4	47
6	2	2	0.098	10.232	4	51
4	4	4	0.094	10.687	4	55
1	5	5	0.091	11.016	4	59

Table 1-5: Reflections for the CdTe in the <011> orientation. The <hkl> indices are generic (signs are ignored).

The effect of atomic species on the image was first examined this way by comparing PPD-type images of CdTe, GaAs, and InP. The thicknesses were on the order of the respective lattice parameters, with 59 beams contributing to the image formation and a constant value of the CTF for all vectors **g,** with $\sin\{\chi(\mathbf{g})\} = -1$ for all of the beams used in the calculation. With this artificial situation then, the results are shown in figure 1-26. Even with the poor grayscale contrast provided by overprinting, the greater degree of contrast could be expected based on atomic scattering factors for electrons, which is a function of the atomic number. In the case of InP, the largest difference in contrast is predicted between indium and phosphorus positions (atomic numbers 49 and 15, respectively). For GaAs, the difference in atomic number is only two, and the atomic species are probably indistinguishable. With a difference of four, CdTe shows some promise of a difference in contrast. In each case, the brighter spots correspond to the heavier species.

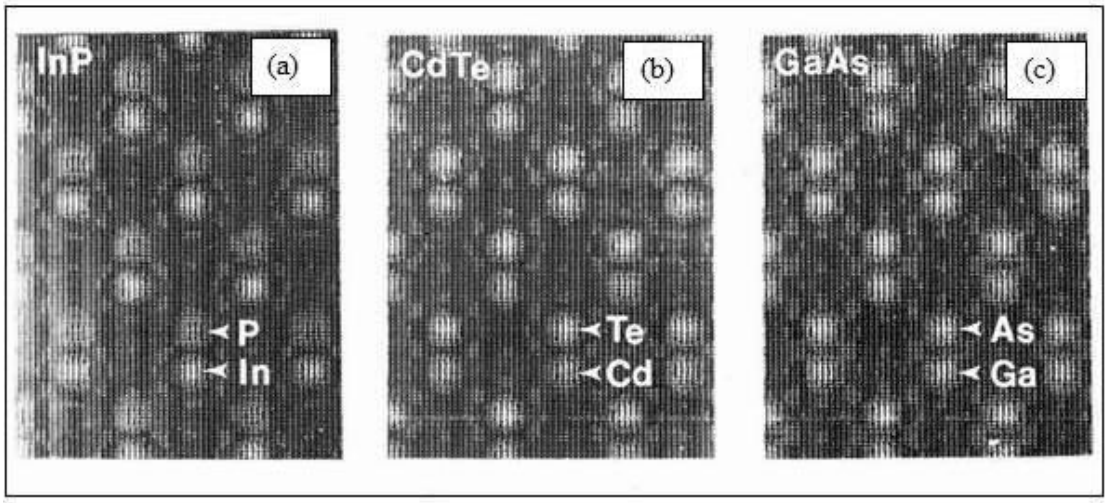

Figure 1-26: PPD-type image calculated with 59 beams out to (155) reflections, and all of the **g** vectors set to $\sin\{\chi(\mathbf{g})\} = -1$. (a) InP, (b) CdTe, (c) GaAs.

The influence of the number of beams, "n" taken through the objective aperture for the same PPD calculation condition as figure 1-26, is shown in figure 1-27. Up to

59 beams are included in the image through the objective aperture. From the figure, it is clear that a minimum of 13 beams (i.e. out to (311) reflections) are required to resolve the individual columns of cadmium and tellurium atoms, a result that is consistent with equivalent calculations for germanium and silicon by Spence et al. [1-17] and by Pirouz [1-48]. The PPD-type images reveal anomalously large spot spacing between the Te and Cd columns along the <100> direction, which decreases to the true dimension of the structure as more beams contribute to the image. The elongation is clearly due to insufficient terms in the Fourier series (equation 1-17) for a true representation of the potential distribution, and becomes negligible when more than 23 beams are involved in the image formation. For the n=13 beam case, the separation between the Cd and Te position along the <001> direction is approximately 0.19 nm vs. the actual 0.162 nm.

For a thicker crystal in a real microscope, the image intensity and the crystal structure are no longer simply related. Therefore, image matching by trial and error must be used to obtain specimen and microscope operating conditions under which the image can be interpreted easily. A series of image-matching calculations covering approximately one Fourier image period (Δf = +10 nm to -260 nm) were carried out to determine the various possible image types. A crystal thickness of 5 nm and 13 beams through the objective aperture were assumed, but ignoring the effect of spatial and temporal coherence for this example. The only defocus range where the calculated images approximate the experimental images occurs at approximately 130 nm underfocus, over a defocus range of approximately $\pm$ 10 nm. The result is shown in figure 1-28. Similar sets of images were obtained at Δf of +5 nm and -250 nm, with the images translated by half the lattice parameter when compared to that at Δf = -130 nm, consistent with the Fourier image period ($\Delta f = 2a_o^2/\lambda$ with a_o= 0.6483 nm) of ~250 nm for CdTe. Structure images at Δf values of +5 nm and -250 nm are considered unlikely because the defocus dependent virtual aperture associated with the finite beam divergence should cut-off the contribution from the (113) type beams at these defocus ranges. A comparison of the experimental image and the calculated image at Δf = -130 nm in figure 1-29 shows that the match is quite good. The elongation of the Cd-Te

column spacing and the intensity difference between the different atomic columns are reproduced in the calculation.

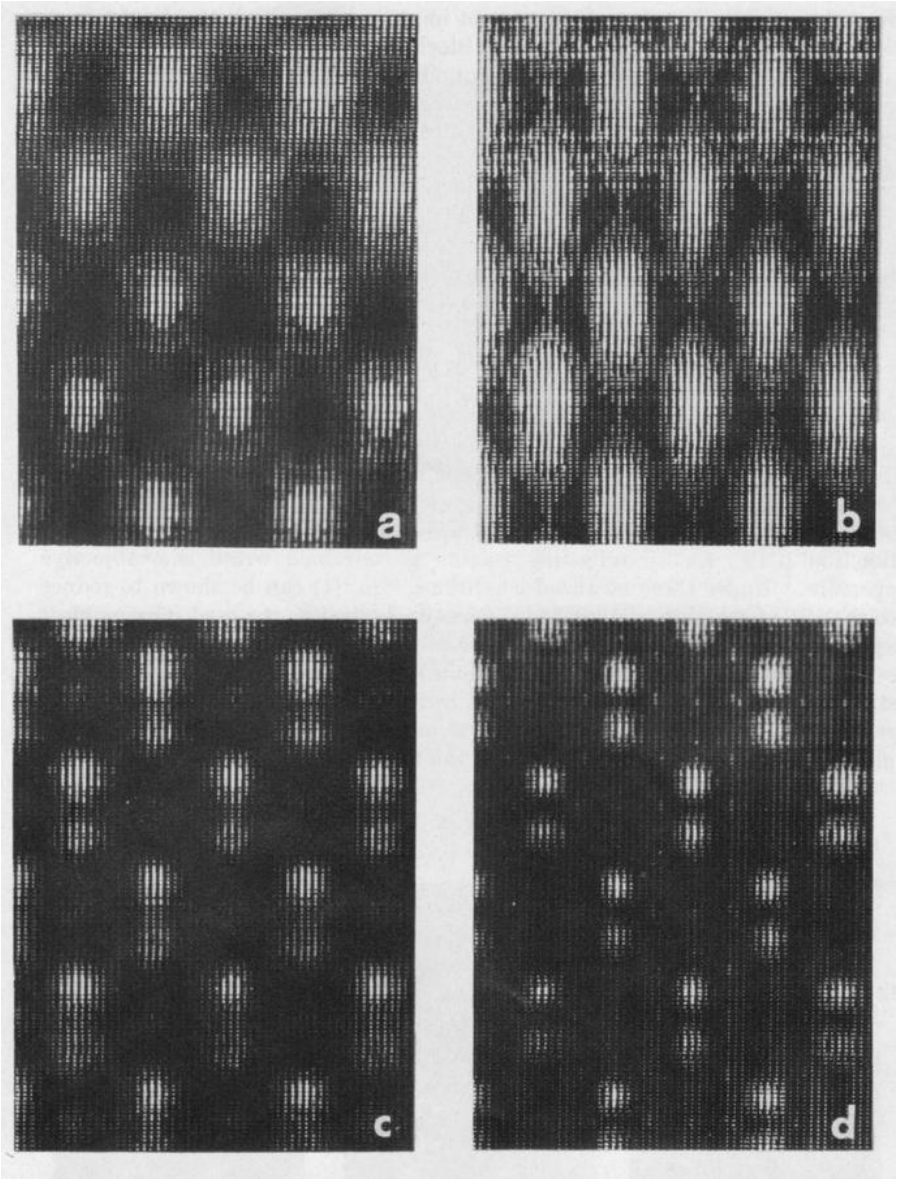

Figure 1-27: PPD-type calculations showing the effects of the number of beams admitted by the objective aperture: (a) n = 7; (b) n = 9, (c) n = 13; (d) n = 23. Atomic columns are not resolved for n = 7 and 9. For n = 13, the spots appear to be separated by a larger distance (~0.19 nm) than in the actual structure (at 0.162 nm), whereas for n = 23 (out to (133) reflections, d = 0.149 nm) the separation is correct.

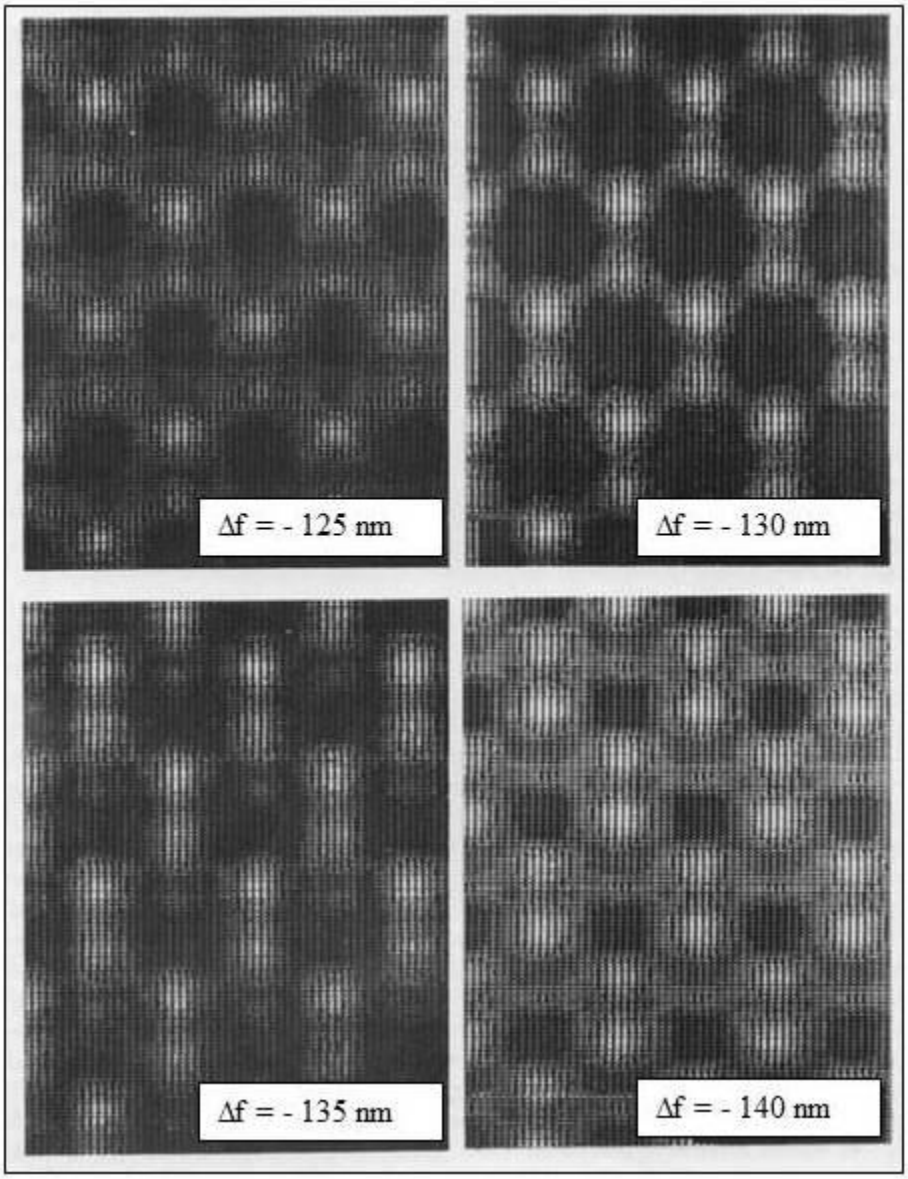

Figure 1-28: Calculated images with t = 5 nm and n= 13 (through the objective aperture) at a defocus interval between Δf = - 125 and -140 nm. Notice the appearance of the high contrast image between Δf = -130 and -135 nm with brighter spots corresponding to tellurium positions. At Δf = -140 nm defocus, the image intensity between cadmium and tellurium positions is reversed. A translation of the bright spots by $a_o/2$ with respect to the PPD in figure 1-27 has occurred because of Fourier optic effects.

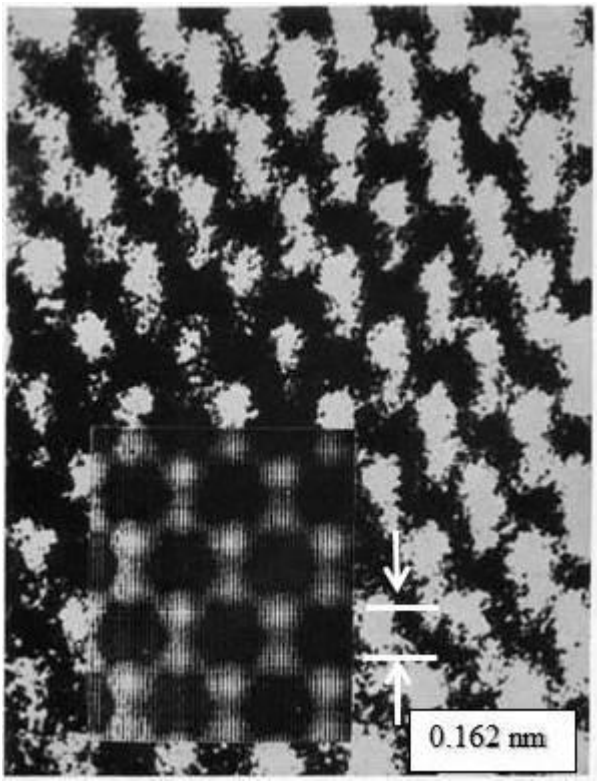

Figure 1-29: A micrograph with a superimposed calculated image (t = 5 nm, Δf = -130 nm and n = 13) in the inset. Both show a similar intensity difference between the cadmium and tellurium positions, and elongation in their relative positions. The simulation shows approximately the same amount of separation (~0.23 nm) as seen in the actual experimental image.

To use the intensity difference to identity atomic species in the image, it is apparent that the defocus value must be known very accurately. The calculated image at Δf = -140 nm shows a slight contrast reversal. It can also be noted that the images shown in figure 1-28 have a *reverse contrast* (white atoms), with the images translated by half the lattice parameter from the actual atomic positions. An image with normal contrast (black atoms) is obtained at other defocus settings, but such an image was not observed experimentally.

Figure 1-30 shows how thickness affects various diffracted wave amplitudes. Owing to the non-centrosymmetry of CdTe, (hkl) and $(\bar{h}\bar{k}\bar{l})$ beams are not equivalent (e.g. $(1\bar{1}1)$ and $(\bar{1}1\bar{1})$ in figure 1-30 (a)). Other diffracted beams have similar behavior. The calculated images are shown in figure 1-31. A high contrast image with the correct symmetry is obtained at thicknesses of 9 to 13 nm. From these results, the approximate thickness for interpreting the experimental lattice images in figure 1-22 was derived.

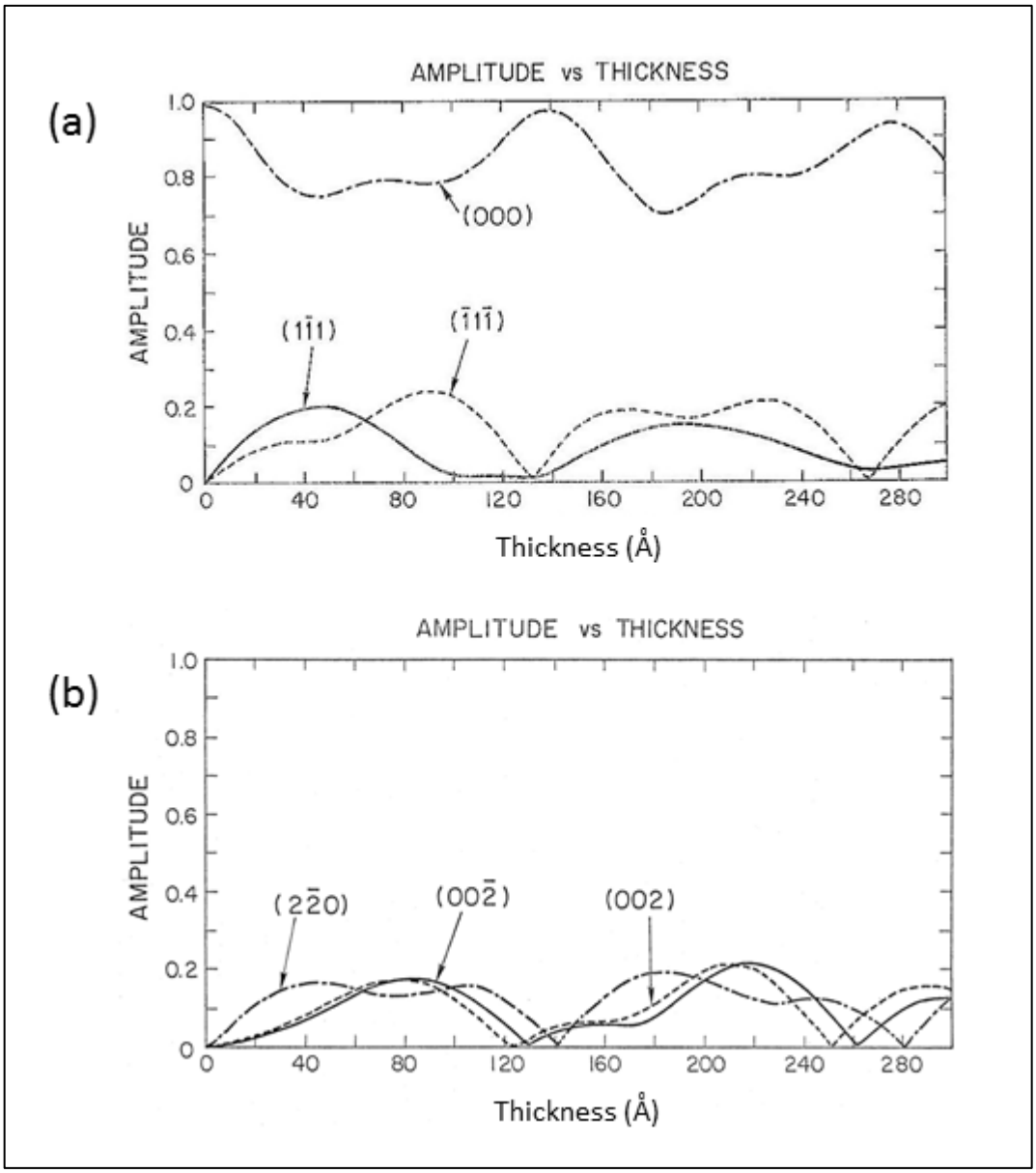

Figure 1-30: Plot of the amplitudes of diffracted beams as a function of specimen thickness. Zone axis is taken as [110]. The x- axis scale is in Å units (1nm = 10 Å). (a) for (000) and {111} type reflections, (b) for $(2\bar{2}0)$, $(\bar{2}20)$ (not indicated), (002), and $(00\bar{2})$ reflections.

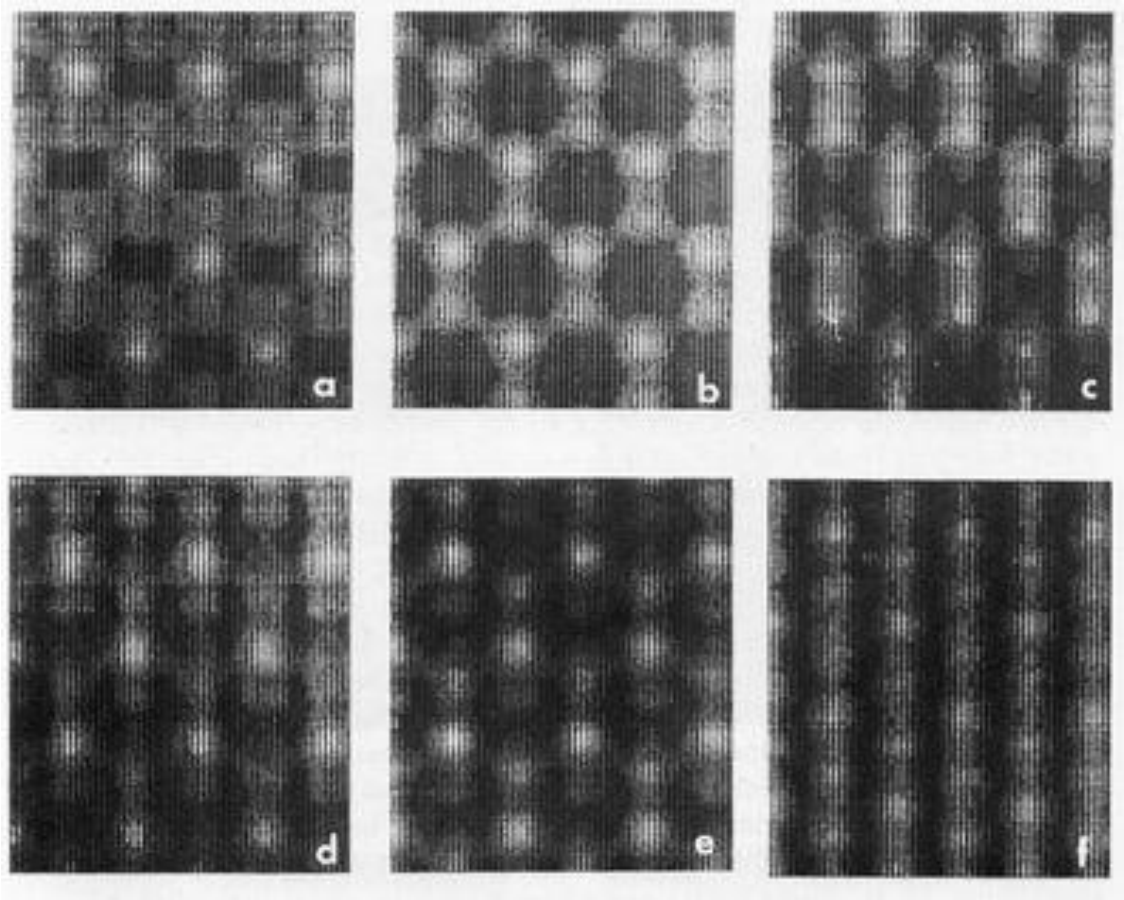

Figure 1-31: 129 beam calculations, with 13 beams through the aperture, for a thicknesses of: (a) 3 nm, (b) 4 nm, (c) 5 nm, (d) 6 nm, (e) 7 nm, and (f) 8 nm. The objective lens defocus is Δf = -130 nm.

In the next step, the effect of partial coherence caused by beam divergence (spatial coherence) and electronic instabilities in the high voltage and the objective lens current (temporal coherence) also were considered. As was described in section 1.1, these factors limit the number of beams that contribute to the image formation, and they are treated as a damping envelope, which modulates the microscope transfer function as described by Wade and Frank [1-49]. It must be emphasized that this is only a first approximation, which may not be valid even for a thickness as small as 5 nm. As Ishizuka indicated [1-50], the use of an envelope function devised for a weakly scattering object should not be applied to crystals of even medium thickness. As was

shown in figure 1-25, the CTF plot shows that only the {111} and {002} type beams (out to 3.08 nm^{-} up to n = 7) are transferred to the image without being severely damped. The effect of the envelope function on the calculated image as a function of beam divergence is shown in figure 1-32. It shows that a beam divergence less than 1.0 mrads is required in order to have all 13 beams contribute to the image for "atomic" resolution showing the *dumbbell* for Cd and Te positions.

For typical lattice imaging work at that time, a fully focused beam was usually used in order to minimize the exposure time. According to the above analysis, only seven beams will contribute coherently, and individual atomic columns will not be resolved. However, an atomic resolution-like image may be obtained at some thickness and defocus, owing to the interference between $\pm${002} and $\pm${111} type beams. Unlike silicon and germanium, the {002} type beams in CdTe have reasonably high amplitude even in the thin part of the crystal, and calculations show that they can play a significant part in the image formation. For instance, the calculated image series shown in figure 1-33 for a crystal thickness of 8 nm (where the {002} type beam amplitude is maximum) shows that a dumbbell-like image can be obtained at a defocus of – 100 nm. The {113}, {004} and {222} periodicities arising from interference between {111} and {002}beams are not due to specimen structure in a simple manner. The spacing between the Cd and Te position in figure 1-33 (c) has the spacing of ~ 0.18 nm, which is closer to the actual of 0.162 nm vs. ~ 0.23 nm in the experimental image. Whether this discrepancy arises from an inadequate theoretical treatment of the effect of partial coherence is not known, but it is clear that the 13 beam calculations (figure 1-28) reproduce the experimental images better, but this calculation was done without the envelope function. The problem remains then, is that the apparent high resolution obtained in images from figure 1-22 cannot be explained based on relatively high beam divergence that was used to form the image. The beam divergence is calculated from the image of the condenser aperture in the diffraction plane with the beam fully focused. This is shown in the diffraction pattern in figure 1-34. One argument that can be made might be that perhaps the actual beam did not completely fill the condenser aperture; therefore, the beam divergence might be better than the 2.1 mrads that were based on

the aperture size alone. Therefore, even a small adjustment in C2 aperture defocus can reduce the beam divergence. However, it is admittedly not a strong argument. On a side note, the selected area diffraction pattern (SADP) aperture used to obtain the diffraction pattern in figure 1-34 covered an area of ~500 nm in diameter on the specimen.

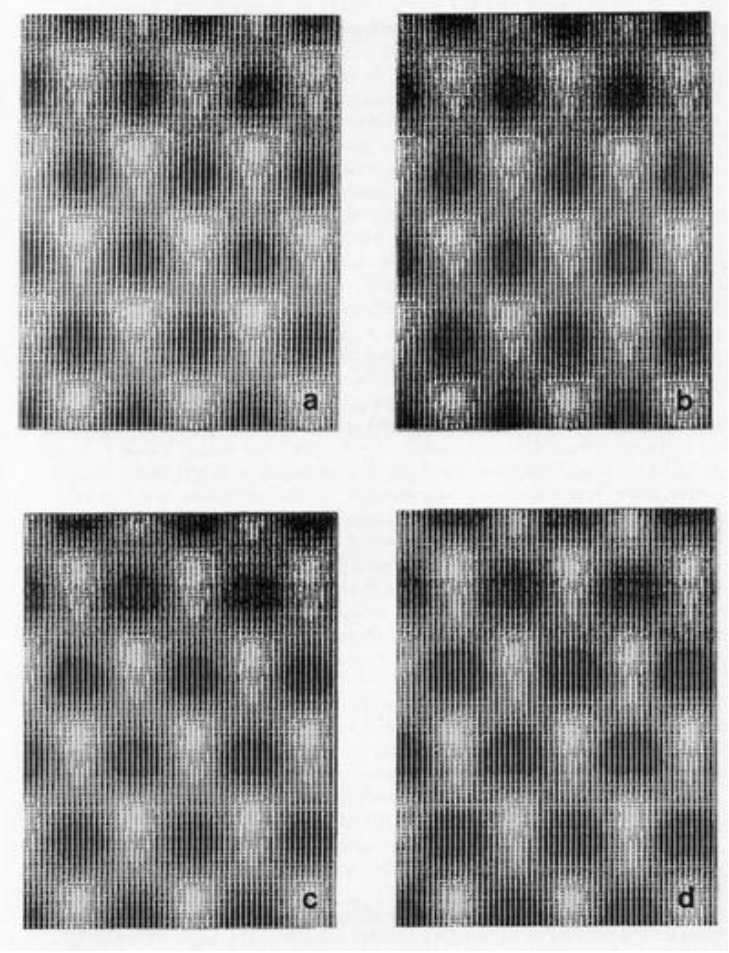

Figure 1-32: Calculated images showing the beam divergence effects for Δf = - 130 nm, t = 5 nm, Δ = 4 nm, and n = 13. (a) $\alpha_{c=}$ 2.1 mrads; (b) $\alpha_{c=}$ 1.5 mrads; (c) $\alpha_{c=}$ 1.0 mrads; (d) $\alpha_{c=}$ 0.5 mrads. For $\alpha_c <$ 1 mrads, dumbbell resolution is obtained.

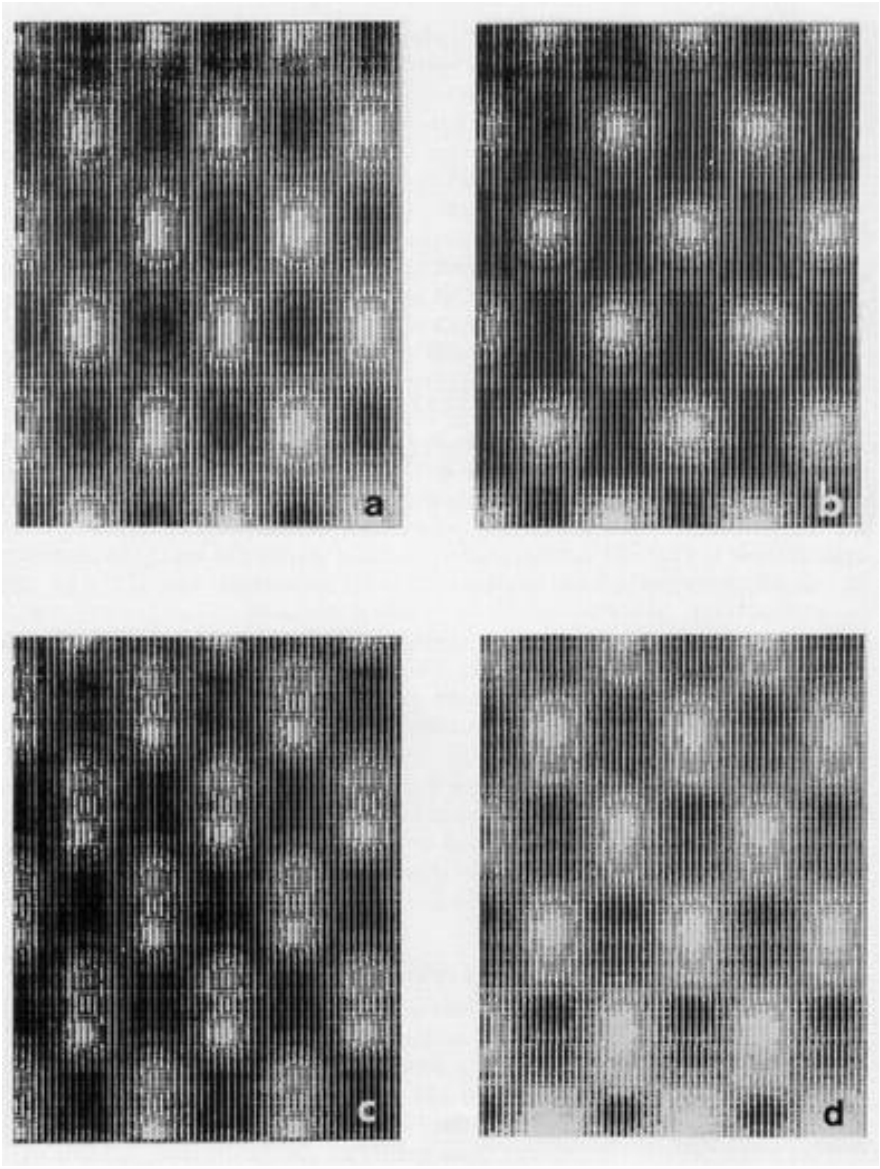

Figure 1-33: Calculated images at t = 8 nm, t = 4 nm, and $\alpha_{c=}$ 2.1 mrads, for 35 beams allowed through the objective aperture; (a) Δf = - 40 nm; (b) Δf = - 80 nm; (c) Δf = - 100 nm; (d) Δf = - 130 nm. It indicates that dumbbell images can be obtained in CdTe using only 7 beams for certain experimental circumstances. However, the spacing between the dumbbell is closer to the actual at approximately 0.18 nm.

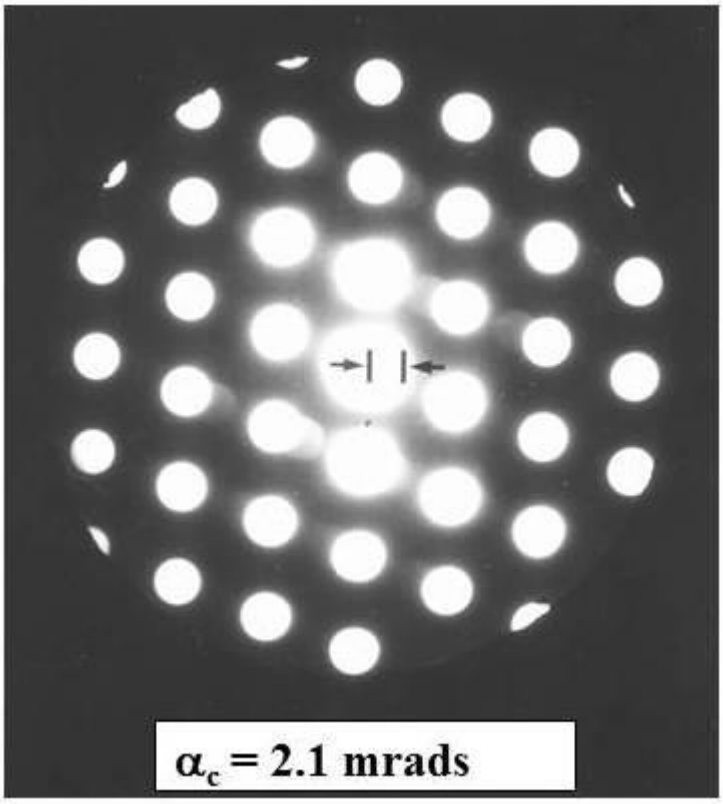

Figure 1-34: Diffraction pattern with the beam fully focused so that condenser aperture can be seen. This would be used for the calculation of the beam divergence, but it will assume that the condenser aperture was completely filled with the beam.

Finally, some attempts were made to simulate the images from thicker parts of the crystal, but the correlation with the experimental images was generally poor. The imaging process is highly non-linear for a thick crystal and it is apparent that such factors as multiple and inelastic scattering must be considered to account for the image correctly.

This exercise in HRTEM for a set of images of CdTe obtained in the [110] projection shows some of the difficulties involved in image interpretation, especially when the image resolution is attempted to be pushed beyond the Scherzer resolution

limit, which is 0.296 nm in the case of the Philips EM400 microscope. It would appear that based on beam divergence consideration alone, an effective aperture was placed on the CTF just below the Scherzer resolution limit. However, the experimental images show that complex images are still possible which may not necessarily reflect the actual specimen potential in the image. Simulations are not very predictive as we never know precisely all the microscope parameters, and the specimen parameters such as the thickness are not known precisely. Even if it can be concluded that Cd and Te spacing at 0.162 nm was actually resolved, the image simulation shows that the intensity can switch between the two atoms and the position also shift with defocus. Therefore, any conclusion that depends on knowing the exact position of individual atoms in an image that shows apparent "high resolution" will be difficult to interpret.

Misorientation of the specimen from the perfect zone axis is one factor that was not considered in the image simulations. It is thought to be critically important for atomic identification based on intensity differences. Calculations on silicon, misoriented from the zone axis by only a few milli-radians, have shown that different image spot brightness arises for the two silicon atomic columns in the <110> projection by Izui et al. [1-16]. In the present exercise, the microscope did not have a tilt-stage. Therefore, it is quite possible that the specimen was slightly out of alignment, although a great deal of care was made in finding the area that was as perfectly oriented based on the diffraction pattern. Figure 1-34 and other diffraction patterns taken at the same time indicate that the specimen was very close to the zone axis. In the image in figure 1-23, the "atomic resolution" that was obtained only within the twinned region, and this may have occurred due to slight misorientation of the crystal from the zone axis. Therefore, it is appropriate to put in quotes the claim of "atomic resolution" becauses it is quite possibly due to a slight misorientation of the crystal, which contributes to such images being obtained. Additionally the images from thicker parts of the specimen can create many complex images, which are due to a combination of inelastic effects and complex interaction of electrons with the specimen potential and the microscope conditions. Figure 1-24 is a clear example, where many different types of image contrast are observed. It would be inappropriate to take just one small area of such an

image from a thicker part of the crystal and claim atomic resolution. An attempt at image simulations in such conditions quickly become intractable. The work on the experimental imaging of CdTe and simulations were summarized by Yamashita et al. in 1982 [1-46].

Probably the best approach to use for HRTEM is to place the objective aperture at or near the Scherzer resolution limit, and keep the image behavior as simple as possible. In the case of CdTe using Philips EM400, this would be an aperture placed at approximately 3.09 nm^{-1} to allow 111 and 002 beams through the objective aperture for 7 beams including the transmitted beam. This will simplify the image characteristics with respect to defocus conditions, and limit image interpretation to the thinnest part of the specimen. Cd and Te atomic positions will not be resolved, and the position of white or dark spots may not necessarily directly correspond to the position of the atoms and they might be displaced by half the lattice parameter. This is illustrated in figure 1-36 where image simulation was made with a modern commercial multi-slice formulation using a Macintosh computer. The MacTempas® program was used which was written by Kilaas [1-22]. Figure 1-35 shows the model and the relative position of Cd and Te atoms in the model and in one of the simulated images. In the simulations, the positions of Te atoms are at the corners of each image. Only 7 beams are allowed through the objective aperture (transmitted, {111}, and {200} reflections). It can be seen that the image characteristics are considerably simplified. A somewhat odd selection of the thicknesses is chosen for the simulation because the program selects the proper thickness to use based on the choice of each slice thickness (approximately 8 slices per unit cell thickness). Generally, the image cycles between *black atoms* to *white atoms* contrast, except for some conditions, the image symmetry changes (e.g., t = 3.7 nm, Δf = 70 nm, and at t = 5.5 nm, Δf = 100 nm). These images have additional image spots that do not reflect the true projection of the actual structure. It is also very difficult to distinguish between the white atom images and black atom images. The eye naturally tends to focus on the brighter white spots in the image, even though such an image may be on the position of the channel in the structure. Some images also show a slight downward shift of image spots with respect to the atom position (e.g., t = 7.3 nm

images). As long as one avoids making too detailed an interpretation regarding the exact positioning of the image spots, the appearance of the image will reflect some general characteristics of the structure of the specimen, even at the defects, so that some general conclusions can be made. Even with 7-beam imaging, very useful information still can be gathered about the specimen and interesting observations can be made. This will be shown in detail as we proceed.

With the aberration-corrected microscopes in use now, using a highly coherent field emission source will allow beam divergence to be very low. This can complicate the image as many beams will now contribute to the image formation if they are allowed through the objective aperture. The resolution limit of the current aberration-corrected microscope is approximately 0.1 nm and if an appropriate objective aperture is used for such resolution, many beams will contribute to the image and interfere. In some respects, the act of interpreting the various interference images will become much more complicated. However, the ability to control and measure the microscope condition has greatly improved. Optical diffractograms can be obtained in-situ and astigmatism correction can be done to near perfection. The specimen can be tilted into exact orientation and kept stable. Specimen parameters such as thickness also can be estimated to a much higher accuracy using tools such as an electron energy loss spectrometer (EELS). Image simulations also are faster and nearly instantaneous to check on the image types that are possible ahead of the actual TEM experiments. The detail of the HRTEM method with the aberration-corrected microscope is described in Chapter 2.

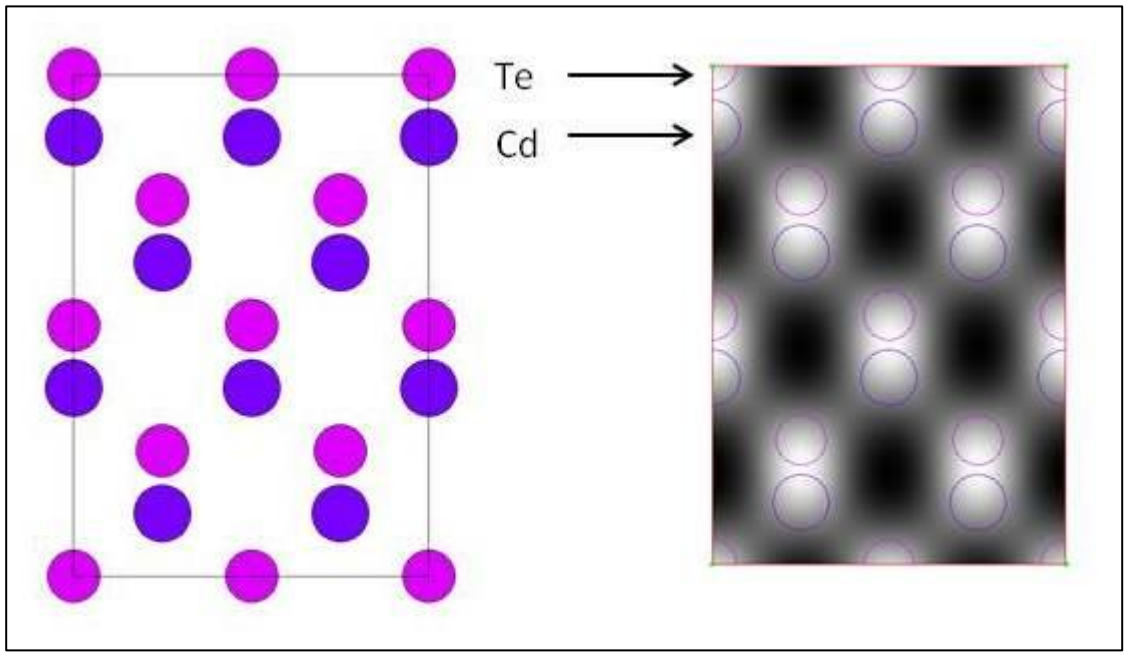

Figure 1-35: CdTe [011] model and the position in the multi-slice calculation on the right (t = 1.8 nm, Δf = -100 nm).

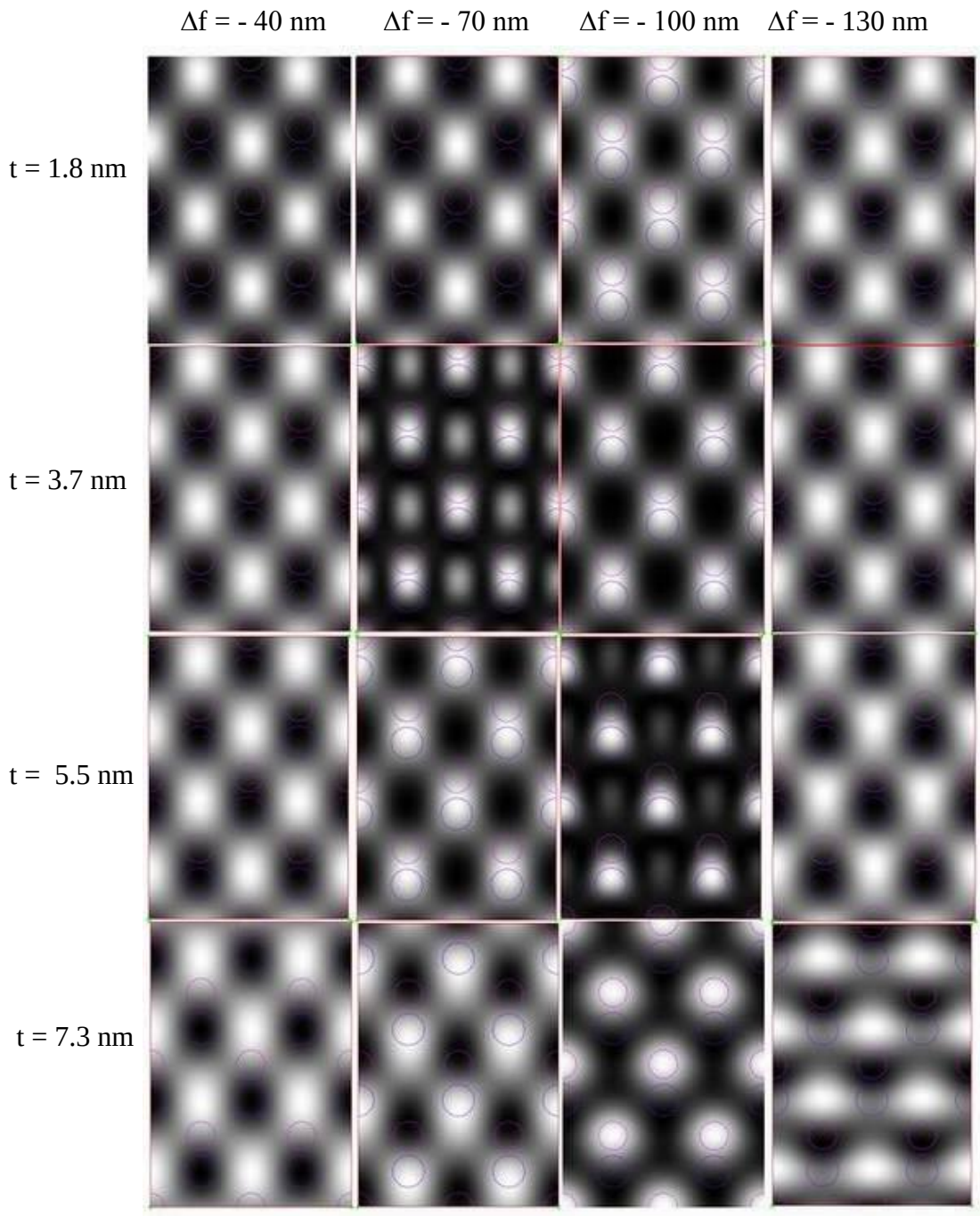

Figure 1-36: MacTempas® Multi-Slice image simulation for EM400 microscope, with objective aperture placed at 3.30 nm^{-1}, effectively putting only 7 beams through the objective aperture. Image series for t = 1.8, 3.7, 5.5 and 7.3 nm, and defocus from -40 nm in 30 nm increments to Δf= -130 nm. Te atoms are positioned at the corners of each image.

1.8.2 CdS in [$2\bar{1}\bar{1}0$] Orientation

CdS has the hexagonal wurtzite structure as previously described in Section 1.5.2. The useful orientation to study CdS by HRTEM is [$2\bar{1}\bar{1}0$], as it is equivalent to the [011] orientation in CdTe, and it is in this direction that was expected to be imaged in the HRTEM of CdS/CdTe heterojunction interfaces. The basal plane {0001} of the CdS is equivalent to the {111} close-packed plane in CdTe sphalerite structure. The displacement of the alternate {0001} plane in CdS by one atomic position would net the diamond cubic packing sequence of AaBbCc. Large letters and smaller letters indicate the different atoms in the interlocking FCC lattice of the diamond cubic material. In the CdS hexagonal packing, the pseudo close-packed basal plane would be an AaBbAa type of stacking sequence.

The indexing notation used for the hexagonal crystal system is the Miller-Bravais convention, which can be a little confusing; therefore, the crystallographic direction convention in the Miller-Bravais system when looking down on the basal plane of the structure was shown previously in figure 1-12a. The projected structure of CdS in the [$2\bar{1}\bar{1}0$] orientation also was shown previously in figure 1-12b. There are five other equivalent directions, which include [$11\bar{2}0$] and [$1\bar{2}\bar{1}0$]. The usefulness of this orientation for HRTEM is that it is equivalent to the [011] projection for CdTe. The Cd and S atoms are imaged end-on as well, and Cd and S atoms alternate in each {0001} layer. Each {0002} type layer is separated by 0.335nm, which is half the unit cell distance, indicated by "C" in figure 1-12(b). Cd and S atoms are separated by 0.146 nm.

A CdS TEM specimen was prepared from a single-crystal wafer following a cleavage plane that occurs along the {$1\bar{1}00$} prism plane of the lattice. Single-crystal CdS typically are produced by physical vapor transport (PVT), and purchased from outside suppliers. Two cleavage planes can be observed edge on, and bisecting the cleavage planes would be the {$2\bar{1}\bar{1}0$} plane. Specimens were prepared according to the description given in figure 1-17.

A diffraction pattern obtained from the sample in the $[2\bar{1}\bar{1}0]$ projection is shown below in figure 1-37. A few things become obvious from the diffraction pattern; there is a large amount of faulting along the {0001} basal planes as indicated by the streaks observed perpendicular to this direction. The {0001} planes are the easy direction of slip for CdS, and in the crystal growth process, a large amount of grown-in faults are introduced. The faults create local regions of cubic sphalerite structure. The tetrahedral coordination is maintained at such stacking faults. There is a stable phase of CdS which has a cubic sphalerite structure. A second detail that can be extracted from the diffraction pattern (in the $[2\bar{1}\bar{1}0]$ projection) is the calculation of the c/a_o ratio for the crystal. The literature value of c/a_o for CdS is 0.6713/0.4136 nm, which is 1.623 from the ASTM X-ray file #6-0314. The ideal c/a_o ratio is 1.633, which indicates that the c lattice direction is slightly shorter than ideal, probably due to a slight ionicity that is exhibited between the Cd and S atoms. Based on the measurement of (0002) and $(01\bar{1}0)$ reflections, a_o and c values can be extracted. The c/a_o ratio from the diffraction pattern is 1.623 which is the same as the ASTM card file value. This result was not verified further by X-ray diffraction analysis.

Lattice images of CdS were obtained using an objective aperture containing beams out to 5.96 nm^{-1}, which incorporates 31 beams out to the (0004) reflections. The Philips EM400 TEM with a fixed specimen holder was used; therefore, there was no capability to tilt the sample into orientation. A rather laborious method of wedging the sample iteratively based on the orientation of the specimen determined from its diffraction pattern needed to be utilized using small pieces of aluminum foil in order to obtain a zone axis orientation that was close to $[2\bar{1}\bar{1}0]$. As was the case with CdTe imaging, the orientation that could be obtained was never perfectly in the zone axis. Therefore, some effect of orientation could contribute to the lattice image. The microscope was operated at 120 kV, and the Cs, beam divergence, etc. were the same as for CdTe imaging, which was Cs = 1.1 mm, and a beam divergence of approximately 2 mrads. In the case of CdS, there was no extensive effort to try to resolve the Cd and S atoms as was the case for CdTe, since the spacing between the two atoms (Cd and S atoms) is 0.146 nm, which is considerably less than for CdTe. As

described in Section 1.8.1, the beam divergence effectively places a virtual aperture on the higher order reflections. Therefore, the reflections beyond the $(01\bar{1}1)$ at 3.17 nm^{-1} are not expected to contribute to the image. A list of reflections in CdS $[2\bar{1}\bar{1}0]$ is shown in Table 1-6.

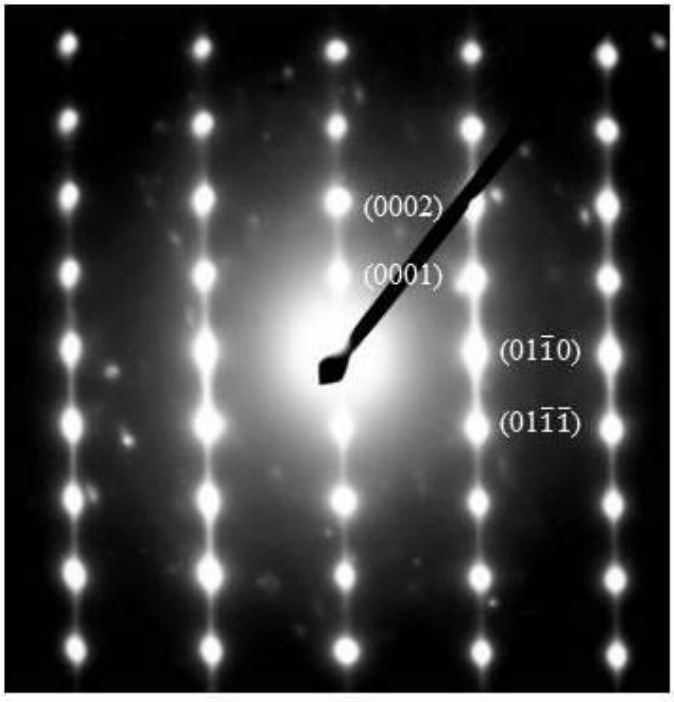

Figure 1-37: Diffraction pattern for CdS in the $[2\bar{1}\bar{1}0]$ projection with indices indicated. Streaking on the (000x) reflections indicate the presence of a high density of stacking faults on the basal planes. Spurious reflections are due to redeposited material on the specimen and slight distortion in the lattice is from the scanner used for the negative (the negative is not lying flat on the scanner bed).

A lattice image of CdS taken with 25 beams out to the (0004) reflection is shown below in figure 1-38. It is interesting to note the slight asymmetry to the image spots which could be coming from the alternate orientation of CdS atomic pairs as shown in the projection model in figure 1-12b. The resolution of the microscope is not

sufficient to resolve the pair of atoms. The atomic numbers of Cd (48) and S (16) are sufficiently different, compared to Cd (48) and Te (52) atoms in CdTe. That atomic scattering would be significantly different. Even though the individual atoms are not resolved, the pair appears asymmetrical and alternate in each layer as would be expected in CdS. Defocus for the image was approximately -100 nm based on the method described for the CdTe in Section 1.8.1.

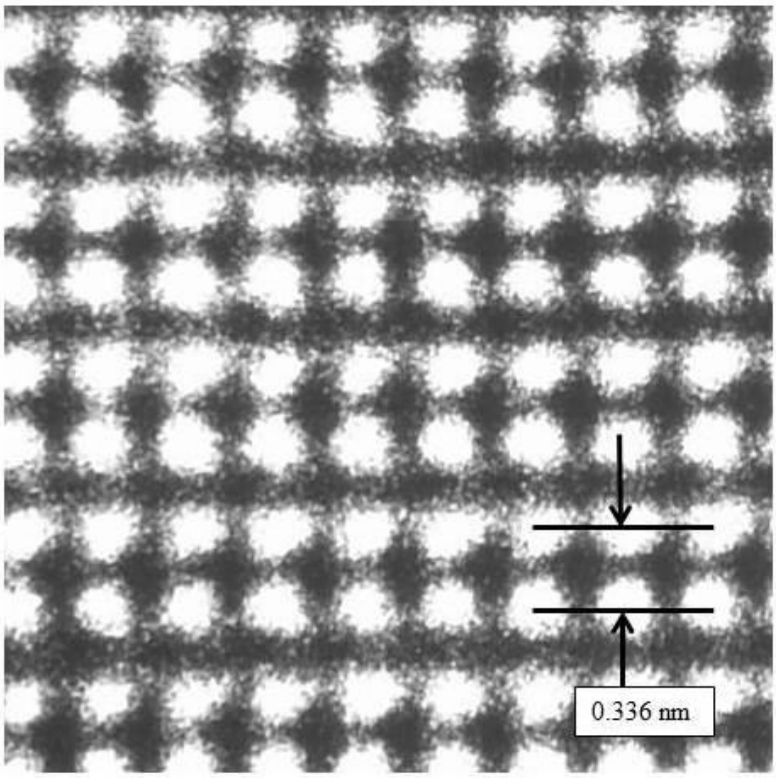

Figure 1-38: HRTEM image of CdS in [$2\bar{1}\bar{1}0$] projection. The bright spots indicate the position of the atoms, which are pairs of Cd and S atoms in an end-on projection. The lopsided nature of the image spots is interesting, reflecting the fact that a pairs of Cd and S atoms that are imaged together is expected to be asymmetrical. Defocus for this image was approximately - 100 nm (underfocus).

Planes	Spacing (Å)	1/d (Å-1)	Multiplicities	total beams
{0000}	0	0	1	1
{0110}	3.581	0.279	2	3
{0002}	3.357	0.298	2	5
{0111}	3.160	0.316	4	9
{0112}	2.450	0.408	4	13
{0113}	1.898	0.527	4	17
{0220}	1.791	0.558	2	19
{0221}	1.730	0.578	4	23
{0004}	1.678	0.596	2	25
{0114}	1.580	0.633	4	29
{0222}	1.520	0.658	4	33
{0223}	1.398	0.715	2	35
{0224}	1.225	0.816	4	39
{0330}	1.194	0.838	4	43
{0331}	1.176	0.850	4	47
{0332}	1.125	0.889	4	51

Table 1-6: Reflections from CdS <$2\bar{1}\bar{1}0$> type orientation. The indices are generic.

Image simulations based on the Bloch Wave formulation are shown in figure 1-39. A total of 25 diffracted beams were considered in the calculation. Conditions are the same as for the experimental image of figure 1-38 with the beam divergence of 2.1 mrads, which should have eliminated most of the higher order beam contributions. The potential plot or the PPD-type image is shown in (a) with the darker spot being the Cd atom position. The CdS image simulation has a peculiar characteristic of showing image spots (whether dark or bright) that are not centered on where the atoms are. They are offset by some amount. Some of the images show the asymmetric image spots, while some do not. Generally speaking, experimental lattice images of CdS showed mostly white atoms. This may be because white atom images are easier to see and have higher contrast, and it is the type of image that is often taken by the operator.

A multi-slice image simulation also was tried with CdS, and the model structure is shown in figure 1-40 and thickness and defocus series in figure 1-41. Basically the same sort of conditions as in the Bloch wave simulation were used, except that the objective aperture was hard set at 3.50 nm^{-1}, which lets 9 beams through, transmitted, (0001), $(01\bar{1}0)$, (0002), and $(01\bar{1}1)$ beams. Asymmetry in the image spots seen in Bloch wave calculation is also seen for some of the conditions, and offset with the projected atomic structure is also observed.

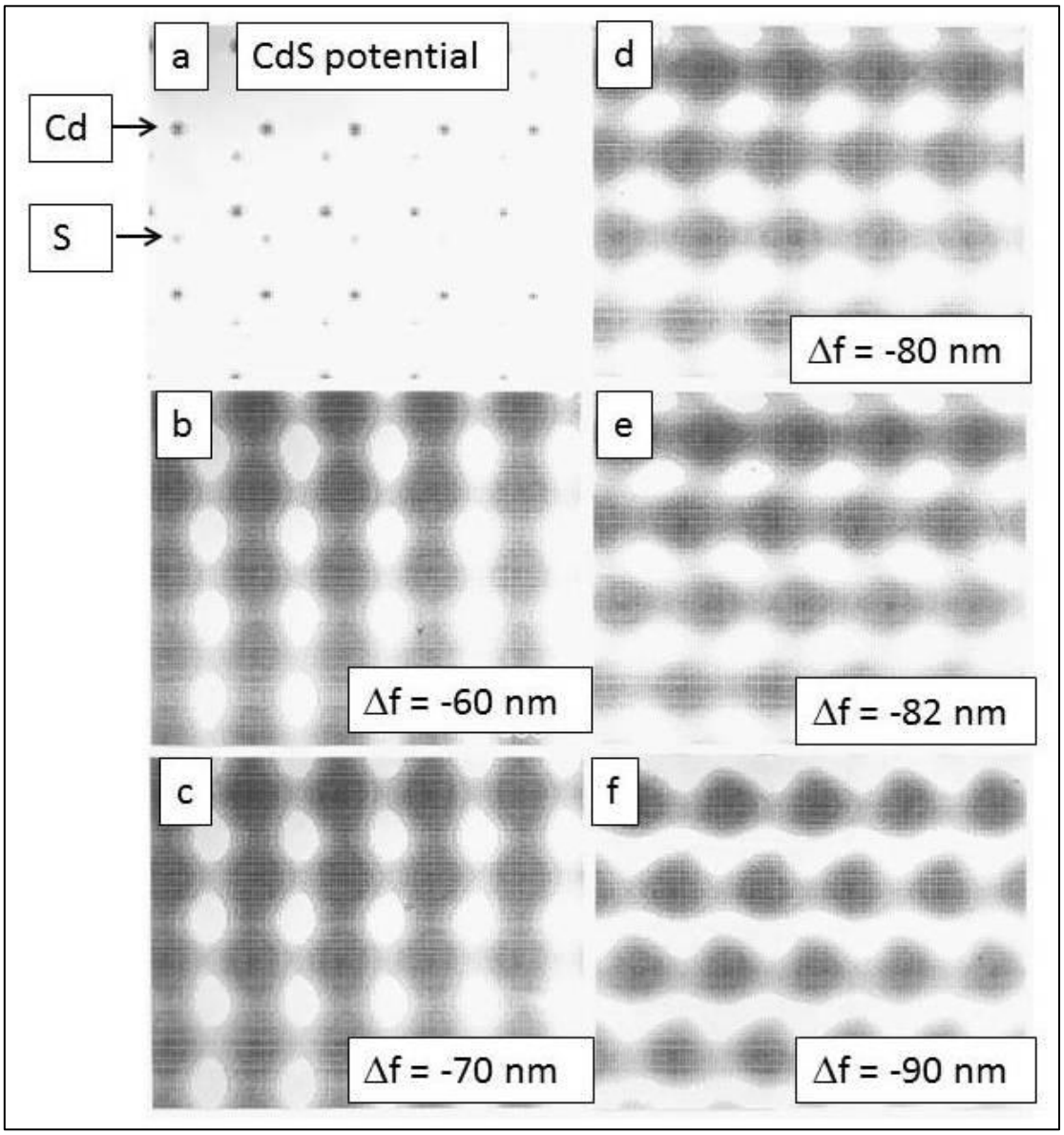

Figure 1-39: Bloch wave image simulation for CdS in the [$2\bar{1}\bar{1}0$] orientation. (a) The PPD-type image. Defocus values are (b) -60 nm, (c) -70 nm, (d) -80 nm, (e) -82 nm and (f) -90 nm. A total of 129 beams were used for the calculation, with 25 beams through the objective aperture. Thickness is 5 nm, and beam divergence α_c = 2.1 mrads.

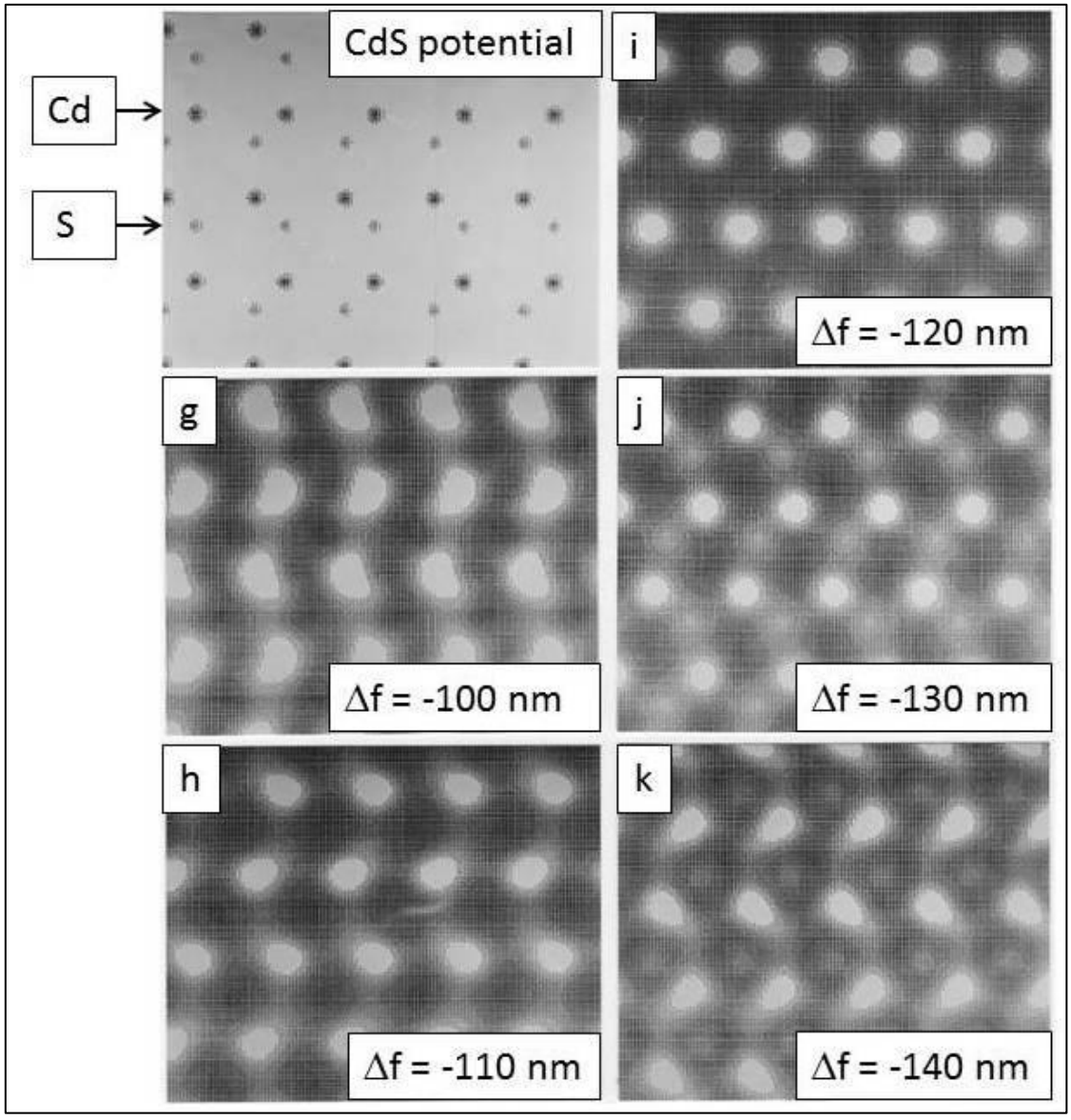

Figure 1-39 (continued): Defocus values at (g) -100 nm, (h) -110 nm, (i) -120 nm, (j) -130 nm and (k) -140 nm. As in the previous page, the position of the image spots (white atoms) is shifted with respect to the potential in an unpredictable manner.

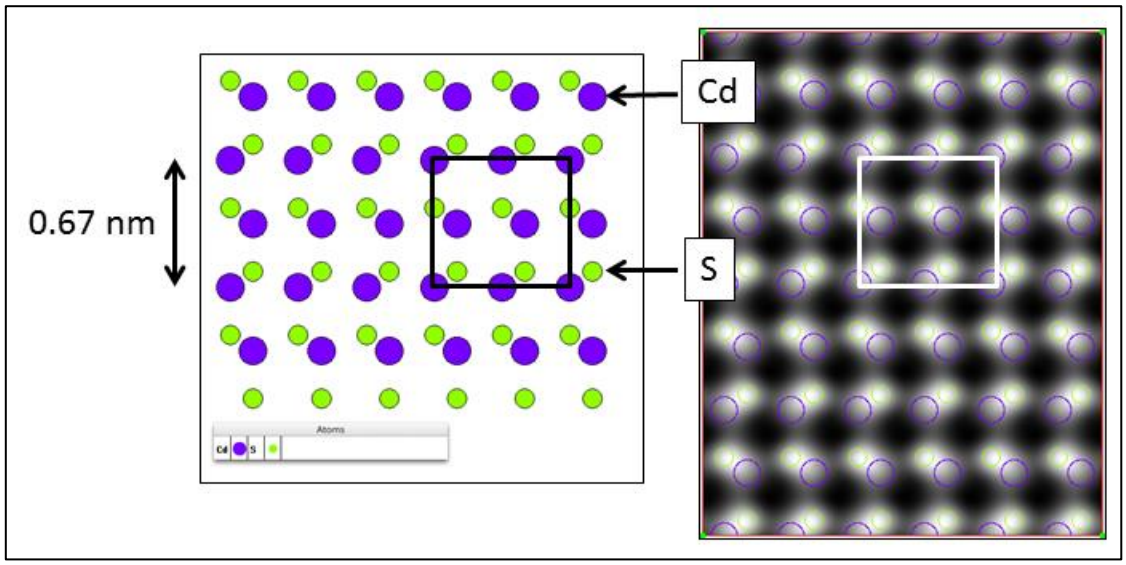

Figure 1-40: CdS [$2\bar{1}\bar{1}0$] MacTempas® multi-slice simulation model (left) and one of the simulated images (right) (t = 6.2 nm, Δf = - 90 nm).

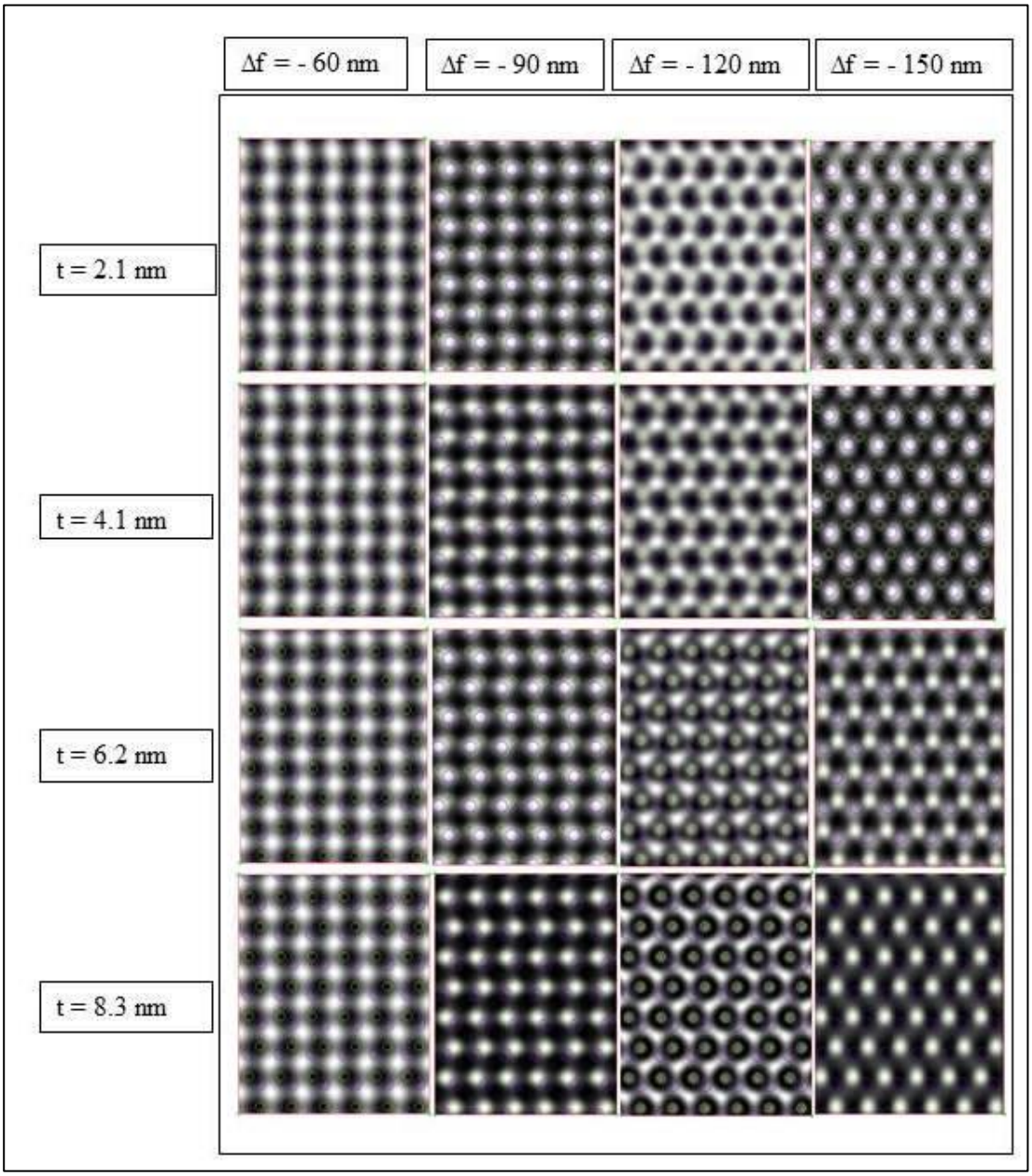

Figure 1-41: Lattice image of CdS [$2\bar{1}\bar{1}0$] by MacTempas® multi-slice program. Imaging conditions: 120 keV, Cs = 1.1 mm, α_c = 2.1 mrads, 9 beams through the objective aperture.

1.9 HRTEM of Defects in CdTe and CdS

1.9.1 Defects in CdTe

Lattice defects in CdTe follow the pattern observed for other cubic sphalerite structure and diamond cubic structure materials such as Si and Ge. Crystals having the cubic diamond structure generally have the {111} planes as the glide planes, and the perfect dislocations have the Burgers vector of the type b = $\frac{a_o}{2}$ <110>. Hornstra described two types of dislocations in silicon, a pure screw dislocation and the 60^o dislocation where the Burgers vector lies at an angle of 60^o to the dislocation line [Hornstra 1-51]. Both the screw and 60^o dislocations have the same Burgers vector, only the sense vectors ξ_g (line direction) are different.

Dislocation Type	Burgers Vector b	Sense Vector ξ_g
Screw	b = $\frac{a_o}{2}$ <110>	b = $\frac{a_o}{2}$ <110>
60^o	b = $\frac{a_o}{2}$ <110>	b = $\frac{a_o}{2}$ <10$\bar{1}$ >

In a diamond cubic structure, there are two distinct {111} planes, one closely spaced and the other wider spaced plane. The closely spaced plane is called the *glide* set and the wider plane is called the *shuffle* set [Hirth and Lothe, 1-52]. The shuffle plane slip requires breaking of one bond for each atom length of dislocation, while the glide set requires three bonds to be broken. For a long time, it was thought that shuffle set dislocation is favored in diamond cubic structure. It was Shockley who first proposed that perfect 60° dislocation in diamond structure can dissociate into partial dislocations bounded by an intrinsic stacking fault in 1953 [1-53], and that this should occur on the glide set of planes. A shuffle set dislocation would create an extrinsic stacking fault. Using weak-beam microscopy, Ray and Cockayne [1-54] determined that both screw and 60° dislocations in silicon are dissociated and that they bound an intrinsic stacking fault, giving support to Shockley's proposal. The dissociated partial dislocations are often called Shockley partials in his honor. The distance between the partials provide the means to calculate the stacking fault energy for the material.

The distinction between the glide and shuffle planes are shown in figure 1-42 with the CdTe in the $[0\bar{1}1]$ projection. Like the diamond cubic structure, CdTe has two interpenetrating FCC lattices, one of which is displaced by (¼, ¼, ¼) with respect to the other. The sequence of {111} planes is AaBbCcAaBbCc as indicated in figure 1-42. Formation of low energy stacking faults on the {111} planes involve insertion or removal of a pair of planes Aa, Bb, or Cc. The nearest neighbor bond angles and spacings remain unchanged across the fault. Therefore, the energy of these stacking faults is relatively low and they are easy to form. In the case of an intrinsic stacking fault, the stacking sequence may be described as AaBbCcAaBb-AaBbCc where the Cc planes were deleted. For an extrinsic stacking fault, the sequence may be described as AaBbCcAaC-cBbCcAa where extra Cc planes were inserted. The dashed line indicates the location of the fault in the stacking sequence. For the intrinsic case, the fault lies with the glide set of planes while, for the extrinsic case, the fault lies in the shuffle plane.

Dislocations and partial dislocations and how they are exactly configured are of great interest, as this would undoubtedly affect how they behave mechanically and electrically. If a sufficient density of these defects exists within the material, it may begin to have significant effects on the electrical transport properties, for example. The site of the dislocation may have dangling bonds which can be a trap for electrons or holes depending upon with which atom type the dangling bond is associated. HRTEM investigation of the compound semiconductors is an extension of much work that has been performed already using conventional TEM methods. Detailed analysis and determination of the type and nature of the defects will shed more light on how they may play a role in the mechanical and electrical properties of these materials. In a sphalerite structure, a convention for labeling dislocation was decided in 1979, at the International Symposium on Dislocations in Tetrahedrally Coordinated Semiconductors [1-55]. Dislocation on the glide plane can be designated as either Cd(g) or Te(g) depending on which atom it terminates with at the core, and the extra plane will point differently, as shown in figure 1-42. For the shuffle plane, the designation will be either Cd(s) or Te(s) depending upon the terminating atom. Another

terminology that is used sometimes for describing the dislocation is whether a dislocation terminates with a cation species (e.g. Cd atom) called α-dislocation, or anion species (e.g., Te atom) called β-dislocation [1-55]. If shuffle or glide cannot be determined, Cd(s) or Te(g) is the α-dislocation, while Te(s) or Cd(g) is called the β-dislocation (Lu and Cockayne) [1-60].

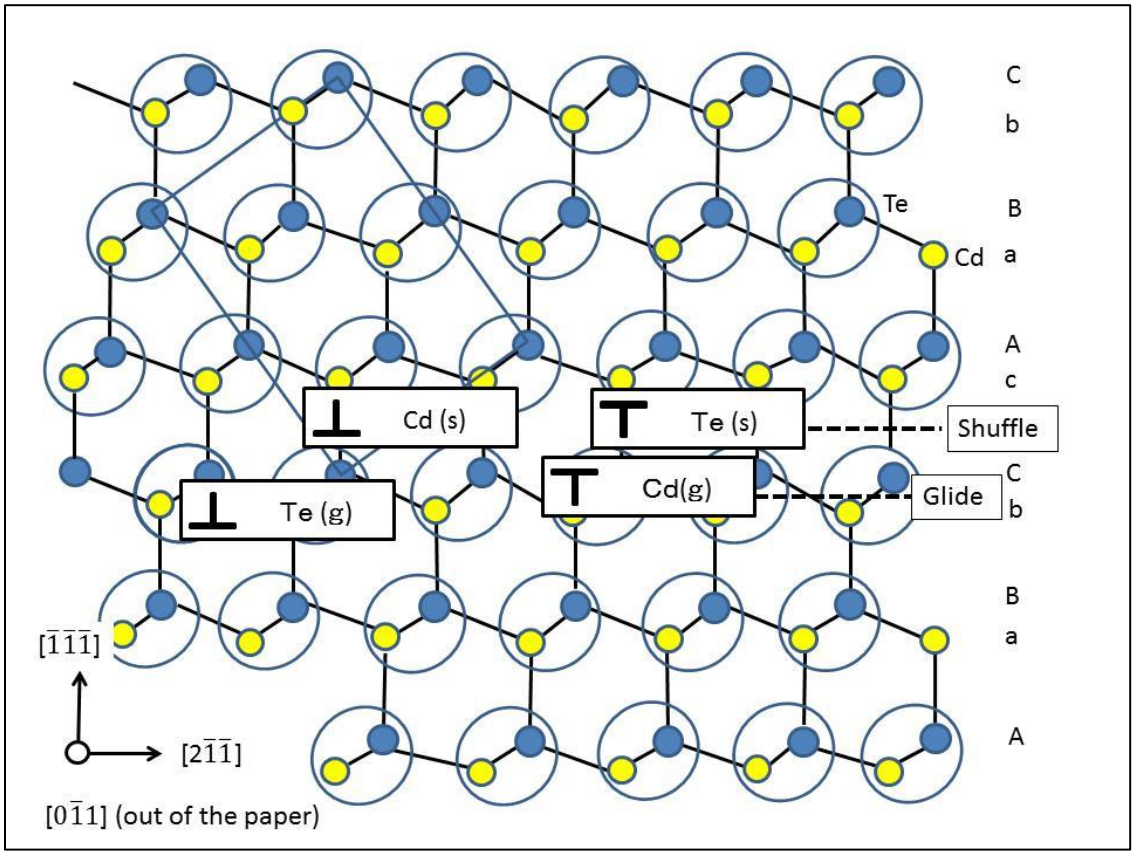

Figure 1-42: CdTe in the [011] projection showing the shuffle and glide planes and {111} plane stacking sequence.

Until only recently, it was not possible to image the dislocation core of tetrahedrally coordinated semiconductors with sufficient resolution to be able to make an unambiguous determination of atomic structure. A STEM imaging method using Z-contrast was used in 1995 for determination of the core structure of 60° and Lomer dislocations by McGibbon et al. [1-56] at the interface of CdTe/GaAs (001), but this method required image matching with calculation of *maximum entropy* or *most likely*

Z-contrast object function for each image [1-57]. This may have been the best method for the study of the dislocation core for compound semiconductors until the advent of aberration-corrected TEM, but it required a STEM tool with 0.13 nm probe size. With the availability of aberration-corrected TEM starting from approximately 2005, it became possible to obtain HRTEM images with sufficient atomic resolution to begin to start looking at the dislocation core and other defect structures of interest in semiconductor materials [1-58]. Aberration-corrected TEM was used to image the grain boundary structure in CdTe solar cell in atomic resolution by C. Li et al. [1-59] for example in 2014, but there is still little work being reported on atomic resolution imaging of dislocation core structure in CdTe.

Since the work on CdTe dislocations by weak beam microscopy by Lu and Cockayne in 1983 [1-60] and by Takeuchi et al. [1-61], it is known that most dislocations in CdTe that are split into partials are of the glide type [1-62, 63]. For the analysis of defects in this thesis, the resolution of the TEM is not sufficient to resolve atomic species, and pairs of atoms (Cd and Te) are imaged together in the [011] projection. Therefore, it is not possible to determine the core structure of dislocations. Nevertheless, some useful analysis can be done on various dislocations, and particularly on dislocation reactions observed by the HRTEM method. For historical reasons, the stacking fault created by vacancy agglomeration is called an *intrinsic* stacking fault, and stacking fault created by interstitial agglomeration is an *extrinsic* stacking fault. Practically speaking, an intrinsic fault is a local slippage of the planes, while an extrinsic stacking fault is characterized by an insertion of an extra layer of {111} plane. The two types of stacking faults can form by a variety of mechanisms. For example, two partial dislocations with the opposite sign can bind an intrinsic stacking fault, and an extrinsic stacking fault can be created by a Shockley dislocations on successive {111} planes. The lattice defects in semiconductor materials have received considerable attention because they can be detrimental to the electrical performance. The defects can trap carriers, reduce electronic transport, and can be the site of impurities that also affect the ultimate performance of the material. It has long been known that deformation in silicon and germanium increases their resistivity

[Gallagher 1-64]. Also the dislocation line can become charged, and their screening effect can be detected by Hall effect measurements [Pearson 1-65]. Generally, a great deal of effort is made to reduce their occurrence for improved device performance. Understanding of the nature of these lattice defects in the material, how they form, and how to reduce them has consumed considerable attention in the industry and in academia.

Dislocations in CdTe have been described in specific detail by Holt and Yacobi [1-66]. CdTe generally contains a much higher density of dislocations compared to other commonly used material such as GaAs, by an order of magnitude at a density of 10^5 to 10^6 cm^{-3}. This comes about due to low shear modulus for CdTe at approximately 19 GPa [1-67] compared to 50.9 GPa for Si [1-68]. It is much more prone to plastic deformation by Peierls mechanism and the dislocations are electrically active, and show large photoplastic effects (change in flow stress by illumination, or deformation induced changes to optical properties) [1-69]. These characteristics cause issues in using CdTe for various electronic applications, and the relationship between dislocations and electronic structure of CdTe has been investigated extensively and reviewed [1-70]. CdTe also is easily deformed at room temperature [1-71], and the deformation mechanism easily can be studied by room temperature indentation methods and characterized by cathodoluminescence for example [1-72]. In a typical II-VI compound semiconductor, the material contains a high level of point defects from residual impurities from crystal growth and it is thought that the interaction of these impurities with moving dislocations cause a variety of photoplastic effects [1-73].

The various types of dislocations that are present in CdTe now can be described in more detail. To maintain proper indices for the Burgers vectors, the description is for dislocations along the $[\bar{1}\bar{1}0]$ direction (for the sense vector $\vec{\xi}$) as seen from the (110) projection, with the slip plane on $(1\,\bar{1}\,1)$ plane. When they dissociate, the 60° dislocations form 30° and 90° dislocations, expressed by the following reactions:

$$\frac{a_o}{2}[10\bar{1}] \rightarrow \frac{a_o}{6}[21\bar{1}] + \frac{a_o}{6}[1\bar{1}\bar{2}] \qquad \text{(Eqn. 1-18)}$$

$\vec{b}_{60°}$ $\vec{b}_{30°}$ $\vec{b}_{90°}$

The $\frac{a_o}{2}[10\bar{1}]$ Burgers vector for the 60° dislocation comes from the fact that if an extra {111} plane is inserted into the projection as shown previously in figure 1-42, the Burgers circuit will give a vector that will not be in the plane of the paper; rather, it will be at a 60° angle with respect to the dislocation line. This will be shown in more detail in the example shown in figure 1-48. The stacking fault that forms between the two dissociated partials is an intrinsic stacking fault, as it has a missing double layers in the {111} plane sequence. Two leading partial dislocations on differing {111} slip planes can meet and combine to form a Lomer-Cottrell dislocation, expressed by a reaction:

$$\frac{a_o}{6}[\bar{1}2\bar{1}] + \frac{a_o}{6}[1\bar{1}2] \rightarrow \frac{a_o}{6}[011] \qquad \text{(Eqn. 1-19)}$$

The schematic for Lomer-Cotrell dislocation is shown graphically in figure 1-43. Lomer-Cottrell dislocations also are called *stair-rod* dislocations because they appear like the rod to hold down the carpet (stacking faults) at the corner of the lattice where they meet [1-52].

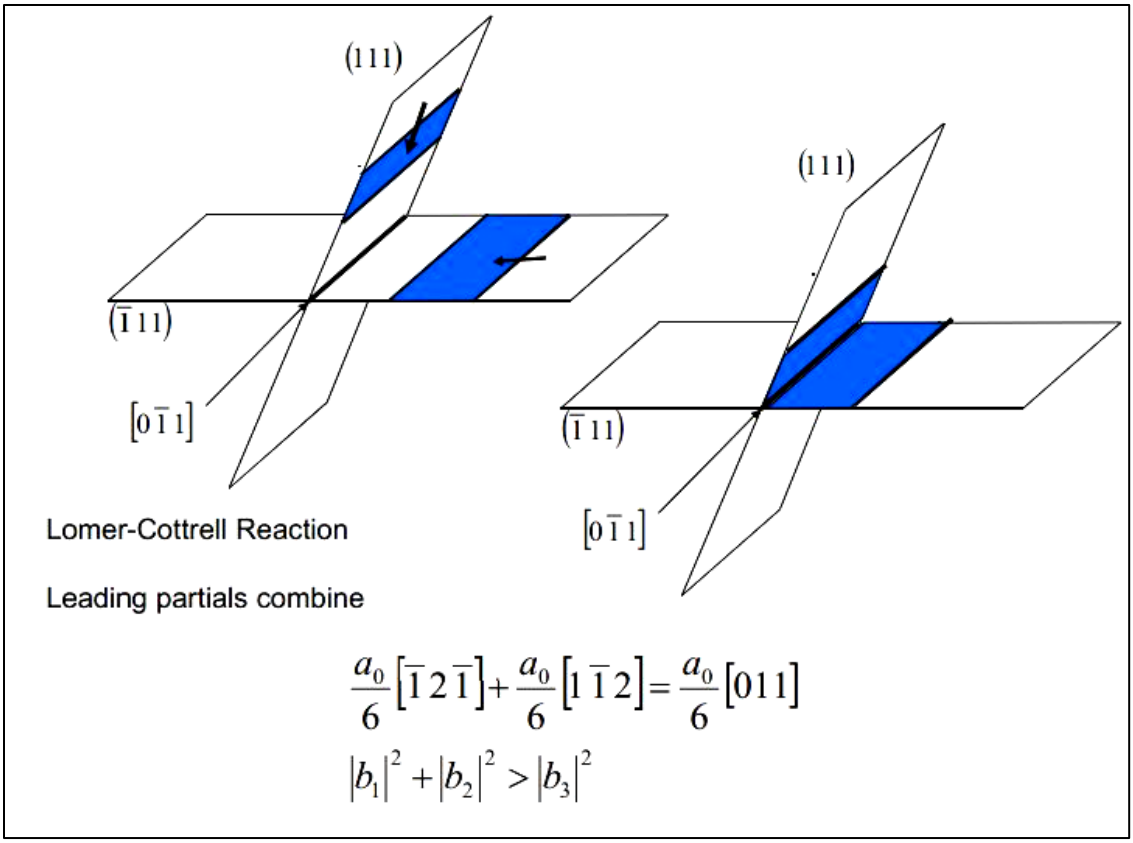

Figure 1-43: Schematic description of Lomer-Cottrell dislocation reaction between two partial dislocations on separate {111} slip planes, creating a sessile dislocation with burgers vector of $\frac{a_o}{6}$ [011].

The extent of the stacking fault bounded by two Shockley partial dislocations is determined by the repulsion force (F) between the partial dislocations and the stacking fault energy γ_{SF}. The width, d_o of the stacking fault can be derived from an equation in Hirth and Lothe (eqn. 10-15, 2nd edition) [1-52], for FCC metals.

$$d_o = \frac{F}{\gamma_{SF}} \qquad \text{(Eqn. 1-20)}$$

The two partials bounding the stacking fault repel each other, and the extent of their separation is smaller as the stacking fault energy becomes larger. The CdTe has relatively small stacking fault energy of approximately 10 mJ/m^2, according to Vere et al. [1-74] and Winkler et al. [1-75]. In comparison, the stacking fault energy in silicon is estimated to be approximately 51 mJ/m^2 based on weak beam microscopy and using anisotropic elasticity theory by Ray and Cockayne [1-54]. Therefore, the stacking faults will be larger in extent in CdTe compared to those in silicon.

Another common type of dislocation in the diamond structure is the Frank partial dislocation. This will occur if a plane is missing or added, and at the edge of such a stacking fault, there will be Frank partials with the Burgers vector of the type $a_o/3$ [111]. Frank partials can only move by climbing, which involves addition or removal of atoms at the dislocation core. Frank dislocations are often in the form of a loop (Frank Loop) and described in more detail by Read (page 96) [1-76]. The stacking faults bounded by Frank partials with an extra {111} plane will be extrinsic, while the faults bounded by a loop that form from vacancy condensation with missing {111} plane will be intrinsic.

A screw dislocation has its Burgers vector in the same direction as the sense vector of the dislocation as shown in figure 1-44. Screw dislocations can also split into two 30° partials as shown below, bounding a stacking fault between the partials:

$$\frac{a_o}{2}[110] \rightarrow \frac{a_o}{6}[121] + \frac{a_o}{6}[21\bar{1}] \qquad \text{(Eqn. 1-21)}$$

A screw dislocation is not very amenable to HRTEM imaging since it is not obvious how the dislocation should appear in [011] projection. If a pure screw dislocation is imaged along the dislocation line, for example, the atomic arrangement in the

projection will form a helical arrangement of atoms along the core, analogous to looking down a circular staircase. If the dislocation line is imaged perpendicular to the line, the disruption in lattice symmetry would only occur along the line and the crystal would be perfect above and below the dislocation line. It would not be obvious how the HRTEM image might look, as it would vary as a function of the amount of material that lies above and below the dislocation line. If the screw dislocation splits and forms partial dislocations, the stacking fault that forms between the partials will become visible if imaged edge-on.

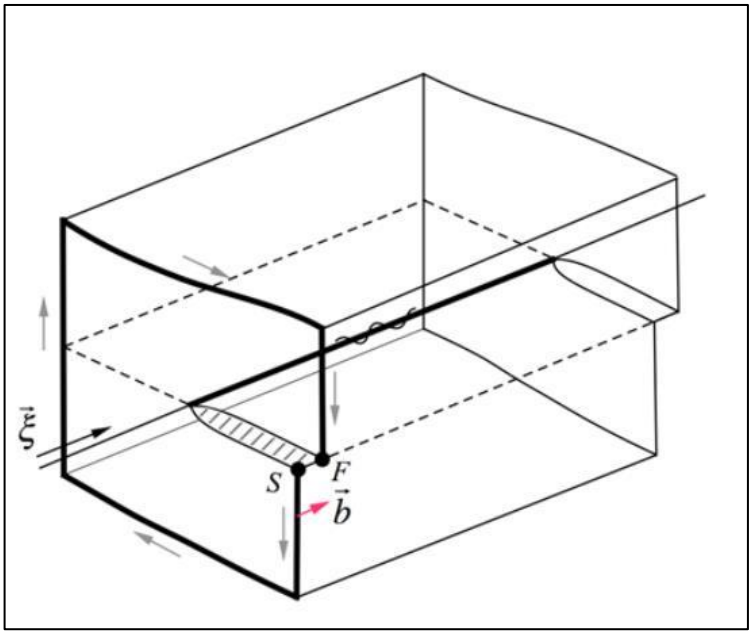

Figure 1-44: Schematic for a screw dislocation, showing the sense vector $\vec{\xi}$ and Burgers vector $\vec{b}$. From Nix [1-77].

Another common form of dislocation is a dislocation loop, as shown in figure 1-45 by Nix [1-77]. A dislocation loop can form from a variety of mechanisms, such as interstitial or vacancy condensation, or by Frank-Reid mechanism [1-78], for example. This loop is composed of edge and screw components, and the sense vectors and the

expected motion of the dislocation components to an applied stress τ are shown in the figure.

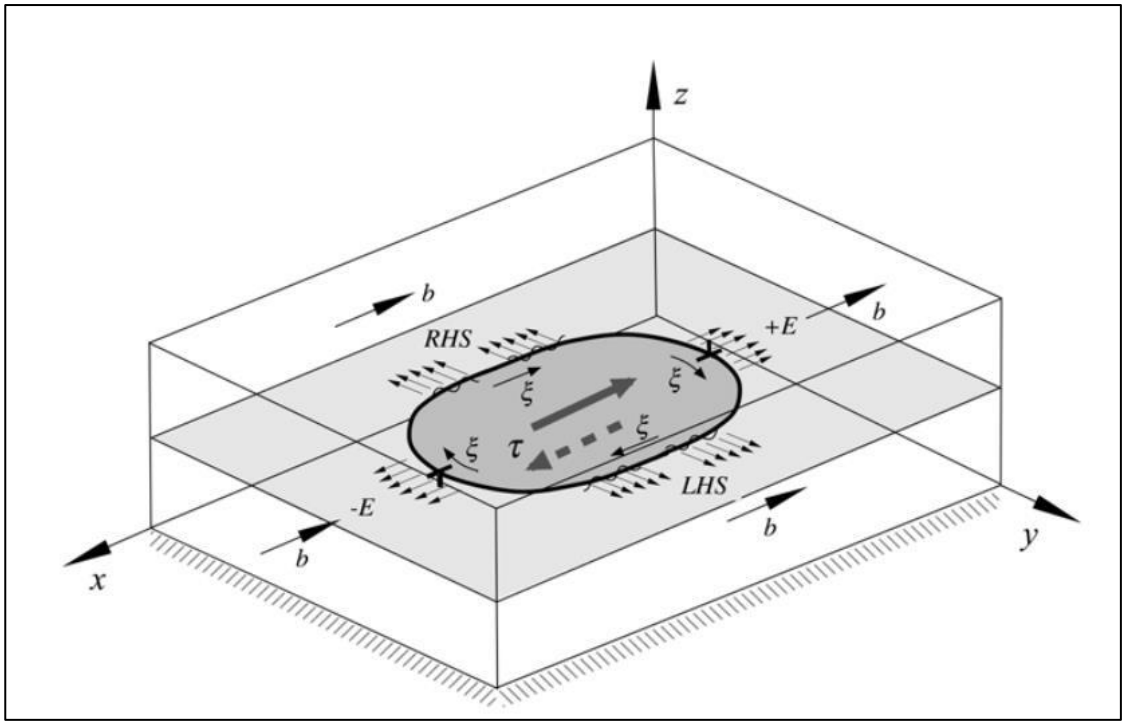

Figure 1-45: Schematic for a dislocation loop containing screw dislocation and edge dislocation components, and the direction that the dislocation will move in response to a shear stress **τ**. From Nix [1-77]. In the figure, the loop will expand with the sheer stress τ as indicated.

HRTEM of CdTe will be limited here to the type of dislocations that can be observed in the [011] projection, and amenable to easy interpretation. It means that only those dislocations can be imaged end-on, with the sense vector $\vec{\xi}$ that is parallel to the electron beam. Therefore, the analysis will be limited to edge dislocations. Additionally, because only a very thin portion of the specimen is imaged, the dislocations possibly will have been affected from their original bulk configuration during specimen preparation. Because of the very close proximity of the surface (at the

top and bottom of the specimen surface) and the edge of the hole formed by the specimen ion-milling, some dislocations would likely have been modified from the bulk configuration by the surface. This would be the case for dislocation loops for example, where the specimen preparation method might have intersected the loop. It may be possible that portions of the loop may remain in the viewing volume of the specimen, but at the edge of the specimen where the HRTEM imaging requires a thickness less than ~10 nm, it is likely that the dislocation loop would have been cut and some relaxation may have occurred along the dislocation line. Much would depend on the effect of the surface on the dislocation (image force for example), and the state of Peirels force on the dislocation line. Screw dislocations when lying on the {111} planes that are imaged end-on in the [011] projection would be difficult to image since there is little displacement in atom positions that occur along the dislocation line, aside from some strain approximately the line along its projection. If the screw dislocation were to lie on a {111} plane that lies 35.3° from the [011] normal, the dislocation line may give some contrast but it would appear as some complex function of specimen thickness and imaging condition. A stacking fault that is bounded by the screw dislocation would also provide some contrast. This situation was not investigated in this work, and only the dislocations (and stacking faults) that are imaged end-on are analyzed herein.

CdTe TEM specimens were prepared from the boule as described in the specimen preparation method in section 1.7. At initial glance the TEM specimen usually contained a very large amount of defects. Two BF images taken with two different two-beam diffracting conditions are shown in figure 1-46. The image contrast is consistent with small dislocation loops. The analysis to determine whether the loops contain intrinsic of extrinsic faults was not done. However, the extraordinarily high density of the defects is clear. A rough estimate of the defect density based on the BF micrographs works out to be ~10^{10}/cm^2. The typical reported value of bulk dislocation density is 10^5 to 10^6 /cm^2 [1-72]. Therefore, the defect density is higher by 5 to 6 orders of magnitude. When the defect density estimation is made using the HRTEM images, the number is even higher at approximately 10^{14}/cm^2 as more defects are counted

compared to BF images. This discrepancy between the published bulk defect density and those observed in the TEM specimens was realized much later, therefore it was unfortunate that a wrong impression was initially obtained about the relative quality of the CdTe sample in terms of defect density. What had happened was that the ion-milling probably had introduced a considerable amount of damage into the sample, and this had skewed the interpretation of the defect density. Although many large-scale twins, stacking faults and long dislocation lines were likely intrinsic to the material, many short length dislocation loops observed as shown in figure 1-46 are probably introduced during ion-milling.

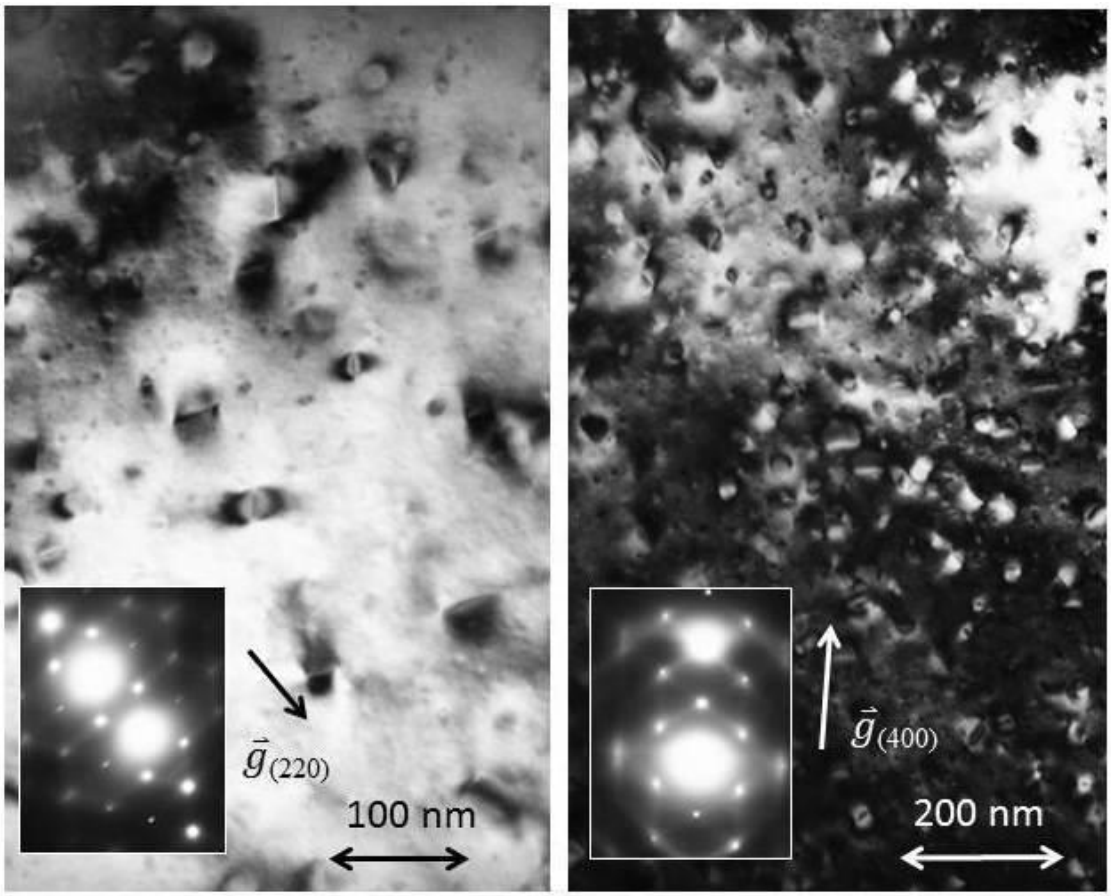

Figure 1-46: Two-beam BF micrographs of CdTe showing the extraordinarily high defect density, estimated to be ~ 10^{10}/cm^2. The sample is after ion-milling. Diffracting conditions for the images are indicated. The specimen was close to the [011] zone axis.

The sensitivity of CdTe to ion-beam damage also is indicated by sample deterioration during imaging at 120 kV. An extensive amount of ablation occurs in the specimen over time, as indicated in figure 1-65 in section 1-10, which was taken over 30 minutes of viewing. Typical current densities used in HRTEM imaging ranged from 10 to 20 A/cm^2. In normal conventional TEM using a LaB_6 filament, the current density is typically between 1 to 5 A/cm^2. Long before the extensive ablation took place as in figure 1-65, the motions of atomic species and dislocation movement were observed and this is described in more detail in section 1-10. Even though the specimens were highly defected, this made it much easier to study and observe various dislocations especially as they moved. Later, CdTe specimens were prepared with much reduced Ar milling conditions of approximately 1 keV at the finish, about half of what was initially used. Figure 1-47 shows a BF image taken under two-beam condition near the (011) zone axis of a specimen prepared with the lower ion-milling condition. The long dislocation lines are probably much more representative of the as-grown dislocations present in the crystal. Smaller features including some of the small loops, may have been produced by ion-milling. The dislocation density for the micrograph comes out to approximately $10^8/cm^2$, still higher than the literature bulk values but a more reasonable value.

The HRTEM images of defects in CdTe were taken with either 7 or 13 beams through the objective aperture. High beam intensity and beam divergence (focused beam) were used in order to keep the exposure times at or below 1 sec. The goal was not to obtain the highest possible resolution, but to obtain high contrast images with moderate resolution and short exposure times. As such, the resolution of the images is at approximately 0.3 nm. Thus, most of the images obtained were with bright spots, which correspond to the positions of Cd and Te atom pairs. The [011] orientation was always used because in this orientation, two sets of {111} planes can be imaged in end-on projection, which allows many dislocations and stacking faults also to be imaged on end-on projection. Typical HRTEM images contained many twinned regions, along with short and long stacking faults. Most of the stacking faults were intrinsic, but there

were many extrinsic faults as well which were associated with Frank dislocations. There also were complex dislocations with stacking faults intersecting along separate {111} planes.

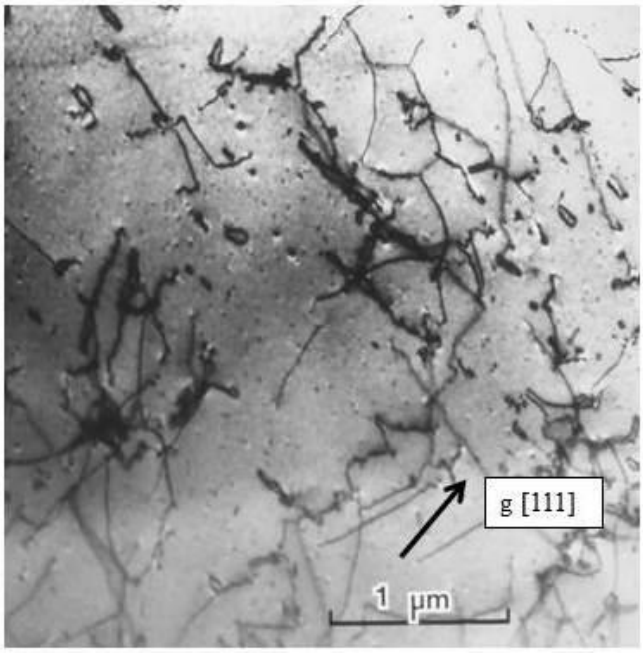

Figure 1-47: BF micrograph of CdTe in two-beam condition. Specimen near <011> zone axis. The dislocation lines were likely present in the bulk prior to ion-milling.

An example of a 60° dislocation which has split into 30° and 90° partials creating an intrinsic stacking fault between them as in equation 1-18 is shown in figure 1-48. A Burger vector circuit according to the RH/SF convention (Right Hand/Start to Finish) is shown in the figure. The zone axis for this image is indexed as [110] in this figure and the crystallographic directions are indicated below the micrograph. The direction of $\vec{b}$ might appear to be $\frac{a_o}{2}[\bar{1}12]$, but the vector to the position of the terminating position of the circuit actually is $\frac{a_o}{2}[\bar{1}01]$ which is inclined 30° to the

surface. The same Burgers vector is then inclined 60° to the sense vector of the dislocation, which is into the paper or $[\bar{1}\bar{1}0]$, hence the name *60° dislocation*.

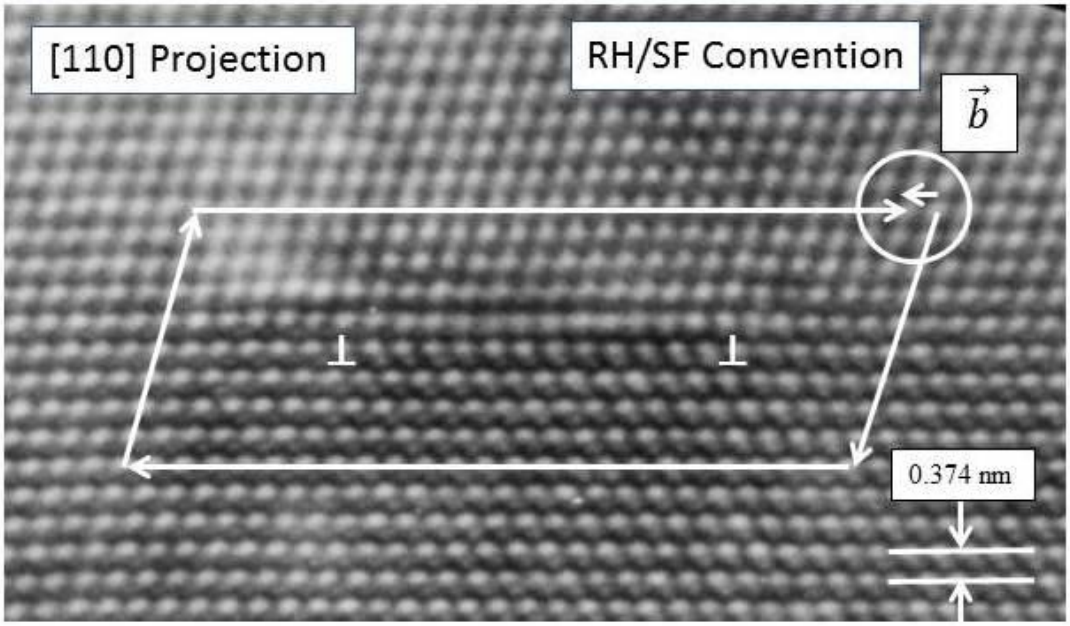

Figure 1-48: Lattice image of 60° dislocation which has split into 30° and 90° partials, creating an intrinsic stacking fault. The Burger circuit indicates that the overall Burgers vector of the dislocation is $\frac{a_o}{2}[\bar{1}01]$. The dislocation to the right is the 90° partial and on the left is the 30° partial.

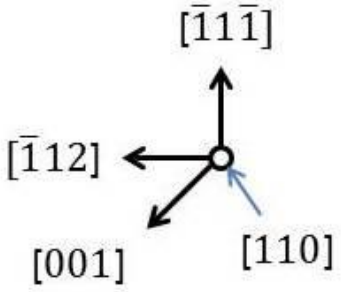

A close-up of the Burgers vector determination for above figure 1-48 is shown in figure 1-49 with Thompson tetrahedron shown in the corner. Thompson tetrahedron construction for the 60^o dislocation into two Shockley partial dislocations is shown in figure 1-50. The notation for the reaction will be as follows with the Burgers vector and the type of dislocation indicated below.

$$\begin{array}{ccccc} BC & = & B\delta & + & \delta C \\ \frac{a_o}{3}[\bar{1}0\bar{1}] & \rightarrow & \frac{a_o}{6}[\bar{2}\bar{1}1] & + & \frac{a_o}{6}[\bar{1}12] \\ 60° & & 30° & & 90° \end{array} \qquad \text{(eqn. 1-22)}$$

The Burgers vector directions for all of the dislocations are indicated in red in the Thompson tetrahedron in figure 1-50.

Figure 1-51 shows the stacking sequence of {111} planes (containing both Cd and Te) for the image in figure 1-48, showing that the stacking fault contained between the two partial dislocations is an intrinsic stacking fault, which has a missing B plane of atoms in the figure. Since we do not have the resolution to resolve individual Cd and Te atoms, the details of the stacking sequence (ABC and abc planes as shown in figure 1-42) cannot be distinguished, nor the details of the core of the structure at the dislocation. Therefore, whether the dislocation is shuffle or glide, or whether it is α or β type cannot be determined from the image. Nevertheless the nature of the dislocation reaction can be established by these lower resolution HRTEM images.

The partial dislocations in figure 1-48 are separated by 5.2 nm. Lu and Cockayne [1-60] and Hall and Vander Sande [1-79] both used weak beam microscopy to determine stacking fault energy in CdTe based on the separation of partials. They plotted the partial separation as a function of dislocation line orientation, and used the elasticity model to calculate the stacking fault energy. Hall and Vander Sande obtained partial separation between 8 to 16 nm for dislocation line angle between 45 to 90°, while Lu and Cockayne obtained separation between 6 to 15 nm for line orientation ranging from 20 to 90°. Hall and Vander Sande obtained stacking fault energy γ_{SF} = 10.1 $\pm$ 1.4 mJ/m^2 while Lu and Cockayne obtained 9.7 $\pm$ 1.7 mJ/m^2. A remarkably close value for CdTe crystal that was prepared differently from different sources. For the specific case of 60° dislocation that separated into 30° and 90° partials, the equilibrium separation between the partial is given by Hirth and Lothe [1-52] in equation 10-15, page 315:

$$r_e = \frac{\mu b_2^2}{8\pi\gamma_{SF}} \frac{(2-\nu)}{(1-\nu)} \left(1 - \frac{2\nu cos2\beta}{2-\nu}\right) \qquad \text{(eqn. 1-23)}$$

where μ = shear modulus = E / 2 (1+ν)

ν = Poisson ratio (0.41 for CdTe)

E = Young's modulus

b_2 = modulus of partial dislocation

γ_{SF} = stacking fault energy

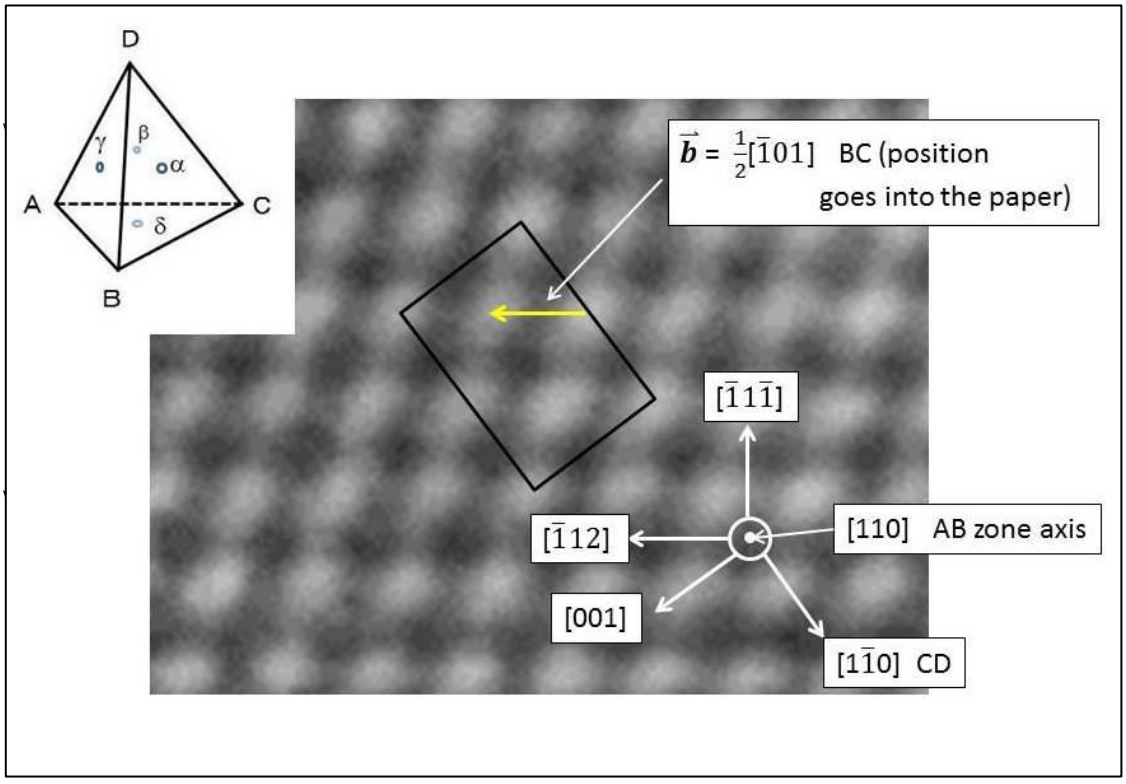

Figure 1-49: Expanded view of the Burgers vector construction for figure 1-48, showing the $\vec{b} = \frac{a_o}{2}[\bar{1}01]$ direction. The direction shown by the arrow points 30° into the plane of the paper.

Figure 1-50: Thompson tetrahedron construction for 60° dislocation dissociating into 30° and 90° Shockley partial dislocations. The line drawing on the left is from Nix [1-77]. Thompson tetrahedron construction is based on Hirth and Lothe [1-52].

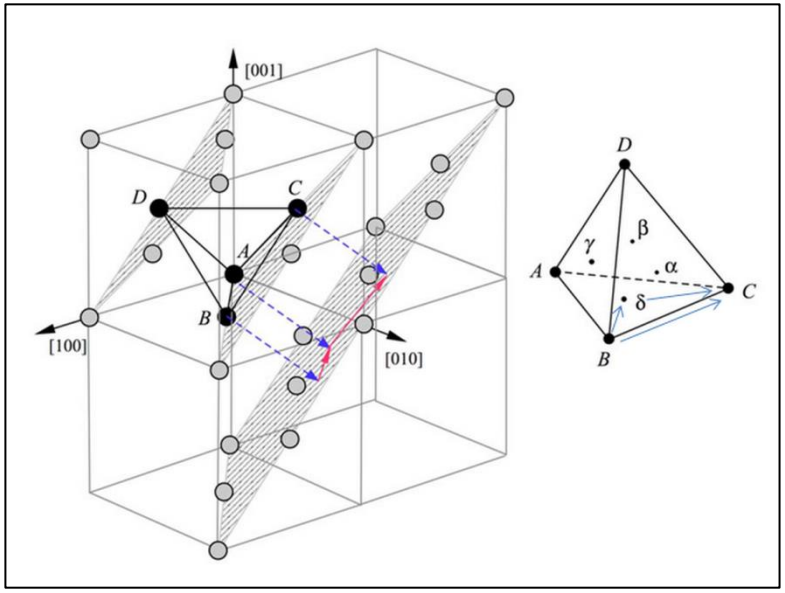

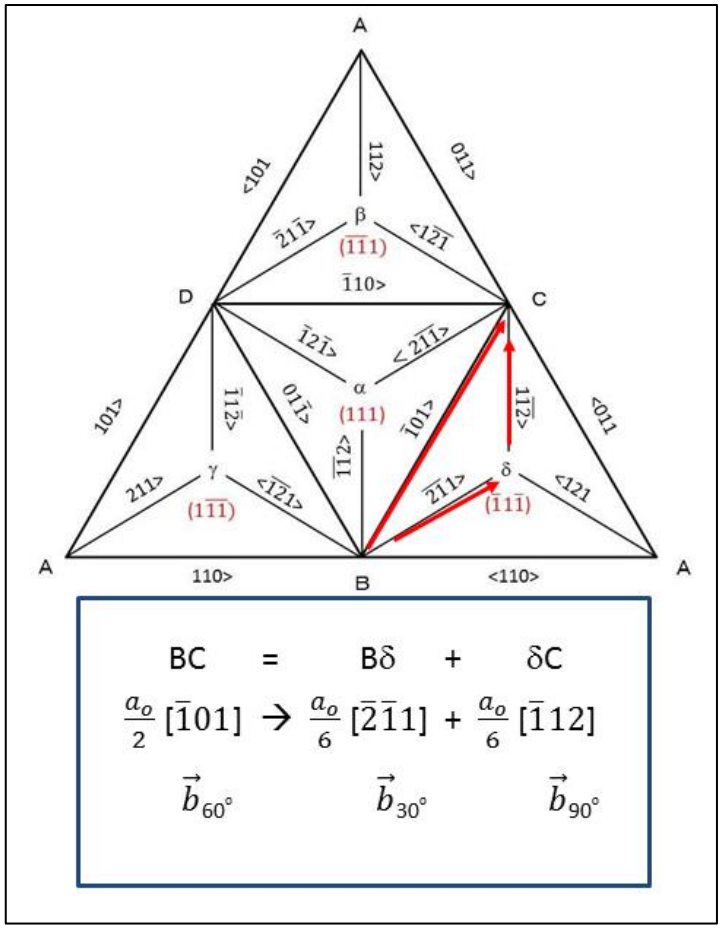

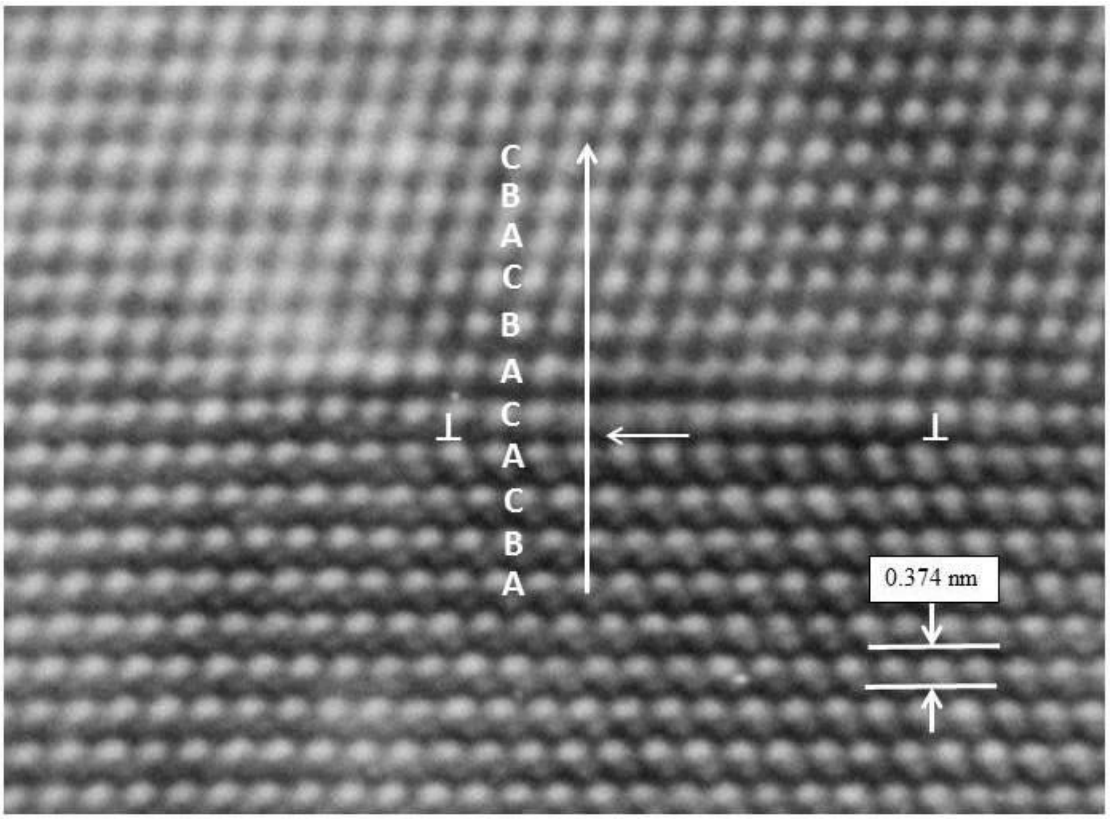

Figure 1-51: Stacking sequence of the {111} planes showing that the fault contained between the partial dislocations is an intrinsic stacking fault (missing B plane indicated by the arrow).

Using 5.2 nm separation to solve for γ_{SF} from eqn. 1-23, the $\gamma_{SF} = 32.7$ mJ/m^2, which is much larger than the calculated value by Lu and Cockayne and by Hall and Vander Sande. Alternatively, using their γ_{SF} values and the Young's modulus of 53.51 GPa that they had used (C_{11} in ref. [1-80]), the calculated value for partial separation r_e is ~18 nm. The experimental separation value for the 60° dislocation orientation reported by Lu and Cockayne is ~10 nm, while the Hall and Vander Sande number is ~12 nm. Therefore, it can be concluded that the simple formula based on Hirth and Lothe in eqn. 1-23 overestimates the γ_{SF} by about 50% for a given partial separation compared to the full anisotropic model used by Lu and Cockayne and by Hall and Vander Sande.

In order to obtain better statistics for the partial separation for the dissociated 60° dislocation, 40 dissociated 60° dislocations of the type shown in figure 1-48 were measured from various HRTEM images. Care was taken to count only those dislocations that were isolated and away from the edge of the specimen. The result is shown below

$r_e = 7.2 \pm 2.1$ nm

Using E = 52 GPa $\gamma_{SF} = 24 \pm 6$ mJ/m^2

Young's modulus of 52 GPa is used, as it is the currently accepted value listed by various CdTe suppliers and current literature lists a range of values between 50.3 to 68.1 GPa based on both the theoretical model and experiments [1-81]. Obviously, the calculated value for the γ_{SF} is considerably larger than the ~10 mJ/m^2 reported in the literature, and the partial separation is shorter. It should be noted that dislocations measured by the weak-beam method were long and meandered in the specimen, having a variety of angles with respect to the Burgers vector. The dislocation line also contained constrictions, and it is not all that clear whether all of the dislocations that were measured were of the same type, as it could not be distinguished whether the faults contained by the dislocations were intrinsic or extrinsic. The partial separations measured here are all of the same type of dislocation and the same character, namely pure 60^o dislocations that had split into partials. In addition, the dislocations are not associated with any other dislocations, and do not contain any reactions or constrictions. One key observation that can be stated here is that when a dislocation reacts with another dislocation, the separation of the partials associated with them becomes much larger. In addition, when one of the partials from the 60° dislocation exits the crystal, the stacking fault length is also much longer. These effects are seen in other examples to follow. It is clear that partial separation is affected by a variety of effects, which is pointed out by Lu and Cockayne and other publications from Cockayne's group [1-82]. An additional qualification is that in HRTEM imaging, the defects are very close to the

surface above and below the dislocation. Therefore, the forces, such as the image force acting on the dislocation cannot be discounted and equation 1-23 does not take into account the proximity of the surface.

Figure 1-52 show an example of several types of dislocations. The HRTEM images were taken with 7 beams admitted through the objective aperture. (1) is a 60° dislocation where one of the partials has moved out of the crystal. It contains an intrinsic stacking fault to the edge of the crystal, bounded by remaining partial 90° dislocation. The intrinsic character of the stacking fault can be determined by the stacking sequence across the stacking fault. (2) is a set of three 60° dislocations on successive {111} planes, which created a small region of twinned area inside the crystal. An enlarged image of this defect is shown in figure 1-53. The inset on the right shows the location of the three partials that form the boundary of the twinned region. The stacking sequence of the {111} planes shows that structure is equivalent to removing three successive planes of Cd-Te atom pairs. On the left side of the defect, the partials are separated further, and the approximate location of the dislocations is indicated. (3) is an example of a locked dislocation that can be described as a reaction of two dislocations. Initially thought to be a reaction of two partial dislocations to form a Lomer-Cottrell lock, it appears to be a reaction between 30° partial dislocation and a Frank dislocation to form a locked dislocation with Burgers vector of the type $\frac{a_o}{6}[\bar{1}10]$. The faulted region that points downward is not clearly imaged, which makes analysis difficult. A somewhat clearer HRTEM image taken at slightly different defocus condition to the figure 1-52 is shown in enlargement in figure 1-54. This image is indexed as [110] orientation and the crystallographic directions are marked on the figure. The Burgers vector of the dislocation at the corner of the two faults is also indicated. The direction of this Burgers vector does not lie on the slip plane of the material; therefore, it is *sessile* and locked. Better examples of this type of dislocation, which are more clearly imaged are shown later in this section. The fault pointing downward contains an extra plane of {111} atoms, hence, it is an extrinsic fault. Some distortion in the lattice approximately this fault, particularly on the right side of the micrograph shows the effect of the extra plane. The fault itself is not imaged very well;

therefore, it is difficult to show the stacking sequence as being an extrinsic fault. The stacking sequence appears complex, perhaps suggesting that there may be additional faulting present in the adjoining plane approximately the extrinsic fault. This is suggested by the termination of this fault at the bottom, shown in figure 1-54. There is a complex twinned region that connects to the fault and other multiple faults intersect this twinned region. This type of complex defect probably formed as a result of multiple interactions of dislocations and faults that reacted and combined. The net effect of these clusters of defects (3) is that various dislocations that intersect it are all locked-up and became immobile. These types of defect structures were very stable under imaging. Other defects that were not as tied-up were observed to move as shown later in section 1-10.

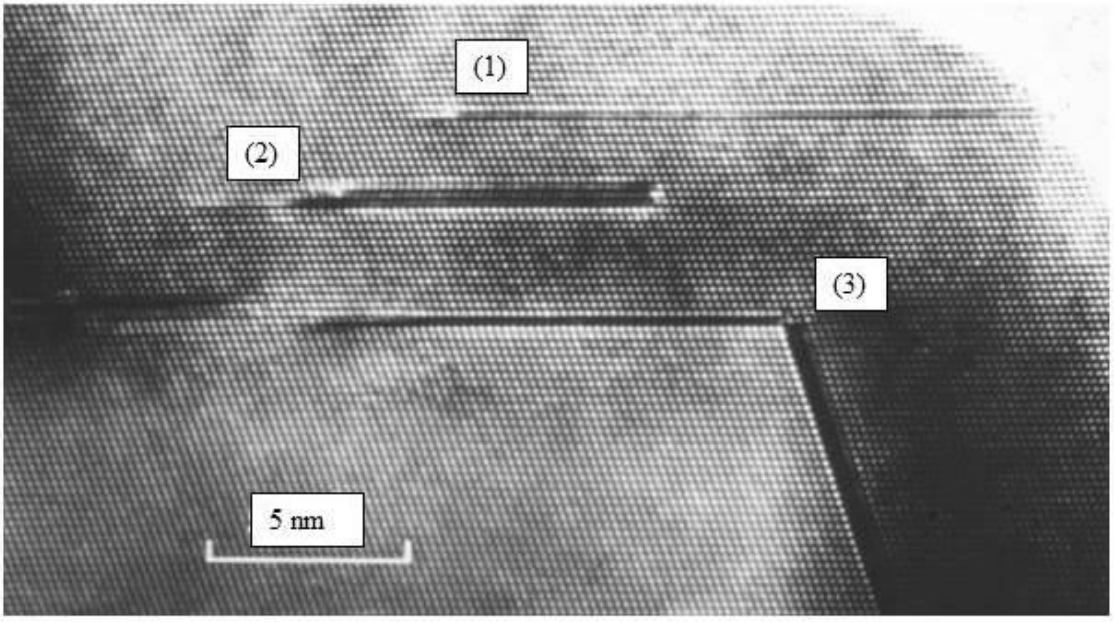

Figure 1-52: Lattice image of several defects. (1) is a 60° dislocation in which one side has passed out of the crystal, (2) is a localized twin region, and (3) is an example of a reaction between a Frank dislocation and the partial from the 60° dislocation, and contains an extra plane of atoms in the fault that is at an angle of 109° with respect to the horizontal fault. At the corner is a sessile dislocation of the type $\frac{a_o}{6}[\bar{1}10]$.

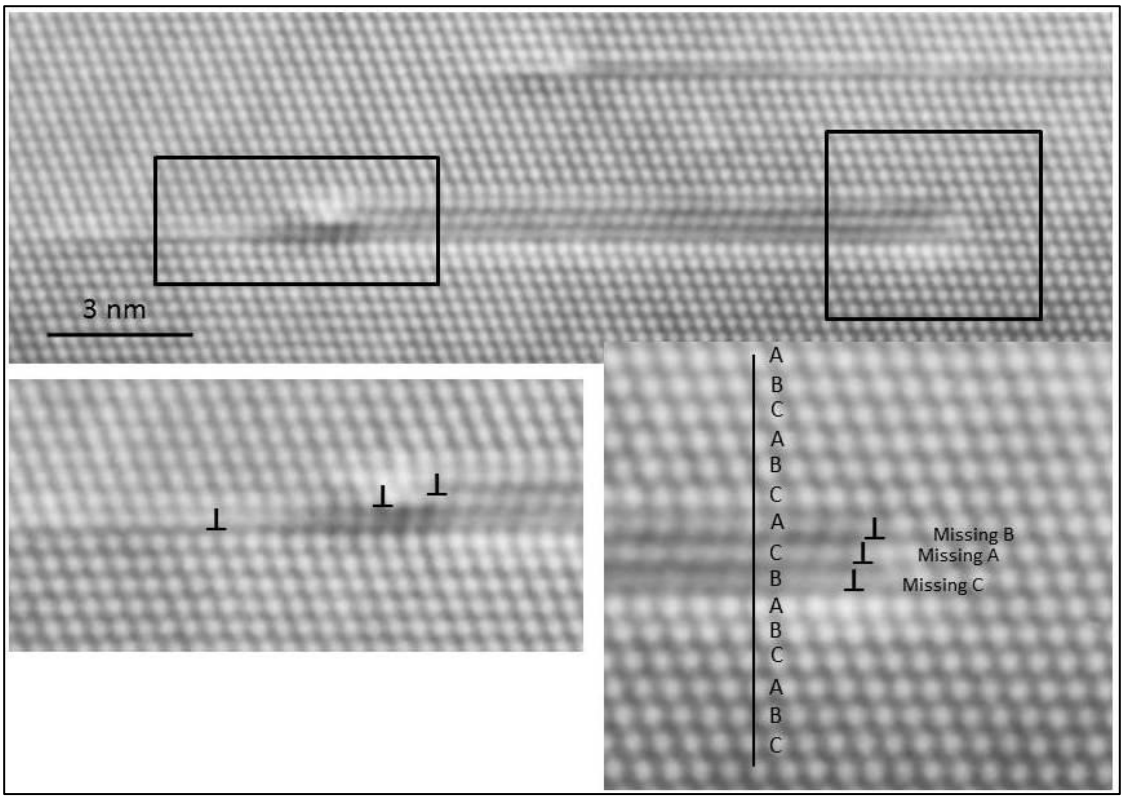

Figure 1-53: Enlarged view of defect #2 shown in figure 1-52. Approximate locations of the partial dislocations on each side of the twinned region are shown and stacking sequence on the right side of the defect.

An example of pure Frank dislocations containing an extrinsic stacking fault between them is shown in figure 1-56. As described earlier, Frank partials have the vector of $\frac{a_o}{3}$[111] type on each side of the extrinsic stacking fault. The extrinsic nature of the stacking fault is quite obvious from the presence of extra {111} atomic pairs at the fault, and from the stacking sequence as indicated in figure 1-57. There is an extra "C" plane inserted into the lattice at the fault. The sign convention on the figure is with CdTe [110] projection (out of the paper). It is believed that the defect being imaged in figure 1-56 must have been a Frank loop in the bulk, probably created by argon ion-milling. The lattice around the Frank dislocation in figure 1-56 is perfect. A Burger circuit around the defect returns to the original starting point.

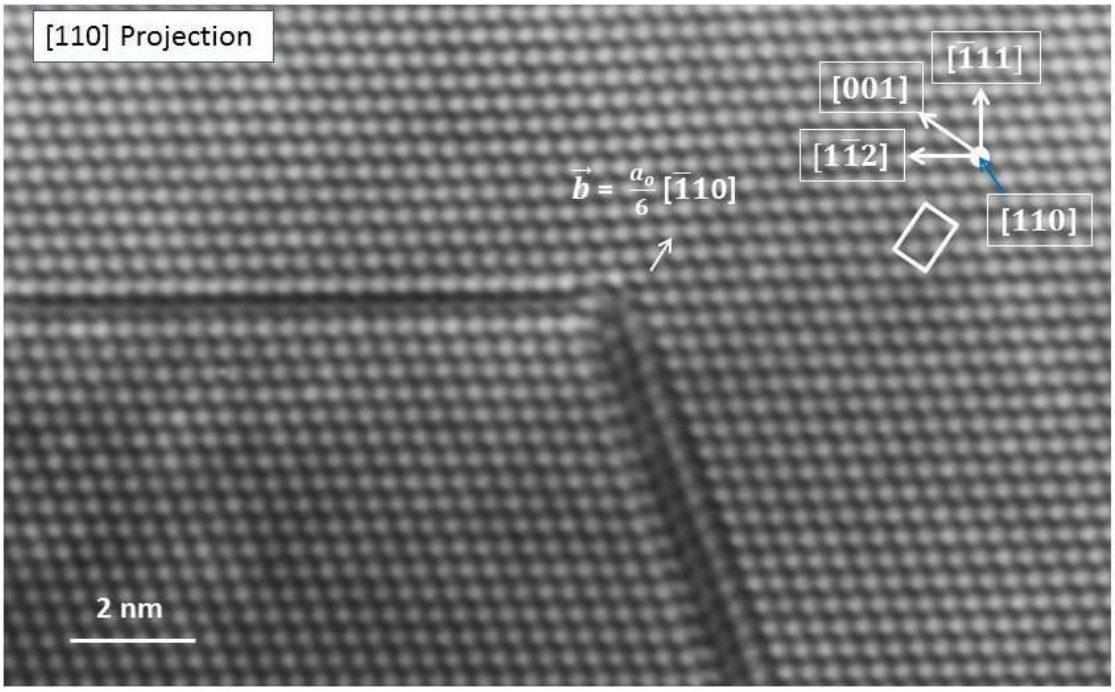

Figure 1-54: Enlarged view of defect #3 shown in figure 1-52. Approximate locations of the partial dislocations on each side of the twinned region are shown and the stacking sequence on the right side of the defect.

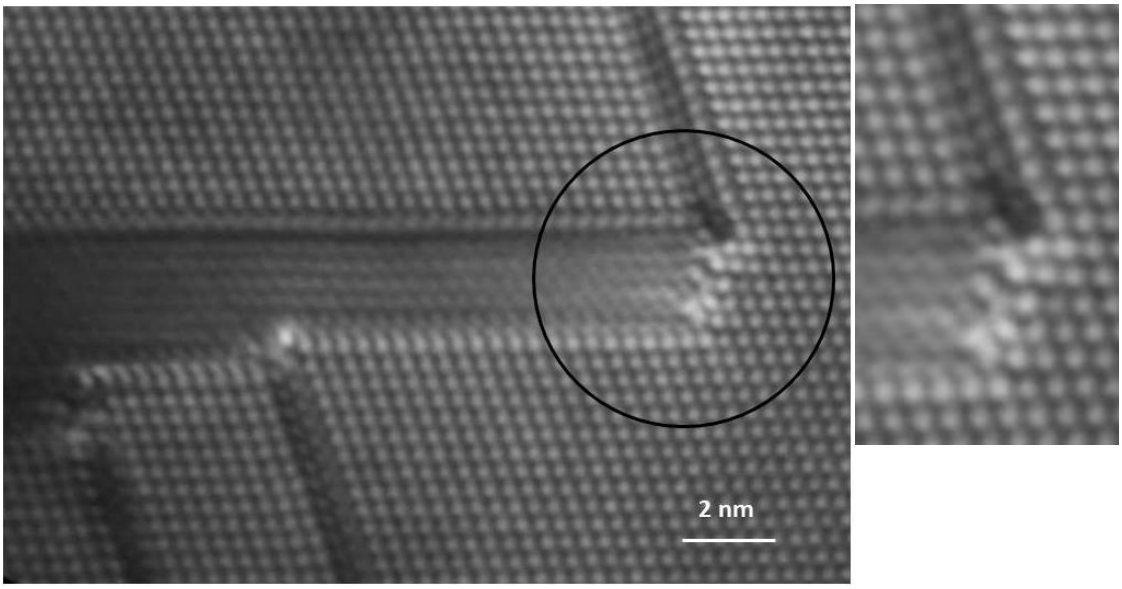

Figure 1-55: Termination of the stacking fault pointing down in figure 1-54, indicated by the circle.

Many defects like these were found in the specimen. During the specimen thinning, the loop was cut and one is imaging the cut loop end-on in the HRTEM image. The clarity of the image at the two Frank partials at the edge indicates that the dislocation is being imaged nearly perfectly parallel to the imaging beam. Frank dislocation occurs by interstitial condensation. The knock-on damage caused by Ar ion-milling should produce many interstitials. The lattice around the extra plane of atoms is highly strained. A rough estimation of the displacement of the {111} planes around the Frank partials shows strains of approximately 10% or more as judged by image spot positions, and the strain field extends out for up to ~10 nm. A Frank dislocation Burgers vector is not in the slip plane of the crystal. Therefore, the only way it can move is by climb, in this case along the $[11\bar{2}]$ or $[\bar{1}\bar{1}2]$ direction, in effect extending or reducing the extrinsic fault. A climb of Frank dislocation very similar to one shown here was observed in HRTEM using the Cambridge University 600 kV TEM and reported in 1982 in *Nature* [1-83, figure 4]. Dislocation climb was recorded using a video camera attached to the TEM, and the dislocation took approximately 100 seconds to climb 4.5 nm. The slow movement reflects the fact that motion can only occur by diffusion of atomic species from the dislocation core.

Figure 1-58 also shows a Frank dislocation, before and after the reaction to form a locked dislocation and a Shockley partial dislocation, in-situ in the microscope, which were taken several minutes apart. In this example, the Frank dislocation on the left has exited the crystal, thereby relieving the lattice strain on that side of the Frank dislocation partial. On the right side, the Frank partial has "reacted" to form a locked dislocation and the other Shockley partial dislocation has exited the crystal. In the process the lattice strain around the original Frank partial has been greatly reduced by the formation of an intrinsic stacking fault. The two inset images of before and after the reaction show the extent of the strain relief. Before the reaction, the strain around the Frank dislocation is large, as much as one lattice spacing (a pair of CdTe atoms) which extends for at least ten {111} layers, which is approximately 10%.

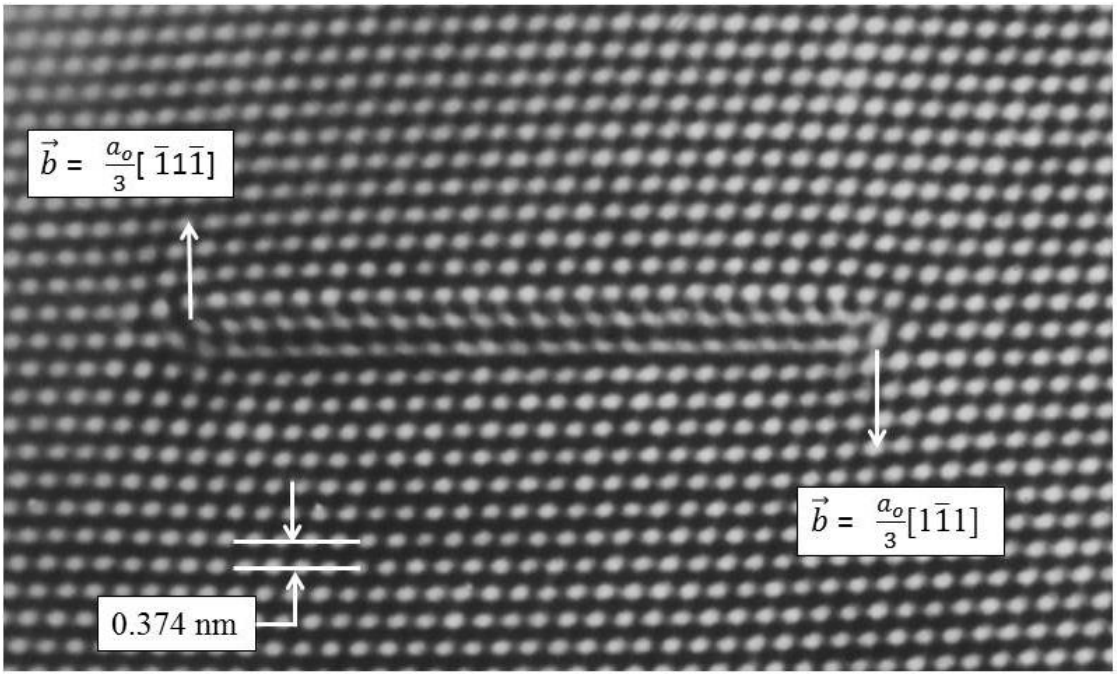

Figure 1-56: Lattice image of Frank dislocations bounding an extrinsic stacking fault. Burgers vector is indicated. From the edge of the photograph, the extent of the lattice strain around the defect is easily visible. Zone axis is [110].

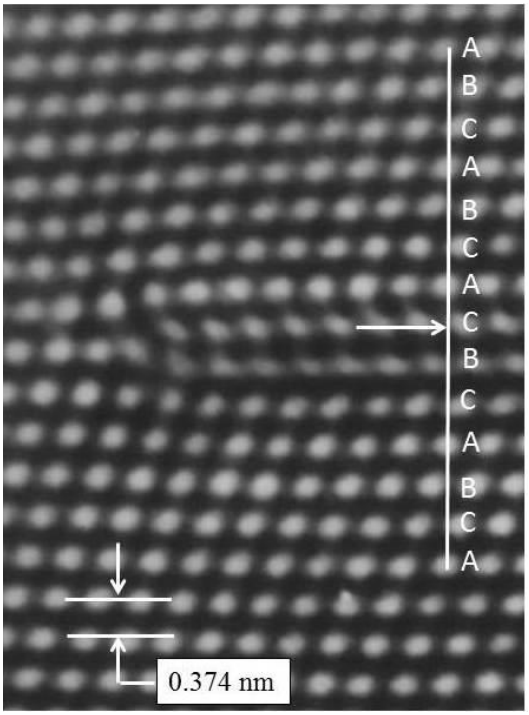

Figure 1-57: Stacking sequence of {111} atomic pairs across the extrinsic stacking fault, indicating the addition of the "C" layer at the fault. Also, the addition of an extra layer of {111} plane is quite obvious in the image.

Once the locked dislocation formed, the resultant intrinsic stacking fault that extends on the alternate {111} plane has greatly reduced the lattice strain. The details of the dislocation core are interesting, but a considerable amount of imaging analysis with atomic displacement modelling and image simulations are necessary to come to any definitive conclusion about the exact atomic rearrangement that is taking place at the core. This dislocation reaction was described by Sinclair et al. in a review article on in-situ TEM in 1988 [1-84]. A more detailed description of the defect reaction will be given now. With the specimen zone axis labeled as [110] orientation, the unreacted Frank dislocation on the right has a Burgers vector of $\vec{b} = \frac{a_o}{3}[\bar{1}1\bar{1}]$. The reaction then can be written as shown in the equation below using the notation based on the Thompson's tetrahedron:

$$\vec{b} = \frac{a_o}{3}[\bar{1}1\bar{1}] \rightarrow \frac{a_o}{6}[\bar{1}1\bar{2}] + \frac{a_o}{6}[\bar{1}10] \qquad \text{eqn. 1-24}$$

$$D\delta \rightarrow D\gamma \qquad \gamma\delta$$

Thompson tetrahedron construction for this reaction is shown in figure 1-59. $D\delta$ is the starting Frank dislocation. $D\gamma$ is the 30° Shockley partial, and $\gamma\delta$ is the locked dislocation with the Burgers vector of $\frac{a_o}{6}[\bar{1}10]$. Once this locked dislocation forms, it becomes very stable and difficult to move. This reaction as described, which is believed to be induced by the heating effect of the imaging beam, shows that such reactions can be studied in situ, at high resolution in the TEM. These observations made in CdTe has led to numerous subsequent studies using this approach in other materials such as silicon, and review of this technique was given by Sinclair in 2013 [1-85].

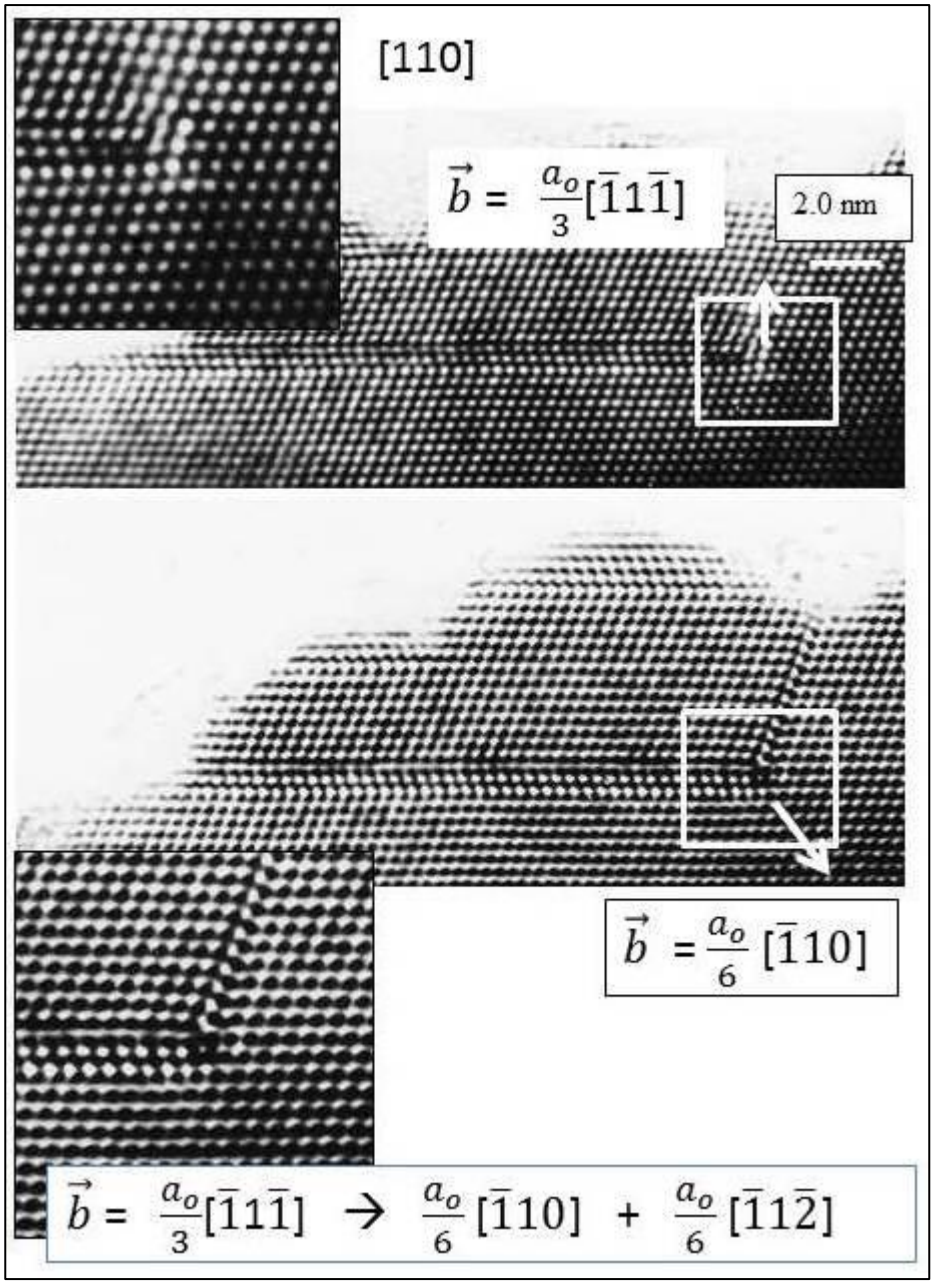

Figure 1-58: A Frank partial dislocation, which formed a Shockley dislocation on another {111} plane to relieve the strain around it, and one Shockley partial has exited the crystal. Images were taken several minutes apart. The resulting dislocation is $\vec{b} = \frac{a_o}{6}[\bar{1}10]$, which is a locked dislocation.

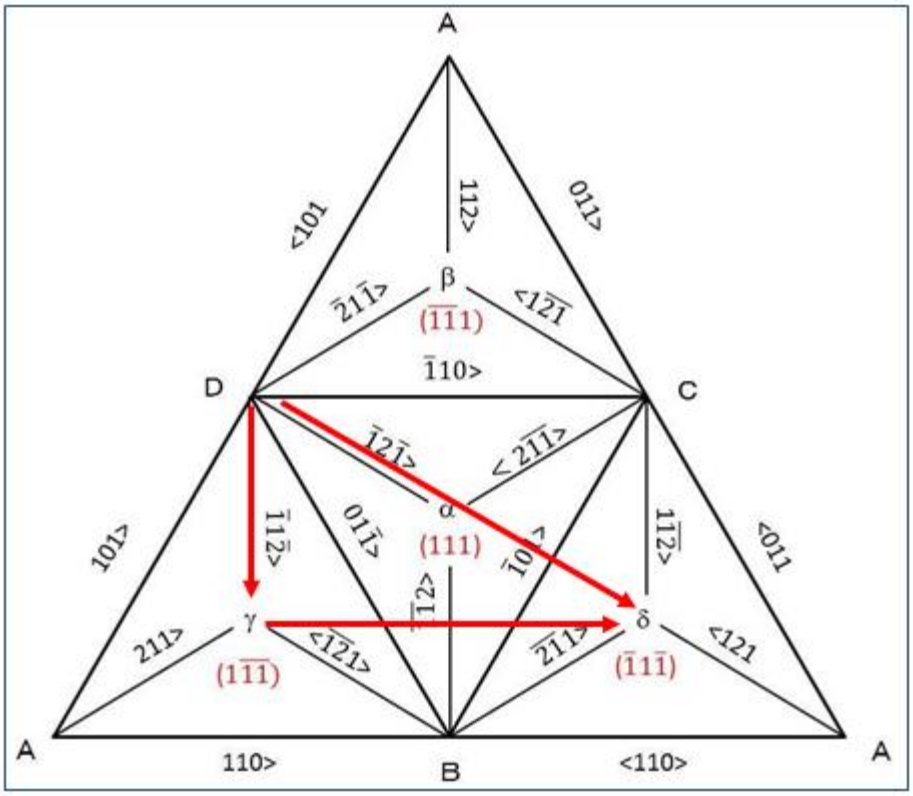

Figure 1-59: Thompson tetrahedron construction for the defect reaction in figure 1-58. Dδ is the starting Frank dislocation. Dγ is the 30° Shockley partial, and γδ is the locked dislocation with the Burgers vector of $\frac{a_o}{6}[\bar{1}10]$.

An example of a network of defects, which were often observed on CdTe is shown below in figure 1-60. (1) is a reaction between a Frank partial and a Shockley partial to form a locked dislocation. The locked dislocation is the same type as described previously for figure 1-58, but it is at an acute angle of 70.5°. (2) appears to be a screw dislocation that has dissociated into two partials, forming an intrinsic stacking fault. A Burgers circuit around the entire defect shows that the outside lattice is perfect. This would be expected if the starting dislocation is a screw dislocation. The intrinsic nature of the stacking fault can be deduced using the stacking sequence. (3) is a Frank partial dislocation at the other end of the same dislocation in (1). (4) is also a Frank dislocation as evidenced by the extra {111} plane, but the other end on the left of

the crystal is perfect. This can occur by passing two Shockley partials on successive planes. (5) is a reaction between two Shockley partials on two different {111} planes to form a Lomer-Cottrell locked dislocation exactly as described in figure 1-43.

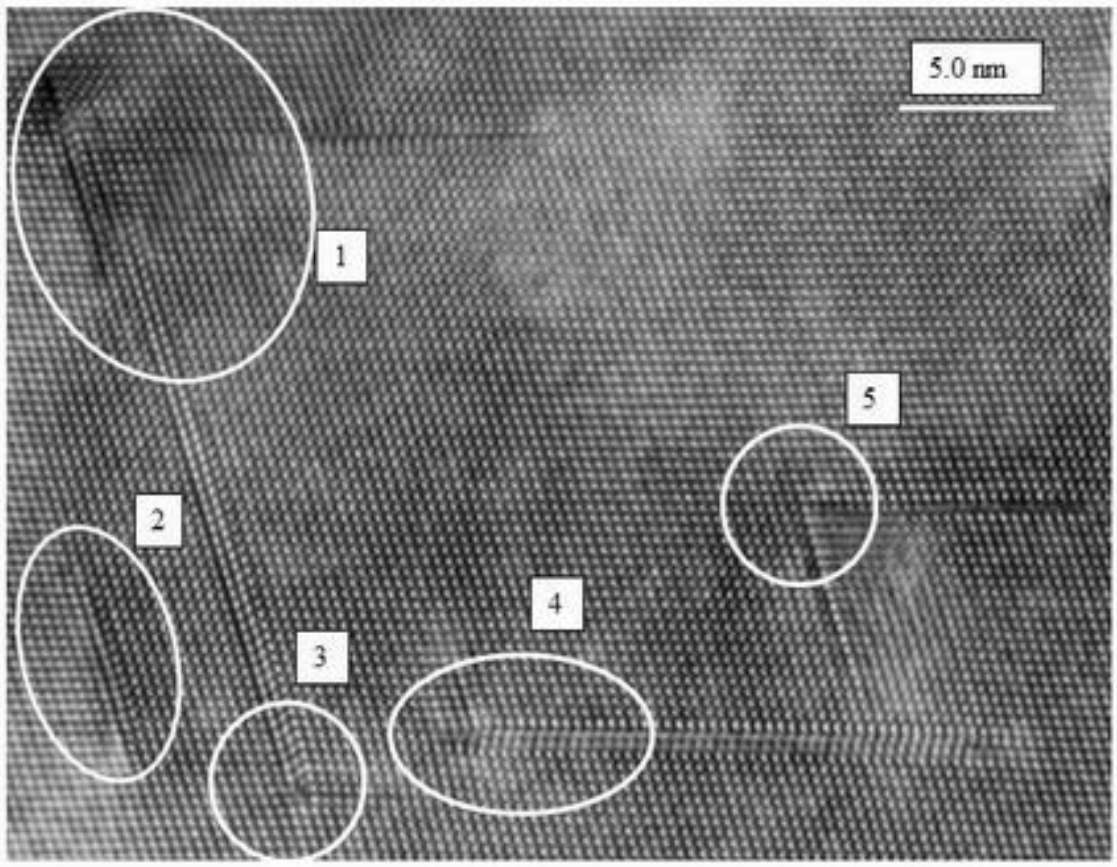

Figure 1-60: Network of various dislocations and small twins that are forming locked dislocations.

As mentioned previously, normally screw dislocations are not amenable for easy imaging and interpretation by the HRTEM method. If the screw dislocation is imaged end-on, there would be no displacement of atomic positions in the direction of the beam because the Burgers vector would be in the same direction as the beam. The only possibility for any contrast would be some telltale indication of strain around the dislocation core, which might show up in the image contrast. Such an attempt was made with $SrTiO_3$ [1-86] but the screw dislocation was identified first by conventional

microscopy before the HRTEM was attempted. If a screw dislocation with the Burgers vector of the type $\frac{a_o}{2}$<110> existed inside of the crystal and imaged top down, the dislocation line would form a spiral. It is possible that figure 1-61 represents such a situation. This type of defect was occasionally observed but only in the thick portion of the specimen. However, the image is difficult to interpret, and its usefulness is probably limited.

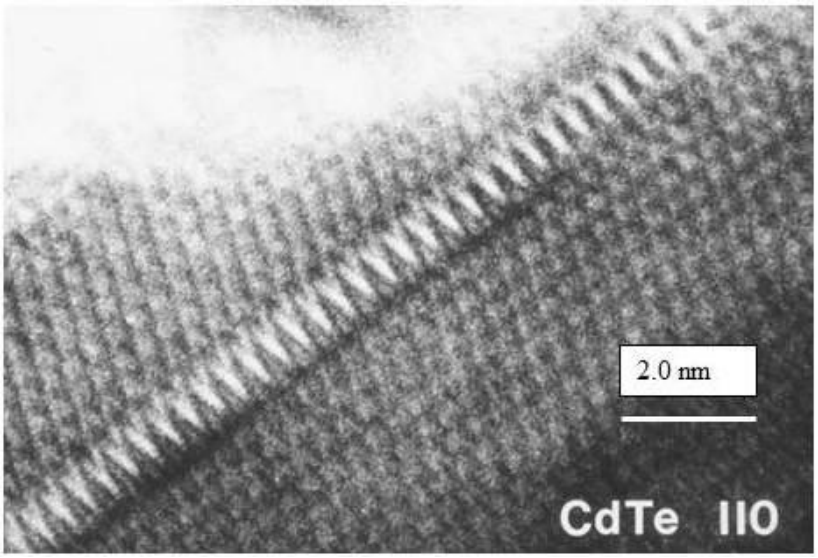

Figure 1-61: An image that could be of a screw dislocation with Burgers vector of the type $\frac{a_o}{2}$<110> viewed top down in the interior of the crystal. It is in a relatively thick part of the specimen.

Figure 1-62 shows a dislocation that appeared quite often in the specimen. At first glance, it looks similar to the 60° dislocation which had split into two Shockley partials as shown previously in figure 1-48. However, a Burgers circuit around the defect returns to the original position. Therefore, the crystal is perfect around the defect. This is shown in the figure with the circuit drawn in yellow. Looking at the {111} planes running 70.5° to the fault plane across the faulted region, it is possible to conclude that dislocations at each end of the faulted region have an opposite sense as drawn in the figure. The stacking sequence across the middle of the fault is shown in the inset image below. It can be seen that there is a missing "C" plane at the fault,

indicating that the fault is intrinsic. At the edge of the fault on either side, it is not possible to make that statement as there is a continuum of fault position. One possibility of what this defect might be is that it was a part of a perfect loop that had been cut across by specimen thinning, leaving behind a $\frac{a_o}{2}$<110> edge dislocation with opposite polarity. It is clear from figure 1-46 that many dislocation loops were created by ion-milling. Some of them may very well have been perfect dislocation loops similar to the drawing in figure 1-45. The question then for the defect in figure 1-62 is why the two dislocations did not annihilate each other as they have opposite polarity and should attract each other. There may be other factors that keep them apart, such as the effect of the surface nearby, or due to impurities that prevent the two from recombining.

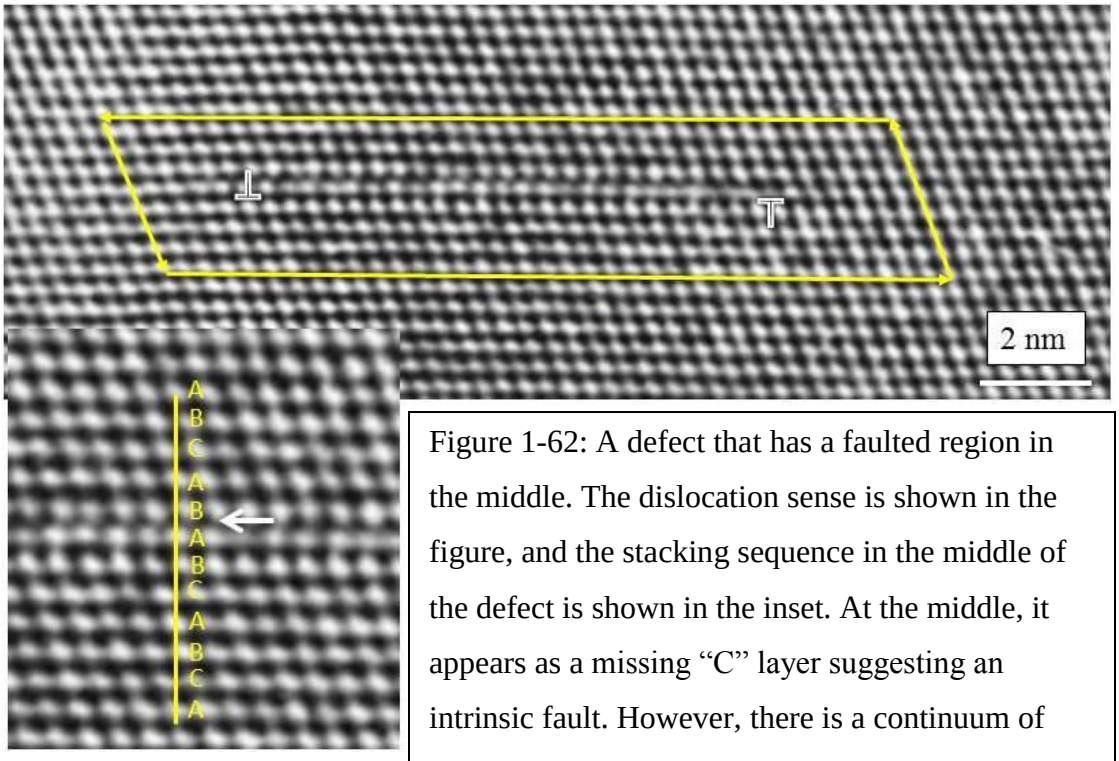

Figure 1-62: A defect that has a faulted region in the middle. The dislocation sense is shown in the figure, and the stacking sequence in the middle of the defect is shown in the inset. At the middle, it appears as a missing "C" layer suggesting an intrinsic fault. However, there is a continuum of positions from one end of the fault to the other.

Partial dislocations associated with an intrinsic stacking fault can easily glide along the {111} slip planes and this was imaged in-situ during HRTEM observations. This is the subject of discussion in the following section, 1.10. Alternatively, Frank partial dislocations must climb, and this can only be accomplished by either deletion or addition of atoms at the core. A slow climb of Frank partials was also observed and recorded in-situ [1-84]. Locked dislocation true to their description, was immobile and none was observed to move.

1.9.2 Defects in CdS

CdS belonging to the hexagonal crystal system has a limited set of slip planes. It is generally accepted that basal planes {0001} and the prismatic plane $\{10\bar{1}0\}$ will be the dominant slip planes in wurtzite structure [Frank & Nicholas 1-85]. Cockayne et al. were the first to observe dissociated dislocations in CdS by weak beam electron microscopy. They also observed their motion in a dissociated state by video microscopy [1-86]. The dislocation that they observed was characterized as a 60° edge dislocation with Burgers vector of $\frac{a_o}{3}[11\bar{2}0]$ that dissociated.

$$\vec{b} = \frac{a_o}{3}[11\bar{2}0] \rightarrow \frac{a_o}{3}[10\bar{1}0] + \frac{a_o}{3}[01\bar{1}0] \qquad \text{(Eqn. 1-25)}$$

Using the radius of curvature of dislocation lines that had bowed due to stress, and a formula relating it to stacking fault energy according to Brown and Thölén [1-87] and elastic constants derived from Berlinkourt et al. [1-88], they calculated the stacking fault energy as γ = 88 $\pm$ 18 mJ/m^2. From the separation distance of the partials, which was 11 nm, they obtained a value of 81 $\pm$ 16 mJ/m^2. In the case of an undissociated dislocation in the basal plane, the extra half plane of an edge dislocation terminates on a row of identical atoms, while on the prismatic plane the

dislocation ends on a row of alternating atoms. A consequence of this is that the basal plane dislocation will carry a charge. The effect of dislocations on various electronic and photonic properties of CdS has been studied extensively. However, the literature on the characterization of defects is rather limited. Suzuki et al. studied extended dislocations, 60°, screw and Frank loops by the HRTEM method and reported a value of 14 $\pm$ 4 mJ/m^2 for the stacking fault energy [1-91]. The large difference in the reported value between result by Cockayne et al. vs. Suzuki may be due to the sample. Cockayne et al. used an oriented crystal, which had been deliberately deformed (by scratching), whereas Suzuki used thin ribbons of crystal grown by vapor transport. Nevertheless, the differences are too large to explain by crystal growth method alone. Additionally, TEM specimen preparation methods were different. Cockayne et al. used chemically thinning while Suzuki used ion-milling which may have introduced more damage to the specimen. In this study, the CdS specimens were much less prone to ion-beam damage compared to CdTe. Therefore, the large difference in reported value between Cockayne et al. and Suzuki et al. is a mystery.

The issues that were discussed in CdTe defects also apply for CdS due to the similarity between the wurtzite and cubic sphalerite structure. As is seen in the model structure in figure 1-37, glide or shuffle type of dislocations are possible depending upon where the atomic discontinuity takes place for the basal plane dislocation. Insertion of extra basal plane of Cd-S pairs would result in Frank loops bounded by a Burgers vector of the type $\vec{b} = \frac{a_o}{2}[0001]$. The easy plane of slip is the basal plane, but since there is only one such plane in the crystal, other slip systems become operative in the wurtzite system when deformed. In comparison, the {111} planes are the slip plane in cubic sphalerite structure and the four planes that are available can accommodate the deformation. The prismatic slip in the wurtzite structure can become quite complicated because of the number of possible slip system that can become operative (page 199, [1-66]). Nevertheless, similar to the HCP (hexagonal close packed) metals compared to the FCC (face centered cubic) metals, the deformation process is much harder in the wurtzite crystal

structure compared to the cubic sphalerite structure. For imaging CdS structure, only the $[2\bar{1}\bar{1}0]$ zone axis was used; therefore the full range of various defects that are possible in CdS was probably not imaged. However, since the slip plane {0001} was imaged end-on, many stacking faults were observed on the basal planes, although terminating dislocations of this specific type were not easy to find as there were few regions on the specimen that were imaged clearly enough to see the line defects.

The CdS specimen used in this study was the same as that previously described in Section 1.7. Specimen was cut from a single-crystal wafer that was commercially obtained. A 3 mm disk was prepared and dimpled, followed by ion-milling at ~2 keV for several hours. Compared to CdTe, the CdS specimen was much more stable under the electron beam, and defects generally stayed static during imaging. An example of undissociated edge dislocation is shown in figure 1-63. In this image, it appears as if there is an extra prismatic plane (indicated by lines), which runs perpendicular to the basal plane, and the Burgers vector direction by running a clockwise circuit would give a $\vec{b} = \frac{a_o}{2}[01\bar{1}0]$, but it more likely to be the pure $\vec{b} = \frac{a_o}{3}[11\bar{2}0]$ edge dislocation at 30° to the frame that is being imaged in projection. The fact that this dislocation did not dissociate may be due to the high stacking fault energy for the CdS as mentioned previously. The $\frac{a_o}{3}$ term reflects that the magnitude of this Burgers vector should be a_o, and the Miller-Bravais indices convention, the magnitude of [u,v,t,w] indices is given by:

$$| [u,v,t,w] | = a\,[3(v^2 + uv + v^2) + (\frac{c}{a_o})^2 w^2]^{1/2}$$

In the Suzuki et al. reference of [1-91], a similar dislocation imaged in the same projection was labeled a "60° dissociated edge dislocation" without any indication of its Burgers vector. However, the $\vec{b} = \frac{a_o}{3}[11\bar{2}0]$ burgers vector, will be inclined 30°

away from the plane of the image, as can be seen from the notation shown in figure 1-36 previously. Suzuki et al. imaged both the undissociated and dissociated 60° dislocations. Although it is difficult to make much sense from the image with regard to the dislocation core structure, the high clarity of the image suggests that there is some consistency in the core rearrangement in the beam direction. If enough defocus series images are compared against extensive image simulations and the core model based on elastic and dynamic models, it may be possible to glean more about the details of the core in this type of dislocation. This was thought to be beyond the scope of the present work. As it stands now, it is not possible to say for certain whether the core is the shuffle or the glide type, and whether the termination is with Cd or with S. It is also interesting to note that there is a slight distortion in the lattice in the vertical direction of the image (along the [0001] direction due to the dislocation. This is evident from the horizontal line drawn on the image. The distortion extends at least 10 or more atomic planes from the core, or approximately 3.4 nm or more, and strain is at least ~10% around the core.

The undissociated dislocation can dissociate into two $< 10\bar{1}0 >$ type partials as shown in equation 1-25, and this would form a stacking fault on the basal plane between the partials. It would be analogous to splitting of perfect 60° dislocations in the cubic Sphalerite structure, forming an intrinsic stacking fault between the partials. Examples of many such stacking faults are seen in figure 1-64. This image was obtained from a CdS film grown on CdTe as a heterojunction cell. Since the film was grown by evaporation and subsequently the TEM specimen was prepared by ion-milling, the film contained a high density of defects from both the grown-in process and possibly by ion-milling. Images were obtained using JEOL 200CX microscope operating at 200 kV. Reflections out to (0004) were included in the objective aperture, which was 25 beams. Beam divergence was approximately 2 mrad. Therefore, only the first 13 or so reflections should have contributed coherently to the image formation. Although the stacking faults are easy to discern by changes in the stacking sequence. across the basal planes, the termination points for the stacking faults (location of the partials) are difficult to pin-point in the image. The lower left section of the micrograph

contains many sets of Frank type dislocations with an extra plane of {0002} basal plane inserted into the lattice deduced from the stacking sequence. Again, the image is quite complicated and it is difficult to discern the exact location of the partial dislocations in this image.

Figure 1-65 shows a Frank dislocation loop with the Burger's vector of $\vec{b} = \frac{c_o}{2}[0001]$, where one extra plane of basal plane atoms is inserted into the lattice. Between the dislocations, there is an extrinsic stacking fault that extends the length of the loop. There is substantial distortion of the lattice that extends out for up to 10 nm or so on either side of the dislocation.

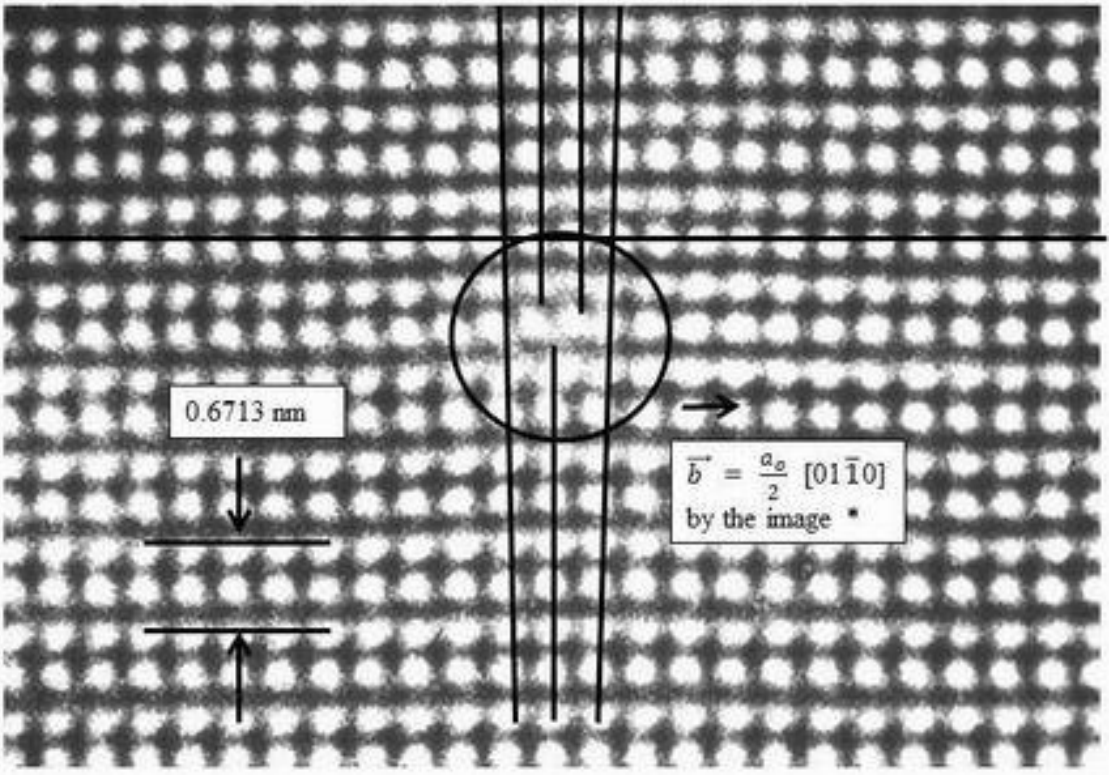

Figure 1-63: Undissociated basal plane dislocation in CdS. The $[2\bar{1}\bar{1}0]$ projection image was taken with a Philips EM400 at 120 keV. The projected Burgers vector as determined from the image is indicated.

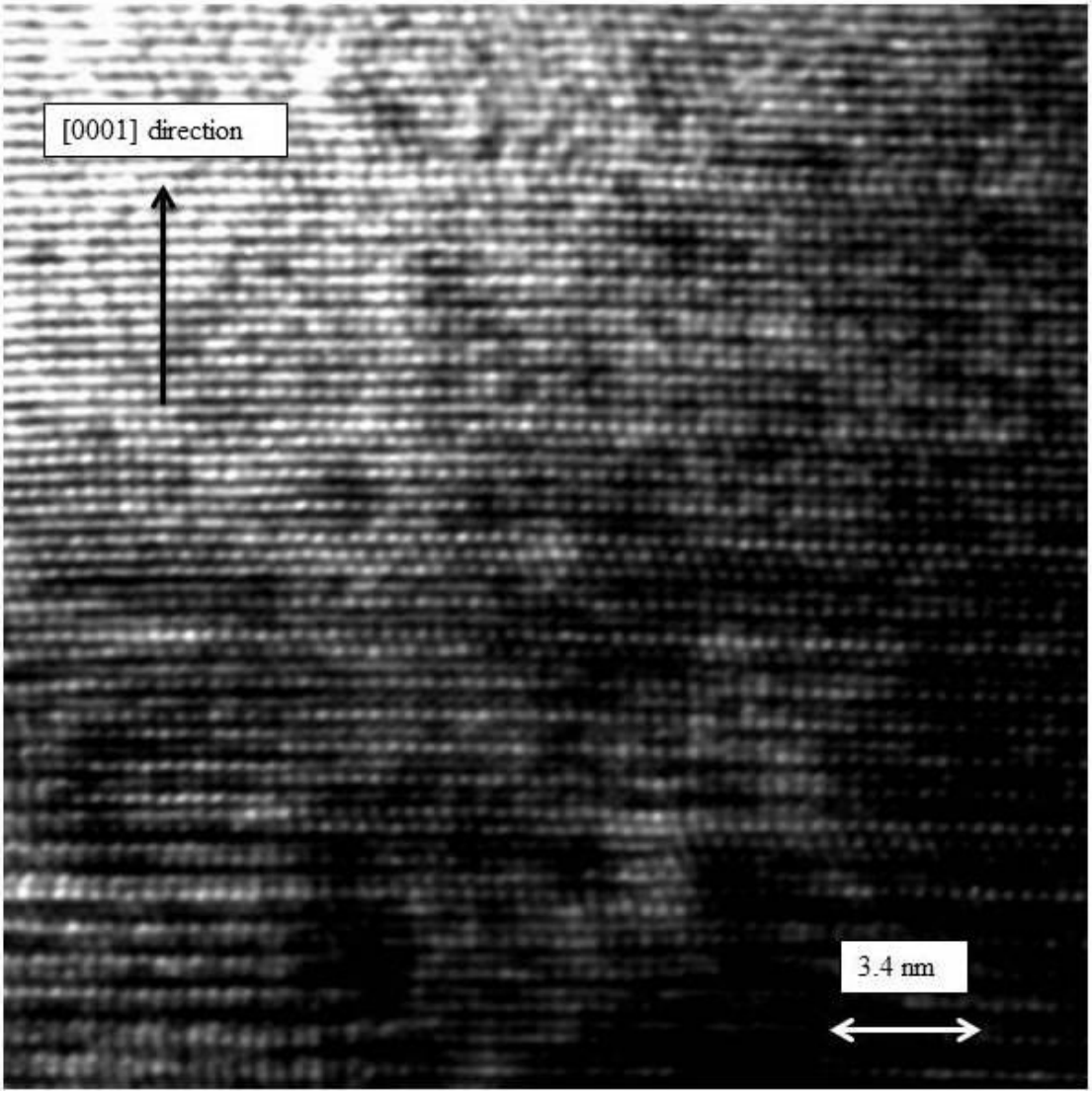

Figure 1-64: HRTEM image of highly faulted CdS in [$2\bar{1}\bar{1}0$] orientation.

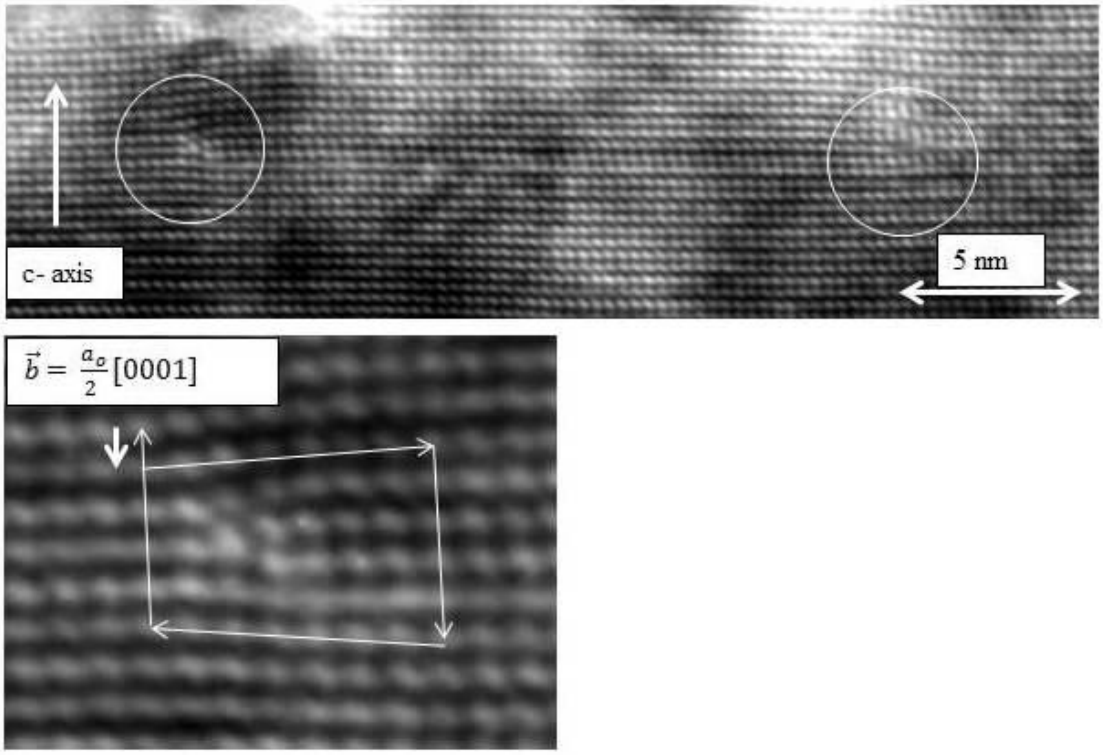

Figure 1-65: Frank dislocation loop in CdS with the ends circled. The loop contains an extrinsic stacking fault in the middle. The c-axis of the CdS points up in the figure. The inset below shows the Burgers vector circuit for the dislocation.

1.10 In-Situ HRTEM Imaging of Atomic Motion and Defects in CdTe

CdTe having the largest lattice spacing of the II-VI compound semiconductors lends itself to high resolution lattice images. The material is susceptible to electron beam-induced damage due to ionization damage combined with specimen heating, and susceptibility to enhanced oxidation of the surface due to the presence of reactive oxygen species that are produced by the electron beam with the residual gasses still present in the column. These processes induced by the beam are interesting to observe. During the initial stages, a rapid appearance and disappearance of the image spots which presumably correspond to a pair of Cd and Te columns in projection can be observed at the edge of the crystal. Formation of crystalline facets of various configurations accompanies this process. Somewhat later, small crystallites can be seen growing on the surface of the CdTe, and they eventually replace the single-crystal CdTe altogether. Some of these crystallites were identified as CdO based on lattice fringe images and their diffraction patterns in this work, which will be described later. In the bulk of the crystal, the motion of dislocations often can be observed. Two basic types of dislocation motion are of interest. The motion of Shockley partial dislocation is the most common, and they tend to move quite rapidly. Another type is the climb of Frank dislocation, which is slower. These processes were recorded by a video recorder using a TV camera attached to the microscope. Magnification at the TV monitor was 17 million times. Images are quite noisy, but digital image processing can be applied to improve the image quality.

Initial high resolution microscopy was performed using Philips EM400 TEM equipped with a high-magnification objective lens (Cs = 1.1 mm at 120 kV) and LaB_6 electron source as described previously, without the specimen tilting capability. Therefore, the single-crystals were sectioned as closely as possible to the desired orientation. Thin foils were obtained by standard ion-milling procedures. The CdTe specimen also was sandwiched between a copper grid as the sample was smaller than 3 mm in diameter. A region of the specimen close to the perfect [110] zone axis orientation was found by translating the specimen in the microscope to make use of the

natural bending of the TEM specimen. The images were taken with large objective aperture, admitting 37 beams with beams out to $(4\bar{4}0)$ reflections at 8.726 nm^{-1}. The magnification was 800,000X, with typical exposure times of approximately 1 sec. for the negatives. This initial work also was done without the use of a video camera. The current density used for typical viewing with a focused beam on the specimen is estimated to be between 10 to 20 A/cm^2. With a slight defocus of the CII condenser lens the current density can be reduced very rapidly. Even with a lower value of current density, these values are quite large, and the TEM was setup to obtain a high beam current in order to obtain short exposure time at the highest magnification of the TEM. In conventional TEM work, ~1 A/cm^2 is more typical. A more detailed discussion of the current density and the method used to determine it follows later.

In typical experimental imaging conditions, it was found that after an initial incubation period of approximately 10 to 20 minutes at moderate beam current (~10 A/cm^2) the specimen deteriorated by the nucleation of new, small crystallites, apparently on the surfaces of the parent crystal. The deterioration time varied from one specimen to another and was typically several hours. This is consistent with gradual heating of the sample rather than instantaneous damage. The applied voltage is well below the threshold for displacement for such high atomic number species as Cd and Te. Close examination of the specimen edge revealed that individual bright image spots were moving about by random jumps. During this process, a clean facet would often form along the edges of the specimen, usually along the {111} planes. Jumps occurred several times per second, usually by a distance equal to the atomic column separation. Not all edge spots were moving simultaneously; rather, one or two would be moving back and forth along a crystal facet. Unfortunately, the time both for transporting photographic plates into position and for exposing the film was too long to allow the motion of individual spots to be studied extensively. The jump rate could not be reduced to an acceptable level, for instance, through decreasing the incident electron beam current density by defocusing the microscope condenser lens. These issues were later overcome by using a higher resolution TEM, and the use of a video camera as summarized in due course by Sinclair et al. [1- 84].

The motion of the surface spots is demonstrated here by the appearance of the specimen after intervals of several minutes. Thus it can be seen in figure 1-66 that the shape of the specimen edge changes noticeably with time, although the crystal structure of the interior is always maintained. The arrowed surface in figure 1-66 (1) corresponds to the (001) surface, and it can be seen that the profile changes over time. The four micrographs were taken over a span of several minutes. The general impression was that small facets were produced, the longer ones being parallel to {111} type planes. The bright spots at the edge move from one lattice site to another. When they become incorporated into the crystal, they extend it and the image is indistinguishable from the perfect crystal image. These observations, therefore, seem to indicate that atomic motion is occurring along the edge of the specimen, and probably across all surfaces. Those atoms that move on the surface normal to the electron beam will coincide exactly with the underlying atomic columns if tetrahedral coordination is to be maintained. Therefore, one would not detect motion of these latter atoms directly. These results are described by Sinclair et al. in 1981 [1-92], and it is the first time that such atomic motion events at the edge of the crystal were reported using HRTEM.

The movement of the image spots represents coordinated motion of a whole or partial atomic column but not the jumping of single atoms. For the observation to be made, the number of atoms that move must be sufficient to produce a detectable image spot. Based on imaging of perfect crystals as described in Section 1.8.1, the thickness of the specimen should be at least ~2.0 nm, or approximately 4 to 5 atomic layers thick. The image spots may coincide with three positions in the projected structure depending on the particular combination of the experimental variables of microscope defocus, spherical aberration coefficient, and specimen thickness. However, the image spot motion is independent of its exact position. Thus the jump of the Cd-Te molecule ‘A’ in the schematic of the CdTe structure at the edge of the specimen in figure 1-67 would be seen as a spot moving whether the spot coincides with the molecule, one atom, or the adjacent column. The argument also holds for other possible migration mechanisms indicated in figure 1-67.

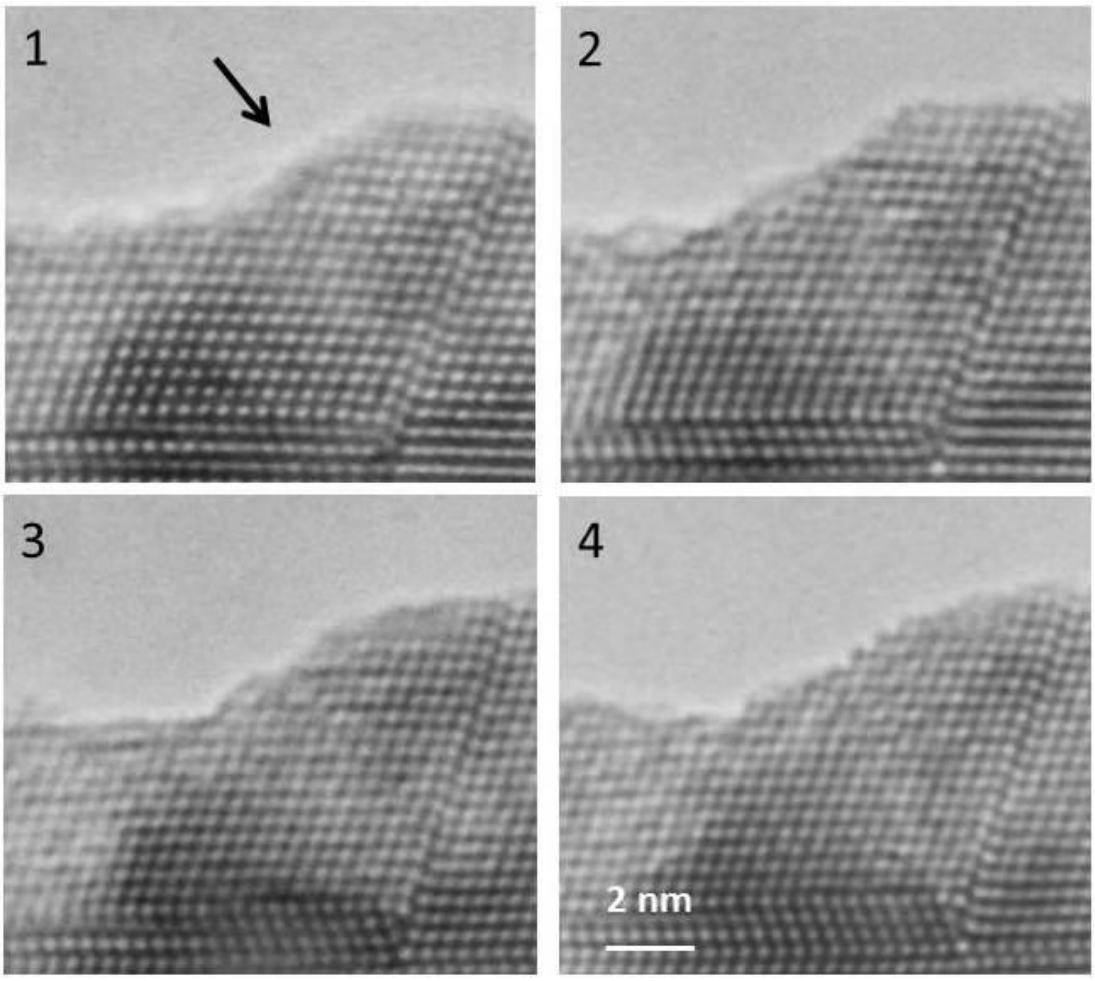

Figure 1-66: Time sequence images showing the specimen edge (arrowed) where *atomic* motion was observed. Gradual change in the surface profile can be seen. The arrowed surface is near [001] surface with the zone axis at [110]. Note that the intrinsic stacking fault on the right is fixed throughout the sequence, which spanned several minutes.

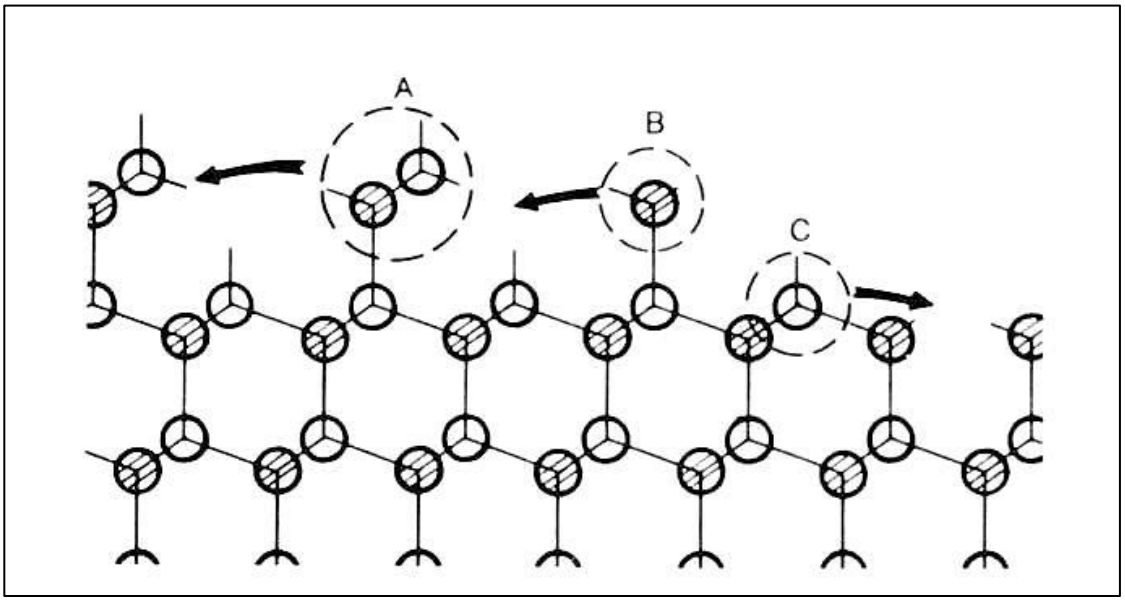

Figure 1-67: Schematic model of possible mechanisms for surface atomic migration in CdTe.

The driving energy for the present behavior is presumably reduction in total surface area. Using a simple formulation for atomic jump frequency ($\upsilon_o \exp - Q/kT$), it is found either that the activation energy (Q) for the present observations is 0.8 eV if they occur at room temperature, or that the specimen temperature is ~100°°C if the activation energy is assumed to be the cohesive bond energy of CdTe (1.03eV) [Harrison, 1-93]. The latter is thought to represent the present situation. Thus, the observations are only made after the specimen temperature rises sufficiently due to heating by the incident electron beam. As exposure continues, the motion becomes rapider with significant surface rearrangement. The variation between specimens can arise from their exact geometry and from the degree of contact between the specimen and the supporting material or holder. Complete isolation of the CdTe is found to result in extremely rapid specimen destruction. Even melting of a small area of the specimen has been observed (the melting point of CdTe is 1041°C). The slow response of the jump rate on reducing the beam current density indicates that the atomic motion is not assisted by direct electron-atom collisions (the electron energy is well below the threshold for Cd or Te displacement) or by ionization effects, and probably arises from

a sluggish heat dissipation from the active area. CdTe also has one of the lowest thermal conductivities of all the semiconductor materials, at 0.07 W/cm°K at 297°K. These unique properties of CdTe come from its high ionicity and low covalent bond energy compared to other semiconductor materials as tabulated in Table 1-7. A plot of various elemental and compound semiconductors and their cohesive energy per bond vs covalency (α_c) is plotted in figure 1-68, which is reproduced from Harrison's book [1-93]. It is believed that weak bonding combined with low thermal conductivity contributes to the observed motion of atomic species under electron beam heating. For other semiconductor materials, a much higher temperature would be needed to observe similar atomic motion if the same mechanism holds. For example, jump frequencies several times per second would be expected at 600°C for silicon (Q = 2.32 eV), 340°C for gallium arsenide (Q = 1.63 eV) and 260°C for cadmium sulfide (Q = 1.42 eV). Indeed, a high temperature heating stage was required to observe the equivalent phenomenon in silicon [1-94].

Along with observation of atomic columns "hopping" along the edge of the specimen, over time, considerable surface rearrangement often took place at the edge of the specimen. At least initially, it appeared that the specimen edge became "cleaner" as surface rearrangement began. This may have been the case as initially the area was ablated and a clean surface exposed. The {111} planes formed most easily followed by {110} to a lesser extent. The {111} plane is presumably the lowest energy configuration for the surface to take because of one missing bond per atom on this surface. A set of micrographs that were taken over a minute or two are shown in figure 1-69. These micrographs were taken with a Philips EM400ST at 120 kV with a tilting stage. Total of 7-beams were used to form the HRTEM images. Current density is ~ 15 A/cm^2, and the image is much sharper now due to the ability to obtain exact zone axis with specimen tilt and using 7 beams, which give better contrast. The specimen also was prepared differently compared to the one in figure 1-66. A square specimen 2.3 x 2.3 mm was cut using a wire saw, and most of the thinning was done by jet thinning using 3% bromine in methanol solution. This was followed by Ar^+ ion-milling at 4 keV for approximately 30 minutes. The size of the specimen was to fit into the TEM holder

without the use of a grid. Using this method provided a much cleaner specimen and easier to handle. In the micrographs, one can observe steps forming on the {111} surface, and an entire row of plane parallel to the facet can be seen forming and disappear in rapid succession. Eventually, a small amorphous *contamination* layer began to form at the edges, and once this occurred, the surface rearrangement of clean edges stopped. However, gross ablation, recrystallization/redeposition, and a reaction/oxidation process occurred if the specimen was left exposed to an intense electron beam.

Even though the observation of atomic motion is clearly due to such phenomena actually occurring in the specimen, one should still be careful not to make direct one-to-one correspondence between the image spots with actual atoms at the edge of the crystal. Since HRTEM is an interference image, the crystal edge presents some issue with regard to its image formation. With highly coherent illumination for example, edges can create their own interference effects that extend well beyond the actual position of the crystal edge. An artificial lattice was constructed to test such effects by image simulation. Bloch wave simulation was used and a large unit cell was constructed with a sharp edge along the $\{1\bar{1}0\}$ surface. Essentially, the unit cell is as shown in the figure 1-70(a) with the atomic position indicated by a small dot. The simulation then assumes that this artificial construction is repeated in space. Two simulation conditions are shown, for the crystal thickness series from one unit cell thickness of 0.458 nm to 1.603 nm at Δf = - 82.2 nm which is close to the Scherzer defocus condition for the Philips EM400ST microscope. The equivalent to 37 beams was used through the objective aperture, but beam divergence attenuates most of the higher order beam contribution. In this condition, the atom positions will have *black atom* contrast, which was expected. This is far from an ideal situation for the simulation since the artificial cell used is probably still too small. It is useful to indicate some interesting image phenomena that take place at the edge, such as at the position shown by the arrow. There will be image spots (white sports) that form outside actual atom positions, which can extend some distance away from the actual specimen edge (e.g., image f) or ¼ of the lattice spacing along the $[1\bar{1}0]$ direction or 0.23 nm. Figure

1-71 is for the case with Δf = -112.4 nm, which gives white atom contrast for the Cd-Te atom position. This time, the actual atomic potential plot is shown in figure 1-71(a). The thickness series goes from 0.458 nm to 1.374 nm. Effectively, it is the spacing of the atom layers in the [110] projection. Again, the *white atom* position extends well beyond the actual position of the atoms, this time by 0.46 nm. Much more intensive simulation and experimental work is necessary to come to a more definitive conclusion about what to expect with the HRTEM imaging at the edge of the crystal, with a single atom or a column of atoms that protrude from it. This effect, known as *delocalization*, is known to be exasperated using a field emission gun source, but can now be overcome in an aberration-corrected TEM.

Specimen damage after prolonged beam irradiation is shown in figure 1-72. This is the same area that was shown in figure 1-52. The deterioration occurred over a period of approximately 30 minutes. A significant amount of specimen area has been ablated, and recrystallized on top of the specimen. The Moiré pattern over the redeposited material clearly shows that it is crystalline. A diffraction pattern and BF image, from the more extensively damaged and recrystallized part of the specimen are shown in figure 1-73. Some of the diffraction rings can be characterized as redeposited CdTe, but there is indication of the presence of CdO in the pattern having a cubic FCC structure with lattice parameter of 4.6953Å (0.46953 nm) (JCPDF#5-0640). Additionally, small crystallites often were found at the edge of the specimen, which showed lattice fringes. A measurement of the fringes and tabulating them indicates the closest fit is for β-TeO_2 (tellurite which has an orthorhombic structure (JCPDF# 9-433).

	Lattice parameter	Thermal conductivity	Cohesive energy	Elastic Constants		
	(Å)	(W/cm° C)	(ev)	(10^{11} dynes/cm^2)		
				c_{11}	c_{12}	c_{44}
C	3.56	2.0	3.68	107.6	12.5	57.7
Si	5.43	1.41	2.32	16.57	6.39	7.96
Ge	5.66	0.61	1.94	12.89	4.83	6.71
GaP	5.45	0.97	1.78	14.12	6.25	7.05
GaAs	5.65	0.54	1.63	11.81	5.32	5.92
AlAs	5.66	0.80	1.89	-----	----	----
InP	5.87	0.68	1.74	10.22	5.76	4.60
InSb	6.48	0.18	1.40	6.67	3.65	3.02
ZnS	5.41	0.26	1.59	10.40	6.50	4.62
CdS	5.58*	0.2	1.42	-----	----	----
ZnSe	5.67	0.13	1.29	8.10	4.88	4.41
CdSe	6.05	0.063	----	-----	----	----
ZnTe	6.10	0.112	1.14	7.13	4.07	3.12
CdTe	6.48	0.07	1.03	5.35	3.68	1.99
HgTe	6.43	0.03	----	----	----	----

Table 1-7: Tabulation of thermal conductivity, cohesive energy and elastic constants of various semiconductor materials. From Harrison [1-93].

W.A. Harrison, *Electronic Structure and the Properties of Solids*, Freeman, San Francisco (1980)
Reproduced with permission.

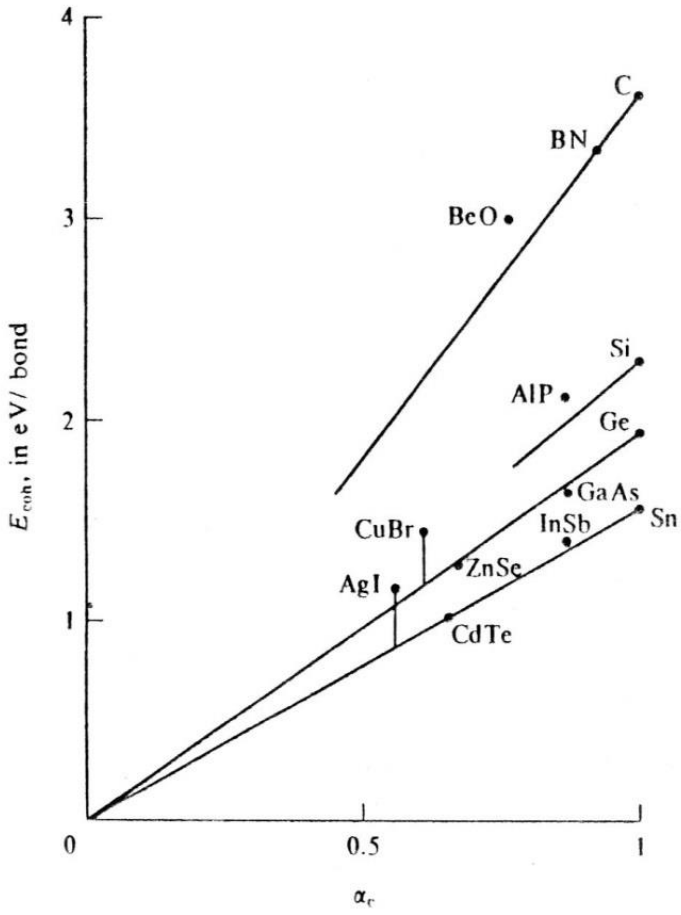

FIGURE 7-2

The cohesive energy per bond (commonly called bond energy) for the homopolar semiconductors and compounds isoelectronic with them, plotted against covalency. The lines represent an extremely simple empirical rule.

Figure 1-68: Plot of cohesive energy per bond for homopolar semiconductors and compounds isoelectronic with them, plotted against covalency. Note that CdTe ranks lowest in terms of cohesive energy. From Harrison [1-93].

W.A. Harrison, *Electronic Structure and the Properties of Solids*, Freeman, San Francisco (1980)
Reproduced with permission.

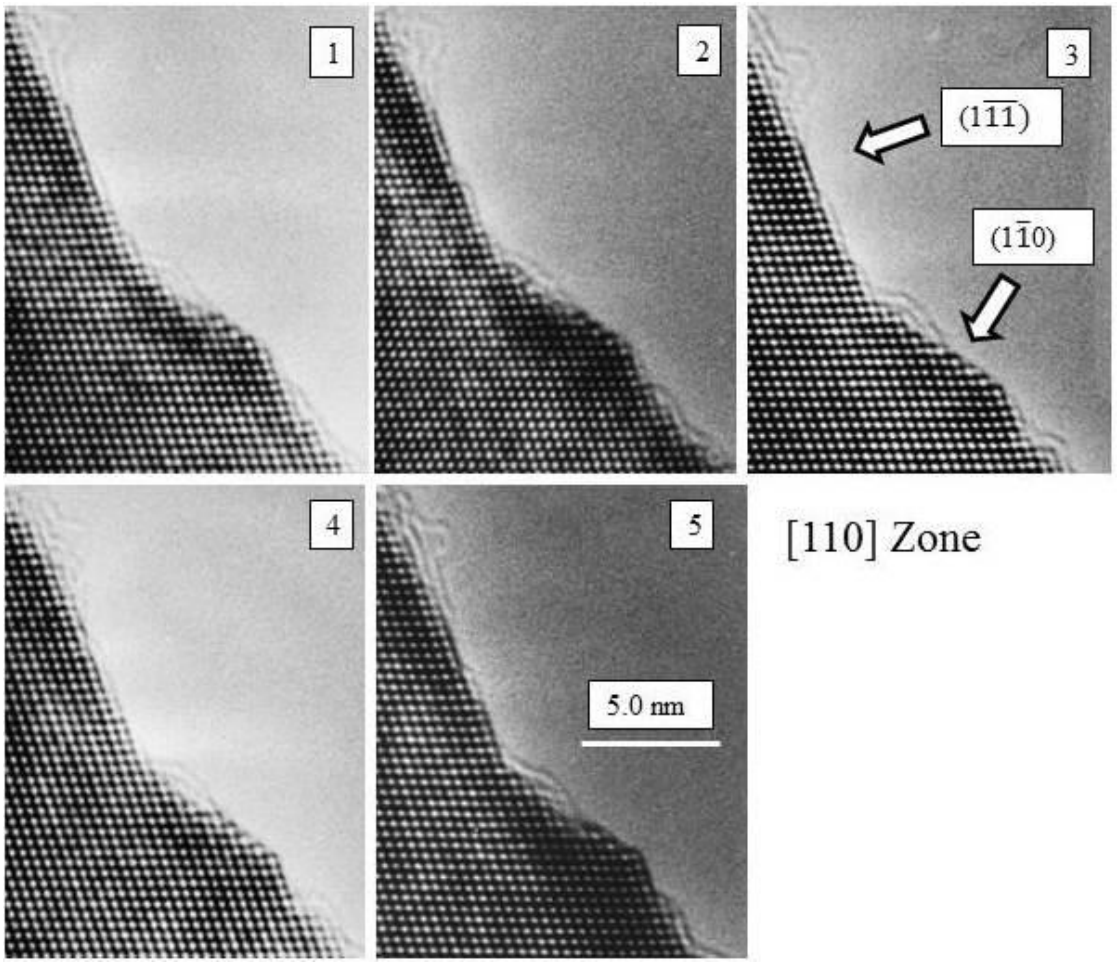

Figure 1-69: Edge of the specimen during a period of approximately 1-2 minutes. The $(1\bar{1}\bar{1})$ planes and $(1\bar{1}0)$ planes are very prominent in rearrangement. The surface rearrangement stops when the amorphous contamination layer builds up at the edge.

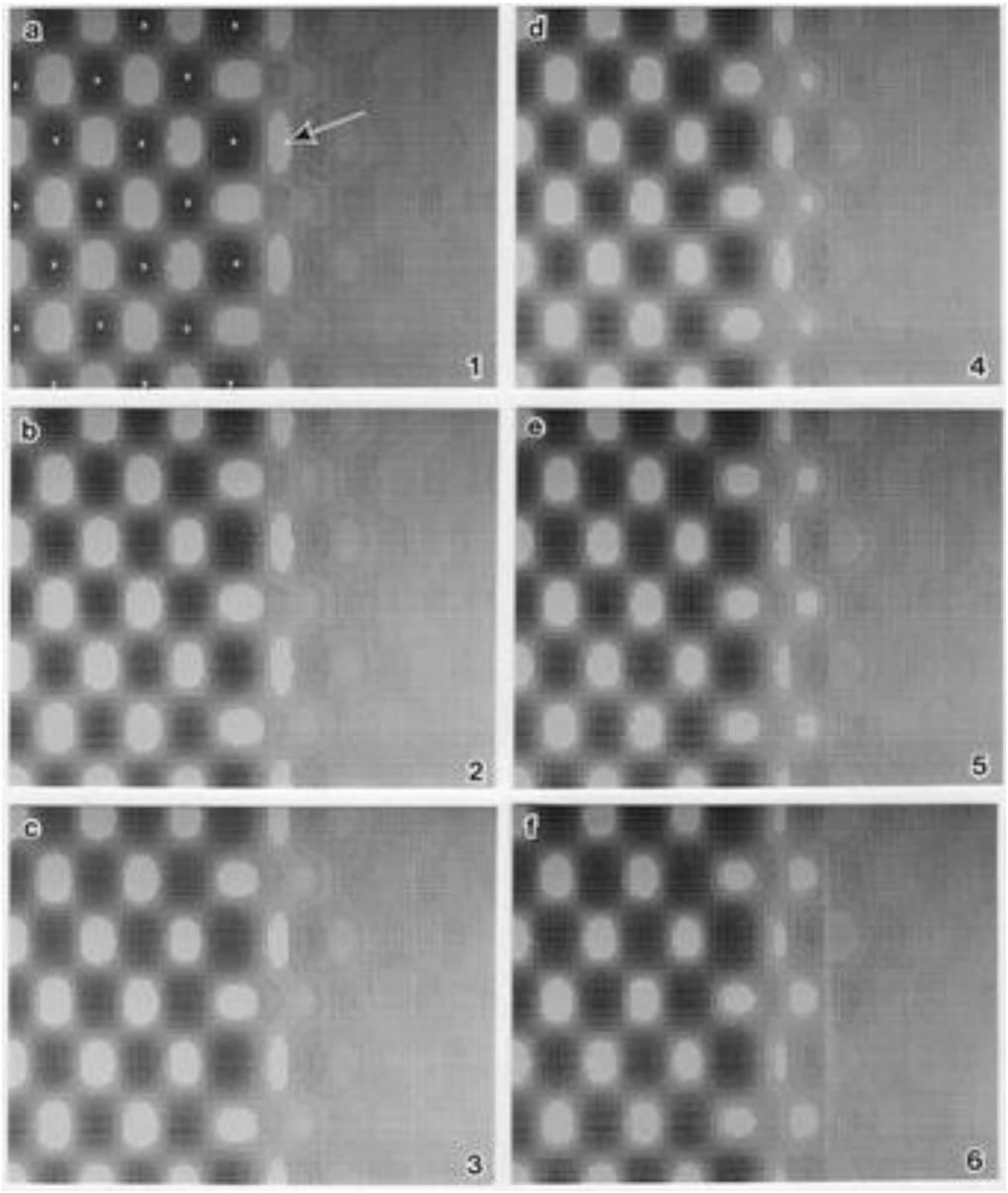

Figure 1-70: Image simulation for testing what happens at the specimen edge at $(1\bar{1}0)$ surface edge, using artificial lattice containing vacuum. Images are thickness series. Note that white image spots will appear well beyond the edge of the specimen. All of the images at $\Delta f = -82.2$ nm which gives black atom images. White dots in image (a) give the position of the Cd-Te atom pairs. (a) t = 0.458 nm, (b) t = 0.687 nm, (c) t = 0.916 nm, (d) t = 1.145 nm, (e) t = 1.374 nm, (f) t = 1.603 nm.

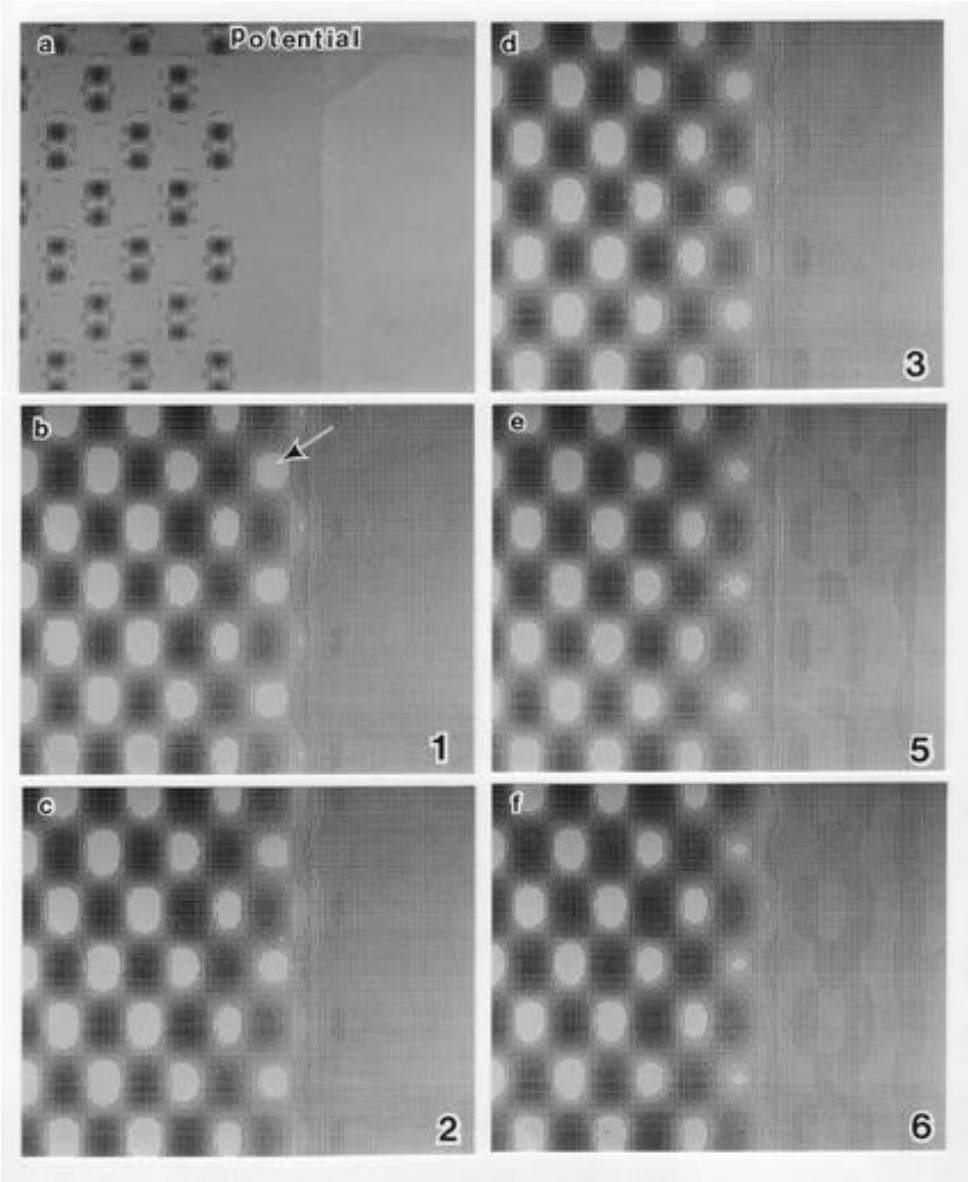

Figure 1-71: Image simulation for artificial lattice containing vacuum. The first image (a) is the atomic potential plot. All of the images at Δf = - 112.4 nm which gives white atom contrast. (b) t = 0.458 nm, (c) t = 0.687 nm, (d) t = 0.916 nm, (e) t = 1.145 nm, (f) t = 1.374nm. Interference fringes that normally appear at the edge of the specimen have been reproduced.

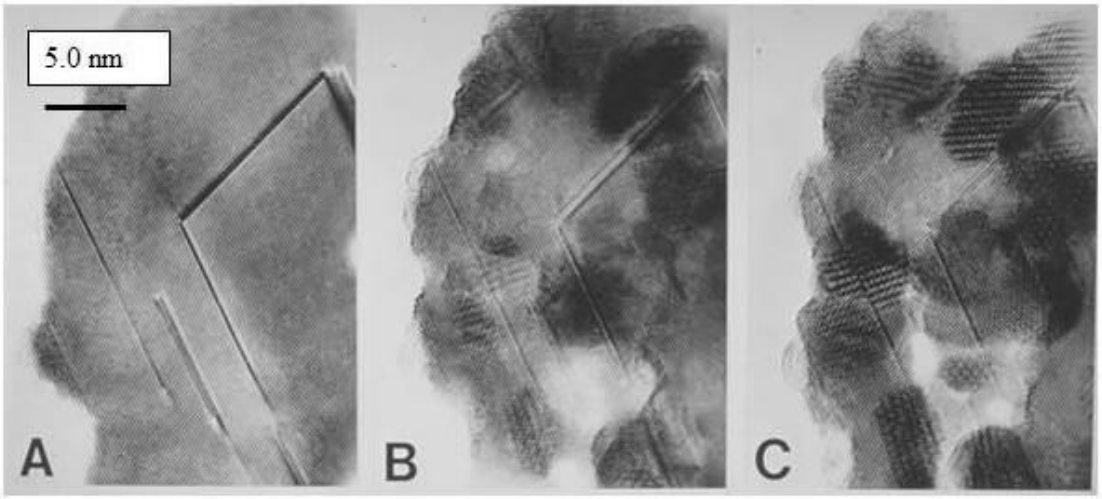

Figure 1-73: Specimen damage from e-beam irradiation over a period of approximately30 minutes of viewing.

Some of the lattice images of particles that formed at the edge of the specimen (TeO_2) are shown in figure 1-75. Since TeO_2 did not show up in any diffraction patterns, a claim for this phase is rather circumstantial. The volume fraction of TeO_2 that forms may also be too small to show in the diffraction pattern. Formation of both CdO and TeO_2, even within the TEM is not surprising in that the heats of formation of these oxides are high (- 62.3 Kcal/mole and - 78.1 Kcal/mole, respectively), and even a small partial pressure of oxygen within the vacuum of the TEM (~10^{-7} torr or lower) is still easily sufficient to drive the reaction to the formation of the oxide, especially in the presence of the ionizing electron beam. Table 1-8 lists the powder X-ray diffraction data for TeO_2 and the matching lattice fringe spacings from the HRTEM images. Only one of the fringe spacings (021) is slightly off. Other materials such as pure Cd (HCP), Te (HCP), CdTe, CdO, and other oxide combinations of Cd, CdTe and Te were considered for example, and there is some matching with Cd. However, since CdO is forming for certain, more than likely, it is not to be the case. Also, one of the crystallites was rectangular (figure 1-75), suggesting that it is likely to be something with cubic or orthorhombic structure. In modern TEM with small STEM probe size and EELS spectrometer, it would have been quite straight forward to determine the

chemical composition and even the chemical signature of small crystalline particles such as those shown in figure 1-75, but at the time of the work, the LaB_6 electron probe and EDS spectrometers were not sufficiently capable to determine the chemical composition of something that is this small.

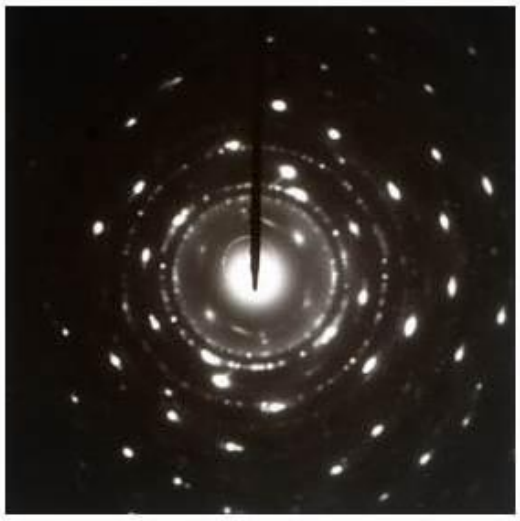

CdO	a = 0.46953 nm		FCC (Fm3m)
JCPDF# 5-0640			
hkl	d (nm)	From DP (nm)	Ratio
111	0.2712	0.268	1.01
200	0.2349	0.229	1.03
220	0.1661	0.162	1.03
311	0.1416	0.140	1.01
222	0.1355		
400	0.1174		
331	0.1077		

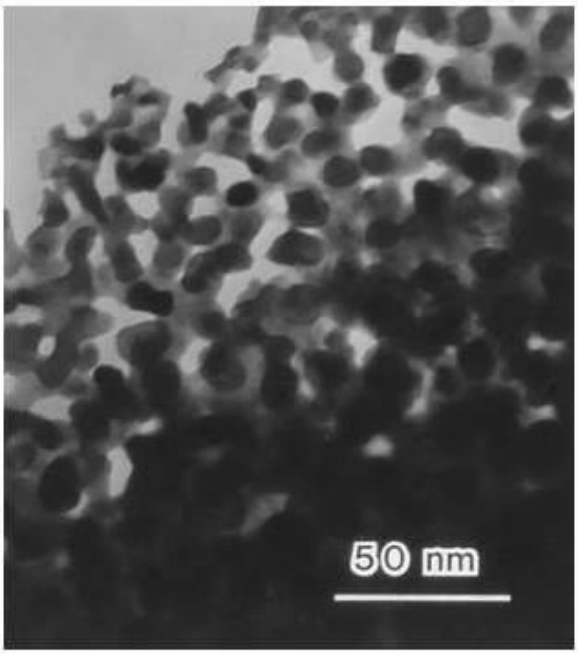

Figure 1-74: Diffraction pattern and BF image from heavily recrystallized CdTe sample. Some of the rings clearly index as CdO. The ratio is the expected/actual value. The spacings based on diffraction rings are slightly off from the PDF file by 1 to 3 %. CdTe reflections were used as a standard to calculate the spacings.

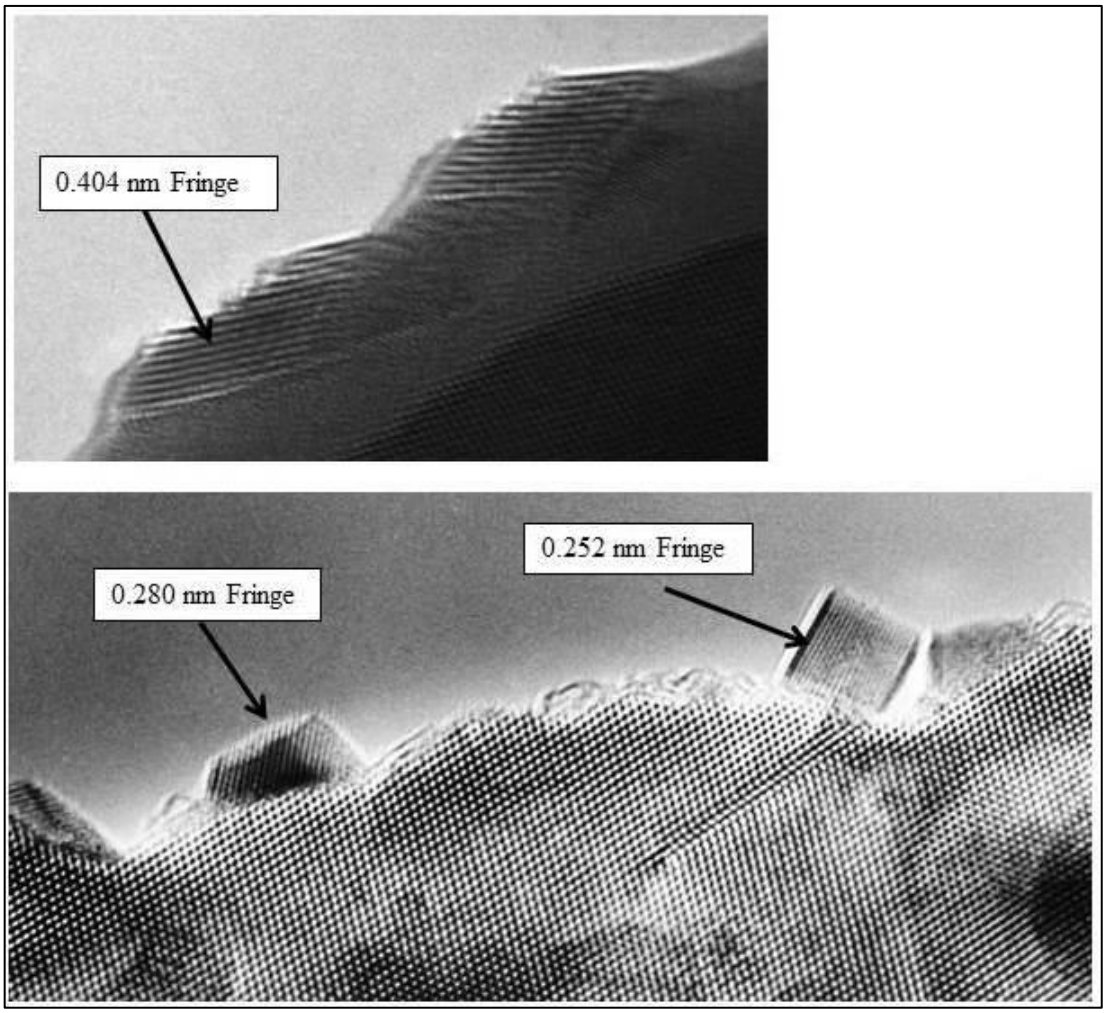

Figure 1-75: HRTEM images from specimen that had been exposed for ~20 min. under the e-beam, which started to form small crystallites at the edge of the specimen. Lattice fringe spacings observed in these crystallites match with the spacing for TeO_2.

TeO_2		Orthorhombic Pbca		
		a=1.20350, b=0.54340, c=0.56070 (nm)		
hkl	d (nm)	I/I_o (%)	From HRTEM image (nm)	Ratio
210	0.40452	11.50	0.40	1.00
111	0.37214	98.00		
211	0.32806	100.00		
400	0.30088	37.90		
311	0.28012	20.80	0.28	1.00
020	0.27320	21.40		
102	0.27304	20.10		
021	0.24560	6.60	0.25	0.97
302	0.22980	22.90	0.23	1.00
511	0.20502	19.10		
420	0.20226	22.00		
122	0.19313	24.70		
611	0.17850	17.90		
322	0.17586	18.10		
113	0.17496	10.00		
131	0.17146	6.00		
213	0.16967	16.50		
231	0.16646	10.20		
522	0.15183	6.20		
702	0.14656	9.30		
http://database.iem.ac.ru/mincryst/s_carta.php?TELLURITE				
CPDS Card # 4673				
IEM (Institute of Experimental Mineralogy)				
Chernogolovka, Moscow				

Table 1-8: Comparison of some of the lattice fringe spacings from crystallites formed at the edge of the specimen after electron irradiation, against powder X-ray data for TeO_2.

Recording and observation of defect motion in CdTe by HRTEM using a video camera was first reported by Sinclair et al. in 1982 using the Cambridge 600 keV TEM with a resolution of 0.2 nm [1-83], using specimens prepared at Stanford. In this work, 500 keV was employed, with current density at the specimen of ~1 A/cm^2, and beam divergence of 0.2 mrads. The objective aperture allowed beams out to 0.12 nm d-spacing. The image pick-up system was an Image-Isocon low light level camera (EEV type P-8041) coupled through fiber optics to a transmission fluorescent screen. At the phosphor, the magnification was ~1.3 million X and on the TV monitor was approximately 10 million X. This system was unique at the time. Images were recorded

on reel-to-reel video tape, and photographs taken directly from the TV monitor using a SRL camera. Each frame of the video was at 0.02 sec (50 frames/sec. – UK standard). The overall resolution of the system including the video recording system was estimated at approximately 0.3 nm. Using this system, the rapid blinking in and out of atomic spots could be recorded and reproduced. In addition, rapid movements of dislocations were recorded, one of them reproduced in figure 1-76. This shows a Shockley partial dislocation moving from left to right, healing an intrinsic stacking fault as it moves. Each frame is 0.02 second apart. The speed of dislocation works out to be approximately 2×10^{-6} cm/sec. This speed is not so unreasonable based on dislocation speed measurement in GaAs by Yonenaga and Sumino [1-95]. One of the results is reproduced in figure 1-77 for the case of β dislocation which is a 60° dislocation with As atoms along the core They also show data for α dislocation (Ga core) and the screw dislocation. They have generally the same characteristics for the velocity vs. shear stress, however the response to the impurity in the lattice have very different effect on each dislocation type. For the TEM observation, the values of applied stress and the temperature are unknown; therefore, it is rather difficult to put into context the observed speed of the dislocation with bulk literature values. In addition, the fact that the surface is very close to the dislocation line could have an effect on the dislocation mobility.

A second type of observation was the slow climb of a Frank dislocation. Figure 1-78 shows a set of 6 photographs obtained from the video showing Frank partial dislocation climbing from right to left and eliminating the extrinsic stacking fault as it climbs. Each photograph is a time-averaged image of 25 frames. The Frank partial dislocation climbed approximately 2.1 nm in 105 seconds, or at a speed of 1.2 nm/minute. Because of the image integration over multiple frames, the picture quality is much better than for figure 1-76, which is unprocessed. A Frank dislocation can only occur by a diffusional process; therefore, it is considerably slower than the slip process for Shockley partial dislocations. As noted in this original article [1-83], the image spots at the dislocation core, terminating the edge dislocation, were rapidly oscillating randomly; this instability also is readily visible in the original recording. The extrinsic

stacking fault associated with the Frank partial is readily recognized by the (111) plane image stacking sequence.

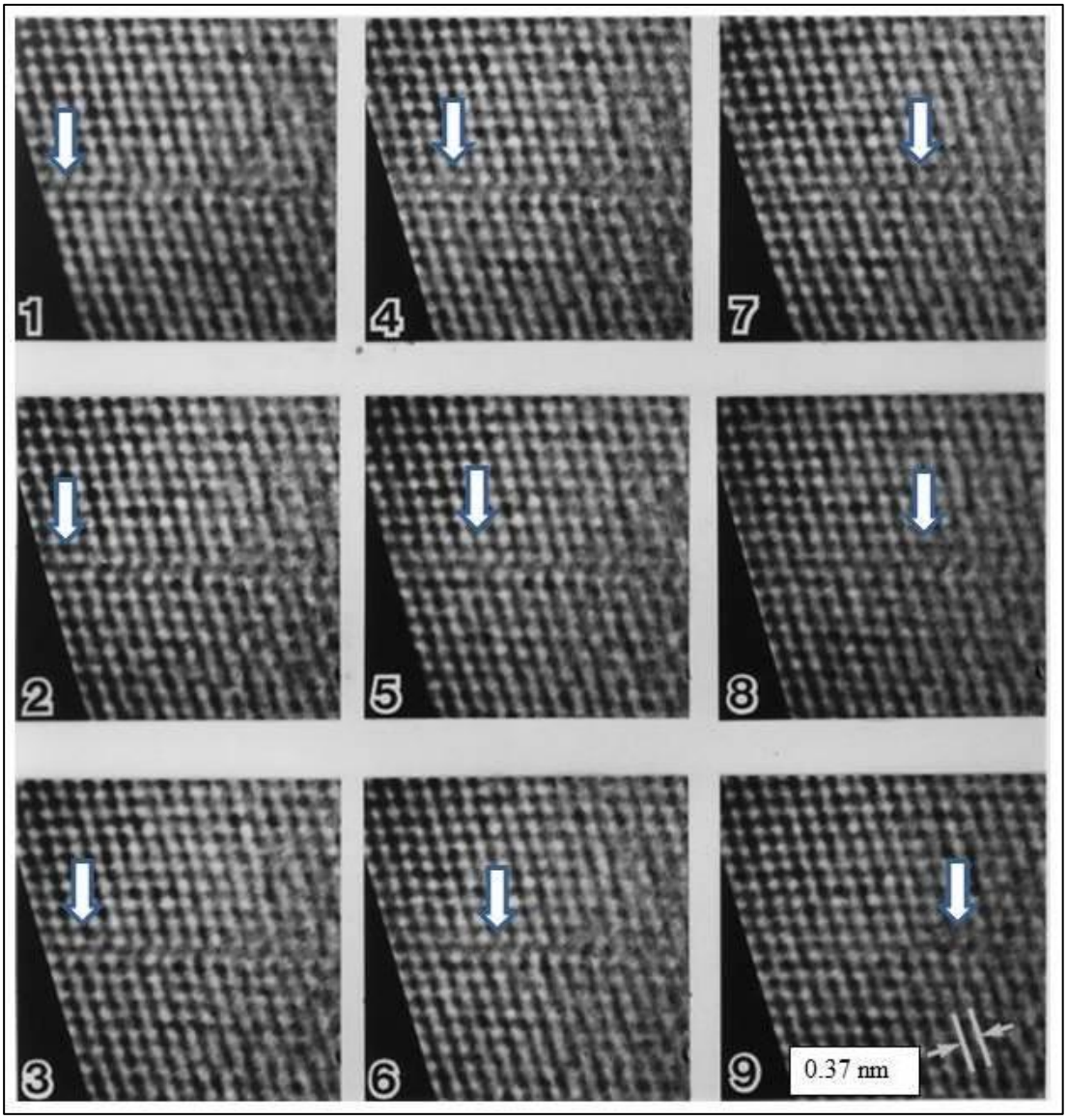

Figure 1-76: HRTEM image of Shockley partial annealing out of the crystal. Successive frame rate is 0.02 sec. apart. The arrow shows the position of the partial dislocation. The intrinsic stacking fault is healed as the dislocation moves from left to right. From Ref. [1-83].

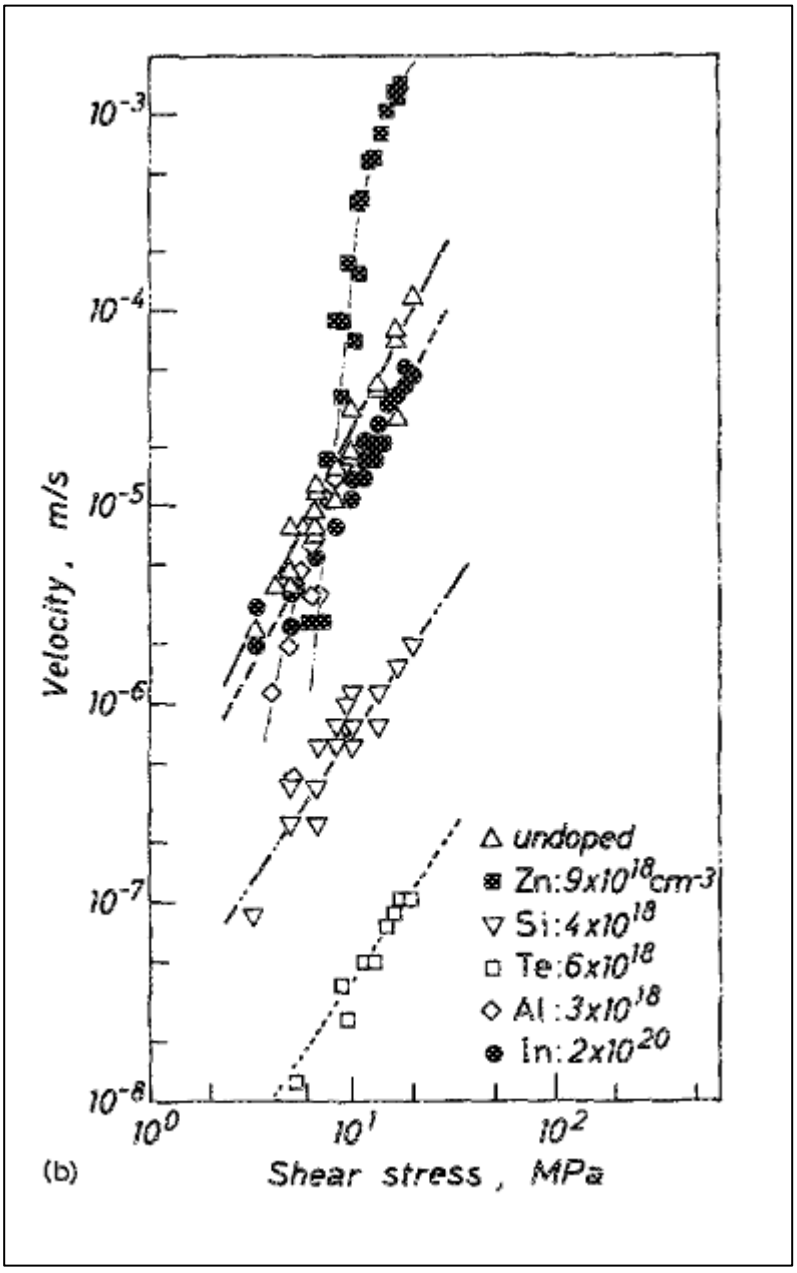

Figure 1-77: An example of dislocation velocity measurement using etch stop technique, by Yonenaga and Sumino (1989)[1-95]. J. Appl. Phys. , AIP publishing. Reproduced with permission.

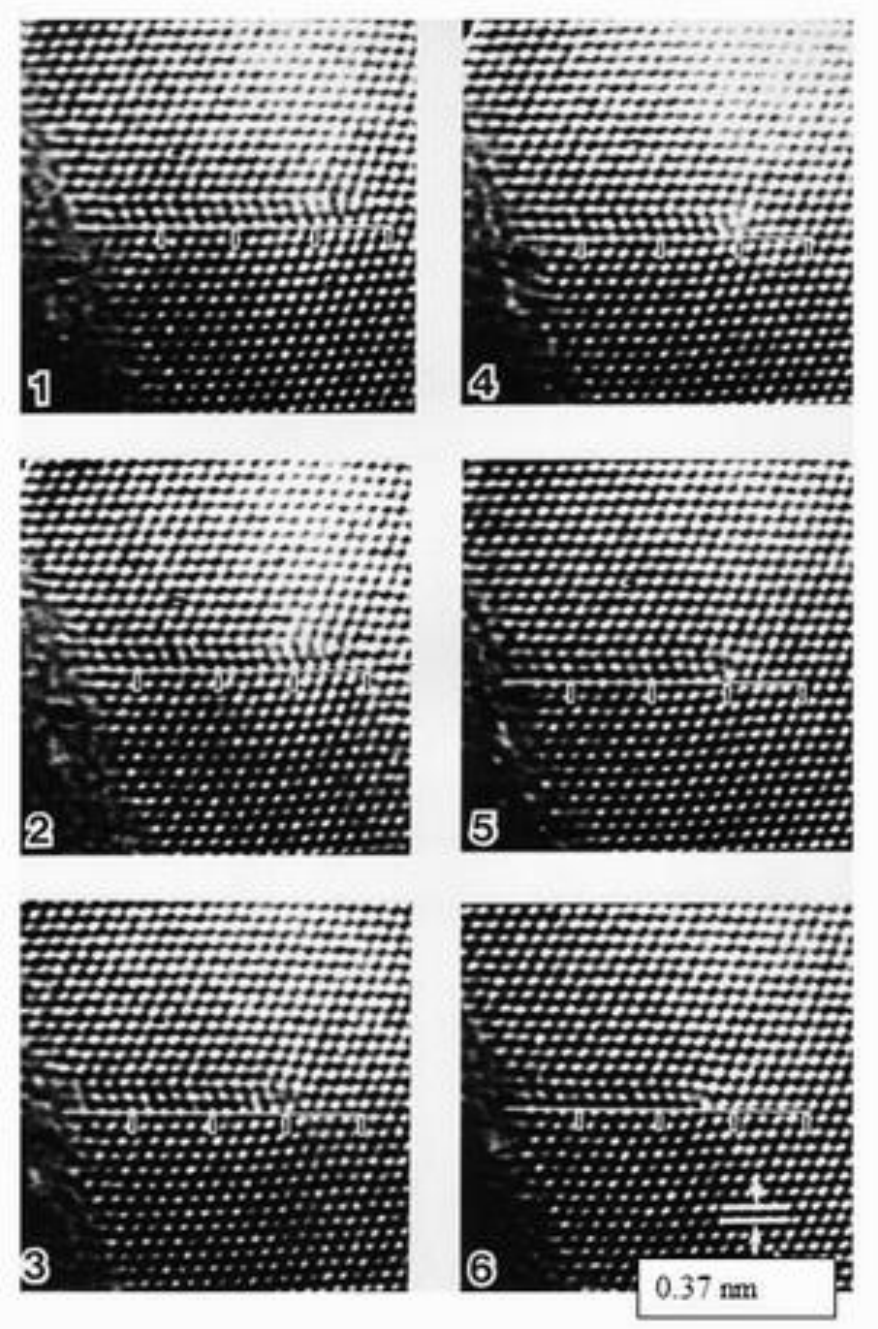

Figure 1-78: Climb of Frank partial dislocation, from right to left. Each ruler marker indicates 5 image spots (~ 1.8 nm). Each image is integrated over 25 frames (i.e., half-second camera exposure). The elapsed time and length of the extrinsic fault is as follows: (1) 0s, 6.3 nm, (2) 28s, 6.0 nm, (3) 48s, 5.6 nm, (4) 71s, 5.3 nm, (5) 85s, 4.5 nm, (6) 105s, 4.2 nm. From Ref. [1-83].

To study the atomic and defect motion in-situ at Stanford, a Philip EM400ST *Super Twin* microscope with the standard side entry stage and two-axis specimen tilting capability was used. The TEM was filled with a video camera made by Philips Co., with a viewing area of approximately 1 inch diameter, and mounted under the microscope as shown in figure 1-79. Similar to the Cambridge video system, a transparent phosphor screen was connected to a fiber optic coupling to the video camera. Combined with 900,000X magnification at the screen with the magnification of the video camera, the total magnification on the viewing monitor was approximately 15 million X. The microscope used a Lab_6 filament; the Cs of this microscope was at 1.2 mm and beam divergence was typically 3 mrads. Compared to the Philip EM400 without the tilt, the ultimate resolution was degraded, but it was still sufficient to obtain lattice images from CdTe. The addition of the two axis tilting stage greatly improved the ability to bring the specimen into the proper orientation for HRTEM imaging.

Since many of the dynamic effects previously observed were thought to be dependent on beam heating, a careful calibration curve was generated for the beam current as a function of condenser lens setting and C2 aperture size. This is shown in figure 1-80. This measurement was taken by measuring the current on the large screen with a Keithley picoammeter. An image of the LaB_6 source is formed on the large screen to just to fill the screen in order to take the measurement. Using a successively larger C2 aperture gives higher probe current and larger beam divergence, which also degrades image quality. Typically, 50 μm aperture was used as the best compromise between image brightness and image quality. A more convenient means of monitoring the beam current was to use the small viewing screen which also was used to measure the exposure time for the negative. By measuring the exposure time on the small screen for a given beam current, a calibration curve can be generated. The curve serves as a convenient indication of the beam current without needing to measure it each time. This curve is shown in figure 1-81. All one needs then is the knowledge of the actual size of the filament image at the specimen to calculate the current density. The large viewing screen for the Philips EM400ST is 8 cm radius, and the magnification at which the filament image just fills the screen at 520,000 magnification. Some care was taken

to determine what part of the LaB_6 filament image contributes mostly to the current to take the measurement. Based on the calibration curve then, at a typical exposure time of 1 sec, the beam current is ~11 nA. This is approximately 15 A/cm^2 at the specimen, which was the typical operating condition. A beam current density as high as 30 to 40 A/cm^2 could be obtained by pushing the filament current and condenser lens current, and using larger apertures. A 15 A/cm^2 beam current density is still a very high current density; therefore, significant specimen heating can occur, especially for CdTe with its low thermal conductivity. For some specimens that had a small or unsupported large thin region, actual melting of the specimen occurred on some occasions. CdTe melting point is 1041°C. Stress could be provided by large uneven thermal stresses that could develop within the specimen. The typical vacuum at the specimen was rated at approximately $2x10^{-7}$ torr.

Video recording was achieved on a studio-grade ¾-inch Sony U-Matic video recorder (Sony Betamax). Editing of the recorded tapes was done at the Stanford Video Services facility. Using the large ¾-inch tape format made some difference in obtaining as clean a signal as possible from the video camera on the TEM, compared to using a ½ inch VHS format, which was becoming popular for consumer applications at that time. Frame speed was 30 /sec. The image as captured on the video camera was already quite noisy, and video recording reduced the quality somewhat more. Edited tape was then transferred to a consumer grade VHS format tape (½-inch width tape) for more easy viewing on consumer grade video players but a significant loss in quality of the image took place in transfer. The VHS tape was then digitally processed using a Quantex model DS-50 digital video processor and model DF-80 digital video filter system [1-96]. Several contrast enhancement schemes were used to try to improve the image quality. First a digital filter was applied to each pixel, with a kernel size of 9 with a 9x9 two-dimensional filter. Fifterrn percent of the unfiltered image was added back in, and a high pass band filtering done. This spatial filtering enhanced the edge contrast significantly. Additionally, a 4 frame running average was used to try to reduced noise and enhance contrast. This comes with some degradation of fast occurring events in the image, but the overall contrast of the image was increased

significantly. These procedures, as with the Cambridge recordings, were pioneering in the early 1980s.

Figure 1-79: Philip EM400 with the video camera attached underneath.

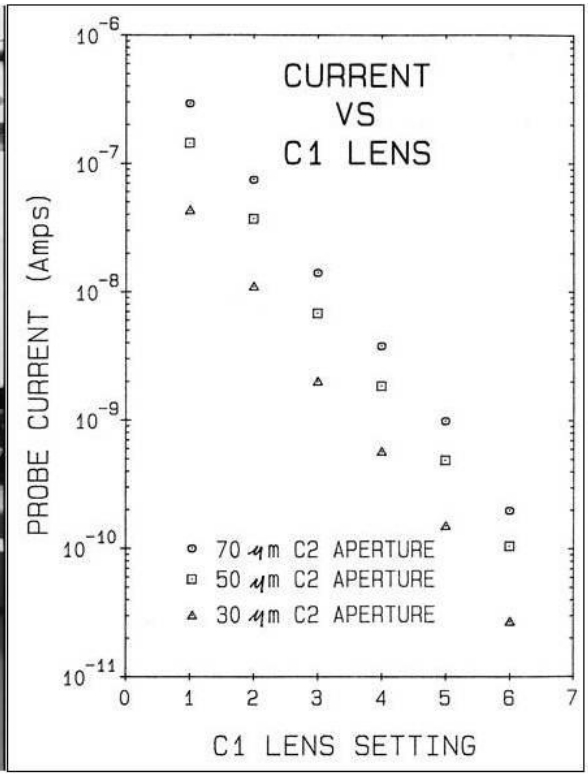

Figure 1-80: Probe current vs. microscope settings.

In in most cases, imaging for the video recording was done with 19 beams out to (004) reflections admitted through the objective aperture. High beam divergence and higher Cs of the microscope should have restricted the contribution to the image to only the four {111} beams, but the lattice resolution of the combined CdTe image spots was easily attained. Most of the specimens for this part of the work were prepared by a chemical jet spray method using 3% bromine in methanol as previously described in Section 1.7.

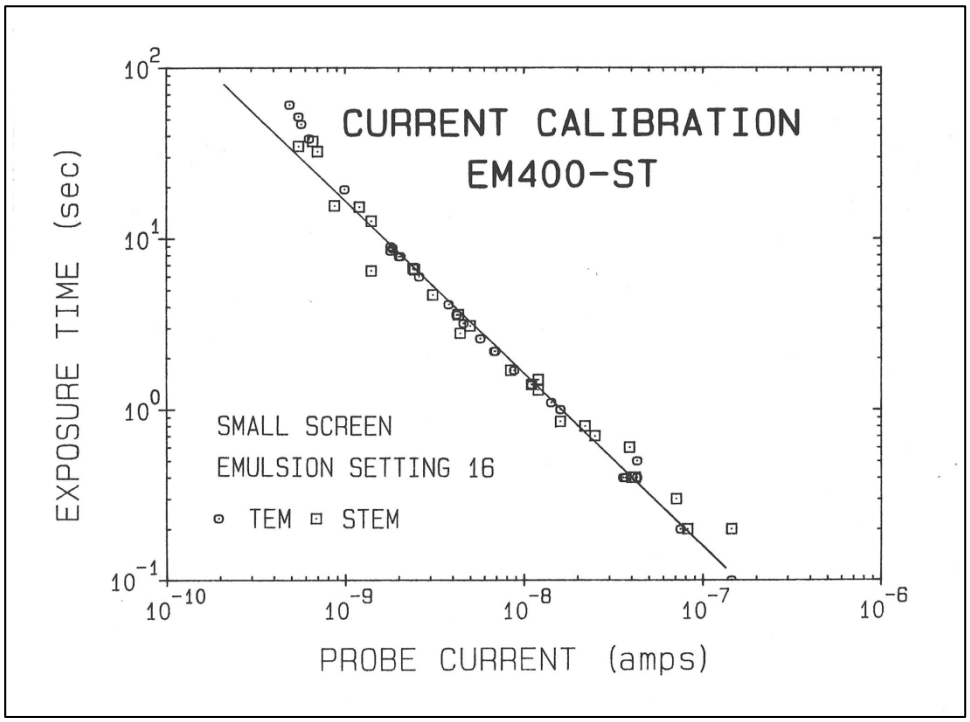

Figure 1-81: Calibration curve between the probe (beam) current and exposure time measured by the small viewing screen.

Figure 1-82 shows the surface rearrangement process as it is occurring in the TEM. A series of steps forms and disappear on the {111} surface as can be seen in the image. These images have been digitally filtered and enhanced with the Quantex image processor. The spatial information that was enhanced (the CdTe lattice) happens to be approximately the same dimension as the camera fiber optic plate and this appears in the area outside the crystal. The facet on the far left is a {110} surface and the other two are {111} planes. The images were taken a few seconds apart. In real time, the individual image spots at the edge make rapid movement of one to two jumps per second.

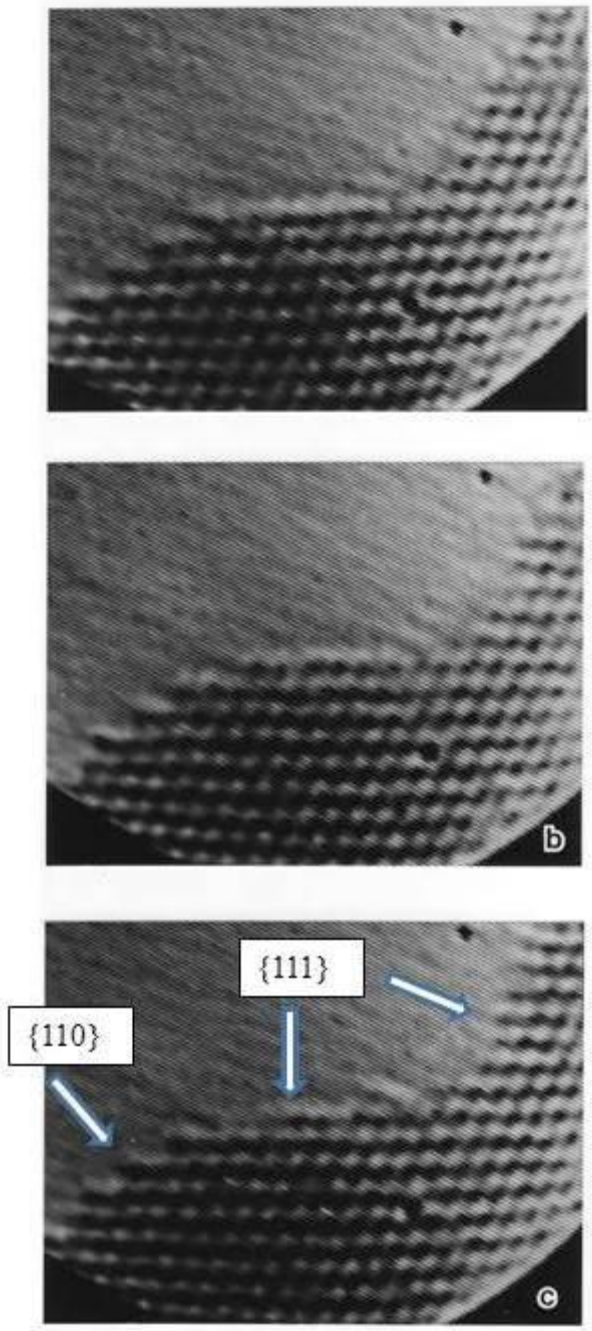

Figure 1-82: Video image from the edge of the specimen where surface rearrangement is taking place. The images are digitally processed and enhanced.

The next series of images are for a Shockley partial dislocation exiting from the crystal at high speed, which could only be captured by the video recording. The entire process took place in 3 TV frames, which is equal to 0.09 sec. In real time, it happens

in just an instant and only frame-by-frame analysis was able to capture the event. This sequence is shown in figure 1-83. Since the image must be viewed as is, no video processing (averaging and combining between frames) was done; therefore, the contrast is low for these images. The approximate position of the partial dislocation is indicated by arrows. As the Shockley partial exits the crystal, the intrinsic stacking fault (identified by its stacking sequence) is eliminated. The speed of the dislocation translates to 2 x 10^{-5} cm/sec, which is consistent with the velocities observed earlier [1-83].

A climbing Frank dislocation with burgers vector of the type $\vec{b} = \frac{a_o}{3}[1\bar{1}1]$ was captured as in figure 1-78 by the Cambridge 600 KeV microscope. This is shown in figure 1-84. In the three images shown, the Frank dislocation with length of approximately 5.0 nm took 2 minutes to climb out of the crystal. This was 2.5 nm/min, or twice as slow compared to the Cambridge microscope observation in figure 1-78. In the process, the extrinsic stacking fault was eliminated. In general, dislocation motion was observed in only a small fraction (< 5%) of the total defect population, and those that did move were mainly near the edge of the specimen.

In figure 1-85, a region containing some amorphous material gradually builds up a new layer of {111} planes to the crystal, while inside the amorphous area, a new crystallite is forming. This occurred over a period of 2-3 minutes. These images have been digitally enhanced using the Quantex processor. The new crystallite appears to be a new CdTe particle, in a twin orientation with the host crystal. It should be noted that current density used in this HRTEM imaging work is quite high, approximately about 10X higher than in conventional TEM work. Generally, larger C1 apertures were used, with a highly focused beam running at highest beam current conditions. A simple heat flow calculation using experimental parameters [1-97] indicates that the expected temperature rise is still considerably below the ~110°C required for the sublimation process to become noticeable [1-92].

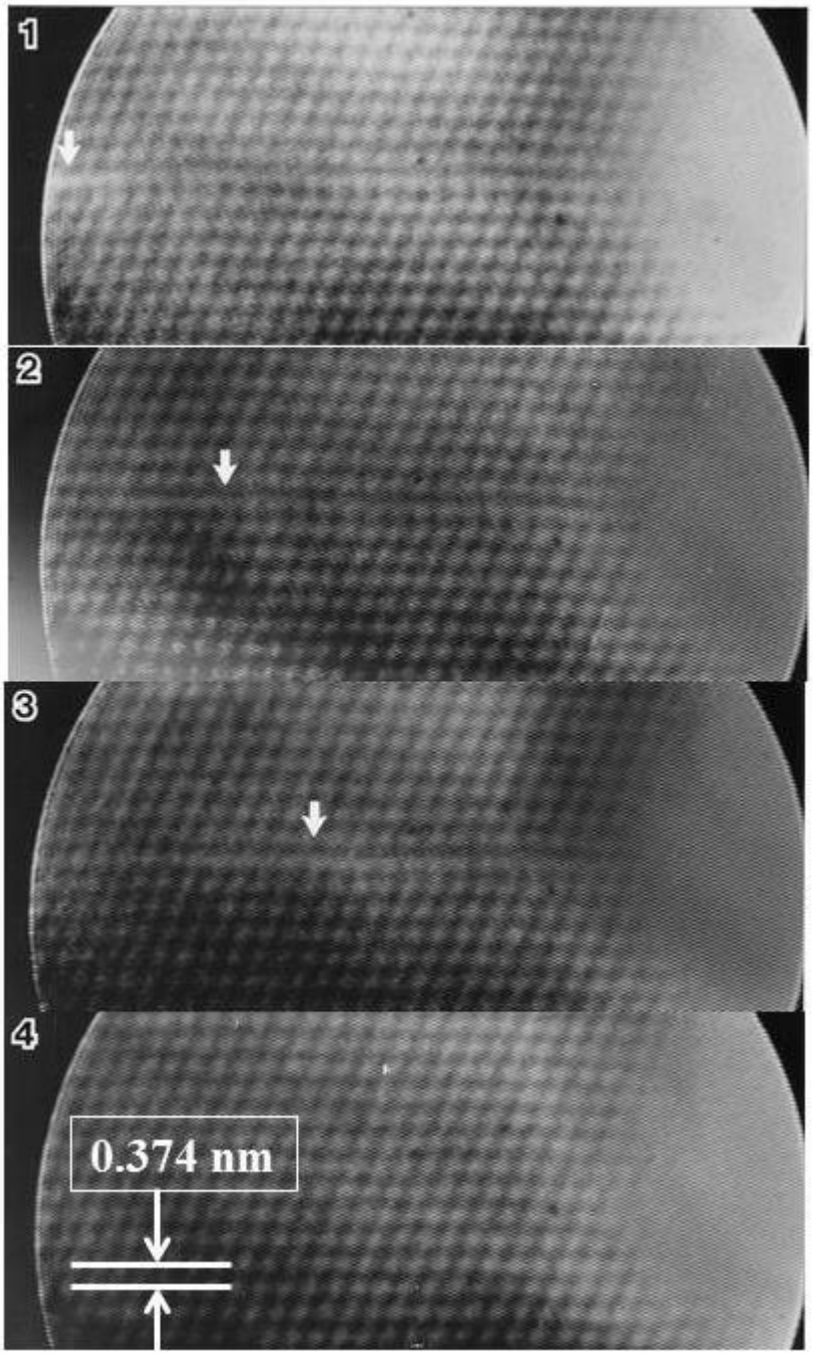

Figure 1-83: A Shockley partial dislocation passing out of the crystal from left to right, eliminating the intrinsic stacking fault in the process. The entire event occurred in 3 TV frames, or in 0.1 sec. Speed converts to 2 x 10^{-4} mm/sec. The image is unprocessed.

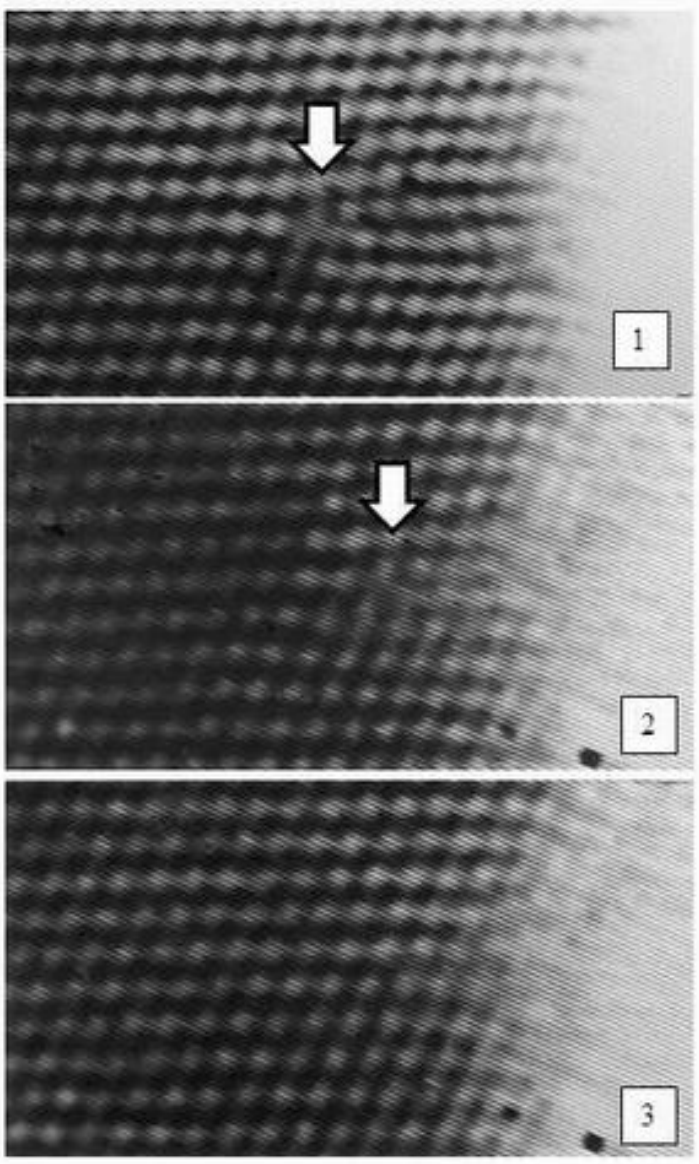

Figure 1-84: Climb of Frank partial dislocation, which eliminates extrinsic stacking faults in the process. Entire process took ~2 minutes to climb 5.0 nm.

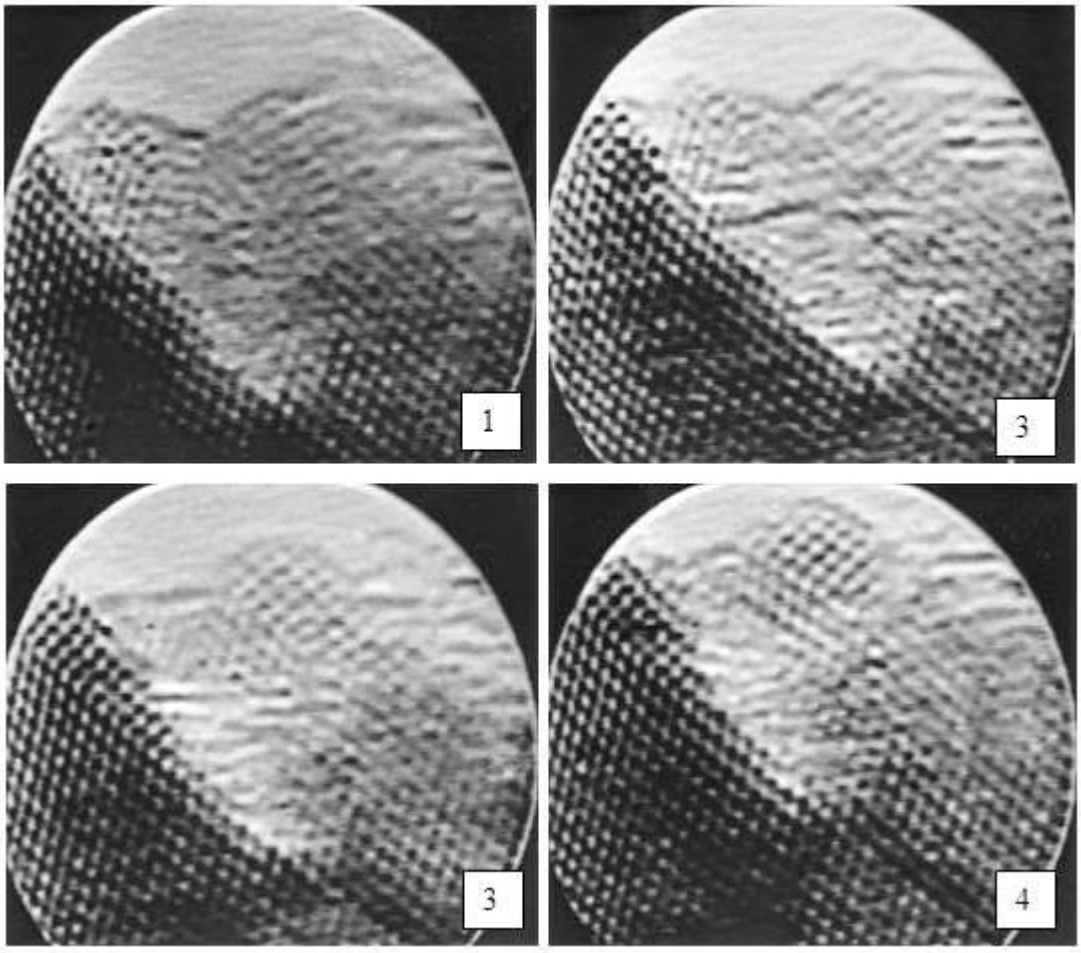

Figure 1-85: New surface being added and growth of new crystallite over a period of approximately 2-3 minutes. The image has been digitally processed.

Much of the temperature rise that occurs can be attributed to some particular geometry of the specimen and low thermal conductivity of CdTe. When the specimen has high thermal conductivity, the beam current needed to induce atomic motion is apparently very high, at approximately 100 A/cm^2, according to Hashimoto for gold particles [1-98]. To obtain more controlled experimental conditions to study defect motion, for example, specimen heating holder combined with a mechanical stage, which can impart a known stress state to the specimen maybe helpful in obtaining more

quantitative results. This combined with higher vacuum conditions to avoid rapid deterioration of the specimen from oxidation and other contamination effects that would complicate analysis would be very useful. However, as mentioned previously, the reaction thermodynamics for oxidation favors the reaction from proceeding even with very low partial pressure of oxygen. The kinetics of reaction also may be affected by e-beam irradiation and better vacuum conditions. These factors need to be tested with further studies with improved modern TEM's.

1.11 Summary of Chapter 1

In this chapter, the HRTEM technique was applied to the study of CdTe material, and to a lesser extent, on CdS. First, various TEM specimen preparation methods that can be applied to all semiconductor materials as well as to other hard materials are described in detail. Methods and tools to use for preparing single-crystal oriented specimen to cross sectional specimen are outlined. The cross section TEM specimen preparation technique and tools that was first developed at HP Laboratories were applied to CdTe, and this methodology came to revolutionalize the specimen-making method for semiconductor material and other materials where the interface has to be viewed in cross section. HRTEM technique was used to image CdTe and CdS to the best resolution capability of the TEM available at the time, which was approximately 0.3 nm. Image simulation methods were applied to determine the effect of various microscope parameters to the image formation.

By virture of its high atomic number and one of the largetst lattice spacing of all semiconductors, CdTe provides exceptionally high contrast images in high resolution. The high density of defects present originally and induced into the specimen during specimen preparation gave unique opportunity to study various dislocation types, which also are present in other semiconductor materials. Dislocations that were dissociated and reacted with other dislocations were

analyzed by HRTEM method to determine their structure at resolution of 0.3 nm. Only some of the simpler reactions were analyzed and compared to known literature results. There are many more complicated reactions and structures that have not been examined in detail that would be useful to analyze in the future to elucidate more details about the reaction mechanisms and the resulting structure.

One of the most interesting outcomes of the study of CdTe material was the observation of dynamic events in-situ in the TEM. Due to the high density of defects and low thermal conductivity of CdTe, there is a significant heating effect that comes from electron beam while examining the CdTe material. Atomic motion and rearrangement of the surface can be observed in real time using a video camera attached to the TEM. Defect motion also was observed, which opened a whole new avenue of study of dislocations and reactions between dislocations. At the time of this study, video system attached to the TEM was relatively rare and more of a curiosity in the field. Today, the video system has become an indispensable part of the TEM, for recording images as well as dynamic events that might take place with the specimen. Digital recording of TEM images have completely done away with negatives and the technology for higher resolution and capture capabilities are constantly being improved. Many interesting phenomena have been investigated using the video system.

Chapter 1 References:

[1-1] L.D. deBroglie, *Recherches sur la théorie des quanta (Researches on the quantum theory), Thesis (Paris), Ann. Phys. Fr.* **3**, 22 (1925)

[1-2] H. Busch, *Berechnug der Bahn von Kathodenstrahlen im Axialsymmetrischen Elektromagnetischen Felde*, Ann, Phys. Lpz. **81**, 974 (1926)

[1-3] E. Ruska, *The Early Development of Electron Lenses and Electron Microscopy*
ISBN-10: 3777603643, ISBN-13: 97-3777603643). Leipzig: S. Hirzel (1980)

[1-4] R. Rudenberg, *"Configuration for the enlarged imaging of objects by electron beams"*, Patent DE906737, May 30, 1931

[1-5] 1986 Nobel Prize for Physics
http://www.nobelprize.org/nobel_prizes/physics/laureates/1986/

[1-6] R. Erni, M.D. Rossell, C. Kisielowski, and U. Dahmen,
Atomic-Resolution Imaging with a Sub-50-pm Electron Probe
Phys. Rev. Lett. **102** (9), 096101 – Published 2 March 2009

[1-7] O. Scherzer, *Über einige Fehler von Electronenlinsen*,
Zeitschrift für Physik. **101**, pp. 593- 594 (1936)

[1-8] R.N. Bracewell, *The Fourier Transform and its Applications*, McGraw-Hill Book Company (1978)

[1-9] P.B. Hirsh, A. Howie, R.B. Nicholson, D.W. Pashley and M.J. Whelan, *Electron Microscopy of Thin Crystals*, London: Butterworths (1965)

[1-10] J.C.H. Spence, *Experimental High-Resolution Electron Microscopy, 2nd Edition*, Oxford University Press, (1988)

[1-11] J. Wu, Center for Ultrastructural Research, Univ. of Georgia, PowerPoint Lectures, jswu@physast.uga.edu. (2005)

[1-12] D.B. Williams and C. Barry Carter, *Transmission Electron Microscope*, Springer-Verlag US (1996)

[1-13] J.C.H. Spence, M.A. O'Keefe, and H. Kolar, *High-resolution image interpretation in crystalline germanium*, Optic **49**, 307 (1977)

[1-14] O. Scherzer, *The Theoretical Resolution Limit of the Electron Microscope*, J. Appl. Phys. **20**, 20 (1949)

[1-15] J. Desseaux, A. Renault & A. Bourret, *Multi-beam lattice images from germanium oriented in (011), Phil. Mag*. **35**, 357-372 (1977)

[1-16] K. Izui, S. Furuno, T. Nishida, H. Otsu, and S. Kuwabara, *High Resolution Electron Microscopy of Images of Atoms in Silicon Crystal Oriented in (110)* J. Electron. Micros., **27**, 1711 (1978)

[1-17] J.C.H. Spence, M.A. O'Keefe, and S. Iijima, *On the thickness periodicity of atomic-resolution images of dislocation cores,* Phil. Mag., A, **38**, 463 (1978)

[1-18] H. Hashimoto, H. Endoh, Y. Takai, H. Tomioka and Y. Yokota, *Direct observation of dynamic behaviour of atoms in crystals and atom clusters by TEM,* Chem. Scr., **14**, 23 (1979)

[1-19] A. Olsen, J.C.H. Spence and P. Petroff, *Compositional analysis of III-V interface lattice images*, Proceedings of the 38th Annual Meeting of EMSA, edited by G.W. Bailey (Baton Rouge: Claitors), p. 319 (1980)

[1-20] P. Pirouz, *The many-beam theory of lattice image formation in transmission electron microscopy*, Phil. Mag.A, **41**, Issue 1, pp 33-40 (1980)

[1-21] P. Goodman and A.F. Moodie, *Numerical Evaluation of N-beam wave functions in electrons in electron scattering by the multi-slice method*, Acta Cryst. A **30**, 280-290 (1974)

[1-22] R. Kilaas, *Interactive simulation of high resolution electron micrographs*, In 45th Ann. Proc. EMSA, G.W. Bailey (ed.), Baltimore Maryland, pp. 66-69 (1987)

[1-23] O.L. Krivanek, *A method for determining the coefficient of spherical aberration from a single electron micrograph,* Optik, **45,** No.1, 97-101 (1976)

[1-24] K.J. Hanzen, *The optical transfer theory of the electron microscope: fundamental principles and applications,* Adv. Opt. Electron Micr. **4**, 1 (1971)

[1-25] K. Zanio, *Semiconductors and Semimetals*, Vol. **13**, CdTe, R.K. Willardon and A.C. Beer, eds., Academic Press, N.Y. (1978)

[1-26] M. Raugei and V. Fthenakis, *Cadmium flows and emissions from CdTe PV: future expectations,* Energy Policy, Vol. 38, Issue 9, pp 5223-5228 (2010)

[1-27] First Solar CdTe solar panel module recycling program.
http://www.firstsolar.com/en/technologies-and-capabilities/recycling-services

[1-28] A. Rogalski, *HgCdTe infrared detector material: history, status and outlook* Reports on Progress in Physics, Vol. **68**, No. 10, 2267 (2005)

[1-29] R. Muller and R, J. Zuleeg, *Vapor-Deposited, Thin-Film Heterojunction Diodes,* Appl. Phys. **35**, 1550–1556 (1964)

[1-30] K. Mitchell, A.L. Fahrenbruch and R, H. Bube, *Evaluation of the CdS/CdTe heterojunction solar cell,* Appl. Phys. **48**, 4365–4371 (1977)

[1-31] T. L. Chu and S.S. Chu, Progress in Photovoltaics: Research and Applications, Vol. **1**, Issue 1, pp. 31-42, Jan. 1993

[1-32] R. Triboulet and P. Siffert, *CdTe and Related Compounds: Physics, Defects, Hetero and Nano-structures, Crystal Growth, Surfaces and Applications*, Elsevier, Oct 22, 2009

[1-33] B. Ray, II-VI Compounds, Monographs in The Science of the Solid State, Vol. 2, Pergamon, Oxford (1969)

[1-34] R.S. Feigelson and R.J. .Raymakers, Center for Materials Research, Crystal Lab, Stanford University

[1-35] South Bay Technology, Inc.
1120 Via Callejon
San Clemente, CA 92673, USA

[1-36] Technics Inc.
Alexandria, VA, USA
Closed in 2002

[1-37] Gatan, Inc.
5794 W Las Positas Blvd, Pleasanton, CA 94588, USA

[1-38] VCR Group, Inc.
(Now part of South Bay Technology, Inc.)
1120 Via Callejon, San Clemente, CA 92673, USA

[1-39] T. Yamashita, *A Mechanical grinding machine for the preparation of TEM specimens,* EMSA Bulletin **10**, 66 (1980).

[1-40] J.C. Bravman and R. Sinclair, *The preparation of cross section specimens for transmission electron microscopy,* J. Electron Microsc. Tech., **1** (1), 53-61 (1984)

[1-41] SYTON®, registered trademark of DA NanoMaterials, LLC

[1-42] Nobel Symposium 47, "*Direct Imaging of Atoms in Crystals and Molecules*", Proceedings of the Forty-Seventh Nobel Symposium held on Lidingö, Sweden (August 6-10, 1979)

[1-43] MRS Conference, Defects in Semiconductors, Symposium Proceedings, Vol. 2, Editors, J. Narayan and T.Y.Tan, North-Holland, Nov. 1980

[1-44] K. Heinnemann, *In-situ measurement of objective lens data of a high resolution electron microscope*, Optik, **34**, 113 (1971)

[1-45] P. Pirouz, *Effect of absorption on lattice images*, Optik, **54**, 69 (1979)

[1-46] T. Yamashita, F.A. Ponce, P. Pirouz and R. Sinclair, *High-resolution lattice imaging of cadmium telluride*, Phil Mag. A, Vol **45**, No 4, 693-711 (1982)

[1-47] P.A. Doyle and P.S. Turner, *Relativistic Hartree-Fock X-ray and electron scattering factors*, Acta Cryst. **A24**, pp. 390-397 (1968)

[1-48] P. Pirouz, *Thin-crystal approximation in structure imaging*, Acta Crystallog. A, **37**, 465 (1981)

[1-49] R.H. Wade and J. Frank, *Electron microscope transfer functions for partially coherent axial illumination and chromatic defocus spread*, Optik, **49**, No.1, 81-92 (1977)

[1-50] K. Ishizuka, *Contrast transfer of crystal images in TEM*, Utramicroscopy, **5**, pp. 55-65 (1980)

[1-51] J. Hornstra, *Dislocations in the Diamond Lattice*, J. Phys. Chem. Solids, Vol. **5,** pp 129-141 (1958)

[1-52] J. P. Hirth & J. Lothe, Theory of Dislocations, Wiley Interscience, New York (1982)

[1-53] W. Shockley, *Dislocations and Edge States in the Diamond Crystal Structure*, Phys. Rev., Vol. **91**, pp. 228 (1953)

[1-54] I. L. F. Ray and D. J. H. Cockayne, *The dissociation of dislocations in silicon*, Proc. Roy. Soc. A **325**, 534 (1971).

[1-55] *International symposium on dislocations in tetrahedrally coordinated semiconductors*:
Journal de physique Colloque, Soc. Franc de Physique, Volume **40**, Volume 46 of 4, Hünfeld/Fulda (FRG) (1979)

[1-56] A.J. McGibbon, S.J. Pennycock and J.E. Angelo, *Direct observation of dislocation core structure in CdTe/GaAs (001)*, Science, Vol 269, pp. 519-521 (July 1995)

[1-57] S.F. Gull and J. Skilling, *Maximum entropy method in image processing*, Communications, Radar and Signal Processing, IEE Proceedings F **131**, 646 (1984)

[1-58] C. Kisielowski, B. Freitag, X. Xu, S.P. Beckman and D.C. Chrzan, *Sub Angstrom imaging of dislocation core structures: How well are experiments comparable with theory?*
Phil. Mag. A **86**, pp. 4575-4588 (2006)

[1-59] C. Li, Y. Wu, J. Poplawsky, T. J. Pennycook, N. Paudel, W. Yin, S. J. Haigh, S. J. Haigh, M.P. Oxley, A.R. Lupini, M. Al-Jassim, S. J. Pennycook, and Y. Yan, *Grain-Boundary-Enhanced Carrier Collection in CdTe Solar Cells,* Phys. Rev. Lett. **112**, 156103, (April 2014)

[1-60] G. Lu and D.G.H. Cockayne, *Dislocation structures and motion in II-VI semiconductors*, Physica B **116**: pp. 646-649 (1983)

[1-61] S. Takeuchi, K. Suzuki and K. Maeda, *Stacking fault energy of II-VI semiconductors*, Phil. Mag. A **50**, p171-178 (1984)

[1-62] C. Braun and H. W. Helberg, *Surface damage of CdTe produced during sample preparation, and determination of dislocation types near micro-hardness indentations*, Phil. Mag. A **53**, 277-284 (1986)

[1-63] J. Schreiber, L. Höring, H. Uniewski, S. Hildebrandt, and H. S. Leipner, *Recognition and Distribution of A(g) and B(g) Dislocations in Indentation Deformation Zones on {111} and {110} Surfaces of CdTe*, Phys. Stat. Sol. (a) **171**, pp. 89-97 (1999)

[1-64] C. J. Gallagher, *Plastic Deformation of Germanium and Silicon*, Phys. Rev. Vol. **88** No. 4, 721-722 (1952)

[1-65] G.L. Pearson, W.T. Read and F.J. Morin, *Dislocations in Plastically Deformed Germanium*, Phys. Rev. Vol. **93**, No. 4, pp 666-667 (1954)

[1-66] D.B. Holt and B.G. Yacobi, Extended Defects In Semiconductors: Electronic Properties, Device Effects and Structures, Cambridge University Press (2007)

[1-67] K. Colakoglu, Y. Ciftci, and E. Deligo, *Elastic, electronic, and lattice dynamical properties of CdS, CdSe, and CdTe,* Physica B **373**, pp. 124–130 (2006)

[1-68] M. A. Hopcroft, W.D. Nix, and T.W. Kenny, *What is the Young's modulus of Silicon ?,* J. Microelectromechanical Systems, Vol. **19**, No. 2, pp. 229-238, (April 2010)

[1-69] E.Y. Gutmanas and P. Haasen, *Photoplastic effect in CdTe,* J. de Pys. Coll. C6, supplement au n06, tome 40, page 26-169 (June 1979)

[1-70] YuA. Osip'yan, V.F. Petrenko, A.V. Zaretskiĭ, and R.W. Whiteworth, *Properties of II-VI semiconductors associated with moving dislocations*, Adv. Phys. **35**, pp. 115-188 (1986)

[1-71] E.L. Hall and J.B.Vander Sande, *Plastic deformation behavior and dislocation structure of CdTe single-crystals*. J. Am Ceram Soc. **61**, pp. 417-425 (1978)

[1-72] H.S. Leipner, J. Schreiber, H. Uniewski and S. Hildebrandt, *Dislocation Luminescence in Cadmium Telluride*, Scanning Microscopy Vol. **12**, No. 1, pp. 149-160 (1998)

[1-73] N.I. Tarbaev, J. Schreiber, and G.A. Shepelskii, *Physical properties of $A^{II}B^{VI}$ semiconductor crystals after plastic deformation at low temperature*, Phys Stat Sol A **110**, pp. 97-106 (1988)

[1-74] A.W. Vere, S. Cole and D.J. Williams, *The origin of twinning in CdTe*, J. Electron. Mater. **12**, 551–561 (1983)

[1-75] M. Winkler, M. Schenk and I. Hähnert, *Deformation induced micro-twins in CdTe ?* Cryst. Res. Technol. **27**, 1047–1051 (1992)

[1-76] W.T. Read, Dislocations in Crystals, page 95, McGraw-Hill, London (1953)

[1-77] W.D. Nix, Materials Science Lecture, Partial Dislocation Tutorial for FCC Metals, Text book in preparation, Stanford University (2015)

[1-78] F.C. Frank, W.T. Read, *Multiplication processes for slow moving dislocations*, Phys. Rev. **79**, 722 (1950)

[1-79] E. L. Hall and J. B. Vander Sande, *On the nature of extended dislocations in deformed cadmium telluride,* Phil. Mag. A, Vol. **37**, No. 1, pp. 137-145 (1978)

[1-80] H. J. McSkimin and D. G. Thomas, *Elastic Moduli of Cadmium Telluride*, J. Appl. Phys., **33**, 66 (1962)

[1-81] E. Deligoz, K. Colakoglu, and Y. Ciftci, *Elastic, electronic, and lattice dynamical properties of CdS, CdSe, and CdTe*, Physica B **373**, pp. 124–130 (2006)

[1-82] D.J.H. Cockayne and A. Hons, Dislocations in semiconductors as studied by weak-beam electron microscopy, J. de Phys. Colloque, **C6**, suppl. LA N. 06, tcme 40, page C6-11, (June 1979)

[1-83] R. Sinclair, F.A. Ponce, T. Yamashita, D.J. Smith, R.A. Camps, L.A. Freeman, S.J. Erasmus, W.C. Nixon, K.C.A. Smith & C.J.D. Catto, *Dynamic observation of defect annealing in CdTe at lattice resolution*, Nature, Vol. **298**, No. 5870, pp. 127 – 131, 8-14 July (1982)

[1-84] R. Sinclair, T. Yamashita, M.A. Parker, K.B. Kim, K. Holloway and A.F. Schwartzman, *The Development of In Situ High Resolution Electron Microscopy*, Acta Crystallogr. Sec. A, **44**, pp. 965-975 (1988)

[1-85] R. Sinclair, *In Situ High-Resolution Transmission Electron Microscopy of Materials Reactions*, Mat. Res. Soc. Bull. **38**, pp. 1065-1071 (2013)

[1-86] Z. Zhang, W. Sigle and W. Kurtz, *HRTEM and EELS study of screw dislocation cores in $SrTiO_3$*, Phys. Rev. B **69**, 144103 (2004)

[1-87] F.C. Frank and J.F. Nicholas, *CXXVIII. Stable dislocations in the common crystal lattices*, Phil. Mag. **44**, Issue 358, pp. 1213-1235 (1953)

[1-88] D.J.H. Cockayne, A. Hons, & J.C.H. Spence, *Gliding dissociated dislocations in hexagonal CdS*, Phil. Mag. A, Vol. **42**, No 6, 773-781 (1980)

[1-89] L.M. Brown and A. Thölén, *Shape of Three-Fold Extended Nodes*, Discuss. Faraday Soc. **38**, 35 (1964)

[1-90] D. Berlincourt, J. Jaffe and L.R. Shiozawa, *Electrostatic Properties of the Sulfides, Selenides, and Tellurides of Zinc and Cadmium*, Phys. Rev. **129**, 1009 (1963)

[1-91] K. Suzuki, S. Takeuchi, M. Shino, K. Kanaya and H. Iwanaga, *Lattice Image Observations of Defects in CdSe and CdSe*, Transactions of the Japan Institute of Metals, Vol. **24**, No. 6, pp. 435-442 (1983)

[1-92] R. Sinclair, T. Yamashita and F.A. Ponce, *Atomic motion on the surface of a cadmium telluride single-crystal*, Nature Vol.290, 2, pp. 386-388 (April 1981)

[1-93] W.A. Harrison, *Electronic Structure and the Properties of Solids*, 176 (Freeman, San Francisco) (1980)

[1-94] M.A. Parker thesis, *In-situ High Resolution Transmission Electron Microscopy*, Stanford University (1988)

[1-95] I. Yonenaga and K. Sumino, *Impurity effects on the generation, velocity and immobilization of dislocations in GaAs*, J. Appl. Phys. **65** (1), pp. 85-92 (1989)

[1-96] Quantex Corporation, 252 North Wolfe Road, Sunnyvale, California 94086

[1-97] L.W. Hobbs, *Introduction to Analytical Electron Microscopy*, J.J. Hren, J.I. Goldstein and D.C. Joy editors, pp 437-480, Plenum Press, New York (1979)

[1-98] H. Hashimoto, Y. Takai, Y. Yokota, H.Endoh, E. Fukuda, *Direct observation of the arrangement of atoms around stacking faults and twins in gold crystals and the movement of atoms accompanying their formation and disappearance.* Jap. J. Appl. Phys., **19**, L1-L4 (1980)

Chapter 2: Imaging CdTe[011] Using Aberration-Corrected TEM

2.1 Aberration-Corrected TEM

Complete correction of spherical aberration in electron optics, long thought to be impossible, became a reality with the Rose corrector, first proposed by Rose in 1990 [2-1] with the first announcement of its demonstration by Haider et al. 1997 [2-2]. By 2002, the first commercial systems started to become available. Aberration corrector for STEM applications also was started in the mid-1990s and proof of the principle was demonstrated by Krivanek et al. in 1997 [2-3]. The development of aberration-free TEM may rank as one of the most significant developments in TEM technology since the instrument's invention by Ruska in 1931. In 2015, there are now hundreds of TEMs around the world fitted with aberration corrector lenses, even though such instruments are very expensive (e.g., $5M compared to $2M for the instrument used in Chapter 1). The investment being made in such tools speaks volumes about the promise that this new technology holds in making new advances in materials science and in other scientific fields using TEM. In the US, an even more ambitious project has been underway since 2004 with the formation of the transmission electron aberration-corrected microscope (TEAM) project (with the goal of achieving 0.05 nm (50pm) resolution with the full correction of spherical aberration, chromatic aberration and off-axial coma for a large field of view without aberration. This project is funded by the Department of Energy (DOE) with participation from Lawrence Berkeley National Laboratory, Argonne National Laboratory, Oak Ridge National Laboratory, and Frederick Seitz Materials Research Laboratory at the University of Illinois at Urbana-Champaign. Industrial participants include FEI and Corrected Electron Optical Systems, (CEOS) GmbH, the companies that are supplying the microscope and the most advanced aberration corrector systems. The TEAM group also has hosted many workshops and promoted the development of techniques that make the best use of the new resolution capability. By 2009, the TEAM project demonstrated a 50 pm imaging capability [2-4].

The current commercially available aberration corrector works on the principle of using two hexapole correction lenses, which are placed after the objective lens. Between the two hexapole lenses, there is a pair of round lenses, which work in unison with the two hexapole correctors. The design principle and mathematics involved in the lens are complex and demanding. A review paper on the history of aberration correction written by Rose is a good reference on the topic (Rose, [2-5]). Insertion of an aberration corrector significantly lengthens the microscope column, and this is a disadvantage for maintaining the mechanical stability needed for high-resolution imaging. Early versions of the TEM with aberration correctors were difficult to use, and the base microscope to which the correctors were fitted was not altogether stable. New microscopes, such as the FEI company's Titan, have been designed with aberration correcting lenses in mind from the ground up, with a larger column size to provide greater mechanical stability. The Titan microscope with aberration correcting lenses became commercially available in 2006. The ease of use and stability of the microscope using the aberration correction also improved.

2.2 HRTEM with Aberration-Corrected TEM

The lens' current settings for the hexapole correctors are calculated by analyzing optical diffractograms obtained from an amorphous film at different beam tilts from the optic axis. The table of diffractograms, called Zemlin tableau [2-6], is constructed to determine the adjustments to be made to the corrector system. Ellipses and asymmetries observed in the diffractograms allow calculation of axial astigmatism correction, coma-free axis alignments, and three-fold astigmatism corrections to be determined. The software automatically calculates the corrections, and allows correction of spherical aberration, four-fold astigmatism and optimizes fifth-order spherical aberration. The process is iterative and requires massive computing power to calculate the corrections. On a Titan microscope, there is a dedicated high power computer for just this function. The ability to obtain digital diffractograms on-the-fly using the high-resolution image acquisition system on the microscope and to rapidly

calculate the diffractogram values automatically make the whole process of operating the aberration corrector possible. At the time that Zemlin et al. proposed the method in 1978, the procedure would have been wholly impractical because it relied on the use of photographic plates and optical diffractogram analysis using lasers (as described in Chapter 1).

When the possibility of eliminating the spherical aberration altogether with the new aberration correctors became a reality, it might have been envisioned that the microscope would be operated at zero spherical aberration condition. With the first term in the $\chi(k)$ function with the C_s going to zero, the equation 1-9 repeated below would leave only the second term with the defocus providing any contrast. Other terms beyond the two terms in the equation may also come into play as well.

$$\chi(k) = \frac{\pi}{2} C_s \lambda^3 k^4 + \pi \Delta f \lambda k^2 + \quad \text{(Eqn. 1-9)}$$

If the $\chi(k)$ function were to go to zero, there would be very little contrast in the image. One of the earliest and most spectacular HRTEM images using the aberration-corrected microscope was of $SrTiO_3$ taken by Jia in 2001 (unpublished data) and reported in 2003 [2-7]. In this work, the oxygen atoms are imaged with high clarity with the HRTEM technique. Upon further analysis of the imaging conditions used to obtain such results, Jia and co-workers had determined that the image was obtained with a small negative C_s correction, with positive defocus. This type of imaging condition was never used or even foreseen prior to this result. The technique even provided a new acronym of NCSI, short for "negative spherical aberration imaging." Further detailed analysis and modeling followed, which put the method on a more sound theoretical footing [2-8].

The aberration corrector allows one to select a C_s value of one's choosing, and this provides an additional degree of freedom to control the $\chi(k)$ value and, hence, the contrast of the image. For low Z elements such as oxygen and carbon, a small negative

value of C_s and using positive defocus provides white atom contrast on a dark background, while still maintaining the good resolution provided by the low C_s value. The contrast from the low Z elements is tremendously enhanced by the NCSI imaging condition, and it has been a boon to the study of materials such as oxides, graphene, etc. For work on graphene and carbon nanotubes, the NCSI method allows imaging of single atoms of carbon in graphene or boron and nitrogen in BN single atomic layer films [2-9, 2-10]. The additional benefit of the aberration corrector lens is that this capability is available at lower kV, at 80 kV for example. For low Z elements that are susceptible to displacement damage at higher voltages, the ability to obtain atomic resolution at low kV has become a very important new capability. A review of the history and recent applications of NCSI was published by Urban et al. in 2009 [2-11].

The other key benefit of elimination or reduction of spherical aberration for HRTEM imaging is that delocalization of lattice images is dramatically reduced, to a point where it does not matter any longer. The use of field emission guns (FEG) increased the information limit of the microscope by reducing the energy spread and beam divergence with its high brightness. However, the gain in information limit was largely negated by the appearance of lattice images at a considerable distance away from the actual structure. At best, this was a nuisance but often this effect severely limited the ability to make conclusions about the lattice images and the local features that created them. The delocalization of lattice images was at least five times worse with a field emission gun (FEG) source compared with the older LaB_6 filaments. One example of the improvement is given by Hossein-Barberi et al. for magnetic recording media [2-12]. Localization R_L is given by [1-13]:

$$R_L = ¼\ C_s\ \lambda^3 g_{max}^3 \qquad \text{(Eqn. 2-1)}$$

g_{max} is the reciprocal of the information limit of the microscope

By dramatically reducing C_s close to zero, the localization is significantly reduced. For example, with 300 kV electrons, g_{max} = 1/0.08 nm, and C_s = 1 mm, R_L is 2.6 nm. In

other words, the lattice fringes can appear up to 2.6 nm beyond from where they originated. Using 20 μm for C_s, the R_L = 0.05 nm with the same g_{max} value.

The optimum C_s value and the defocus to use for the best NCSI condition are given by:

$$C_s = - 64 / (27 \lambda^3 g_{max}^4) \quad \text{(Eqn. 2-2)}$$

$$\Delta f = 16/(9 \lambda g_{max}^2) \quad \text{(Eqn. 2-3)}$$

These were derived by Lentzen by equating Scherzer defocus, $\Delta f_{Scherzer}$ to Lichte defocus, Δf_{Lichte} and solving for C_s [2-14]. The Lichte defocus [2-15] is given by:

$$\Delta f_{Lichte} = -3/4\ C_s \lambda^2 g_{max}^2 \quad \text{(Eqn. 2-4)}$$

The Lichte defocus is the one that gives the best (i.e., least) delocalization. By equating Scherzer to Lichte defocus, the purpose is to maximize the CTF for flat response out to the information limit g_{max} and to minimize the delocalization effect. The influence on the CTF function can be seen in figure 2-1 for the Titan microscope operating at 300 kV, with g_{max} = 10 nm^{-1}, which is the resolution limit for the microscope without the use of a monochrometer. With the monochrometer, the resolution specification of the microscope is 0.07 nm (g_{max} = 14.3 nm^{-1}).

Optimized C_s = - 31.1μm

Optimized Δf = + 9.0 nm

C_c = 1.2 mm, beam divergence = 0.5 mrad, δ = 4.6 nm

With the aberration corrector and very low value of C_s, the envelope function to the CTF is dominated only by the temporal component, which includes the chromatic aberration and terms comprising energy spread, lens fluctuations and accelerating voltage fluctuations (eqn. 1-13). This envelope is the blue dotted line and it defines the information limit of the microscope. When the microscope is set to this condition and

near it, the atoms will appear white on a dark background. The delocalization effect, if any, will be also minimized. Comparison to the case without the aberration corrector is now obvious. With the slightly negative C_s setting, the operating defocus condition will be positive, and the values are much smaller than in the non-corrected case by a factor of 10.The microscope can now be operated at near the information limit as defined by the envelope function (in large part determined by the chromatic aberration).

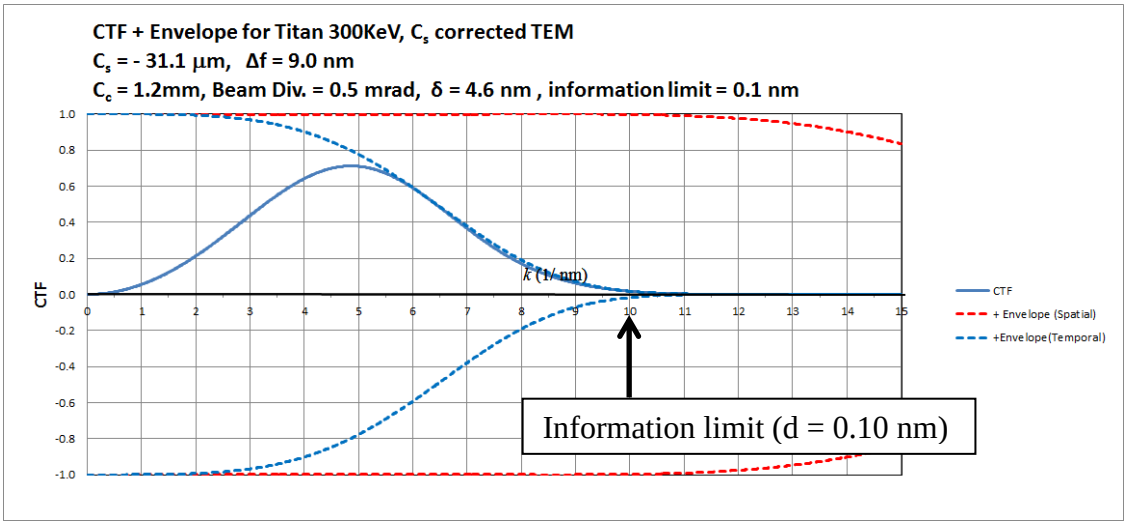

Figure 2-1: CTF for Titan with aberration corrector, at C_s = -31.1 µm. Optimized defocus value is +9.0 nm, and the CTF function is positive out to the information limit of the microscope at 0.1 nm (k = 10 nm^{-1}).

2.3 Imaging CdTe in [011] Using Aberration-Corrected Titan TEM at 300 kV

Imaging CdTe in the [011] orientation is now described using a FEI Titan operating at 300 kV, equipped with the CEOS aberration corrector. Although the optimum C_s calculated for this microscope is at -31.1 µm, other users of the microscope suggest that the practical optimum setting is actually approximately -20 µm. This is based on obtaining the best contrast at the best resolution for the microscope. It is based on empirical experience with the machine, but if such is the case, then it

suggests that the information limit is somewhat better than the specified value of 0.10 nm. The value of g_{max} that would give -20 μm as the optimized value for C_s would be 0.09 nm and δ value will have to be adjusted to approximately 4.0 nm from 4.6 nm. These values are a significant improvement over those of the TEMs available in the 1980s.

The aberration corrector goes through a procedure of collecting the Zemlin tableau of diffractogram data taken at various beam tilts. Several iterations are done to determine the best condition that the lens settles to, and a determination is made about whether all of the other aberration parameters are optimized to the minimum value possible. An amorphous carbon specimen is used for this procedure, and it takes some time to complete the entire process, typically 20 to 30 minutes. The procedure is done during each session of microscope work, and the optimization is slightly different each time. At the start of the session, -20 μm was the target for Cs, but the system settled down to -18.3 μm. More iteration could have been done to try to reach - 20 μm but it would probably not have given any significant improvement in imaging results, and it would only take that much session time away from the actual work on the specimen. Therefore, the work commenced using -18.3 μm as the C_s setting. Table 2-1 shows the listing of all the aberration coefficients that the system calculated based on the final setting of the corrector. The calculations must be quite demanding because the system uses a dedicated high-end Dell workstation (T7600) using a pair of Intel Xenon E5-2600 processors. It also supports vast memory capacity as well.

A new CTF calculation based on C_s of -18.3 μm is plotted in figure 2-2. Defocus Δf value of + 7.3 nm is the optimized value if C_s of -20 μm had been used. It can be seen that the CTF function does not change much between the two settings. Also added are the CdTe reflections in the [011] projection. There are 43 reflections represented out to the (600) reflection, which is 0.108 nm or $1/d = k = 9.26\ nm^{-1}$.

Latest accepted measurements				
	Value	Angle	Confidence	Δt
C1	-281.1 nm	–	1.413 nm	27 min
A1	1.48 nm	18.0 °	1.175 nm	28 min
A2	16.69 nm	0.4 °	35.84 nm	28 min
B2	19.49 nm	172.6 °	31.25 nm	28 min
C3	-18.3 µm	–	3.161 µm	28 min
A3	223.7 nm	84.2 °	451.1 nm	28 min
S3	107.3 nm	175.2 °	268.4 nm	28 min
A4	10.19 µm	134.8 °	12.14 µm	28 min
D4	2.178 µm	133.1 °	7.46 µm	28 min
B4	11.73 µm	57.0 °	14.06 µm	28 min
C5	4.582 mm	–	2.072 mm	28 min
A5	1.363 mm	132.0 °	340.4 µm	28 min
C1q				
A1q				
A1G				
B2G				

C1	nm	Defocus
A1	nm	2-fold astigmatism
A2	nm	3-fold astigmatism
B2	nm	Axial coma
C3	µm	3rd order spherical aberration
A3	µm	4-fold astigmatism
S3	nm	Star aberration
A4	µm	5-fold astigmatism
D4	µm	3-lobe aberration
B4	µm	Axial coma
C5	mm	5th order spherical aberration
A5	µm	5-fold astigmatism

Table 2-1: Table of aberration coefficients for the Titan microscope after the optimization process. The table on the right explains the code. C3 is the third order aberration coefficient, which is the C_s.

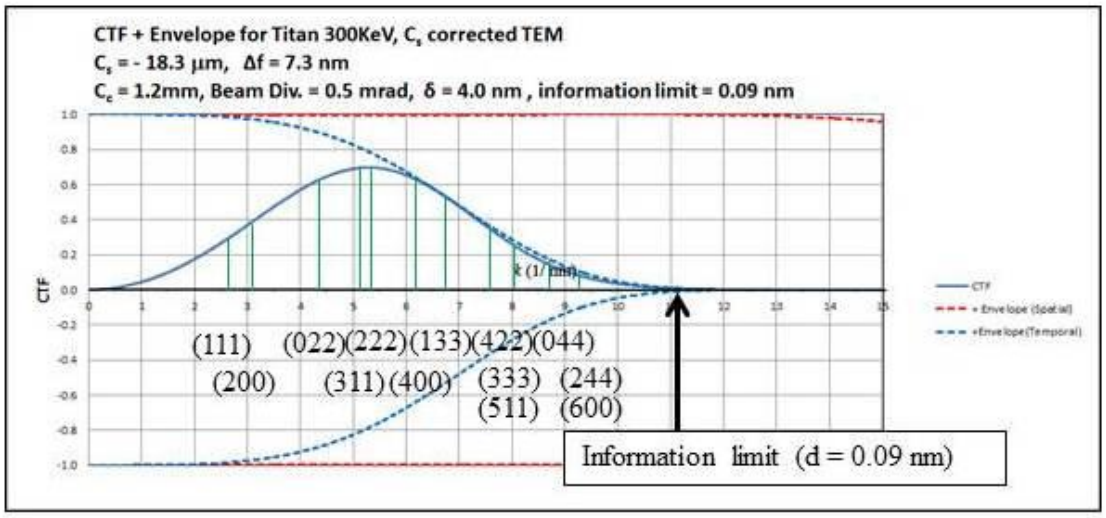

Figure 2-2: CTF for Cs = -18.3 µm, Δf = +7.3 nm, δ = 4.0 nm.
The information limit is at 0.09 nm, or 11.1 nm^{-1}. Green lines indicate the reciprocal lattice spacings of CdTe [011] reflections out to (600).

The Titan model 80-300 is an environmental transmission electron microscope (ETEM) capable of conducting in-situ reactive gas experiments with the specimen. It is capable of operating from 80 to 300 kV. In this work, only 300 kV was used. It is equipped with a CEOS aberration corrector and a monochrometer to provide energy resolution of less than 0.2 eV. For this work, the monochrometer was not used because it reduces the beam brightness. The standard double tilt specimen holder was used. Aperture sizes were as follows:

CI	2000 μm
CII	150 μm
CIII	2000 μm (not used–only in STEM mode)
Objective	70 μm (out to (600) reflections $k = 9.26\ \text{nm}^{-1}$)

The microscope defocus setting was estimated from the point of lowest contrast in the image, which is given by the following for conventional positive C_s imaging (Heinemann1971 [2-16]):

$$\Delta f_{\text{minimum contrast}} = -(\tfrac{1}{2} C_s \lambda)^{\tfrac{1}{2}}$$

Although this does not apply in the case of the NCSI condition, the minimum contrast condition occurs close to zero defocus, at approximately 1 to 2 nm positive Δf for the -18.3 μm C_s that had been chosen. Objective lens current and defocus values are accurately calibrated, especially in the case of aberration-corrected TEM as this is very critical in generating accurate Zemlin tableau for C_s correction.

The CdTe material was an undoped p-type <100> wafer with dimensions of 5x5x1mm, which was purchased from MTI Corporation [2-17]. The <110> surface was obtained by cleaving, followed by lapping with diamond coated film to about 100 μm

thickness. The specimen was then glued to a copper slot grid and ion-milled from 4 kV to 1 kV in successive steps to thin the sample.

The atomic resolution images of CdTe in [011] projection were obtained only in the thinnest regions of the specimen. Such areas on the specimen are considerably farther in from the extinction thickness, which for the CdTe is approximately 15 nm. Such regions are prone to beam damage, and the specimen starts to perforate after approximately 10 minutes of viewing. Figure 2-3 shows such a region after some holes were already created by the electron beam on the specimen. Various types of image appearance are observed, some areas showing well-resolved *dumbbell* spots representing the columns of Cd and Te atoms. This image was taken at aaproximately +10 nm overfocus. Figure 2-4 shows an image from another area taken at a defocus value of approximately +16 nm with the atomic resolution. The unit cell dimension is indicated. The enlarged image in (b) shows considerable detail in the image beyond the dumbbell resolution. There are contrast features in-between atoms that are different in each area, and some of the atoms have slightly different shape and contrast. It is not clear as to what they signify, but the HRTEM imaging with low C_s has the capability to distinguish individual atoms. It may signify some difference in the atomic species present in the column or difference in the number of atoms in the particular column for example. The improvement in image resolution compared to the ones shown in Chapter 1 (eg, figure 1-23) is quite striking. The crystal orientation of the CdTe specimen was not tracked so that it is not known which image spot corresponds to which atoms. The contrast difference between the individual Cd and Te was not expected in any case, as they are only separated by 4 atomic numbers (48 and 52, respectively). If it is possible to image features such as vacancies, dopant atoms and interstitials, HRTEM with C_s corrected microscope will be a useful tool for future work on CdTe. Such point defects are an important subject for the study of electronic properties of CdTe [2-18].

In thicker parts of the specimen farther away from the specimen edge, only lower resolution images with image spots corresponding to Cd-Te atom pairs were obtained, much like the images shown in Chapter 1 taken with a TEM without

aberration correction. Figure 2-5 is a low-resolution multi-beam image of the specimen edge. Atomic resolution images were obtained only within the narrow band about 50 nm wide at the edge of the specimen. The specimen contained a high density of microdefects in the thick parts of the specimen while the edge was pristine. It was as if the defects were absent from the specimen all along the edge. It is possible that clearing out of the defect at the edge took place during the ion-milling process. The CdTe used in this chapter was an undoped CdTe while the ones used in Chapter 1 were heavily doped with phosphorus. The higher purity CdTe might have made the defects at the edge of the crystal move easier and out of the crystal during specimen preparation.

Figure 2-6 is an experimental thru-focus series at 2 nm focus increments from +2 nm overfocus to +20 nm overfocus. Focus steps are based on lens current settings and taken automatically by the microscope at 0.2 sec exposure for each image. White atom images with atomic resolution are obtained between +10 to +18 nm overfocus. The +6 nm image might have had some image drift. At a small positive defocus of 1 to 2 nm, CTF values will be small, and the image should have low contrast. This may be the case with the experimental images. At zero defocus, a black atom image with low contrast can be expected, but the +2 nm image is not quite this situation. The CTF plot in figure 2-7 (a) at Δf = 0 nm shows that the function has a small negative value for most of the reflections which should give a black atom image. At higher defocus, the CTF starts to fluctuate more so that higher order reflections start to be transferred with negative values of CTF (egg, figure 2-7c).

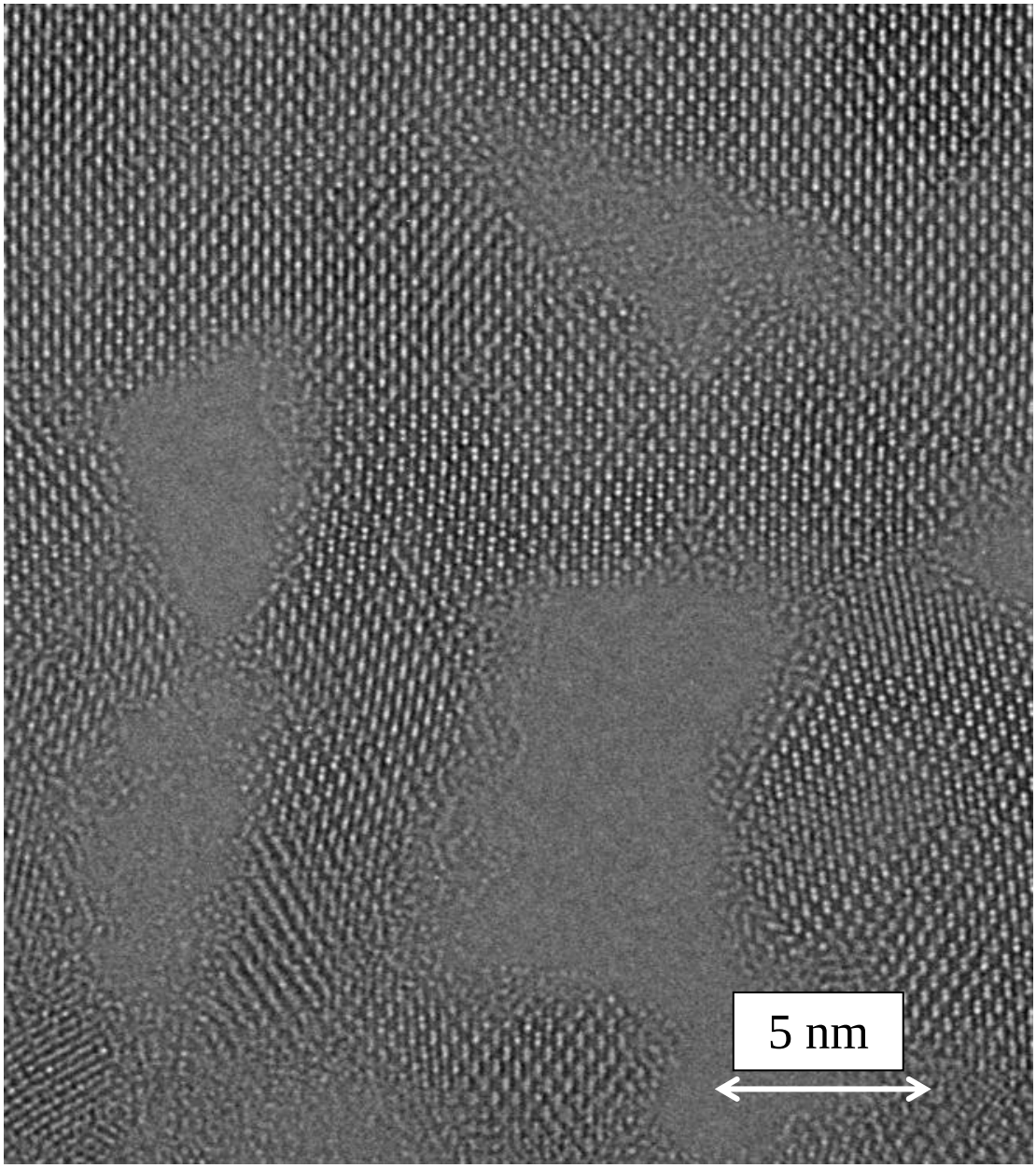

Figure 2-3: Atomic resolution image of CdTe [011] in a very thin part of the specimen after the area has stated to ablate and become perforated due to beam damage. Many regions show the characteristic *dumbbels* representing the Cd and Te atomic columns. Defocus for this image was approximately +10 nm overfocus. Objective aperture contained 43 beams out to (600) reflections.

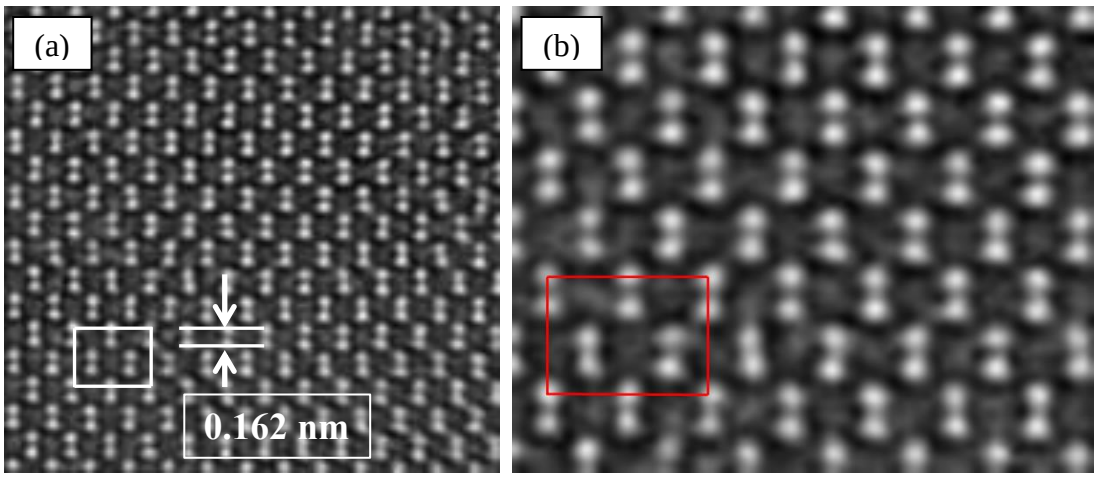

Figure 2-4: (a) Atomic resolution image of CdTe [011] taken at approximately +16 nm overfocus, (b) enlargement from one area. There are considerable details beyond the resolution between the two "dumbells" representing Cd and Te atomic columns.

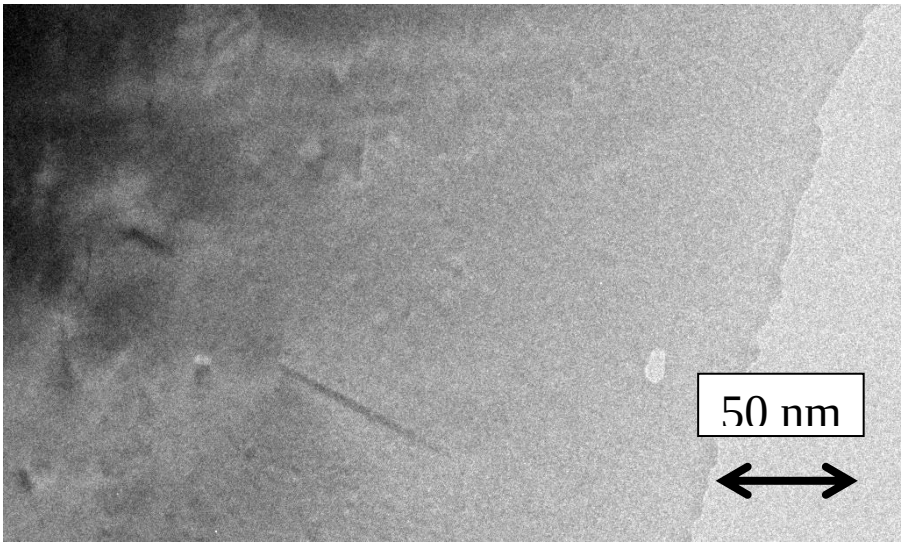

Figure 2-5: Low-resolution image (multi-beam) of the specimen edge. The thick region of the specimen at the far left contained a high density of micro-defects, while the 100 nm wide band along the edge was free of defects. Atomic resolution images were only obtained within approximately 50 nm of the edge of the crystal.

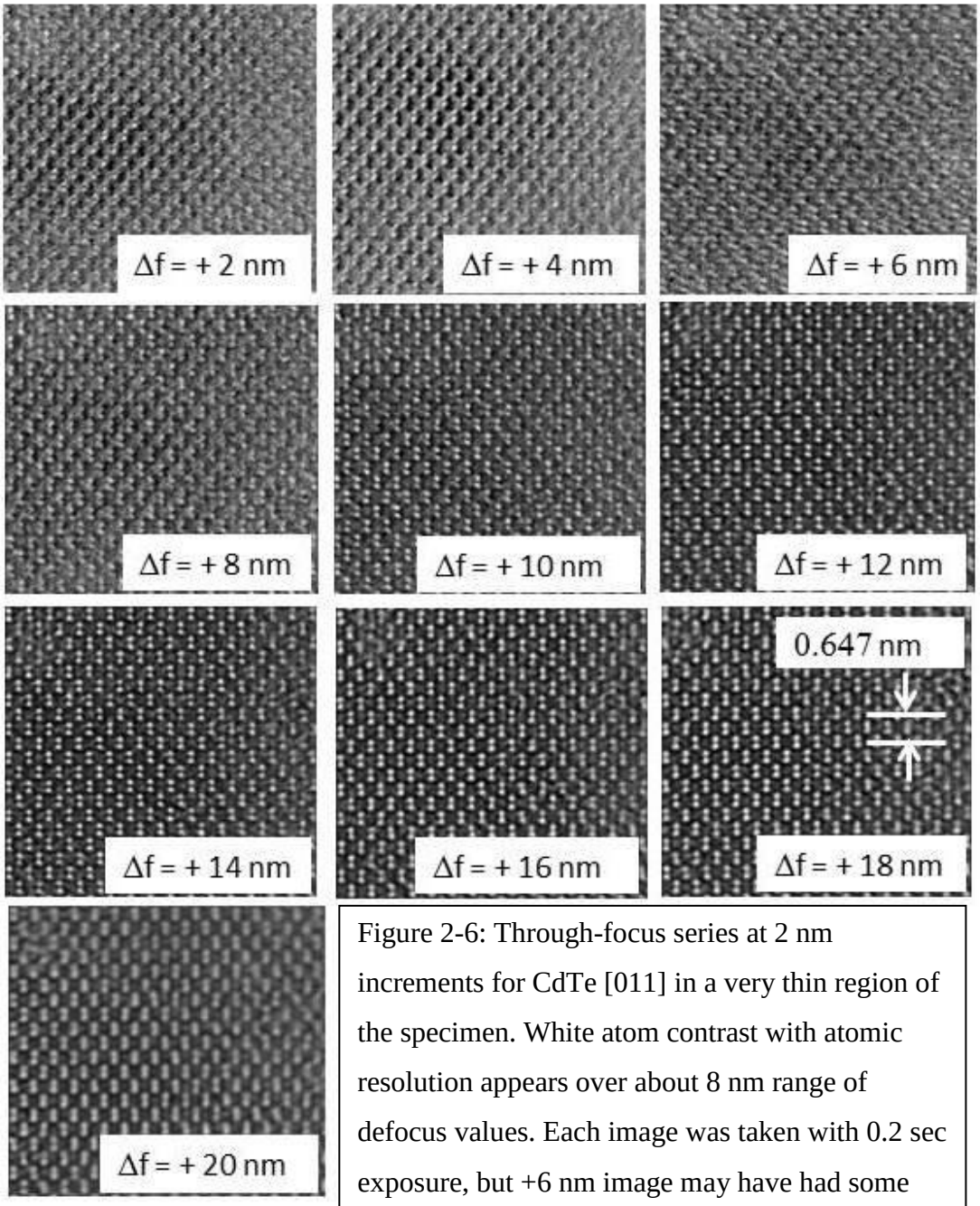

Figure 2-6: Through-focus series at 2 nm increments for CdTe [011] in a very thin region of the specimen. White atom contrast with atomic resolution appears over about 8 nm range of defocus values. Each image was taken with 0.2 sec exposure, but +6 nm image may have had some specimen drift.

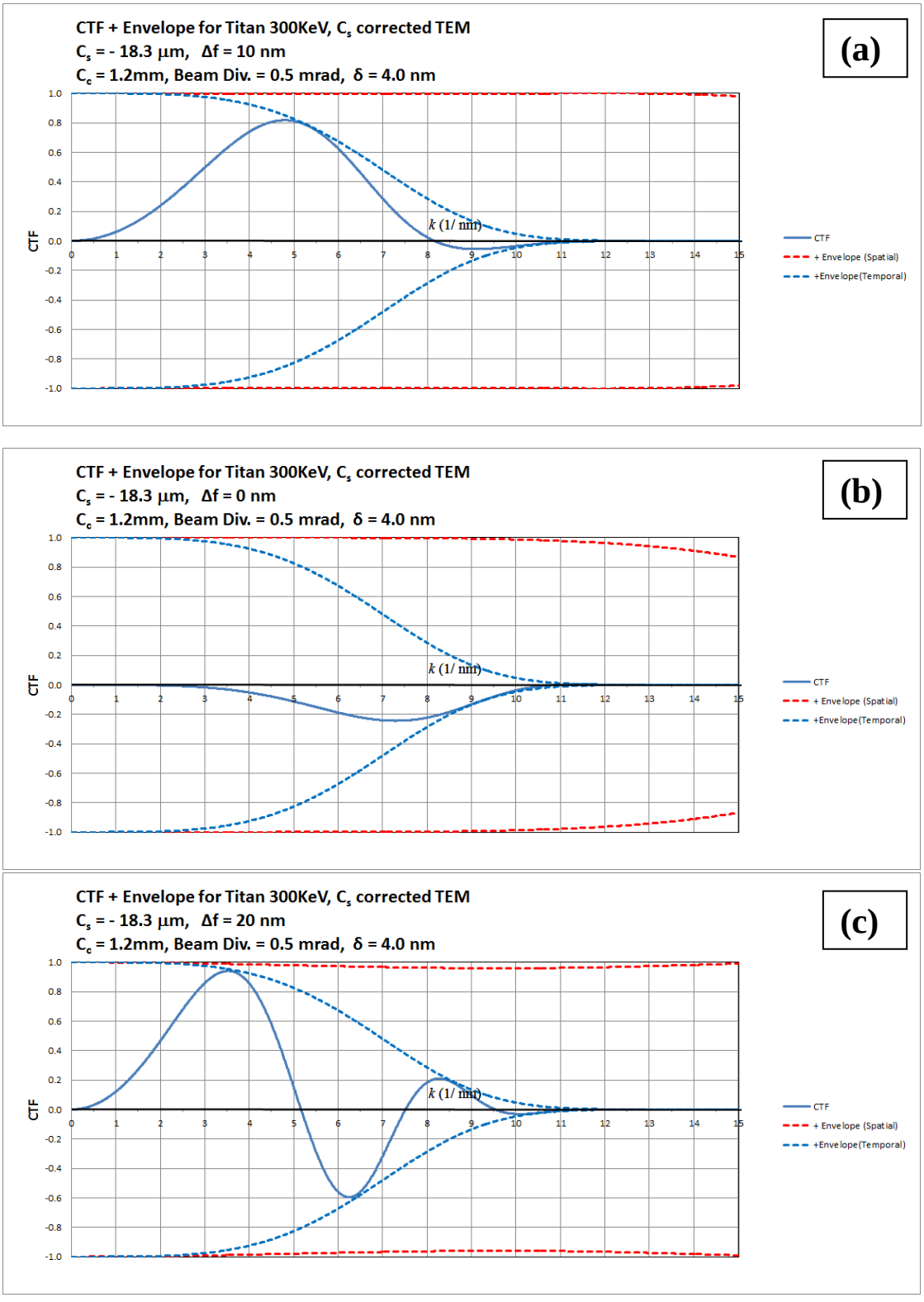

Figure 2-7: CTF at (a) 0 nm, (b) +10 nm and at (c) +20 nm overfocus.

Image simulations were done using the MacTempas multi-slice software [1-22] to compare against the experimental images. The projected potential plot of CdTe [011] is shown in Figure 2-8, with the atomic positions and unit cell indicated in the figure on the right. Each atomic column is circled with a different color to indicate the atomic species (eg, bright purple for Te). Figure 2-9 shows the calculated diffraction pattern for [011] CdTe, with the red circle indicating the objective aperture used for the calculation, which includes reflections out to (600), at d = 0.108 nm (g = 9.255 nm^{-1}). Calculated amplitudes vs. thickness plot is shown in figure 2-10 for the transmitted and several diffracted reflections. The behavior with thickness is similar to the calculation shown for 120 kV in figure 1-30 in Chapter 1. Pendellösung extinction contour would be expected at approximately 9 nm thickness, but the effect may not be so pronounced because some of the beams (e.g. $(\overline{1}\overline{1}1)$) still have high amplitude at this thickness.

First, a survey covering a large range of specimen thicknesses and defocus conditions was calculated, this is shown in figure 2-11. Specimen thickness covers 0.915 nm to 201.30 nm in 0.915 nm thickness increments and defocus covers 0 to +40 nm overfocus in 4 nm increments. The unusual thickness intervals are because the program picks only unit cell dimensions for the thickness intervals. 0.915 nm is the unit cell dimension in the [110] direction (0.647 nm x $\sqrt{2}$). Details of other simulation parameters are listed in figure 2-10. The purpose of showing the large simulation image space is to observe the general tendencies for the calculated images as a function of specimen thickness and defocus. It can be seen that black atom images are obtained for 0 and +4 nm defocus at all thicknesses within the range covered. There are regions of low contrast images (dark images) at some defocus conditions, such as at +8 and +12 nm defocus between the thicknesses of 10.8 nm to 19.9 nm, and in the left lower quadrant between +24 to +36 nm overfocus in the thickness range between 1.6 to 8.46 nm. In the right lower quadrant, there is a large region of defocus and thicknesses where the images are a white atom type that does not vary much with defocus and thickness. The most interesting images are actually in the upper left quadrant of the simulation space, and this detail can only be seen in the closer view as shown in figure 2-12 covering the specimen thickness from 0.915 nm to 91.5 nm in 0.915nm

increments and Δf defocus from 0 to 30 nm overfocus in 5 nm increments in this figure. The black atom image contrast seen at the zero defocus condition is clearer, and the upper left quadrant shows images with atomic resolution where Cd and Te atomic columns are resolved. The close up view of this region is shown in figure 2-13, covering the thickness range from 0.915 nm to 4.575 nm and defocus from zero to 16 nm overfocus in 4 nm increments. It can be seen that there are atomic resolution images with white atom contrast that appear between 4 to 12 nm overfocus and in the thickness range of the figure. The range of defocus where the dumbbell resolution appears is narrower in the simulation than in the experimental images in figure 2-6. It is also possible in the experimental images the defocus values are offset from the actual because of uncertainty in choosing where the point of minimum contrast is. Fast Fourier transform (FFT) of the experimental images did not give sufficient contrast in the diffractogram rings to provide any information on the defocus condition.

Although simulated images similar to the experimental image in figure 2-4 are observed in some settings, there are many image types at other settings that were not observed experimentally, for example at the lower right quadrant in figure 2-12. Therefore, it is not very clear how representative the image simulation is to the actual experimental images. About the only conclusions that can be drawn if any from the simulation are that true dumbbell resolution is observed in very thin specimens, and that some black atoms on a white background are possible at or near zero defocus conditions. Similar dark atom images were indeed observed experimentally, but they were more infrequent (or rare) during the observations. Alternatively, the simulation suggests otherwise, as it should have been more visible across a greater range of thicknesses and this was not the case. Whether this is due to an inadequacy of the calculation was not explored further.

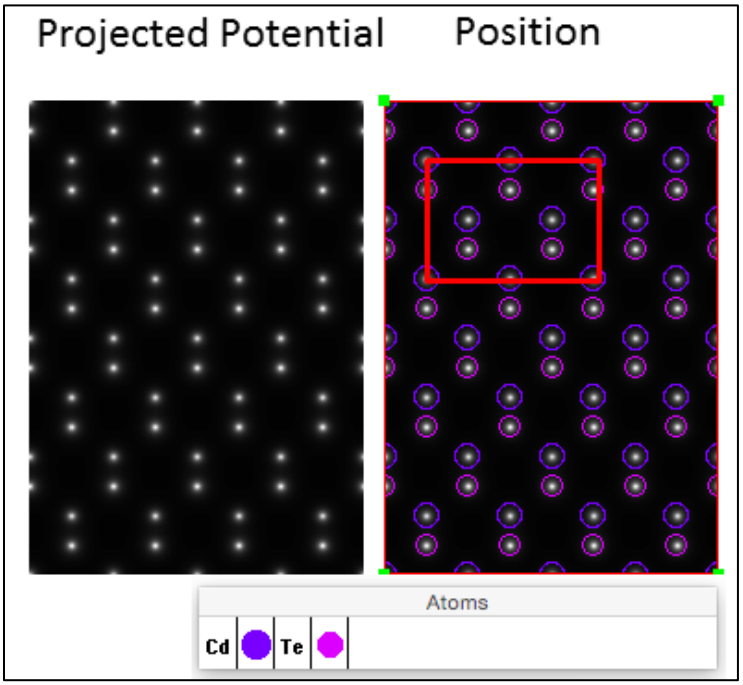

Figure 2-8: Projected potential plot from the MacTempas® multi-slice simulation program, and the position of the atoms as indicated for CdTe [011]. The unit cell is indicated in red.

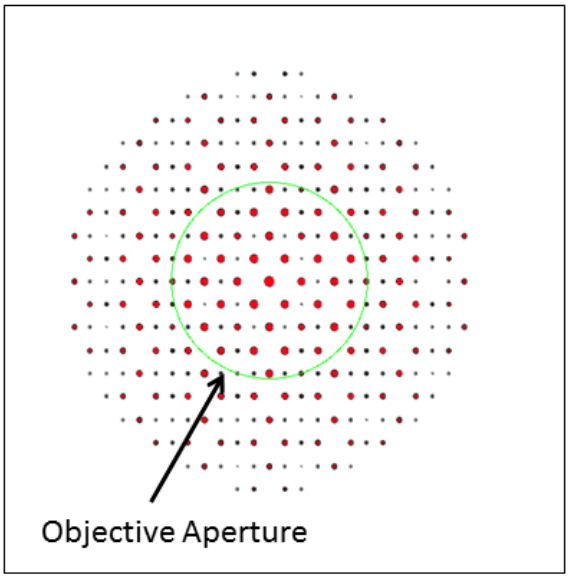

Figure 2-9: Computed diffraction pattern and the size of the objective aperture used for the calculation, matching the experimental condition. Red colors indicate the main reflections. Black dots represent very weak reflections, which are never observed experimentally.

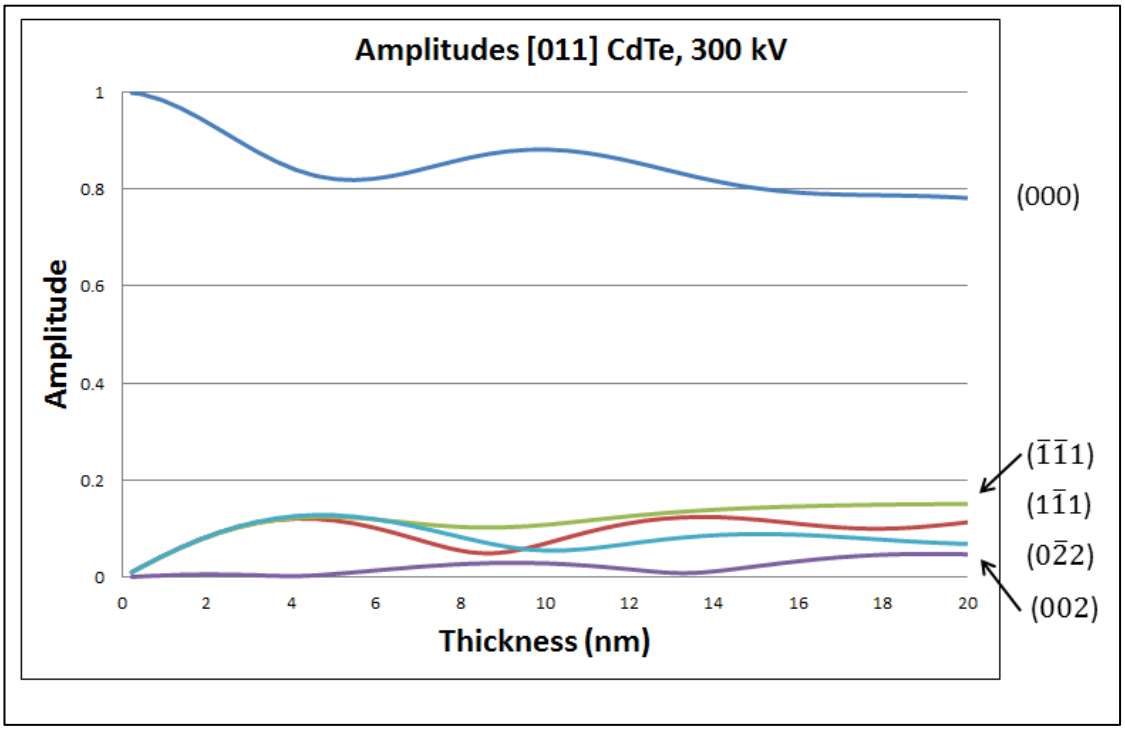

Image Simulation Parameters Detail:

Cs	-18.3 μm
Cs (5th order)	4.6 mm
Convergence angle	0.5 mrad
Spread of defocus	4 nm
Obj. aperture	9.3 nm^{-1} (43 beams)
2 fold astig./coma	1.5 nm
3 fold astig./coma	16.7 nm
Coma	19.5 n
#slices/cell	4

Figure 2-10: Calculated amplitudes vs. thickness for selected reflections. Images with weak contrast are expected at approximately 9 nm due to low amplitudes from some of the reflections. Image calculation parameters are listed below the plot.

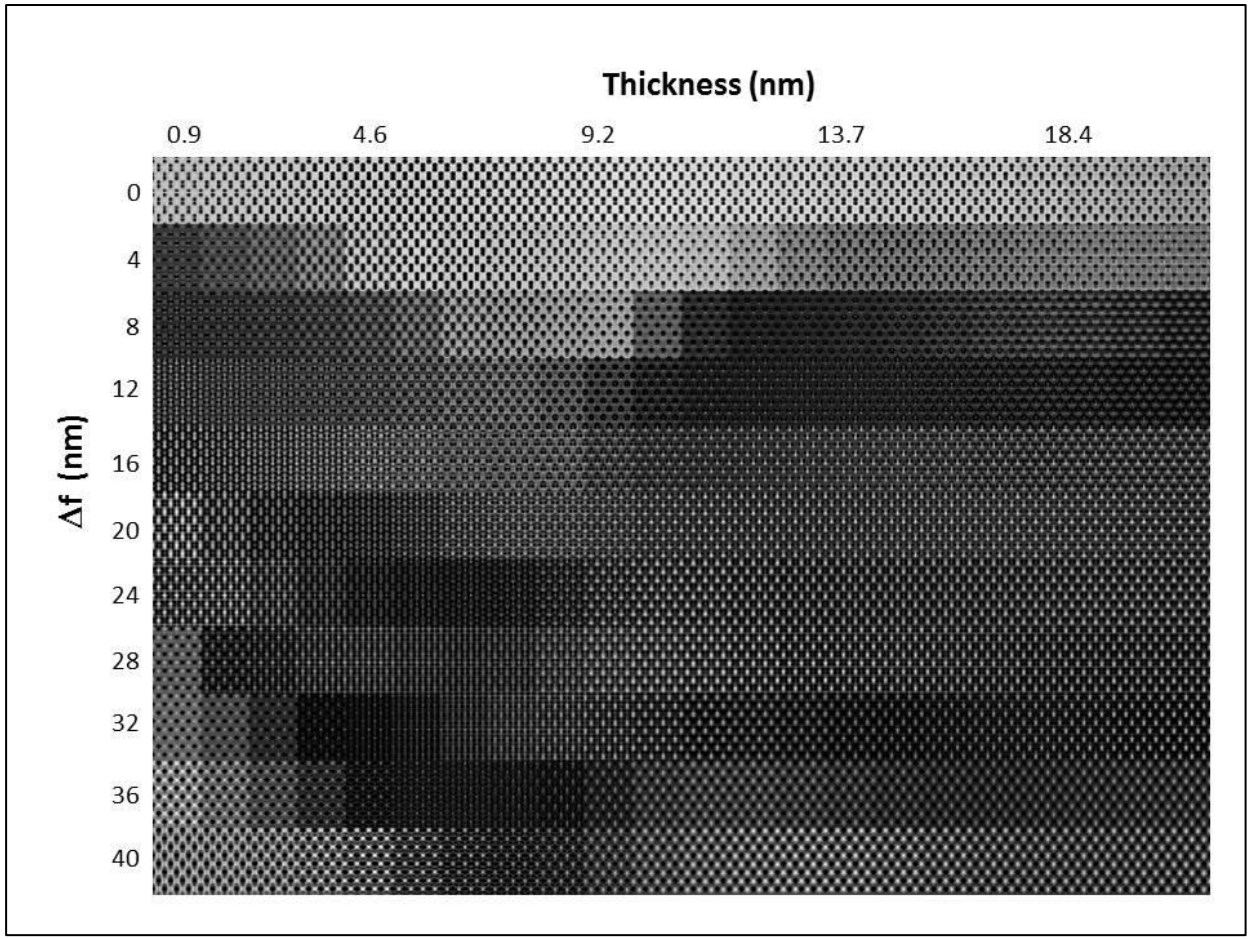

Figure 2-11: Multi-slice image simulations covering thickness from 0.9 nm to 19.9 nm, and Δf from 0 to +40 nm overfocus. MacTempas® software was used [1-22].

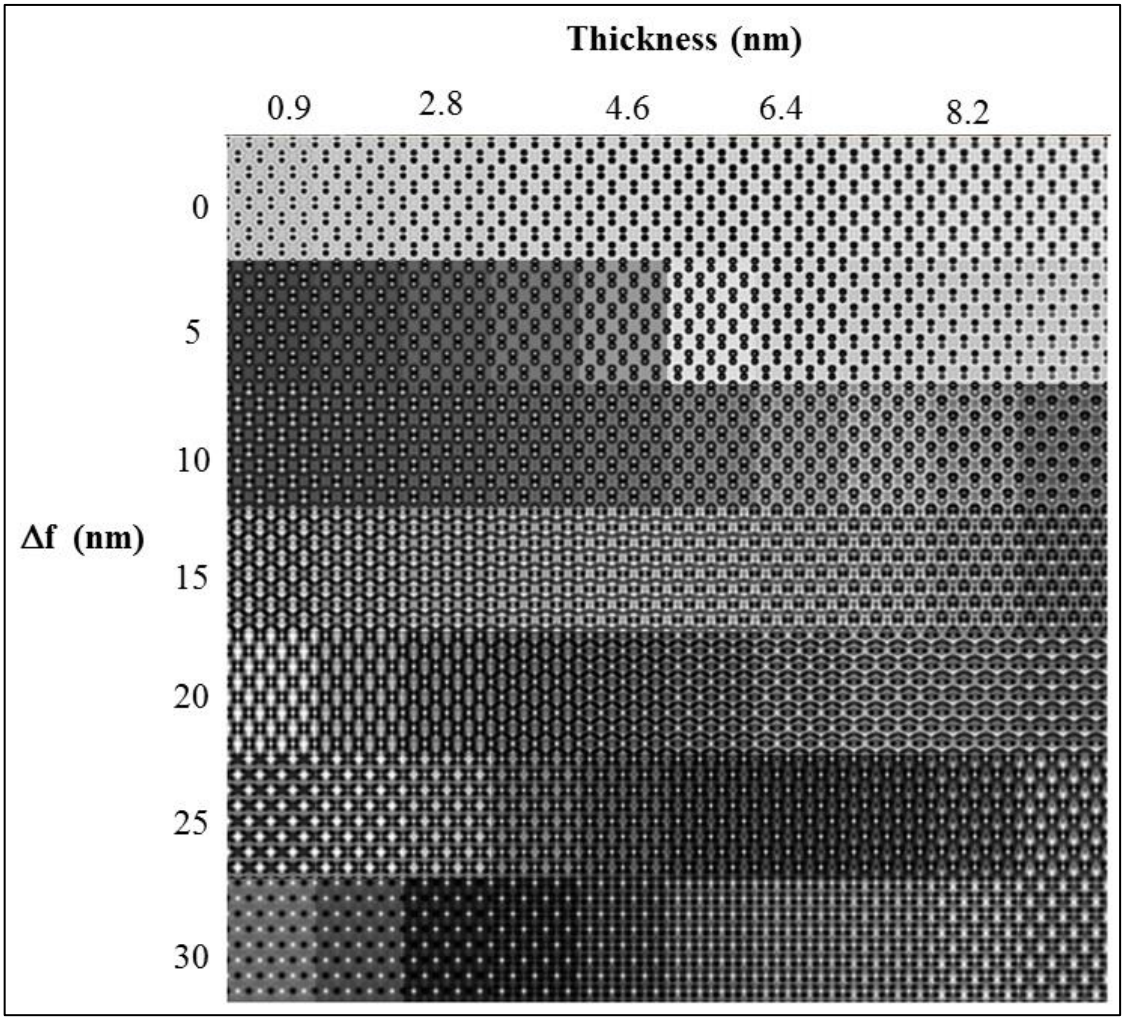

Figure 2-12: Multi-slice image simulation matrix covering a narrower range of thickness and defocus from upper left quadrant of figure 2-11. Δ*f* defocus values are all overfocus conditions.

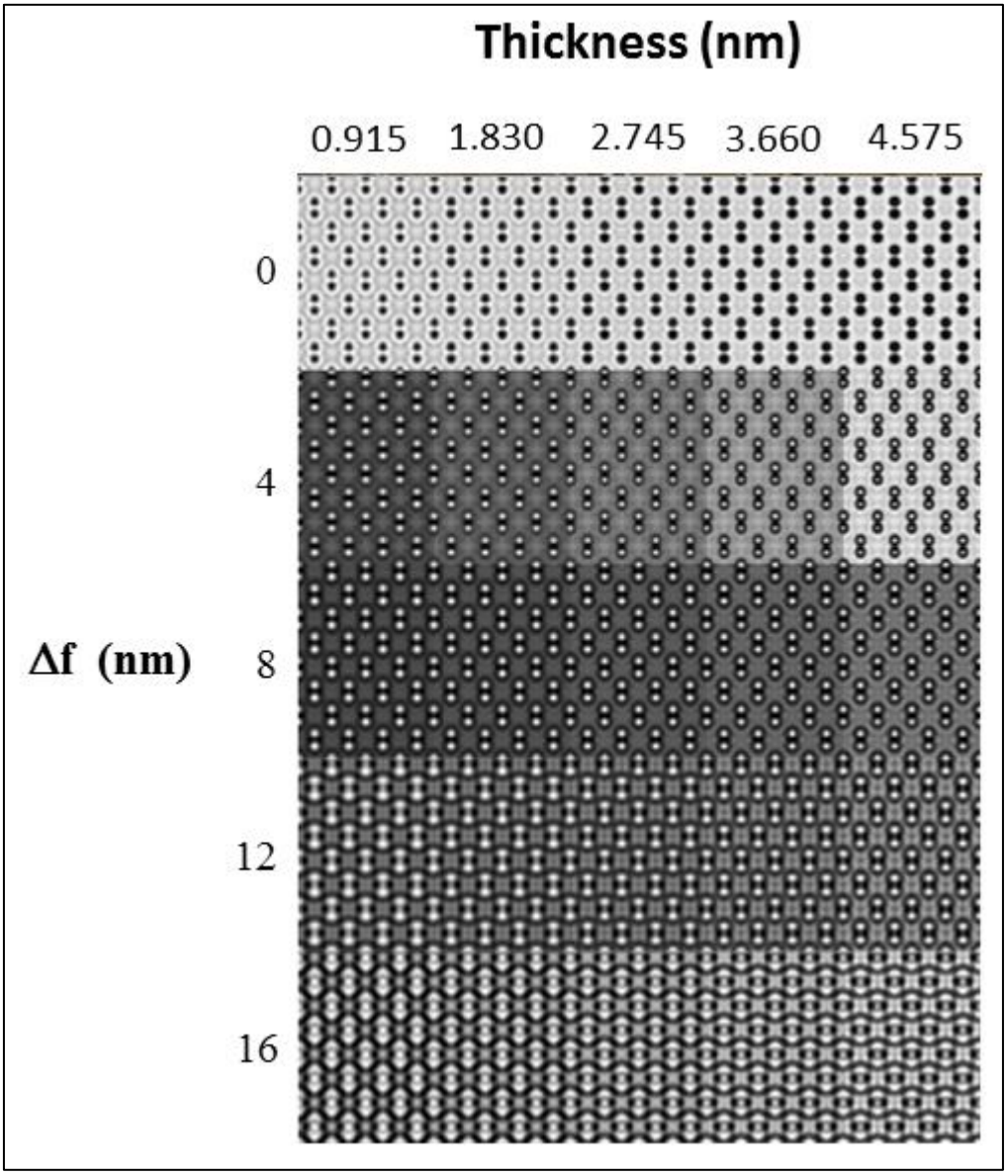

Figure 2-13: Multi-slice image simulation matrix from upper left quadrant of figure 2-12, covering thinner specimen thickness and narrow defocus conditions (overfocus) where atomic resolution images are obtained.

A side-by-side comparison between the experimental image as shown in figure 2-4 for Δf = +16 nm and simulated image at t = 3.66 nm and Δf = +12 nm is made in figure 2-14. Atomic positions are similar. Other simulated images between Δf = +4 to +12 nm in figure 2-13 could have been chosen for comparison. There are features in the channels between the atoms in both, although their intensities do not match perfectly. An example of a black atom image on white background is shown in figure 2-15. A simulated image at zero defocus at 0.9 nm thickness is inserted in the image on the left corner. The defocus condition used to obtain this image was not tracked. However, it can be said that this type of image was relatively rare. As in white atom images, the black atom images were only observed in very thin areas of the specimen.

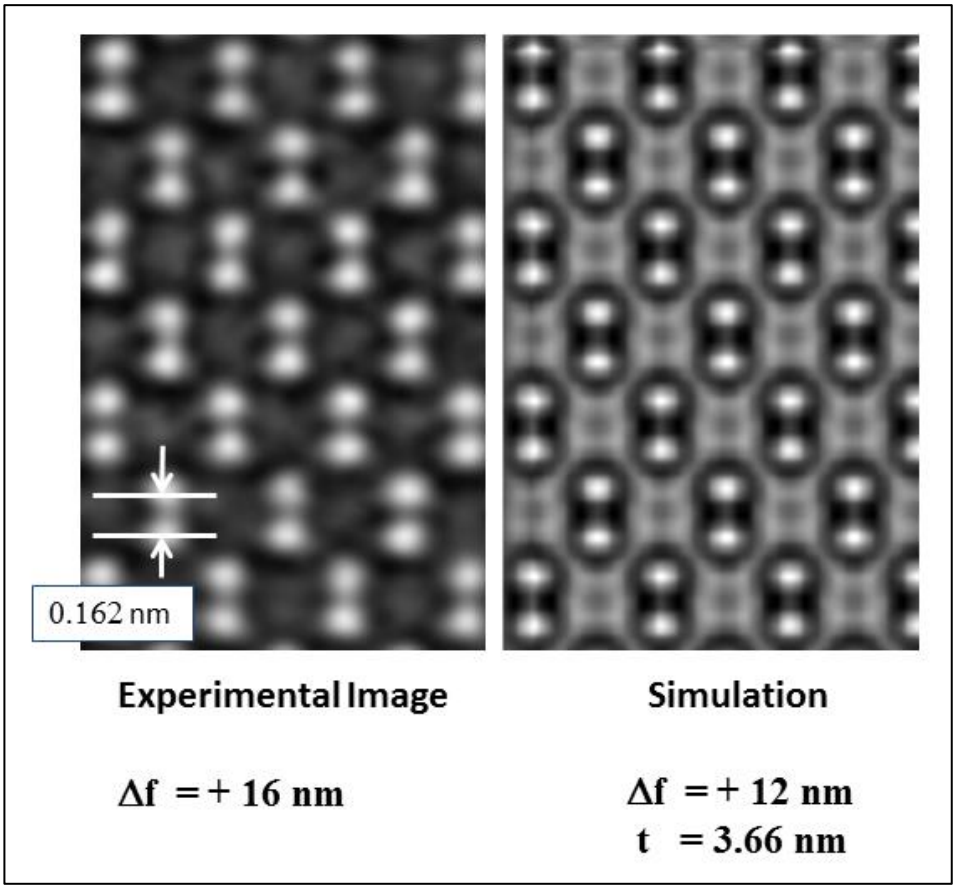

Figure 2-14: Comparison between the experimental image and the simulated image at thickness of 3.66 nm and Δf = +12 nm.

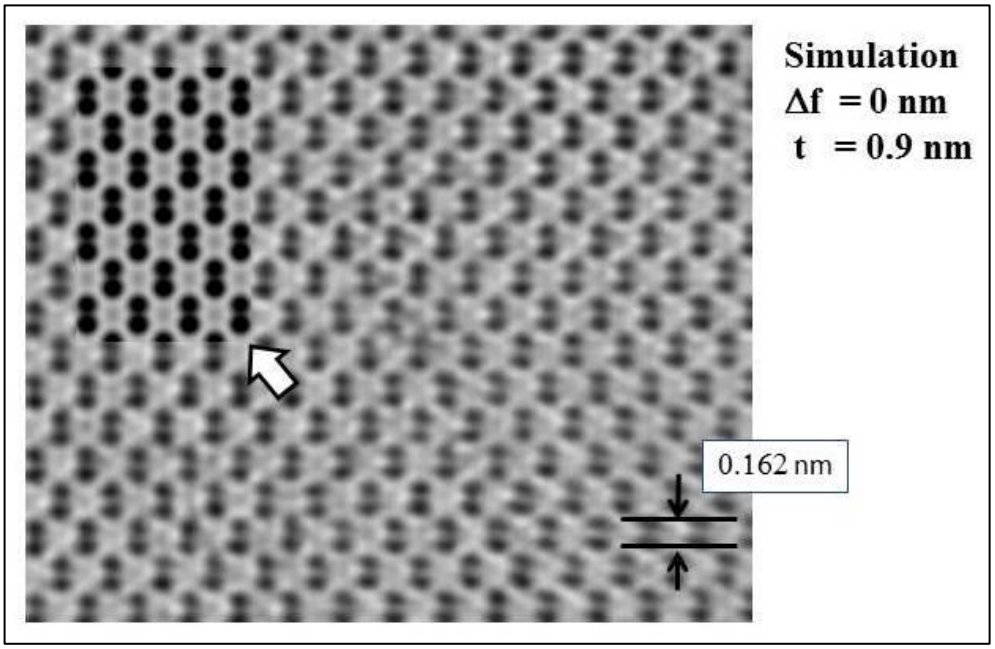

Figure 2-15: Experimental image of black atom contrast on white background. Image simulation at Δf = 0 nm and thickness at 0.9 nm inserted at the left corner (arrowed).

A more typical image even in the thin region of the specimen consisted of one image spot for the Cd-Te pair, as it was the case in Chapter 1 with lower resolution TEM. An example is shown in figure 2-15, which was taken near the edge of the specimen. Image spots were generally elongated in this type of image at the edge of the crystal. It is thought that even though the area is at the edge of the specimen, the thickness is still higher than in the region as in figure 2-3, which gave dumbbell images. The area that gave dumbbells always deteriorated quicker than in an area such as figure 2-15. The specimen perforated very quickly within several minutes of viewing as shown in figure 2-3.

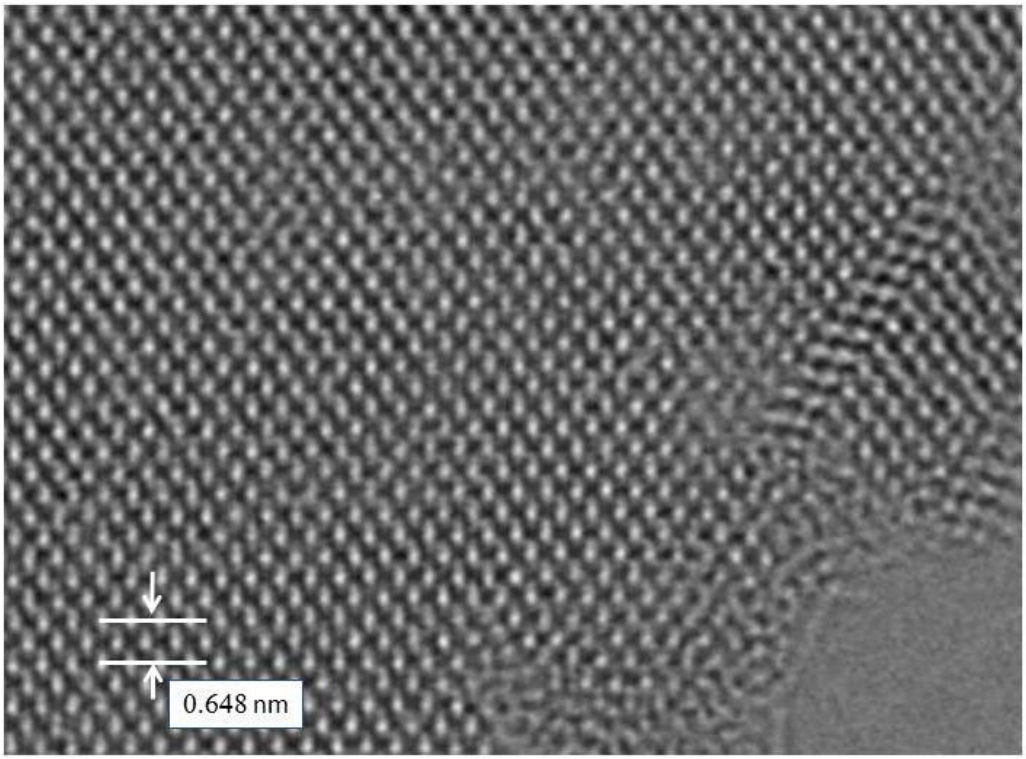

Figure 2-16: Typical HRTEM image from the edge of the specimen with lower resolution which did not separate the Cd and Te atomic species.

2.4 Observation of Defects and Atomic Motion at 300 kV

As was explained previously with figure 2-4, the CdTe crystal used in this chapter contained relatively few lattice defects within the first ~100 nm of the edge of the specimen. The CdTe crystal obtained from MTI Corporation was undoped, while the crystal used in Chapter 1 was highly doped with phosphorus to $10^{17}/cm^3$ carrier density, but the actual phosphorus concentration in the crystal could have been one to two orders of magnitude higher due to self-compensation that occurs in CdTe [2- 19]. Phosphorus is an acceptor atom on the Te position, but it can also go into the Cd position and push out Cd interstitials which is a donor. It is possible that phophorus doping may affect dislocation mobility, although there is no previous literature on this topic. The specimens in Chapter 1 had a strikingly high density of defects at the edge

of the specimen which made it possible to study many of them and observe them in motion. The undoped specimen in this chapter was nearly completely devoid of defects within the ~ 100 nm-wide region of the specimen edge. There were few short defects often found right at the edge of the specimen such as the ones shown in figure 2-16 in the right corner. These may have been formed as a result of reconfiguration that takes place either during ion-milling or during imaging at the very edge of the specimen. Dislocations near the surface can experience strong attractive image force, and if their motion is not impeded by a solute atoms for example, it is quite possible that dislocations are depleted near the surface.

In a very simple analysis, if an image force given by the equation below [1-52] is larger than the Peierls force, a dislocation might be expected to pass out of the crystal.

$$F_{\text{image}} = \frac{-Gb^2}{4\pi(1-\nu)d} > F_{\text{Peierls}} \qquad \text{(eqn. 2-5)}$$

b = | b| of Burgers vector
d = distance of the dislocation from the surface
ν = Poisson ratio (0.41 for CdTe)

If a 15^{o} tapered edge for the TEM specimen is assumed as shown in figure 2-17 with a 120 nm region at the edge of the crystal where the dislocations have disappeared, then solving for $F_{Peierls}$ with the values of G = 51 GPa, b = 0.45 x 10^{-9} nm, d = 32 nm gives the value of 79 MPa. If the depleted region were narrower, the calculated $F_{Peierls}$ would be even larger. Gutemanas et al. [2-20] reported $F_{Peierls}$ of 21 MPa using CdTe single-crystal and polycrystalline material with unspecified dopant type and concentration. Alternatively, Lirtsman et al. [2-21] obtained a value of 6.5 MPa using p-type CdTe but dopant type and concentration was not specified. Their result was obtained from a stress relaxation measurement. It does appear that $F_{Peierls}$ is relatively low for CdTe for dislocation motion, even though the above analysis using eqn. 2-5 provides a relatively

larger value when it is applied to the TEM specimen. However, many dislocations observed in the specimen in both Chapter 1 and 2 are locked dislocations, and there are many Frank dislocations, which will require far higher force, high temperatures, or both to move them. Equation 2-5 would only apply to the isolated edge or screw dislocations. Therefore, it is somewhat mysterious as to why the undoped CdTe is behaving so differently compared to the phosphorus doped CdTe in Chapter 1.

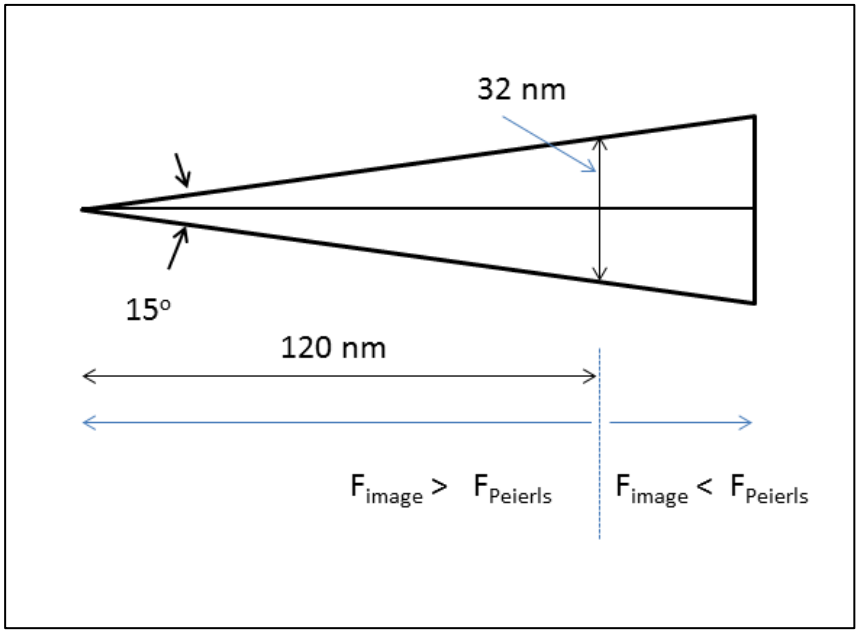

Figure 2-17: Schematic representation of TEM specimen edge, with 15° taper. 120 nm represents the region without dislocations. Blue arrows indicate where $F_{image} > F_{Peierls}$ in the thin region, and $F_{image} < F_{Peierls}$ in the thicker region at the center of the specimen.

Figure 2-18 shows a low magnification BF image taken with many beams (same as HRTEM with 43 beams) showing the distribution of many defects in the specimen. As was shown in figure 2-5, a region approximately 100 nm wide at the edge of the specimen does not have many defects. Further in, there is a high density of defects that are visible out to approximately 600 nm and beyond into the specimen. If

the TEM specimen geometry were similar to figure 2-17, the specimen thickness at 600 nm from the edge would be approximately 160 nm. With the 300 kV electrons, we see much deeper into the specimen than it was possible in Chapter 2 with 120 and 200 kV electrons.

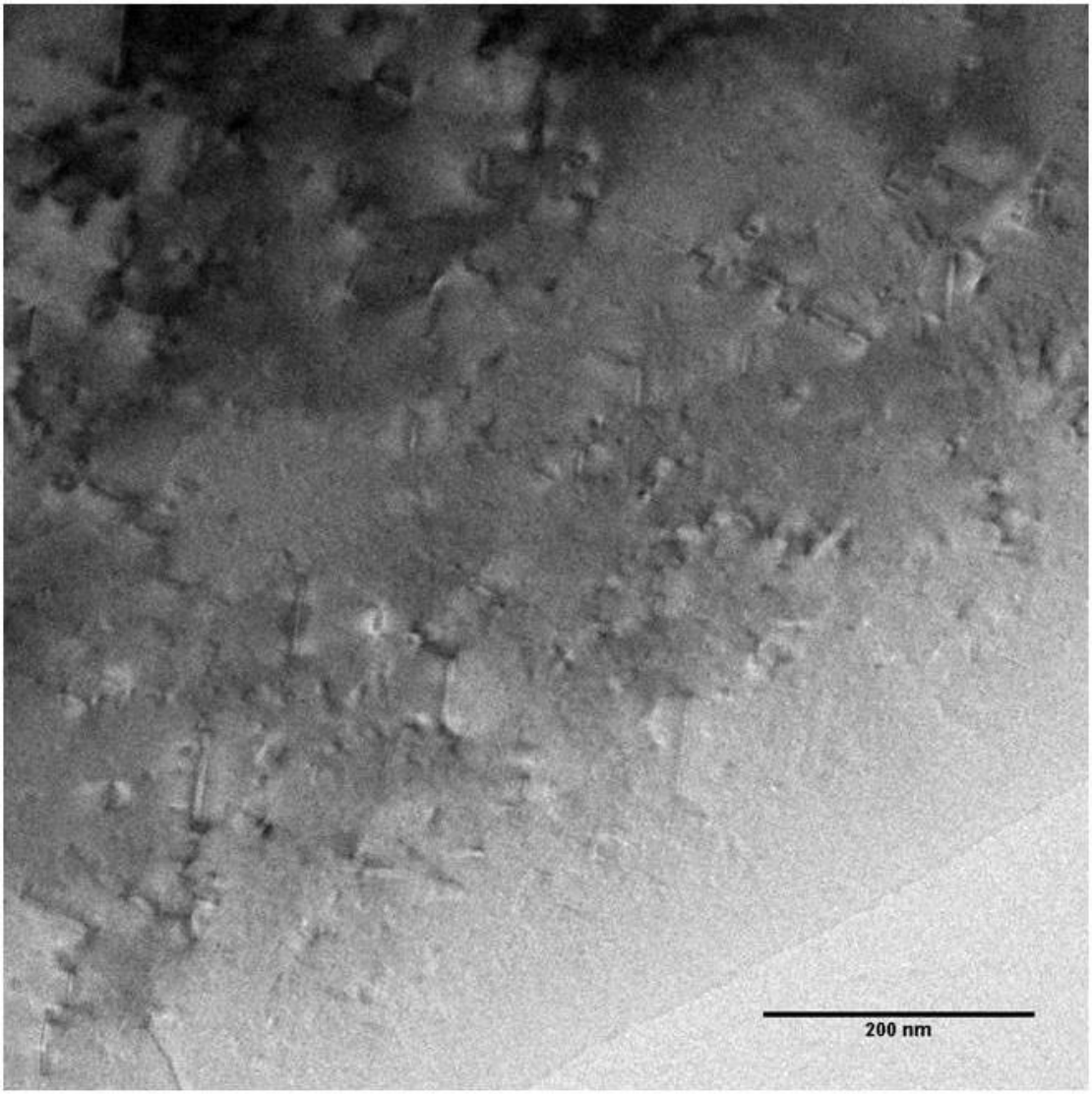

Figure 2-18: Low resolution BF TEM image taken with many beams (43) as in HRTEM. The edge of the disk is depleted in defects, while the interior contains many defects.

An example of typical defects found in the thicker part of the specimen is shown in figure 2-19. This defect is located approximately 300 nm from the edge of the specimen. Again, if the TEM specimen edge profile were like figure 2-17, the specimen thickness would be expected to be approximately 80 nm, which is quite thick for HRTEM imaging. Consequently, the image is not very clear and it is difficult to determine the type of fault it may contain at the center. Looking from the edge of the paper from the side, the defect clearly contains an extra layer of {111} plane at the defect. Therefore, it is likely to be an extrinsic fault with Frank dislocations at each end. A Burgers circuit around the entire defect indicates that the lattice is perfect, which further supports the conclusion. The width of the defect is approximately 18 nm; therefore, the specimen thickness is likely to be much thicker than the width of the defect. This type of defect is likely to be a loop as described in Chapter 1, section 1.9.1 in the bulk. Since the specimen thickness is probably much larger than the width of the defect, it is possible that the defect is being imaged as a loop with perfect crystal surrounding the defect above and below the defect. It may explain why the image is difficult to interpret. Additionally, the lattice appears very different above and below the defect, and it is not clear to what this is due. There is significant distortion in the lattice around the Frank dislocations and the extrinsic stacking fault that forms between them. It is possible that this distortion, which might vary along the imaging direction could cause a change in image character. There were other planar defects that were similar that were analyzed but it was usually difficult to determine what they were, whether they are Shockley partials bounding an intrinsic stacking fault or the Frank type as in figure 2-19.

Other common defects observed in the thick part of the specimen were a network of dislocations, which are tied together by locks. One example is shown in figure 2-20, which is formed by the reaction of various partial dislocations to form a parallelepiped-like structure. This structure is also located approximately 300 nm in from the edge of the specimen. Because the specimen is thick around this defect, it is difficult to determine what each lock is composed of and the nature of the stacking

fault, whether they are intrinsic or extrinsic. However, the structure appears very similar to those already described in Chapter 1, section 1.9.1. Defect #1 is an obtuse angle lock similar to the one described in figure 1-58. The fault running horizontally is a Shockley partial, and the vertical fault appears to be a Frank dislocation that had reacted with the Shockley partial. There is an extra plane of {111} atoms in the planes running 70.5^{o} to the horizontal. Defect #2 is an acute angle version of #1. Defect #3 is an intersection of a Shockley partial with the intrinsic stacking fault running on an alternate {111} plane. It is probably not a lock because it is possible for the dislocation to pass through the stacking fault. This appears to have happened at defect #4 which is an acute angle version of #3.

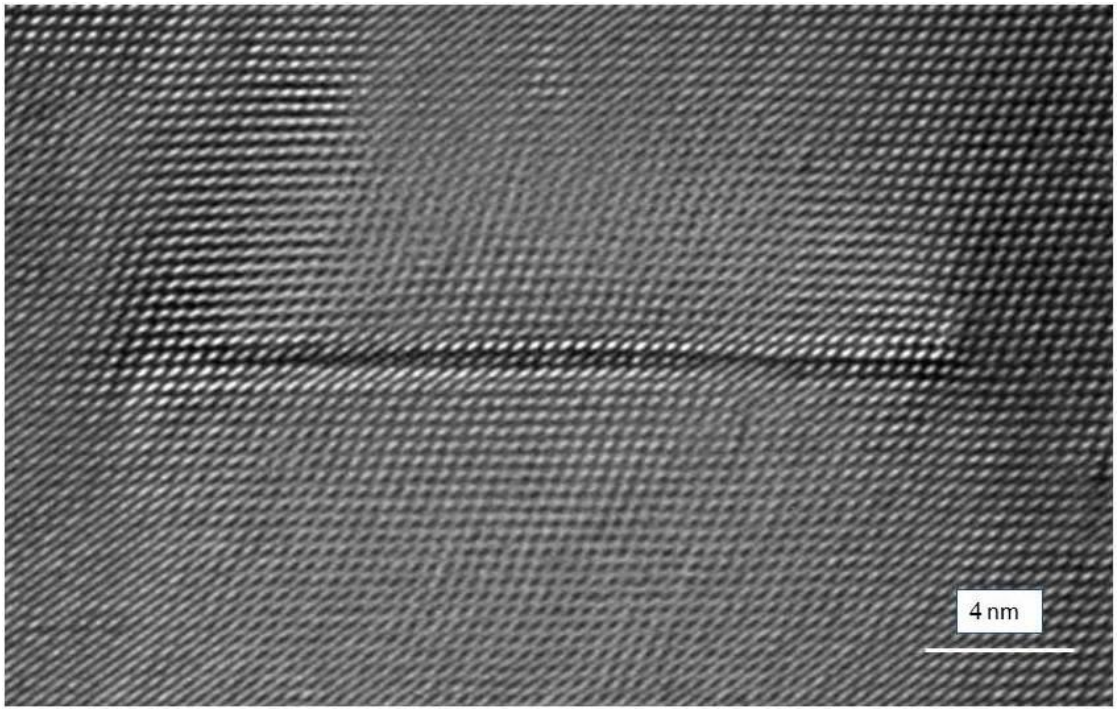

Figure 2-19: HRTEM image of Frank dislocations bounding an extrinsic fault with an extra {111} plane inserted in the middle. Specimen thickness is probably approximately ~ 80 nm at this location.

Defect #5 is a reaction between two 30^{o} Shockley partials on different {111} to form an obtuse angle *Hirth lock* which is described by Hirth and Lothe [1-52]. The two partial dislocations form a new dislocation with the Burgers vector of the type *a*/3<001>. According to Nix [2-22], this configuration is metastable, and the two partials should pass each other further to form a more stable acute angle Lomer-Cottrell lock as shown in figure 1-43. It is difficult to tell exactly what defect #6 may be due to; the lattice image is very fuzzy and difficult to discern. It appears to be the acute angle dislocation lock with the classical Lomer-Cottrell lock configuration.

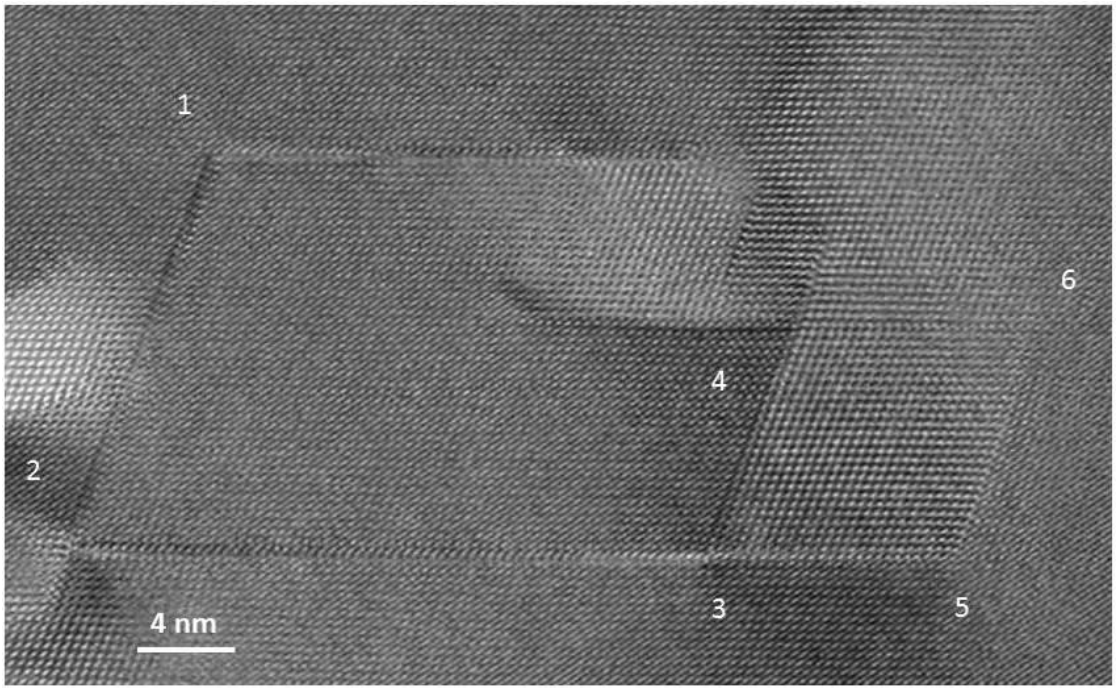

Figure 2-20: HRTEM image of network of dislocations which have become locked. Located approximately 300 nm in from the edge of the specimen. #1 and #2 are reaction between Shockley partial and Frank dislocations. #3 and #4 are intersection of Shockley partial with intrinsic stacking faults formed by Shockley partials on alternate {111} planes. #5 is an obtuse angle reaction between two Shockley partials forming a metastable lock. #6 appears to be a Lomer-Cottrell lock between two Shockley partial dislocations.

Nearly all of the defects such as the ones described in figure 2-19 and 2-20 were located in the thick part of the specimen and the image quality was not very good to make a clear analysis.

A video camera attached to the Titan TEM was used to take video images of CdTe in HRTEM, as it was done in Chapter 1.9.1. Titan was equipped with a x-FEG high brightness gun with beam current capability up to 20 nA. A typical current for HRTEM work on the Titan TEM is 2 to 3 nA. The operating current used in this work was 1.1 x 10^4 electron-sec/Å^2 or 17.6 A/cm^2. This value is roughly the same current density that was used in Chapter 1.9.1 with approximately 15 A/cm^2. Most of the defects in the specimen were in the thick part of the specimen, and they were immobile during imaging. The few defects that were at the edge of the specimen were also immobile, but beam ablation and reconfiguration of the edge occurred first before the defect motion was observed. The specimen edge perforated within several minutes of viewing as described earlier. During the perforation process, the edge of the crystal was reconfigured, but rapid motion of individual image spots as described in Chapter 1.10, figure 1-66 were not observed, perhaps obscured by small amounts of amorphous material that were always present at the very edge of the crystal. Figure 2-21 shows a series of images at approximately 5 second interval, taken at the edge of the crystal. Images are at atomic resolution at the top of the image. There is a crystal with different orientation at the bottom center which had formed because of reconfiguration at the edge of the crystal. The spacing of this crystal closely resemble the <112> orientation projection. This projection is shown in figure 2-22. The closely spaced Cd and Te atoms are separated by 0.132 nm and they are not resolved in the image. It was not unusual to see small crystallites that nucleate at the edge of the specimen with a different orientation than the parent crystal. A close-up of the top middle section of the image is shown in figure 2-23, which makes it easier to see the changes taking place in this region of the crystal. The video was not taken in continuous 30 frames per second in these images. Instead, each frame was averaged over approximately one-half a second, so that each frame is a discrete sequence of “still” images when viewed in acontinuous mode. This was done in part to obtain better contrast and signal strength

in the images. To see a fast-changing event such as atomic motion at the edge of the crystal, more work must be done to obtain higher SNR in the video images. The microscope conditions were not specifically setup for atomic motion imaging, and the Titan microscope has enough capabilities to optimize for recording fast-moving events. For example, the beam current on the specimen can be increased and magnification can be reduced to trade for higher brightness on the camera screen. Nevertheless, it would be advantageous to have a video camera with higher sensitivity and higher resolution so that the camera can be operated at high frame rates with good SNR.

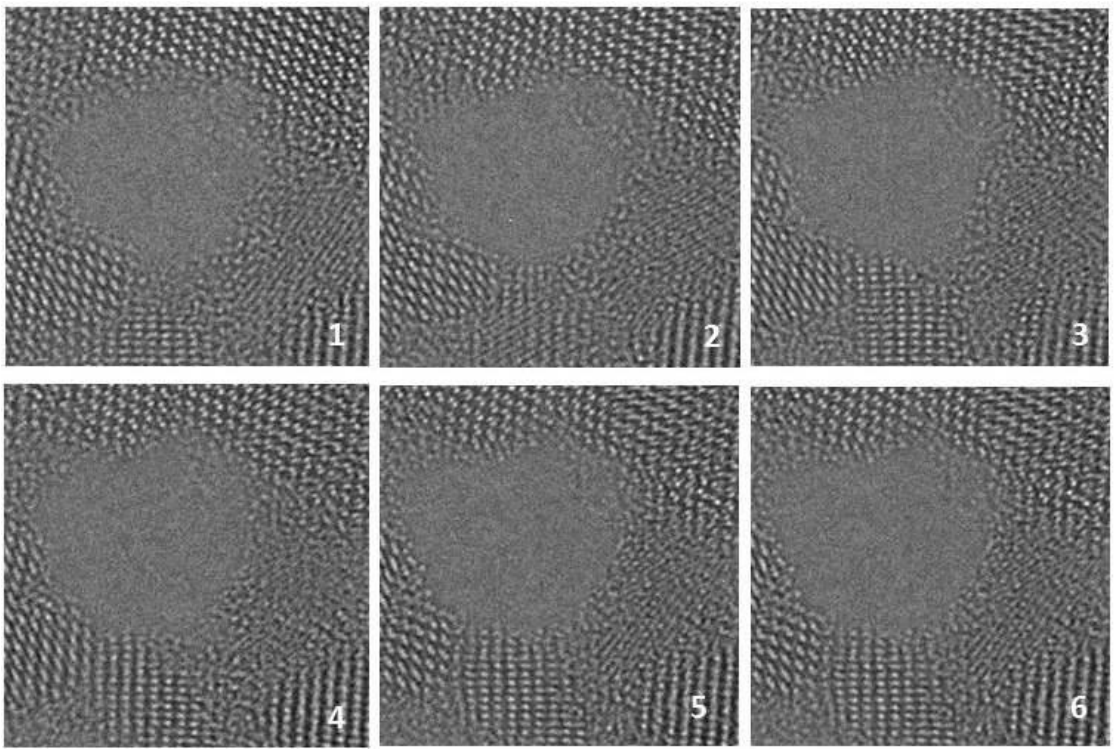

Figure 2-21: HRTEM image from a video taken at the edge of the crystal. Interval between each image is about 5 seconds. Top portion of the image is at atomic resolution. Bottom center of the image contains a small crystal with an orientation that closely resemble <112> projection.

The newest cameras available from the vendors have both higher resolution and sensitivity, which should improve the ability to record fast-moving events at the microscope operating conditions used in this work without having to increase beam current, which may cause much faster deterioration of the specimen and may contribute to degrading the resolution of the microscope.

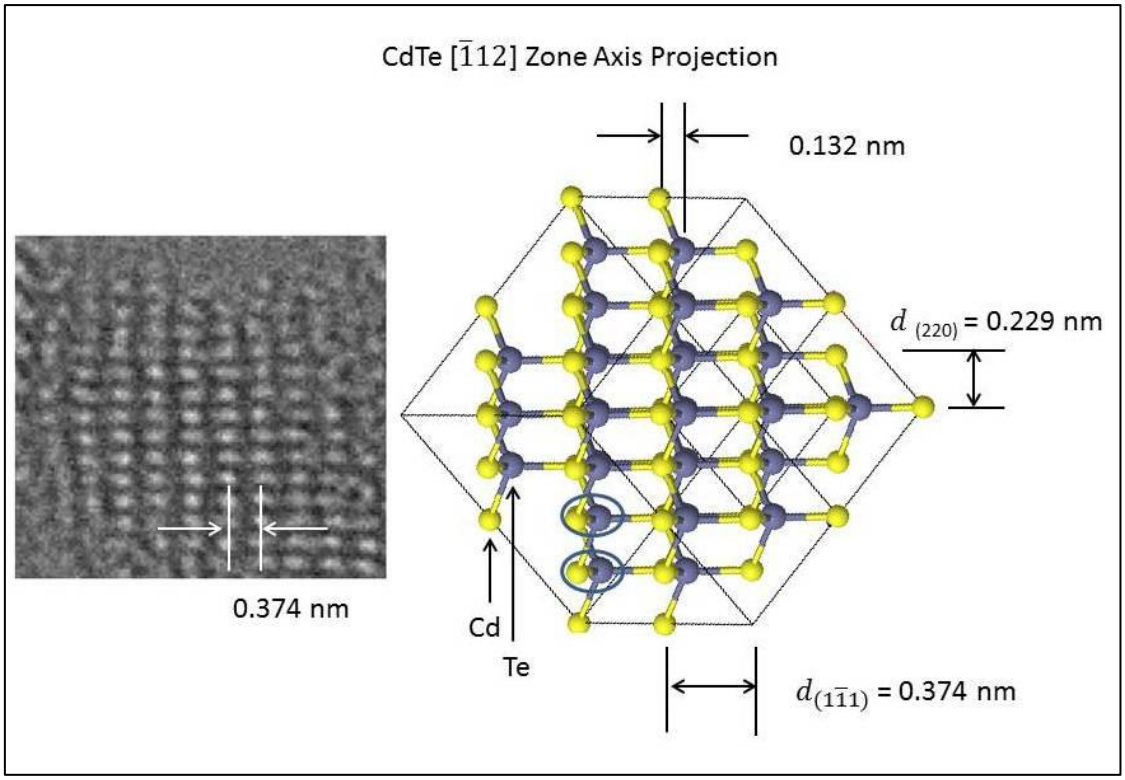

Figure 2-22: Insert image from figure 2-21 at the bottom center of the figure, with the schematic of the CdTe [$\bar{1}12$] projection. Each image spot is Cd-Te pair separated by 0.132 nm, which is not resolved.
Model based on ChemTube3D, © 2008-2014 The University of Liverpool [3-44].

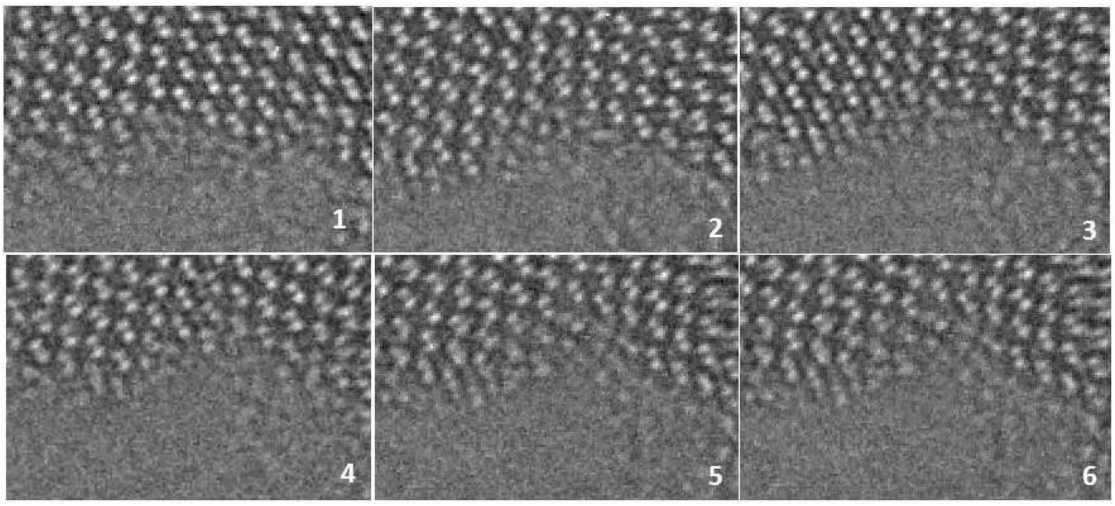

Figure 2-23: Higher magnification images of the same sequence in figure 2-21, from the top middle section of the image where atomic resolution was obtained. Changes in the edge shape are discernable. Each sequence is approximately a 5-second interval.

2.5 Summary of Chapter 2

In summary, a Titan 80-300 HRTEM with an aberration corrector was set up for NCSI conditions with C_s = -18.3 μm in order to image the CdTe [011] projection and to obtain 0.162 nm resolution between the Cd and Te atomic columns. A comparison of experimental images with the multi-slice image simulation shows some similarities in the images, but the match was not useful for many other thicknesses and defocus conditions. The parameters for the simulation will likely need to be adjusted in order to obtain a better match. A lack of knowledge about the precise thickness of the specimen where the images are obtained hampers the image matching exercise. Some method to calibrate the thickness accurately is needed. It is possible that EELS can be used to obtain a calibration curve between thickness and the energy loss peak profile for example. Switching to STEM mode imaging maybe necessary to obtain the best result for the EELS analysis and the specimen degradation may make it difficult to obtain the calibration. The e-beam causes rapid deterioration of CdTe at the thin region

of the specimen so that obtaining enough data about the specimen and generating enough through-focus series images to use for image matching experiments is difficult. Investigating the resolution capability of the microscope at 80 kV may be worthwhile to determine whether the e-beam damage could be minimized. In previous work at 120 kV in Chapter 1, we have already seen e-beam damage taking place. With the use of the NCSI technique, it may be interesting to study CdTe doped with various point defects to see if such defects can, in fact, be imaged. Such defects are a continuing subject of investigation into obtaining a better understanding of electronic properties of CdTe.

The results shown here for imaging CdTe with the aberration-corrected TEM clearly show striking improvement in image resolution over conventional TEM, even though such resolutions are obtained in restrictive conditions for the specimen as demonstrated here. The aberration-corrected HRTEM shows great potential for advancing the understanding of the structure of materials that have been inaccessible before. Combining the high-resolution capability of aberration-corrected TEM with the high-resolution chemical analysis tools that come with modern state-of-the-art TEM provides the unprecedented capability to analyze and probe the structure and chemical properties of materials at atomic resolution. Several atomic resolution imaging sessions of CdTe has been reported recently using STEM instruments. In 2014, Li et al. [2-23] analyzed the core structure at the two ends of intrinsic and extrinsic faults using aberration-corrected Nion UltraSTEM 100 and 200 microscopes, and used STEM - high angle annular dark field (HAADF) and Z-contrast imaging to determine the atomic species at the core. They found single Cd and Te columns at the opposite end of the faults and determined that they have three-fold and five-fold coordination at the site, suggesting that the cores have dangling bonds. They also took STEM movies of intrinsic faults that appeared and disappeared while imaging. In 2014, Paulauskas et al. [2-24] imaged Lomer-Cottrell and Hirth lock dislocation cores in CdTe using an aberration-corrected JEOL JEM ARM-200CF STEM tool at 200 kV. Atomic resolution Z-contrast imaging and XEDS (X-ray energy dispersive spectrometry) mapping were used to determine the atomic core structure in these dislocations. In 2014, Li et al. [2-

25] analyzed Σ9 grain boundaries in polycrystalline CdTe in CdS/CdTe thin film solar cell film using an aberration-corrected Nion UltraSTEM 200 microscope using Z-contrast imaging to determine the atomic structure there. The EELS line scan also was taken at the same grain boundary to determine that there was chlorine segregation taking place within an approximately 5 nm-wide band at the grain boundary. This recent work using STEM tools equipped with aberration-corrected lenses and powerful EELS and XEDS systems clearly show the capability of these tools for the study of the dislocation core structure and atomic arrangements at the grain boundaries. An HRTEM imaging TEM/STEM tool using an aberration-corrected lens should also provide similar information when operated in the STEM mode, with the added versatility of applying conventional TEM techniques to the analysis of defects. The TEM imaging mode should be more suited for imaging rapidly changing events such as dislocation motion and other dynamic events taking place at the edge of the crystal as described in this chapter and in Chapter 1. HRTEM with aberration-corrected lenses has not yet been applied to the study of CdTe material in any substantial way. Therefore, there is still a good opportunity to make a significant contribution to the field.

Chapter 2 References:

[2-1] H. Rose, *Outline of a spherically corrected semiaplanatic medium-voltage transmission electron microscope*, Optik **85**, 19-24 (1990)

[2-2] M. Haider, S. Uhlemann, E. Schwann and B. Kabius, *Development of a spherical aberration of a 200kV TEM by means of a hexapole corrector*, In Proc. Dreiländertagung, Regensberg, Germany, Optik **106** (Suppl. 7) 7, (1997)

[2-3] O.L. Krivanek, N. Dellby, A. J. Spence, R.A. Camps & L. M. Brown, *Aberration correction in the STEM. In Electron Microscopy and Analysis* 1997: Proc. EMAG97 Conf., Cavendish Laboratory, Cambridge, UK, (ed. J. M. Rodenburg). Institute of Physics Conference Series, vol. **153**, pp. 35–40. Bristol, UK: Institute of Physics (1997)

[2-4] U. Dahmen, R. Erni, V. Radmilovic, C. Kisielowski, M-D. Rossell, and P. Denes, *Background, status and future of the Transmission Electron Aberration-corrected Microscope project*, Phil. Trans. A, **367**, 3795-3808 (2009)

[2-5] H. Rose, *Optics of high-performance electron microscopes*, Sci. Technol. Adv. Mater. **9** (2008)

[2-6] F. Zemlin, K. Weiss et al,, *Coma-free alignment of high resolution electron microscopes with the aid of optical diffractograms*, Ultramicroscopy **3**:49-60 (1978)

[2-7] C.-L Jia., M. Lentzen and K. Urban, *Atomic-resolution imaging of oxygen in perovskite ceramics*. Science **299**, 870–873 (2003)

[2-8] C.-L. Jia, M. Lentzen and K. Urban, *High resolution transmission electron microscopy using negative spherical aberratio*n, Microsc. Microanal. **10**, 174–184 (2004)

[2-9] J.C. Meyer, C. Kisielowski, R. Erni and M.D. Rossell, *Direct imaging of lattice atoms and topological defects in graphene membranes*, Nano Lett. **8**, 3582–3586 (2008)

[2-10] J.H. Warner, M.H. Rümmeli, A. Bachmatiuk and B. Büchner, *Atomic Resolution Imaging and Topography of Boron Nitride Sheets Produced by Chemical Exfoliation,* CS Nano, **4** (3), pp 1299–1304 (2010)

[2-11] K. W. Urban, C.-L. Jia, L. Houben, M. Lentzen, S.-B. Mi & K. Tillmann, *Negative spherical aberration ultrahigh-resolution imaging in corrected transmission electron microscopy*, Phil. Trans. R. Soc. A **367**, 3735–3753 (2009)

[2-12] F. Hossein-Babaei, A. L. Koh, K. Srinivasan, G. A. Bertero and R. Sinclair, *Aberration Corrected Transmission Electron Microscopy of the Intergranular Phase in Magnetic Recording Media*, Nano Lett. **12** (5), pp. 2595–2598 (2012).

[2-13] M. Lentzen, *Progress in aberration-corrected high-resolution transmission electron microscopy using hardware aberration correction*, Mirosc. Microanal. **12**, 191-205 (2006)

[2-14] M. Lentzen, B. Jahnen, C.-L. Jia, A. Thust, K. Tillmann & K. Urban, *High-resolution imaging with an aberrationcorrected transmission electron microscope*.
Ultramicroscopy **92**, 233–242 (2002)

[2-15] H. Lichte, *Optimum focus for taking electron holograms*, Ultramicroscopy **38**, 13–22 (1991)

[2-16] K. Heinemann, *In-situ measurement of objective lens data of a high-resolution electron microscope*. *Optik* **34**, 113–128 (1971)

[2-17] MTI Corporation, Richmond, California

[2-18] P. Fochuk, R. Grill and O. Panchuk, *The Nature of Point Defects in CdTe*, Journal of Electro. Mater., Vol. **35**, No. 6, pp.1354-1359 (2006)

[2-19] H. Zhao, *Impurty and bulk contact effects on CdTe/CdS thin film solar cells*, page 46, Ph.D. Thesis, University of South Florida, Dec. 5 (2007)

[2-20] E. Y. Gutmanas, N. Travitsky and P. Haasen, *Negative and positive photoplastic effect in CdTe*, Phys. Status Solidi A, **51** (1979) 435

[2-21] G. Lirtsman, S. V. Lubenets, V. D Natsik and L. S. Fomenko, *The influence of Peierls relief on low-temperature plasticity of CdTe single-crystals*, Mat.Sci.Engr. A**164**, pp. 364-367(1993)

[2-22] Discussion with W.D. Nix – March, 2015

[2-23] C. Li, Y. Wu, T.J. Pennycook, A.R. Lupini, D.N. Leonard, W. Yin, N. Paudel, M. Al-Jassim, Y. Yan and S.J. Pennycook, *Carrier separation at dislocation pairs in CdTe*, Phys. Rev. Lett. **111**, 096403 (2013)

[2-24] T. Paulauskas, C. Buurma, E. Colegrove, B. Stafford, Z. Guo, M.K.Y. Chan, C. Sun, M.J. Kim, S. Sivananthan and R.F. Klie, *Atomic scale study of polar Lomer-Cottrell and Hirth lock dislocation cores in CdTe*, Acta Cryst. A **70**(6) (2014)

[2-25] C. Li, Y. Wu, J. Poplawsky, T. J. Pennycook, N. Paudel, W. Yin, S. J. Haigh, M. P. Oxley, A.R. Lupini, M. Al-Jassim, S. J. Pennycook, and Y. Yan, *Grain-Boundary-Enhanced Carrier Collection in CdTe Solar Cells*, Phys. Rev. Lett. **112**, 156103, (2014)

Chapter 3: CdS/CdTe Heterojunction Solar Cell

3.1 CdS/CdTe Heterojunction Solar Cell

Solar cell structures based on CdTe have been promoted since the 1950s owing to their bandgap of 1.44 eV, which matches well with the solar spectrum. Bube was one of the early pioneers in the study of CdTe and other II-VI compound semiconductor materials for their photoelectronic properties [3-1, 3-2]. A comprehensive review article was published by Bube et al. in 1983 [3-3]. For commercial application, a thin film structure is needed in order to reduce the cost. Because of high absorption constant, CdTe is well suited to be used in a thin film form as most of the photons will be absorbed within 1-2 μm from the surface. In recent times, a thin film structure based on the CdS/CdTe heterojunction has emerged as a competitive device [1-31] that competes favorably with silicon-based materials and the other commercially important thin film structure based on copper indium gallium selenide ($CuIn_xGa_{1-x}Se_2$) or CIGS. To understand the basic properties of the CdS/CdTe heterojunction cells, the work should be first spent on a junction formed on well-controlled surfaces using oriented single-crystal CdTe in order to relate the structure and electrical properties to the fabrication method of the heterojunction. The purpose of this study was to examine the interface between CdS and CdTe and attempt to correlate it with its electrical properties.

In a solar cell, the photon created carriers must be separated and collected before they recombine, and this is achieved by introducing a field generated by a p-n junction. For material such as CdTe with a large absorption constant, surface recombination can dominate; therefore, the junction must be placed away from the surface. This requires a long minority carrier diffusion length, which is often not a common feature of most materials. A one sided n^+ -p or p^+ -n junction often is chosen as it makes the best use of a large absorption constant material. Since electrons have longer minority carrier life than holes, an n^+ -p junction is used, using a wide bandgap CdS as the n^+ layer and p-type CdTe. This structure then is the definition of the

heterojunction. A CdS film on single-crystal CdTe with the efficiency of 7.9% was achieved at Stanford by Mitchell, Fahrenbruch, and Bube in 1977 [3-4]. An efficiency up to 12 % was being reported at approximately the same time [3-5, 3-6]. Additionally, a thin film version using a silk screening process with the efficiency of 9% was obtained [3-7]. Comprehensive review articles have been written about CdTe by Strauss [3-8], Wald [3-9], and Zanio [3-10]. More recent review articles on thin film CdS/CdTe heterojunction solar cells also are available by Kumar and Rao [3-11] and on recent developments in high efficiency cells by Gloeckler et al. [3-12].

One of the key advantages of a heterojunction cell is a large short circuit current J_{sc}, owing to the efficient collection of carriers near their generation. A disadvantage is the relatively low open circuit voltage, V_{oc}. A key characteristic of a heterojunction that makes it advantageous for solar cell application over simpler p-n junction cells is that surface recombinations are significantly reduced, which helps with carrier collection efficiency. The space charge that results from joining two dissimilar semiconductors together with bandgap matching helps to efficiently separate the carriers generated by photon absorption in the absorber material. The large I_{sc} (short circuit current), V_{oc} (open circuit voltage) and fill factor ff = $\frac{P_{max}}{I_{sc}V_{oc}}$ characterize the best efficiency for the solar cell figure of merit. The low V_{oc} for the CdS/CdTe often reported is thought to be due to interfacial defects, which provide leakage paths. They could be lattice mismatch defects (e.g., dislocations at the interface, interfacial reaction and compound formation at the junction). A generic and idealized current density-voltage (J-V) curve for a solar cell is shown schematically in figure 3-1 in the dark and under illumination, and the equivalent circuit is shown in the inset.

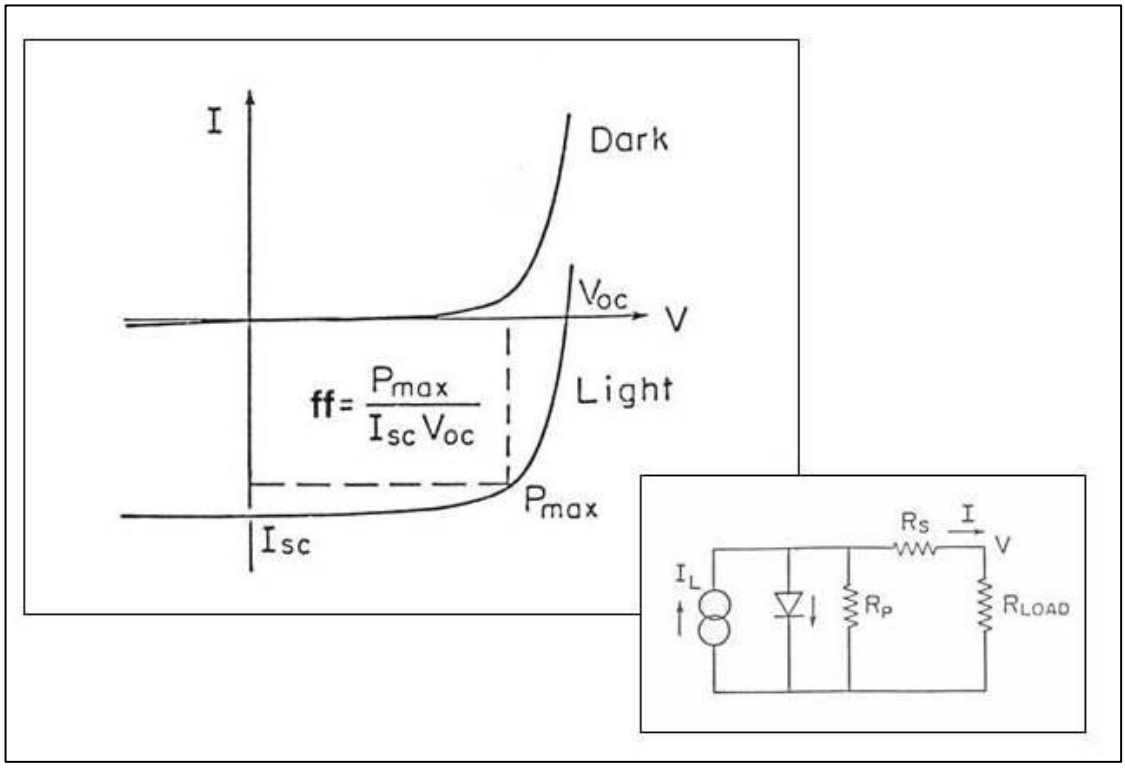

Figure 3-1: Idealized schematic drawing of a JV current -voltage curve for solar cell with the equivalent circuit in the inset. Some of the best actual CdS/CdTe solar cells have very similar JV characteristics as shown. From Werthen thesis [3-19].

The equivalent circuit in figure 3-1 is described by:

$$J = J_o \left[\exp\left(\frac{qV}{AkT}\right) - 1 \right] + G_p V - J_L \quad \text{.....(Eqn. 3-1)}$$

where J_o = reverse leakage current

A = diode factor

G_p = shunt conductance = 1 / R_p

J_L = photo-generated current

The voltage applied to the junction V is equal to:

$$V = V_{appl} - IR_S$$

where V_{appl} = voltage applied to the terminal of the diode

R_s = total series resistance as seen from the terminal of the diode

I = total diode current, JA_c

Ac = total area of the diode

Since the key characteristic of a heterojunction cell depends so much on the condition at the metallurgical interface, it is useful to understand the nature of that interface as well as possible. CdS normally exists in the hexagonal wurtzite structure, while CdTe has a cubic sphalerite structure. This adds additional complications to what might take place at the interface. A high density of misfit dislocations is expected if there is epitaxial growth of CdS on CdTe. A typical substrate preparation before the deposition of CdS may leave a thin layer of oxide or contaminants at the interface which could interfere with CdS film growth. The electrical effects of misfit dislocations and thin interfacial phases are still not well known or understood. Therefore, the comparison of junction properties to the details of the interface provides some useful insight into the development of better processing methods for the formation of the heterojunction.

The orientation relationship between CdS (hexagonal wurtzite) and crystals with cubic sphalerite structure (including CdTe) has been studied [3-13, 3-14, and 3-15]. It was found that {0001} and $\{11\bar{2}0\}$ faces of CdS are nearly always parallel to the $\{111\}$ and $\{1\bar{1}0\}$ faces of the cubic CdTe structure. For example, Igarashi deposited CdS by chemical vapor deposition on CdTe with {110}, {112}, and {221} orientations, and saw a small deviation from the exact CdS {0001} // CdTe {111} orientation using the back reflection Laue technique [3-15]. Igarashi used the

dislocation model of small-angle grain boundaries developed by Read and Shockley [3-16] and it was possible to relate the degree of misorientation to the amount of lattice mismatch between the CdS and the substrate crystal. However, the fit to the model was not good for CdS deposited on a {110} CdTe surface, which was only attributed to the large lattice mismatch between the two materials in this orientation. More recent analysis on the CdS/CdTe interface has been dominated by work on thin film solar cells, based on CdTe deposited by closed spaced vapor deposition (CSVT) or sublimation onto CdS films [3-17, 3-18].

Our objective was to determine in more detail the relationship between the CdS and CdTe for CdS deposited by e-beam evaporation and chemical vapor deposition (CVD) on several orientations and surface treatments of the CdTe substrates. CdS/CdTe heterojunction cells were prepared by Werthen and Nishimura, and their electrical properties were reported by them in their respective theses [3-19, 3-20]. Some of the TEM results also were already reported there. The present thesis will describe in more detail the TEM analysis for the various junctions.

3.2 CdS/CdTe Heterojunction Solar Cell Preparation Method

CdS films in this study were deposited by two different methods, first by e-beam evaporation by Werthen [3-19] and second by Nishimura for CVD [3-20]. CdTe crystals used in this work were grown by a modified Bridgman method by Robert Raymakers at the Center for Materials Research at Stanford [3-21]. In this technique, the crystals are grown in quartz ampules coated with pyrolytic graphite. A phosphorus dopant is added during the second regrowth step, and its concentration in CdTe is approximately 10^{17} cm^{-3} [3-19]. The addition of phosphorus to CdTe makes it p-type. Group V elements such as P and As can substitute for Te to become acceptor sites, or exist interstitially in the lattice [3-21]. The actual measured hole density of the CdTe substrate was approximately $5x10^{16}$ cm^{-3}, and the Hall mobility was 40 cm^2/V-s [3-19, page 45-46]. Carrier density is determined by capacitance measurement and mobility by the Van der Pauw method [3-22]. Vibration is also added during growth to increase

grain size. Typically, many large grains that are many millimeter in size, as shown earlier in figure 1-14, are obtained within the boule, with many of the grains oriented in the <111> direction along the long axis of the boule. The grains also contain many large twins. Typical CdTe boules are 40-50 mm long by 15- 20 mm in diameter. A cut surface of the boule was planarized with 600-grit SiC paper, followed by a polish with a 1 μm alumina slurry. This surface was then chemically polished with 5% bromine in methanol (Br_2:MeOH) solution. This was necessary in order to obtain visible reflections from Laue X-ray diffraction which was used to determine the crystallographic orientation of the grains in the boule. A boule was mounted on a goniometer stage so that a wafer with the desired orientation could be cut from it. Thin wafers were cut with a wire saw, and the same polishing process was used to obtain rectangular pieces for further work, the dimensions of which were typically ~4.5 x 3.5 mm, and 1mm thick. The surfaces of these pieces were again polished with 1 μm alumina slurry followed by etching in Br_2:MeOH solution to obtain a shiny surface and remove surface damage from the alumina polish.

Some of the rectangular pieces were cleaved to obtain a {110} surface once the <111> orientation had been determined by the Laue technique. A number of different orientations were prepared to produce CdS/CdTe heterojunction cells. The terminology used for the substrate surface condition or treatment and their description used by Jan Werthen [3-19, page 46 and 109] are as follows:

1) As cleaved {110} surface - (C)

2) As cleaved and etched with 2% Br_2:MeOH on CdTe {011} surface - (CE)

3) $\{111\}_{Cd}$ or $\{111\}_{Te}$ surface, polished and etched in 2% Br_2:MeOH - (PE)

4) $\{111\}_{Cd}$ or $\{111\}_{Te}$ surface, polished and etched in 2% Br_2:MeOH, followed by hydrogen anneal at 420°C for 5 minutes - (PEH). Hydrogen annealing was carried out in the quartz tube with flowing hydrogen prior to CdS deposition in a separate vacuum system.

For the Br_2:MeOH treatment on the substrate surface, the term *etching* is used when 2% Br in methanol is employed when the surface is oxidized. At lower Br concentrations, the solution oxidizes the surface. It is reported by Werthen [3-19, page 47] that $\{111\}_{Te}$ surface is blackened while the $\{111\}_{Cd}$ face remains shinier. For compound semiconductors with the cubic sphalerite structure, it is well known that the {111} surface exhibits different behavior depending on which atomic species is on the surface. If the lattice terminates with Cd atoms, it is termed $\{111\}_A$, and $\{111\}_B$ if it terminates with Te atoms [3-23]. Etching methods have been developed to determine the two types of surfaces, as described by Warekois et al. [3-24] and Inoue et al. [3-25]. Warekois' etching process was tested on the two {111} surface types, and the results are shown in figure 3-2. The etching process involves the following steps:

1. 3 parts HF, 2 parts H_2O_2, 1 part H_2O for 2 minutes

2. Concentrated HCl for 3 minutes

However, the results that we have obtained were reversed from Warekois' results. What was labeled as Cd $\{111\}_A$ was in fact Te $\{111\}_B$ and vice versa in our results based on a check of surface properties based on X-ray photoelectron spectroscopy (XPS). In our convention then, the Cd surface or $\{111\}_A$ is the side that pits heavily, vs. Te $\{111\}_B$ for Warekois. For the {111} surface identification used by Werthen and Nishimura, our convention (reversed from Warekois) was used. A 1983 publication by Fewster and Whiffen [3- 26] arrived at a same result as ours with the Warekois etch, showing that the Cd $\{111\}_A$ surface pitted much more than the Te $\{111\}_B$ surface. They confirmed the result of A and B surface identification using the X-ray diffraction method, making use of the asymmetry that occurs in the {333} higher order reflections depending upon which surface is viewed. More detailed analysis of various techniques used to identify the A and B surface for CdTe was made by Brown in 1988 [3-27]; Fewster and Whiffen also confirmed the results [3- 26]. Warekois et al. issued an erratum to their 1962 paper in 1966 for making a similar type of error in identification of $\{0001\}_{Cd}$ and $\{0001\}_S$ surface for CdS using a different etch [3-28]. The confusion in the literature caused by the Warekois reference is outlined in the Brown reference.

However, it appears that no such erratum was issued for CdTe etch. We are confident with our result on A and B surface identification, as it was backed by XPS analysis and the work by Fewster and Whiffen, and by Brown.The geometrical description of the $(111)_A$ and $(111)_B$ surface is shown in the ball and stick model in figure 3-3. The naming convention for the surface is also shown, although it is not strictly followed by everyone. A good description of the convention is given by Egan [3-29].

Br_2:MeOH at 5% concentration is very effective in polishing the surface, as it removes mechanical damage and creates a shiny polished appearance. In addition, it has been reported previously that this solution produces a residue-free surface suitable for forming heterojunctions [3-30]. However, the XPS analysis of the etched surface shows that it becomes Te-rich, with a Cd:Te ratio between 0.45 to 0.57 based on the ratio of Cd $3d_{5/2}$ and Te $3d_{5/2}$ peaks [3-31], and small amounts of bromine were detected by Auger analysis [3-19]. A compound such as $TeBr_4$ or other hydrolyzed forms of Te are thought to form on the surface, which is strongly dependent on the rinsing process after the etching [3-32].

Heat treatment with hydrogen was performed at 420°C for 5-10 minutes. A higher temperature was not picked as a Schottky barrier study on such surfaces by Werthen [3-19] showed significant degradation in J_o values. Hydrogen treatment leaves a stoichiometric surface on CdTe, and the mechanism is thought to be due to the formation of hydrides of Cd or Te, which can vaporize from the surface [3-31].

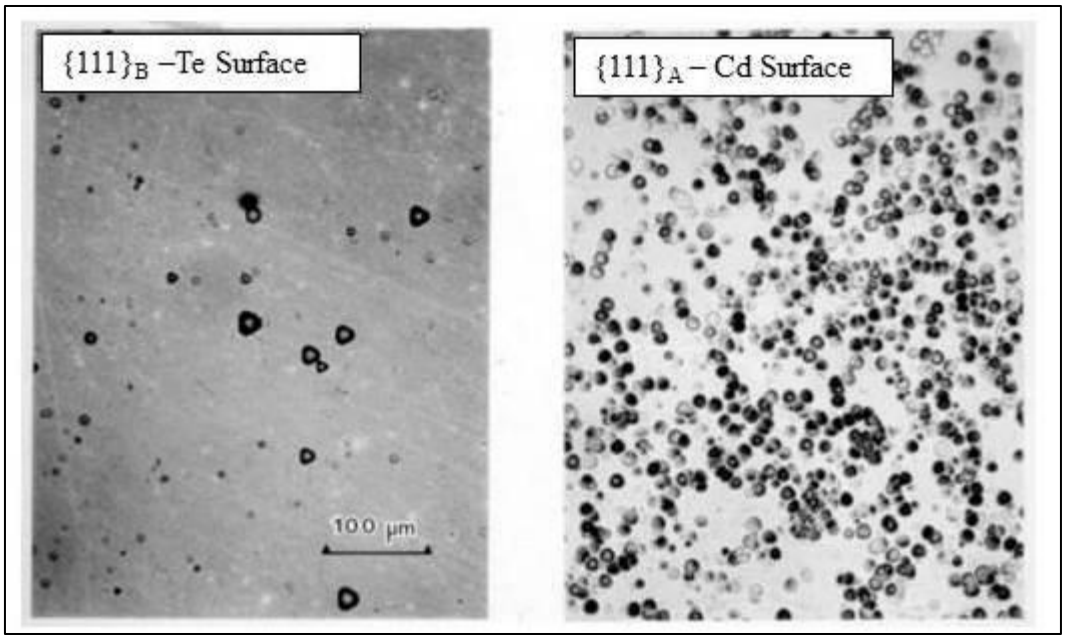

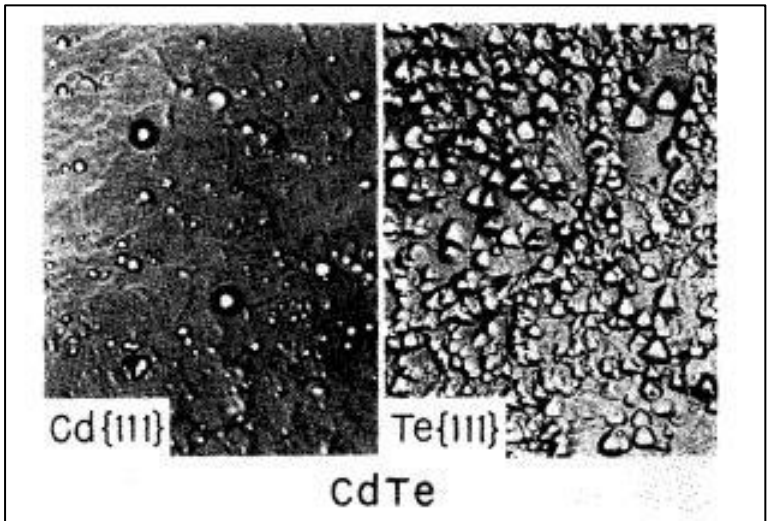

FIG. 7. The {111} surfaces of CdTe after etching in 3 (parts by volume) 48% HF+2 30% H_2O_2+1 H_2O for 2 min at 25°C. The film, present on both surfaces, was removed by rinsing briefly in conc. HCl. Triangular etch pits are formed on the tellurium surface and can be seen to be aligned in grain boundary arrays. The cadmium surface is very nearly polished and the shallow figures shown in the photomicrograph flatten even further with continued etching. Samples cut from crystals obtained from two sources gave identical results; 200×.

Figure 3-2: Above, CdTe {111} surface identification method based on Warekois' etch, except that identification of $\{111\}_{Cd}$ and $\{111\}_{Te}$ is reversed from Warekois' results. Figure 7 in the inset below is from the Warekois reference [3-24]. AIP Publishing, Reproduced with permission.

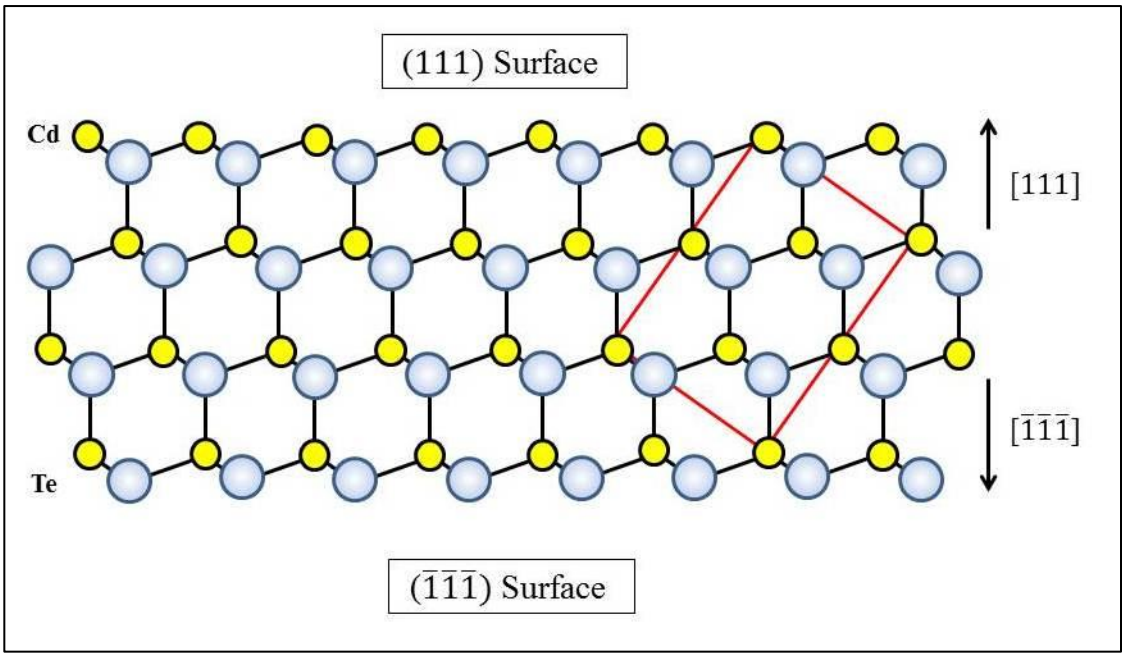

Figure 3-3: Schematic showing the convention used for naming the (111) surface in compound semiconductors, shown in <110> projection. $(111)_A$ surface terminates in a metallic surface (Cd) while $(\overline{111})_B$ surface terminates in a non-metallic surface (Te). $(111)_{Cd}$ surface terminates with Cd atoms on the (111) surface so that it is tetrahedrally coordinated with three Te atoms below. For the $(\overline{111})_{Te}$ surface, the situation is reversed.

Thermal evaporation of CdS was done in a diffusion-pumped vacuum system at about 2 x 10^{-6} torr. The CdS starting material was an undoped sintered powder, which was electron beam evaporated using a Varian 6 KeV four-crucible electron gun. The substrate was typically heated to 130-140°C with an infrared quartz lamp during evaporation, and the deposition rate was ~1 nm/sec. It has been observed that CdS films generally grow with <0001> preferred orientation based on X-ray diffraction. The grain structure of the film becomes more visible with higher substrate temperature by optical microscopy and SEM. The typical thickness of the CdS film was approximately 1.0 to 1.5 μm. Well-developed granular structured films have grain sizes that are similar to the film thickness based on SEM observation of films in cross

section (Werthen [3-19]). For thermally grown CdS, a two-phase mixture of cubic sphalerite and hexagonal wurtzite has also been reported [3-33]. Above 200°C, a pure hexagonal structure forms [3-34]. Heteroepitaxy of CdS has been observed on other substrate materials such as GaP [3-13], InP [3-35], and ZnTe [3-36]. The orientation relationship between the cubic sphalerite and CdS has been reported to be <011> - GaAs / $<\bar{1}2\bar{1}0>$ CdS [3-37]. CdS, as evaporated on glass slides, shows the hexagonal structure as revealed by X-ray diffraction analysis. Optical microscopy of CdS on a cleaved (C) {110} CdTe surface showed only the features related to cleavage steps on the surface. A cleaved and etched (CE) CdTe surface also showed no visible features, while for polished and etched (PE) and polished, etched and heat-treated (PEH) $\{111\}_{Te}$ surfaces, the optical microscopy showed a grain structure in the CdS film. On PE and PEH $\{111\}_{Cd}$ surfaces, no visible features were observed in the CdS films. Epitaxial film is expected to give a smooth surface, the film has a fine grain structure, or it is amorphous.

The CVD system used for CdS growth consisted of an in-house built 36-inch three-zone temperature controlled furnace. The system can use either N_2 or H_2 as the carrier gas or a mixture of the two. CdS and indium dopant in spoons are initially placed in the cold zone, and moved into the hot zone to start the deposition. Details of the system and the method of deposition are described by Nishimura [3-20, pages 31, 99]. When CdS is evaporated, Cd and S dissociate, and some of the S reacts with hydrogen to form H_2S. Partial pressures of Cd, S, S_2, and H_2S factor into the growth rate of the film. The CdTe substrate was annealed for 5 minutes at 425°C with an H_2 flow. The CdS was evaporated at 890°C, while the CdTe substrate temperature typically varied between 260°C to 400°C. A much higher substrate temperature is needed for a CVD process compared to e-beam evaporation in order to obtain high quality CdS film that is optically transparent and has good heterojunction properties [3-20, page 109]. H_2 was used as the carrier gas for the CVD growth. Typically, two flow conditions were used, 130 cc/min and 390 cc/min. The deposition time was fixed at 80 minutes and the substrate temperature was varied in order to obtain the desired film thickness. The Arrhenius plot of the film growth that was obtained by Nishimura is

reproduced in figure 3-4 (figure 6.1 in Nishimura's thesis [3-20, page 121]). The y-axis on this curve is the total film thickness after 80 minutes of deposition instead of the usual deposition rate.

Once the CdS deposition was completed, the substrate and the CdS spoon, which holds CdS powder, were moved back to the cold zone and the heater turned off. A nitrogen purge was carried out and the specimen was allowed to cool overnight. For CVD CdS deposition, it is known that hexagonal wurtzite structure film grows epitaxially on {111} CdTe surface with the basal plane of CdS {0001} matched to the CdTe {111} planes. Additionally, if the CdTe has $\{111\}_{Cd}$ surface, CdS will grow with $\{0001\}_S$ as the starting layer, or with a Cd layer if the surface is $\{111\}_{Te}$ [3-38, 3-39]. Nishimura observed that the CdS growth rate on $\{111\}_{Cd}$ was much lower than for $\{111\}_{Te}$ [3-20]. Nishimura obtained growth rates that follow the classic Arrhenius equation of the form:

$$R = r_0 \exp(-\Delta E/kT) \qquad \text{(Eqn. 3.2)}$$

where r_0 is the pre-exponential factor

Following are the Arrhenius values obtained for growth rates on both surfaces at H_2 flow rate of 390 cc/min.

$\{111\}_{Cd}$: Rate (Å/min) = $3.1 \times 10^9 \exp(-0.68\ eV/kT)$

$\{111\}_{Te}$: Rate (Å/min) = $5.4 \times 10^{12} \exp(-1.15\ eV/kT)$

For the TEM sample (Δ symbol) on curve A′ in figure 3-4 for $\{111\}_{Cd}$ at 667°K (394°C), the CdS film growth rate is approximately 260 Å/min (26 nm/min) [3-20, page 121]. The film growth rate is calculated from figure 3-4. For $\{111\}_{Te}$ at the same temperature and the H_2 flow rate on curve B, the extrapolated growth rate would have been 6000 Å/min (600 nm/min, which is 23X higher. Consequently, the TEM

specimen ((Δ symbol) on curve B was prepared at 556°K (283°C), keeping the total deposition time to the same 80 minutes. Changing the substrate temperature to control the thickness is rather unconventional, as it would likely change the properties of the CdS film itself for a given thickness for different substrate treatments. However, it was likely done for practical reasons, because the deposition rate is very different for curve A and A′ vs. curve B. It was easier to change the temperature of the processing which can be varied easily by changing the position of the substrate in the reaction tube.

Nishimura speculates that the difference in the growth rate comes from some rate-limiting step that involves the reaction of Cd or S with the growing film. Nishimura writes that there are two possible surface configurations for the CdTe {111}/CdS {0001} surface. Type 1 will have one dangling bond on the surface, whereas type 2 will have three. Additionally, it is claimed that type 1 surface with only one dangling bond will be thermodynamically favored. This description is the same as the *shuffle* and the *glide* planes for semiconductor {111} planes as shown in figure 1-42. The shuffle plane is type 1 and the glide plane is type 2 in Nishimura's terminology. More bonds must be broken in order to create a glide plane than for a shuffle plane. Nishimura assumes that CdS film grows in double-layer fashion with both Cd and S layers forming one right after the other, except that the order of their formation is reversed between the $\{111\}_{Cd}$ and $\{111\}_{Te}$ surfaces of the CdTe. The sulfur layer is the first to form on $\{111\}_{Cd}$ and a cadmium layer on the $\{111\}_{Te}$ surface. The formation of type 2 (glide) surfaces is assumed to be the rate limiting step in the growth of the CdS film. The glide surface for $\{111\}_{Cd}$ CdTe is the $\{000\bar{1}\}_{S}$ plane, while for the $\{111\}_{Te}$ CdTe surface, it will be the $\{0001\}_{Cd}$ planes. The double-layer growth mechanism model then assumes that the formation of type 2 (glide) surfaces is thermodynamically unstable due to the presence of multiple dangling bonds, and the type 1 (shuffle) layer will grow spontaneously. The growth rate will depend on impingement rate, which should be proportional to the sticking coefficient of Cd on the S layer or S on the Cd layer. Nishimura experimentally derived the values for the sticking coefficients, with $\alpha_{Cd} = 0.89$ and $\alpha_S = 0.03$ based on the growth rate as a function of Cd and H_2S concentration [3-20, page 182-185]. The value of α_S being so small is not unreasonable

since H_2S must first decompose in order to make S atoms available to attach to the growing CdS film.The difference in the ΔE_A and ΔE_B activation energies corresponds to the difference in growing the type 1 (glide) layers, which are the S layer for the $\{111\}_{Cd}$ and Cd layers in $\{111\}_{Te}$. The difference in the r_{0A} and r_{0B} values is due to the difference in the surface density of activated species, N_s and N_{cd}.

The surface preparation of the CdTe substrate for CVD differed somewhat from those used for e-beam deposition. Mechanical polishing was done with 600-grit SiC-coated paper, followed by 3 μm diamond, then 0.3 μm α- alumina, followed by 0.05 μm γ-alumina. This was followed by etching with 4% Br_2:MeOH solution for 3 minutes, which removed approximately 12 μm of the material. The term *etch* was used by Nishimura, but at this concentration of bromine, the surface should have been left in a polished condition.

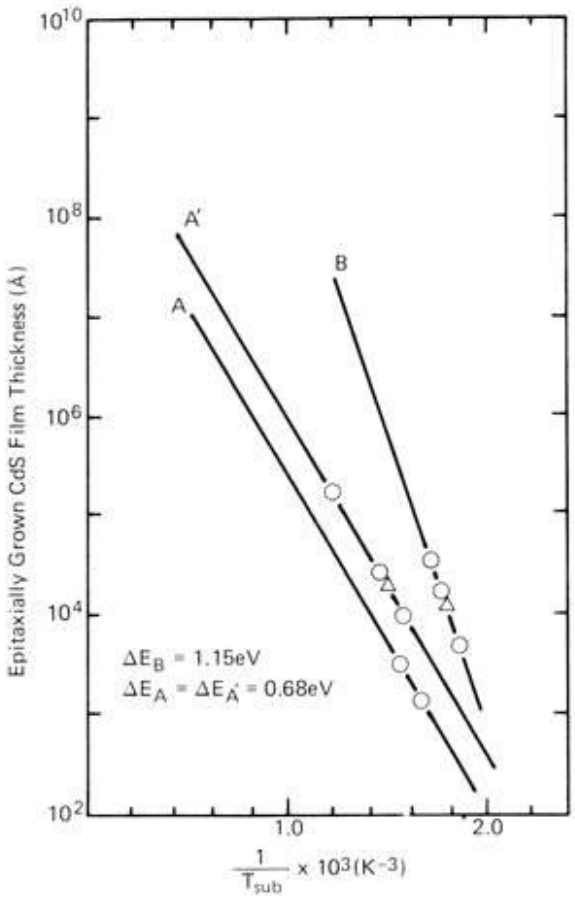

Figure 6.1. CdS film thickness *versus* inverse substrate temperature during CdS film growth $1/T_{sub}$ by CVD. The films were grown on (111) oriented CdTe single-crystal substrate. A was grown on (111_A) CdTe surface with H_2 flow rate of 130 cc/min. A′ was grown on (111_A) CdTe surface with H_2 flow rate of 390 cc/min. B was grown on (111_B) CdTe surface with H_2 flow rate of 390 cc/min. ○ CdS film thickness measured by alpha step. Δ CdS film thickness measured off photograph of TEM image.

Figure 3-4: Reproduced from Nishimura thesis [3-20, page 121], showing the growth rates obtained for $\{111\}_A$ (or Cd) and $\{111\}_B$ (or Te) surfaces. Two triangles mark the samples that were examined by TEM.

3.3 Electrical Properties

A schematic diagram of the heterojunction cell used to make electrical measurements as described by Nishimura [3-20, page 113] is shown in figure 3-5. Indium contacts were evaporated on CdS surface through a mask, and Au or Au-Cu contacts were also evaporated on the back of the CdTe surface after it had been polished, and etched with chromate solution ($K_2Cr_2O_3$:H_2SO_4:H_2O). This treatment before Au-Cu deposition is known to provide low-resistant *ohmic-like* contact to p-CdTe [3-40]. TEM specimens were always obtained from heterojunction cells shown in figure 3-5.

The resistivity of the e-beam evaporated CdS film determined by four-point probe measurement varied considerably as a function of CdTe surface characteristics and treatments. For cleaved and etched {110} and $\{111\}_{Cd}$ surfaces, the resistivity was approximately 0.01 Ω-cm. For the etched $\{111\}_{Te}$ surface, the resistivity was 0.5 Ω-cm, and on the as-cleaved {110} surface, the resistivity was much higher at > 1 Ω-cm. Werthen did not report on the resistivity value of CdS on PEH $\{111\}_{Cd}$ or $\{111\}_{Te}$. Mobilities of the holes in CdS were between 30 to 60 cm^2/V-s in all cases. In comparison, Si has hole mobility of ~450 cm^2/V-s. The numbers of samples measured for light J-V characteristics by Werthen were limited.

Light J-V characteristics for C, PE, and PEH surfaces with 1 μm thick e-beam evaporated CdS are shown in figure 3-6. The light J-V curves were taken with a 85mW/cm^2 solar simulator. The latter consisted of a 600 W quartzline lamp filtered with water and a Corning 1-62 filter, and was calibrated using a NASA Si standard cell [3-19, page 53]. The current standard in 2015 for solar cell evaluation is AM1.5G, which is 100 mW/cm^2 [3-41]. Therefore, the numbers reported for junction performance here underestimate the value based on today's measurement method because the power input to the cell was lower. The PE cell had an efficiency of 6.2% and the PEH cell had an efficiency of 7.5%. Unfortunately, Werthen failed to identify the Cd and Te faces for the PE and PEH samples in his thesis. The specimens provided for TEM analysis were both labeled as $\{111\}_{Te}$. Therefore, it is assumed that the same

cells were used in the electrical measurements. Junction characteristics of other cells such as CE {110}, PE, and PEH $\{111\}_{Cd}$ were not reported by Werthen.

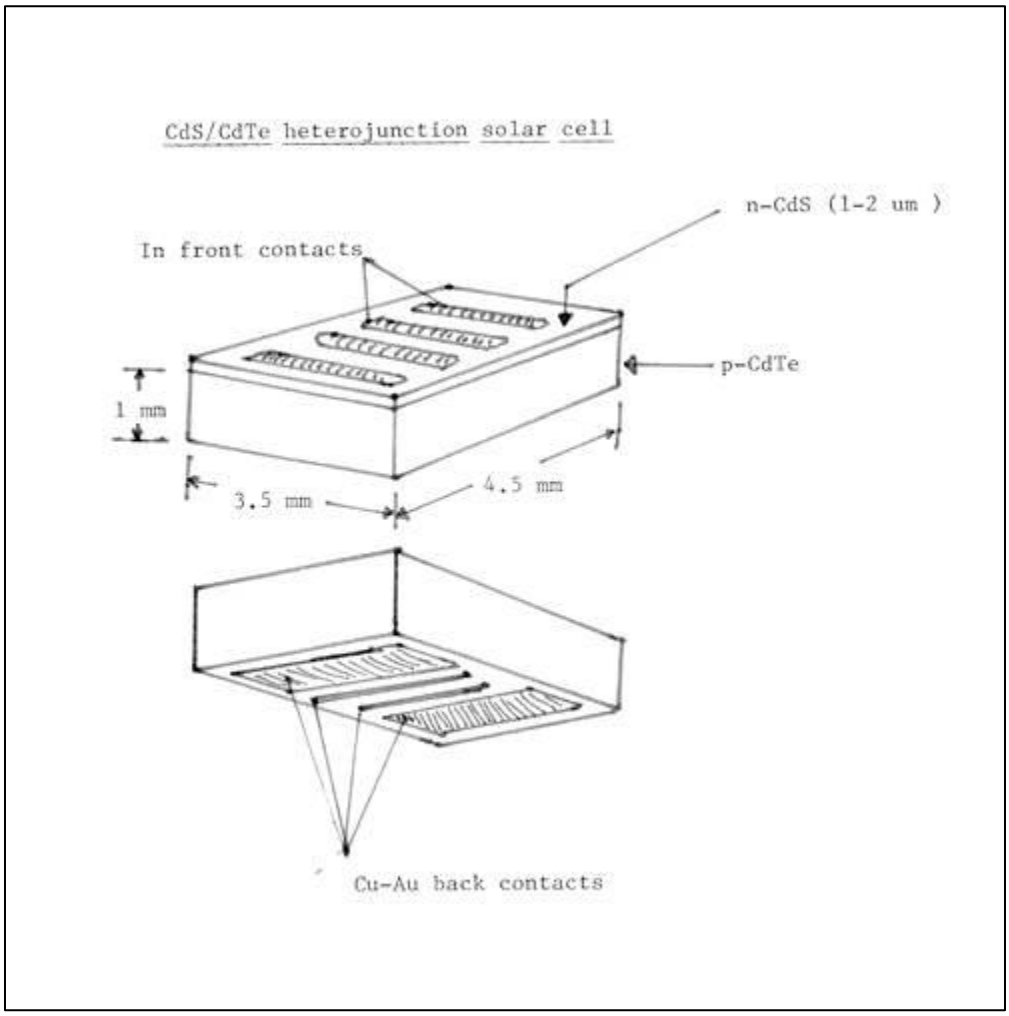

Figure 3-5: Schematic of CdS/CdTe heterojunction cell created by Werthen thesis and [3-19] and Nishimura thesis [3-20].

For the C specimen, the light J-V curve has V_{oc} = 0.62 V, J_{sc} = 12 mA/cm^2, and a low fill factor. This poor characteristic came about due to the high series resistance of this CdS film. The spectral response of the junction reported by Werthen showed

typical characteristics for true CdS/CdTe heterojunction behavior [3-42]. In the Cr/CdTe Schottky device, characteristics reported by Werthen where the Cd or Te face was kept track of, $\{111\}_{Cd}$ surface always performed slightly better than $\{111\}_{Te}$ for the V_{oc} of the light J-V characteristics for both PE and PEH surface treatment [3-19, page 79]. Additionally, PEH surfaces always performed much better than PE surfaces, especially for the V_{oc} values and provided higher efficiency. It is likely that the CdS/CdTe junction followed similar characteristics because it is expected that the interface condition played an important and similar role in both junction types.

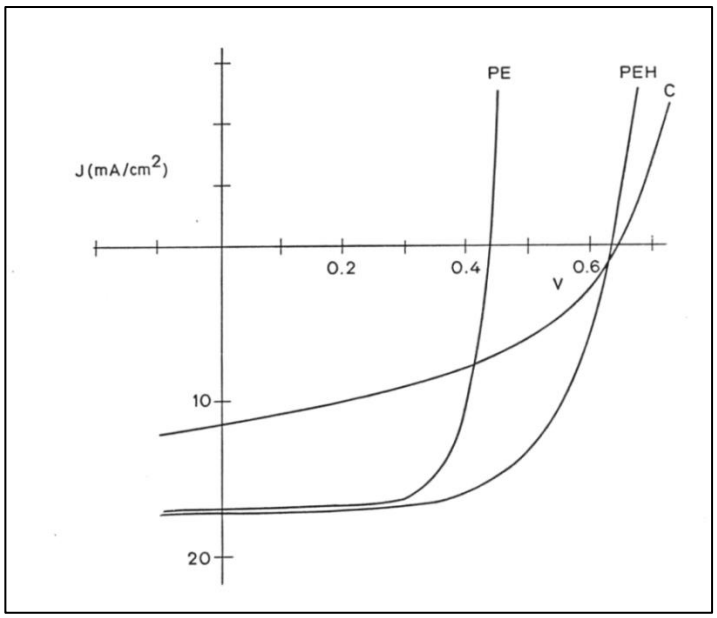

Figure 3-6: Light J-V characteristics of CdS/CdTe junctions formed on C, PE, and PEH surfaces. The figure was reproduced from J. Werthen's thesis [3-19, page 110]. It is thought that PE and PEH samples were both $\{111\}_{Te}$ face specimens, since all three specimens were provided for TEM analysis together and the PE and PEH specimens were labeled $\{111\}_{Te}$ face. The curves were reproduced from actual data taken by the measurement system (analog measurements).
From Werthen thesis [3-19].

3.4 HRTEM imaging of e-Beam CdS/CdTe Interfaces

TEM samples in cross section were prepared according to the encapsulation method described in Section 1-6, in Figure 1-18. A dimpler was used to mechanically thin the specimen to ~30-50 μm which was then ion-milled at ~4 keV for several hours to obtain thin electron transparent areas at the interface. The Philips EM400ST and JEOL 200CX microscopes were used and both were equipped with a LaB_6 filament. HRTEM images were obtained at 900,000X magnification for the EM400ST, operating at 120 kV, and 850,000X magnification for the JEOL 200CX operating at 200 kV. EM400ST used a side-entry double tilt specimen holder, and JEOL 200CX used a top-entry double tilt specimen holder.

3.4.1 E-Beam CdS on Freshly Cleaved CdTe {110} Substrate - (C)

The CdS film was grown on a freshly cleaved CdTe {110} surface by e-beam evaporation with the substrate temperature at 135°C. A HRTEM image of this interface was obtained with CdTe oriented in the <110> projection. This CdS film had the cubic sphalerite structure. A bright-field (BF) micrograph of the interface taken under a two-beam condition using $\mathbf{g} = (02\bar{2})$ reflection is shown in Figure 3-7. In this imaging condition, one set of stacking faults on the {111} planes inside CdS is visible, which emanate from the interface. The CdTe contains many dislocations. Energy dispersive X-ray spectroscopy (EDS) also was used to verify the chemical identity of the material being imaged. The CdS film thickness was ~1 μm, and a large area over many hundreds of microns in length indicated that the CdS film exists as a single-crystal, close to epitaxy with CdTe as observed by the diffraction pattern along the interface (not shown). The CdS film has the same cubic sphalerite structure as the CdTe substrate, as determined by the selected area diffraction pattern (SADP) as shown in figure 3-8, which was taken from the interface area containing both CdS and CdTe. Both CdTe and CdS diffraction patterns are indexed as [011] (i.e., the same) and some of the reflections are indexed in the figure. The spots marked with the “o” symbols are the CdS reflections. By this notation, the CdTe plane that is matched to CdS will be

indexed as $(01\bar{1})$ or $(0\bar{1}1)$. The diffraction pattern is properly oriented with respect to the BF image in figure 3-7. The streaks in the CdS diffraction pattern come from the stacking faults, which lie on $(\bar{1}1\bar{1})$ or the $(1\bar{1}1)$ planes as indexed in the figure. The $[01\bar{1}]$ direction, which is the CdS film growth direction in the BF image, is pointing up in the diffraction pattern. It can also be noticed that the CdS lattice is rotated by ~2° with respect to the CdTe lattice about the [011] axis toward the [100] direction as indicated in figure 3-8. The lattice parameters of CdTe and CdS (cubic phase) are listed below, as previously tabulated in Chapter 1, sections 1.5.1 and 1.5.2. The actual CdS a_o value as calculated based on CdTe being at the theoretical value is listed as well.

$a_{o\ CdTe} = 0.648$ nm

$a_{o\ CdS} = 0.581$ nm (theoretical value), $a_{o\ CdS}$ (as measured) = 0.589 nm

Therefore, the measured CdS lattice parameter is slightly larger by 1.4%. It is not certain why this is the case. It could arise from coherency with a larger CdTe lattice parameter.

It should be noted the unusually large size of the diffraction spots in figure 3-8 is a consequence of having used a very large condenser aperture (200 μm), which was needed in order to obtain sufficient beam intensity for the HRTEM observations. The cubic phase of CdS is often observed when grown on other substrate materials as well, such as InSb [3-43] and mica [3-44].

Figure 3-9 shows a HRTEM image of the CdS/CdTe interface. The image was taken on Philips EM400ST with 19 beams taken through the objective aperture out to (004) reflections or to 6.170 nm^{-1}. The spherical (C_s) and chromatic (C_c) aberration coefficient for this microscope were 1.4 mm and 1.1 mm, respectively. The Scherzer resolution for the microscope was 0.31 nm and Scherzer defocus was at -79.1 nm. Individual Cd and Te atoms could not be resolved with this microscope in the <110> projection, and the pair of atomic columns forms one image spot. Point resolution was further degraded by the use of high beam divergence, usually between 1 to 2 mrad, which was a consequence of using large condenser aperture to increase image

brightness. The Philips EM400ST used a double tilt holder, which made it more convenient to orient the specimen, but it came at the expense of a higher C_s value compared to the EM400 model, which used only the single tilt holder. The typical defocus condition was between -100 to -300 nm underfocus based on the objective lens current setting. Within this defocus range, high contrast, white image spots corresponding to the position of the atomic pairs could be obtained. This is consistent with the CTF calculation for the microscope. The interface in figure 3-9 appears very abrupt and free of any visible foreign material with different contrast and structure. Although EDX chemical analysis was performed at the interface, the resolution of the technique was not sufficient to determine whether any foreign elements exist at the narrow region of the interface. Fine probe capability and EELS chemical analysis were not available on the TEM during this period. In addition, the light elements such as oxygen could not be detected by the EDX tool even with low spatial resolution then. The lack of any visible interface phase was surprising in that the cleaved CdTe surface had been exposed to air for probably several hours before the CdS was deposited. Formation of an oxide film or contamination layer even a few atomic layers thick would have been clearly visible in the HRTEM image. The existence of them would also have disrupted the subsequent growth of CdS film to a much greater extent. The interface appears as clean as the GaAs films grown on GaAs substrate under very stringent substrate preparation and ultra-high vacuum condition, which are discussed in Chapter 4.

It is obvious that many stacking faults in the CdS layer emanate from the interface, and they lie exclusively on one set of {111} type planes. It is not known why this is the case. The image spots in the CdS clearly show the same lattice symmetry as those on the CdTe side, confirming the cubic sphalerite structure of the film. The approximate location of the interface is indicated by black arrows and by a green line drawn along the interface in figure 3-9. The CdTe {110} plane is indicated by the red line, and it can be seen that the actual interface is tilted with respect to the $\{110\}_{CdTe}$ plane by approximately 1.5°. When the CdTe {111} planes are followed into the CdS {111} planes, the angular tilt is very small, at approximately 1°. This is somewhat

inconsistent with a larger tilt of approximately 2° observed in the diffraction pattern. The diffraction pattern is sampling over a much larger area than the HRTEM image in figure 3-9; therefore, the atomic arrangement seen in the HRTEM image must be a local phenomenon.

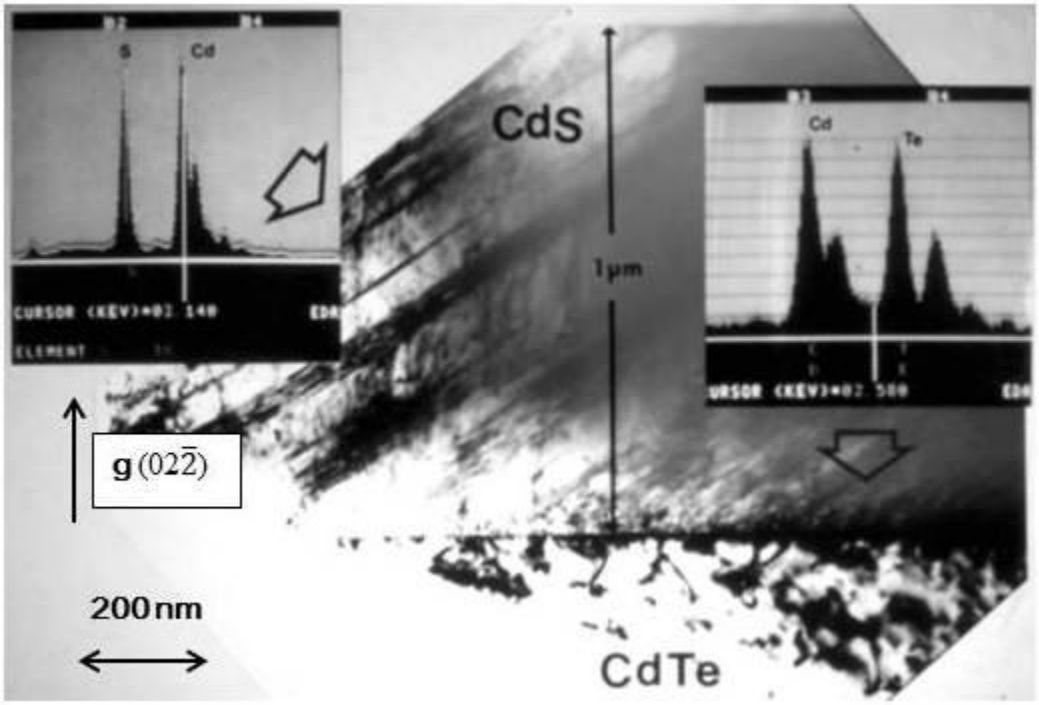

Figure 3-7: BF image of cubic CdS (01$\bar{1}$) / CdTe (01$\bar{1}$) interface. EDS (insets) aids in chemical identification of the material in the image. Corresponding SADP image is shown in figure 3-8.

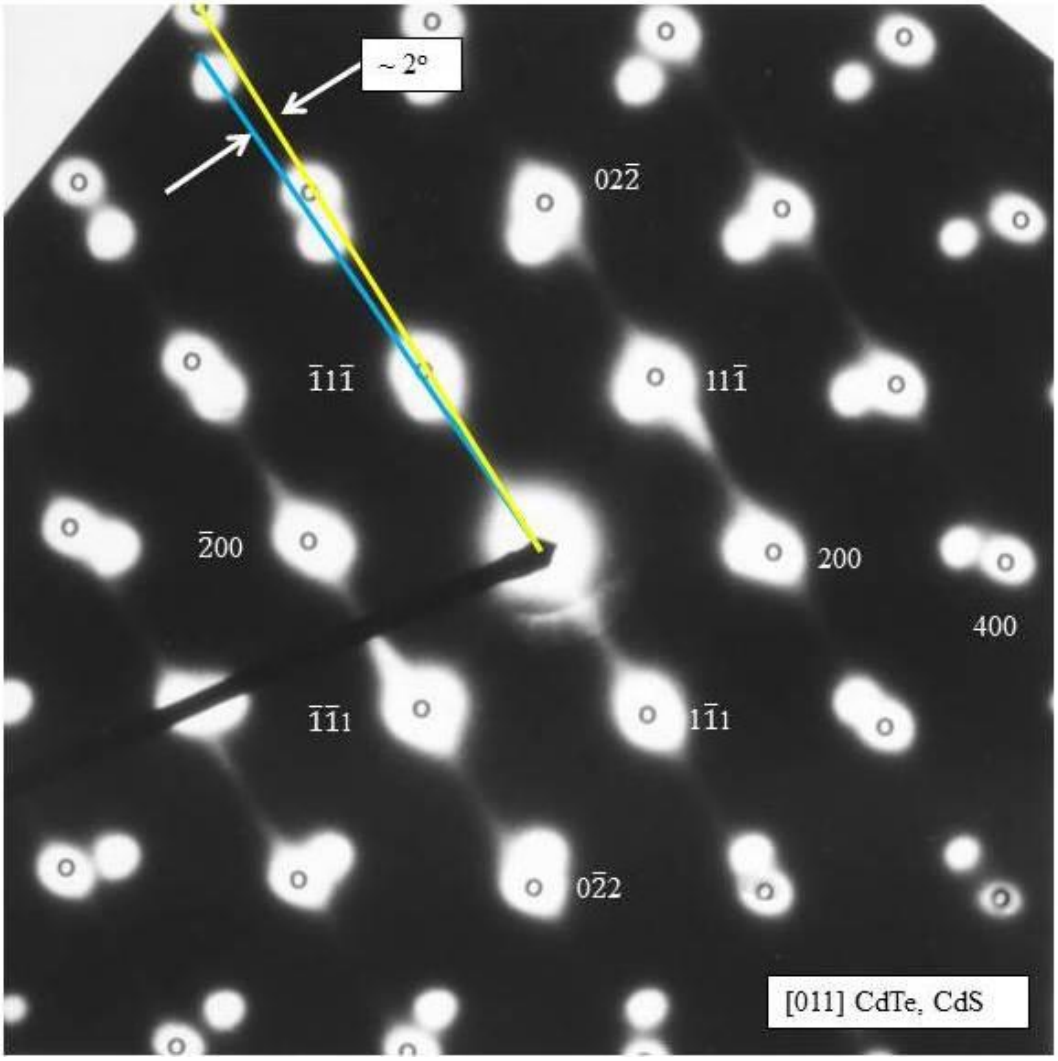

Figure 3-8: Selected area diffraction pattern (SADP) from the CdS/CdTe interface for CdS deposited on freshly cleaved {110} CdTe surface. SADP is indexed as [011] zone for both CdTe and CdS and it is properly oriented with respect to the BF image in figure 3-7. Condenser aperture of 200 μm was used. The CdS diffraction spots are indicated by "o" marks. The streaks on the CdS pattern comes from the high density of stacking faults lying on the {111} planes (e.g. $(\bar{1}1\bar{1})$ planes). The CdS lattice is rotated ~ 2° with respect to the CdTe lattice as shown by CdTe (blue) and CdS (yellow) $[\bar{1}1\bar{1}]$ directions. Lattice parameters with $a_{o\ CdTe}$ = 0.648 nm as a reference leads to $a_{o\ CdS}$ = 0.589 nm, which is slightly larger by 1.4% vs. accepted value for bulk CdS.

An image taken from a nearby region of figure 3-9 is shown in figure 3-10 with higher enlargement. This image was taken using a JEOL 200CX microscope at 200 KeV, with 850K magnification. This microscope had a top entry double-tilt stage, with Cs of 1.2 mm. Scherzer defocus for this microscope was at -63.3 nm, and the point resolution was at 0.245 nm. The image was taken at approximately -100 nm underfocus, based on objective lens current settings. The objective aperture allowed 23 beams out to $(13\bar{3})$ and equivalent reflections. The condenser aperture was 100 μm, corresponding to beam divergence of approximately 0.5 mrads. JEOL 200CX provided an image with slightly better quality and resolution compared to the EM400ST.

Based on the lattice spacings determined by the SADP in figure 3-8, the misfit between the CdS and CdTe lattice is 13.9%. The lattice misfit is defined as:

$$\text{Lattice misfit} = (a_{o(\text{Substr})} - a_{o(\text{Film})}) / a_{o(\text{Film})}\ ^{*} \qquad \text{(Eqn. 3-3)}$$

* Strictly speaking, this only applies to two cubic crystals. Specific lattice planes to be matched needs to be considered if the two lattices have different crystal systems.

How this large misfit is accommodated at the interface is of some interest. It is clear from the HRTEM images that how the mismatch is accommodated is quite complex. In addition, there is a tilt to the CdS lattice with respect to the CdTe lattice, and the interface is not exactly along the $(01\bar{1})$ surface as indicated in figure 3-9, the effect of which must also be considered.

Enlargements of the image in figure 3-10 are shown in figure 3-11 and 3-12. Both figures show that the interface has regions of clean epitaxy where the CdTe lattice extends into the CdS layer without any breaks, and there are periodic regions of disruption at the interface where the mismatch between the two lattices is accommodated (circled in both figures). In these regions of the interface, the lattice images are considerably distorted, and it is in these regions that one can find extra CdS $(\bar{1}1\bar{1})$ planes. When the stacking fault in the CdS is clearly imaged as in figure 3-11 in the circled region, the fault is clearly extrinsic in nature, showing an extra set of {111}

CdS planes when followed from the CdTe side of the interface. Most of the faults are usually not resolved very well, as in figure 3-11 and 3-12, but the few that are visible indicate that they are extrinsic faults. Therefore, this is one of the means by which the CdS lattice accommodates the mismatch with the CdTe lattice.

The CdS and CdTe $(\bar{1}1\bar{1})$ planes were counted across the interface from the images such as figure 3-9 and 3-10 to determine how many extra planes were in the CdS for the CdTe planes. The numbers are tabulated below in Table 3-1. There are some uncertainties in the numbers as the planes are often obscured around stacking faults. The value of 1.09 for the ratio of CdS to CdTe $(\bar{1}1\bar{1})$ planes was obtained. This is somewhat less than expected based on the 13.9% lattice mismatch.

CdS planes	CdTe planes	Ratio CdS/CdTe planes
86	80	1.08
66	60	1.10
75	70	1.07
90	82	1.10
56	52	1.08
	Average	1.09
	Std. dev.	0.01

Table 3-1: The count of $(\bar{1}1\bar{1})$ planes across the interface from HRTEM images including figure 3-9 and 3-10.

A schematic construction of the interface is drawn in figure 3-13. Tilting the CdS lattice with respect to the CdTe lattice is quite effective in reducing the misfit for the $(\bar{1}1\bar{1})$ planes. For example, 3.6° tilt of the CdS $(\bar{1}1\bar{1})$ will be sufficient to eliminate the misfit at least for this particular plane. For the actual tilt of 2° and interface tilt of 1.5° taken into account, the geometrical misfit value for the $(\bar{1}1\bar{1})$ planes becomes 8.6%. For the $(\bar{1}1\bar{1})$ planes then, the number of misfit dislocations counted along the

interface is more consistent with this value of the misfit. This construction is for the $(\bar{1}1\bar{1})$ planes and it says nothing about the lattice accommodation in the z-direction (into the paper or $[01\bar{1}]$ direction). This information is not available from the images.

The notation to properly describe the relationship between the two crystals in epitaxial growth is given by providing the planes of the interface for the two crystals, and one direction in the plane of the interface. The proper notation is quite simple for this present case, as both the CdS and CdTe have the same crystal structure and the same orientation, and given by the following notation:

$(01\bar{1})$CdS//$(01\bar{1})$CdTe; [011] CdS//[011]CdTe

The poor electrical performance of CdS on cleaved [011] CdTe can be attributed to the cubic phase CdS that has high electrical resistivity. It is possible that high n-type conductivity that comes from sulfur vacancies in hexagonal CdS is disrupted in the cubic phase material, but this is purely speculative. The resulting high series resistance for this CdS film results in poor J_{sc} and fill factor. The high level of perfection seen for the CdS film and the cleanliness of the interface did little to change the poor overall performance of the junction.

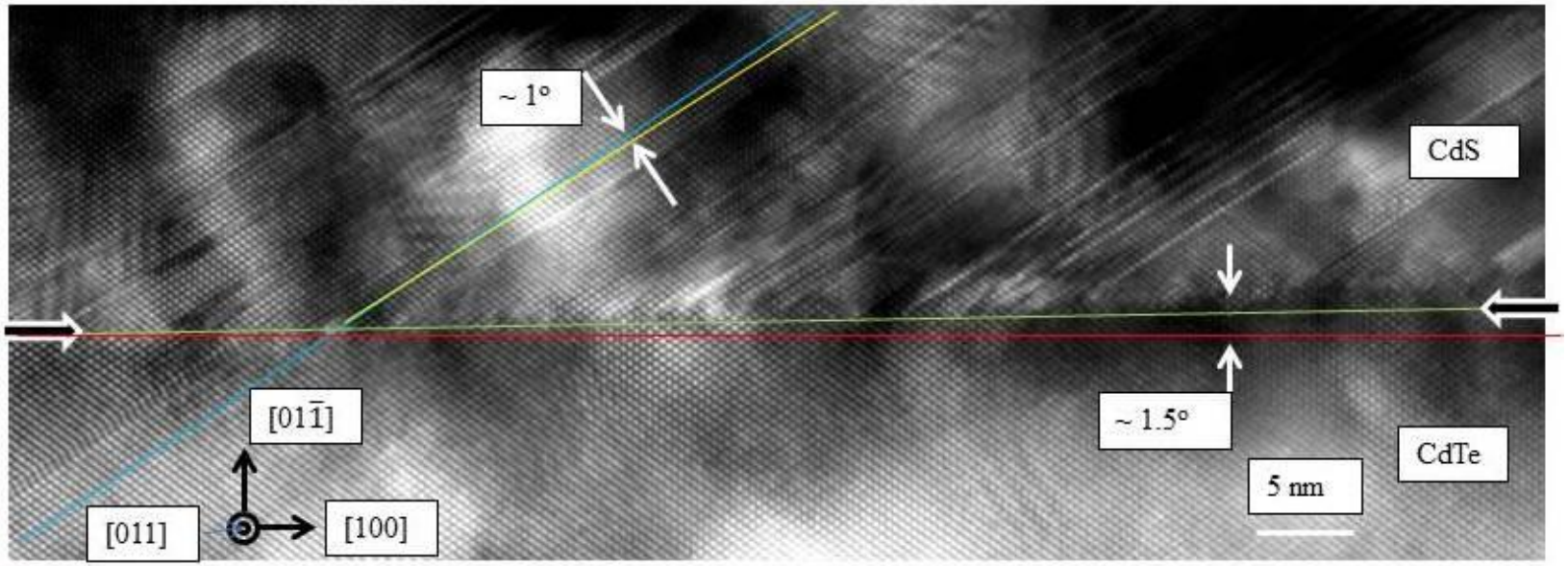

Figure 3-9: HRTEM image of CdS (cubic) on cleaved (011) CdTe. CdS has the cubic structure, and CdTe ($\bar{1}1\bar{1}$) planes extend into CdS ($\bar{1}1\bar{1}$) planes with an angular tilt of less than 1° as indicated by the trace of CdTe ($\bar{1}1\bar{1}$) – blue line into CdS ($\bar{1}1\bar{1}$) – yellow line. The nominal CdTe ($0\bar{1}1$) plane at the interface is indicated by the red line. The actual interface – green line - is tilted away from this line by approximately 1.5°.

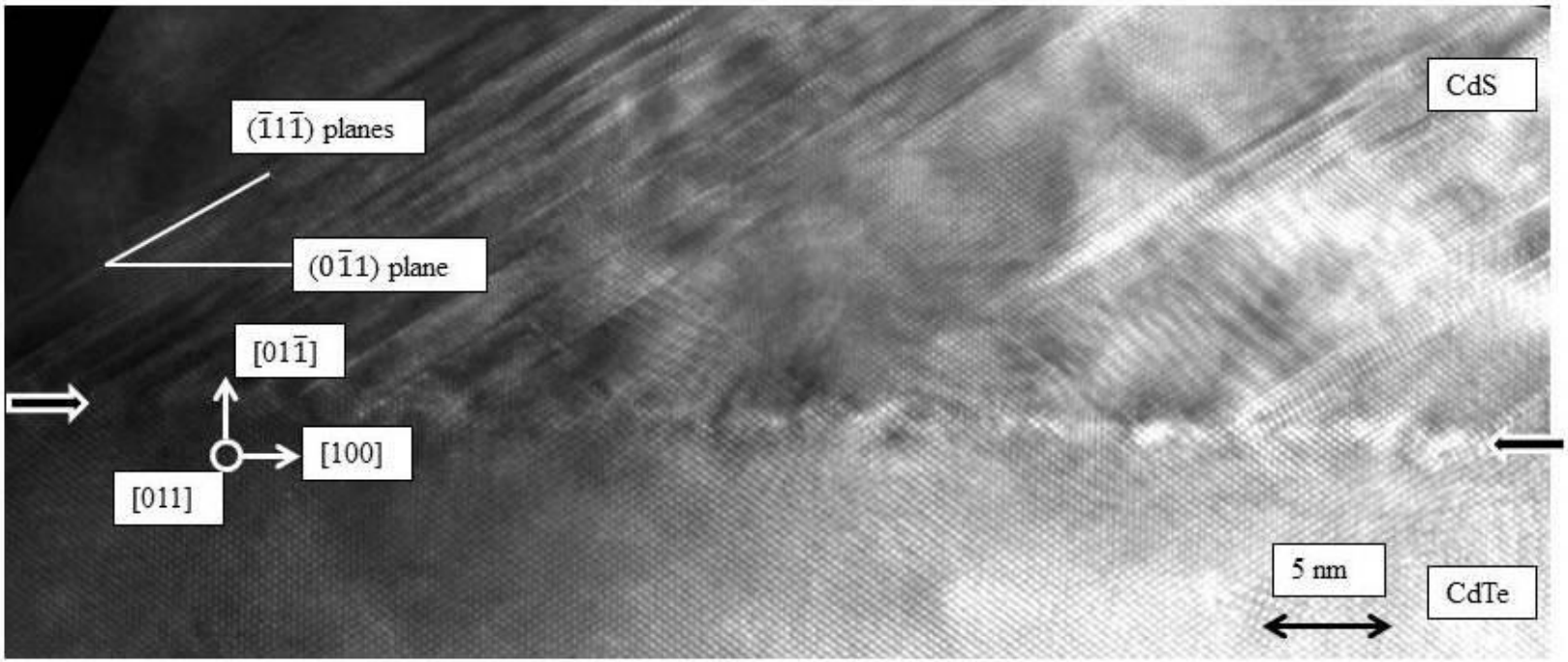

Figure 3-10: HRTEM image of CdS/CdTe (011) surface, cleaved and CdS deposited. Different region from figure 3-9. Interface is again approximately 1.5° away from the perfect [011] orientation. There are periodic ~1-2 nm region spaced about 5 nm apart which shows some contrast that could be due to strain, contaminants or steps at the interface. They do not necessarily create defects at the interface. Image taken on JEOL 200CX at 850K magnification.

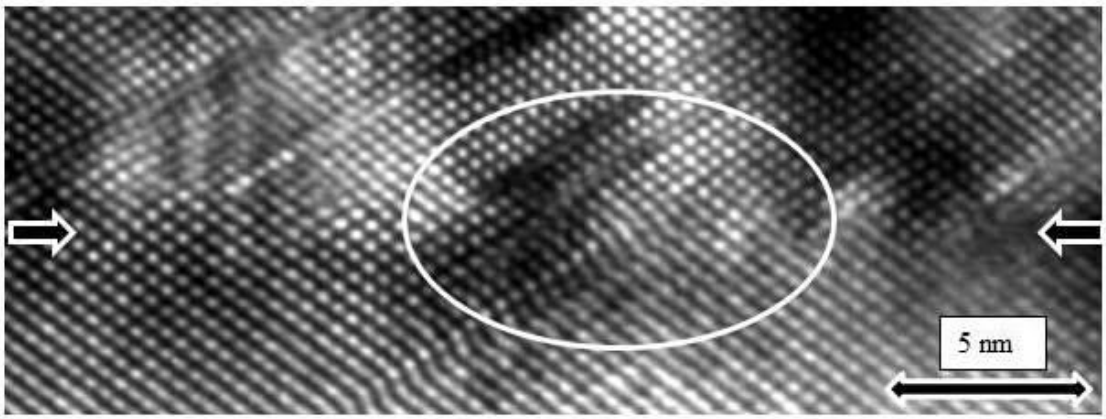

Figure 3-11: HRTEM image of CdS (cubic) on cleaved (011) CdTe. Closer detail of the interface is shown. The black arrow indicates the location of the interface. The location of the interface on the left may appear to be inside the CdTe, but an extended view of the interface shows that the arrow correctly points to the location of the interface.

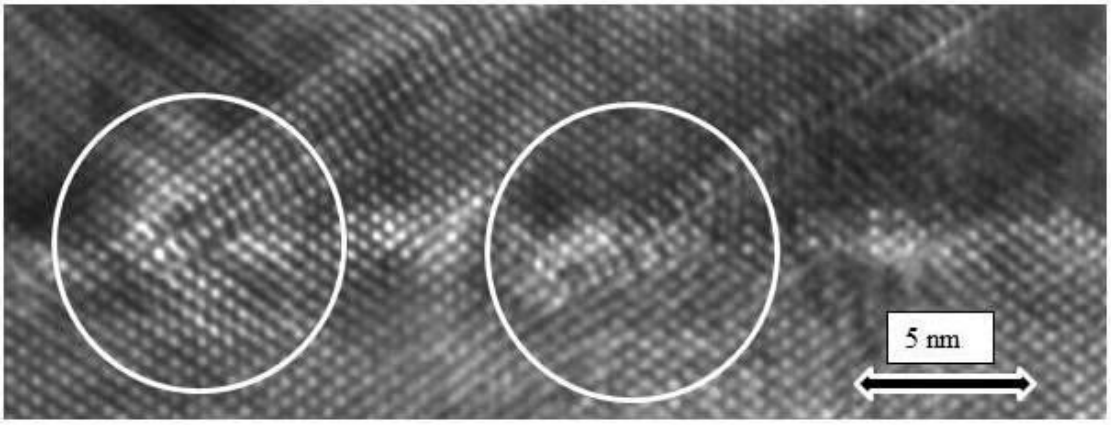

Figure 3-12: Closer view of the interface where the stacking fault is clearly visible indicates the presence of an extrinsic type stacking fault (containing extra {111} plane) in the CdS film (circled).

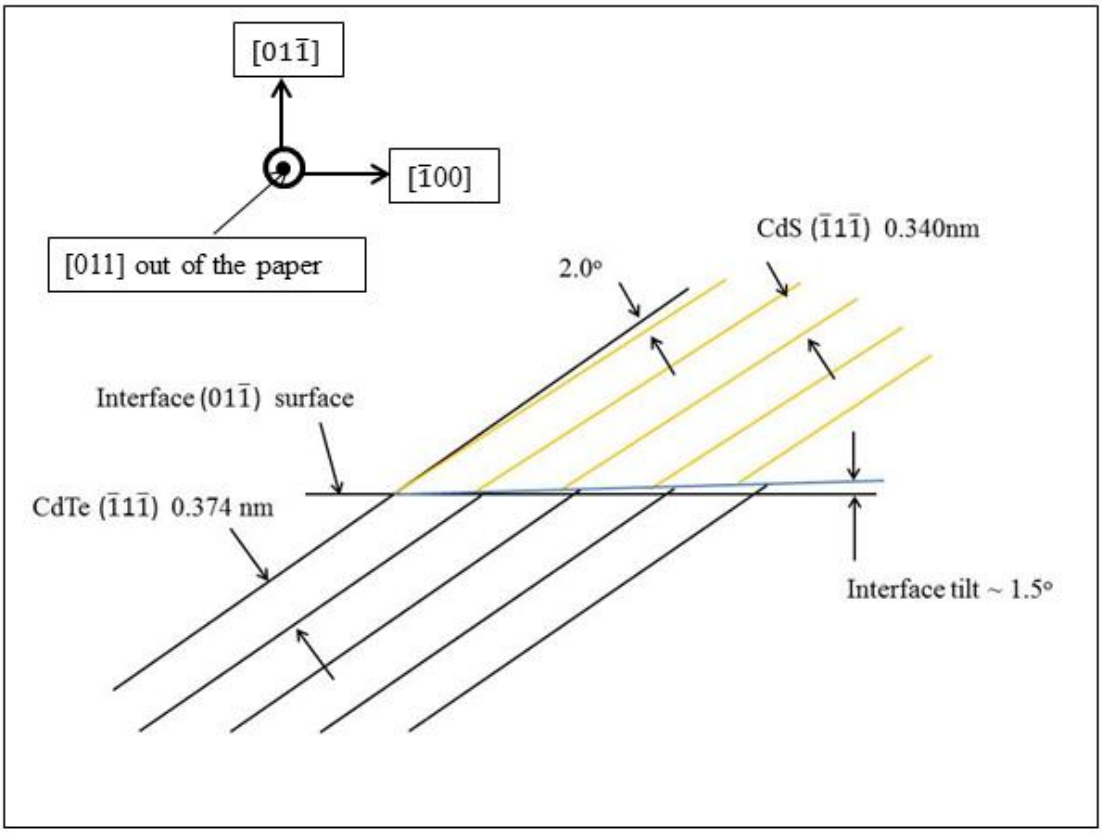

Figure 3-13: Interface construction for CdS/CdTe, matching CdTe ($\bar{1}1\bar{1}$) planes to CdS ($\bar{1}1\bar{1}$) planes on (01$\bar{1}$) surface of the interface. For a perfect (01$\bar{1}$) surface, CdS can be tilted by 3.6° to match with CdTe. With the interface tilt of 1.5° and CdS lattice tilt of 2.0° as indicated above, the lattice misfit for the ($\bar{1}1\bar{1}$) plane becomes 8.6%.

3.4.2: E-Beam CdS on Cleaved and Etched {110} CdTe Surface - (CE)

CdS on a CE substrate was examined in cross section by TEM. Unfortunately, the electrical performance of this specimen was not reported by Werthen [3-19]. The behavior of the surface can be inferred from a more extensive surface treatment matrix on Cr/CdTe Schottky barrier devices which Werthen tabulated [3-19, table 5.3, page 80]. Schottky barrier devices are very sensitive to the semiconductor/metal interface, in particular, the abruptness and cleanliness of the interface. Cleaved {110} CdTe had

high V_{oc} and low J_o values indicative of ideal Schottky barrier device function. Jo is obtained from dark J-V characteristics of the junction.

$$J = J_o (\exp (qV/AkT)-1) \qquad \text{(Eqn. 3-4)}$$

A is the diode factor between 1 and 2.

In a Schottky barrier device, the dark current typically involves one or more of four different types of current mechanisms: injection current, recombination current, tunneling current, and thermionic emission [3-45]. The thermionic emission component is usually the dominant dark current mechanism in a practical Schottky barrier device. When various CdTe surfaces were etched, and they all had much lower V_{oc} by a third to half as much compared to the cleaved (110) surface, and the J_o value was 3 orders of magnitude higher. Three types of surfaces were reported.

PE {110}

PE $\{111\}_{Cd}$

PE $\{111\}_{Te}$

The fact that they all had uniformly poorer V_{oc} and J_o indicate that etching left some interfacial material that interfered with the Schottky barrier function. Heat treatment of the etched surfaces in hydrogen results in V_{oc} and J_o values that are similar to the cleaved specimens. Light J-V characteristics also were reported, and heat-treated samples again showed much superior V_{oc} values and fill factor. These electrical results imply that Br_2:MeOH etch leaves some oxide or contaminant on the surface, which interferes with the ideal Schottky barrier function of the device. Heat treatment in hydrogen removes the contaminant, leaving a clean surface again.

CdS film on the CE {110} surface had a mixed morphology. In some areas, the CdS had a polycrystalline structure, while in other regions the film was epitaxial to the substrate. The grain size was in the range of 200 - 400 nm, but not enough grains were imaged to make a statistically meaningful determination. The CdS film thickness was

approximately 1 μm. The specimen quality was poor, and it had only a small area that could be imaged. The images were obtained using Philip EM400ST microscope, operating at 120 kV. The HRTEM imaging condition was similar to the one described in the previous section for figure 3-9. The magnification on the negative was at 900,000X. Figure 3-14 is a low magnification BF image of the specimen in cross section where the CdS film appears to be largely a single-crystal. Many stacking faults emanate from the interface. The interface is surprisingly flat and smooth, and it does not show much evidence of a secondary phase that might be expected from the Br_2:MeOH etch that was applied to the surface.

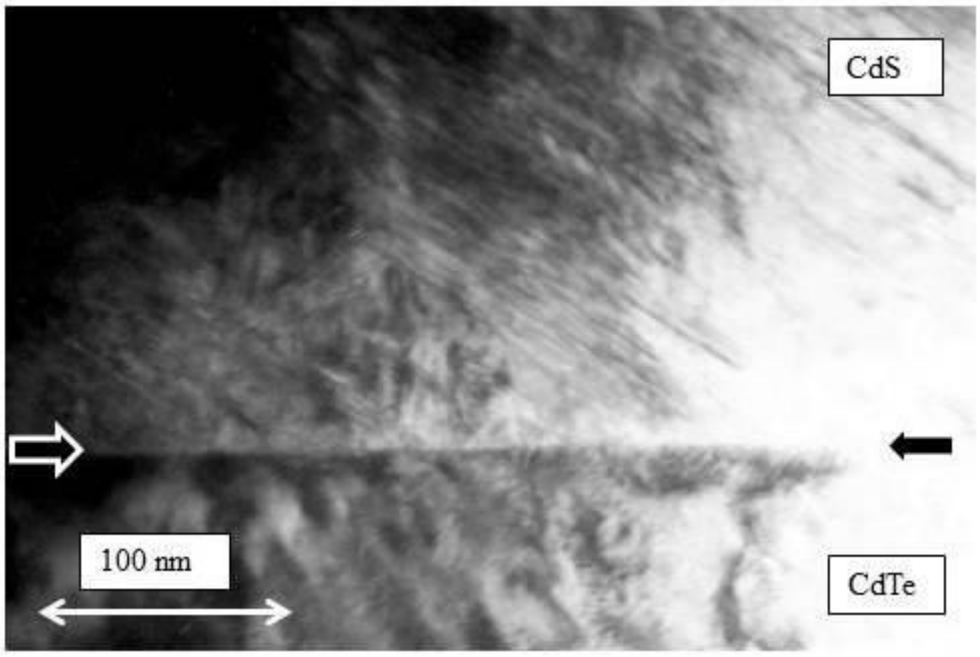

Figure 3-14: BF micrograph of the CE (011) specimen in cross section. Interface is indicated by the arrows.

Figure 3-15 shows the area where there was epitaxy between CdTe and CdS. The TEM specimen quality was relatively poor due to it being too thick and obtaining clear HRTEM images was difficult. The interface was quite complex and the CdS film

was difficult to analyze, as clear and interpretable lattice images could not be obtained. As it can be seen in the figure, the image consists largely of lattice fringes on both sides of the interface. Black arrows indicate the location of the interface. The angle markers indicate the angle that lattice fringes make with the interface plane. CdTe lattice fringes, which are observed in some of the areas in the micrograph are at 35° with the interface and these fringes clearly belong to $(\bar{1}1\bar{1})$ planes by the indexing convention used. The precise angle between CdTe $(\bar{1}1\bar{1})$ and $(01\bar{1})$ planes is 35.26°. Near the interface in the CdTe side, the lattice shows alternating intensity in the fringes, as if each layer has a potentially different structure. This is shown in the circled regions in the micrograph. A magnified view of the interface is shown in figure 3-16. The approximate spacing of the dark fringes is 0.76 nm, which is slightly larger than twice that of CdTe $(\bar{1}1\bar{1})$spacing. The CdTe $(\bar{1}1\bar{1})$ fringes extend into this material and there is a complex structure between the CdTe and the new phase separated by dislocations. It is surmised to be dislocations because the lattice fringes that extends from the CdTe into the interface phase terminates and form additional planes in the interface phase. It should be also noted that only this region was imaged in high resolution, and it is a small area of the specimen. It is not known whether the same situation exist elsewhere in the specimen.

In the CdS side, the numerous faults that extend from the interface at the angle of 34° are the basal plane direction of the hexagonal CdS with the wurtzite structure. This can be ascertained from the diffraction patterns shown in figure 3-17, which will be described in more detail shortly. The faults lie on the basal plane of the CdS. Since the basal planes makes the same angle to the interface as the CdTe $(\bar{1}1\bar{1})$ planes except in the opposite direction, the situation is analogous to the formation of a twin across the interface. However, there is another set of {111} planes that are not visible in the image which also makes the 35° angle to the interface, which is the $(11\bar{1})$ plane. It can be said that the CdS basal plane is merely the extension of this plane from the CdTe side. The formation of a new phase at the CdTe side of the interface, presumably due to Br_2:MeOH etch could have promoted the formation of a hexagonal CdS. Alternatively, simply the presense of a discontinuity at the interface by the

contaminants may have promoted the hexagonal CdS film formation as well, but this latter possibility does not explain the fact that CdS film appear to have an orientation relationship with the CdTe lattice. The lattice fringes on the CdS side, which makes an angle of 57° with the interface, have the spacing of 0.362 nm as measured directly from the micrograph. This spacing is close to the 0.358 nm spacing of $(01\bar{1}0)$ planes in hexagonal CdS. In comparison, CdTe (111) spacing is 0.374 nm. The measured spacing is closer to the CdS $(01\bar{1}0)$ plane spacing. The $(01\bar{1}0)$ plane should make an angle of 54.7° to the $(01\bar{1})$ CdTe plane (90° - 35.3°). Therefore, the basal plane that is perpendicular to the $(01\bar{1}0)$ planes is tilted toward the $[\bar{1}00]$ CdTe direction by 2.3° based on the direction convention shown below in figure 3-15.

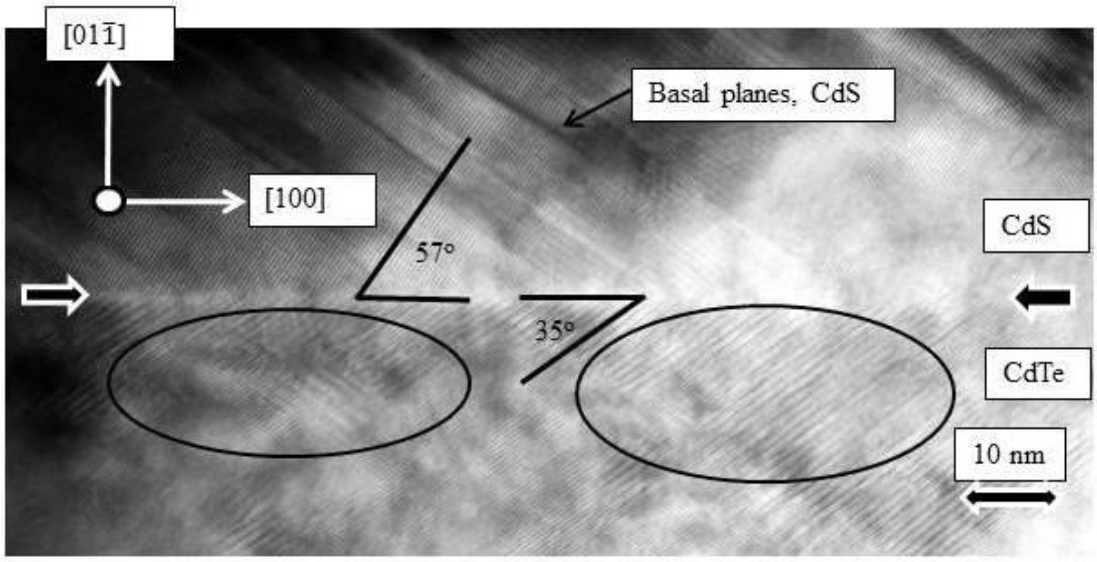

Figure 3-15: CdS on CE CdTe [011] substrate. The interface is indicated by black arrows. The circled regions are the interfacial phase on the CdTe side of the interface with a different structure than CdTe. This phase acts to continue the CdS growth with CdS (0001) planes that extend CdTe $(\bar{1}1\bar{1})$ planes. This occurs only in some locations. In many locations, the CdS was polycrystalline and not epitaxial to CdTe.

The diffraction pattern from the area shown in figure 3-14 is shown in figure 3-17. The SA aperture covered an area about 0.5 μm in diameter which was sufficient to cover both the CdS film and part of CdTe substrate. The pattern is oriented properly with respect to the image. The crystallographic direction convention is indicated in the left bottom corner. The main reflections belong to the CdTe [011] zone, and some of the reflections are indexed. Other reflections are consistent with the CdS hexagonal wurtzite structure in the $[2\bar{1}\bar{1}0]$ orientation. However, not all of the reflections are present in the image. The negative was overexposed due to operator error, and it is possible that some of the reflections did not reproduce in the image shown. Detailed analysis of the diffraction pattern is shown in figure 3-18. White grid corresponds to the CdTe [011] pattern and yellow grid to the CdS $[2\bar{1}\bar{1}0]$ pattern. It can be seen that the CdTe $[11\bar{1}]$ direction corresponds to the CdS [0002] direction, with a slight tilt of approximately 2° toward the CdTe [100] direction. This is consistent with the lattice fringe images of the $(01\bar{1}0)$ planes in figure 3-15 and 3-16. Lattice spacings for CdS determined from the diffraction pattern are listed below in table 3-2, against the theoretical value. The values are quite close.

Table 3-2: Theoretical and measured lattice spacing

	Theoretical	From SADP	From lattice fringes
CdS (0002)	0.336 nm	0.339 nm	(not observed)
CdS $(01\bar{1}0)$	0.358 nm	0.358 nm	0.362 nm

There are additional faint and diffuse diffraction rings observed in figure 3-18, which are tabulated in table 3-3:

Table 3-3: Diffuse diffraction rings in figure 3-16.

1/d (nm^{-1})	d (nm)	$1/d^2$ (nm^{-2})	$(1/d^2)/7.069$
6.030	0.166	36.36	4.8
5.517	0.181	30.44	4.0
4.683	0.214	21.93	2.9
3.689	0.271	13.61	1.8
2.758	0.363	7.609	1.0

It is not clear what is producing the diffuse rings. It is crystalline but very fine-grained and exists over a broad region. Based on the ratio of reflections by factoring the first ring spacing into each successive ring as shown in the table above, it appears that ring spacing is consistent with a phase having a primitive crystal structure. The SADP also contains many reflections that cannot be indexed. Presumably, they belong to other variants of CdS grains and other phases that may be present in the film.

Figure 3-19 is a diffraction pattern from a region of the CdS film that contains many variants of CdS orientations, showing the polycrystalline nature of the film. The diffraction pattern is oriented so that interface plane is horizontal in the pattern. It can be seen that the white grid has the same orientation as the CdS $[2\bar{1}\bar{1}0]$ pattern seen in figure 3-18. The yellow grid is also the CdS $[2\bar{1}\bar{1}0]$ pattern, which is rotated by 61° with respect to the white grid. Many reflections do not fall on the grids, and they are presumably from other orientation variants of CdS. Both grids show streaks along the <0001> direction, which is consistent with basal plane stacking faults in the hexagonal CdS.

The orientation relationship between CdS and CdTe where epitaxy exists is as follows:

$(01\bar{1}3)$ CdS // $(01\bar{1})$ CdTe; $[2\bar{1}\bar{1}0]$ CdS // CdTe [011]

As described earlier, the notation for describing the interface consists of defining the interface planes for both CdS and CdTe which are $(01\bar{1}3)$ and $(01\bar{1})$ planes, respectively, followed by defining one direction within the plane of the interface for both lattices, which was chosen above with $[2\bar{1}\bar{1}0]$ CdS // CdTe [011]. The $[01\bar{1}3]$ CdS direction is at an angle of 32° with respect to the basal plane direction of [0001] which is close to the observed 33° (90° – 57°) in the figure 3-15. The odd index for the CdS plane is the consequence of using the Miller-Bravais notation. It is not immediately intuitive as to which plane in the crystal this index represents.

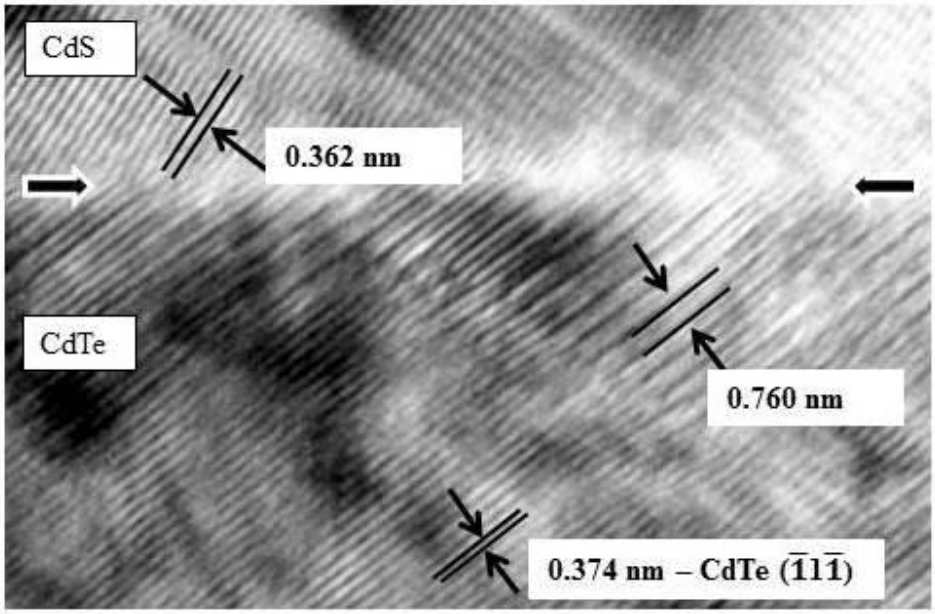

Figure 3-16: Close up view of the interface from figure 3-13. It appears as though some of the CdTe material has transformed to a new material, but it is continuous with respect to the CdTe $(\bar{1}1\bar{1})$ planes.

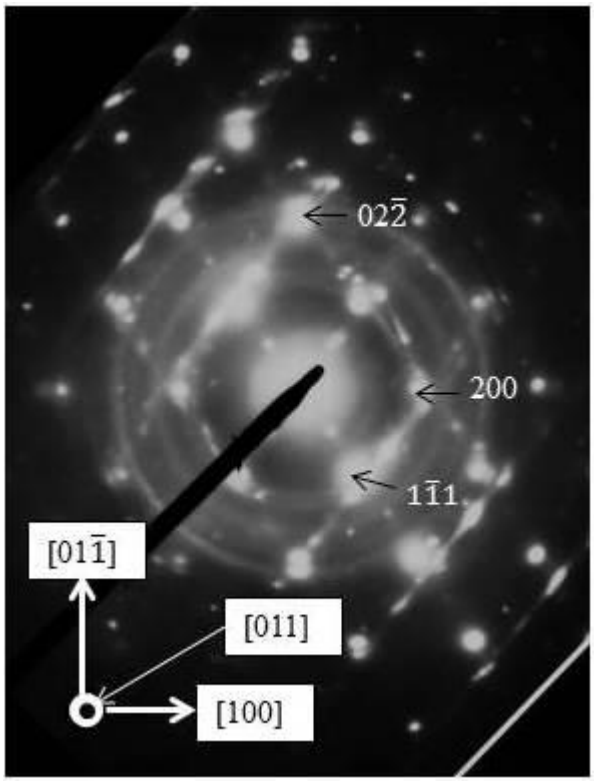

Figure 3-17: Diffraction pattern of sample area in figure 3-14. The image is properly oriented with respect to the image. The main strong reflections belongs to [011] CdTe. Other weaker reflections with streaks are close to hexagonal CdS in the $[2\bar{1}\bar{1}0]$ orientation. The streaks are consistent with the direction of the stacking faults in the CdS film. A more detailed analysis of the diffraction pattern is shown in figure 3-18.

In summary, Br_2:MeOH etch on cleaved {110} CdTe forms a crystalline material of unknown structure and composition at the interface while maintaining a flat surface. In some regions, an epitaxial hexagonal CdS can form which appears to extend one of the {111} CdTe plane into the (0001) basal plane of the CdS, with a slight tilt of the lattice by approximately 2° to the CdTe $(01\bar{1})$ interface plane in the direction of [100], based on both the diffraction pattern and HRTEM images. Many region contained the polycrystalline phase. Werthen reported that in general, Br_2:MeOH etch forms a Te-rich surface by Auger analysis [3-19]. Also some amount of bromine was detected on the surface which disappears quickly once the Auger analysis starts. Unfortunately, no photovoltaic properties were reported by Werthen on this cell structure. Some indication of what it would have behaved like could be taken from light J-V characteristics of Cr/CdTe junctions. Etched CdTe (110) behaves similarly to etched $\{111\}_{Cd}$ and $\{111\}_{Te}$ surfaces, with poor V_{oc} of between 0.15 to 0.25 volts, while PEH surfaces yields V_{oc} of 0.50 to 0.55 volts. During the period of

this analysis, a high-resolution EELS spectroscopy tool with sufficient spatial resolution did not exist, and such analysis would have produced much more detailed information on the chemical nature of the interface material. The interface phase is quite thin, on the order of 5-10 nm, and it is quite remarkable that CdS film can form with the extension of CdTe {111} type planes into the basal CdS {0002} type planes across the interface containing this interface phase. Unfortunately, the specimen quality was not sufficient to obtain much more detailed HRTEM images showing the more precise nature of the interface lattice matching between CdTe and CdS.

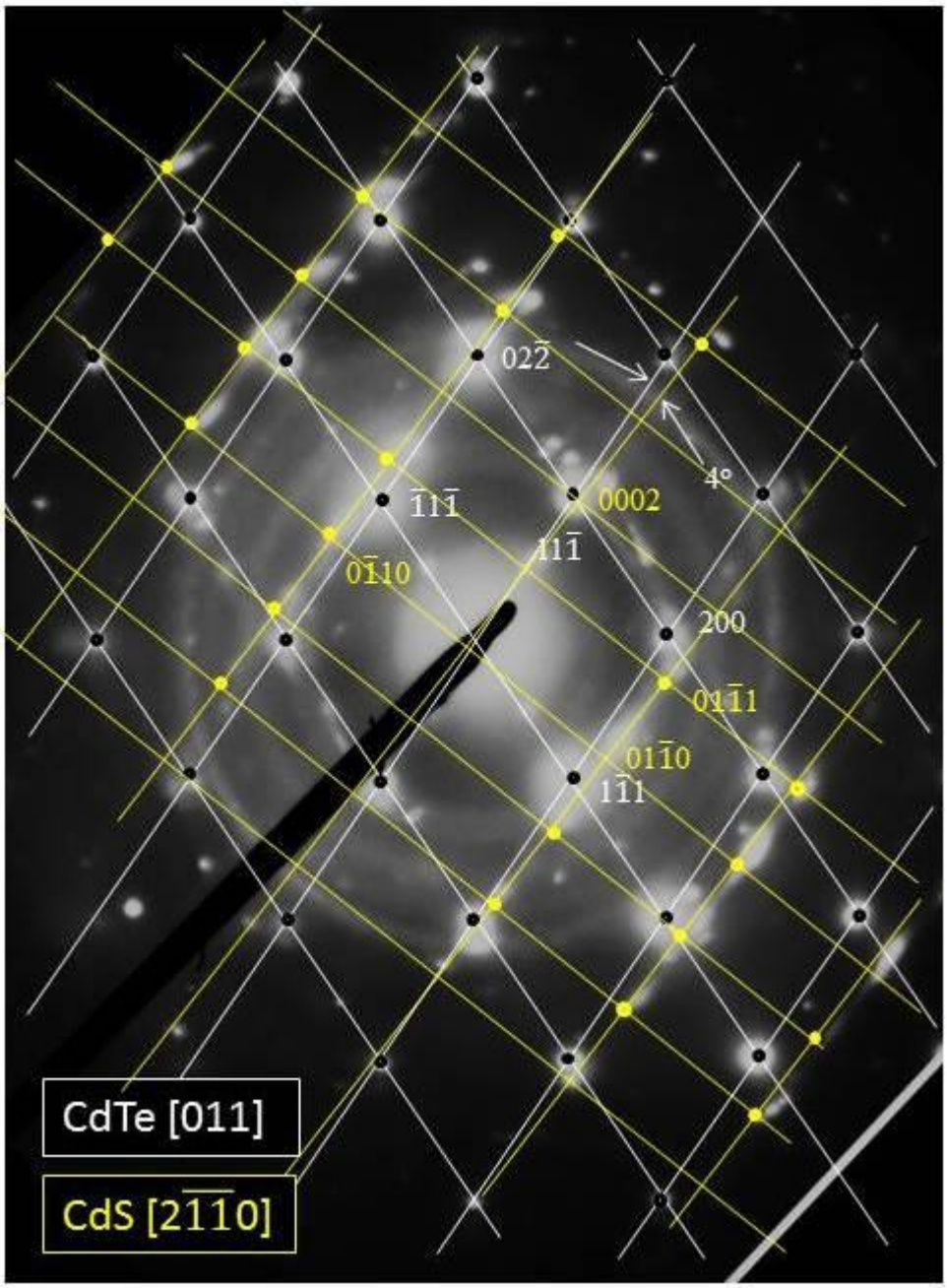

Figure 3-18: The white grid corresponds to the CdTe [011] pattern, while the yellow grid corresponds closely to the CdS [$2\bar{1}\bar{1}0$] pattern. In the CdS pattern, not all the reflections are present. Also, many of the spots cannot be explained.

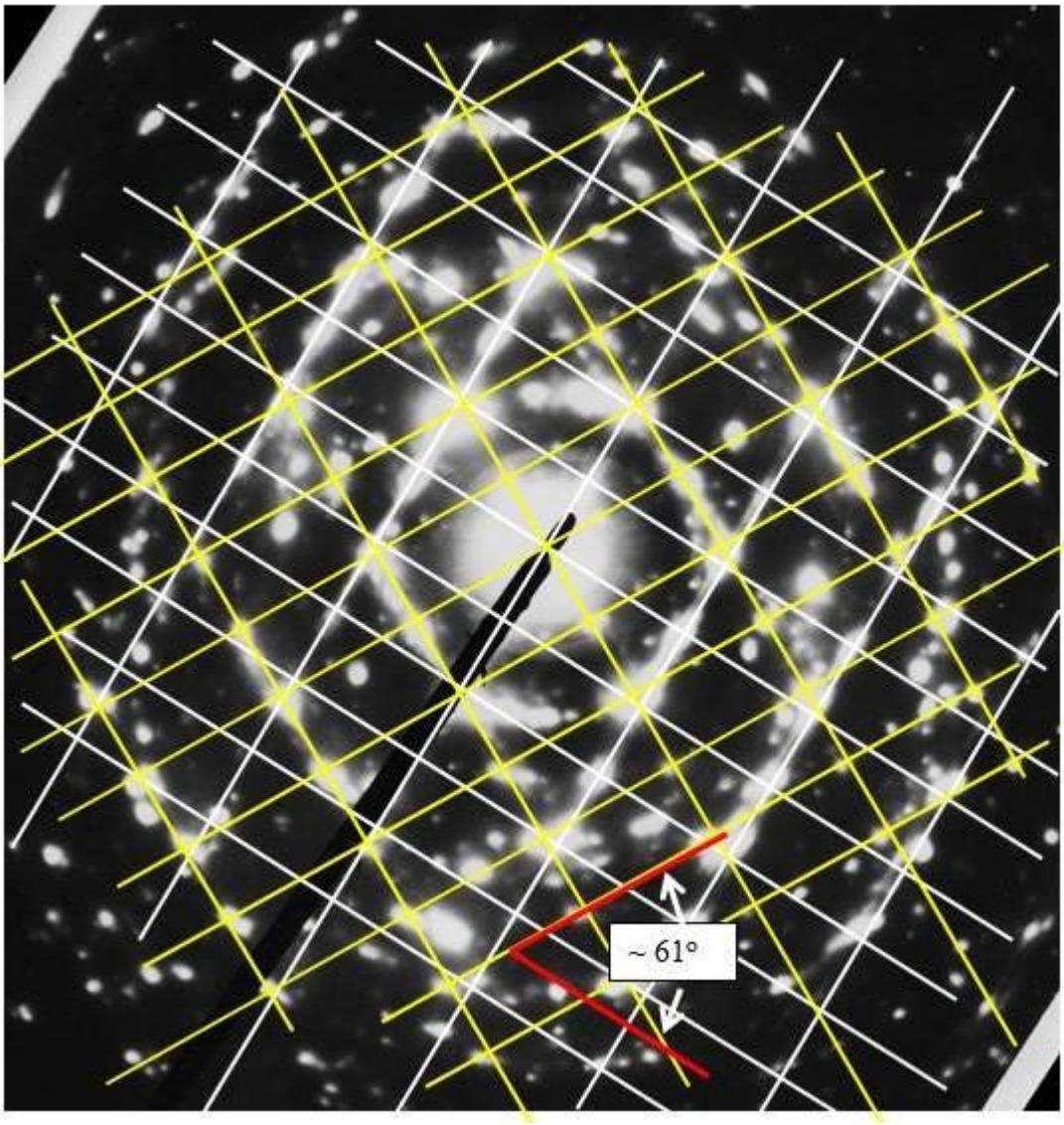

Figure 3-19: Diffraction pattern from mostly the CdS side of the interface. The white and yellow grids are CdS $[2\bar{1}\bar{1}0]$ patterns that are rotated by ~61°. There are many other reflections that do not fall on the grid, which are presumably other orientations of CdS.

3.4.3: E-Beam CdS on Cleaved and Etched {112} CdTe Substrate – (CE)

This specimen had CdS evaporated on a cleaved and etched {112} CdTe surface. The specimen was originally labeled by Werthen as a cleaved and etched CE {110} surface as in section 3.4.2. This probably occurred because the {112} plane is a possible alternative cleavage plane in CdTe. Figure 3-20 shows the BF low-resolution micrograph image of this interface. The thickness of the E-beam evaporated CdS film was approximately 350 nm in this specimen. The thickness also is unusually thin, as the expected thickness was 1.0 μm or more. It is not clear whether the low thickness was the consequence of the {112} surface (e.g., low growth rate - or a mistake was made during the CdS deposition). The BF, DP, and HRTEM images in this section were taken using a JEOL 200CX microscope at 200 kV. The CdS film was largely single-crystal and contains a very high density of stacking faults. It will be shown that these stacking faults are basal plane faults in the hexagonal CdS structure. Identification of CdS being hexagonal, and the CdTe surface as having {112} surface were deduced from the diffraction pattern shown in figure 3-21, and from the HRTEM image of the interface shown in figure 3-24. The indexing notation used for the CdTe and CdS orientations can be seen in the SADP in figure 3-21, and in figure 3-22. The CdTe zone axis is indexed as [011] as done previously, while the CdS zone axis is indexed as $[2\bar{1}\bar{1}0]$ as also done in section 3.4.2. By this notation, the specific {112} surface for the interface will be indexed as $(2\bar{1}1)$ in CdTe. The equivalent plane in the hexagonal wurtzite structure does not yield easily visualized plane indices. In the $[2\bar{1}\bar{1}0]$ zone, the interface plane will be close to $(01\bar{1}9)$. This is more easily understood and visualized in terms of the planes and directions that extends from CdTe to the CdS lattice, which are specifically CdTe $(1\bar{1}1)$ // CdS (0002) and the same for the directions, CdTe $[1\bar{1}1]$ // CdS [0002]. The $(2\bar{1}1)$ plane in CdTe makes an angle of 19.47° with the CdTe $(1\bar{1}1)$ plane as shown in the ball and stick model in figure 3-22. In the lattice, the two lattices are drawn as if they have the same equivalent lattice spacing. The $(2\bar{1}1)$ surface, looking down on it from the top is easily visualized using the computer aided model shown in figure 3-23. The $(1\bar{1}1)$ planes are at 90° to the $(2\bar{1}1)$ surface and form distinct rows of atomic planes. Lattice parameters were

calculated from the SADP for the CdS film, and the values were within 1% of those expected. The measured c/a_o ratio came out to be 1.613 as opposed to the expected value of 1.621.

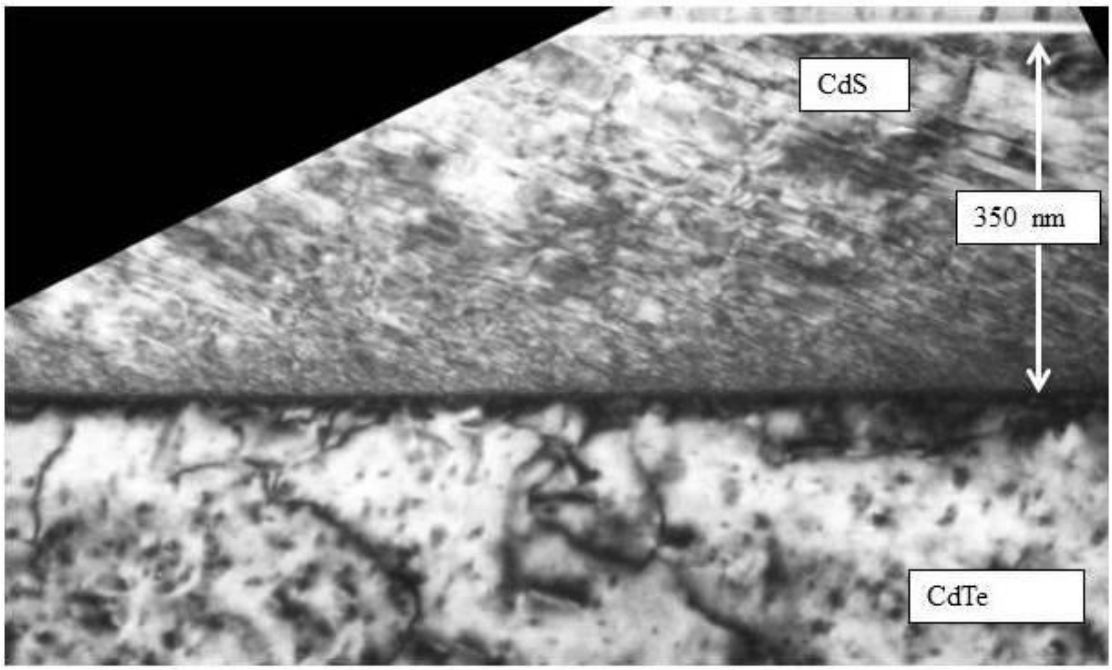

Figure 3-20: BF image of E-beam evaporated CdS on $(2\bar{1}1)$ CdTe that has been cleaved and etched in Br-Methanol solution. CdS is single crystalline in the region imaged, and contains a high density of stacking faults which are on the basal plane of the CdS lattice. The top of the CdS film is seen as a white line on top of the micrograph.

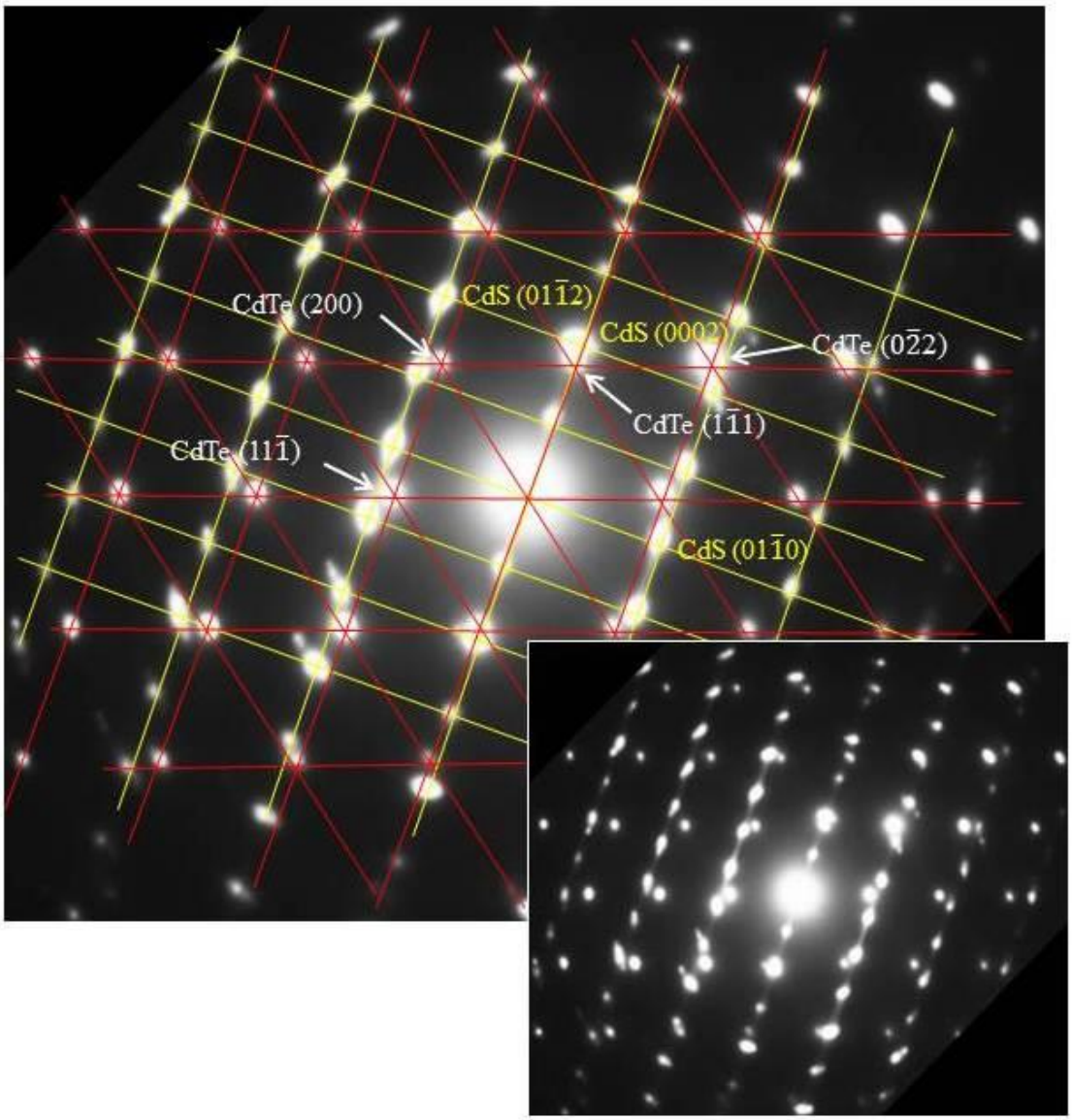

Figure 3-21: Diffraction pattern from CdS and CdTe showing the overlapping CdTe [011] and CdS [$2\bar{1}\bar{1}0$] reflections. The image is properly oriented with respect to the BF and HRTEM images. CdS reflections are indicated by yellow grids and CdTe by red grids. Streaks in the CdS reflections are due to stacking faults on the basal planes and runs perpendicular to the faults observed in the BF image of figure 3-20 and HRTEM images in figure 3-24 and 3-25. The CdS lattice is tilted slightly byapproximately 1° toward the CdTe [200] direction.

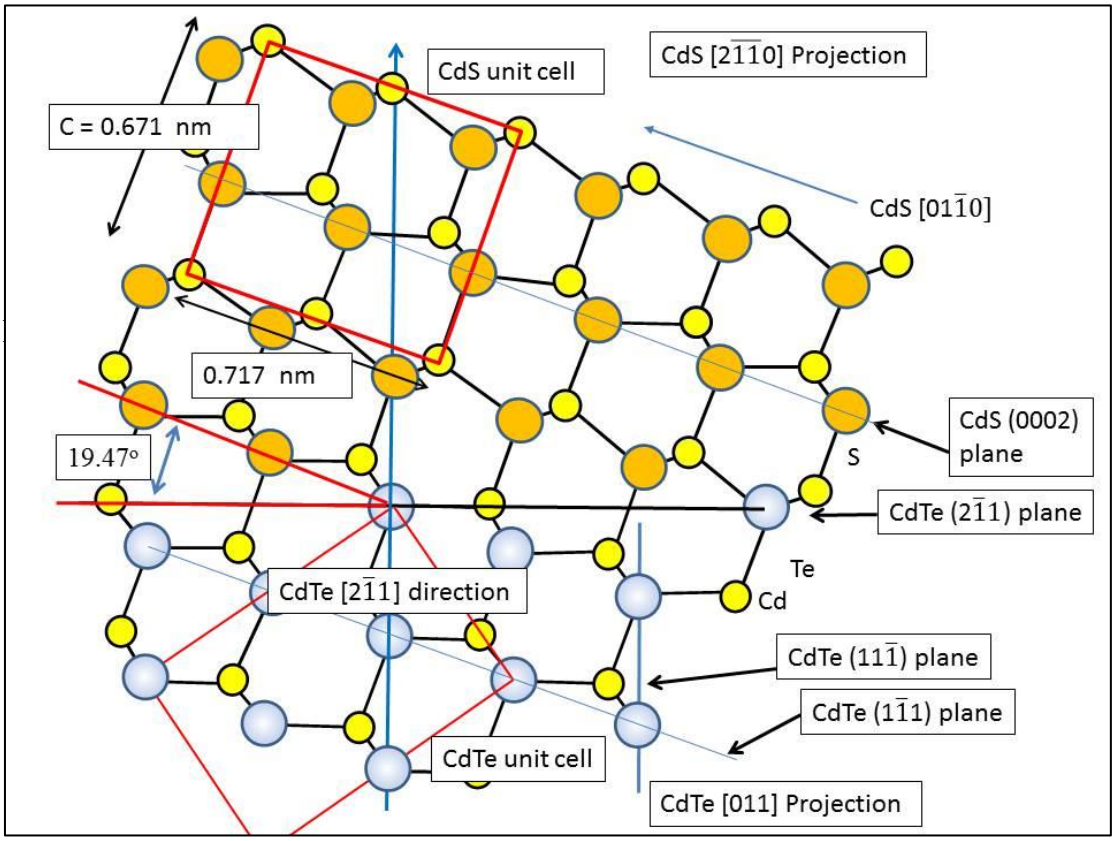

Figure 3-22: Model of the interface between CdS and CdTe (2$\bar{1}$1). CdTe (11$\bar{1}$) makes an angle of 90° to the (2$\bar{1}$1) surface, while (1$\bar{1}$1) is at 19.47° to the same surface. The model was drawn as if CdS has the same equivalent lattice parameter as CdTe. The equivalent CdS surface to CdTe (2$\bar{1}$1) is close to (01$\bar{1}$9). Miller-Bravais index notation for hexagonal system makes it difficult to visualize the

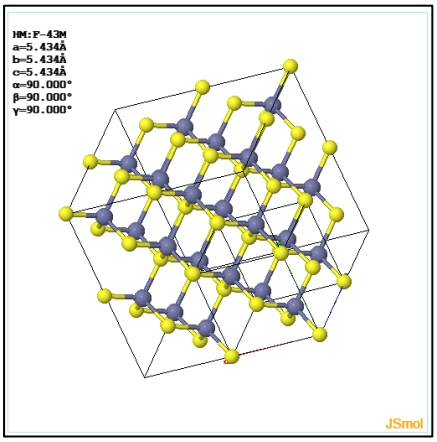

Figure 3-23: Model of cubic sphalerite, looking down on the <112> projection. (11$\bar{1}$) planes are at 90° to the surface.

Model based on ChemTube3D, © 2008-2014 The University of Liverpool [3-47].

The HRTEM image in figure 3-24 was taken with 19 beams, out to (400) reflections. Images were taken at approximately 100 nm underfocus where the best contrast was obtained for the CdTe lattice (white atom pairs). It can be seen that CdS film contains a very high density of faults. In some regions, the characteristic lattice of CdS in the $[2\bar{1}\bar{1}0]$ projection is evident, as was already shown in figure 1-40 in Chapter 1. The precise details of the faults are difficult to discern because the lattice are highly faulted, and individual image spots for the Cd-S pairs are not usually distinguished around the faults. However, it can be said that the faults are running along the basal plane of the CdS lattice. Drawn in figure 3-24 is a line that corresponds to the CdTe $(2\bar{1}1)$ plane. It can be seen that the actual interface is several degrees away from this plane, by roughly ~2.5° in the localized area seen in the micrograph. At the same time, the interface is not altogether smooth and regular. This cannot be detected from the diffraction pattern, but the analysis of the SADP in figure 3-21 shows that CdS is rotated by only 1° with respect to the CdTe $[1\bar{1}1]$ direction.

Figure 3-25 is an enlargement of the interface at the left side of figure 3-24. CdTe $(1\bar{1}1)$ planes extends smoothly into CdS (0002) planes, indicated by the white line. Much of the lattice disruption occurs slightly away from the actual interface for the CdS (0002) planes. When the CdTe $(1\bar{1}1)$ planes are tracked into the CdS, there is one to one correspondence with the CdS basal planes. There is a slight tilt of the CdS (0002) planes toward the interface by about 1°. It is barely discernable, but it can seen by viewing the image at a shallow angle. Stacking faults are much more clearly imaged, and some regions (in the middle of the figure) show narrow band where the atomic stacking is FCC.

The lattice mismatch between CdTe {111} with 0.374 nm spacing and CdS {0002} with 0.336 nm is 11.5%, which is a large value. It might be expected that an interface with such a large mismatch maybe incoherent because it would be very difficult for the two lattices to accommodate each other. However, the interface is surprisingly coherent, as there is a smooth continuation of CdTe {111} planes into CdS {0002} planes. This is even more surprising because Br_2:MeOH etch was expected to

leave some oxide or residue on the surface, which should have disrupted the interface. As was shown in figure 3-13, it is possible for the misfit to be accommodated by a CdS lattice tilt across the interface. This is shown schematically in figure 3-26. It is possible to accommodate the misfit by tilting the CdS (0002) planes by 2.0° from the matching CdTe ($1\bar{1}1$) plane across CdTe ($2\bar{1}1$) interface. The actual tilt measured in the SADP was 1°, and the HRTEM image gave approximately the same amount. The interface tilt of 3^{o} could also play a role to accommodate the misfit.

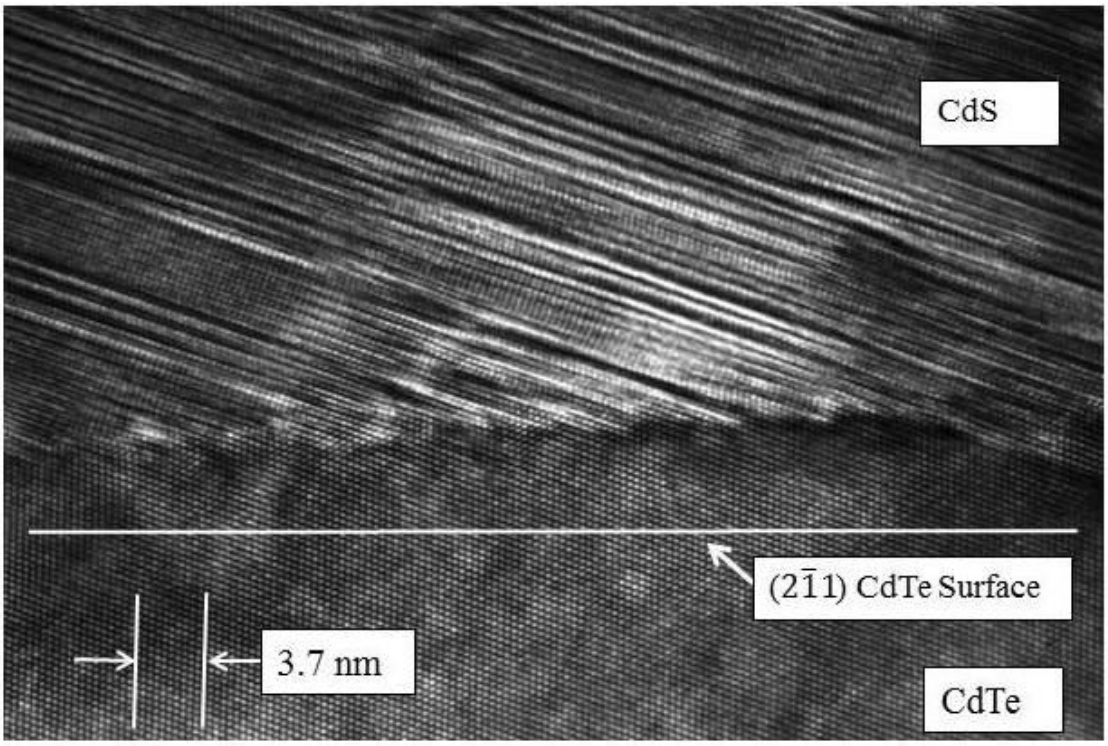

Figure 3-24: HRTEM image of the interface. The white line indicates the ($2\bar{1}1$) CdTe plane, and the actual interface is tilted slightly by about 2.5° and appears rough on the scale of approximately 1-2 nm.

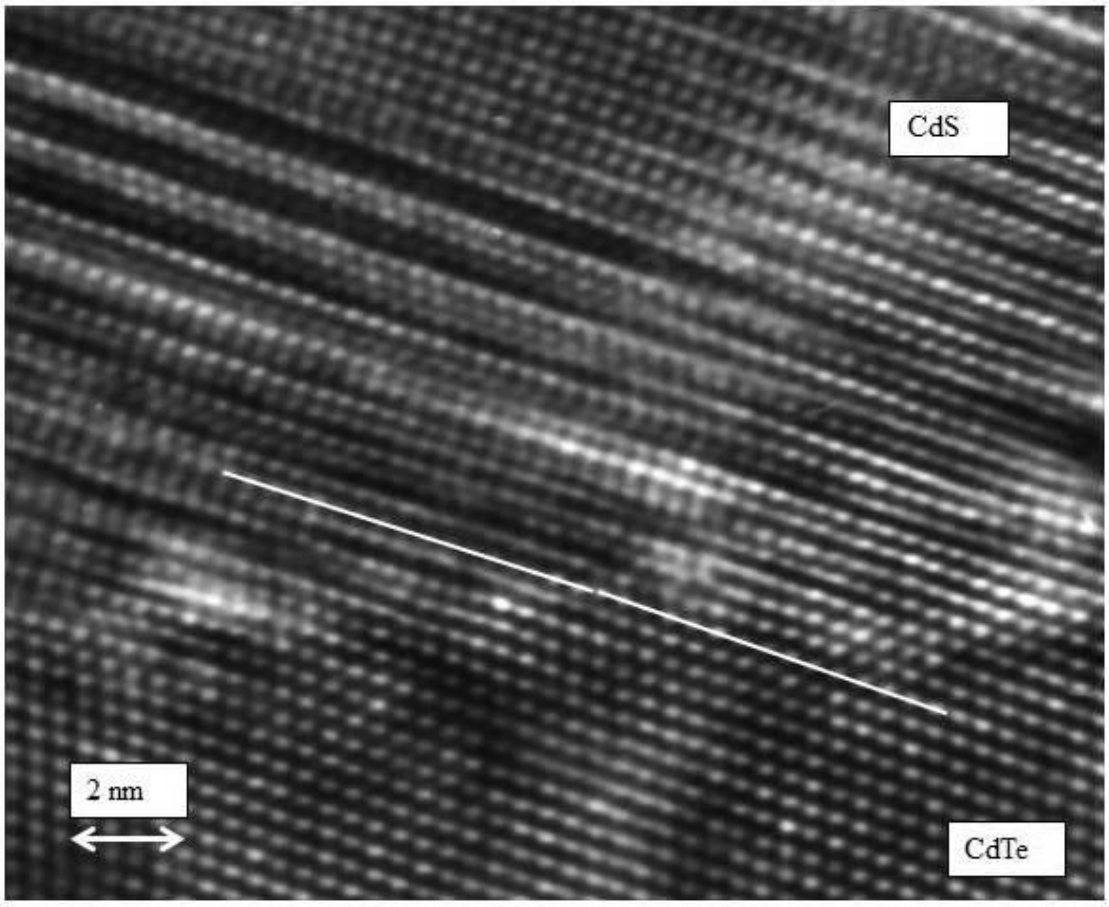

Figure 3-25: Enlargement from figure 3-23 showing the details of the interface. CdTe $(1\bar{1}1)$ planes extend smoothly into CdS (0002) planes, indicated by the white line. Much of the lattice disruption occurs slightly away from the actual interface for the CdS (0002) planes. In the above interface, there are no extra CdS planes for each of the CdTe $(1\bar{1}1)$ planes. There is slight tilt of the CdS (0002) planes toward the interface by about 1^{o}. It is barely discernable, but can be seen by viewing the image at a shallow angle.

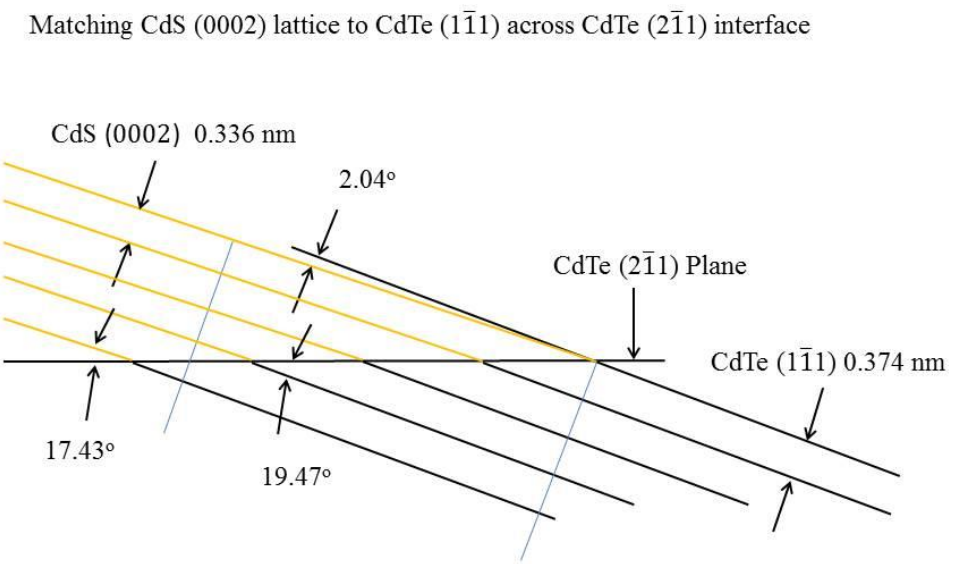

Figure 3-26: Matching CdTe (1$\bar{1}$1) planes to CdS (0002) planes across CdTe (2$\bar{1}$1) interface, one requires a lattice tilt of 2.0^{o} for the CdS lattice. The analysis only accounts for the mismatch in the plane of the paper, and says nothing about accommodating the mismatch into the plane of the paper. The lattice mismatch between CdS and CdTe lattice for CdS (0002) and CdTe (1$\bar{1}$1) planes is 11.5%.

Figure 3-27 is a HRTEM image of the interface where CdS lattice is imaged more clearly. Stacking faults are much more clearly imaged, and some regions show narrow band where the atomic stacking is FCC. The transition from CdTe to CdS is smooth, with no visible indication of additional planes in most of the region. A greatly magnified image from figure 3-27 is shown in figure 3-28. A circled region indicates where the extra CdS (0002) plane is detected. There should be such extra planes for every 11 CdTe (1$\bar{1}$1) planes, but the actual values appear to be far fewer. It is possible

that the combination of CdS lattice tilt and interface tilt help to accommodate the misfit between CdS and CdTe lattice.

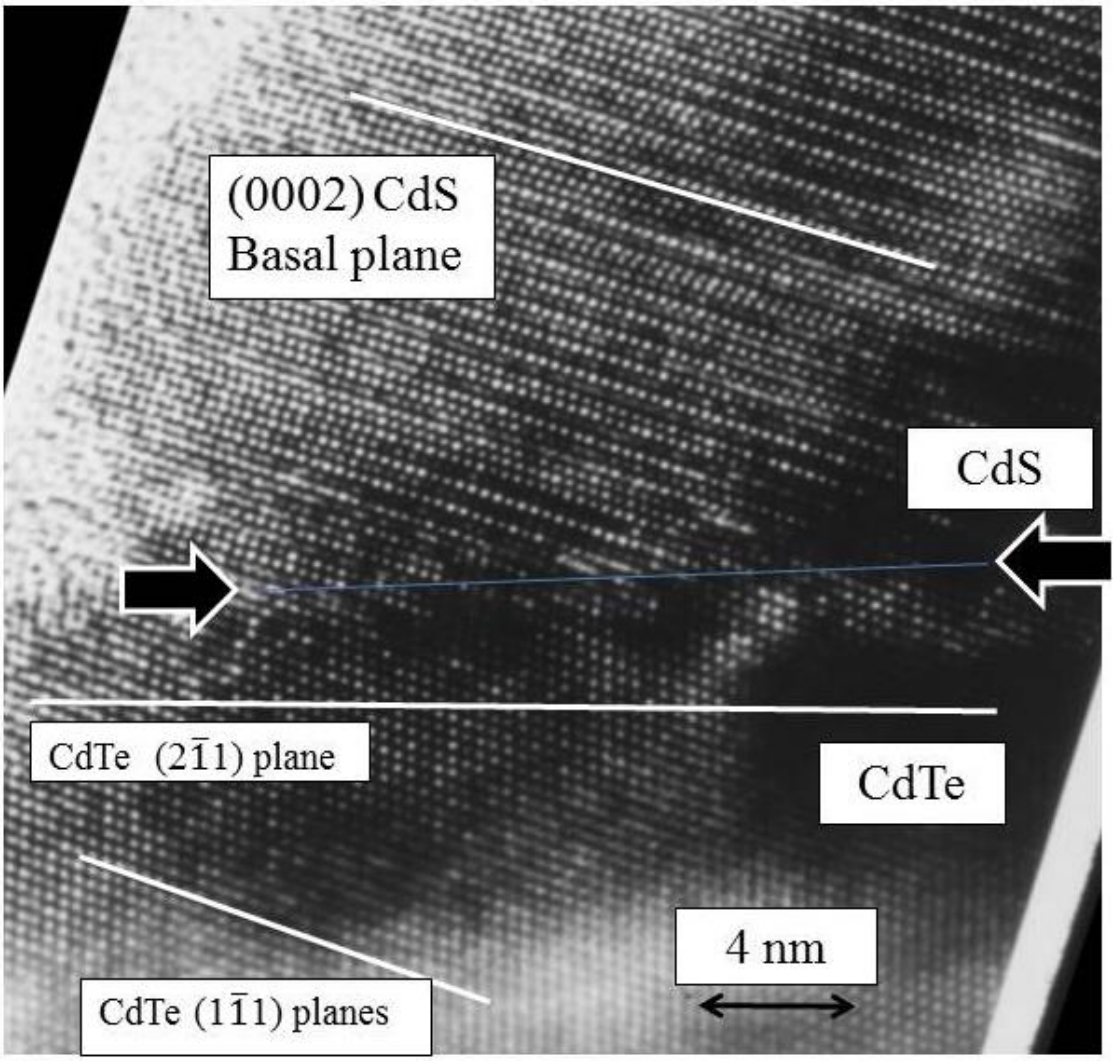

Figure 3-27: HRTEM image of the interface, where the CdS lattice is imaged more clearly. Stacking faults are much more clearly imaged, and some regions have a narrow band where the atomic stacking is in the cubic sphalerite structure. The actual interface is marked by large arrows and a thin blue line which is at an angle with respect to the CdTe (2$\bar{1}$1) plane. The interface is at an angle of approximately 2.5° with respect to the CdTe (2$\bar{1}$1) plane. The transition from CdTe to CdS is smooth, with no visible indication of additional planes, or of any discontinuity or contaminant layer.

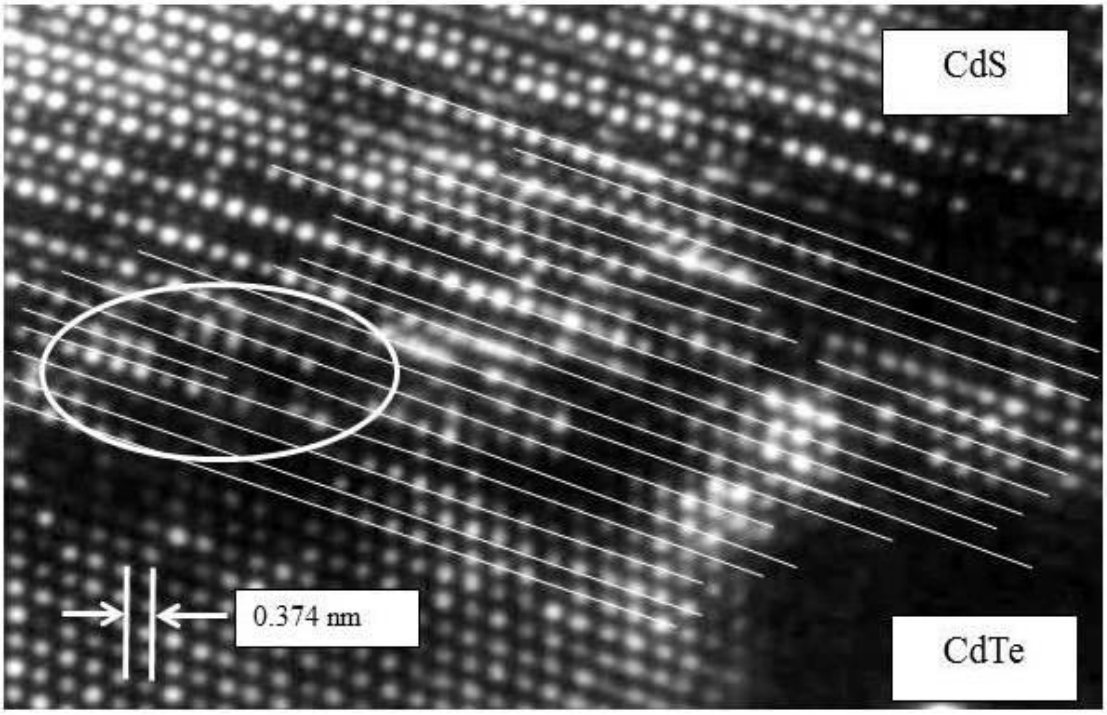

Figure 3-28: Maginified view of figure 3-27 showing the presence of an extra CdS (0002) plane. Other planes follow smoothly across the interface into the CdTe lattice. The number of misfit planes on the CdS (0002) is far fewer than that expected based on the lattice misfit. There should be one extra CdS plane every 11 CdTe planes, but the actual count is far fewer.

Figure 3-29 is another HRTEM image of the interface in a different location of the same TEM specimen. This interface is at an angle of 5° with respect to the CdTe $(2\bar{1}1)$ plane as indicated by a blue line. The basal plane of CdS is at an angle of 17.5° with respect to the $(2\bar{1}1)$ plane, which is to say that it is tilted by about 2° with respect to the CdTe $(1\bar{1}1)$ plane. This is the same situation as drawn out in figure 3-26. The CdTe interface plane is not smooth and has the appearance of being stepped. The magnified view of the interface is shown in figure 3-30. There is a region of confusion around the interface, which gives the impression that there are steps there.

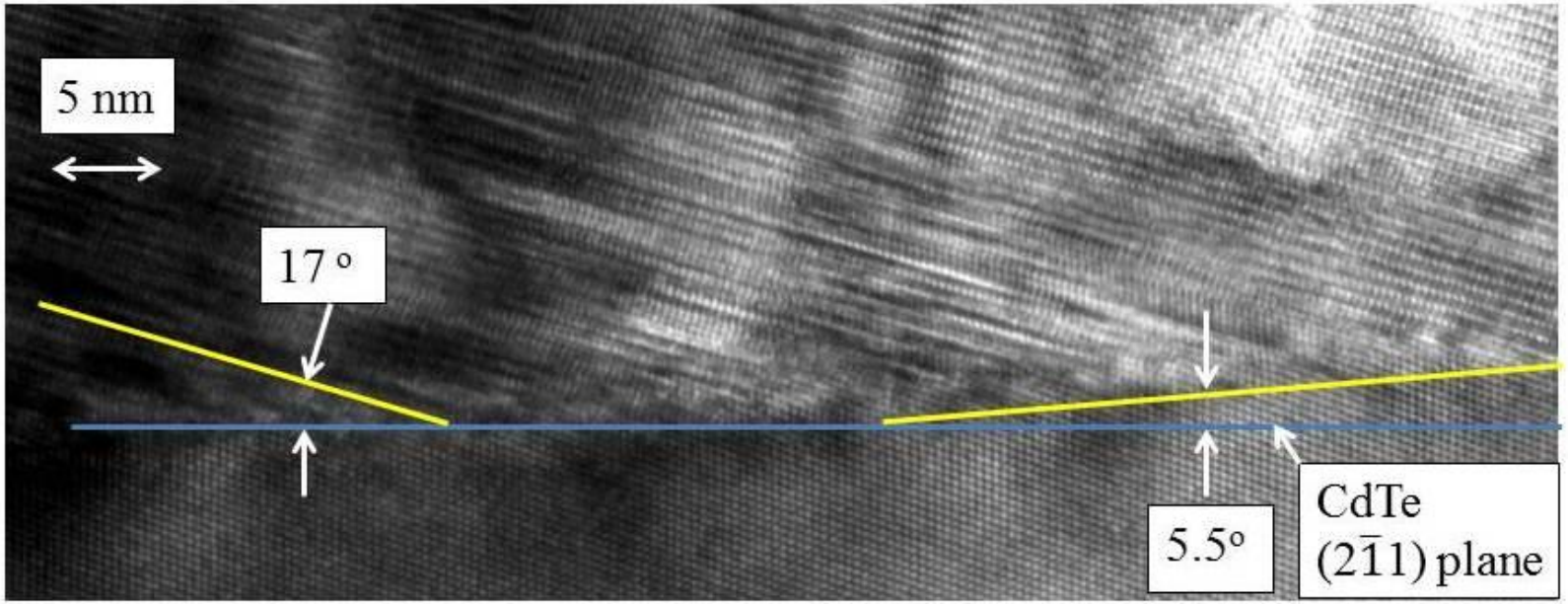

Figure 3-29: HRTEM image of the interface of E-beam evaporated CdS on CE (2$\bar{1}$1) CdTe. The (2$\bar{1}$1) CdTe plane is drawn in blue. The actual interface is at an agle of 5^{o} with the (2$\bar{1}$1) plane. The basal plane of CdS is at an angle of 17.5° with respect to the (2$\bar{1}$1) plane. The (112) CdTe surface is not smooth and has the appearance of being stepped. This feature of the interface maybe the consequence of the Br_2:MeOH etchant on the CE (2$\bar{1}$1) CdTe surface. Taken with JEOL 200CX at 850K X magnification. Stacking faults are also seen in the CdS layer.

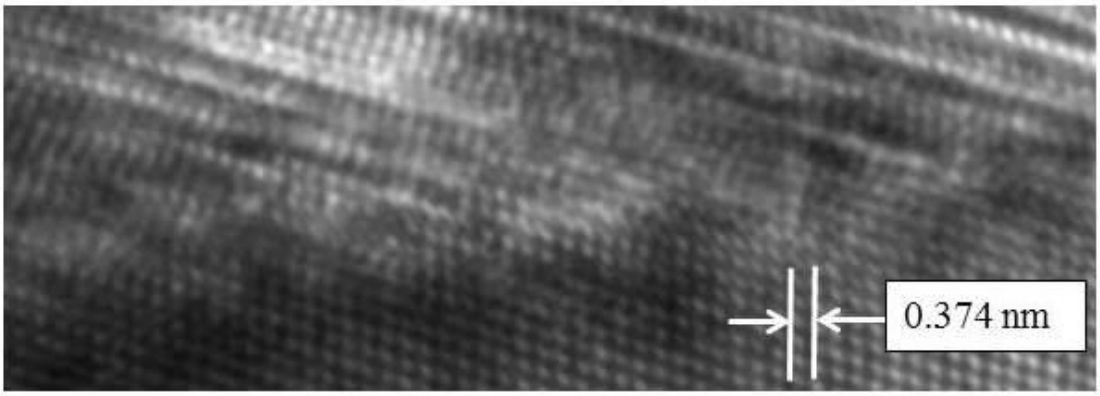

Figure 3-30: Magnified view from figure 3-29 showing details of the interface between CdS and CdTe. There is a region of confusion at the interface, which gives the impression that there are steps at the interface.

In summary, the CdTe {112} specimen was unique in providing an epitaxial hexagonal CdS film even though the surface had been etched. Lack of any oxide or secondary phase at the interface to disrupt the growth suggests that the surface is uniquely resistant to etching. In other specimens and orientations, Werthen noted that Br: MeOH etch turned the surface dark, but with respect to this specimen, nothing was apparently noticed. Nothing was said about the electrical performance of this particular specimen, but it is possible that Werthen had grouped them together as another etched surface. As a group, apparently the etched surface led to generally poorer V_{oc} values, presumably due to poor interface characteristics, such as high recombination rates. This specimen might have produced a good junction performance, but because the CdS film was very thin, it would have suffered lesser PV performance from thickness effects such as shunting and perhaps a higher film resistance. Therefore, it would have inferior properties for reasons other than having a poor interface. The orientation relationship between CdS and CdTe is as follows:

$(01\bar{1}9)$ CdS // $(01\bar{1})$ CdTe; $[2\bar{1}\bar{1}0]$ CdS // CdTe [011]

The film thickness was much lower than in other specimens were, perhaps because the favorable growth direction of CdS which is (0001) direction, is highly inclined to the

substrate surface. However, the drastic difference in the film thickness from that of other specimens is difficult to explain.

The CdS film contained very high density of stacking faults. A rough calculation based on HRTEM images indicates a density of approximately 300 faults/μm length along the interface. The CdTe substrate appeared normal in comparison to the bulk specimens that were examined in Chapter 1. There were some microdefects that were put there by ion-milling during specimen preparation, but they were present in about the same frequency as seen in the bulk specimen. The low magnification BF image in figure 3-20 shows dislocations and microdefects in the CdTe substrate and this appeared normal in comparison to the bulk CdTe specimens.

3.4.4 2nd Specimen, Cleaved and Etched {112} CdTe – Plan View TEM Analysis

An attempt was made to examine the CdS on cleaved and etched {112} CdTe in plan view in an effort to elucidate more details about the nature of the CdS film growth. One of the problems with looking at the interface in cross section is that one can only see the interface projected into one dimension, and one cannot see what is taking place beneath the surface. Additionally, one can only look at a very thin ~10 to 20 nm slice through the interface and it is possible to make a misleading conclusions about the film structure and what is actually taking place at the interface. One difficulty with preparing a planar TEM specimen is that one must capture the substrate and the film at the same time. With a thick ~1 μm thick CdS film, a precise amount of the film must be milled away while thinning the substrate at the same time to leave a thin region that contains both phases in order to image the interface and ascertain what might be happening there. This is difficult to do.

To make a plan view TEM specimen, a simple jet thinning method was developed which used a 50-50 mixture of 3% Br_2:MeOH solution in ethylene glycol. Br_2:MeOH is highly dangerous, and protective gear must be worn to shield oneself at all times. It is also very volatile and the fumes are toxic and dangerous. The work must

be done inside an efficient fume hood. Ethylene glycol was added to thicken the solution to avoid splashing and so that it is more controllable during jet thinning. A simple squeeze bottle with a fine nozzle was sufficient for the purpose, and this was turned upside down to allow gravity to provide a steady stream of etchant to the specimen. Several minutes of etching was usually sufficient to obtain a nicely concave surface with the thin part at the center. A frequent check in the optical microscope with lighting from beneath indicates whether the specimen was approaching the desired thickness as CdTe allows light to come through when it becomes thin. A 3mm disk was protected with methyl methacrylate wax, leaving only the center of the specimen exposed. Jet thinning was done from the CdTe substrate side and final thinning achieved by ion-milling at 3 keV from both sides. For this part of the investigation, the Philips EM400ST was used with a double tilt holder. The operating voltage was 120 kV.

The main surprise with the specimen is that the orientation was not what was expected. The CdTe was in the {112} orientation, but the CdS was in the $\{10\bar{1}0\}$ orientation. The expected orientation was for CdS to be close to the {0002} orientation, tilted by about 17° with respect to the CdTe {112} zone axis. The diffraction pattern containing the reflections from both CdTe and CdS is shown in figure 3-31. The SADP aperture covered a large area about 5 μm in diameter. The pattern is quite complex. The main pattern correspond to CdTe in the <112> orientation as expected, here indexed as the $[\bar{1}12]$ zone axis. Main CdS reflections, which are closely matched to the CdTe reflections, are indexed as $[01\bar{1}0]$ zone axis. CdTe $[\bar{1}12]$ reflections are indicated in a white grid, and CdS in a yellow grid in figure 3-31. For the CdS zone axis, the prism planes lie on the plane of the substrate with the c-axis aligned with the <111> direction of the CdTe {112} plane of the substrate. This orientation relationship is clear from the fact that CdTe $(\bar{1}1\bar{1})$ reflection is closely aligned with the CdS (0002) reflection. There are many reflections associated with each diffraction spots and some are difficult to interpret. There is one pattern labled with blue lines that correspond to the reflections as indicated in the figure which can be indexed as belonging to the CdS

$[\bar{2}7\bar{5}\bar{3}]$ zone axis. The angles between the reflections and the lattice parameters are all self-consistent with the CdS lattice parameters to within 1% of the expected values.

The four weak reflections marked with red circles in figure 3-31 that are approximately ½ $(2\bar{1}\bar{1}2)$ distance has the lattice spacing close to that of CdS $(10\bar{1}0)$ at 0.358 nm, the measured value at 0.353 nm which is 1.4% of the $(10\bar{1}0)$ value. It is tempting to index these reflections as belonging to the CdS [0002] zone axis, which was expected based on the analysis in the previous section. However, the angles between the reflections are not at 60° for the [0002] zone; instead, they are at about 63° in one direction and 57° in the other. The discrepancy is too large; therefore, it is uncertain as to what the reflections are due to. It is possible that CdS lattice is highly distorted due to high density of faults in the film, but in the previous analysis with the cross section specimen, distortion in the lattice was not observed in the diffraction pattern. A dark field image should have been taken using the weak reflections to determine where the intensity is coming from, but this was not done. Although most of the large reflections can be identified as belonging to CdTe or CdS, there are additional weak reflections that cannot be clearly identified. Since there was at least one additional CdS phase besides the main $[01\bar{1}0]$ zone axis phase, it is quite possible that the specimen contains grains with other orientation. Additional oddity of the diffraction pattern is the lack of streaking in the CdS [0002] direction. All the previous CdS films showed varying density of stacking faults and the same should be exected here, but the diffraction pattern did not show any indication of their presence.

The relationship between the CdS $[01\bar{1}0]$ zone axis and CdTe $[\bar{1}12]$ zone axis can be vidualized better by seeing the ball and stick model of CdS in the $[01\bar{1}0]$ projecton as shown in figure 3-32. The basal plane of the CdS matches well with one of the CdTe {111} planes (CdTe $(\bar{1}1\bar{1})$ in the $[\bar{1}12]$ projection).

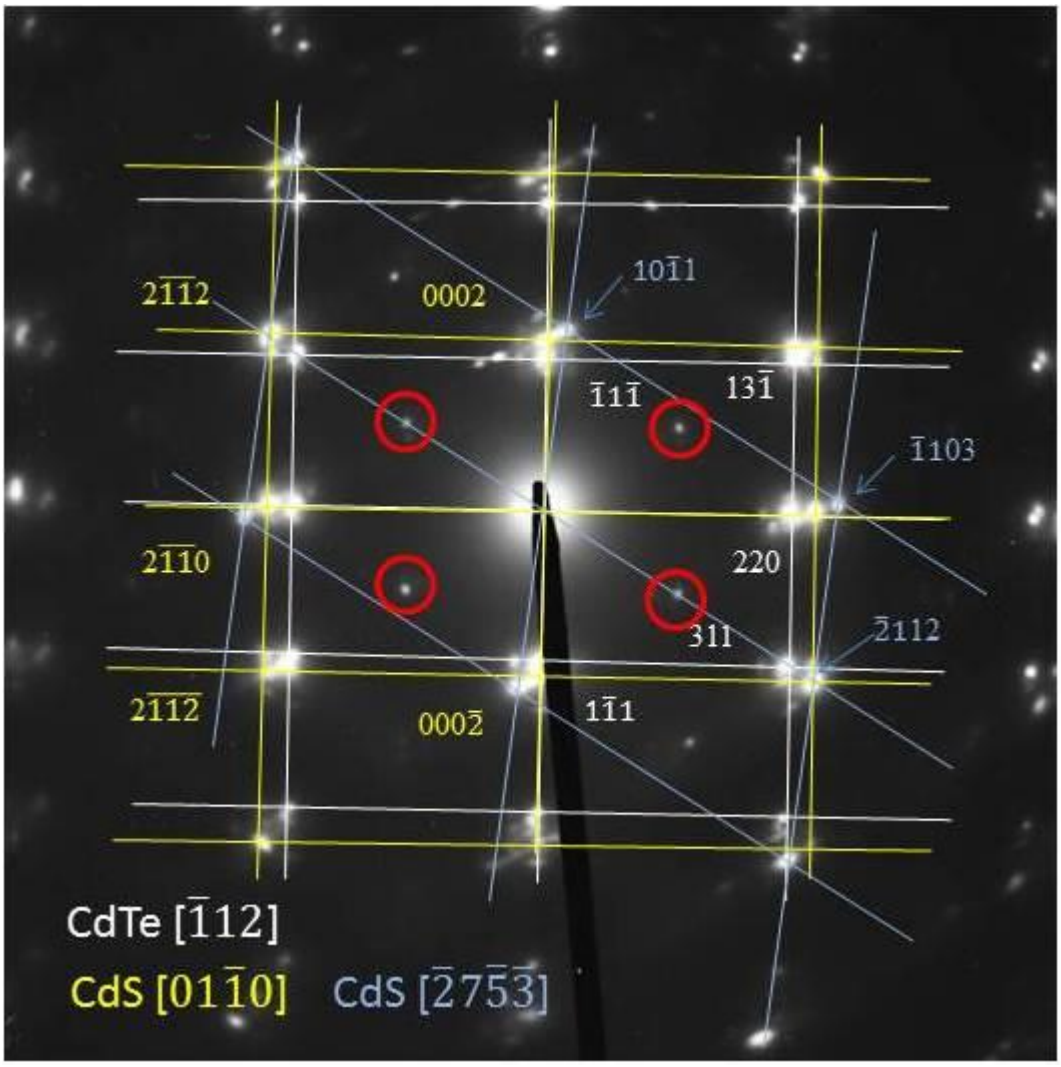

Figure 3-31: Diffraction pattern taken from the planar specimen containing both CdS and CdTe from the area as shown in figure 3-33. CdTe is indexed as $[\bar{1}12]$ zone axis with white grid and indices. CdS lattice is indexed as $[01\bar{1}0]$ zone with yellow grid and indices. There are additional strong reflections from the CdS which belongs to the $[\bar{2}7\bar{5}\bar{3}]$ zone axis which is marked in blue grid and indices. Four weak reflections circled in red are close to the CdS $(10\bar{1}0)$ lattice value, with the pattern close to the CdS (0002) zone axis. However, the angles are significantly off at 63° instead of the expected 60° between the reflections. Two other reflections are obscured by CdS (0002) and CdTe $(\bar{1}1\bar{1})$ above and $(000\bar{2})$ and $(1\bar{1}1)$ reflections below.

The orientation relationship between the two lattices is as follows using the same convention used earlier:

$(01\bar{1}0)$ CdS // $(1\bar{1}2)$ CdTe; [0001] CdS // $[11\bar{1}]$ CdTe

The $(01\bar{1}0)$ CdS and $(1\bar{1}2)$ CdTe planes are the matching interface, and [0001] CdS and $[11\bar{1}]$ CdTe directions are the two equivalent directions in the interface. The other two orientations that were identified, were the $(01\bar{1}9)$ CdS face from the previous section and CdS $[\bar{2}7\bar{5}\bar{3}]$ zone axis which has the approximate interface plane of $(\bar{2}, 7, \overline{5.3}, \bar{5})$, this value obtained by the method prescribed in Edington [3-46, page 295]. The formation of these odd orientation relationships are probably the consequence of attempting to grow CdS films on the CdTe {112} type surface. This surface clearly has less degree of freedom to form low index interface with CdS lattice compared to the {111} and {110} faces of CdTe. The degree of freedom loosely defined as the availability of low index planes on the CdTe surface that can be matched to the CdS lattice. Nevertheless, the CdTe {112} surface did not result in completely random polycrystalline film for the CdS.

The basal plane of CdS is the preferred growth direction and when the basal plane is lying on its side to the substrate such as for the $(01\bar{1}0)$ CdS orientation, the film growth rate should be slow. Therefore, it is likely that the CdS film was thin or even thinner than the CdS films from the previous section. The actual thickness was not measured as the specimen was made into a planar sample. With this specimen, we do not have any specific information about its electrical characteristics. It was likely thought to be similar to other CE {110} specimen as its true crystallographic characteristic was not suspected.

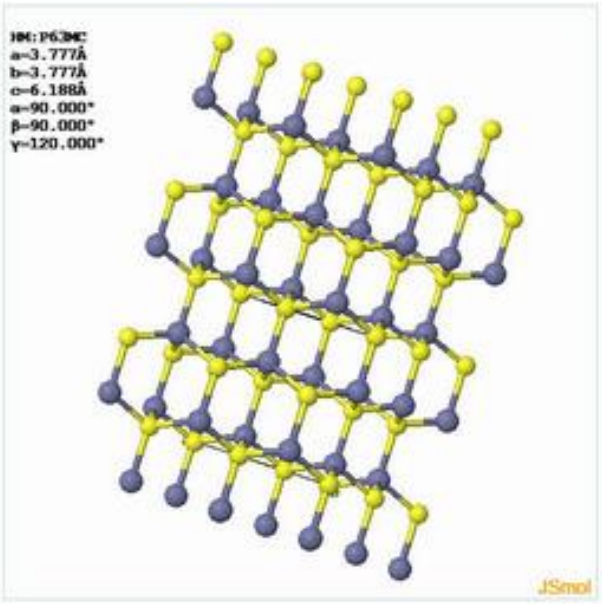

Figure 3-32: Computer generated ball and stick model of wurtzite in <01$\bar{1}$0> projection. The basal plane of CdS can match well with the CdTe {111} planes that are at 90° to the ($\bar{1}$12) surface.
Model based on ChemTube3D, © 2008-2014 The University of Liverpool [3-47].

A BF micrograph of the CdS film and CdTe which is oriented with respct to the SADP in figure 3-31 is shown in figure 3-33, and it can be seen immediately that the microstructure is very complex. The CdS film apparently contains many grains with different orientations, but it is not very obvious from the image as to where the boundaries are, and what is causing the different contrast features in the image. It may have been helpful to conduct DF imaging using isolated diffraction spots to determine the microstructure more clearly; however, many of the diffraction spots for the CdS phases are close together and it would have been difficult to isolate individual reflections. 2½-D imaging technique [5-25] would have been helpful in this situation; however, this was not attempted with this specimen. It is suspected that some contrasts are due to grain boundaries and others are due to strain contrast from the CdS/CdTe interface.

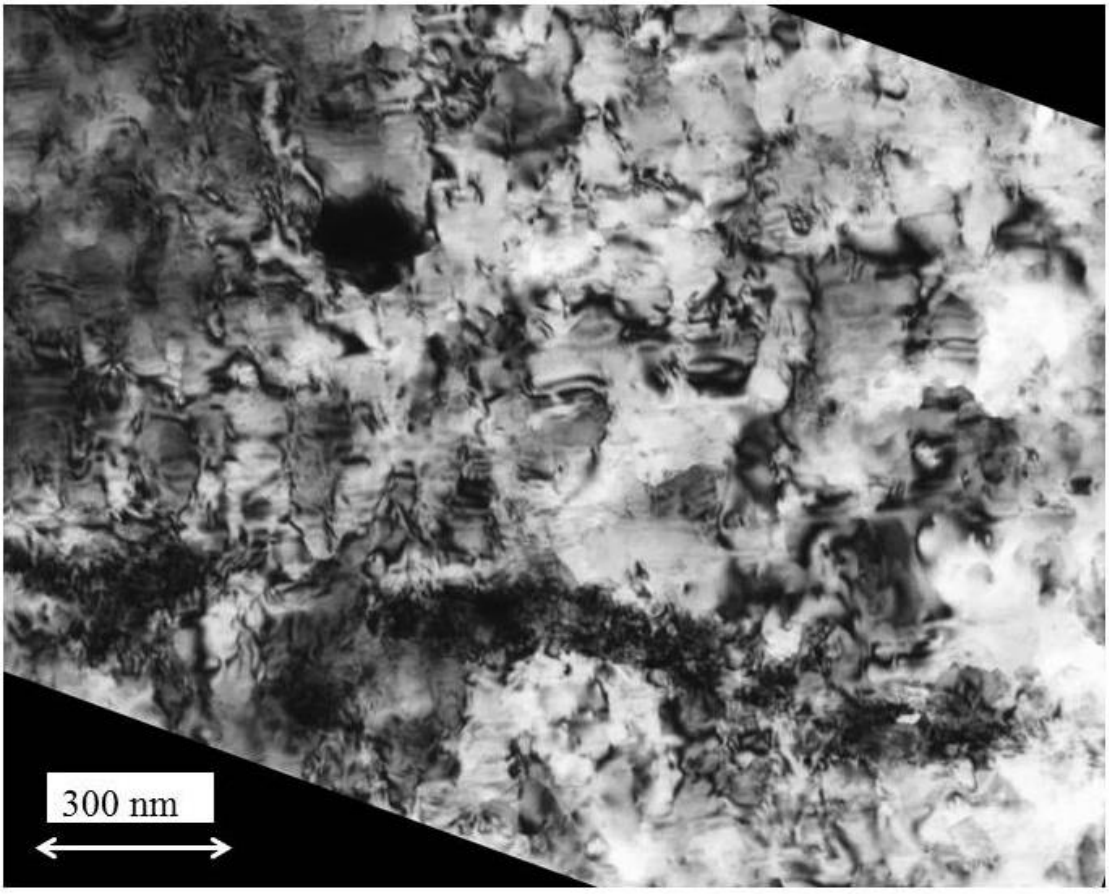

Figure 3-33: BF micrograph of the plan view TEM specimen, looking through both CdS and CdTe. The image is very difficult to interpret due to its complex contrast features.

One TEM method that is useful in this type of situation where some level of epitaxy exists between the substrate and the film is to look for Moiré patterns that originate from the two lattices that are on top of each other. A key rquirement for Moiré pattern is that two crystals have almost the same lattice parameter, and that the beam diffracted by by both crystals is allowed to recombine with the transmitted beam to form the final image. Double diffraction is an essential prerequisite for the Moiré pattern formation. The two crystals are brought into strong two-beam diffracting condition and either BF or DF image is obtained with the objective aperture containing the closely spaced double diffracted beams in the aperture. Different Moiré patterns

occur when two lattices overlap, depending upon the type of misalignment that occurs between them [3-46, 3-48, 3-49, 3-50].

A Moiré pattern imaging that was attempted used CdS in $\boldsymbol{g}$ = [$\bar{2}$110] diffracting condition, and CdTe in $\boldsymbol{g}$ = [220] condition, as these two reflections are located close together (see figure 3-31). The attempt was only moderately successful and other reflections are also strong. Figure 3-34 shows the diffracting conditions with the indices indicated in the figure. Additional problem is that double diffraction effects are not so evident around the transmitted beam, or on the diffracted beam. They maybe present in the transmitted beam but washed out due to proximity to the strong beam intensity. On the diffracted beam, there are many other beams nearby including the beams from other grain orientation. Some of the reflections may or may not be double reflection spots. Note that image of the objective aperture in the figure was not the one used for the actual Moiré imaging. Only the transmitted beam was used to obtain the BF image.

With the above caveat with respect to the diffracting conditions that was used, the actual BF image that was obtained is shown in figure 3-35, which is properly oriented with respect to the DP in figure 3-34. The fringes that appear are spaced approximately 2 nm apart and runs predominantly in one direction. Given the direction of the g-vector and the direction of the fringes, it is thought that fringes are due to two different overlapping lattices (CdS ($\bar{2}$110) and CdTe (220)) that are slightly rotated with each other; therefore, the spacing is given by eqn. 3-5 [3-46].

$$D \approx \frac{d_1 d_2}{[(d_1 - d_2)^2 + d_1 d_2 \beta^2]^{1/2}} \qquad \text{[Eqn. 3-5]}$$

β is the angle of rotation between the two lattices

d_1 = CdTe (220) = 0.229 nm

d_2 = CdS ($\bar{2}$110) = 0.207 nm

An optical bench was used to obtain diffractograms from the negative from an area about 100 nm in diameter in order to attempt to average the fringe spacings, and four measurements were taken from the original negative of figure 3-35. The four measurements are shown in table 3-4 with the calculated rotation angle β.

Table 3-4:

D spacing of Moiré fringes for CdS/(112) CdTe planar specimen, calculated from eqn. 3-5.

D (nm)	β (degrees)
2.0	4.3°
2.0	5.5°
1.9	6.0°
1.9	6.6°

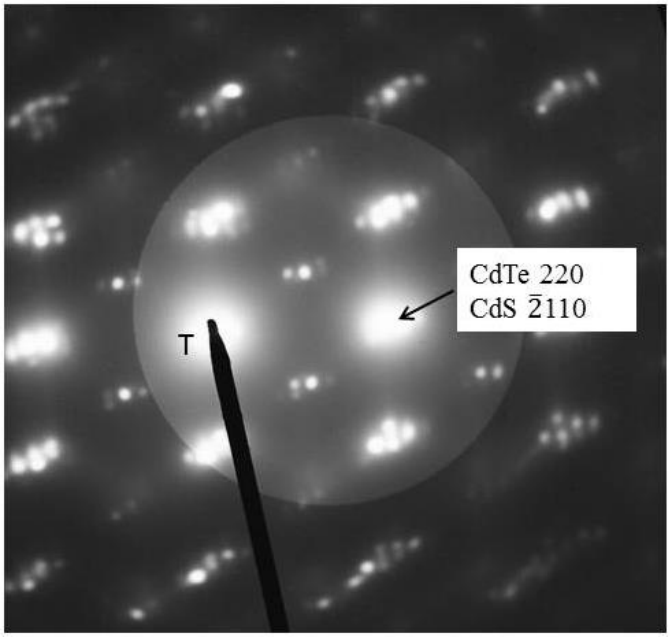

Figure 3-34: DP setup for the Moire pattern imaging in figure 3-35. Two-beam condition was attempted for CdTe (220) and CdS ($\bar{2}$110) reflections, but they were not strongly diffracting, with the intensities still strong on other reflections. Objective aperture that is shown, is not the one used for imaging.

The angles are large in comparison to the very slight angular tilt between the CdS and CdTe lattice seen in the SADP of figure 3-31, which is less than 1^{o}. It appears that the Moire analysis is problematic, and it may be due to the relatively low intensity of double diffraction, and the fact that there are several reflections with large intensity that may be contributing to the image, which complicates the situation. It may suffice to note from the image that Moire appears in clumps of area 20 to 50 nm in size, with slight angular spread between each region. This must be the actual situation that exists in the CdS film. The detail of this feature is shown in the enlargement in figure 3-36. The appropriate description of this type of structure is a mosaic microstructure. It is a consequence of many nucleation sites for the growth of CdS grains which are slightly misoriented from each other and they converge once the film reaches a certain thickness. The subgrain-like structure then continues through the film growth. The approximate density of dislocations at the CdS/CdTe interface as determined by the number of terminating Moiré fringes corresponds to a density of approximately $10^{13}/cm^{2}$. This is the approximate figure that would be expected based on ~10% lattice mismatch between CdS and CdTe. The Burger's vector of the dislocations as implied in figure 3-35 should be some fraction of $<\bar{2}110>$ based in the CdS lattice, which is in the plane of the interface. Moiré fringe analysis provides complementary data to high resolution imaging in cross-section.

Planar specimen and Moiré fringe analysis would have been very useful for analyzing other specimens in different CdTe orientations, but {112} orientation CdTe (CE specimen) was the only specimen looked at in planar mode. The reason for this was that in order to prepare a planar specimen, one can obtain just one specimen from each junction sample which typically measured 4.5 x 3.5 mm as shown in figure 3-5.

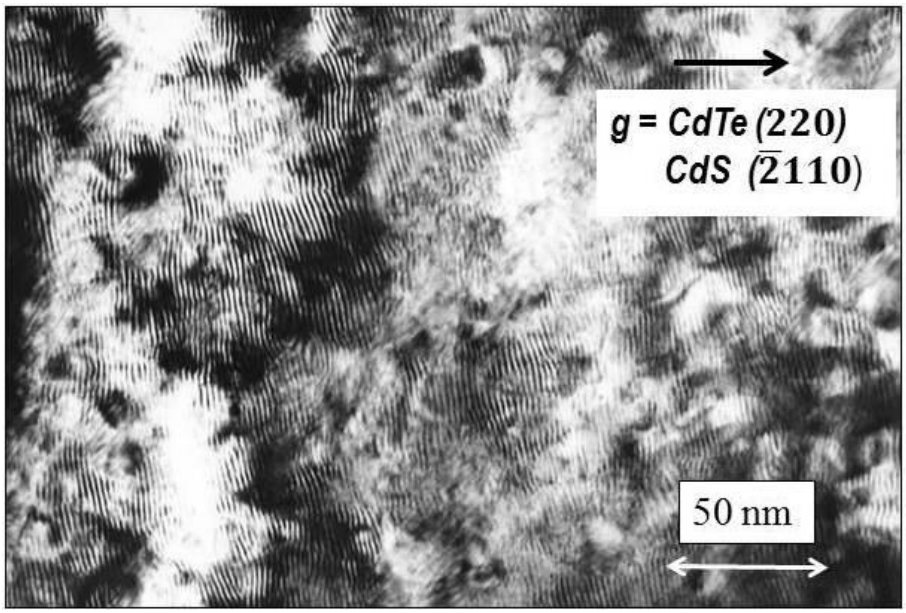

Figure 3-35: Moiré patterns from CdS / CdTe grains that are mis-oriented with respect to each other. The spacing of the fringes suggests that two lattices are rotated with respect to each other by an average of 4.3 to 6.6^{o} based on diffractogram analysis of above image.

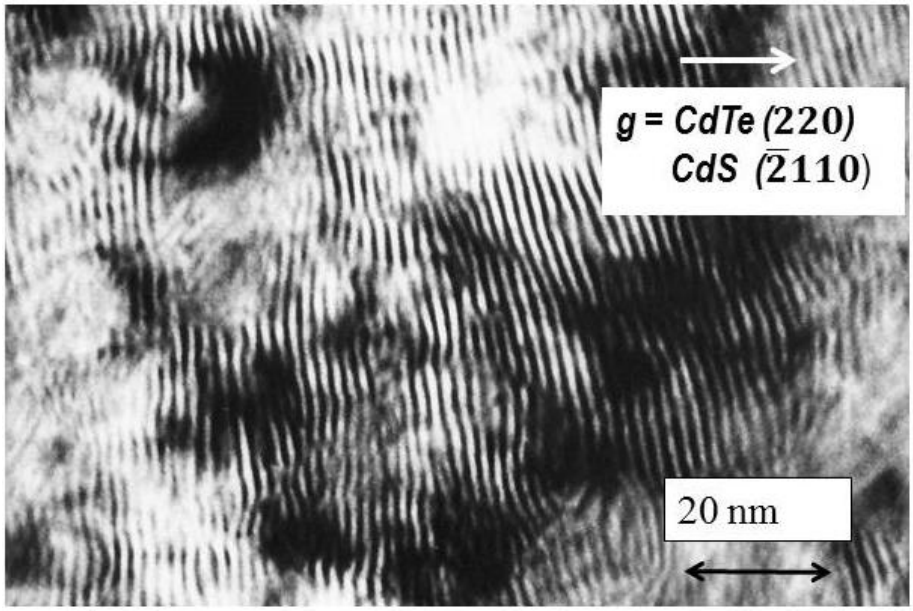

Figure 3-36: Magnified view of the Moiré fringes showing the complexity of the interface between the CdS film and CdTe.

3.4.5: E-Beam CdS on Etched $\{111\}_{Te}$ CdTe Substrate - (PE)

The CdS deposited on {111} CdTe that had been polished and etched in a 2% Br_2:MeOH solution has a polycrystalline structure. The specimen examined had a $(111)_{Te}$ surface. The CdS structure has a hexagonal wurtzite structure and is randomly oriented based on X-ray diffraction intensities as shown in figure 3-37. The X-ray powder card for the hexagonal CdS (greenockite) is shown in figure 3-38 [3-51]. The relative intensities of various reflections in figure 3-37 mirrors the intensity ratios listed in the powder file. Therefore, the crystallites have a random orientation. A Read camera photograph [3-52] of the CdS film shown in figure 3-39 also confirms the polycrystalline nature of the film and the hexagonal crystalline structure of CdS. The Read camera is a useful tool to examine thin films on a crystalline substrate because it can capture a much larger diffraction angles on a single film and provide a more detailed view of the structure of the film compared to a single scan by Bragg-Brentano geometry.

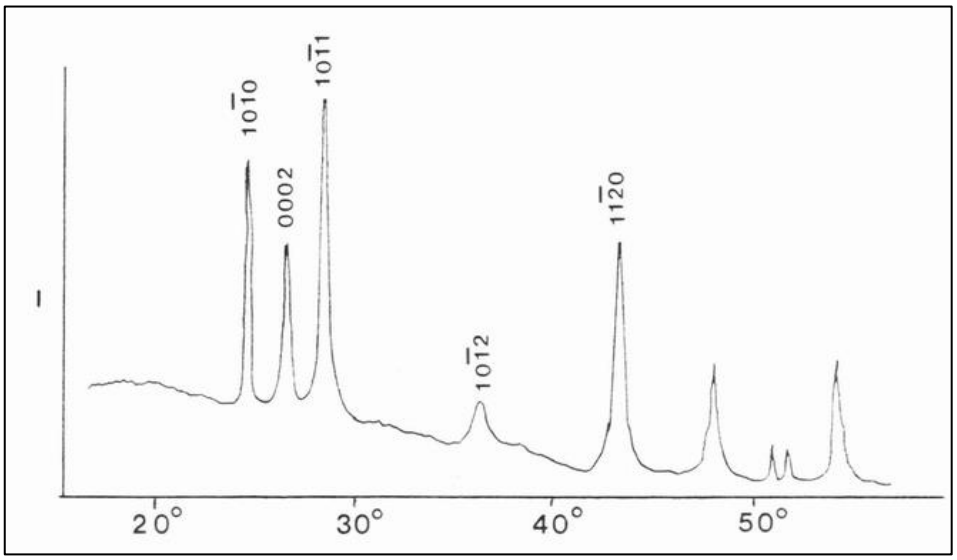

Figure 3-37: X-ray diffraction pattern of the evaporated CdS film on PE CdTe {111} substrate, using CuKα X-ray. Using standard Bragg-Brentano geometry. CdTe reflections were not observed. This is probably due to it being single crystal, and the reflections were not intercepted by the detector.

All TEM images in this section were taken with the Philips EM400ST at 120 kV using a double-tilt specimen holder. HRTEM images were taken with 19 beams through the objective aperture, out to (400) reflections. As in other sections, the defocus condition was several tens of nanometer underfocus beyond the Scherzer defocus condition to obtain the best possible contrast in the images with a white atom spot representing Cd-Te atom pairs. In the low-resolution BF image of the interface shown in figure 3-39, the polycrystalline character of CdS film is evident. The CdS layer had been eroded by the ion-milling in this micrograph. Other micrographs showed CdS film to be about 1 μm in thickness. PE {111} CdS/CdTe specimen was difficult to prepare due to uneven ion-milling between CdS and CdTe, with CdS being ion-milled much faster than CdTe. Energy dispersive X-ray spectroscopy (EDS) analysis of the region as shown in the inset in figure 3-40 indicates a presence of an interfacial material containing Br. Probe size used was approximately 100 nm. Apparently some of the bromine remained on the surface after cleaning before CdS deposition.

The grain size of the CdS film is approximately 50 nm, based on estimation of their size in cross section TEM images. The HRTEM image of the PE sample shown in figure 3-41 at the CdS/CdTe interface is quite confused, as one is imaging multiple grains of CdS in different orientations. Some of the CdS is shows lattice fringes that happen to be in the right orientation for imaging. Otherwise, the image is indistinct. The CdTe surface is quite close to the {111} orientation, but there are undulations on the scale of approximately 10 nm width to the surface, which is more visible in the inset which is a magnified view of the white square in the micrograph. The height of these long wavelength undulations is approximately two to three {111} plane spacings, which is ~1 nm in length. There is no clearly distinguishing interfacial compound, but at least at this section of the interface, there are small oval mounds that appear to have CdS that is oriented with (0001) basal orientation aligned with the CdTe (111) planes at the right side of the inset, as well as mounds that appear to have cubic sphalerite structure on the left side of the inset. They are undoubtedly CdS as they lie on CdS side of the interface. There are stacking faults at the base of the mounds, which suggests

that they are part of the deposited CdS film. The SADP pattern from the CdTe and CdS at the interface is shown in the inset, indicating CdS with many different orientations within the area of the diffraction pattern. The SADP was obtained from a small region at the interface approximately100 nm in diameter containing both the CdTe substrate and part of the CdS film. There is a correlated relationship between some of the CdS reflections with the CdTe as the CdS reflections do not form completely random rings. The actual interface is very rough and complex. The light J-V characteristic of the PE $(111)_{Te}$ specimen is shown in figure 3-6. The performance is much worse compared to the PEH sample, and it is thought to be due to the interface which is complex and full of defects. Many grain boundaries present in CdS also must contribute to such factors as higher film resistivities and carrier traps. A high density of defects at the interface probably causes recombination losses which reduce the V_{oc} of the junction.

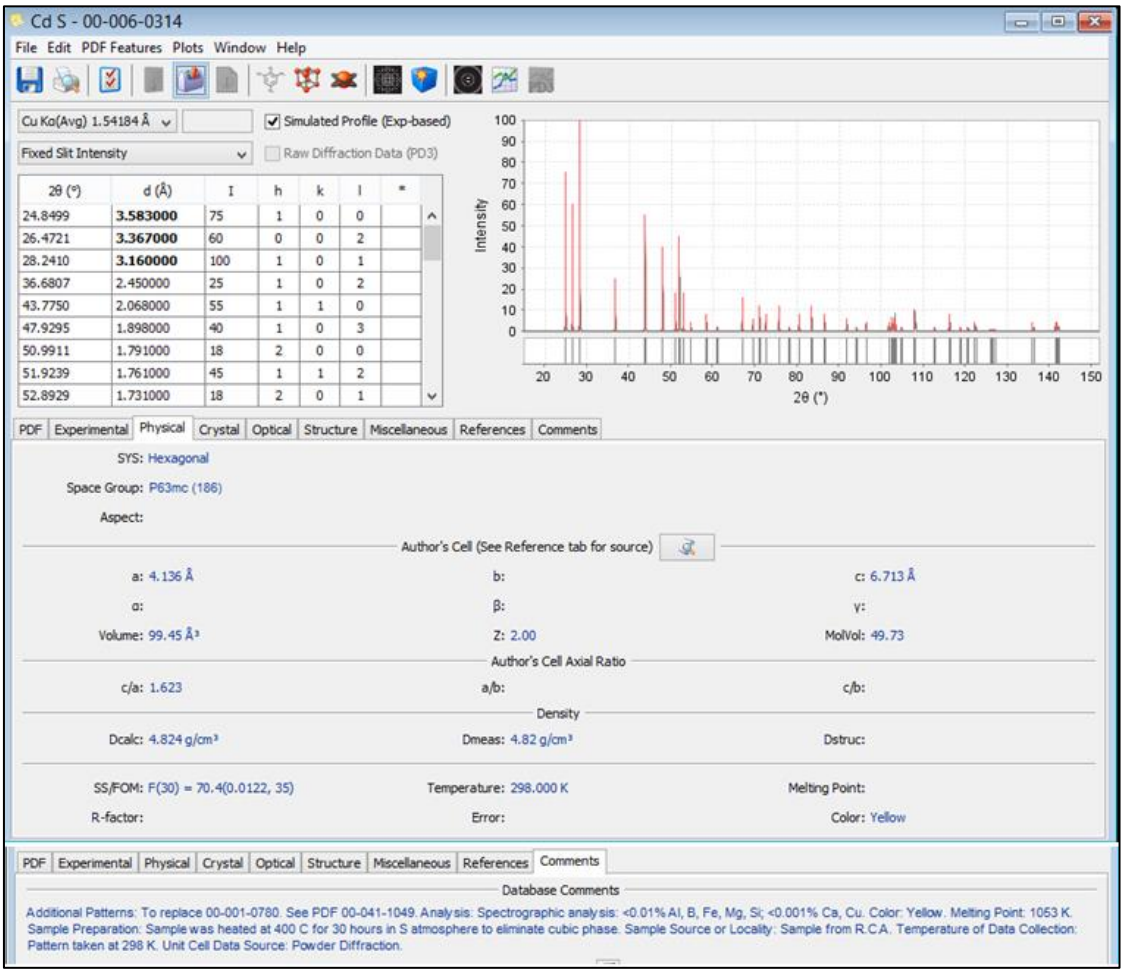

Figure 3-38: X-ray powder diffraction data file for hexagonal CdS (Greenockite) [3-51]. The X-ray intensities for the data on Figure 3-37 can be compared against those on this card and it can be concluded that the CdS phase is randomly oriented. Reproduced with permission from ICDD. International Center for Diffraction Data.

Figure 3-39: Read camera X-ray photograph of CdS film on PE sample showing the polycrystalline nature of the film. Grains are small and fine, and randomly oriented as indicated by the smoothness of the rings. Individual bright spots are coming from the CdTe substrate.

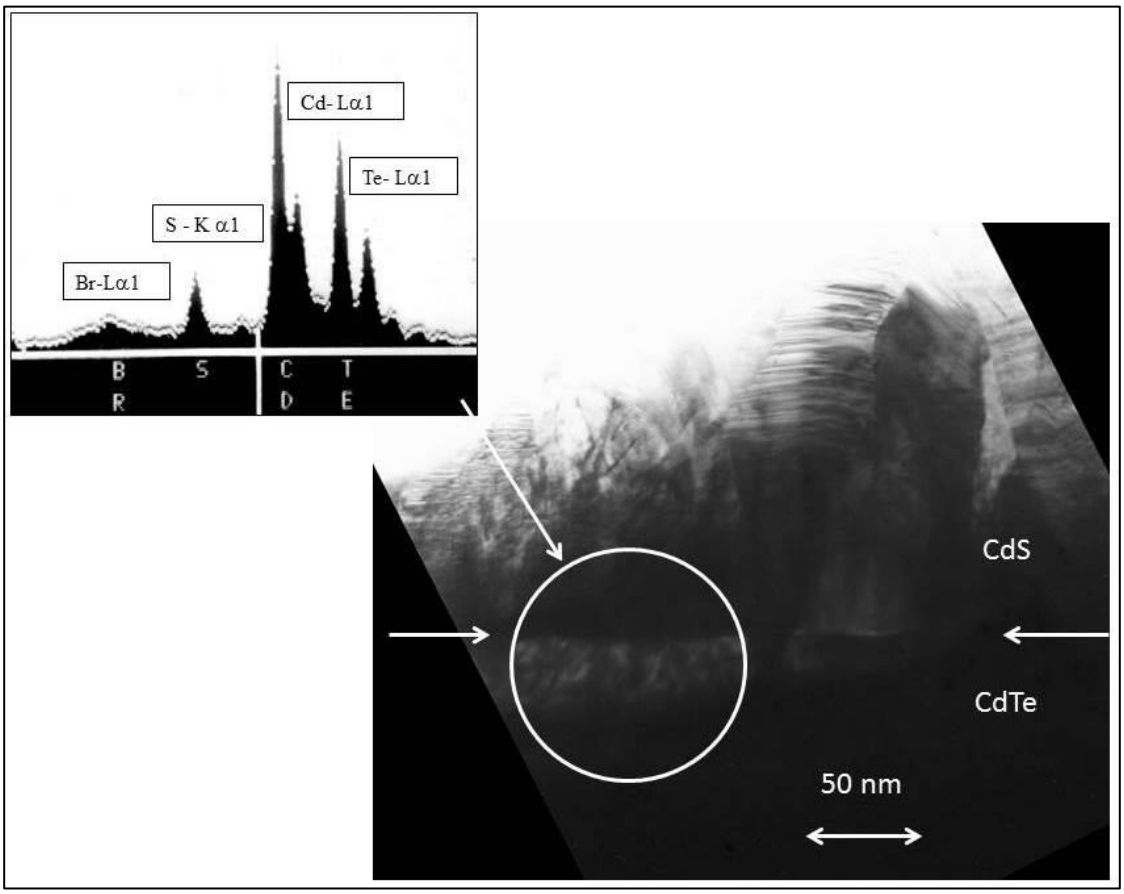

Figure 3-40: BF micrograph of PE **{111}$_{Te}$** specimen. Original CdS film thickness was 1 μm, and the film was ion-milled away in the specimen. Horizontal arrows indicate the location of the interface. EDS spectra taken with ~100 nm diameter probe is shown in the inset, with the circle showing the approximate size of the probe. EDS spectra shows the presence of bromine at the interface. The poor quality of the micrograph was due to the difficulty in obtaining TEM specimen that had both CdS and CdTe thin, with CdS milling much faster than CdTe.

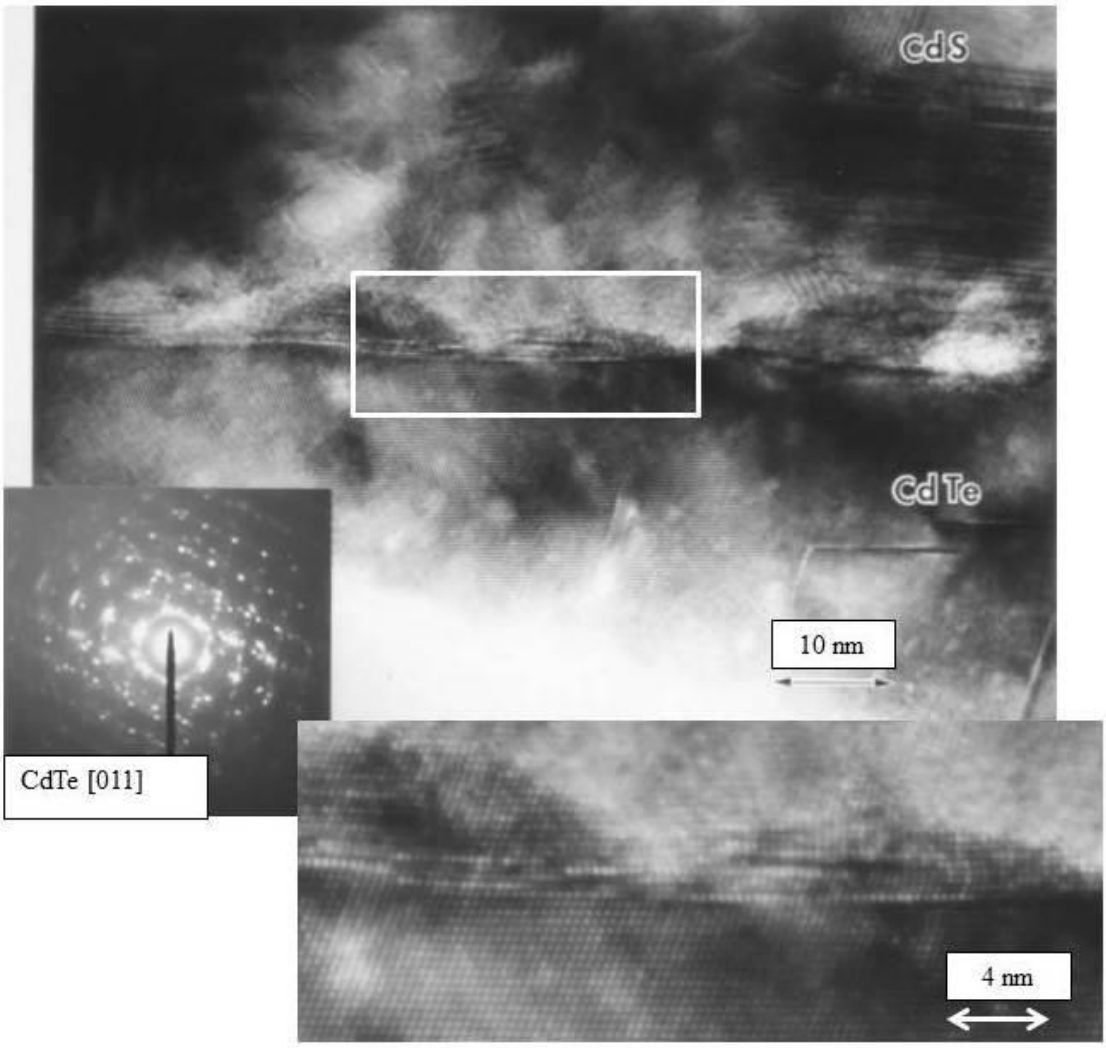

Figure 3-41: HRTEM image of the CdS/CdTe interface for PE sample. Bcause CdS is polycrystalline with random orientation, only some of the grains show lattice fringes. There is a small *island* of epitaxial (0001) wurtzite-like structure at the interface (inset) as well as the cubic phase, but there are many grains with different orientations. There is some correlated structural relationship between the CdS grains and CdTe near the interface as indicated by the SADP (inset).

3.4.6: E-Beam CdS on Etched and Heat Treated $\{111\}_{Cd}$ CdTe Substrate-(PEH)

The E-beam evaporated CdS film deposited on the Br_2:MeOH polished and hydrogen heat-treated (111) CdTe sample was very smooth and did not show much visible features under optical microscope examination and by SEM. A BF image of the film showed a large area at least several hundred nanometers in length that was a single-crystal and a few regions with many grains, which were 50 - 100 nm wide. The film thickness was 1 μm, and some of the single-crystal regions were approximatelyt the same size. The large grains were oriented with the basal plane of CdS aligned parallel to the interface. Even the small grains often were aligned the same way.

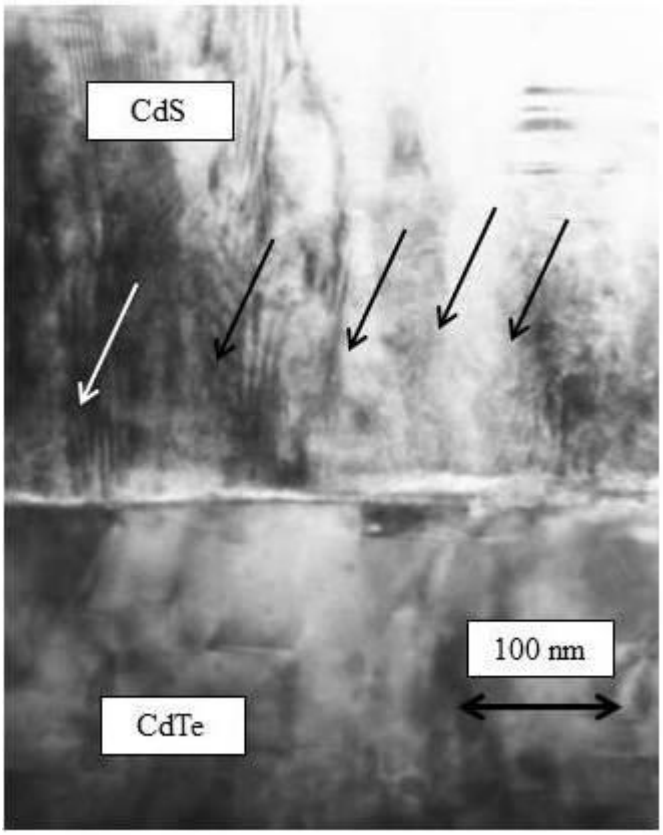

Figure 3-42: BF micrograph of a multi-grained region in the PEH specimen. Most of the grains were much larger, some as large as 1 μm in width. Arrows indicate the locations that are thought to be grain boundaries.

A typical lattice image of the interface is shown in figure 3-43. This image was taken using the a Philips EM400ST operating at 120 kV. For the CdTe, 17 beams were admitted through the objective aperture out to (222) CdTe reflections. Typically, a defocus of 30 to 50 nm was applied beyond the Scherzer defocus condition to obtain high-contrast lattice images. In this specimen, the CdS forms a distinct epitaxial film over the {111} CdTe surface and its structure along the $[2\bar{1}\bar{1}0]$ projection is clearly visible. With the same zone axis indexing used previously with CdS in $[2\bar{1}\bar{1}0]$ zone and CdTe in [011] zone axis orientation, the orientation relationship is (0002) CdS // $(1\bar{1}1)$ CdTe and $[2\bar{1}\bar{1}0]$ CdS // [011] CdTe. When the CdTe is oriented as closely as possible to the [011] zone axis, the CdS $[2\bar{1}\bar{1}0]$ zone axis often was slightly tilted away from its perfect orientation and this affected the CdS HRTEM image. Consequently, it was difficult to obtain clear lattice images for both CdS and CdTe. In the example for the diffraction pattern shown in figure 3-45, the CdS film appears to be oriented approximately 3° away from the exact $[2\bar{1}\bar{1}0]$ orientation toward $[0\bar{1}12]$ direction. This tilt of the CdS lattice with respect to the CdTe varied between 3 to 9° from one location to another as determined from the diffraction patterns. The unusual light to dark alternating contrast seen in the (0002) planes of CdS is likely due to this misorientation of CdS from the exact zone axis. Even though the surface of the CdS film was featureless by optical microscopy and by SEM, the film must exist as subgrains on CdTe, each with some misorientation with respect to the CdTe. This is shown in the BF micrograph in figure 3-46. The slight tilt of the CdS lattice presumably exists to accommodate lattice mismatch. Examination of a much larger specimen area in plan view of the CdS film would have revealed the exact nature of this arrangement as was done with the a CE {112} specimen, but was not performed for this specimen.

The interface shown in figure 3-43 is smooth, but there are several areas that have defects in the CdS side of the interface, for example on the left side of the micrograph. More detailed micrographs are shown later. The CdS film contains many stacking faults. Area density of these defects over small sampling area inherent in the HRTEM images translates to approximately $6 \times 10^{10}/cm^2$. It should be mentioned that

more typically, the stacking fault density is defined as stacking fault length over unit area. This requires that length of each stacking fault to be measured and this is not so easily accomplished with HRTEM images such as in figure 3-43. The termination point of each fault is not easily determined. If one assumes that the length of the faults as seen in figure 3-43 are approximately 10 nm in length, the stacking fault density becomes 6 x 10^6 /cm. Many of them are extrinsic faults and examples are circled in figure 3-43. Enlargement of these two areas are shown in figure 3-44. Stacking faults in the basal plane of hexagonal wurtzite structure can have intrinsic and extrinsic stacking as it is the case in cubic sphalerite structure. There are two types of intrinsic stacking fault, the first type involve one breach of the wurtzite stacking rule where they exhibit the stacking sequence of ABABCBCBC. The second intrinsic fault type involves two breaches of the wurtzite stacking sequence and has the sequence of ABABCACAC. The extrinsic stacking fault involves three breaches in the wurtzite stacking sequence and has the stacking sequence of ABABCABAB [3-53]. For the intrinsic stacking fault, the fault is formed by the change from one hcp lattice to another one, i.e. from AB stacking to BC or AC. For the extrinsic fault, it is formed by insertion of an extrinsic layer, i.e. a C layer in an AB sequence. In the case of first intrinsic fault case, the termination results in Frank type dislocation with Burger's vector of $\mathbf{b} = a_o/6[20\bar{2}3]$, the second intrinsic type fault will terminate with Shockley type partial dislocation with Burger's vector of $\mathbf{b} = a_o/3[1010]$. For the extrinsic type fault as shown in figure 3-42, the Burger's vector witll be $\mathbf{b} = \frac{c_o}{2}[0001]$ which is the Frank type dislocation which was described earlier in chapter 1 in figure 1-65.

In figure 3-42 and in the additional HRTEM image shown in figure 3-47, the abruptness of the interface can be determined accurately to within two image spot spacings, or 0.74 nm, which is aided by the fact that CdS now has the wurtzite structure which makes it distinct compared to the cubic CdTe structure. Figure 3-47 shows a region that has a step or a ledge in the CdTe $(1\bar{1}1)$ surface that causes considerable disruption in the CdS lattice. The CdS in this region contains several extrinsic stacking faults, and the lattice is highly distorted along the (0002) planes. Even in the smooth region of the interface on the right side of the image, the CdS film contains extrinsic

faults near the interface which cause distortion in the (0002) lattice for approximately 5 nm into the CdS film.

For figure 3-47, the lattice image is clear enough for both CdTe and CdS to be able to count the number of planes on both sides over an extended distance along the interface. A total of 100 planes of CdS $(01\bar{1}0)$ and CdTe $(\overline{11}1)$ were counted along the interface. When the two planes were matched at the end of 100 counts, there were 10 more CdTe $(\overline{11}1)$ planes. The ball and stick model of the interface is shown in figure 3-48. This time, the CdS and CdTe lattice is drawn approximately to scale. The projection of CdTe $(\overline{11}1)$ planes to the CdTe $(1\bar{1}1)$ which is the interface plane makes spacing of 0.404 nm as shown in the figure. This spacing then is to be matched to CdS $(01\bar{1}0)$ planes which has a spacing of 0.358 nm. Using these two values then, the lattice misfit for CdTe $(\overline{11}1)$ and CdS (0110) planes becomes 12.8%. An interesting aspect of this lattice mismatch is that there is no obvious indication of lattice distortion on CdS $(01\bar{1}0)$ or CdTe $(\overline{11}1)$ lattice planes that is associated with the mismatch or misfit dislocations in the CdS side of the interface. The misfit dislocations are not observed. There are defects that exist along the interface that may be accommodating the mismatch but it is not clear from the image how this might occur. In some areas as in the inset image, there are extended distances (30 planes) where the interface appears perfect and there is one to one matching of the CdS and CdTe planes.

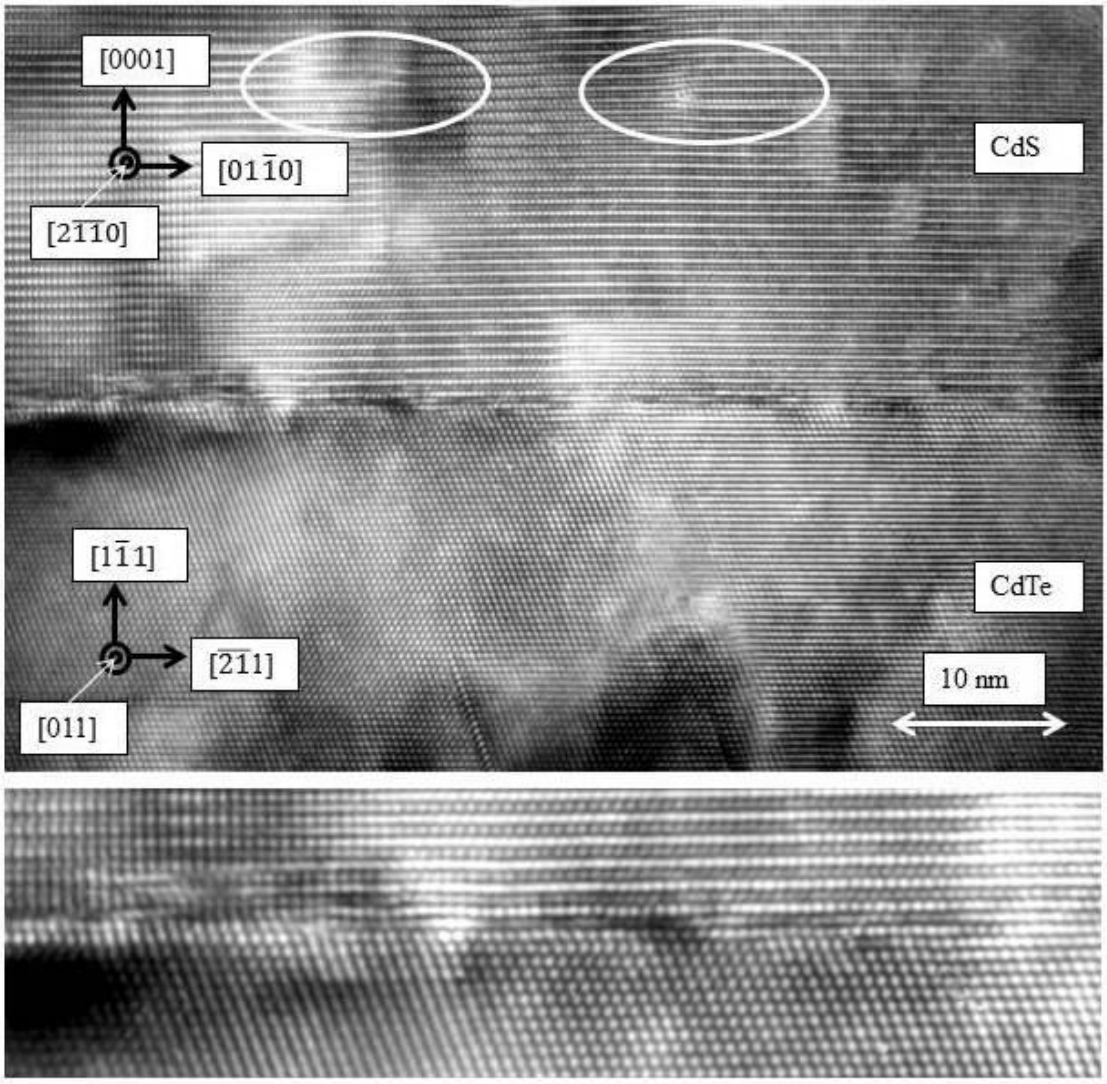

Figure 3-43: HRTEM image of E-beam CdS on PEH CdTe substrate with {111} orientation. The orientation relationship is (0001) CdS // (1$\bar{1}$1) CdTe; [2$\bar{1}\bar{1}$0] CdS // [011] CdTe. Enlargement of the interface is shown below in the inset. The interface is very smooth and abrupt over the entire distance. The circled region indicates areas with extrinsic stacking faults in the CdS film. Enlargemnt of the circled area is shown in figure 3-43. Alternating light/dark contrast of the basal planes in the CdS film is thought to be due to the slight misorientation of the CdS lattice from the perfect [2$\bar{1}\bar{1}$0] zone axis when CdTe is in [011] zone axis.

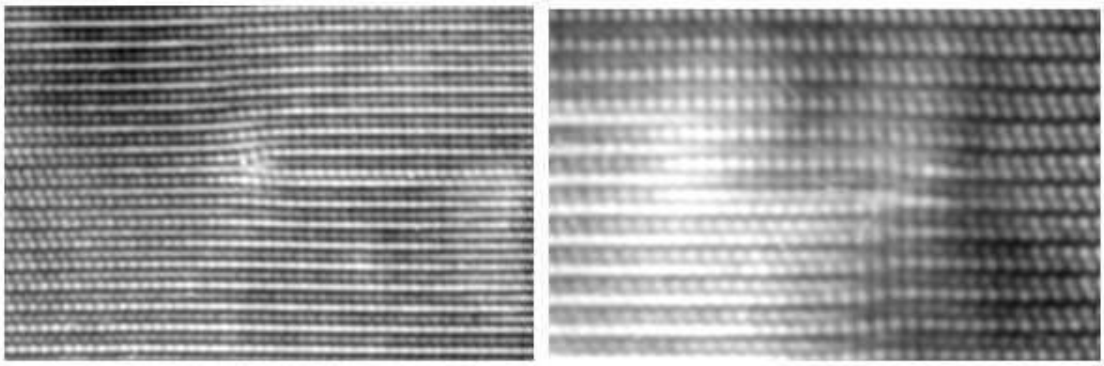

Figure 3-44: Enlargement of CdS film from previous figure 3-43, showing the extrinsic stacking fault in the film. Burgers vector of the dislocation is $\vec{b} = \frac{c_o}{2}[0001]$, a Frank-type dislocation.

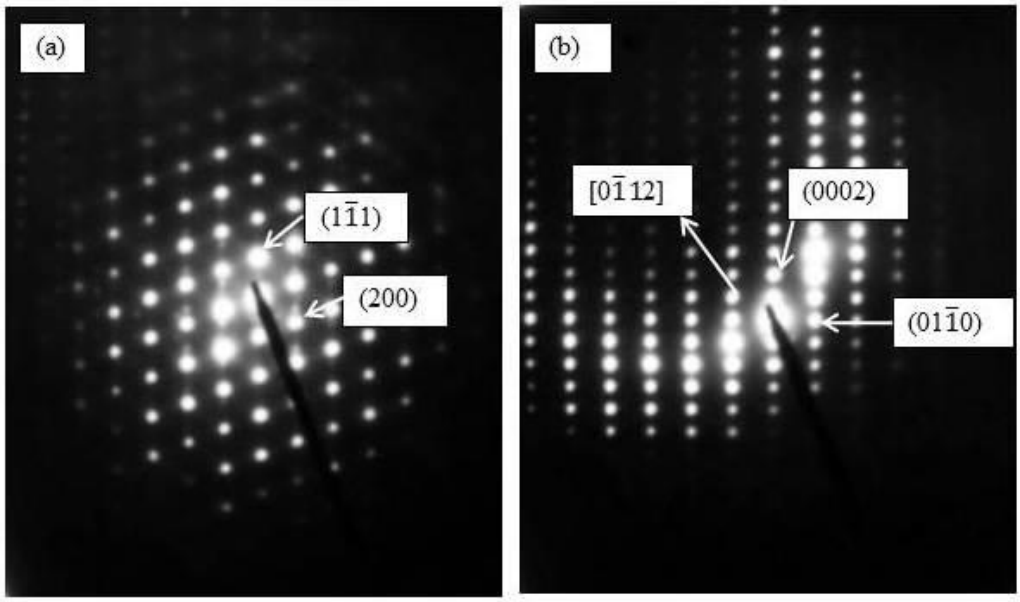

Figure 3-45: Diffraction patterns from CdTe (a) and CdS (b) for e-beam evaporated CdS deposited on PEH {111} CdTe. SADP's were obtained individually from CdTe and CdS, with CdTe oriented at the [011] zone. The two SADP's are oriented properly with respect to the image in figure 3-43. The CdTe pattern has a small amount of CdS reflections contained within it. Indication of the Ewald sphere in (b), from the ring of bright reflections, can give measurement of the misorientation of CdS from the perfect $[2\bar{1}\bar{1}0]$ zone axis. In the above example, CdS $[2\bar{1}\bar{1}0]$ zone axis is tilted along the $[01\bar{1}2]$ direction as indicated in (b) by approximately 3°.

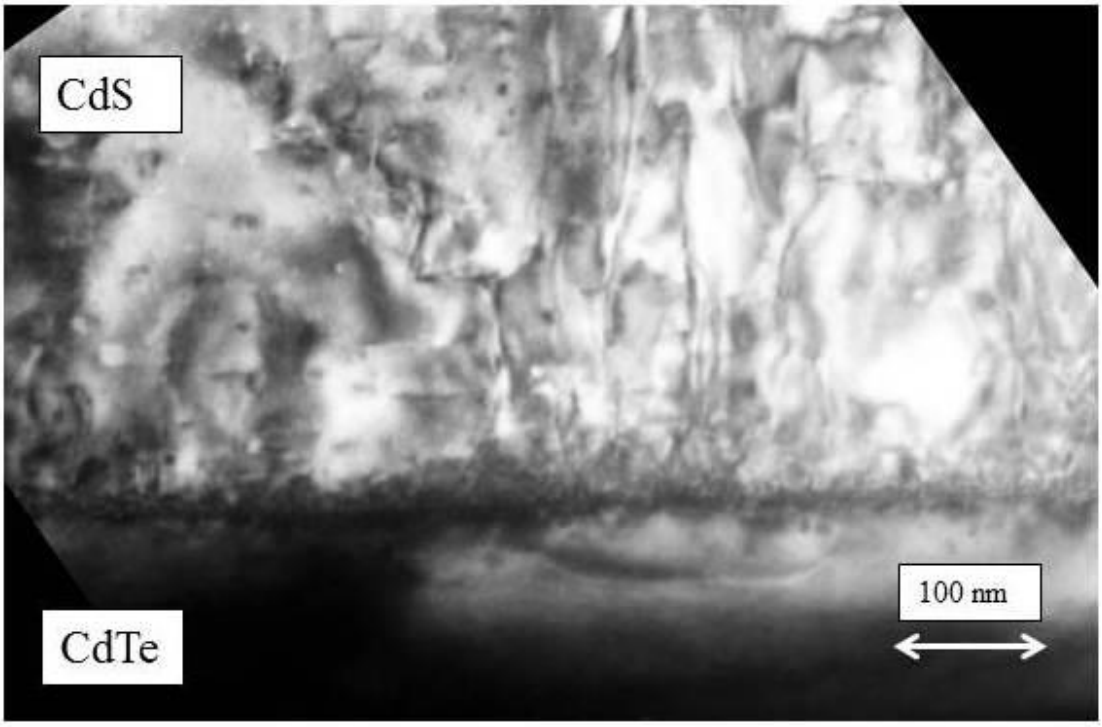

Figure 3-46: BF micrograph of the CdS/CdTe interface. CdS has a large area where it is single crystalline, but in some areas (center), there are subgrain-like structures, which are at slightly different orientation with respect to the neighboring regions.

The ball and stick model in figure 3-48 is just one of many possible configurations of the interface that can be drawn. In this figure, the CdTe surface terminates with Te atoms in the *shuffle* plane as was previously described in figure 1-42 in Chapter 1. It is thought that termination in the shuffle plane is more thermodynamically stable since there is only one dangling bond that comes out of each Te atom in this arrangement. With the Te in the shuffle position, the first layer of CdS will have a Cd atom attach itself to the Te atom. The choice of which plane to examine for the bonding across the interface is somewhat arbitrary, but the obvious low index planes will be CdTe $(\bar{1}\bar{1}1)$ planes which make an angle of 70.53° with the interface with CdS $(01\bar{1}0)$ planes. The added complication in trying to understand the misfit is the slight tilt of the CdS lattice with respect to the CdTe lattice as seen in the SADP and in the HRTEM images, and the projection yields nothing about the misfit into the

specimen, along the CdTe [011] direction. For the projection shown, it might be expected that insertion of an extra CdS $(01\bar{1}0)$ plane should cause distortion in the CdS lattice and in CdTe as well, but such distortion was not observed. To explain this phenomenon, it may be necessary to invoke that some form of bond rearrangement is occurring across the interface, and that the lattice is not continuous. This may allow CdS to still achieve *epitaxy* without having to match bond for bond in the CdTe side. This interface may then actually be described as being *incoherent*.

The PEH {111} CdTe surface was remarkable for the atomically clean surface that it had before the CdS deposition, as inferred by the abruptness of the CdTe/CdS interface after the CdS film deposition. A large part of the CdS film is a single-crystalline, with some subgrains that are slightly misoriented with respect to each other but still all epitaxially formed on the CdTe surface. It can be suggested that an H_2 anneal leaves the CdTe surface clean and atomically perfect so that even by low temperature e-beam evaporation of CdS, the crystallographically high-quality film can be grown on the substrate. Imperfections in the CdS lattice occur when there are steps in the CdTe. The CdS film generates stacking faults from such steps as was imaged by HRTEM. Werthen did not identify which {111} surface (Te or Cd face) corresponded to the junction characteristics reported in figure 3-6 for the PEH {111} surface. This specimen is surmised to be $\{111\}_{Te}$ face based on the specimen records. It was noted that CdS grown on $\{111\}_{Cd}$ surface of CdTe grew without visible features while CdS on CdTe $\{111\}_{Te}$ showed large visible areas [3-19, page 108]. The specimen provided for analysis for this section fits the description for the $\{111\}_{Te}$ surface. The J-V characteristics for the specimen were some of the best cell characteristics obtained, with V_{oc} of 0.63 V, and J_{sc} of 17 mA/cm^2. With the 85 mW/cm^2 simulated solar source, the solar efficiency was 7.5%, compared to 6.2% for the PE $\{111\}_{Te}$ sample in figure 3-6. Werthen did not complete a more thorough examination of the effect of the CdTe surface type (e.g., the difference between $\{111\}_{Cd}$ and $\{111\}_{Te}$ surface with different surface treatments) as he did for the Schottky barrier study.

The quality of the CdS/CdTe interface, such as abruptness of the interface and lack of high density of dislocations together with having a hexagonal wurtzite CdS structure apparently leads to better photovoltaic JV characteristics. A higher quality CdTe surface also leads to better Schottky barrier device characteristics as well [3-19, figure 5-16, page 77]. PE process followed by hydrogen heat treatment leads to significantly increased V_{oc} values compared to PE alone, from 0.15- 0.26 V to 0.5 V after hydrogen annealing. In more recent work on CdTe {111} characteristics based on STM, it was noted that the $\{111\}_{Cd}$ surface is more stable, and has less surface reconfiguration under various surface treatment condition [3-54]. It is possible that Werthen might have seen better junction properties from the $\{111\}_{Cd}$ surface if he had measured it.

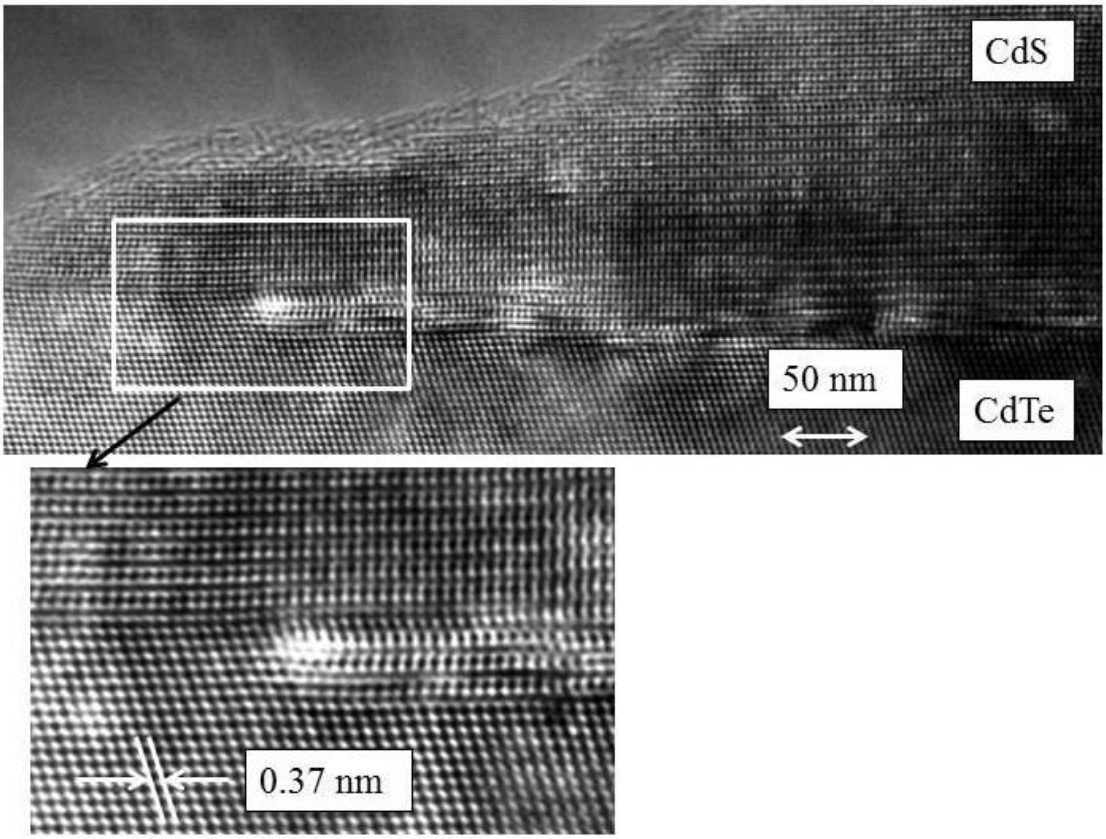

Figure 3-47: HRTEM image of PEH {111} CdTe /CdS specimen, showing details of the interface. The inset area has a step in the CdTe where the CdS lattice forms extrinsic stacking faults. There is considerable distortion in the lattice around the step. When CdS $(01\bar{1}0)$ planes are counted against CdTe $(\overline{1}\overline{1}1)$ planes as indicated in the inset image, there are extra CdS planes for every ~10 CdTe $(\overline{1}\overline{1}1)$ planes. In some areas such as on the left side of the inset image, there is no apparent distortion of the CdS lattice with the extra $(01\bar{1}0)$ plane. In the region shown above, the CdS lattice is tilted by approximately 1° with respect to the CdTe $(1\bar{1}1)$ plane.

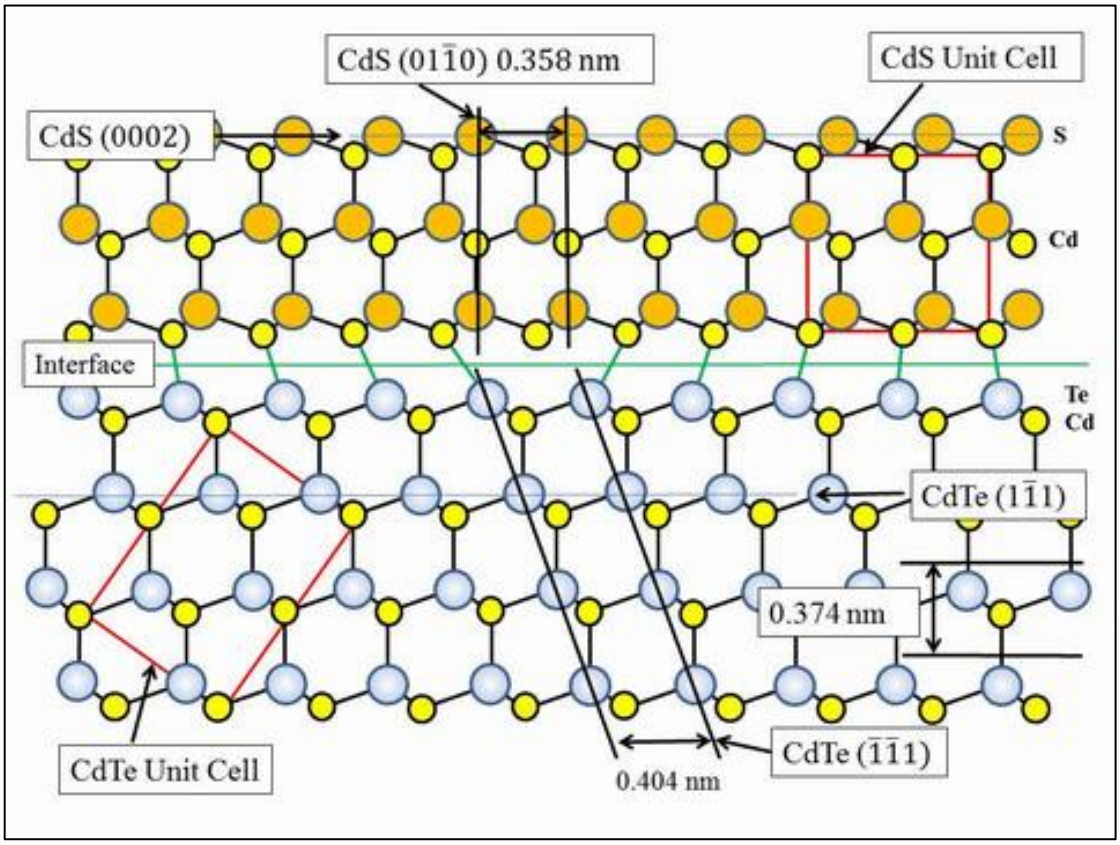

Figure 3-48: A model of CdS (0002) plane matched to the CdTe (1$\bar{1}$1) surface in the CdTe [011] and CdS [2$\bar{1}\bar{1}$0] projection. In this diagram, CdTe ($\bar{1}\bar{1}$1) planes extends into the CdS (01$\bar{1}$0) planes. The width of CdTe ($\bar{1}\bar{1}$1) planes projected onto the CdTe (1$\bar{1}$1) surface will be 0.404 nm, whereas CdS (01$\bar{1}$0) plane spacings are 0.358 nm. The lattice mismatch between CdS (01$\bar{1}$0) planes and CdTe ($\bar{1}\bar{1}$1) planes will be 12.8%. The interface is constructed with a Te face on the CdTe placed in the shuffle plane. The cadmium atoms are the first to form the plane of CdS on the Te face of the CdTe. The mismatch implies one extra CdS (01$\bar{1}$0) plane for every eight CdTe ($\bar{1}\bar{1}$1) planes.

3.5: HRTEM Imaging of CVD-CdS/CdTe Interface

CdS deposited on a {111} CdTe surface by the CVD method was compared with those prepared by e-beam deposition. The CVD process requires much higher substrate temperatures, approximately 300-400°C compared to approximately 130°C for e-beam evaporation. The CdTe substrate was polished with a Br_2: MeOH solution and hydrogen annealed prior to CdS deposition. H_2 gas also is used as a carrier gas during deposition; in effect, the CdS film growth takes place in a reducing atmosphere. The best CVD CdS/{111} CdTe cells typically have V_{oc} of 0.6 - 0.7 V and J_{sc} of 15 - 17 mA/cm^2, and a fill factor of 0.70. Such a solar cell had an efficiency of 8.4% [3-20]. Nishimura worked exclusively with oriented {111} CdTe wafers for CdS/CdTe junctions, and kept track of which face was used, $(111)_A$ or Cd and $(111)_B$ or Te face. Although the $(111)_{Te}$ surface had a higher growth rate for CdS, the electrical properties of the junction did not matter as much on which face was used. Nishimura used the the $(111)_{Cd}$ surface for most of his work on the junction. X-ray diffraction based on Bragg-Brentano configuration analysis of a very thick CdS film (deliberately made thick) shown in figure 3-49, has only the (0002) and (0004) reflections, indicating that the CdS has a highly preferred (0002) orientation. A small indium signal in the X-ray diffraction pattern is from the contacts made on the CdS film. The indium also appears to be highly oriented. The CdTe (111) reflection appears at the theoretical value, and CdS (0002) reflection has corresponding lattice spacing that is about 3% smaller than the theoretical value of 0.335 nm. A SEM micrograph of the same thick CdS film imaged from the top, shown in figure 3-50 using secondary electrons, clearly shows a preferred growth characteristic of the film. The hexagonal shape of the grains is also another indication of a hexagonal crystal structure of the CdS film. Also note that orientations of each hexagonal grain are all aligned in the same way. The grain size was about the same as the film thickness at approximately 100 μm. A small powder-like material on top of the hexagonal crystals is believed to be residual deposition that took place during cool-down after CVD growth.

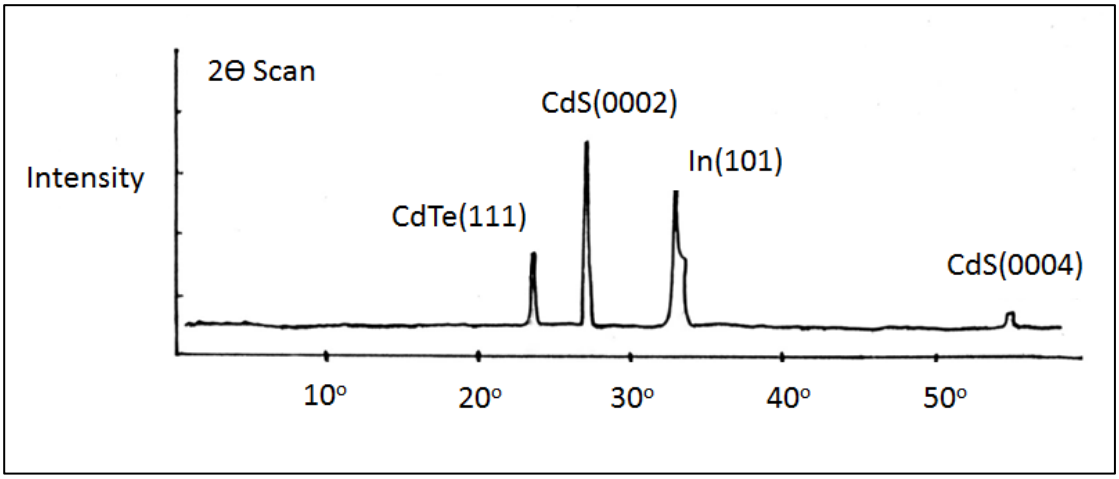

Figure 3-49: X-ray diffraction pattern from CVD-CdS on {111} CdTe. The specimen is for films grown deliberately very thick (~100 μm). A highly oriented film is indicated by the absence of other CdS reflections. The indium peak is from the top contact on the CdS film.

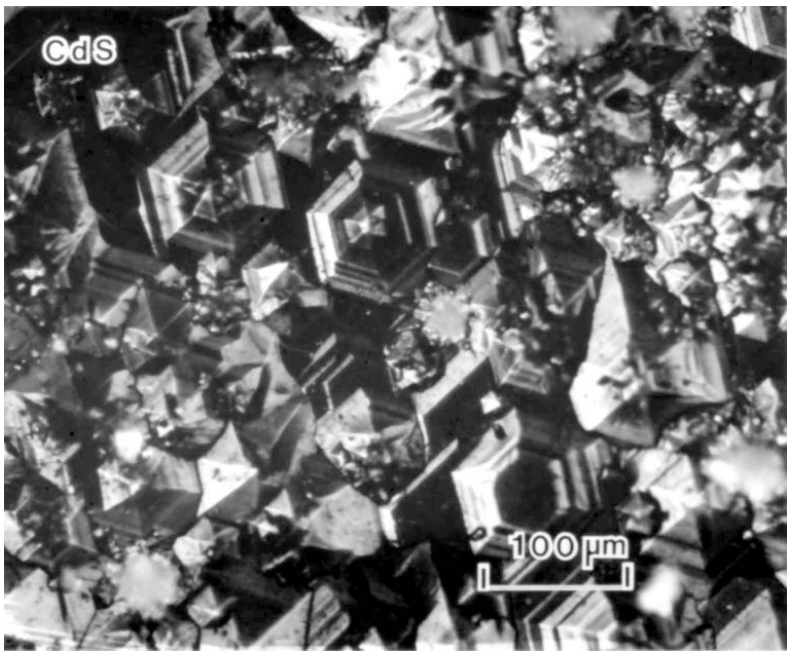

Figure 3-50: SEM micrograph of the surface of CVD-CdS grown on {111} CdTe. The film deliberately is made very thick at approximately 100 μm or more to be able to see the film structure that develops. The grain size in the CdS film is over 100 μm. The image is taken with secondary electrons.

A typical BF TEM micrograph of the CVD CdS/CdTe interface is shown in Figure 3-51.The CdS film was deposited on a $\{111\}_{Cd}$ surface, and the film thickness was 1.9 μm. Based on orienting the diffraction pattern correctly with the image shown in the inset, the substrate surface was approximately 8° off the exact {111} orientation. This was unintentional. The Laue X-ray diffraction method was used to orient the crystal and the (111) wafers were cut from the boule using a wire saw. Some misorientation from the exact (111) direction was easily possible since the wire-saw often did not cut exactly straight. Subsequent surface lapping and polish can also introduce additional misorientation. The crystallographic directions for CdS indexed as the $[2\bar{1}\bar{1}0]$ zone axis and CdTe in the [011] zone axis is indicated in the figure. The image was taken using a Philips EM400ST at 120 kV.

The CdS image contains parallel lines which are thought to be stacking faults on the basal planes of the film based on the streaking in the diffraction pattern. The density of faults based on the BF image comes out to about $10^{10}/cm^2$. This is similar to the e-beam deposited the PEH {111} specimen. The SADP taken from the interface region clearly shows that the orientation relationship is (0001) CdS // $(1\bar{1}1)$ CdTe and $[2\bar{1}\bar{1}0]$ CdS // [011] CdTe the same as in the previous section on PEH {111} specimen. The CdS in the SADP region is essentially a single-crystal, leading to a highly oriented film which is within 1-2° of the perfect alignment between the CdTe $[1\bar{1}1]$ and CdS [0001] directions. Lattice spacings of CdTe and CdS derived from the diffraction patterns is consistent with the standard bulk values for these materials. It was previously mentioned that XRD results for CdS film was about 3% smaller than the theoretical value for the (0002) reflection but the XRD specimen was with CdS film that was deliberately made thick. There are streaks that run approximately perpendicular to the faults that run in the c-axis directions in the CdS film. The specimen was thinned on both sides of CdS and CdTe during ion-milling so that only a sliver of both materials remain in the BF image. A more detailed analysis of the diffraction pattern is made in figure 3-52. The yellow grid is for the CdS $[2\bar{1}\bar{1}0]$ zone axis, and the blue circles are for the CdTe [011] reflections.

The analysis is the same as in figure 3-21 for the CE {112} and PEH {111} in figure 3-44, as the orientation relationship between CdTe and CdS is the same.

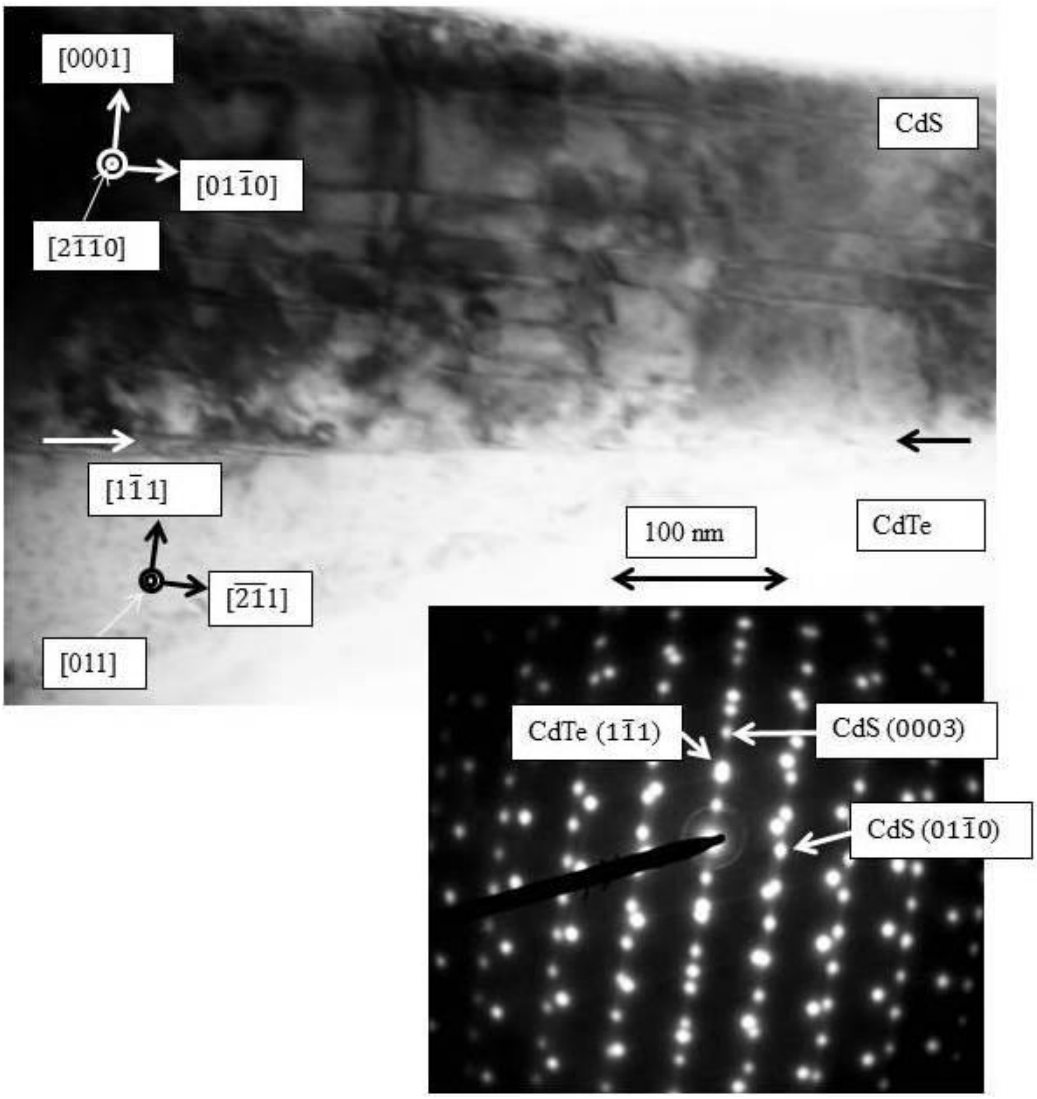

Figure 3-51: BF micrograph of CVD-CdS on {111} CdTe. The diffraction pattern in the inset clearly shows that orientation relationship is CdS(0001)//CdTe(111). It is properly oriented with respect to the BF image. Streaks in the CdS lattice run perpendicular to the faults in the CdS layer. Arrows indicate the location of the interface. Crystallographic directions in the CdS and CdTe are indicated. CdS [0001] is tilted from vertical (by ~8°) due to the CdTe (111) interface being tilted by the same amount.

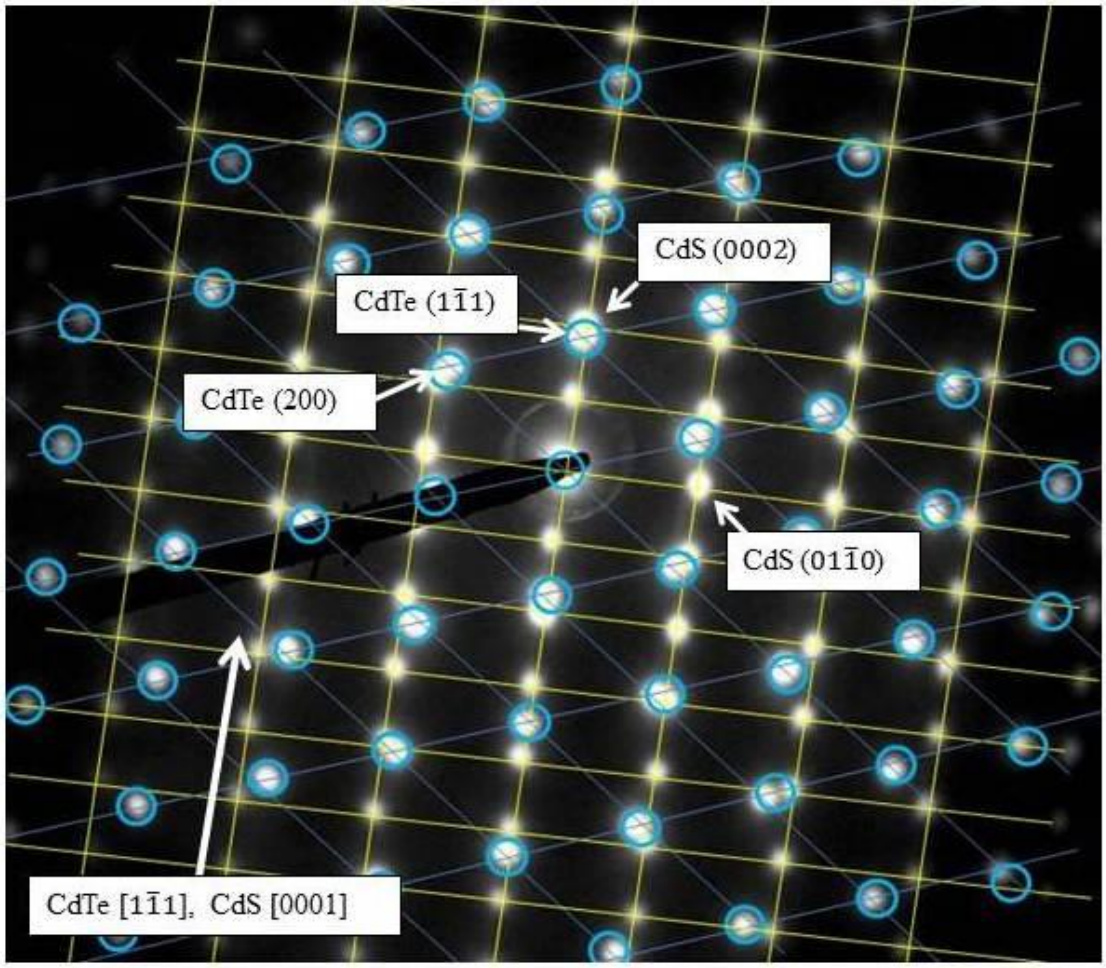

Figure 3-52: Detailed diffraction analysis of CVD CdS on {111} CdTe from figure 3-51. The blue circles indicate the CdTe reflections in the [011] zone axis, and the yellow lines indicates the CdS lattice in the [$2\bar{1}\bar{1}0$] zone axis. The directions of CdTe [1$\bar{1}$1] and CdS [0001] are pointing close to vertical in the figure and are indicated by the large white arrow. The deviation between the two directions is within 1-2°.

An HRTEM image of the interface is shown in figure 3-53. The specimen had been ion-milled further, and the specimen is not very good quality. There is some beam damage (or contamination) or uneven milling evident in the CdS film as seen by blotches of high and low brightness regions. The interface is not very straight, and it

meanders across the micrograph as shown. Overall, the interface is diffuse and slightly tilted. At the right side of the micrograph, the tilt is approximately 8° between the CdTe ($1\bar{1}1$) and CdS (0002) planes. It also is diffuse and disordered in some regions as shown in the enlarged image in the inset. It is possible that such an interface is a consequence of higher substrate temperatures used in CVD CdS deposition compared to the e-beam evaporation (260-400°C for CVD vs. 130-140°C for e-beam evaporation).

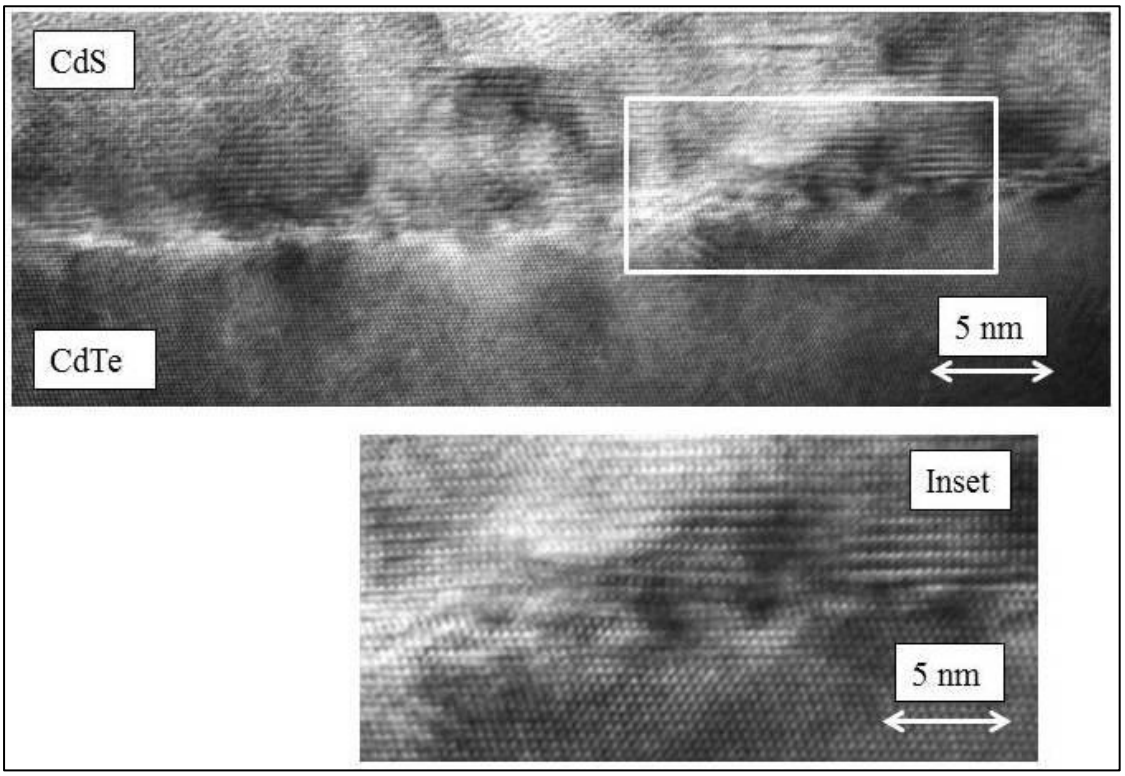

Figure 3-53: HRTEM image of the CVD CdS/CdTe interface. The interface is not smooth, and appears diffuse and disordered as seen in the inset. The CdS film has some variation in orientation, but the TEM specimen quality is not very good which makes interpretation difficult.

Another specimen examined in HRTEM had considerable variability in CdS morphology and in orientation. There were regions of a polycrystalline phase and the interface that was more disordered and diffuse. CdS was deposited on the $\{111\}_{Cd}$ face. This specimen had substrate annealing applied at 620°C followed by CdS deposition at 355°C. The H_2 flow was 120 cc/min. and the CdS film thickness was 1.9 μm. The junction characteristics were poor, with J_{sc} of only 2.62 mA/cm^2 and V_{oc} of 0.76 V, a fill factor of 0.71 and solar efficiency of only 1.8%. Other characteristics such as CdS film resistivity were normal compared to other cells. The low J_{sc} is characteristic of a low collection efficiency, often due to a high recombination rate. The HRTEM image from this specimen is shown in figure 3-54. In this image, CdS film has [0001] direction pointing up in the micrograph, but with a tilt of about 6° from the CdTe $[11\bar{1}]$ direction. There is variability in the direction of the CdS [0001] and the film is composed of ~30 to 50 nm-sized islands. There is a high density of defects in the CdS film, and the interface is complex and diffuse. It is not clear from the image what is really taking place at the interface. There is a region of Moiré -like contrast at the center of the image, and it is not clear whether it is due to the interface that is at an angle to the normal surface, or due to something else. Inclined interface is probably the likely cause.

The diffraction patterns from the above area taken individually from CdS and CdTe are shown in figure 3-55. While the CdTe is in exact [011] zone axis in (b), CdS is some distance away from the exact $[2\bar{1}\bar{1}0]$ zone axis as indicated by the arc of strong diffraction spots (intersection of Ewald sphere with the Laue zone plane) that has its center of the ring some distance away toward the $[0\bar{1}1\bar{1}]$ direction as indicated in (a) but the arrow pointing toward left corner of the micrograph. The actual tilt angle away from the zone axis is about 3.8^o.

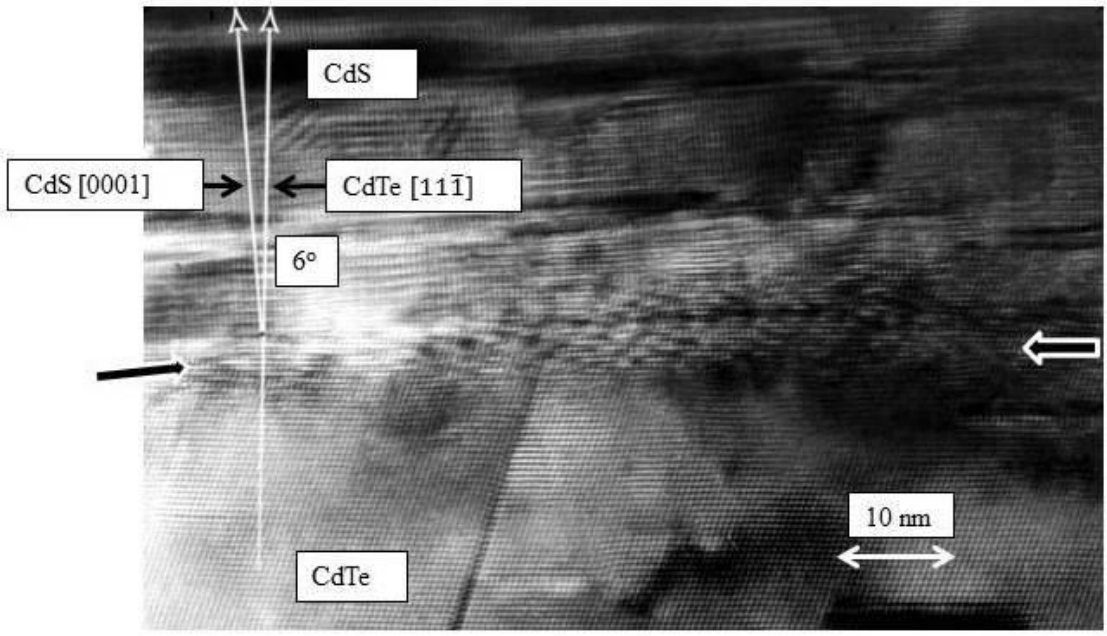

Figure 3-54: HRTEM image of CVD-CdS/CdTe(111) interface. In this case CdS [0001] is tilted by 6° away from CdTe [11$\bar{1}$]. Two black arrows point to the location of the interface, but the exact location is hard to tell.

The second HRTEM image from a different region of the same specimen in figure 3-54 is shown in figure 3-56. The CdS film is generally oriented with [0001] direction pointing up vertically from the interface, but there are local variations in the CdS contrast on the scale of 10 nm which suggests different subgrains or crystals with slightly different orientation. The [0001] direction is slightly tilted by approximately 1-2° from the CdTe [11$\bar{1}$] direction. There are also hemi-spherical, dark features that extend into the CdTe lattice below the interface line. They also have the lateral dimension of approximately10 nm and some have a CdTe lattice structure, while others have a structure that is different. There are lateral stacking fault-like features right at or just above the interface. It is not clear whether they exist in the CdS or in the CdTe lattice. Since CdS is many degrees away from the [2$\bar{1}\bar{1}$0] zone axis, the lattice is not imaged very clearly. If STEM/EELS capability were available, then it would have been possible to determine the chemical composition of these features at this scale to

determine what they are. The diffraction pattern from both CdS and CdTe is shown in figure 3-57. CdTe is close to the [011] zone axis while CdS $[2\bar{1}\bar{1}0]$ zone axis is tilted away along the $[000\bar{2}]$ direction. CdS is rotated by approximately 5° with respect to the CdTe lattice in a counterclockwise direction. This is consistent with the HRTEM image in figure 3-56.

In this specimen, the individual columnar grains of CdS that are growing slightly differently with respect to each other are being sampled by HRTEM imaging. Since the latter images are taken from a highly localized areas of the specimen, it is important to sample as much of the interface as possible in order to obtain a clearer understanding of the interface structure. Unfortunately, this is often not possible with a cross section TEM specimen, as it is usually possible to obtain only two areas that are thin on both sides of the interface across the hole made by ion-milling. The differential milling rate between the two materials also leaves one side too thick to image while the other side is milled away very quickly. Repeated sample insertion into the TEM specimen holder to ion-mill more parts of the cross section specimen to expose additional areas of the interface often leads to specimens falling apart because they are quite delicate. Despite these difficulties, it was possible to observe several different regions with this specimen, and wide variations in morphology were observed. It is tempting to speculate that it is this variability at the interface that may have contributed to the particularly poor light junction characteristics of this cell compared to other cells that were examined.

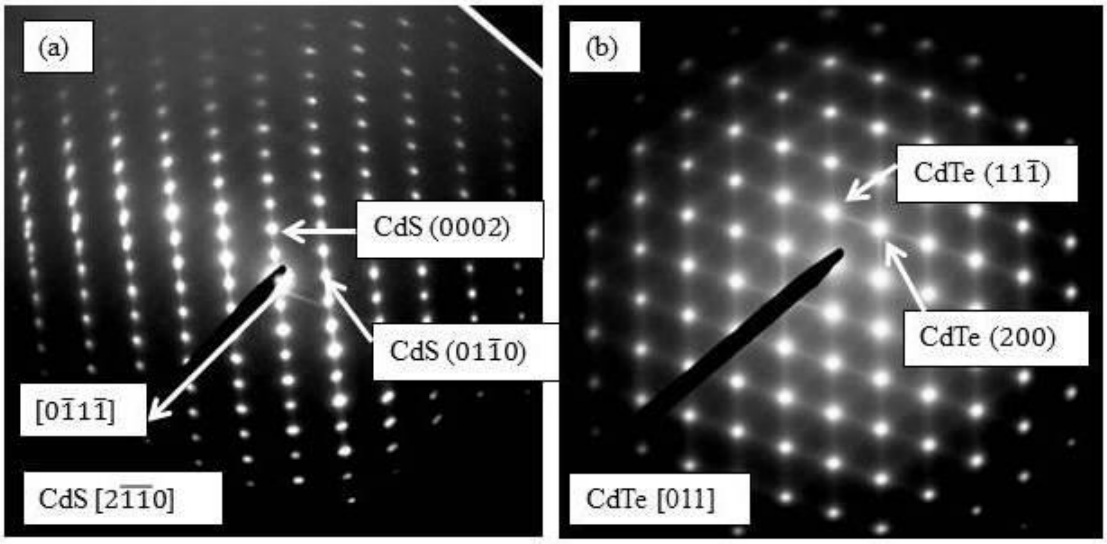

Figure 3-55: Diffraction pattern from CdS (a) and CdTe (b) from figure 3-54. (a) has reduced magnification to show higher order splitting due to several different variants of CdS grains. The CdS is away from the exact $[2\bar{1}\bar{1}0]$ zone axis toward the $[0\bar{1}1\bar{1}]$ direction as indicated by the arrow. The actual tilt is approximately 3.8° away from the zone axis. Diffracation patterns are oriented properly with respect to the micrograph in figure 3-54. Streakes in the CdTe reflections in (b) are due to stacking faults in the two {111} planes that are perpendicular to the [011] projection.

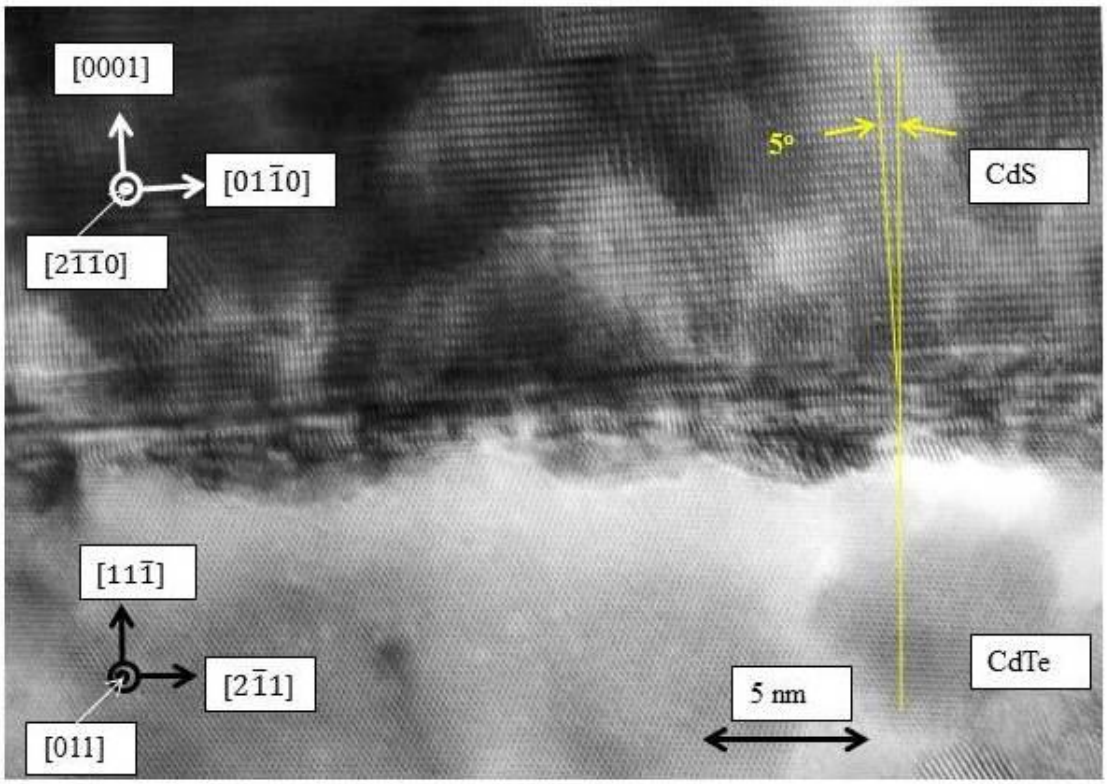

Figure 3-56: HRTEM image of an interface that has hemi-spherical features that penetrate into the CdTe side of the interface. The interface also contains faults, but it is not clear whether they are in the CdTe or in the CdS layer. The CdS [0001] direction is tilted by approximately 4° from the CdTe [11$\bar{1}$] direction.

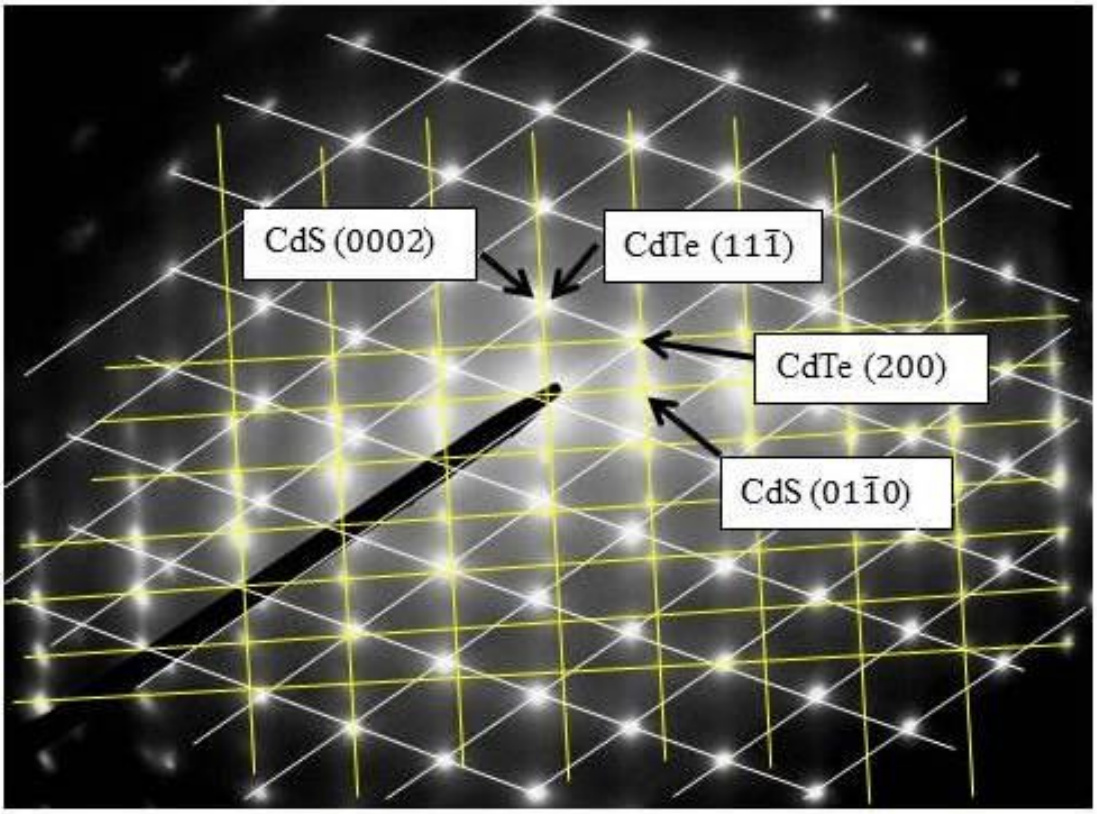

Figure 3-57: Diffraction pattern from figure 3-56, for both CdS and CdTe. The white grid mark the CdTe reflections while CdS is marked with a yellow grid. The CdS lattice is rotated counterclockwise with respect to the CdTe lattice in the above figure by approximately 6°. CdTe is at the [011] zone axis while the CdS [$2\bar{1}\bar{1}0$] is off axis. The center of the Laue zone for CdS [$2\bar{1}\bar{1}0$] is tilted away by about 2.8°.

3.6 Summary of HRTEM Results on CdS/CdTe Heterojunction Interfaces

1. Five different heterojunction cells made with e-beam deposited CdS on various CdTe surfaces were examined by HRTEM method. The CdTe surface types were as follows: C {110}, CE {110}, CE {112}, PE $\{111\}_{Te}$ PEH $\{111\}_{Te}$.

2. C {110} and PEH $\{111\}_{Te}$ specimens had the cleanest and sharpest interfaces between the CdS film and the CdTe substrate surface showing epitaxy between the CdS and CdTe lattices. Both films were largely single-crystalline films. C {110} had the cubic phase (sphaelite) CdS while PEH $\{111\}_{Te}$ had the hexagonal (wurtzite) phase CdS. A cleaved surface and heat-treatment after etching leaves a clean CdTe surface that is free of interface contaminants that could disrupt the epitaxy. This occurs even though the CdTe surface is still exposed to air before CdS deposition. No surface cleaning was carried out in a vacuum before e-beam deposition of the CdS film.

   All three etched surfaces resulted in hexagonal wurtzite phase CdS films, with varying degrees of crystallinity and crystalline perfection. CE {110} had a mixed morphology, with a polycrystalline CdS film with some areaa showing an epitaxial relationship with the substrate. There was evidence of a new phase that had formed on the CdTe surface prior to CdS deposition in the HRTEM image. The CE $\{111\}_{Te}$ had a random polycrystalline CdS film. A small bromine signal was detected by EDX at the interface, which suggests residual bromine or a bromine compound there. The CE {112} sample was an oddity, the first specimen showing a CdS film with a single-crystalline hexagonal wurtzite structure with no evidence of an interfacial compound in the HRTEM image. The orientation relationship for this specimen was $(01\bar{1}9)$ CdS // $(01\bar{1})$ CdTe; $[2\bar{1}\bar{1}0]$ CdS // CdTe [011]. This film has the CdS basal plane inclined by 17.4° to the substrate surface. A second specimen, which was observed only in plan view, had the orientation relationship of $(01\bar{1}0)$ CdS // $(\bar{1}12)$ CdTe; [0001] CdS // $[11\bar{1}]$ CdTe. In this configuration, the CdS c-axis lies in the substrate

plane. Moiré fringe pattern analysis was applied to this specimen, and it was determined that the film formed a mosaic pattern in an epitaxial relationship with the {112} CdTe surface, with a grain size of 20 to 50 nm, and grain rotation between 4.3 to 6.6° within the area that was measured.

3. The {112} cleaved and etched surface was a special case, where the CdS film formed with an unusual epitaxial orientation relationship with CdTe. Apparently, the {112} surface is not very susceptible to etching (and oxidizing) by the Br_2:MeOH etching solution. This can be said because in the other orientations such as {110} and {111}, Br_2:MeOH etching leaves some contaminants or oxide layer which disrupt the CdS epitaxy. For {112} surface, there were no evidence of such layer and the CdS film formed epitaxially over the CdTe surface.

4. Photovoltaic measurements were not done on all the specimens that were analyzed by conventional TEM and HRTEM methods. Therefore, only partial conclusions can be drawn about the relationship between the observed structure and electrical properties. Electrical properties were measured on only the following specimens: C {110}, PE $\{111\}_{Te}$, PEH $\{111\}_{Te}$.

   C {110} had a high V_{oc} with a low J_{sc} and fill factor. The low J_{sc} and fill factor are very detrimental to the light junction performance. This poor performance was ascribed to high series resistance for the cell by Werthen [3-19]. This likely comes from the higher resistivity of the cubic phase CdS film. Werthen only reported that the resistivity value was > 1 Ω-cm. PE $\{111\}_{Cd}$ and PEH $\{111\}_{Cd}$ films had a resistivity of 0.01 Ω-cm. PE $\{111\}_{Te}$ had a resistivity of 0.5 Ω-cm, and visible grain structure on the surface of the CdS. The resistivity of PEH $\{111\}_{Te}$ film was not mentioned. Based on available evidence then, it is likely that single-crystal CdS (hexagonal) film has a lower film resistivity, while the polycrystalline phase has higher values, which would be expected due to grain boundary scattering of charge carriers. Stacking faults in hexagonal CdS

structure creates local cubic atomic structure; hence, it might be expected to cause higher resistivity in the film if there was high density of stacking faults.

The PE $\{111\}_{Te}$ specimen had a high J_{sc} and fill factor, but a low V_{oc}. With everything being equal, the quality of the CdS films such as grain size and preferred orientation can affect V_{oc} by changing the collection efficiency of carriers [3-55, page 129]. Larger grain size and oriented columnar growth are also associated with improved J_{sc} and V_{oc}, and an epitaxial CdS film (e.g., single-crystalline) can have excellent low film resistivity. An epitaxial CdS film on GaAs grown by closed spaced vapor transport (CSVT), for example, show resistivity between 0.01-0.05 Ω-cm with moderate substrate heating of approximately 400°C [3-56, page 299]. Therefore, the PEH $\{111\}_{Te}$ film with good epitaxy and a single-crystalline film had the best light junction properties, with J_{sc} of 18 mA/cm^2, V_{oc} of 0.63 volts and solar efficiency of 7.5% using an 85 mW/cm^2 solar simulator. With the current AM1.5G standard using a 100 mW/cm^2 solar spectrum [3-41], the performance would have been proportionally higher.

5. Heat treatment of the Br_2:MeOH etched surface in H_2 is very effective in cleaning the CdTe surface so that the CdS film can grow epitaxially as indicated by the HRTEM analysis of a PEH $\{111\}_{Te}$ specimen. The lattice mismatch for CdS $(01\bar{1}0)$ and CdTe $(\bar{1}\bar{1}1)$ planes across the CdTe $(1\bar{1}1)$ surface is 12.6%. Despite this large value, the CdS $(01\bar{1}0)$ planes appear largely unaffected despite the fact the required number of extra CdS planes are present. CdS film does not show locally strained lattice which might be indicative of the presence of misfit dislocations at the interface. This suggests that the interface is not necessarily coherent. The lattice misfit must be still accommodated which does not involve actual tetrahedral bonding across the interface between CdTe and CdS, otherwise there will be high density of dangling bonds at the interface. In order to understand the mechanism that is at play in this interface, an atomic resolution imaging of the interface together

with chemical mapping at atomic scale are probably necessary to shed more light on the issue.

6. For CVD CdS/CdTe junction cells, fewer specimens were examined compared to the e-beam CdS films. Only the specimen having $\{111\}_{Cd}$ substrate surface was examined. All of the TEM specimens showed a hexagonal CdS film structure, with strong preferred orientation with a [0001] CdS growth direction. CdS had large grains or subgrain structure with a varying degrees of misorientation with respect to the CdTe {111} substrate plane. The interface was considerably more disordered compared to the PEH {111} specimens made by e-beam deposition. More disordered interface seen in the CVD specimen may be due to the higher substrate temperature used in CVD CdS deposition at 300 and 355°C for the specimens that were examined versus 135°C used for the e-beam evaporation. The specimen prepared at 355°C had particularly poor junction performance and it showed considerably more variation in the structure at the interface.

7. The best light junction performance of CVD CdS/CdTe cells matched or slightly exceeded the performance of the best e-beam CdS/CdTe cells. At first glance, it could be concluded that sharpness or high crystalline quality of the junction interface may not matter as much to the light junction performance, comparing the e-beam CdS/PEH $\{111\}_{Te}$ substrate to the best CVD CdS/$\{111\}_{Cd}$ CdTe cell, or to the presence of some granular structure in the CdS film as opposed to a film with largely single-crystal structure. The junction electrical characteristics of all the cells examined by HRTEM are tabulated in Table 3-5. Some of the parameters were not available. Werthen did not report the A value (diode factor) and J_o (reverse saturation current) for the e-beam CdS specimens. Table 3-6 lists the characteristics observed for each TEM specimen.

Electrical Properties of Solar Cells

Surface Orientation	CdS deposition method	T_{sub}	T_{anneal}	CdTe hole density	A	J_o	V_{oc}	J_{sc}	Fill Factor FF	efficiency η	CdS thickness	CdS resistivity	CdS hole mobility
		°C	°C	(cm^{-3})		mA/cm^2	(V)	mA/cm^2	(%)	(%)	(μm)	(Ω-cm)	$cm^2/V\text{-}s$
C {110}	e-beam	135	NA	$2x10^{16}$			0.632	11.3	47	not reported	1	> 1	30-60
CE {110}	e-beam	135	NA	No data available		→					1	0.01	30-60
CE {112} #1 specimen	e-beam	135	NA	No data available		→					0.35	0.01 *	30-60
CE {112} #2 specimen	e-beam	135	NA	No data available		→					NA	0.01 *	30-60
PE $\{111\}_{Te}$	e-beam	135	NA	$2x10^{16}$			0.435	16.7	73	6.2	1	0.5	30-60
PE $\{111\}_{Cd}$	e-beam	135	NA	No data available		→						0.01	30-60
PEH $\{111\}_{Te}$	e-beam	135	400	$2x10^{16}$			0.645	17.2	60	7.5	1	not reported	30-60
PEH $\{111\}_{Cd}$	e-beam	No data available	→										30-60
$\{111\}_{Cd}$ - high quality	CVD	300	520	$2.2x10^{16}$	1.67	$2.5x10^{-7}$	0.707	15.5	71	7.0	1.9	0.048	9.68
$\{111\}_{Cd}$ - low quality	CVD	355	620	$3.5x10^{16}$	2.64	$4x10^{-10}$	0.796	2.64	53	1.8	1.9	0.026	17.9
$\{111\}_{Te}$	CVD												

85 mW/cm^2 simulated light

C	Cleaved
CE	Cleaved & Etch
PE	Polish & Etch
PEH	Polish, Etch & Heat Treated

* For CE(112), the specimen was assumed to be CE (110)

Table 3-5: Solar cell parameters of CdS/CdTe heterojunctions

Surface Orientation / Treatment	CdS deposition	T_{sub} °C	T_{anneal} °C	Electrical data	TEM data	CdS thickness µm	CdS Phase	Poly/ Single	Orientation	grain size nm
C {110}	e-beam	135	NA	✓	✓	1	Cubic	Single	$(01\bar{1})$CdS//$(01\bar{1})$CdTe; [011] CdS//[011]CdTe	
CE {110}	e-beam	135	NA		✓	1	Hex	Mixed	$(01\bar{1}5)$CdS//(011)CdTe; $[2\bar{1}\bar{1}0]$CdS//CdTe[011]	200-400
CE {112}	e-beam	135	NA		✓	0.35	Hex	Single	$(01\bar{1}9)$CdS//$(2\bar{1}\bar{1})$CdTe; $[2\bar{1}\bar{1}0]$CdS//CdTe[011]	
CE {112}	e-beam	135	NA		✓	NA	Hex	Mosaic	$(01\bar{1}0)$ CdS//$(\bar{1}12)$CdTe; $[0001]$CdS//$[11\bar{1}]$CdTe	20-50
PE $\{111\}_{Te}$	e-beam	135	NA	✓	✓	1	Hex	Poly/Random		50
PE $\{111\}_{Cd}$	e-beam	135	NA				Hex			
PEH $\{111\}_{Te}$	e-beam	135	400	✓	✓	1	Hex	Mosaic (?)	(0001)CdS//$(1\bar{1}\bar{1})$CdTe; $[2\bar{1}\bar{1}0]$CdS//CdTe[011]	50-1000
PEH $\{111\}_{Cd}$	e-beam	135	400							
$\{111\}_{Cd}$ - high quality	CVD	300	520	✓	✓	1 - 2	Hex	Mixed	(0001)CdS//$(1\bar{1}\bar{1})$CdTe; $[2\bar{1}\bar{1}0]$CdS//CdTe[011]	1-2
$\{111\}_{Cd}$ - low quality	CVD	355	620	✓	✓	1 - 2	Hex	Mixed	(0001)CdS//$(1\bar{1}\bar{1})$CdTe; $[2\bar{1}\bar{1}0]$CdS//CdTe[011]	1-2
$\{111\}_{Te}$	CVD			✓						

Table 3-6: List of TEM Specimen and their characteristics

In summary, it can be stated that the CdS/CdTe heterojunction structure is remarkably versatile, producing solar cell efficiency in the 8 to 9% range with relative ease, using a simple and low-cost deposition techniques such as e-beam evaporation and CVD for the CdS film. The CdTe surface can be made remarkably clean using the Br_2:MeOH etch followed by a simple H_2 annealing at moderate temperatures of 400 – 600^oC. The XPS and Auger data taken by Werthen [3-19] support this finding. The CdTe surface can maintain this state for a while in air, for the time it takes to transfer the prepared surface to the deposition system. This suggests that this heterojunction is suitable for the manufacturing process where stringent vacuum conditions often cannot be maintained or that to do so would be very expensive. This is borne out by the success that this heterojunction has had in recent times in commercialization as described in the following section. A CdS film with high transparency and good electrical properties can be made with relative ease as well, and it is well suited for use with CdTe. The hexagonal wurtzite structure of CdS can be made with low resistivity, and it is straight forward to grow with both e-beam and CVD methods. When the CdTe surface is relatively clean with the proper etch and heat-treatment, the CdS film grows epitaxially over the CdTe surface. Even when the CdS film was not perfectly single-crystalline the cell performance did not deteriorate much, suggesting a pathway to produce an all-thin film version of the heterojunction cell which is important for commercialization This, in fact, was achieved in recent years [3-56].

The conventional and HRTEM analyses of the heterojunction interfaces show the complexity of the actual structures made by the deposition methods, using substrates that are more often than not, far from ideal. A proper understanding of the electrical behavior of heterojunction cells require an extensive amount of theory and modeling. However, the typical electrical model of the interface is highly idealized and the TEM analysis quickly shows how different and complex the reality actually is. This in itself is useful so that undue emphasis is not placed on theory and the modeling to explain the practical behavior. The present work also points out many limitations of the TEM analysis for understanding of the interface. One of the key issues is in the problem of sample size. Ideally, several specimens should be examined from parts

having similar electrical properties, to be sure that TEM analysis is consistent from one part to another. However, TEM analysis by its very nature is made difficult by specimen preparation. Not many specimens can be made and examined, and only a very small area about few hundred nanometer dimensions of the TEM specimen can be imaged. Preparation of cross section specimens only exacerbates this problem. Other techniques such X-ray diffraction and surface topographic methods such as SEM and AFM for example can provide additional insights about the specimen. The combination of planar and cross section TEM analysis is also very powerful in obtaining a more complete picture of the microstructure. This was attempted in the present work, but it was successful for only specimen type.

The microstructural analysis must be connected to the electrical properties of the heterojunction cell, as this is the ultimate goal of the TEM analysis. Making this connection is difficult. Not all electrical properties are explainable by microstructure, or by anything that can be seen by TEM. For example, J_{sc} appears to be affected strongly by the CdS phase (cubic or hexagonal) and by the defect density, while Voc appears to be more sensitive to interface condition. Such factors as the presence of contaminants or the quality of the interface in terms of how abrupt it is, appears to affect the V_{oc}. Therefore, the objective must to be set to a limited number of electrical characteristics that can be related to the microstructure. In this situation, it is useful to compare specimens with widely different electrical characteristics that are made nominally the same in most parameters. For instance, the substrate CdTe used all the same dopant characteristics, made from a single boule of crystal and CdS films made the same way using the same starting material to the same thickness. Only a few parameters were changed to observe the effect of those changes to the microstructure of the CdS film, such as the CdTe surface orientation and surface treatments.

One of the key developments in TEM analysis that was not available at the time of this work is the use of EELS and EDX using a sub-nanometer sized electron probe. Being able to probe the chemical composition on a nanometer scale at the heterojunction interface would have greatly added to the usefulness of the analysis. In

addition, the higher resolution capability available on modern microscopes would have provided additional details about the interface structure.

3.7 Current State of CdS/CdTe Heterojunction Solar Cells

Much has happened in the past 30 years or so concerning the technology around CdS/CdTe solar cells. One company, First Solar, has become a major supplier of solar cell panels based on this heterojunction structure. This company based in Tempe, Arizona has a market capitalization of $4.4B as of January 2015, and estimated 2014 sales of $4B. They have become the second largest manufacturer of solar cells in the world. It was started in 1999 and was the first to break the $1/W module cost barrier in 1999, and the cost in 2014 stood at 55¢/W. They had 10 GW of installed base at the end of 2014 [3-57]. Their success is based on perfecting the manufacturing of high efficiency, low cost thin film version of CdS/CdTe solar cells. The company originated with the purchase of a prior company, Solar Cells Inc. (SCI) by the investment arm of the Walton family, of the Walmart fame. Today, First Solar produce modules with efficiencies of approximately 13.4% [3-58] compared to polycrystalline silicon with efficiencies of approximately 15 to 16% and single-crystal silicon at 21.5% achieved by Sun Power, the industry leader in panel efficiency [3-59]. In 2014, First Solar demonstrated cell efficiency of 20.4% on a laboratory device [3-60]. This can be compared to the best laboratory demonstration of 25.6% efficiency for single-crystal silicon achieved in 2014 [3-61]. Cell efficiency and module efficiency must be considered separately because different factors go into the performance. Cost of the module can be influenced by such factors as ease of manufacturing and the manner in which the individual cells must be incorporated into the module.

First Solar's future is somewhat cloudy due to some dramatic changes taking place currently in the solar cell industry. The cost per watt for the silicon-based modules has been falling dramatically, and three manufacturers announced in 2014 that their cost fell below 50¢/W [3-62] below those of First Solar. With the silicon having

higher efficiency compared to CdTe thin film, First Solar must now improve both the cost and efficiency of their cells. The low cost for silicon cells and modules are all being reported by the Chinese manufacturers, and some argue that the cost figure is artificially lowered due to subsidies given to them by the government [3-63].

The basic structure used for the CdTe thin film cells is shown below in figure 3-57 [3-64]. Is is thought that First Solar's film structure is similar, but the details of their construction is a well-kept secret. There are several critical discoveries that have aided the success of the CdS/CdTe heterojunction solar cell. First is the discovery of $CdCl_2$ treatment to the CdTe film by Nakayama et al. in 1976 [3-65]. Post growth CdTe heat treatment in $CdCl_2$ can raise efficiency from 1 to 5% to double digit values for thin film CdTe cells. A second critical step forward in CdS/CdTe structure was made by Chu et al. in 1991 when it became possible to thin the CdS film to 100 nm and lower, and the use of close spaced sublimation method (CSS) to make the CdTe thin film to achieve solar cell efficiency of 13.4% [3-66]. CSS method was developed earlier, but it became important for making CdTe film growth manufacturable. Further gains in efficiency to 16.5% was achieved by Wu et al. in 2001 by using cadmium stannate (Cd_2SnO_4 (CTO)) as transparent conductive oxide (TCO), and inserting high resistivity zinc stannate (Zn_2SnO_4 (ZTO)) buffer layer between the TCO and the CdS film [3-67].

First Solar started to use CSS deposition method with advisory help from Chu, but later adopted a vapor transport method [3-68, 3-69]. The CdTe thickness is approximately 4 μm, and the CdS is 0.3 μm in these references. It should be noted that the same process (called close-spaced vapor transport (CSVT)) was investigated by the Bube group at Stanford for growing CdTe thin films in the early 1980s and CdS/CdTe thin film solar cell with efficiency of 6% was obtained [3-70].

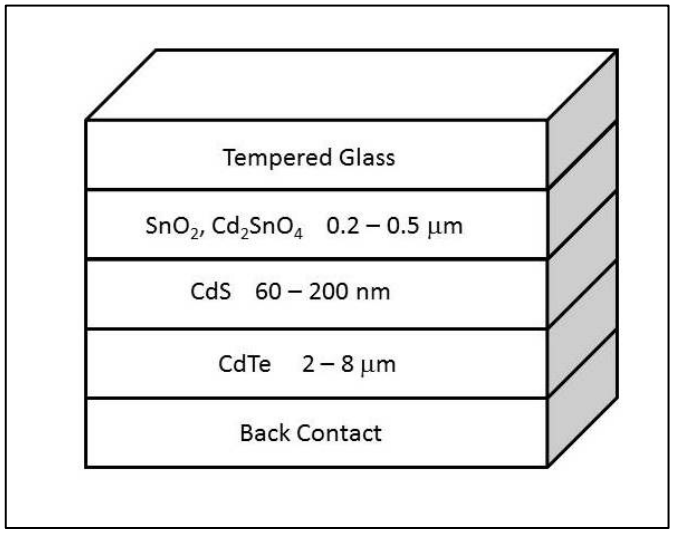

Figure 3-58: Structure of CdS/CdTe thin film solar cell based on ref [3-64].

The structure of the thin film CdS/CdTe heterojunction solar cell as shown in figure 3-58 uses a low cost substrate such as soda-lime glass produced by the float process, which is coated with a fluorine doped transparent conductive oxide (TCO) (SnO_2, Cd_2SnO_4). It is important to note that for the thin film structure, the order of the film deposition is reversed when compared to making a device on a single-crystal. The structure is *upside down* as CdTe absorber layer is at the bottom of the structure, deposited after the CdS film. The light enters the device through the top tempered glass in the above figure. A *buffer layer* of Zn_2SO_4 or ZTO (not shown) is deposited on top of the TCO layer. The buffer layer is a high resistivity SnO_2 that plays a crucial role in being able to thin the CdS layer to approximately 100 nm or lower as previously described, which significantly aids in improving V_{oc} and J_{sc}. Having a buffer layer helps to prevent formation of a short-circuit where CdS coverage is thin [3-71]. Thin CdS can have pin holes where a short circuit can develop between the CdTe and TCO layer during subsequent heat treatment of the structure during $CdCl_2$ treatment which typically occurs at 350 – 450°C. The buffer layer of ZTO also helps with the adhesion between CdS and TCO, which can become weak during $CdCl_2$ treatment process [3-71].

Thin CdS allows more light to be absorbed near the heterojunction region for greater efficiency. CdS can be deposited by CVD, CSS or more recently by sputtering. The CdTe film is then coated by CSS or vapor transport methods. The entire finished structure is then annealed in $CdCl_2$ vapor. It is apparent that $CdCl_2$ is the magic elixir that has been missing in improving the efficiency of the CdS/CdTe junction cells. The exact role that it plays is still an active area of research. A recent review article by Dharmadasa provides insight into the current understanding of the mechanisms involved with the treatment [3-72]. The $CdCl_2$ can cause grain growth in CdTe film but the improvement in cell performance still occurs when there is no grain growth. It is thought that defect passivation and reduction of pinholes in the CdTe film may be also occurring. Oxygen is also required during $CdCl_2$ treatment to be effective. $CdCl_2$ heat treatment is often done in ambient atmosphere condition, and it was also demonstrated that 0.1 mbar of oxygen partial pressure was sufficient to obtain the benefit of $CdCl_2$ heat treatment [3-73]. The role of oxygen is not certain and one of the suggestions is that it promotes formation of CdO at the CdTe grain boundaries to passivate them [3-73]. Grain boundaries in CdTe are thought to be pathway for shunting the device, as evidenced by excess junction current which reduce photovoltages and low fill factors [3-74]. Additionally, Cl (and other halogens) is a known dopant to improve carrier lifetime in CdTe [3- 75]. Typical laboratory thin film cells using the latest methods have V_{oc} of 0.85 V, J_{sc} of 26 mA/cm^2, a fill factor of 76% and cell efficiency of 16.5% [3-64]. These are siginificant improvements from the numbers shown in Table 3-4 for the cells analyzed in the present work.

Being able to make a thin film CdS/CdTe solar cell with high efficiency is what makes it possible to construct low-cost solar cells and this was the ultimate goal of the fundamental work taking place on this heterojunction in the 1980s. It has taken nearly 25 years to make it into a commercial reality. It is hoped that some of the basic work taking place with single-crystal CdTe and deposited CdS, and understanding various aspects of this structure from the electrical and microstructural aspect, helped in obtaining the commercial success that this heterojunction has achieved today in the

marketplace. A summary of the TEM work on e-beam evaporated CdS on single-crystal CdTe was reported in 1983 [3-76].

More recent work on the CdS/CdTe interface was done in 2000 by Boieriu et al., working with CdTe $(\overline{111})_B$ which was deposited on Si (111) by molecular beam epitaxy (MBE) [3-77]. The reason for working with CdTe $(\overline{111})_B$ is that CdS film does not grow very well on the $(111)_A$ surface, forming a rough surface and poor crystalline quality [3-78]. It was not specified what *poor crystalline quality* was meant. The CdTe $(\overline{111})_B$ substrate was prepared prior to CdS film deposition by etching in 0.1% Br_2:MeOH, which passivates the surface. Te on the surface was then removed in the MBE chamber with heat-treatment, exposing a fresh Cd-rich surface. First, a buffer layer of additional CdTe $(\overline{111})_B$ layer 150nm thick was grown, followed by CdS film growth by MBE at substrate temperatures between 150 – 350°C. The CdS film grows with a hexagonal wurtzite structure with the same orientation relationship as was reported in this work, which is $(01\bar{1}0)$ CdS // $(\bar{1}12)$ CdTe and [0001] CdS // $[11\bar{1}]$ CdTe. HRTEM images of the interface were obtained in the CdTe <110> zone axis. Detailed analysis of the interface was not done in this work, but the images presented showed CdS film with some defects, and the interface was defect-free. The situation is complicated by the fact that the buffer layer of CdTe grown just prior to CdS deposition is contaminated by the incorporation of S into the CdTe by as much as 10%. This occurred apparently as a consequence of the process used. It was noted that the interface appeared abrupt between the CdTe buffer layer and the CdS film. Use of MBE and Si coated with epitaxial CdTe provides much more control over the growth of CdS over a very precisely fabricated surface. However, the MBE process itself introduces other variables such as S incorporation into CdTe buffer layer that complicates the practicality of the results to more conventional cell fabrication.

A second article published in 2001 by Yan et al. describes CdTe thin films grown by the CSS method onto a single-crystal CdS (0001) and CdTe (111) substrates [3-79]. The paper is by the National Renewable Energy Laboratory (NREL) group, based in Golden, Colorado which has been a leader in solar cell research for many years. They have spearheaded the work on CdS/CdTe heterojunction cell development.

This work is of some importance as the commercial CdS/CdTe junction cell relies on the use of the CSS method for deposition and CdTe is deposited onto a CdS film. The approach of first growing well-characterized CdTe films by CSS on a single-crystal CdTe, followed by the deposition on single-crystal CdS mirrors the same approach used by Anthony in 1984 in the Bube group at Stanford to develop the CSVT CdTe film growth method [3-56]. Yan et al. showed that CdTe film grows epitaxially on the (111) CdTe substrate using HRTEM. The A or B surface type was not specified for the (111) surface. The substrate temperature for the CdTe film growth was 550°C. Both conventional BF and HRTEM images show high density of planar defects, which by HRTEM indicates that they are region with twins and intrinsic stacking faults. The interface also contained stacking faults, and a region that is completely free of visible features and defects. They claim to have calculated the *formation energy* based on first principles calculation for the intrinsic and extrinsic faults, and "lamellar" twins of 32, 34 and 16 mJ/m^2, respectively. It is not clear what is meant by formation energy and what the first principles calculation is in the paper. Also the definition of lamellar twins is unclear. The twins were in thin sheets few hundred nm wide and few tenths of microns long which ran parallel to the interface based on their BF micrograph. Perhaps the term "lamellar" refers to these thin twin sections. The formation energy must refer to the stacking fault energy.

Yan et al. also grew CSS CdTe films on the CdS (0001) substrate, and showed that CdTe grows epitaxially with the orientation relationship of $[111]_{CdTe} \parallel [0001]_{CdS}$ and $[110]_{CdTe} \parallel [11\bar{2}0]_{CdS}$ based on HRTEM images. Using the convention for defining the epitaxial relationship in the present work, it should be written as (0002) CdS // $(1\bar{1}1)$ CdTe and $[11\bar{2}0]$ CdS // [110] CdTe, which is equivalent to the orientation relationship that was determined for CdS film deposited on (111) CdTe in the present work. They show exceptionally clear HRTEM images of both CdTe and CdS across the interface, indicating a well-oriented CdTe [110] zone with the CdS $[11\bar{2}0]$ zone axis. The HRTEM image shown indicate that mismatch dislocations exist along the interface spaced about 5 nm apart, with the Burgers vector described as ½ [001]. They do not specify which planes are being matched across the interface, but it

is likely to be between the $(1\bar{1}00)$ CdS planes with the $(1\bar{1}\bar{1})$ CdTe planes which lies 70.5^{o} to the $(1\bar{1}1)$ CdTe interface plane according to the HRTEM image that is shown. It should be also mentioned that it is not clear from their HRTEM image whether the mismatch dislocations are in fact that, as it is hard to tell from the image whether there are distortion in the CdTe $(1\bar{1}\bar{1})$ planes around the misfit dislocation if it is to be called as such. Additionally the assignment of the Burger's vector is not accompanied with any detailed analysis. They also show steps in the CdS (0002) plane over which the CdTe $(1\bar{1}1)$ planes forms around it, causing what they describe as step dislocations, which cause strong strain contrast and lattice distortion in both the CdTe and CdS lattice. The step shown in the paper appears to be on a single (0002) plane in the CdS substrate. In this present work, the steps in CdTe (111) surface were larger (figure 3-46) which caused considerably larger disruption in the CdS lattice.

Yan et al. used EDX to show that sulfur atoms diffused into the CdTe lattice and tellurium atoms into the CdS lattice. The probe size was not specified, only that the data shown was collected 100 nm away from the interface. The amount of diffusion was also not quantified, but the EDX spectrum indicates that amount was small, less than ~ 5-10 %. They conclude that this interdiffusion should helps to reduce the lattice parameter of CdTe, and increase it for CdS, thereby helping to decrease the density of mismatch dislocations at the interface. They found a large region (~ 20 nm wide in the HRTEM as shown) where the interface was perfect with no misfit dislocations as evidence. Analysis of the HRTEM image does indicate that there is one for one correspondence between the CdTe $(1\bar{1}\bar{1})$ planes and CdS $(1\bar{1}00)$ planes over about 50 lattice planes. Actual lattice spacing measurements at the interface and away from it would have been more convincing.

Similar work to Yan et al. was done in 1983 by Anthony and Ponce [3-76, figure 14] where HRTEM image was shown of a CdTe film deposited on a (0001) CdS substrate by CSVT method. Shown below in figure 3-59 is a HRTEM image reproduced from the original micrograph. The image was taken on JEOL 200CX at 200 kV, with CdS in the $[11\bar{2}0]$ projection and CdTe in the [110] projection, same as in Yan et al. The interface is not level and it is difficult to determine exactly where it is

due to faults running horizontally near the interface. The image was not analyzed in detail in the original report [3-76], and is is now done to see whether more can be made of the micrograph. The CdTe $(1\bar{1}\bar{1})$ planes and CdS $(1\bar{1}00)$ planes were counted away from the interface, and the ratio of the number of CdTe $(1\bar{1}\bar{1})$ planes to CdS $(1\bar{1}00)$ planes is 0.91 over the distance of about 80 planes. Theoretical value is 0.96. Therefore the mismatch is actually larger than theoretical, in the opposite direction than reported by Yan et al. [3-79]. The mismatch ought to cause misfit dislocation at the interface, but if it did exist, it would be very difficult to place it's location in the image shown in figure 3-59, because the exact location of the interface is difficult to place in the image. The center part of the image appears to contain a step or a mound of CdS that are several (0002) layers thick. Tracking either the CdTe (111) or CdS (0002) across the image by viewing the image from the side shows that there is one extra layer of image spots at the center. It is possible that such steps on the CdS substrate helps in accommodating the lattice misfit between the two lattices. CdTe film contains many twins similar in appearance to what Yan et al. reported [3-79]. Both CdS and CdTe are being imaged rather clearly, and suggest that both lattices are near the zone axis. There is no obvious tilt in the two lattices either, although the diffraction pattern was not reported in ref. 3-76, therefore it is not certain just how close the two lattices are oriented with the orientation relationship as shown earlier.

The current TEM work on CdS/CdTe interfaces appears to be concentrated on the practical analysis of actual structures that are close to the commercial cells, with thin film CdS/CdTe junctions made by CSS or by a chemical bath deposition technique. A recent publication by Han et al. in 2015 describes the analysis of CdS film deposited by chemical bath deposition (CBD) vs. CSS method [3-80]. CdS was deposited first on a commercially available SnO_2:F coated soda lime glass. CSS was carried out at a 520^oC substrate temperature. For CBD, a cadmium acetate and thiourea solution was used at bath temperature of 75^oC. A CdTe layer of 5 μm thickness was then deposited on top of CdS film by CSS at a substrate temperature of 520^oC. This was followed by $CdCl_2$ treatment at 400^oC. The structures were analyzed in the TEM in cross section. Both CdTe and CdS have a random polycrystalline structure and have rough surfaces,

so the HRTEM images are difficult to interpret. The CSS CdS forms large grains which are as thick as the film thickness, about 70-80 nm. These grains form sharp boundaries with CdTe grains which are as large or larger. CBD CdS grains on the other hand are very small at 5-10 nm, and the interface with CdTe is difficult to make out clearly. It is claimed that by XPS depth profile that CSS CdS has sharper boundary with CdTe compared to CBD CdS, but this is hard to tell from the actual plot of the depth profile. The junction performance was also shown, but despite the large differences in CdS film morphology, the performance was only slightly different, with CSS CdS film performing better. For example, CSS CdS film had 9.5% efficiency while CBD CdS had 8.9 % efficiency. The work illustrates the fact that electrical performance of a junction does not necessarily follow or track the features that are observable by TEM.

One of the key contribution to the understanding of the role of $CdCl_2$ that remained a mystery for so many years was made by Li et al. in 2014 [2-25]. As already discussed in chapter 2, Li et al. used a combination of EBIC (electron beam-induced current), STEM imaging and EELS to demonstrate for the first time that chlorine atoms migrate to the CdTe grain boundaries and that they contribute to electrical activities there. The fact that chlorine segregation occurs within a ~ 5nm narrow band at the grain boundary can only be demonstrated by using powerful STEM and TEM capabilities that are available now. The microstructural and chemical analysis by TEM is sure to play an important role in obtaining better understanding of the behavior of the CdS/CdTe heterojunction solar cells.

Even though the commercial solar cell structure based on CdS/CdTe heterojunction use all-thin film design now, it is important to note that single-crystal based structure as described in the present work still have an important role to play in improving the thin film solar cell design and process. First Solar Inc. for example, is funding research on single-crystal CdTe and CdS based heterojunction cell design to obtain the highest possible solar cell efficiency and compare the results to thin film design [3-81]. In so doing, they hope to understand which factors limit the efficiency of the thin film design from achieving the ultimate theoretical efficiency. This work is very important in that CdS/CdTe solar cell must improve the module efficiency in

order to compete with the silicon based solar cell that have achieved considerable cost reduction in recent times.

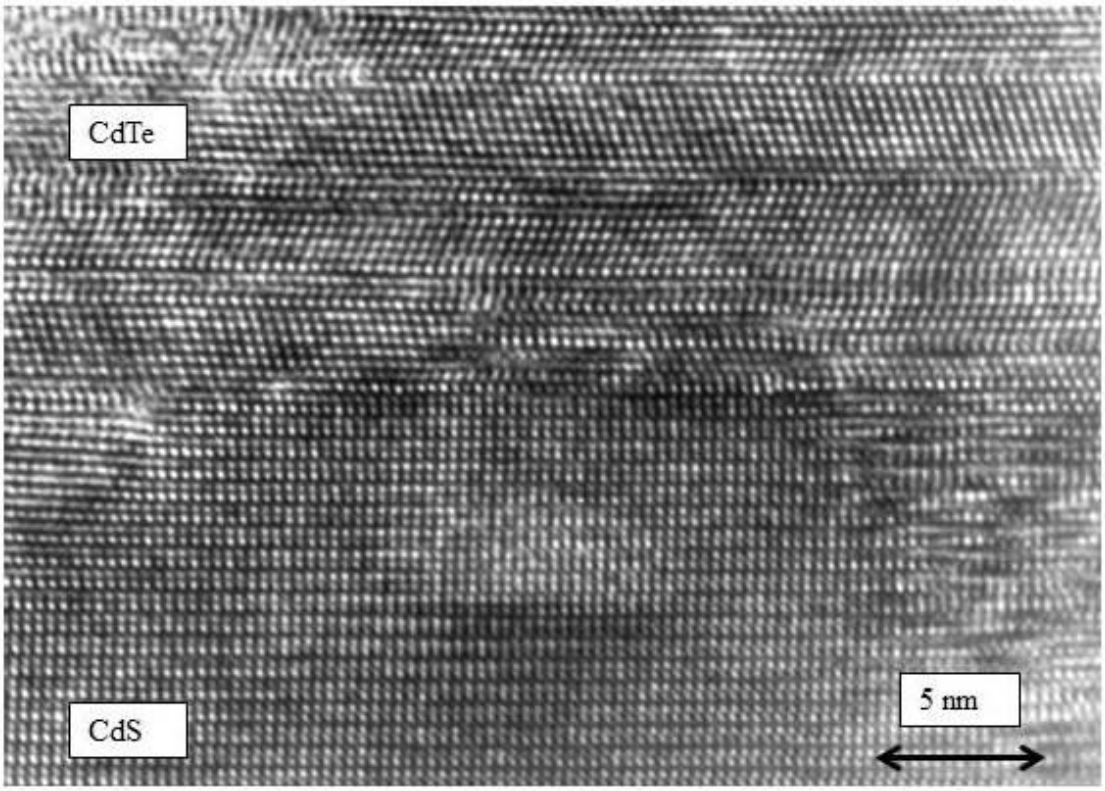

Figure 3-59: HRTEM image of the CSVT CdTe film grown on CdS (0001) single crystal substrate. Substrate temperature was between 500 – 550^{o}C. CdS is in the [11$\bar{2}$0] zone and CdTe is in the [110] zone orientation. Micrograph taken by F. Ponce.

Chapter 3 References:

[3-1] D. A. Jenny and R. H. Bube, *Semiconducting CdTe*, Phys. Rev. **96** (5), p. 1190 (1954)

[3-2] R. H. Bube, *Photoconductivity of the Sulfide, Selenide, and Telluride of Zinc or Cadmium*, Proceedings of the IRE **43** (12), pp. 1836–1850 (1954)

[3-3] R.H. Bube, *Cadmium Telluride Solar Cells, Proc. of Sympos. on Materials and New Processing Technologies for Photovoltaics*, J.A. Mick, V.K. Kapur and J. Dietl, eds., Proc. Vol. **83-11**, pp. 359-376, Electrochem. Soc., Pennington, N.J. (1983)

[3-4] K.W. Mitchell, A.L. Fahrenbruch and R.H. Bube, *Evaluation of the CdS/CdTe heterojunction solar cell*, J. Appl. Phys. **48**, pp. 4365- 4371 (1977)

[3-5] K. Yamaguchi, H. Matsumoto, N. Nakayama and S. Ikegami, *Photovoltaic Effect in CdTe-CdS Junctions Prepared by Vapor Phase Epitaxy*, Japan J. Appl. Phys., **15**, No. 8, p. 1575 (1976)

[3-6] K. Yamaguchi, N. Nakayama, H. Matsumoto and S. Ikegami, *CdS-CdTe Solar Cell Prepared by Vapor Phase Epitaxy*, Japan J. of Appl. Phys. **16**, No. 7, pp. 1203-1211 (1977)

[3-7] H. Uda, H. Matsumoto, Y. Komatsu, A. Nakano and S. Ikegami, *All screen-printed CdS—CdTe solar cell*, 16th IEEE Photovoltaic Specialist Conf. pp. 801-804 (1982)

[3-8] A.J. Strauss, *The physical properties of cadmium telluride*, Rev. Phys. Appl. **12**, pp. 167-184 (1977)

[3-9] F.V. Wald, *Applications of CdTe. A Review*, Rev. Phys. Appl. **12/2**, pp. 277-290 (1977)

[3-10] K. Zanio,
Semiconductors and Semimetals, Vol. 13: CdTe
R.K. Willardson and A.C. Beer, Eds., Academic Press, New York (1978)

[3-11] S. G. Kumar and K.S.R.K. Rao, *Physics and chemistry of CdTe/CdS thin film heterojunction photovoltaic devices: fundamental and critical aspects*, Energy Environ. Sci., **7**, pp.45-102 (2014)

[3-12] M. Gloeckler, I. Sankin, Z. Zhao, *CdTe Solar Cells at the Threshold to 20% Efficiency*, , IEEE Journal of Photovoltaics, Vol. **3** , Issue 4, pp. 1389 – 1393, Sept (2013)

[3-13] M. Weinstein, G.A. Wolff and B.N. Das, *Growth of wurtzite CdTe and sphalerite type CdS single-crystal films,* Appl. Phys. Lett. **6**, 73 (1965)

[3-14] O. Igarashi, Japan. J. Appl. Phys. **9**, 642 (1969)

[3-15] O. Igarashi, Japan J. Appl. Phys. **42**, 4035 (1971)

[3-16] W.T. Read and W. Shockley, *Dislocation Models of Crystal Grain Boundaries,* Phys. Rev., **78**, 275, (1950)

[3-17] R. G. Dhere, M. M. Al-Jassim, Y. Yan, K. M. Jones, H. R. Moutinho, T. A. Gessert, P. Sheldon and L. L. Kazmerski, *CdS/CdTe interface analysis by transmission electron microscopy*, J. Vac. Sci. Technol. A **18**, 1604 (2000)

[3-18] C.S.S.R. Kumar, *Transmission Electron Microscopy Characterization of Nanomaterials*, Chapter 2, Springer Science and Business Media, (2013)

[3-19] J.G. Werthen, *Effects of Surface Preparation of the Properties of Single-crystal CdTe Junctions*, Ph.D. Thesis, Stanford University (1982)

[3-20] K. Nishimura, *Investigation of the Phenomena Involving Junction Formation of n-CdS/p-CdTe by Chemical Vapor Deposition*, Ph.D. Thesis, Stanford University (1982)

[3-21] CdTe crystal made by R. Raymakers of the Center for Materials Research, Crystal Growth Laboratory at Stanford University

[3-21] H. Wiedemeier and G.H. Wu, *Defects in CdTe single-crystals grown by very fast vapor growth technique*, Journal of Electronic Materials, **24**(8), pp. 1007-1015 (1995)

[3-22] L.J. van der Pauw, *A method of measuring specific resistivity and Hall effect of discs of arbitrary shape*, Philips Research Reports **13**: pp. 1–9. (1958)

[3-23] S.A. Hatfield, *Heteroepitaxial growth of MnSb on III-V semiconductor substrates*, Ph.D. Thesis, University of Warwick, 2006

[3-24] E.P. Warekois, M.C. Lavine, A.N. Mariano and H.C. Gatos, *Crystallographic Polarity in II-VI Compounds*, J. Appl. Phys., **33**, 690 (1962)

[3-25] M. Inoue, I. Teramoto and S. Takayanagi, *Etch Pits and Polarity in CdTe Crystals*, J. Appl. Phys., **33**, 2578 (1962)

[3-26] P.F. Fewster and P.A.C. Whiffen, *Crystallographic polarity and etching of cadmium telluride*, J. Appl. Phys., **54**, 4668 (1983)

[3-27] P.D. Brown, *Structural defects in II-VI epitaxial layers*, Ph.D. Thesis, Durham University, (1988)

[3-28] E.P. Warekois, M.C. Lavine, A.N. Mariano and H.C. Gatos, Erratum: *Crystallographic Polarity in II-VI Compounds*, J. Appl. Phys., **37**, 2203 (1966)

[3-29] C. K. Egan, *Morphology, Structure and Electronic Properties of CdTe Surfaces Studied by Scanning Tunneling Microscopy*, Ph.D. Thesis, Durham University (2011)

[3-30] R.N. Zitter, Surf. Sci. *Ramon Detection of Tellurium Layers on Surfaces of CdTe*, **28**, 335 (1971)

[3-31] J.-P. Haring, J.G. Werthen, R.H. Bube, L Gulbrandsen, W. Jansen and P. Luscher, *Study of cleaved, oxidized, etched and heat-treated CdTe surfaces*, J. Vac. Sci. Technol., **A** 1(3), pp. 1469 – 1472, July-Sept. (1983)

[3-32] P. Dupuy, *Sur la preparation et les proprieties du tetrabomure de tellure*, Compt.Rend., **237**, 718 (1953)

[3-33] K.B. Shalimova, A.F. Andrushko, V.A. Dmitriev and L.P. Pavlov, *Crystal structure of thin films of cadmium sulfide as affected by deposition conditions*, Kristallografiya **8**, No. 5, pp. 774-777, (1963); translated source: Sov. Phys. Crystallogr. **8**, No. 5, 618-20 (1964)

[3-34] L.S. Palatnik, M.N. Naboka and V.E. Marincheva, Izv. Akad. Nauk SSSR, Inorg. Mater. **6**, 1526 (1970); Inorg Mater. (USSR) **6**, 1344 (1971)

[3-35] M.J. Tsai and R.H. Bube, *Electrical properties of n type epitaxial indium phosphide film*, J. Appl. Phys. **49**, 3397 (1978)

[3-36] M. Aven and W. Garwacki, *Epitaxial growth and properties of ZnTe-CdS Heterojunctions*, J. Electrochem. Soc. **110**, 401 (1963)

[3-37] B.J. Curtis and H. Brunner, *The epitaxial growth of cadmium sulfide on gallium arsenide substrates*, J. Cryst. Growth **6**, No. 6, 269 (1970)

[3-38] D.B. Holt, *Misfit dislocations in semiconductors*, J. Phys. Chem. Solids **27**, 1053 (1966)

[3-39] R. S. Mueller and R.J. Zuleeg, *Vapor-Deposited, Thin film Heterojunction Diodes*, J. Appl. Phys. **35**, 1550 (1964)

[3-40] T. C. Anthony, A.L. Fahrenbruch and R.H. Bube, *Low resistance contacts to p-type cadmium telluride*, J. Electro. Mater. 11, pp. 89-109 (1982)

[3-41] IEC 60904-9 Edition2 and ASTM E927-10 standard
American Society for Testing and Materials (ASTM) Terrestrial Reference Spectra for Photovoltaic Performance Evaluation, ASTM G-173 NREL

[3-42] J.G. Werthen, A.L. Fahrenbruch, R.H. Bube and J.C. Zesch, *Surface preparation effects on efficient indium-tin-oxide-CdTe and CdS-CdTe heterojunction solar cells*, J. Apple. Phys. **54** (5), pp 2750-2756, May 1983

[3-43] H. Holloway and E. Wilkes, *Epitaxial growth of cubic CdS*, J. Appl. Phys., **39**, 5807 (1968)

[3-44] K.L. Chopra and I.H. Khan, *Polymorphic transformation in epitaxial CdS films*, Surface Science, Vol, **6**, Issue 1, pp 33-41, (1967)

[3-45] A.L. Fahrenbruch and R. H. Bube, Fundamentals of Solar Cells, Academic Press, 1983

[3-46] J.W. Eddingron, in Practical Electron Microscopy, p. 190, Van Nostrand Reinhold (1976)

[3-47] University of Liverpool, online atomic model viewer
Chem Tube 3D.
ChemTube3D by Nick Greeves is licensed under a Creative Commons AttributionNoncommercial-Share Alike 2.0 UK: England & Wales License
© 2008-2014 The University of Liverpool

[3-48] W.C.T. Dowell, J. Phys. Soc. Japan, **17**, suppl. B-11, 175 (1962)

[3-49] G.A. Bassett, J.W. Menter and D.W. Pashley, *Moiré patterns on electron micrographs, and their application to the study of dislocations in metals,* Proc. Roy. Soc. **A 246**, 345 (1958)

[3-50] D.B. Williams and C.B. Carter, Transmission Electron Microscopy, A Text Book for Materials Science, 2nd Edition, Springer Science and Business Media, (2009)

[3-51] ICDD, International Centre for Diffraction Data
ICDD (**2014**), PDF-4+ 2014 (Database). International Centre for Diffraction Data, edited by Dr. Soorya Kabekkodu (Newtown Square, PA, USA).

[3-52] K. Tao and C.A. Hewett, *Thin film X-ray analysis using the Read camera: a refinement of the technique*, Rev. Sci. Instrum. **58**, 212-214 (1987)

[3-53] J. Lähnemann, U. Jahn, O. Brandt, T. Flissikowski, P Dogan and H.T. Gahn, *Luminescence associated with stacking faults in GaN*, J. Appl. Phys. D, Vol. **47**, No. 42, 423001 (2014)

[3-54] C.K. Egan, *Morphology, structure and electronic properties of CdTe surfaces studied by scanning tunneling microscopy*, Ph.D. Thesis, Durham University, (2011)

[3-55] K.L. Chopra and S.R. Das, Thin Film Solar Cells, Plenum Press (1983)

[3-56] T.C. Anthony, *Preparation and Properties of CdTe Films and Junctions using Close-Spaced Vapor Transport*, Ph.D. Thesis, Stanford University (1984)

[3-57] google finance, https://www.google.com/finance?fstype=ii&q=NASDAQ:FSLR

[3-58] from Yahoo® finance: http://seekingalpha.com/article/2108263-first-solars-revised-panel-efficiency-road-map-could-bode-well-for-its-future

[3-59] M. Osborne, "SunPower lifts lid on new record 21.5% efficient X-series solar modules", PVTech, 03 April 2013. http://www.pvtech.org/news/sunpower_lifts_lid_on_new_record_21.5_efficient_x_series_solar_modules

[3-60] First Solar Investor Relations News, August 5, 2014, "First Solar builds the highest efficiency thin film PV cell on record", http://investor.firstsolar.com/releasedetail.cfm?ReleaseID=864426

[3-61] K. Masuko, M. Shigematsu, T. Hashiguchi, D. Fujishima, M. Kai, N. Yoshimura, T. Yamaguchi, Y. Ichihashi, T. Mishima, N. Matsubara, T. Yamanishi, T. Takahama, M. Taguchi, E. Maruyama, and S. Okamoto, *Achievement of more than 25% conversion efficiency with crystalline silicon heterojunction solar cell*, IEEE Journal of Photovoltaics, Vol. 4, No. 6, pp. 1433-1435 (2014)

[3-62] M. Munsell, Greentechsolar, Sept.15, 2014, "Yingli drops Q2 solar module manufacturing cost to less than 50 cents per watt", http://www.greentechmedia.com/articles/read/Yingli-Drops-Solar-Module-Manufacturing-to-Below-50-Cents-per-Watt-in-Q2

[3-63] E. Wesoff, Greentechsolar March 4, 2014, "Module costs dip below 50 cents per watt in JinkoSolar's strong Q4", http://www.greentechmedia.com/articles/read/Module-Costs-Dip-Below-50-Cents-Per-Watt-in-JinkoSolars-Strong-Q4

[3-64] R. Noufi, *High Efficiency CdTe and CIGS Thin Film Solar Cells: Highlights of the Technologies Challenges*, National Renewable Energy Laboratory, Invited talk at 2006 IEEE 4th World Conference on Photovoltaic Energy Conversion (WCPEC-4), May 7-12, 2006, Waikoloa, Hawaii

[3-65] N. Nakayama, H. Matsumoto, K. Yamaguchi, S. Ikegami, Y Hioki, *Ceramic thin film CdTe solar cell*, Jap. J. Appl. Phys. 15, pp. 2281-2282 (1976)

[3-66] T.L. Chu, S.S. Chu, C. Ferekides, C.Q. Wu, J. Britt and C. Wang, *13.5% efficient thin film CdS/CdTe solar cells*, J.Appl. Phys. **70** (12) pp 7608-7612 (1991)

[3-67] X. Wu, R.G. Dhere, D.S. Albin, T.A. Gessert, C. DeHart, J.C. Keane, A. Duda, T.J. Coutts, S. Asher, D.H. Levi, H.R. Moutinho, Y. Yan, T. Moriarty, S. Johnston, K. Emery, and P. Sheldon, *High-Efficiency CTO/ZTO/CdS/CdTe Polycrystalline Thin film Solar Cells*, NCPV Program Review Meeting Lakewood, Colorado 14-17 October 2001

[3-68] US Patent 5,248,349 A, *Process for making photovoltaic devices and resultant products*, Publication Date: Sep 28, 1993

[3-69] US Patent 6,037,241, *Apparatus and method for depositing a semiconducting material*, Filed February 19, 1998

[3-70] T.C. Anthony, A.L. Fahrenbruch, M.G. Peters and R.H. Bube, *Electrical properties of CdTe films and junctions*, J. Appl. Phys. 57(2), pp. 400-410 (1985)

[3-71] X. Wu, P. Sheldon, Y. Mahathongdy, R. Riebelin, A. Mason, H.R. Moutinho, and T.J. Coutts, *CdS/CdTe Thin film Solar Cell with a Zinc Stannate Buffer Layer*, National Center for Photovoltaic Program Review Meeting, Denver, Colorado, Sept 8-11 (1998)

[3-72] I.M. Dharmadasa, *Review of the $CdCl_2$ Treatment Used in CdS/CdTe Thin Film Solar Cell Development and New Evidence towards Improved Understanding*, Coatings, **4**, 282-307 (2014)

[3-73] A. Rios-Flores, J.L. Pena, V. Castro-Pena, O. Ares, R. Castro-Rodriguez, A. Bosio, *A study of vapor $CdCl_2$ treatment by CSS in CdS/CdTe solar cells*, Solar Energy, **84**, pp. 1020–1026 (2010)

[3-74] T.L. Chu and S.S. Chu, *Thin film II-VI photovoltaics*, Solid State Electron. **38**, 533-549 (1995)

[3-75] T.K. Tran, J.W. Tomm, N.C. Giles, B.K. Wagner, A. Parikh, and C.J. Summers, *Strong room temperature excitonic resonance in CdTe: I*, J. Cryst Growth, **159**, 368-371 (1996)

[3-76] Progress Report #8, *Photoelectronic Properties of II-VI Heterojunctions*, for the period Dec. 1, 1982- Nov. 30, 1983, Materials Science Program, Division of Basic Energy Sciences, Department of Energy, DE-AT 03 76ER700 47, Principal Investigator: Richard H. Bube, Professor, Department of Materials Science and Engineering, Stanford University, Stanford, California, 94305

[3-77] P. Boieriu, R. Sporken, Yan Xin, N.D. Browning, and S. Sivanathan, *Wurtzite CdS on CdTe Grown by Molecular Beam Epitaxy*, J. Electro. Mater. **29**, No.6, 718 (2000)

[3-78] Y. Xin, S. Rujirawat, N.D. Browning, R. Sporken, and S. Sivananthan, *The effect of As passivation on the molecular beam epitaxial growth of high-quality single-domain CdTe (111)B on Si (111) substrates*, Appl. Phys. Lett., **75**, 349 (1999)

[3-79] Y. Yan, R.G. Dhere, K.M. Jones, and M.M. Al-Jassim, *Influence of substrate structure on the growth of CdTe thin films*, J. Appl. Phys. **89**, 5944 (2001)

[3-80] J. Han, G. Fu, V. Krishnakumar, H-J. Schimper, C.Liao, W. Jaegermann, and M.P. Besland, *Studies of CdS/CdTe interface: Comparison of CdS films deposited by close space sublimation and chemical bath deposition techniques*, Thin Solid Films, **582**, pp 290-294 (2015),

[3-81] D.N. Weiss, *Introducton to First Solar Technology*,
Stanford Optical Society Seminar, May 6, 2015
Comments made on questions from the audience.

Chapter 4: Characterization of MBE GaAs on LEC GaAs

4.1 Analysis of Defects in LEC GaAs Substrate

Single-crystal GaAs used for optoelectronic application are grown by the liquid encapsulated Czochralski (LEC) method. To reduce the amount of dislocations present in the crystal, high concentrations ($>10^{18}$ cm^{-3}) of doping impurities such as selenium, sulfur or tellurium are used [4-1, 4-2, 4-3]. The impurities cause solution hardening, which reduces the propagation and multiplication of dislocations introduced at the periphery of the crystal due to thermal stresses that develop during crystal growth. The conventional method for detecting and measuring the number of dislocations present in the crystal had been by etch pit density (EPD) or by transmission X-ray topography. However, it was realized that so-called *dislocation-free* crystals obtained in this way still contain a high density of microdefects, such as dislocation loops and stacking faults, which are often not visible by EPD or by X-ray topography [4-2, 4-4, 4-5]. Several TEM investigations on Te-doped LEC GaAs crystals have shown the presence of large stacking faults, and a high density of Frank-type faulted loops, which are both extrinsic in character [4-4, 4-6]. Tellurium precipitation is suspected in both of these types of defects, and formation of a layer of Ga_2Te_3 which has a cubic sphalerite structure with a lattice parameter of 0.588 nm was proposed in both types of defects based on defect contrast analysis and radiation damage experiments [4-4, 4-7]. In the present analysis, conventional TEM and HRTEM techniques were used to image the defects in as-grown Te-doped LEC GaAs as a function of the position in the crystal boule. Undoped and Si-doped GaAs were also examined for the purpose of comparison.

GaAs crystals that were analyzed were <111> orientation LED single-crystals, which were pulled at a rate of 0.7 cm/hr. The diameter of the boule was 6 cm, and the length approximately 8 cm. The silicon doped crystal was grown in the <100> orientation. Dopant concentration (electrically active) and the EPD of the three types of crystals analyzed are listed below in Table 4-1. Dopant concentration is based on a Hall measurement.

Table 4-1: Carrier density, N_D-N_A (cm^{-3}) and etch pit density EPD (cm^{-2}) for Te, Si and updoped GaAs wafers.

	Ingot ID	N_D-N_A (cm^{-3})	EPD (cm^{-2})
Te-doped	A172	$6 \times 10^{17} - 7 \times 10^{18}$	$2 \times 10^4 - 4 \times 10^4$
Si-doped	H163	$10^{17} - 10^{18}$	200 - 2000
Undoped	H155	semi-insulating	1×10^4

Transmission X-ray topographs were obtained from cross section bars cut across the diameter of the crystal as (112) orientation bars approximately 4-5 mm in width and 1mm thick, and TEM samples were obtained from the same or similar bars cut from the upper and lower portion (~2/3 of the length down from the neck) of the boule. The geometry of the boule and where the topograph sections and the TEM specimens were obtained are shown schematically in figure 4-1. TEM specimens were made by chemical jet-thinning, using 3% bromine in methanol solution. The specimens were ion milled further at 5 keV for 20 minutes to obtain electron transparent regions. Two different orientation samples were made, with the orientation of <110> and <112>, with the former used for HRTEM. A JEOL 200CX microscope with a point-to-point resolution of 0.26 nm was used at an operating voltage of 200 kV.

The transmission X-ray topograph of a bar cut across the diameter of a Te-doped ingot at the bottom of the boule is shown in figure 4-2. The peripheral region of the crystal has a high density of grown-in dislocations. The dislocation density decreases abruptly toward the center of the crystal, and this region is characterized by growth striations from the Czochralski process. For comparison, an X-ray topograph of a bar cut from the top of the ingot is shown in figure 4-3. Most of the larger straight lines seen in figures 2 and 3 are saw marks from cutting the bar. Dislocations are fine striations and the mass of smaller lines in the image. It is not easy to obtain a clear

picture of how the dislocations are organized in the specimen from the X-ray topographic images.

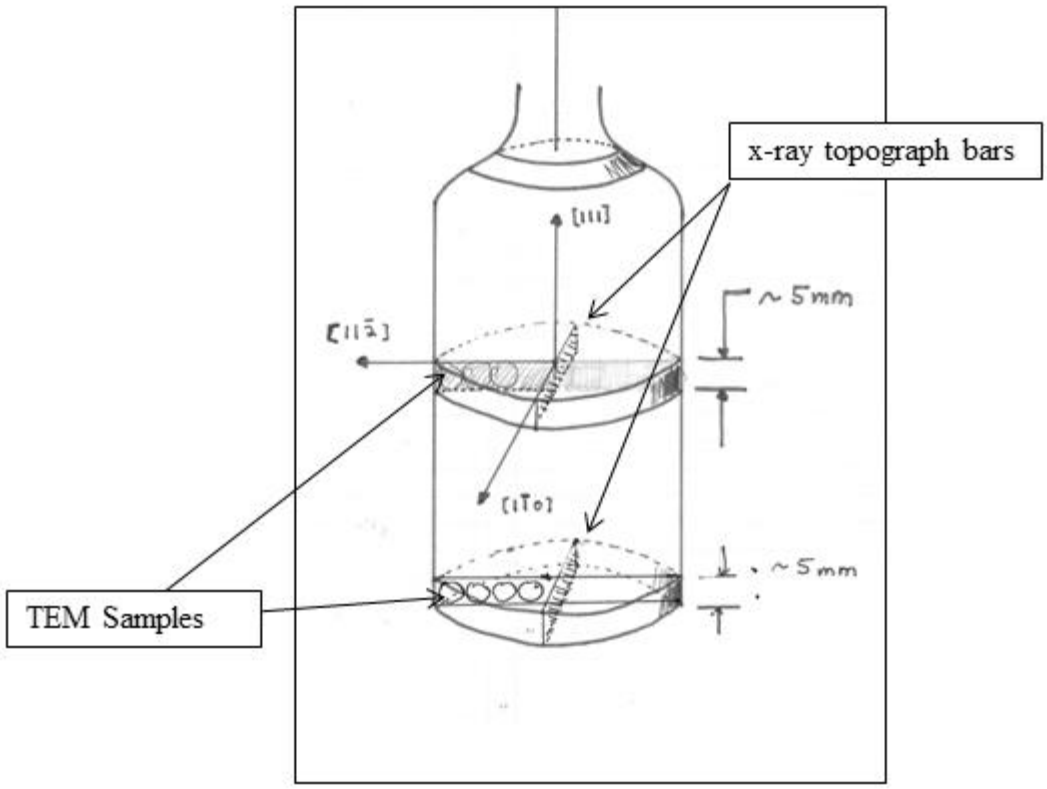

Figure 4-1: Schematic diagram of LEC GaAs crystal boule, and the locations where the (112) orientation X-ray topograph bars were obtained. TEM specimens were obtained in [110] and [112] sections as indicated in the diagram.

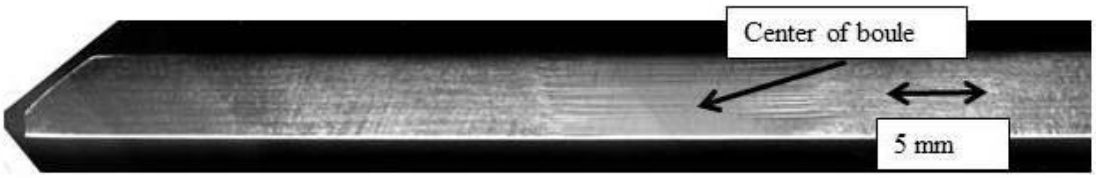

Figure 4-2: X-ray topograph of LEC GaAs with Te doping. The bar was obtained from bottom section of the boule. The center region has striations. Dark contrast on both sides of the center striations are dislocations. (Ingot A172, using Mo Kα and (220) reflection)

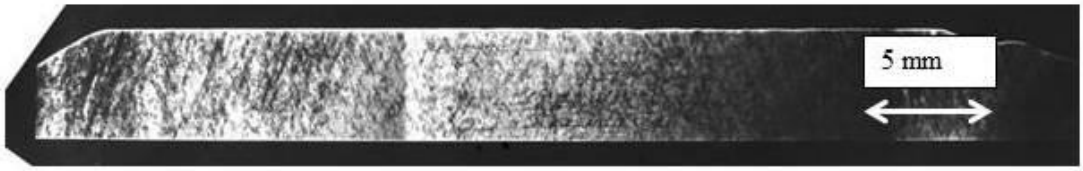

Figure 4-3: X-ray topograph of LEC GaAs with Te doping from the top section of the boule. (Ingot A172, using Mo Kα and (220) reflection)

As a comparison, X-ray topographs of the Si-doped and undoped ingot are shown in figure 4-4 and 4-6, respectively. These specimens are cut from the boule as wafers are normally cut, which is length-wise across it. An example is shown in figure 4-5. The top of the boule where the crystal growth starts is also at the top of the photograph. Si-doped GaAs has the lowest etch pit density, and the X-ray topography shows less dislocation contrast, especially in the midsection of the boule as shown in figure 4-4. The image quality is poor, but it is clear that there are higher concentration of dislocations at the periphery and lower in the center.

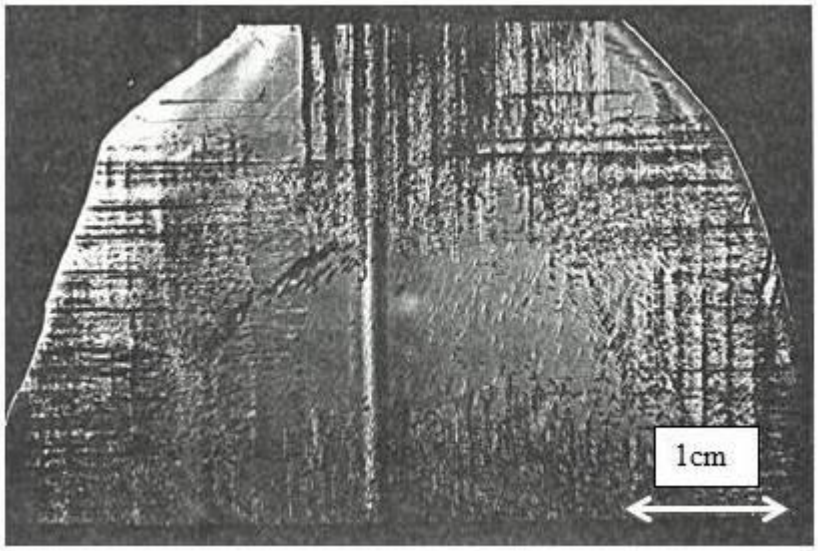

Figure 4-4: X-ray topograph of Si-doped GaAs ingot from the top section of the boule. The large horizontal and vertical lines are saw marks. (Ingot H163, using Mo Kα and (220) reflection)

Figure 4-5: Undoped GaAs ingot H155, cut length-wise across the boule to obtain wafers. The image on the right is the same wafers shown on the left, taken with higher contrast to show the different wafers that were cut.

The X-ray topograph from the wafer cut from the bottom section of the undoped GaAs shown below in figure 4-6 shows the network of dislocations that develop in the crystal. The dislocation network is more easily seen, as the wafer had been better prepared with some polishing. It is evident that lacking solution- or precipitation-hardening that prevents dislocations from moving and multiplying, the cell-like structure of the dislocation network can develop in the undoped crystal. Etch pit density for undoped GaAs did not show much difference in dislocation density compared to the Te-doped GaAs, but it did show significantly less for the Si-doped GaAs even though it is not clear from the X-ray topograph that there is a great difference between Si-doped and Te-doped GaAs, for example. Therefore the EPD technique is seeing something different than the X-ray topography and it should not be relied upon as the only indicator of dislocation density. TEM specimens were prepared only from the Te-doped GaAs bars.

For the Te-doped GaAs, mostly straight dislocation lines were found at the periphery of the crystal. An example is shown in figure 4-7. These dislocations were often associated with small spherical precipitates, which were ~ 60 nm in diameter (arrowed in the figure), which may be pinning the dislocation lines. EDS analysis of the particle showed the presence of Te, but it was not possible to discern chemical composition since the GaAs matrix above and below the particle interferes with the composition analysis. The fact that any Te is detected at all suggests the high amount of segregation of Te in the particle. In the region slightly toward the interior of the crystal, bowed and helical dislocations were often observed, as shown in figures 4-8 and 4-9. Small microdefects were often attached to these dislocations, some apparently pinning the dislocations as seen in both figures.

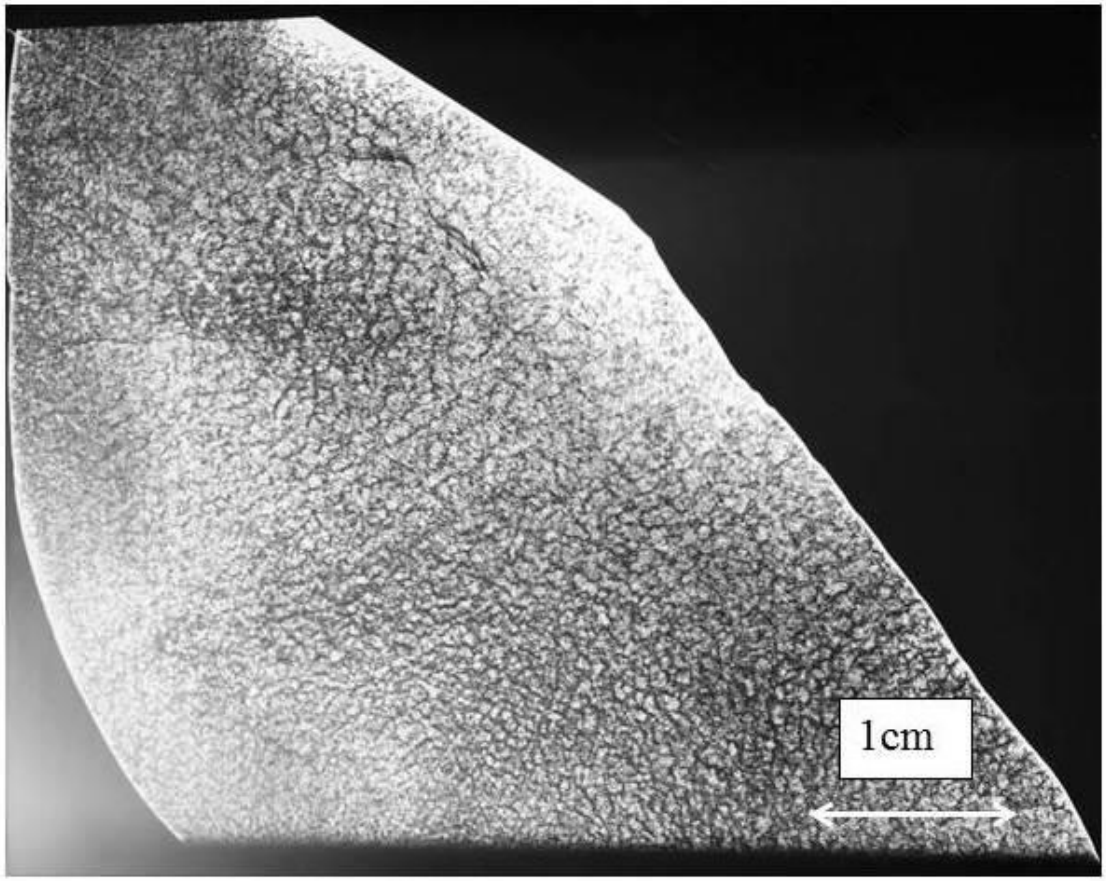

Figure 4-6: X-ray topograph of undoped GaAs ingot from bottom section of the boule showing cellular network of dislocations. This wafer came from different cut than the ones shown in figure 4-5. (Ingot H155, using Mo Kα and (220) reflection)

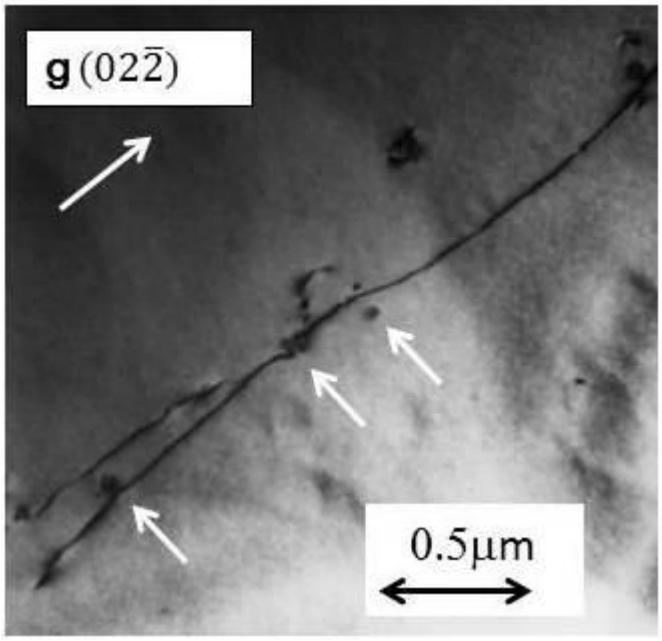

Figure 4-7: Straight dislocation from Te-doped LEC GaAs. White arrows point to circular precipitates that are associated with the dislocation line. They maybe pinning the dislocation. Small amount of Te was detected at the precipitates.

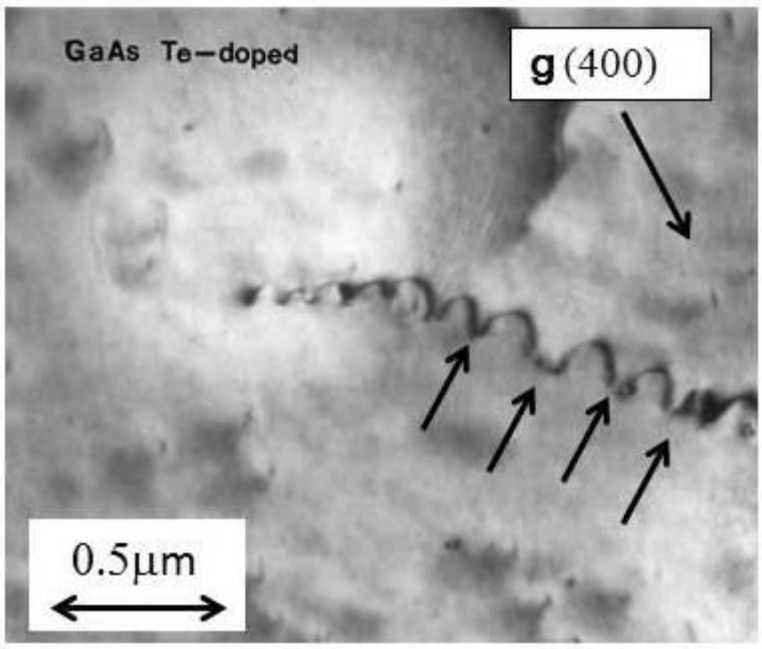

Figure 4-8: Dislocation line showing Orowan type bowing due to pinning by small microdefects (arrowed).

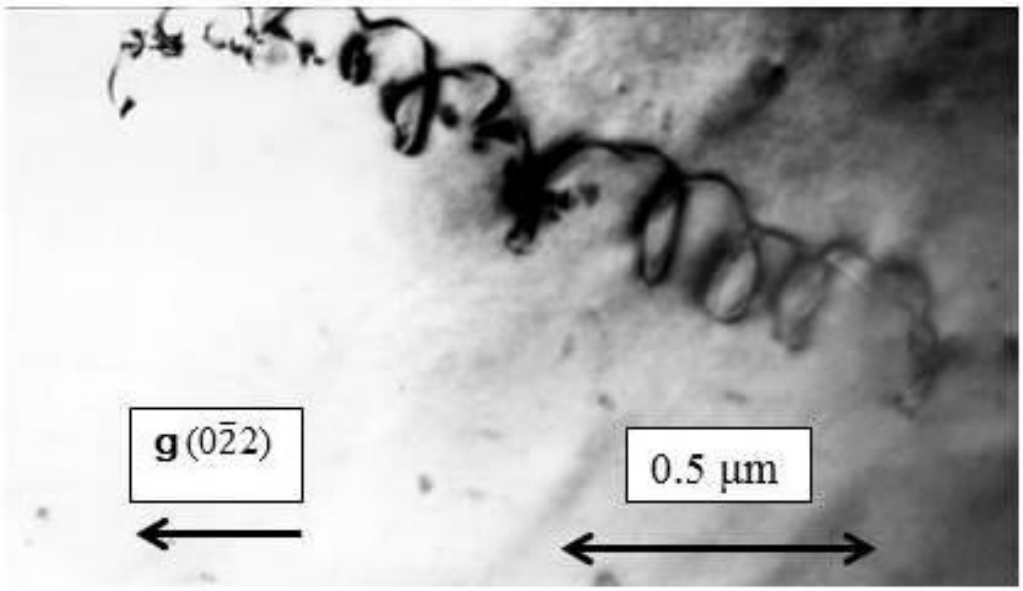

Figure 4-9: Helical dislocations in LEC GaAs. Dark spots are microdefects. Many are associated also with helical dislocations.

The center of the crystal was virtually free of dislocations, but it contained a high density of microdefects at a density of approximately 10^{14} cm^{-3} as shown in figure 4-10. The density of the latter at the periphery of the crystal was lower than that at the center by about two orders of magnitude. Roughly 30 to 40 of these defects lying close to the edge of the foil were imaged in end-on projection in the [110] specimens by HRTEM. Examples of such microdefects are shown in figure 4-11 and 4-12. The HRTEM of these microdefects always showed the presence of an extra plane of image spots at the fault, clearly indicating the extrinsic nature of the defect. Lattice images of the larger microdefects were more complex, having steps in the fault as shown in figure 4-13 and often containing additional faults on alternate (111) planes, forming a Lomer-Cottrell type locked dislocation. Lomer-Cottrell dislocation forms as a result of a reaction between two Shockley partial dislocations lying on a different slip plane, forming a sessile dislocation. Chemical analysis using EDS was attempted on the microdefects, but the results were inconclusive. Each image spot corresponds to a Ga-

As atomic pairs, and it cannot be ruled out that the chemical composition of the extra plane of image spots could consist of Te atoms for example. Many intrinsic stacking faults are associated with the extrinsic faults, as was observed in CdTe as shown in Chapter 1. Ion-beam damage is not a factor for GaAs, as there were specimens that did not contain microdefects and the specimens were all prepared in the same manner. The microdefects are clearly intrinsic to the crystals as they were grown.

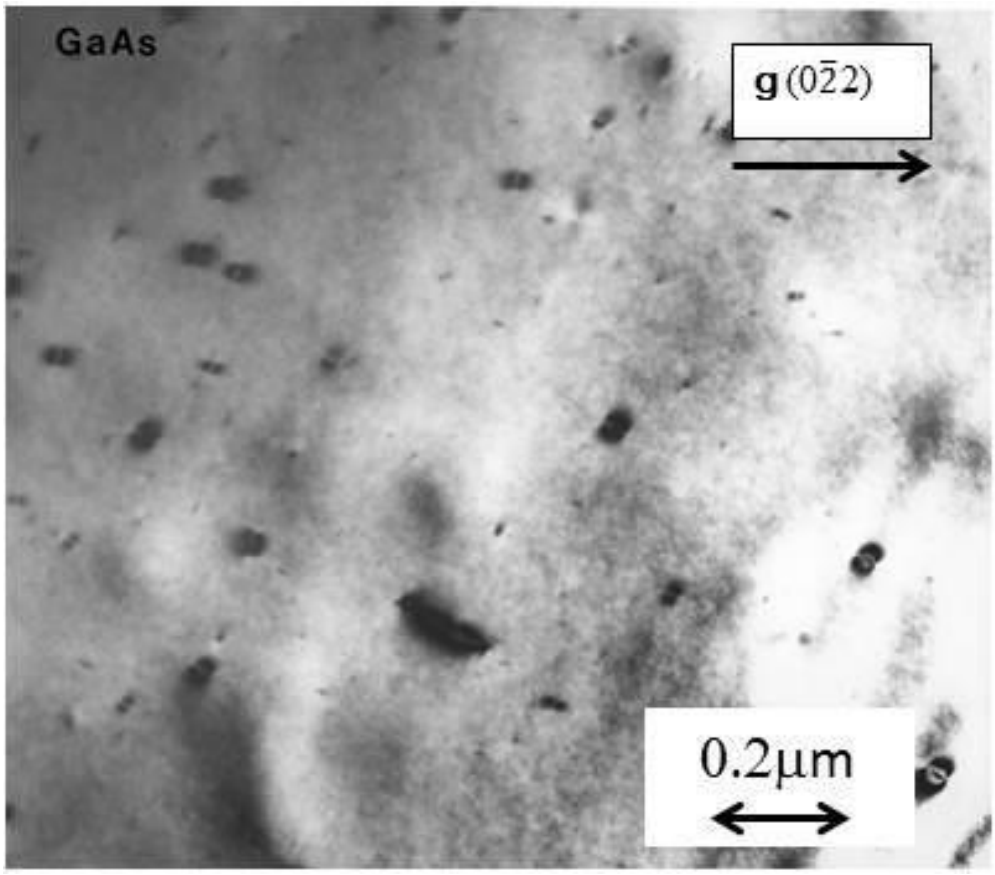

Figure 4-10: Two-beam BF image of microdefects in the central region of the boule. The density of microdefects is approximately 2 x 10^{14}/cm^3.

The small Frank loops, which are cut in cross section in HRTEM sample preparation, had the appearance of a pure extrinsic stacking fault; therefore, the extra layer of atoms at the fault could be GaAs. There may be an atmosphere of Te within

these faults but whether this is the case or not could not be discerned by the HRTEM method. The fact that these types of faults form suggests the Suzuki atmosphere effect around the defect. Suzuki effect is where solute atoms in the material segregate at stacking faults to change their character such as stacking fault energy and its mobility.

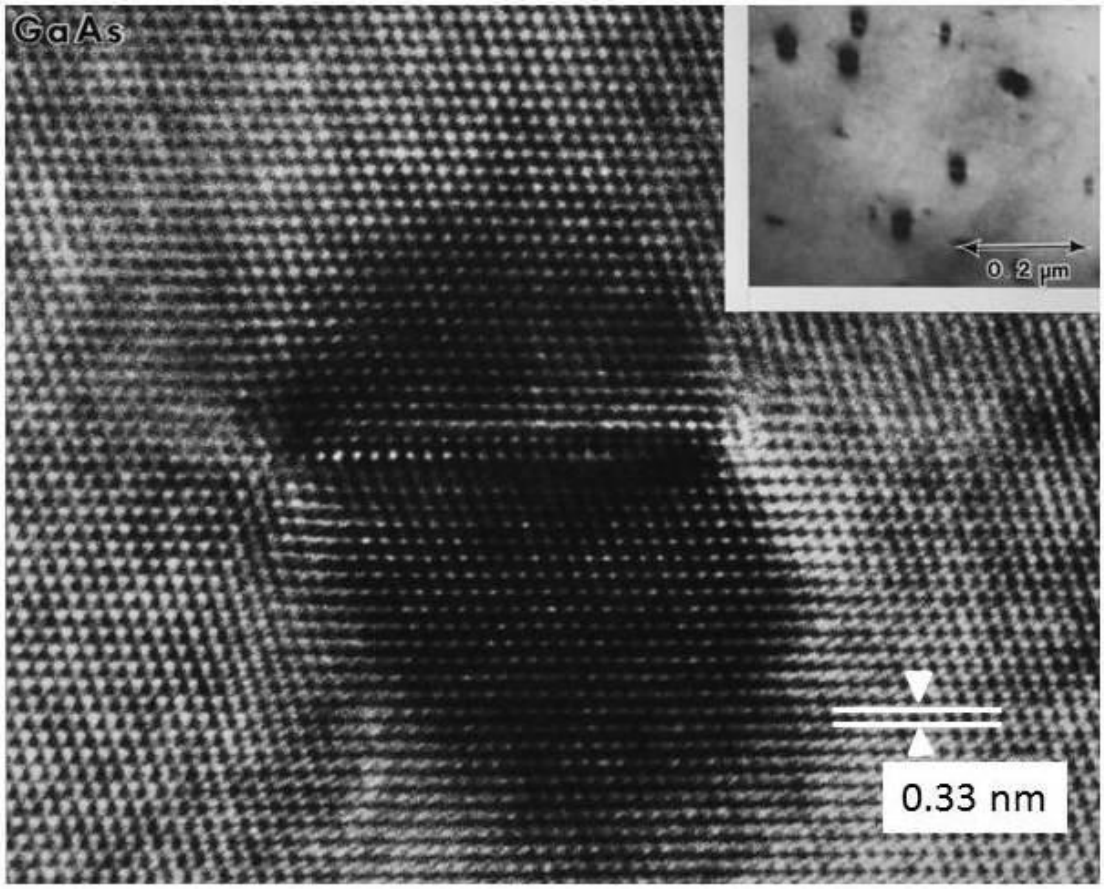

Figure 4-11: HRTEM micrograph of a microdefect imaged in the [110] projection, clearly showing the extrinsic nature of the microdefect. All of the small microdefects imaged were interstitial defects. In thicker parts of the TEM specimen, it is thought that these defects would be small Frank loops. As in the CdTe examples in Chapter 1, these defects would have Burgers vector of the type $\vec{b} = \frac{a_o}{3}[111]$ with opposing sign on each end. Insert image is a BF micrograph of the microdefects, shown as an example (not the HRTEM image in the figure).

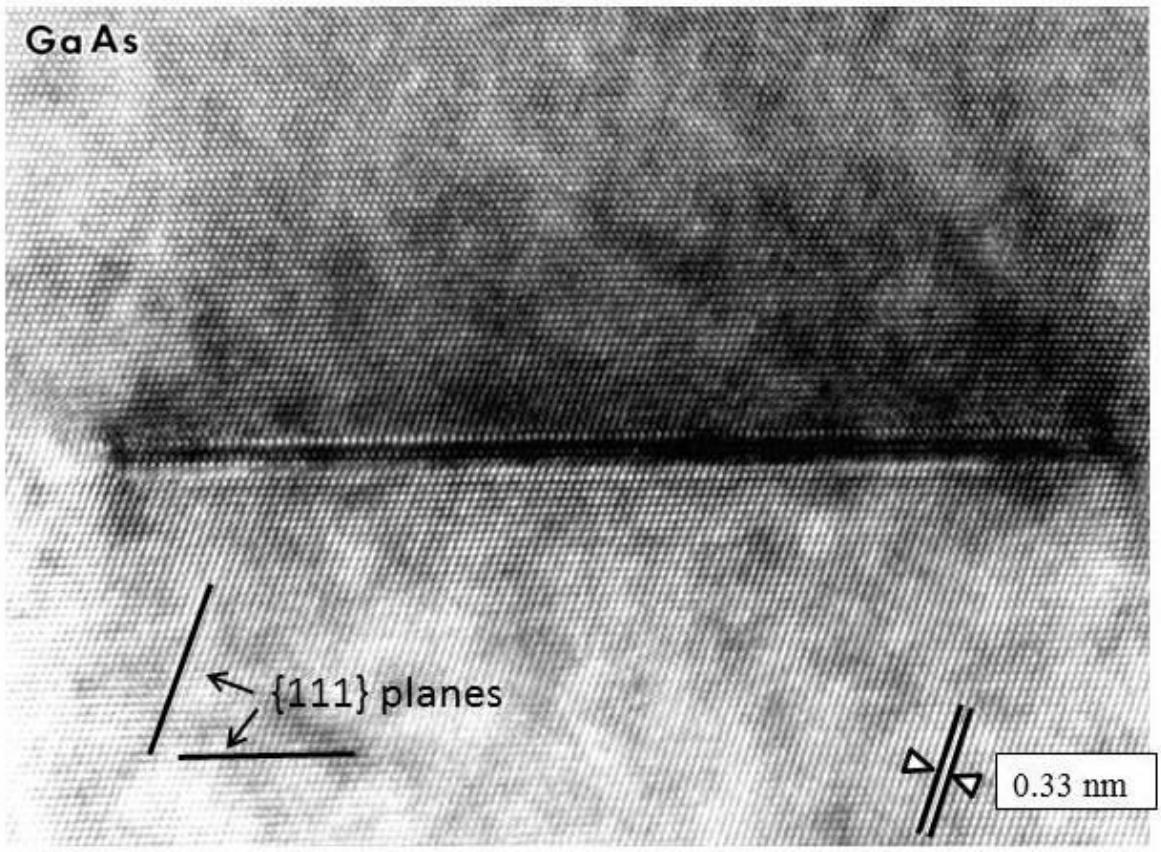

Figure 4-12: HRTEM image of LEC GaAs microdefect. This defect is larger than typical microdefects in the crystal. It also contains an extra (111) plane.

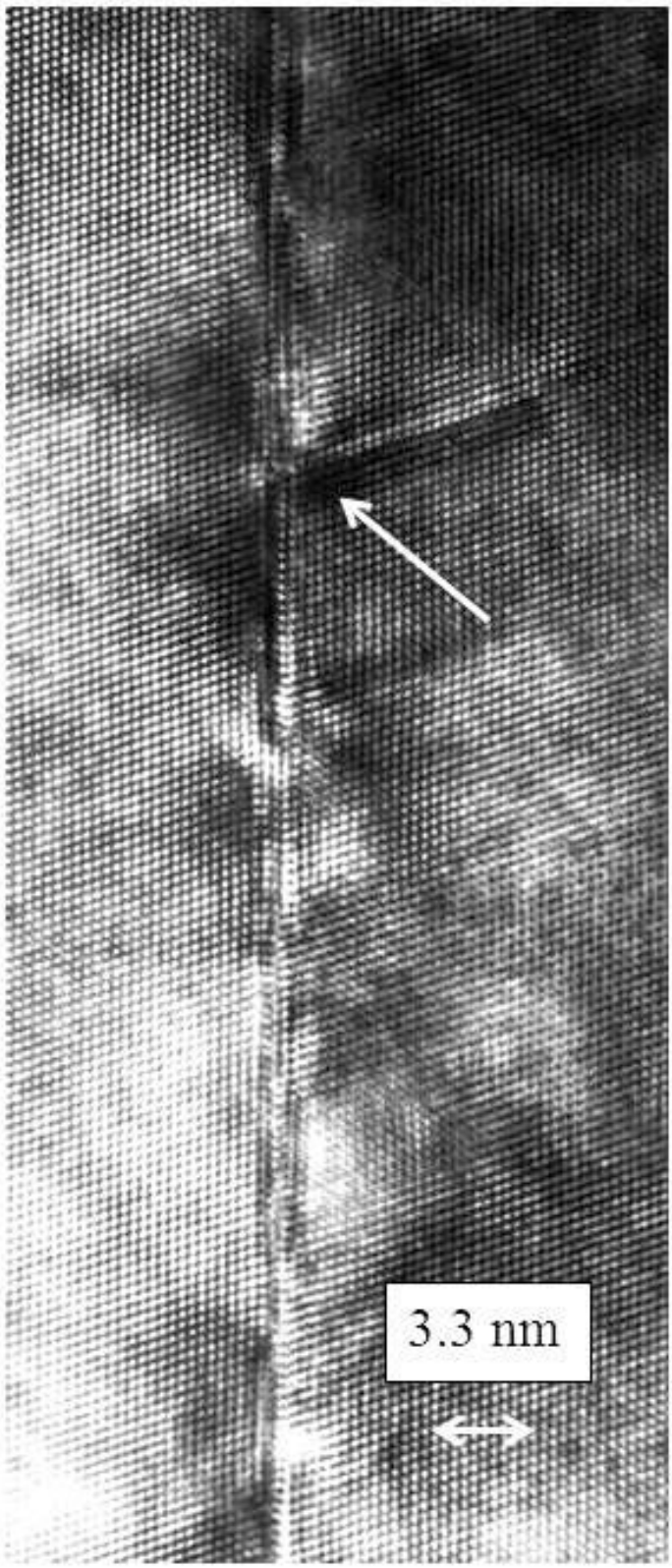

Figure 4-13: HRTEM of extended microdefects in the LEC-GaAs crystal with defects on multiple (111) planes, which may have formed because of the merging of multiple microdefects. It also contains a locked dislocation (arrowed). Similar locked dislocation was described for the CdTe in Chapter 1, figure 1-54.

In summary, the cellular dislocation network that forms in undoped crystals as seen by X-ray topography shows that there are no impediments to dislocation motion except by each other. The greater effectiveness of silicon in reducing dislocation density may be explained in terms of the stronger interaction of point defects in silicon-doped GaAs than in tellurium-doped GaAs, which produce more effective solution hardening. This contradicts a model based on chemical bond energies [4-9] that predicts the greater effectiveness of tellurium in providing solid solution hardening. However, the model is based on InP; therefore, GaAs may behave differently. Spherical Te-rich precipitates also form in the periphery of the crystal, which also act to hinder dislocation movement. Furthermore, it is apparent from the analysis of the microstructure of Te-doped crystal that microdefects may play a large role in the pinning of dislocations, and part of the mechanism responsible for reduction of dislocations in the interior part of the crystal may be due to precipitation hardening. There is a very high density of microdefects present in the interior of the boule. Based on the BF TEM analysis, the density is approximately $2 \times 10^{14}/cm^3$. The microdefects are small extrinsic Frank loops, which may contain tellurium. The formation of Frank loops is a good indication of precipitation effects occurring inside the crystal. However, it should be stated that factors such as thermal history and melt stoichiometry can sometimes affect the defect structure and their distribution within the crystal to a far greater extent than the choice and amount of dopant used [4-10].

4.2 Defects in Homo-Epitaxial MBE GaAs on GaAs

Optoelectronic devices using GaAs typically use GaAs substrates made by the LEC method, and device structures are built up on top of the substrate by first growing a fresh new layer of GaAs, often by molecular beam epitaxy (MBE) or by organo-metallic vapor phase epitaxy (OMVPE), which is also called metal organic chemical vapor deposition (MOCVD). MBE and MOCVD methods are used to build complex layers of compound semiconductors on top of the substrates to create devices such as lasers, LED's, and other unique optoelectronic devices. The present study involved

deposition of a fresh GaAs layer on LEC-GaAs by MBE, and studying the defects that occur in the MBE grown GaAs to elucidate its structure, possible sources, and mechanism of their formation in order to improve the quality of the grown GaAs film on which additional structures are to be built. Many review papers exist on the MBE process, which has been practiced extensively since the early 1970s [4-11]. The MBE method allows epitaxial film growth by the reaction of one or more thermal molecular beams with a crystalline surface under ultra-high vacuum conditions. MBE is related to vacuum evaporation, but the control over the incident atomic or molecular fluxes is much better so that sticking coefficient differences may be taken into account. The beam species can be rapidly changed so that it is possible to produce superlattice structures consisting of alternating layers only a few atomic layers thick. Electrically active impurities are added to the growing film with separate beams so that the doping profile can be controlled with a precision that is difficult to achieve by any other means. MBE is widely used in the fabrication of various GaAs-based devices.

The MBE apparatus typically consist of a stainless steel bell-jar system, ion-pumped and normal base pressure reaching into the low 10^{-10} torr. Many systems are often equipped with electron guns and energy analyzer optics for Auger electron spectroscopy (AES), low-energy electron diffraction (LEED) and reflection electron diffraction (RHEED) units. A quadrupole mass spectrometer for residual gas analysis and analysis of the molecular beam is usually standard equipment on an MBE system. Sources are thermal effusion cells the temperatures of which are accurately controlled. The source ovens are surrounded by the liquid nitrogen-filled chamber to reduce outgassing. Externally controlled mechanical shutters are used to intercept the beam to turn it on and off. The source is a Knudsen cell containing vapor and condensed phase at equilibrium [4-12, 4-13]. The flux, F at the substrate is given by:

$$F = \frac{P_T a}{\pi L^2 \sqrt{2\pi m K_B T}} \quad \text{molecule / cm}^2\text{-sec} \qquad \text{Eqn. 4-1)}$$

Where P_T is the equilibrium pressure (kg-m^2/s^2) at the cell temperature T (Kelvin), *a* is the area of the cell aperture, L is the distance to the substrate, K_B is the Boltzmann constant and m is the mass of the effusing species. The units can be either molecule or atoms. For GaAs, the effusing species are As_2 and Ga. The crucible material is often made of pyrolytic BN or high purity graphite. A typical schematic of the MBE is shown in figure 4-14.

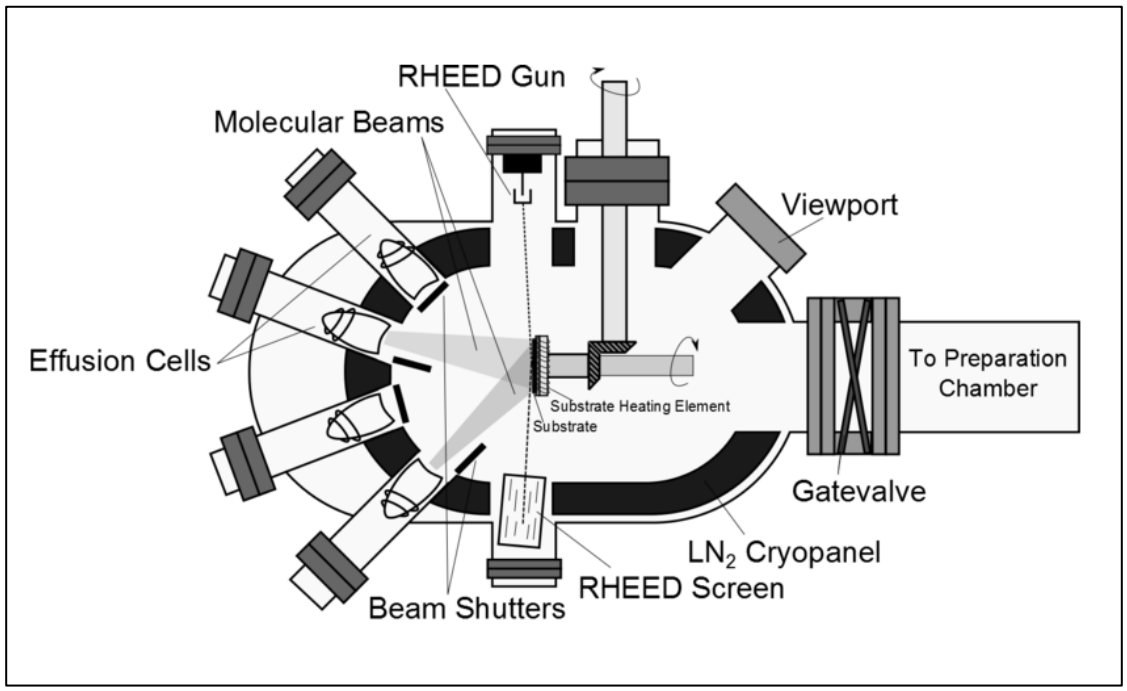

Figure 4-14: Schematic diagram of a MBE system, Wikimedia.org Commons [4-14]. http://commons.wikimedia.org/wiki/File:Molecular_Beam_Epitaxy.png

In the growth of GaAs, it is possible to use pure elemental sources or GaAs itself. When solid GaAs is heated above 637°C, As_2 evaporates preferentially, leaving liquid Ga on the solid surface [4-15, 4-16]. When used as sources, the III-V compounds provide constant beam flux of the group V element until it is nearly exhausted from the cell because the solubility of the group V element in liquid group III metal is low at normal effusion cell temperatures. When the pure arsenic source is used, one of the

disadvantages cited is that it can oxidize when the vacuum system is opened to air. Removal of the oxide can be achieved by heating the source to its operating temperature for some period prior to actual deposition. The elemental sources are still preferred since purer films can be produced.

The growth process in GaAs has been studied by surface replica analysis, and a step-growth model has been proposed [4-17]. The fact that the film surface became flatter with growth is cited as evidence of the mechanism. The kinetics of the reaction of Ga and As_2 molecular beams incident on GaAs surface have been investigated by modulated beam mass spectrometry [4-18, 4-19]. In these experiments, the incident Ga and As_2 beams were modulated by a rotating chopper wheel prior to arrival on the GaAs substrate. A mass spectrometer viewing the substrate was used to measure desorption rate as a function of the varying surface population of ad-atoms. This method provides direct measurement of lifetime adsorption or the mean residence of atoms on a surface. It is found that Ga follows a first order desorption process, given by:

$$\Gamma(t) = F\,(1-e^{-t/\tau}) \qquad \text{(Eqn. 4-2)}$$

Where $\Gamma(t)$ is the rate of desorption, and τ is the surface lifetime. Activation energy for desorption, E_d is given by:

$$\tau = \tau_o \exp\,(E_d/RT) \qquad \text{(Eqn. 4-3)}$$

The As_2 molecule on the GaAs surface does not desorb according to eqn. 4-2. The lifetime of As_2 on clean, heated GaAs is very short, and it is dependent upon the amount of Ga present on the surface. A distinction is made between a so-called Ga-stabilized and As-stabilized surface [4-20], and As_2 can bind to only the Ga-stabilized surface. About ½ of the monolayer of As can be incorporated into the surface heated at 550^oC, upon which the surface structure becomes As-stabilized. When the As_2 beam is

shut-off, the surface reverts to the Ga-stabilized structure with the evolution of a ½ monolayer of As atoms. A model consistent with these observations shows that As_2 molecules are first absorbed into a mobile weakly bound precursor state. Dissociation of absorbed As_2 can occur when the As_2 molecules encounter paired empty As sites. At elevated temperatures, recombination of As atoms to molecules and subsequent desorption is possible. The growth rate is then limited by the Ga arrival. Above 230^{o}C, there is no appreciable adsorption of As_2 unless Ga atoms had previously been deposited. Therefore, stoichiometry can be achieved by providing a sufficiently greater flux of As_2 than Ga to ensure that all of the Ga is reacted. Arsenic can evaporate as As_4 or As_2. In the case where GaAs is used as a source, As_2 evaporates preferentially and it has a higher vapor pressure by several orders of magnitude compared to As_4. The growth rate of MBE GaAs is given by:

$$R = \alpha F_{Ga} \qquad \text{(Eqn. 4-4)}$$

$$\alpha = 6.18 \times 10^{14}$$

where F_{Ga} is Ga flux in atoms / cm^2-sec, and R is in μm/hour. α is obtained experimentally [4-20].

The substrate holder is capable of heating the substrate uniformly to temperatures up to ~ 650^{o}C. This is usually accomplished by mounting the substrate on an internally heated Mo block, using a thin layer of Ga or In between the block and crystal to provide good thermal contact without the necessity for rigid clamping. The metal layer is molten at the growth temperature. Rigid clamping can cause strain in the wafer, which can introduce dislocation in the growing film. Surface contamination on the substrate can be analyzed inside the MBE chamber using AES. However, the sensitivity of AES is limited, with the surface sensitivity of approximately 2 nm and detection limit of about 0.1 at% for most elements. Additionally, the spatial resolution was approximately 1μm at the time of the present work, making it impossible to see the type of contamination on the surface that will be shown later. For GaAs, the major

surface contaminant is oxygen and carbon. The carbon contamination can be minimized by flushing the substrate with water after chemical polishing. The GaAs surface is passivated in this manner, and the surface is stable to laboratory air. Oxygen can be removed by heating GaAs in a vacuum to 525 - 535^{o}C [4-21, 4-22]. Ar^{+} ion bombardment can be used to clean the surface further, but leaves the surface disordered. Annealing at 350^{o}C is required to obtain an ordered surface again. Recontamination of the clean surface by background gas is usually not a problem at pressures below 10^{-9} torr. The sticking coefficients of most gasses are quite low (< 10^{-3}) [4-23, 4-24]. These findings have been obtained through extensive use of RED and LEED on the III-V compounds [4-17, 4-25, and 4-26].

The LEC GaAs substrate typically has a high defect density as previously described, and the MBE GaAs film has a higher quality in terms of defect density and electrical properties. However, even though the interface between the substrate and deposited GaAs is lattice matched, sometimes problems occur during the deposition process where the film has considerably more defects than it should have or its electrical characteristics are not what they should be. Typically, great care is taken to prepare the substrate surface before it is introduced into the MBE chamber. In a typical process, the substrate is etched lightly using an ammonium hydroxide/hydrogen peroxide/water solution followed by a double DI water rinse. The preparation coats the surface with a thin layer of oxide material, which passivates the surface until it can be removed by in-situ heating inside the chamber at a temperature typically above 580^{o}C. Separate Ga and As_4 sources are used in the MBE system. In this work, two types of substrate preparation are compared. In the first case, the in-situ heating was done at 610^{o}C under As_4 flux for 5 minutes to assure oxide removal before the GaAs growth commences and, in the second case, the substrate was heated only up to 550^{o}C without the complete removal of the oxide layer (which was determined later) before the film deposition. In both types of films, the growth rate of GaAs is 0.5 μm / hr, and As_4 / Ga flux ratio was 2 to 1. The final film thicknesses are 2 to 3 μm. The GaAs substrate in each case was a (100) orientation wafer, grown by LEC method. In the normal MBE

GaAs growth process where the substrate surface was properly prepared, the quality of the film is very high.

A typical bright field cross section TEM micrograph showing the interface is shown in figure 4-15. The MBE layer is free of any visible defects. Typically, the dislocation density in the substrate material is ~ 10^4 cm^{-2} by chemical etching and by X-ray topography. These substrate dislocations are largely transmitted to the grown layer. In the cross section specimens, the amount of material being examined is very small so that chances of encountering these dislocations are expected to be exceedingly rare in a typical specimen. Even for the plan view TEM specimen with viewable area of 10 x 10 μm, for example, the chance of encountering a dislocation is only 1% for a dislocation density of 10^4 cm^{-2}. The actual incidence of finding dislocations in a plan view specimen was much higher; therefore, the EPD and X-ray topography underestimates the number of dislocations present in the specimen. Nevertheless, the chance of encountering a dislocation in a cross section specimen is still very small. Figure 4-16 shows the HRTEM micrograph of the interface. In this case, the interface is nearly impossible to distinguish. It can only be said that the quality of the interface in terms of the structure is indeed very high, and that the precise location of the interface can only be inferred from the lower magnification BF images and a slight contrast difference between the two layers. The reason why the contrast exists is not clear. There may be slight thickness difference between the substrate and the MBE layer as evidenced by the shift in the thickness contours in figure 4-15.

A transmission X-ray topograph of the sample receiving incomplete oxide removal (sample #B-017) is shown in figure 4-17. Part of the wafer was covered with a mask during MBE GaAs growth so that there is no film there, and the boundary is indicated by two arrows. The MBE film shows a complex web-like structure with detail too fine to be resolved by X-ray topography. A high-resolution X-ray rocking curve scan was taken over the area with and without the mask using the (200) diffraction peak. Figure 4-18(a) is the epilayer region, and 4-18(b) is the masked substrate region. The epilayer GaAs film region has a half-width of 90 sec. while the substrate region has a half-width of 49 sec. Typical high-quality GaAs film has a half-

width comparable to those of the substrate as shown in figure 4-19 for sample #A-047 with the half-width of 45 sec. Clearly, the samples with an incomplete cleaning show problems with the GaAs film, indicating that the film has some spread in the orientation.

Figure 4-15: BF micrograph of MBE GaAs on (100) LEC-GaAs substrate. The interface is relatively perfect and there are very few features to see. The interface is indicated by two arrows.

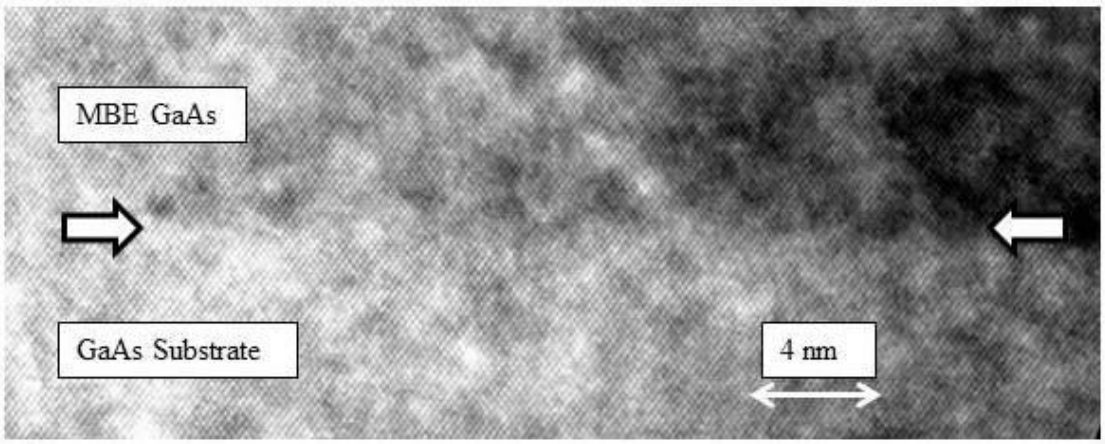

Figure 4-16: HRTEM micrograph of interface between MBE GaAs on (100) LEC-GaAs substrate. The interface is all but impossible to tell from the image.

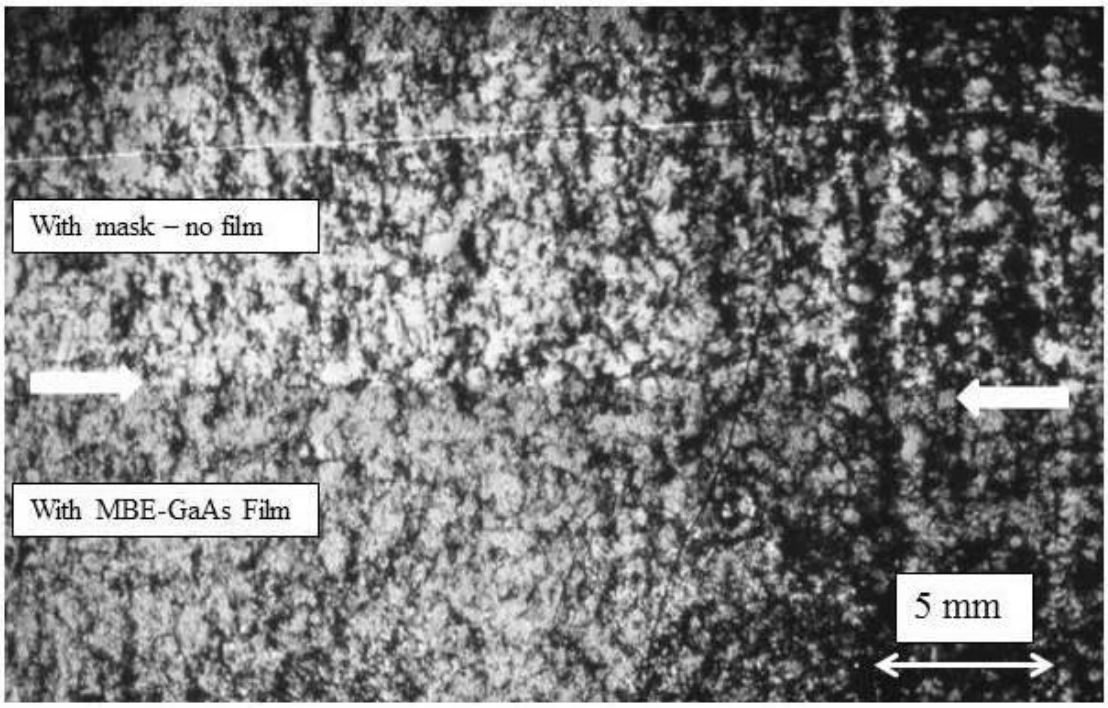

Figure 4-17: Transmission X-ray topograph of the MBE-GaAs with incomplete surface cleaning. Arrow indicates where the mask was placed. Below it has MBE-GaAs deposited, while above it is bare LEC GaAs substrate. A fine mottled contrast is seen in the MBE-GaAs film side.

Figure 4-20 is a BF micrograph of the through-foil specimen from the GaAs film from the sample #B-017. The TEM specimen was prepared by jet-thinning using a Br-methanol solution as described in Chapter 1.7. The image was taken under the two-beam condition using $\boldsymbol{g}$ = <220>. Since the MBE-GaAs film is ~ 5 μm thick, the through-foil specimen can only image a small section of the total thickness of the film. It is believed that figure 4-16 came from the top layer of the GaAs film based on the manner in which the specimen was prepared (polished from the bottom of the specimen). The image shows that the film contains a high density of stacking faults. The estimated density comes out to approximately 10^8 cm^{-2}. From the through-foil TEM analysis, it can be said that the web-like structure seen in the X-ray topograph is a

characteristic of the high density of stacking faults present in the film, which also contributes to the larger rocking curve half-width.

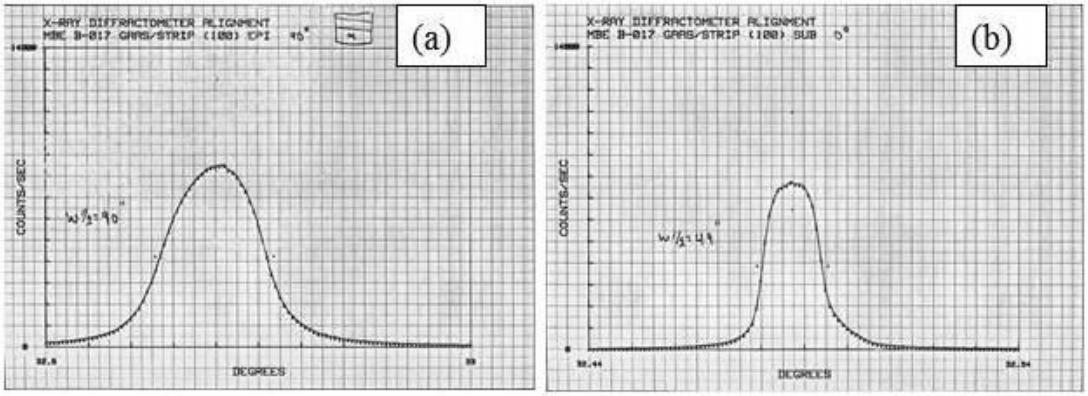

Figure 4-18: X-ray rocking curve measurement from X-ray topograph sample in figure 4-13: (a) from area with MBE-GaAs film, (b) from bare substrate. The MBE film has a half-width of 90 sec, while the bare substrate has a half-width of 49 seconds.

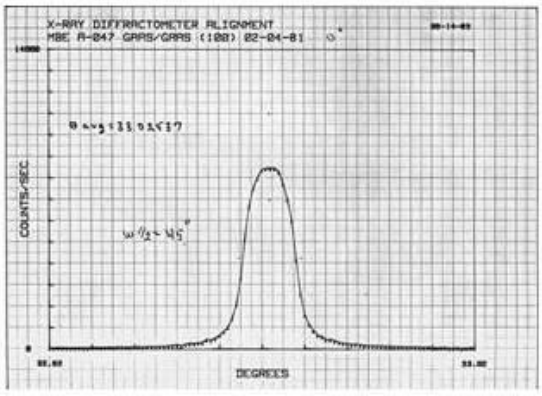

Figure 4-19: Sample A-047 X-ray rocking curve. Typical of good MBE-GaAs film, which has good characteristics, and a narrow rocking curve half-width.

A BF image of the #B-017 sample in cross section with 2-beam condition using $\boldsymbol{g}$ = <220> is shown in figure 4-21. It is clearly evident now that there is a very high density of dislocations originating at the interface between the substrate and the deposited layer. The dislocations are closely intertwined and crisscross through the thickness of the deposited layers. The resolution available in a typical BF image does not reveal the cause of the problem at the interface. This can only be achieved by the

cross section HRTEM method, as shown in figure 4-22 and 4-23. The micrographs were taken using the JEOL 200CX using 7 beams admitted through the objective aperture, out to (200) reflections. The operating voltage was 200 kV, and the micrographs were taken at 850,000X magnification. Typical beam divergence was 0.5 mrads, and the specimen orientation is <011>. Figure 4-23 shows a complex set of stacking faults originating at the interface. Upon closer inspection shown in figure 4-22 and 4-23, there is a small quantity of amorphous material at the interface, which is apparently disrupting the GaAs growth. The thickness of the oxide phase is not much greater than 1.0 nm.

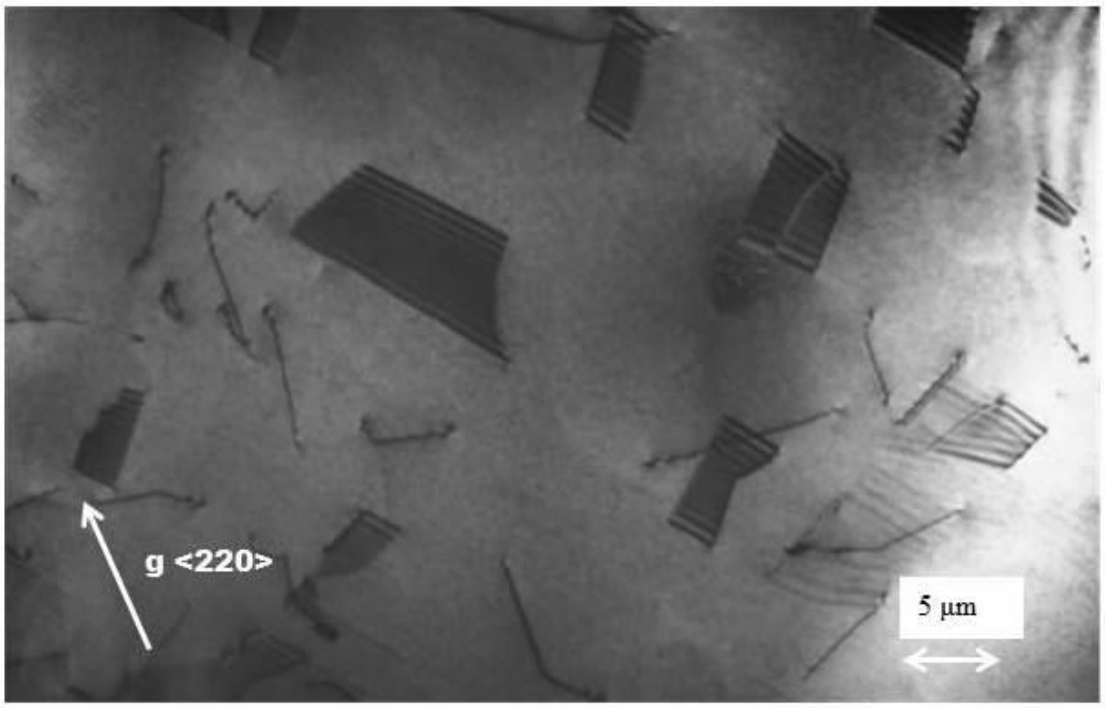

Figure 4-20: Thru-foil BF image of MBE-GaAs with incomplete substrate surface cleaning. 2-beam imaging condition was used, with ***g*** = <220>. The upper part of the MBE film is imaged, and the specimen contains a high density of stacking faults.

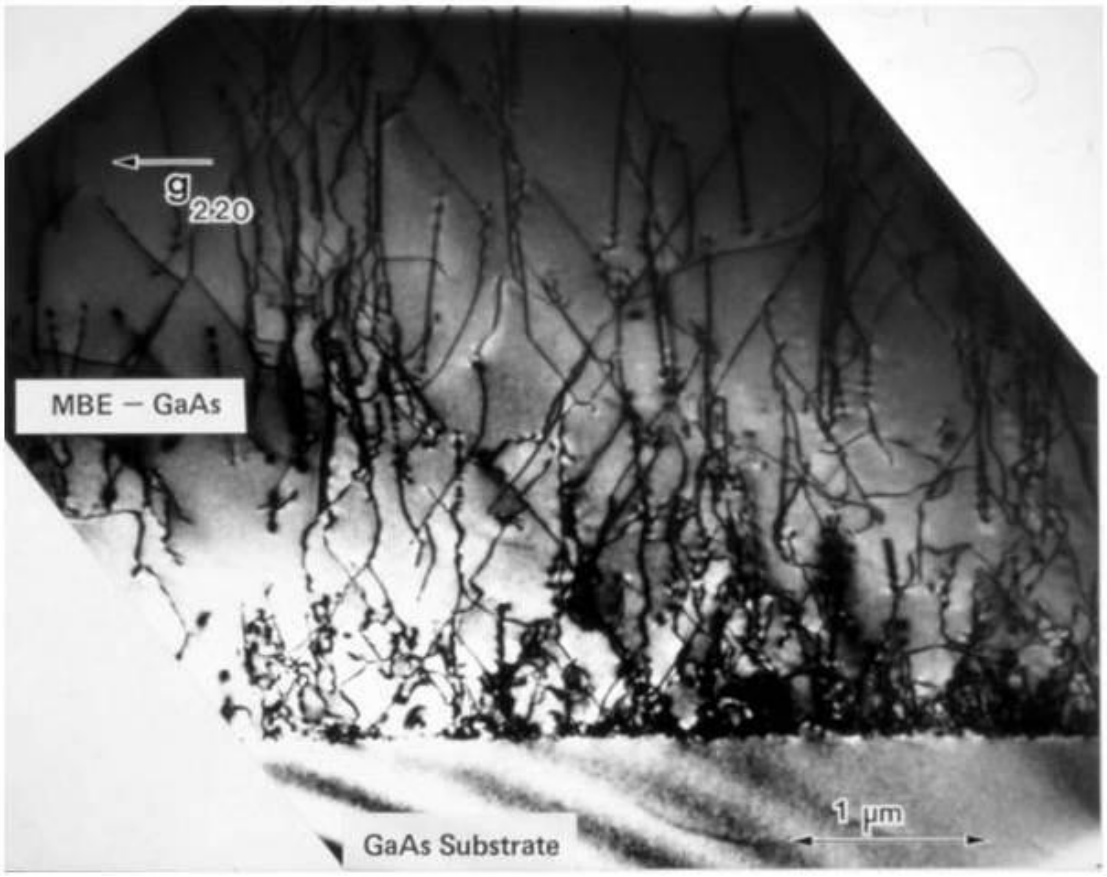

Figure 4-21: BF cross section image of a MBE-GaAs with incomplete substrate surface cleaning. Image was taken with 2-beam condition, with g = <220>.

It would have been difficult to detect and determine by any other means what the impact is to the film growth of the presence of the oxide phase and what it does to the MBE-GaAs. Even with the presence of a contamination layer at the interface, the epitaxial growth of GaAs still occurs. A substantial amount of it is still necessary to disrupt the growth. The exact nature of the amorphous contamination was not possible to elucidate at that time of analysis. Today, with much more sensitive and powerful STEM and EELS capability in the TEM, it would probably be possible to obtain much more detailed information about the chemical nature of the contaminants and even determine what it is. The conclusion from this work was that more thorough cleaning,

at a higher temperature of ~ 610^{o}C, is necessary to ensure complete removal of oxide from the GaAs substrate for high-quality growth of the MBE GaAs layer. The mechanism that leads to a high density of defects with lower temperature cleaning was also elucidated by HRTEM imaging of the interface and the results were correlated with conventional TEM and X-ray techniques.

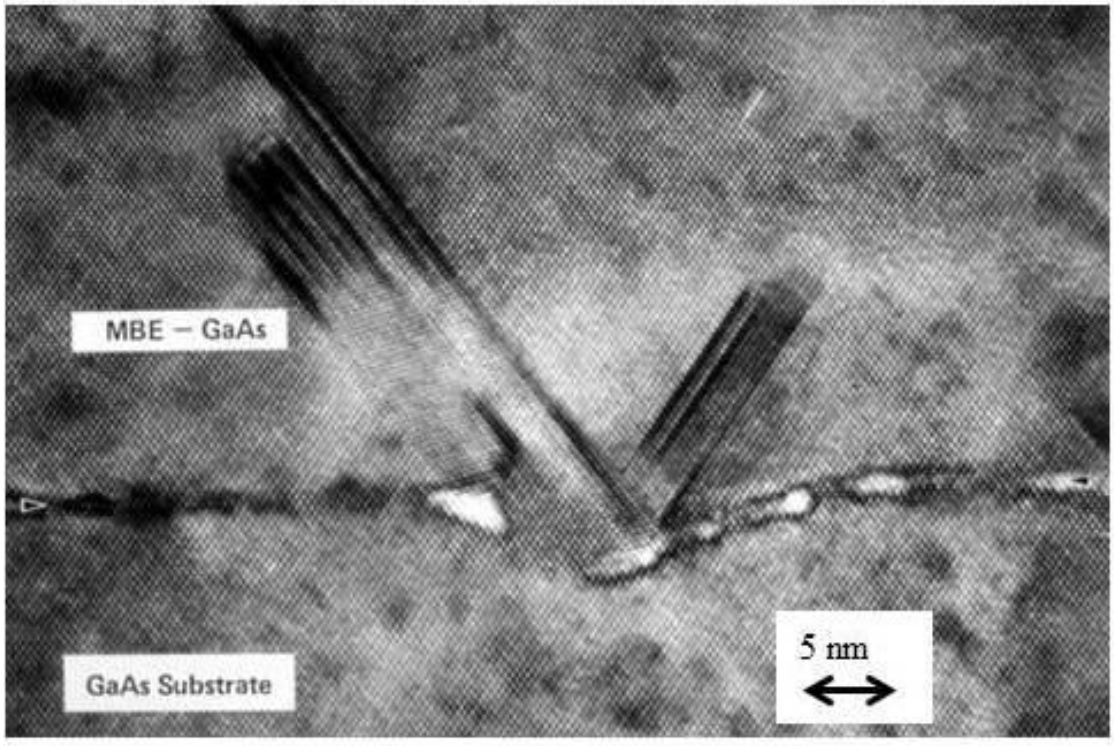

Figure 4-22: HRTEM micrograph of MBE GaAs/GaAs interface with incomplete cleaning. Amorphous oxide phase at the interface cause formation of faults and dislocations at the interface that grows into the MBE-GaAs layer.

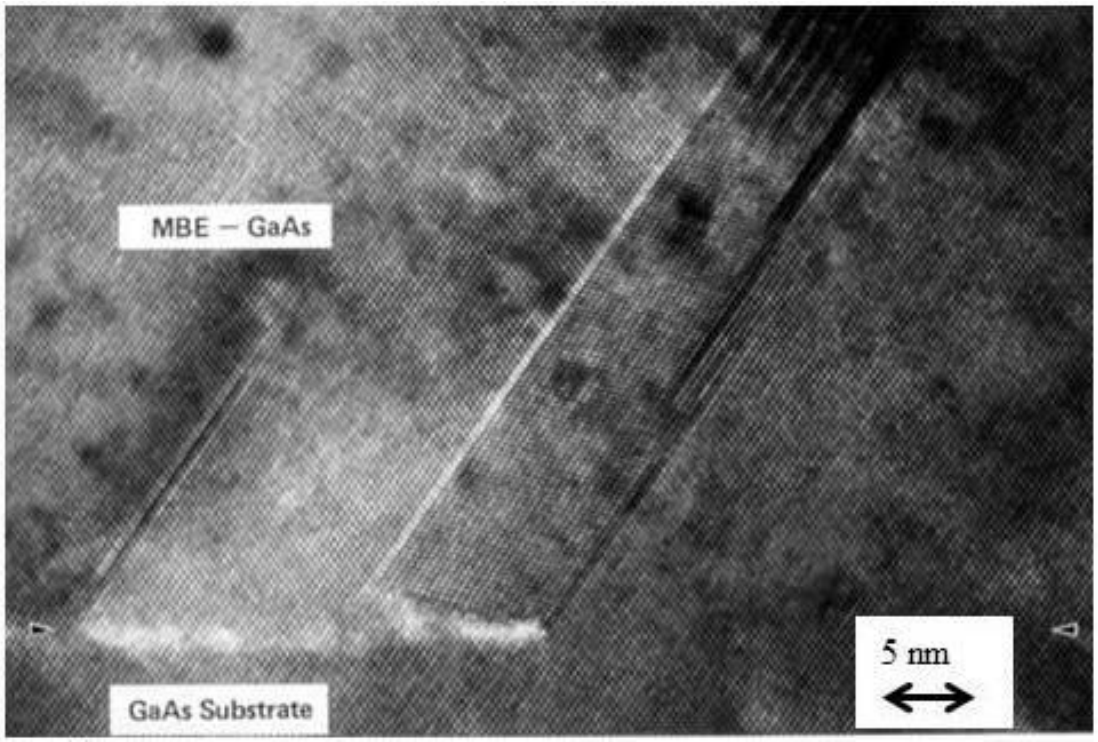

Figure 4-23: HRTEM micrograph of MBE GaAs/GaAs interface with incomplete cleaning. Arrow points to the interface. Where there is a contamination, the defect growth occurs.

4.3 HRTEM Analysis of AlAs/GaAs Heterojunction Interface

In this investigation, the interface between the AlAs and GaAs layers grown by MBE was analyzed in cross section by HRTEM. The MBE structure consisted of 50 nm of GaAs grown on (100) LEC-GaAs substrate, followed by 100 nm of AlAs and 50 nm of GaAs. The images were obtained in (110) orientation as usual. The purpose was to study how sharp the interface could be imaged by HRTEM and to calibrate the MBE growth rate with the precise HRTEM measurements. The MBE technique allows fabrication of high-quality multiple layer heterojunction devices based on $Ga_{1-x}Al_xAs$/GaAs system [4-27]. In some cases, the layers can have dimensions that are only a few atomic layers thick [4-28, 4-29]. Therefore, it is important to be able to

control the layer thickness as precisely as possible with several techniques including HRTEM so that electrical properties of these devices can be related to their actual structure. A notable feature of GaAs and AlAs is that they have nearly identical lattice parameters; therefore, the compositions involving GaAlAs also have the same lattice parameter. The lattice parameter of GaAs is 0.565 nm and AlAs is 0.566 nm. Cohesive energy is also relatively close, at 1.63 eV for GaAs and 1.89 eV for AlAs. Elastic constants are not listed for AlAs in Harrison's text [1-10] and the calculated value based on near-infrared Brillouin scattering [4- 30] is listed below with GaAs values as a comparison in Table 4-2.

Table 4-2 Lattice parameter, cohesive energy, elastic constants, and Poisson ratios for GaAs and AlAs.

	Lattice Parameter	Cohesive Energy (eV)	C11 (GPa)	C12	C44	ν
GaAs	0.565 nm	1.63 eV	118.1	53.2	59.2	0.31
AlAs	0.566 nm	1.68 eV	119.9	57.5	56.6	0.32

ν (Poisson Ratio) = C12/ (C11 + C12)

GaAs and AlAs are ideal for creating a nearly perfect interface as the lattices are nearly perfectly matched. The structural parameters of interest are the thickness of the layers, the abruptness of the interface, and overall chemical and structural perfection of the layers. Some of the difficulties involved in this analysis are the lack of sufficient contrast difference between $Ga_{1-x}Al_xAs$ and the GaAs layers by conventional TEM imaging methods. One imaging method that provides some contrast between GaAs and $Ga_{1-x}Al_xAs$ is the dark-field imaging technique using the (200) reflection, which emphasizes the structure factor difference between the Ga, Al and As [4-31]. However, the resolution available from this technique is limited by the diffraction effects from the objective aperture used in this imaging mode, which is typically about

1.0 nm. HRTEM can use the ultimate resolving power of the TEM, which at the time was approximately 0.26 nm.

To study the capability of the HRTEM method applied to this problem, a special structure was made representing the extreme in the mole fraction of Al, namely, a pure AlAs sandwiched between two GaAs layers to determine the applicability of HRTEM method to this task. A MBE film was made in a Varian Gen II system, on a Cr-doped LEC semi-insulating (100) GaAs substrate. Standard ammonium hydroxide-peroxide etch was used to prep the wafer, and the substrate was thermally treated at 610^{o}C under As_4 flux for 2 minutes. As, Ga and Al source temperatures were 312, 1151, and 1308^{o}C respectively, for the growth rate of 0.9 μm/hr. for GaAs and 0.4 μ/hr. for AlAs, and As_4/Ga flux ratio of 2:1. GaAs layers were grown at 582^{o}C substrate temperature. The AlAs was grown at 700^{o}C. Background pressure was at 6.1 x 10^{-8} torr. The growth was not interrupted between the layers as the substrate temperature was changed.

The specimen preparation method for the cross section samples was the method described by Bravman and Sinclair [1-24] and already described in Chapter 1.7. Ion milling was done at 4 keV for 4-5 hours. The microscope used in the analysis was a JEOL 200CX operating at 200 keV. HRTEM lattice images were always formed using 7 beams through the objective aperture, and images were taken typically at 850,000X magnification. Specimens had to be examined immediately after ion milling to prevent oxidation of the AlAs layer. This layer would oxidize within a day if left in the air, always greatly expanding as it oxidized. The thickness of the specimen at the area of interest can be estimated to within 2 - 3 nm based on the position of the Pendellösung thickness fringes. Multi-slice image simulations were done to calculate the behavior of beams vs. thickness to obtain the thickness position of the Pendellösung fringes. Since the image contrast was an important consideration for exact placement of the interface, the thickness estimation for GaAs and AlAs was an important consideration. In addition, the issue was the difference in milling rate between GaAs and AlAs, potentially resulting in thickness difference between the materials across the interface.

This could not be controlled. It did appear that AlAs was milling slower than GaAs based on observation of many samples. Thicker AlAs might have led to darker image contrast, but as it turned out, AlAs always appeared with lighter contrast than the GaAs in the HRTEM images, suggesting that contrast due to atomic scattering dominated.

The BF micrograph of the structure showing the relative thickness of each layer is shown in figure 4-24. Figure 4-24(a) was taken in an axial orientation, with the specimen aligned to the (011) zone axis as close as possible. A relatively sharp demarcation can be seen between the top GaAs and AlAs layer, and between the AlAs and the bottom GaAs layer. However, the demarcation between the bottom deposited GaAs and the substrate cannot be seen, as was the case earlier. The top GaAs film thickness was 52 nm while the AlAs layer was 73 nm thick, which was considerably less than the 100 nm that had been planned. The bottom GaAs, which should have been the same thickness as the top because they were deposited under the same condition, did not show any distinguishable interface with the substrate at that location. However, there is a region of contrast difference at approximately 130 nm deep below the AlAs layer, which shows lighter contrast above and mottled contrast feature below it. It is not clear what this contrast is due to. The contrast is not always present under different diffraction conditions. It could be due to thickness variances in the specimen, but the demarcation line between the light and darker mottled contrast is too sharp to be explained as simply thickness difference. Therefore, this feature of the contrast in the cross section specimen remained a mystery. Figure 4-24(b) was taken using a two-beam condition with $\boldsymbol{g} = <02\bar{2}>$ (with the correct vectors for the direction notation maintained). Since the substrate is (100) orientation, and the specimen is in the (011) orientation, setting the two-beam condition to $<02\bar{2}>$ means tilting the specimen along the direction of the interface. Therefore, the interface is still imaged end-on.

It has been noted that there is a difference in the value of the valence band discontinuity between the AlAs/GaAs and GaAs/AlAs interface [4-32]. That is, the ΔEv depends upon the MBE growth sequence in the AlAs/GaAs system, and this non-commutivity effect has been attributed to the structural difference between the two

interfaces or to the presence of impurities. The lattice images of the two interfaces were examined carefully for such details as presence of contrast features at the interface (evidence for the presence of impurities or strain) and abruptness of the interface, but no significant difference in the interface structure was detected in the lattice images to within the resolving power of the HRTEM technique. The bottom GaAs/AlAs interface is shown in figure 4-25, and the top AlAs/GaAs interface is shown in figure 4-26.

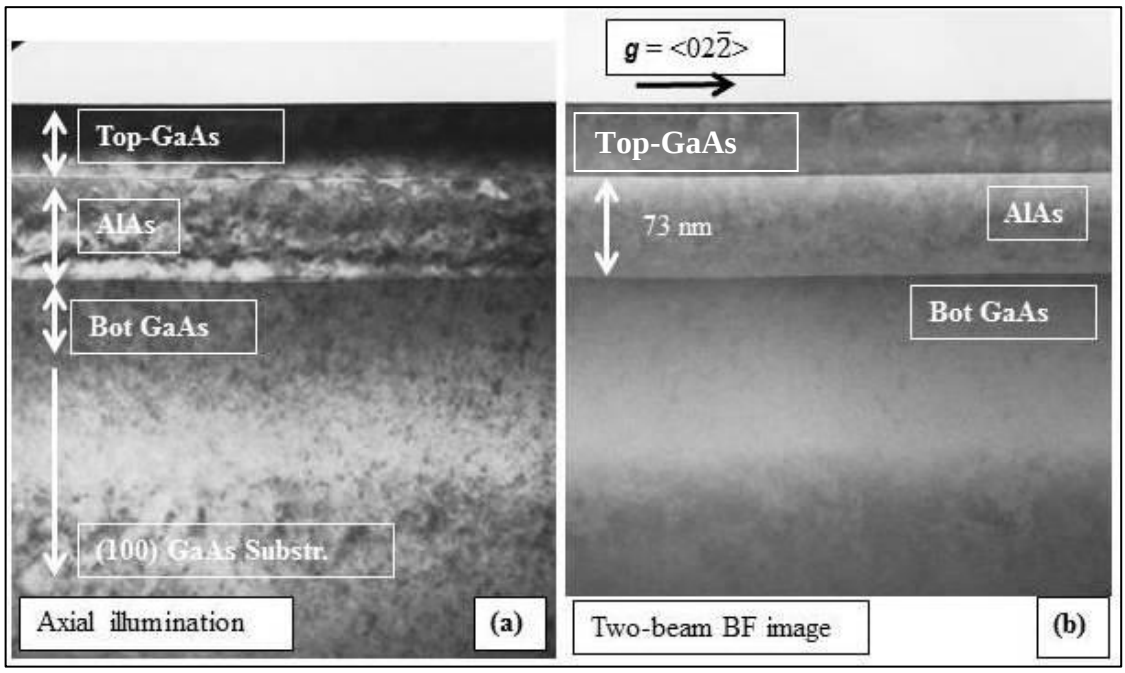

Figure 4-24: (a) BF micrograph of GaAs/AlAs/GaAs MBE films on (100) GaAs substrate, taken at axial illumination. Contrast features present in various layers and near the interface are probably due to some strain contrast, but some of the features could be defects; (b) is the BF image taken with $\boldsymbol{g}$ = <02$\bar{2}$> two-beam imaging condition. Note that contrast features change with the diffracting condition.

From the lattice images of the top and bottom interfaces, it is difficult to discern that there are obvious differences in the interface. There is no visible evidence of contamination, segregation or any defects that delineate the interface and makes the two interfaces appear differently. With the maximum extent of composition difference represented by AlAs vs. GaAs, a composition that is in-between for $Ga_{1-x}Al_xAs$ would be even more difficult to discern against GaAs using the HRTEM method. GaAlAs heterojunction with GaAs was not examined in this study; therefore, any optimization that could be made for HRTEM imaging of the interface was not made. However, under the conventional TEM method, it is possible to discern some contrast between the interface due to existence of strain and some other factors, including specimen preparation effects such as difference in milling rates between the two materials. Therefore, unless some particular features such as physical defects or interface problems such as contaminations are being looked for as in the previous section, it is not possible for the HRTEM technique to precisely identify the location of the interface. In a modern TEM with high-resolution EELS and EDX capabilities, it is possible to precisely locate the interface with near atomic resolution using chemical mapping.

For the purpose of completeness, image simulations using the multi-slice program were done for the AlAs and GaAs, and the supercell that includes the interface between AlAs and GaAs. Amplitudes of various reflections for GaAs and AlAs are shown in figure 4-27(a) and 4-27(b) for GaAs and AlAs, respectively. GaAs and AlAs reflections have considerably different amplitude behavior vs. thickness, which could be used to some advantage in HRTEM imaging. At some specimen thickness for example approximately 10 nm, for example, AlAs (200) reflection peaks while GaAs (200) reflections are quite weak. This would have the effect of enhancing the AlAs image characteristics, which might be more visible in the HRTEM imaging. It is essentially the same argument that was used by Petroff [4-31] in using (200) dark field imaging.

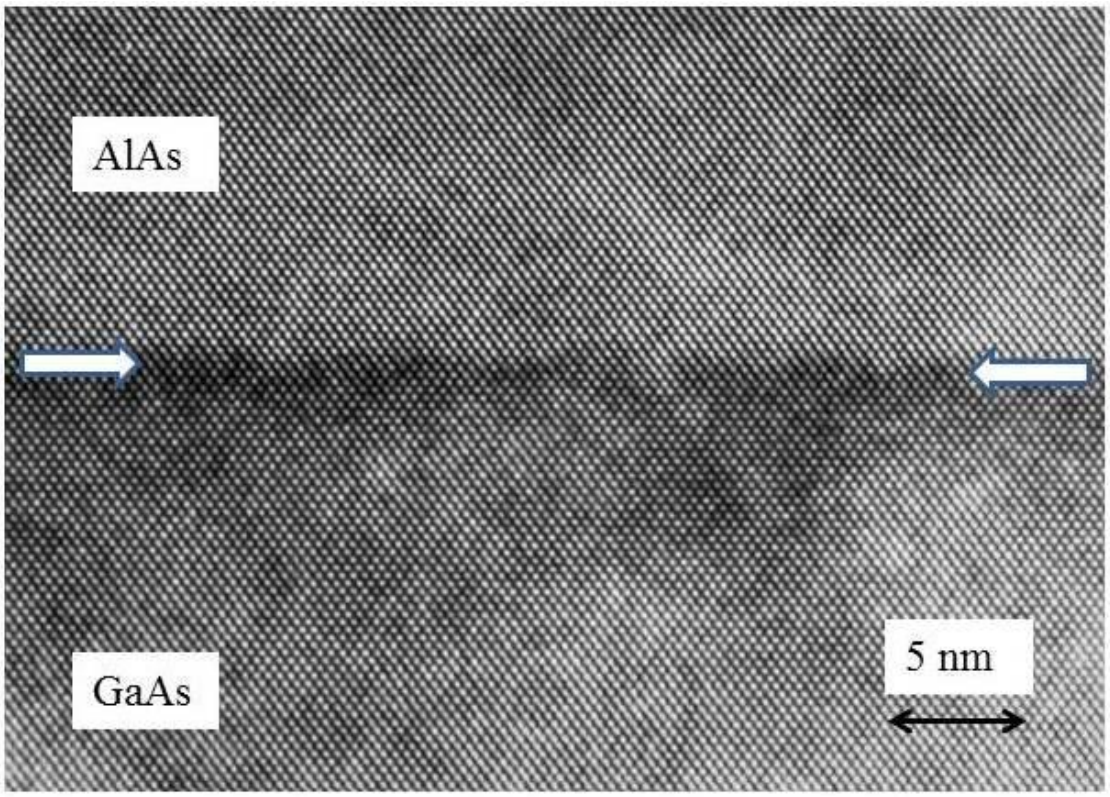

Figure 4-25: HRTEM image of the interface between the bottom GaAs MBE layer and the AlAs layer. The arrow indicates the approximate location of the interface. Aside from the dark shadowy contrast at the interface, it is quite difficult to discern a sharp interface between the GaAs and AlAs. The dark band could be due to a subtle thickness difference at the interface due to a small amount of lattice strain at the interface.

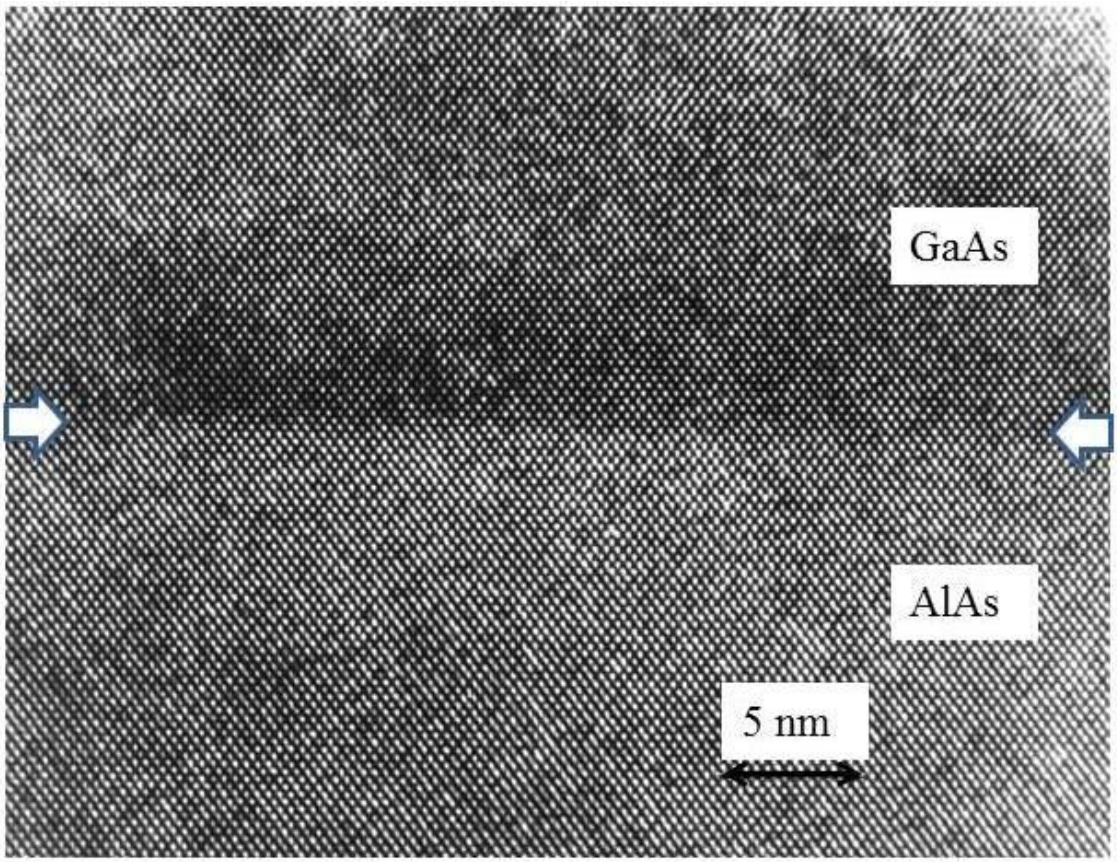

Figure 4-26: HRTEM image of the top GaAs/AlAs interface, showing the perfection of the lattice match and difficulty in discerning the exact location of the interface. The location of the interface is shown by the arrows. There is a dark band on the GaAs side that makes it somewhat easier to see the interface compared to the bottom GaAs/AlAs interface shown in Figure 4-21.

Image simulation using a supercell constructed out of GaAs and AlAs interface was calculated. 6774 Fourier coefficients out to (26, 38, 0) were used. The unit cell contained a total of 96 atoms; 48 As, 24 Al and 24 Ga atoms. The defocus series for the thickness of 2.0 nm is shown as an example of this type of image simulation in figure 4-28. Defocus is in increments of 10.0 nm from -50 to -130 nm underfocus. The main problem with the simulation is that the objective was to look for intensity difference or contrast between the two materials, and with the overprinting method used in this case

using a line printer, it is difficult to determine whether there is a contrast difference. It had been shown by Krakow [4-33] that multi-slice simulation can actually simulate actual intensities in experimental images if proper settings for the intensities are used and with grayscale that properly represent the actual experimental conditions. However, even in the modern case with more sophisticated intensity scaling, the proper calibration of intensities in the simulation to the experimental images difficult to achieve. As mentioned previously, it is more convenient to use chemical mapping to determine the exact location of the interface in a modern microscopes.

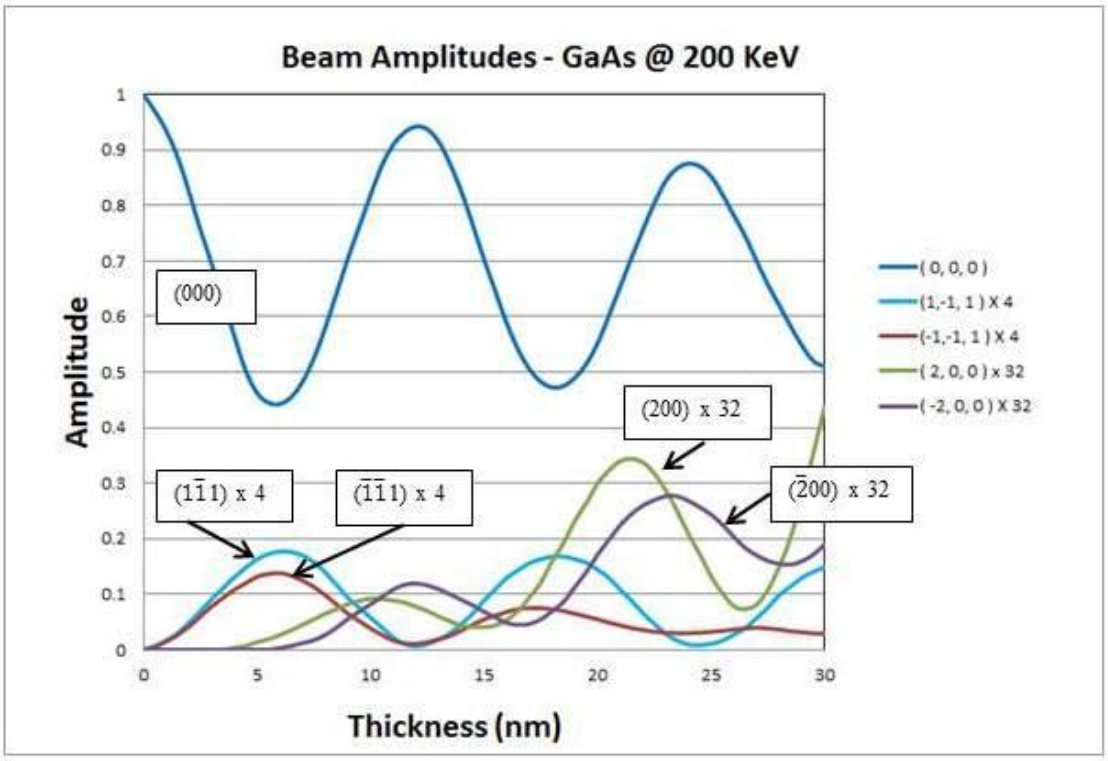

Figure 4-27(a): Beam amplitude vs. thickness for GaAs reflections based on multi-slice simulation. Note that (200) and (111) reflections are relatively weak and they multiplied by 32X and 4X, respectively.

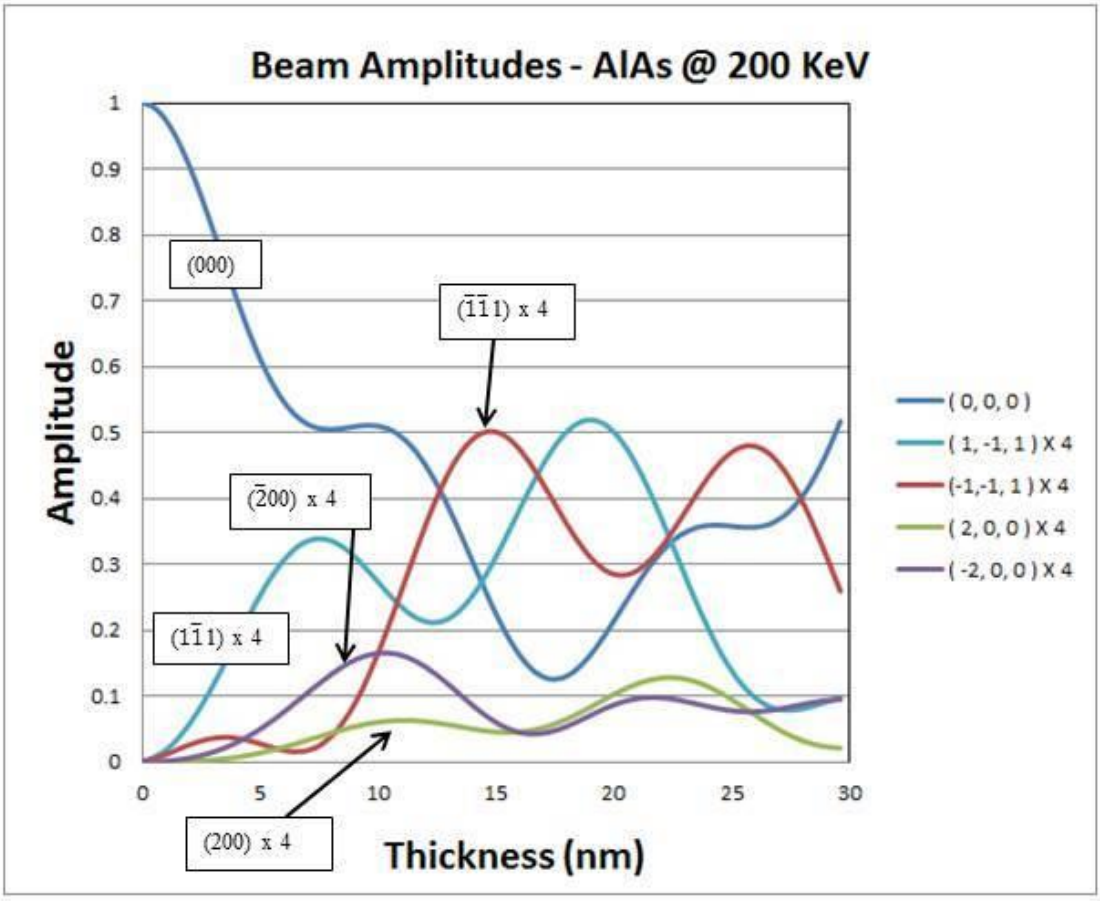

Figure 4-27(b): Beam amplitude vs. thickness for AlAs reflections based on multi-slice simulation. The reflections have considerably different behavior compared to the GaAs. The (200) reflections are much stronger for AlAs, which could be used to advantage for imaging. Note that (200) and (111) amplitudes are expanded 4X in the figure.

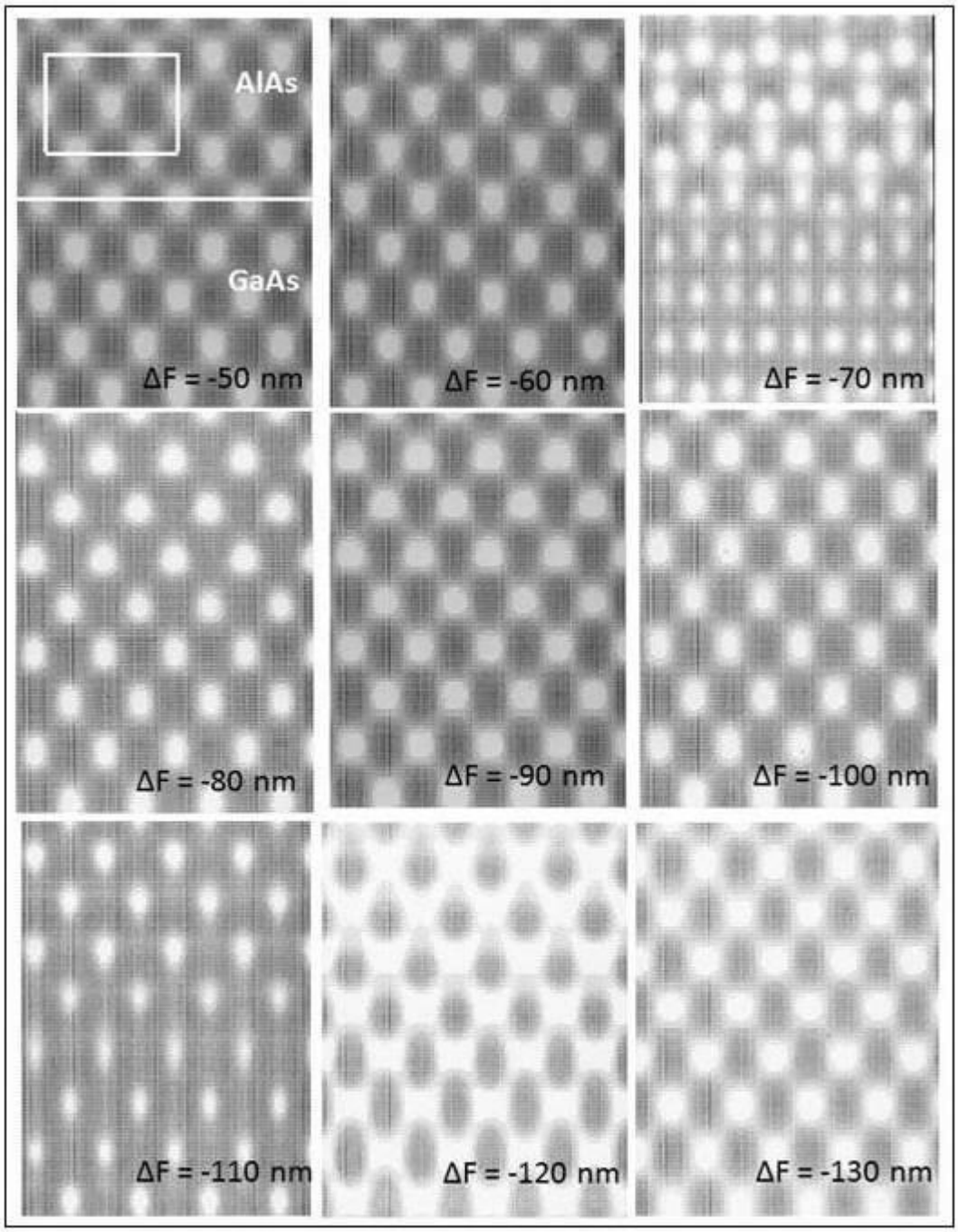

Figure 4-28: Multi-slice simulation of AlAs/GaAs interface. Specimen thickness at 2 nm. Δf defocus series from -50 nm at 10 nm increments. Imaging conditions are for JEOL200CX microscope at 200 keV with Cs = 1.2 mm. Position of the interface is indicated by the white line in Δf = -50nm image. Unit cell for GaAs or AlAs is also indicated in the same figure.

For the GaAs/AlAs/GaAs interface, dislocations that penetrate through several interfaces were observed in a small region of the specimen. Figure 4-29 is a BF image taken near axial illumination. What is interesting about the image is that some of the dislocation originates within the first deposited GaAs layer and extends through the AlAs. Some abruptly terminate at the top AlAs/GaAs interface while others that originate within the AlAs layer continue through to the top GaAs film. The location of the substrate is well below what is shown in the micrograph. It appears that initial dislocation occurs partly through the first GaAs layer. It is not very clear from the image how or why the dislocation started in the first place. HRTEM imaging was attempted on the specimen but it was too thick to obtain useful images. It is easier to understand that a discontinuity in elastic constants and cohesive energy may present some barrier to dislocation motion or continuation of its growth between AlAs and GaAs lattices.

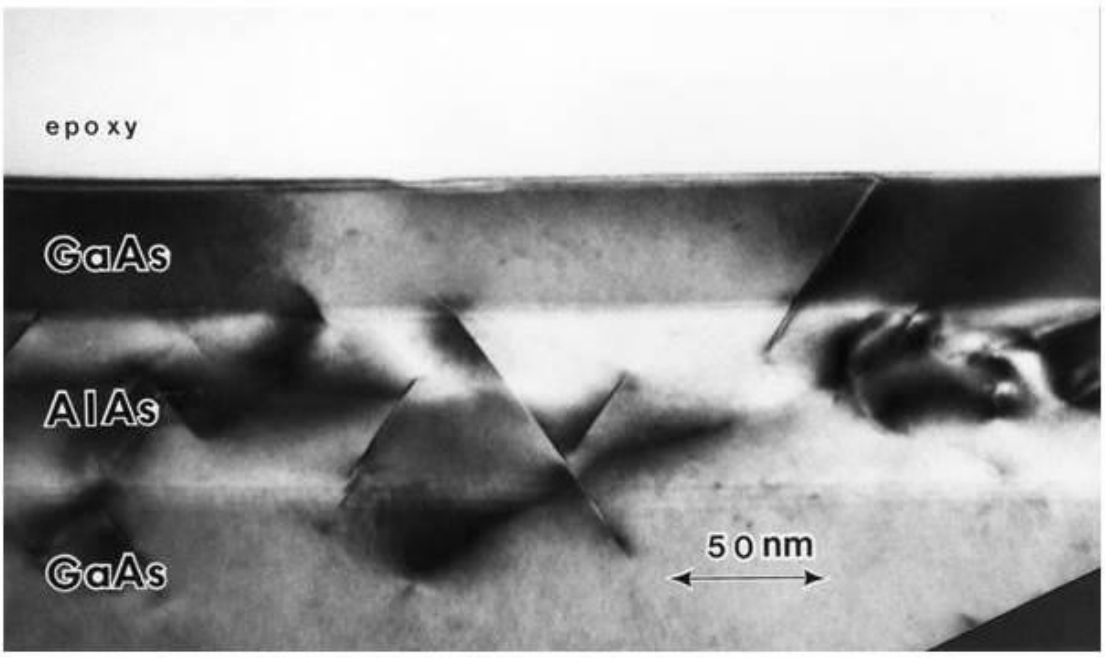

Figure 4-29: Dislocations in the MBE-GaAs and AlAs film layers. The location of the substrate is well below what is shown in the micrograph.

In summary, HRTEM technique is well suited to study thin epitaxial structures such as the MBE-GaAs hetero-structures. The quality of the interface and the film can be determined quickly in cross section specimen and exact thicknesses of the layers can be measured so that deposition conditions can be adjusted to obtain very precise control over the fabrication of devices. The precise control and reproducibility that the MBE process offers for depositing different layers of material makes HRTEM the ideal tool to use for process monitor and trouble-shooting. High-resolution chemical mapping capability of the modern analytical TEM makes them even more useful.

4.4 Characterization of Oval Defects in MBE GaAs

This section describes the characterization of so-called *oval defects* in MBE GaAs, which was a significant problem in MBE GaAs film growth in early 1980s. The description of the defect comes from its distinct oval shape, which is crystallographically oriented with respect to the (100) GaAs substrate. The defect is a mound or a shallow protrusion on the surface of the GaAs film, and has a dimension of approximately 5-15 μm or more along the long axis and less than half of the long axis dimension on its short axis. On the (100) wafer, the long axis of the oval defects were always aligned with the <110> direction. The shape and size vary considerably, but they are easily visible under an optical microscope. These defects interfere significantly with the device structure on the MBE GaAs film, and they often exist in high density to cause significant issues in quality and yield of devices fabricated from the film. Typical density was in the range of 10^2 to 10^4 defects /$cm^{2,}$ and the density was often correlated with the condition of the Ga effusion cell. What was known or was suspected at that time was that some form of vapor-liquid-solid (VLS) growth [4-34] is involved with spitting of Ga droplets from the Ga effusion cell, as many oval defects contained what appeared to be small foreign solid materials inside the defect. Additionally, it was known that Ga oxidation in the effusion cell could lead to oval defect formation [4-35]. It was thought that spitting of involatile oxide particles onto the GaAs substrate lead to the formation of oval defects. The oval defect problem was “solved” more than once according to many publications and apparently it took until around the 1990s to

completely solve the problem. There were many analyses and characterizations done on the defects that were published into the late 1980s [4-36, 4-37]. Therefore, there were several sources and mechanisms involved in the formation of oval defects [4-38].

A typical optical micrograph of oval defects is shown in figure 4-30. The numbers next to the defect were a part of an effort to classify the defect type, and considerable statics were gathered on their frequencies. It can be seen from the micrograph that the oval defect direction is oriented in one direction.

The typical film structure used for the oval defect analysis was with 0.5 μm of undoped MBE GaAs, followed by 1.0 μm of undoped AlGaAs (Al=28%), and capped with 4.0 μm of Si-doped AlGaAs. SEM micrographs of several oval defects are shown in figure 4-31. These types of oval defect have faceted edges and sometimes contain white material inside. This material tends to charge-up under SEM viewing and appear bright white. It did appear that the white phase goes through several stages of growth. Some are very small as shown in the center micrograph, and some grew much larger, as shown in figure 4-32. These oval defects are always a hillock, protruding from the surface of the MBE-GaAs. The faceted edge appears to be close to the {111} plane in the GaAs. In the (100) wafer surface, the facet face could be two of the possible four {111} types of planes depending upon which <110> direction the defect is facing.

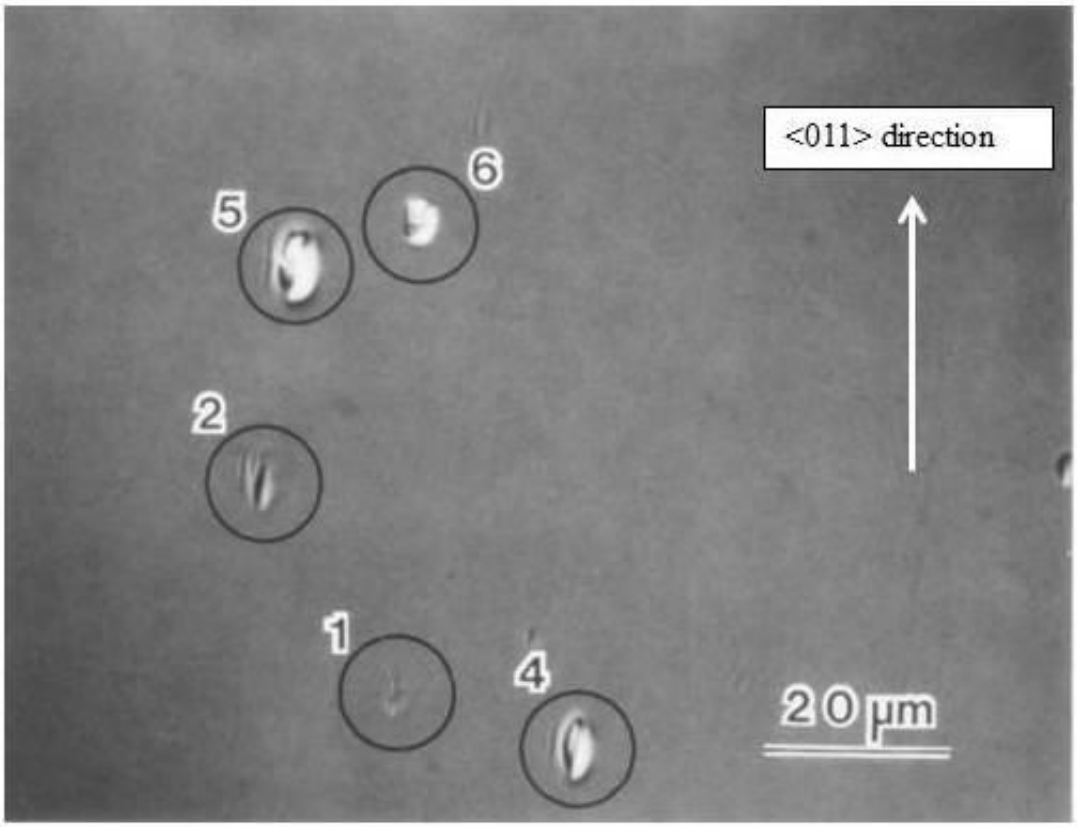

Figure 4-30: Example of some of the variety of *oval defects* on MBE GaAs on (100) a LEC-GaAs substrate (optical micrograph).

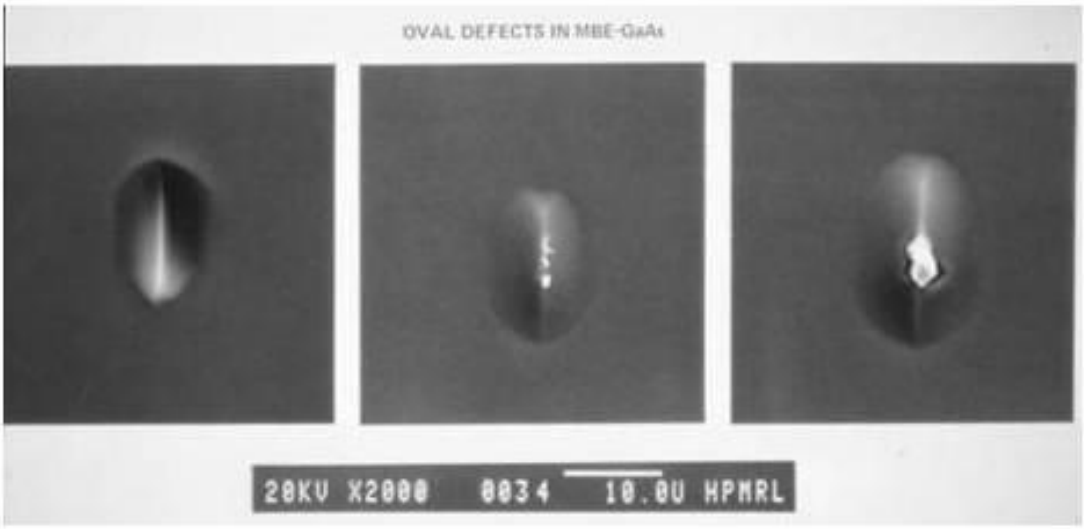

Figure 4-31: SEM micrographs of several oval defects with facet face.

The two <110> directions are not equivalent due to non-centrosymmetry of the GaAs when it comes to the {111} planes. One set will be a Ga-rich face while the other is As rich-face. Anisotropic etch consisting of 3 part H_2SO_4, 1 part H_2O and 1 part H_2O_2 can determine which direction the oval defect is facing and which {111} face would be the A face (Ga) and the B face (As) [4-39]. The etch creates a trough on the GaAs (100) face, and $\{111\}_A$ face would have a narrow edge while the B face will have a wide sloping face. The etch results showed that if the oval defect facet face is close to {111} face, it would have an "A" face or Ga-rich face. However, having determined this, not much else could be deduced or understood about why this is the case. Additional SEM images of oval defects with white particles or other structures inside of it are shown in figure 4-32. The white "ball" defect was quite common with the oval defects, and initial SEM-EDX analysis had mistakenly led to the conclusion that these "balls" are Ga-rich. In fact, by SEM EDX analysis, it was quite difficult to come to any conclusion because the features were small, and there were always stray signals from the surrounding GaAs matrix to confuse the data. Since Ga spitting and Ga oxide formation inside the effusion cell had been implicated in the oval defect formation already, it was easy to think that the white balls were associated with Ga from the effusion cell. Naturally, the Ga oxide would be less conductive and would charge up in the SEM and expected to appear white.

Some of the so-called "oval" defects were actually irregularly shaped, as shown in figure 4-33, and they also contained whitish powderly material inside. These irregular defects had more of a "spitting" impact crater-like appearance as if something had landed on the substrate surface and affected the subsequent MBE film growth. A survey of these various types of defects made it clear that one was probably dealing with more than just one mechanism that was causing these surface defects on MBE-GaAs. The next logical step was to undertake a TEM-based characterization of the defects.

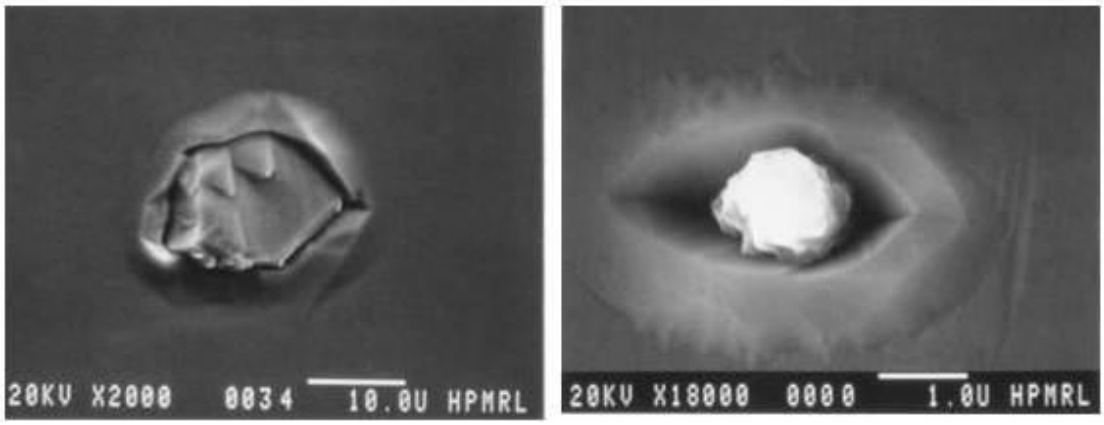

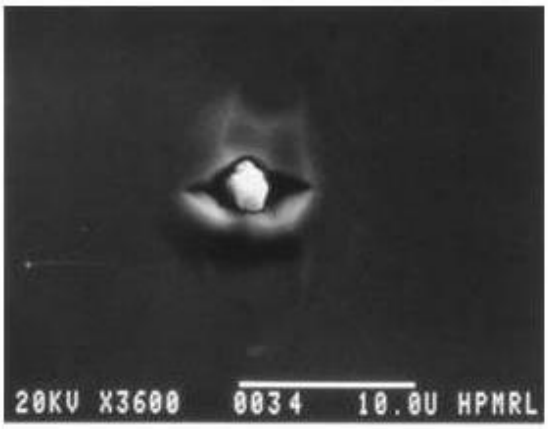

Figure 4-32: Additional SEM photographs of oval defects with various appearances. Oval defects with a white "ball" inside were quite common.

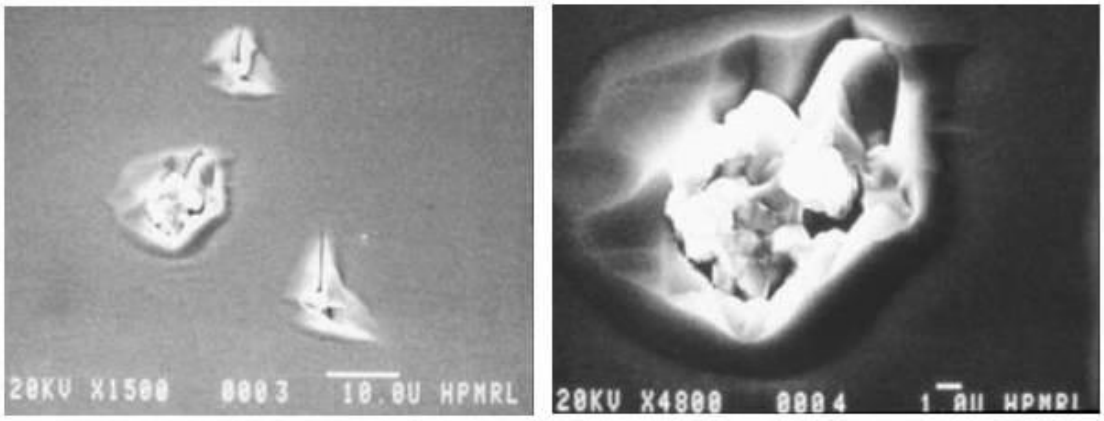

Figure 4-33: SEM micrographs of irregularly shaped "oval" defects. They also contained white particles inside, but often they were also irregularly shaped and polycrystalline. They have the typical appearance of external "impact" defects, where a particle fell on the substrate and film grew around it.

TEM analysis of the oval defects presented some challenges in terms of specimen preparation. Planar samples were attempted at first, but to capture the defect in the thin part of the specimen was quite difficult. Many attempts were made without capturing the defect in plain view. The defect density was high but still not high enough to conveniently capture the defect in the TEM specimen. However, once found, the problem was that the defect feature was quite large and covered considerable thickness of the specimen. Total thickness of the deposited GaAs and GaAlAs MBE films were over 5 μm thick, and the defect that was caught appeared to cover the entire thickness of the film, which could only be imaged partially because the specimen was thinned. It was difficult to obtain a clear picture of what part of the defect was actually being imaged. Attempt to capture the defects in cross section was even more difficult, as it would have to be a complete stroke of luck to catch the defect in a thin slice of cross section specimen even with the high density of oval defects. Recently, this issue has been solved by the use of a focused ion-beam (FIB) tool, which can zero-in on a small surface defect and obtain a precise cross sectional TEM sample to determine what is taking place with the defect. At the time of this analysis, the FIB tool was still perhaps 10 - 15 years into the future.

There was only one instance where something was caught in cross section, and it occurred for one of the GaAs/AlAs/GaAs/LEC-GaAs specimen that was discussed in Section 4-3. A large defect was caught in cross section that resembled an oval defect in terms of their scale on top of the specimen. This micrograph is shown in figure 4-34. It shows a massive amount of dislocation that is clearly in the substrate that causes considerable disruption in all of the MBE layers, and the surface profile that is on the same scale as the oval defect. Therefore, this one micrograph showed a connection between the substrate-based defect to the subsequent formation of the oval defect. The difference with this sample was that MBE film thickness was only approximately 170 nm, made deliberately thin. The fully developed oval defects were always on a thick MBE films, therefore the thickness of the MBE films definitely played a role in the formation of the oval defects.

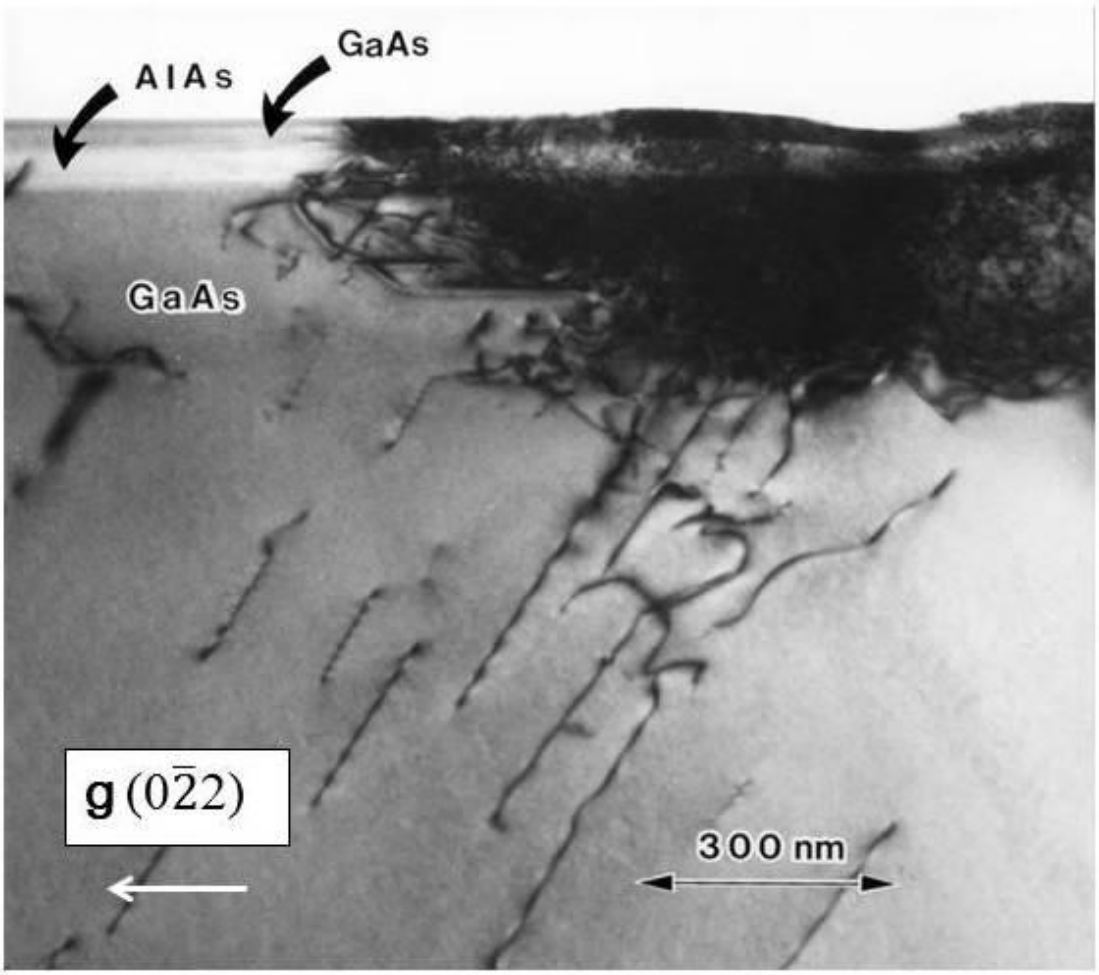

Figure 4-34: Massive pile-up of defect in the MBE GaAs/AlAs/GaAs on LEC GaAs that appear to be made of tangles of dislocations that originate in the substrate. Surface feature is on the same sort of scale and shape that would be expected from an oval defect. Compared to previous specimens, this particular structure only had approximately a 170 nm thick MBE layer; therefore, the defect would not have had a chance to develop further compared to the 5 .5 μm thick film parts with fully developed oval defects.

4.5 Characterization of GaAs Whiskers Grown by MBE GaAs

While the investigation into oval defects was taking place, a new and more urgent issue needed to be addressed. The MBE process went completely out of control at HP Labs because whisker growth phenomenon started to take place during MBE film growth, which completely overwhelmed the process. Apparently, whisker growth had been observed from time to time, but it was at a nuisance level, and not much attention had been put on it. The oval defect was a much greater concern. Now, the entire process was shut down due to whisker growth. Initially, the reason why the process had fallen apart so much could not be identified, and significant effort was expended in troubleshooting the MBE system and attempting to understand what the whiskers were, and to try to understand why it was forming. Under normal conditions that were being used at the time with the growth of ~ 5-6 μm of MBE films, the whisker covered the entire surface of the wafer. The whiskers were typically a few microns thick at the base and often grew to a length of a few hundred microns. The thickness gradually tapered to a point at the end, and there was no evidence of liquid droplets at the tip. Therefore, vapor-liquid-solid (VLS) growth mechanism was ruled out. Incomplete cleaning of the substrate, as it was done for the GaAs film growth study in section 4-2, made things much worse. The example of this is shown in figure 4-35 in the SEM micrograph where the surface is covered in whiskers, which are several hundred microns long. The growth rate of the whiskers was estimated to be between 10 to 50 μm/hr, which is extremely fast.

Some of the MBE samples were run with shorter times, and they had much shorter whiskers compared to the one shown in figure 4-35 with full deposition times. Optical and SEM micrographs of shorter whiskers are shown in figure 4-36. It was noted by both optical inspection and SEM that whisker growth direction was directional, and it followed the same long axis as the oval defect, namely, along the <110> direction if projected onto the substrate. The whiskers tended to grow more or less equally along the two <110> direction on the (100) substrate surface.

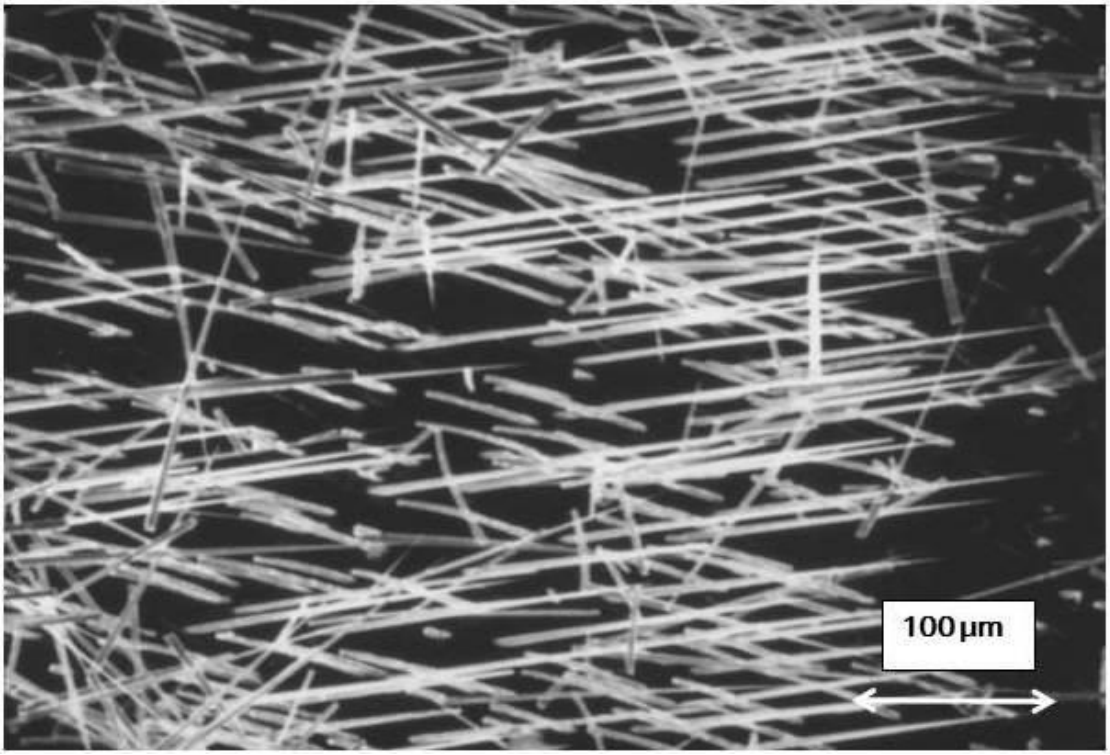

Figure 4-35: SEM micrograph of GaAs whiskers after full MBE deposition run, showing massive growth of whiskers, which were several hundred micrometers long. Note the preferred directionality in the whisker growth direction.

Two close-up SEM micrographs of the short and long whiskers are shown in figure 4-37. Shorter whiskers show that whisker growth is the outcome of the growth of the white balls often seen inside of the oval defect. A close-up view of the whisker surface shows a rough, faceted surface. Under the SEM, the whiskers were quite resistive and tended to charge up during imaging. As the whiskers grew, it creates characteristic shadowing marks underneath it. Additional detail of the whisker growth direction is given by figure 4-38, showing the two <110> direction growth of the whisker on (100) the GaAs wafer surface and schematic of the whisker shown below. It can also be deduced that the whisker growth direction is close to the <111> direction with respect to the GaAs surface, and more specifically, it corresponds to the $<111>_A$

direction or the Ga face of the <111> direction. This was determined by the anisotropic etching method that was described previously.

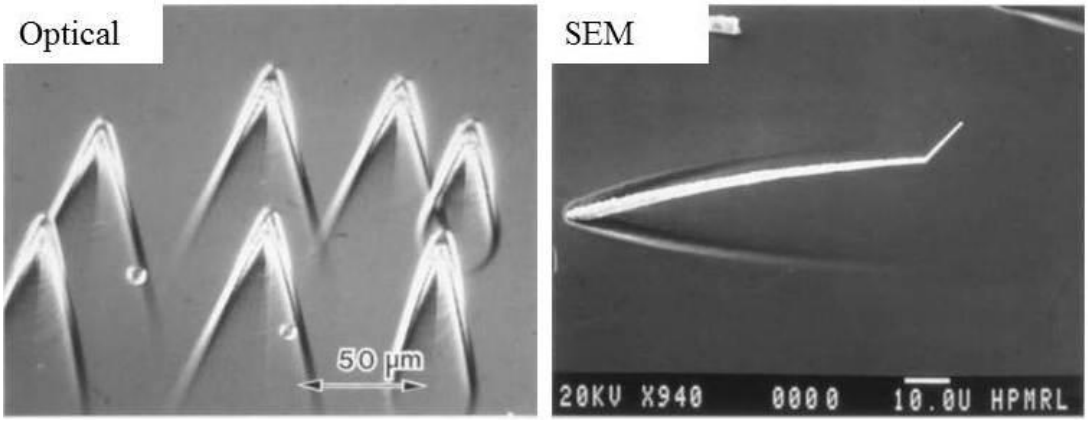

Figure 4-36: Optical and SEM micrograph of the whiskers on an MBE-GaAs wafer. Many of the whiskers had broken off or were damaged during handling so that there were small fragments on the surface and the tip of the whiskers had bent or broken-off as seen in the SEM micrograph.

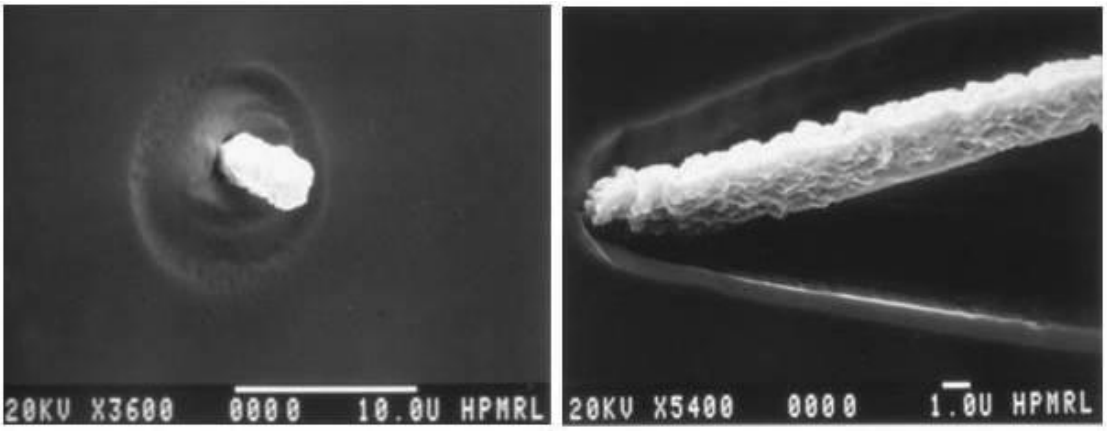

Figure 4-37: SEM micrograph of shorter GaAs whiskers showing more detail of its morphology. The image on the left clearly shows that the base of the whisker is the same oval defects that were being seen earlier, and that whiskers appear to be the outgrowth of the white balls seen inside of the oval defects.

The next step was to try to identify the whisker material, and a conventional powder X-ray diffraction scan was taken by collecting the whiskers onto a tape. The X-ray diffraction pattern revealed that it is consistent with the hexagonal phase of GaAs. The lattice parameter and the reflections are consistent with wurtzite phase of GaAs, which is highly unusual because it was relatively unknown and unheard of at the time. There were only reports of hexagonal phase GaAs under very high pressure [4-40]. XRD results are shown in figure 4-39.

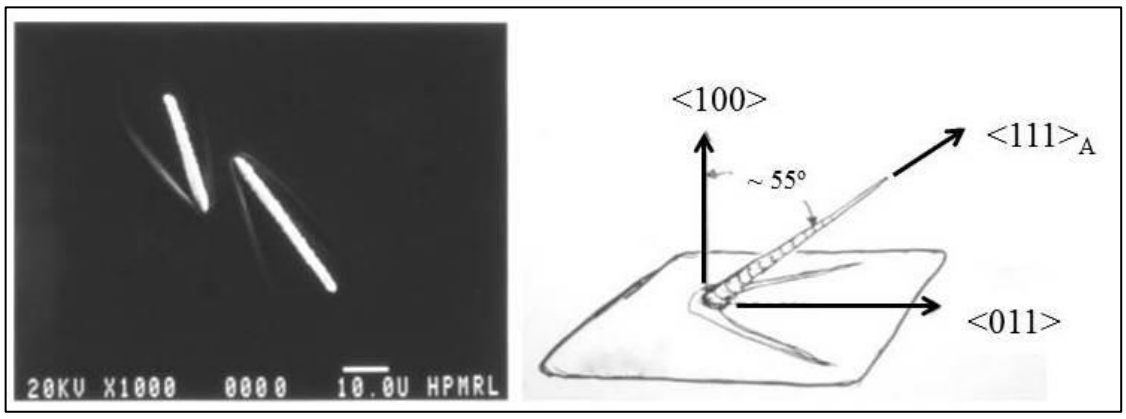

Figure 4-38: Left, a SEM micrograph of a short segment whisker showing growth along the two opposing <011> directions on the GaAs (100) surface and right, a schematic of the crystallographic direction of the whisker growth. The whisker growth is along the $<111>_A$ direction with respect to the GaAs substrate.

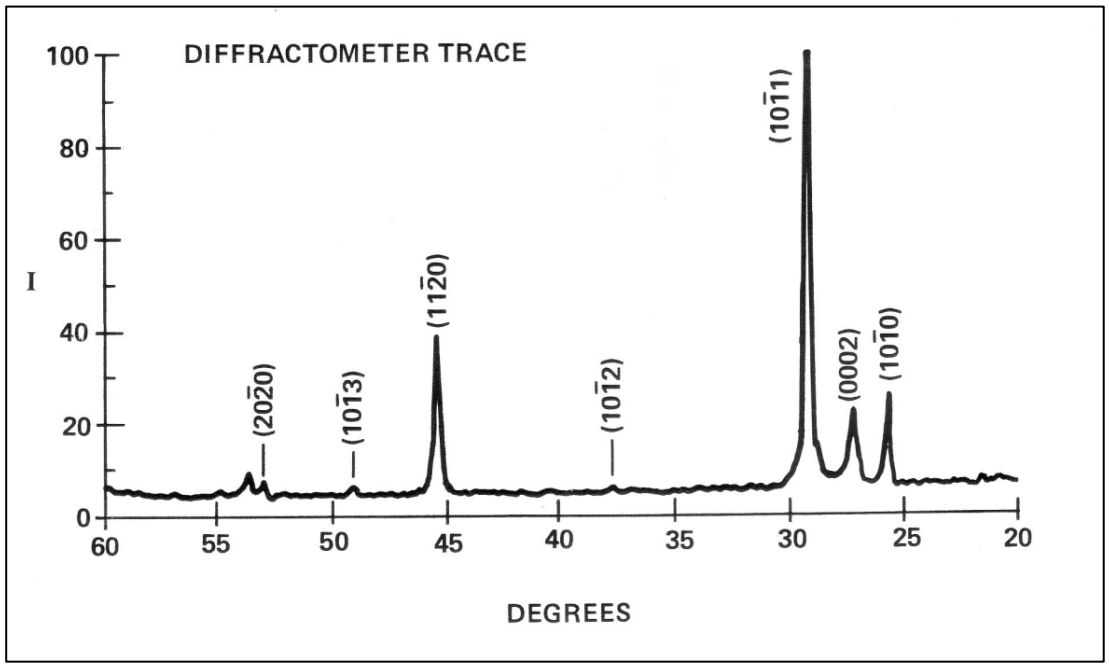

Figure 4-39: XRD trace from whisker collected from GaAs surface. The trace is consistent with the wurtzite structure for GaAs. Note that the direction of the scan was from higher to lower angles.

Table 4-3 tabulates the reflections for the GaAs cubic phase and hexagonal wurtzite phase. The lattice parameter for the whisker was consistent with the cubic phase being translated into a wurtzite structure.

Table 4-3: Reflections for the cubic and hexagonal phase GaAs and expected X-ray reflections

Cubic GaAs:		a_o = 0.56534 nm	
ASTM card #14-450			
d (nm)	I/I_o	hkl	2θ (deg)
0.3260	100	111	27.32
0.2832	<1	200	31.65
0.1999	35	220	45.37
0.1704	35	311	53.78
0.1413	6	400	66.11
0.1297	8	331	72.94
0.1154	6	422	83.83
0.1088	4	333	90.23
0.0993	2	440	100.95
Hexagonal GaAs:		a_o = 0.39976 nm	
		c_o = 0.65280 nm	
d (nm)	I/I_o	hkl	2θ (deg)
0.3462		1011	25.73
0.3264		0002	27.36
0.3059		1011	29.2
0.2375		1012	37.88
0.1999		1120	45.37
0.1842		1013	49.47
0.1731		2020	52.89

TEM analysis followed for the GaAs whiskers. Whiskers were collected from the surface using acetate tape, using a standard method for obtaining extraction replica of surfaces [4-41]. Approximately 10 nm of carbon was evaporated onto the acetate, and the acetate was then dissolved in acetone. The whiskers were left attached to the remaining thin carbon film. The carbon film was then placed on a 3mm-diameter grid

for TEM analysis. Philips EM400ST was used for conventional TEM analysis and JEOL 200CX for the HRTEM imaging. Additionally, the plan view image of the whiskers was obtained using 1.5 MeV high voltage microscope at The National Center for Electron Microscopy at Lawrence Berkeley Laboratory in order to make use of the higher penetrating depth of the 1.5 MeV electrons. The higher surface density of the whisker defects combined with the greater thickness that could be imaged using the higher voltage made it worthwhile to attempt a plan view specimen to try to capture the defects. The BF micrograph of the whisker captured in carbon film is shown in figure 4-40. The image was taken using the two-beam condition, with $\boldsymbol{g} = (01\bar{1}0)$. It is clear that the whisker contains many stacking faults.

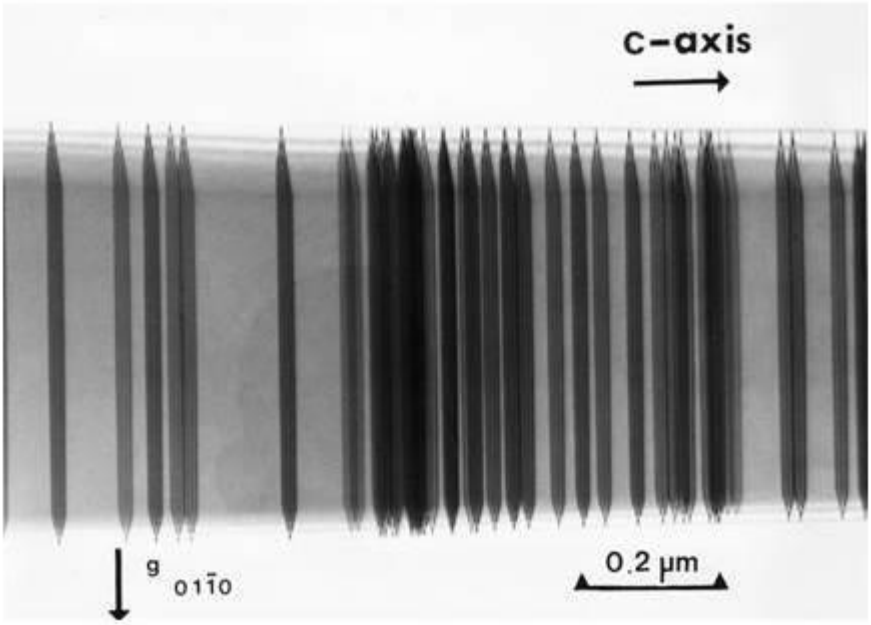

Figure 4-40: BF micrograph of a whisker taken under the two-beam condition, showing many stacking faults within the whisker

Chemical identification of the whisker was done with the EDX system on Philips EM400ST. There seems to be a slightly higher signal for As from the whisker compared to the EDX signal from a plan view GaAs specimen, but it may be due to the shape of the whisker. Using the EDAX® software, the excess As in the whisker was as

much as 5% higher. There is a small amount of Cu signal from the TEM grid. EDX spectra are shown in figure 4-41 below.

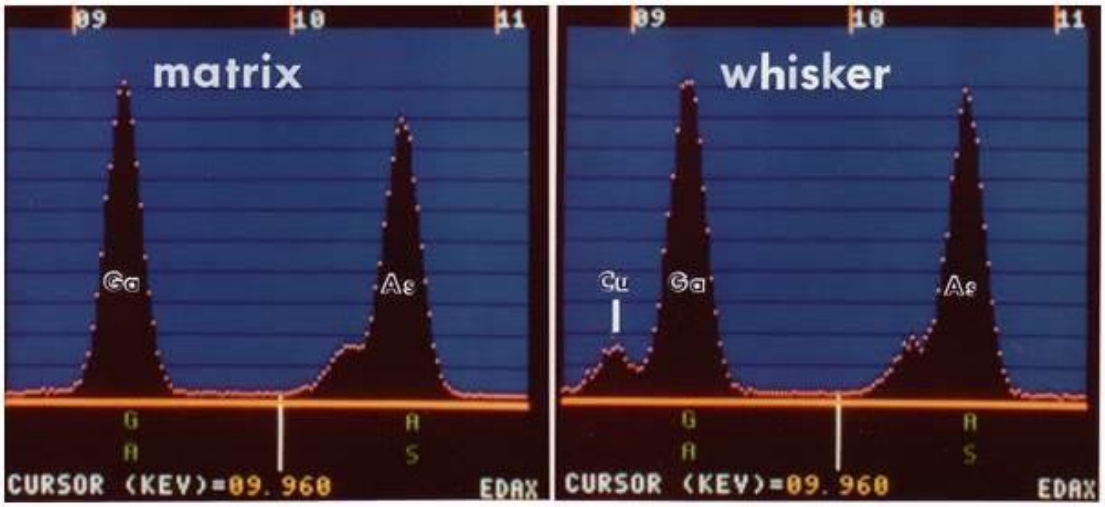

Figure 4-41: EDX spectra from the whisker (right) compared to the spectra obtained from a plan view specimen of GaAs (left-labeled as matrix). It is possible that the whisker may be slightly more As-rich compared to the bulk of the GaAs.

Crystallographic verification of the whisker as being hexagonal was done by rotating the whisker around its diameter and obtaining diffraction patterns from it. The results are shown in figure 4-42, with the correctly identified index shown. The HRTEM micrograph of the whisker is shown in figure 4-43, with the whisker oriented in the $[2\bar{1}\bar{1}0]$ orientation as it was done for CdS in Section 1.7.2. The model structure of GaAs in wurtzite structure is shown in the inset. The projected structure of the GaAs with hexagonal wurtzite structure is shown in Figure 4-44 with the lattice parameter and unit cell indicated in the figure.

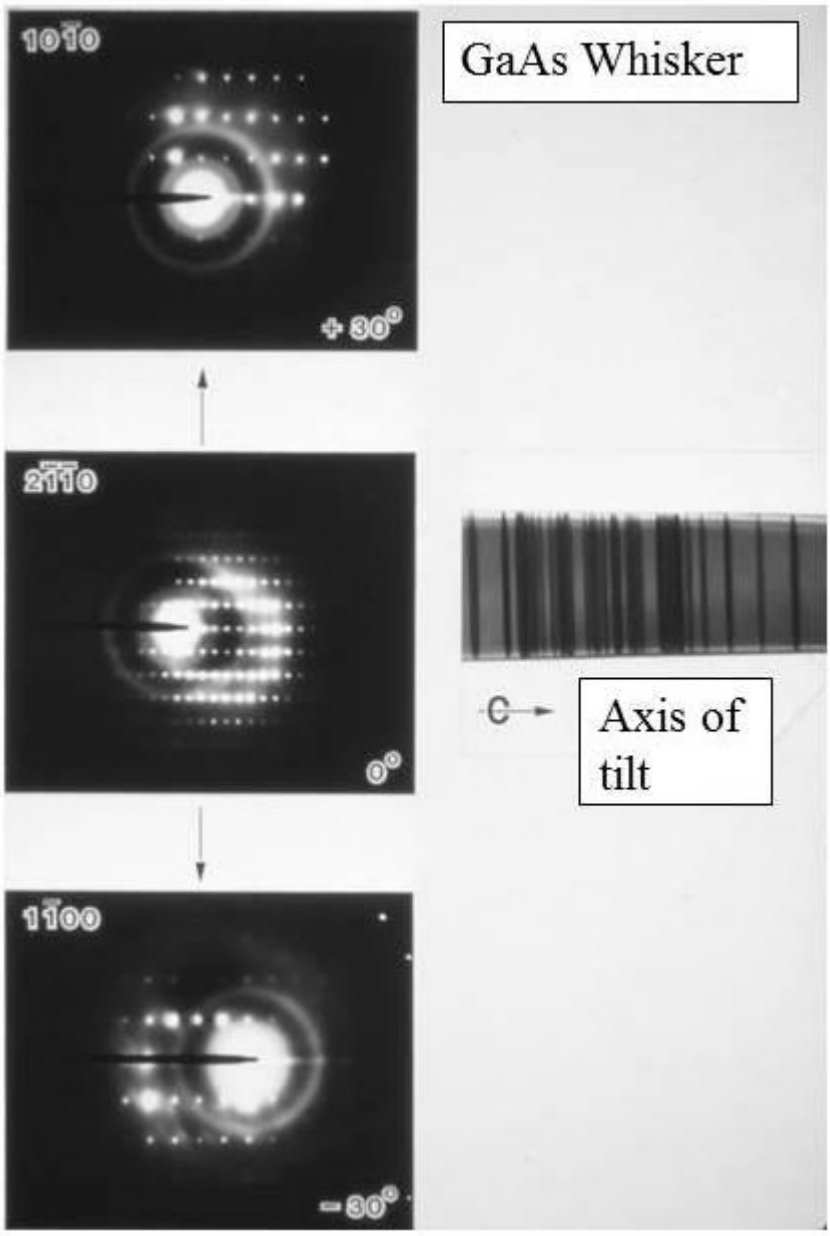

Figure 4-42: DP from a whisker rotated about its axis as shown in the BF image inset, and the corresponding diffraction pattern obtained at $\pm$ 30^{o} rotation.

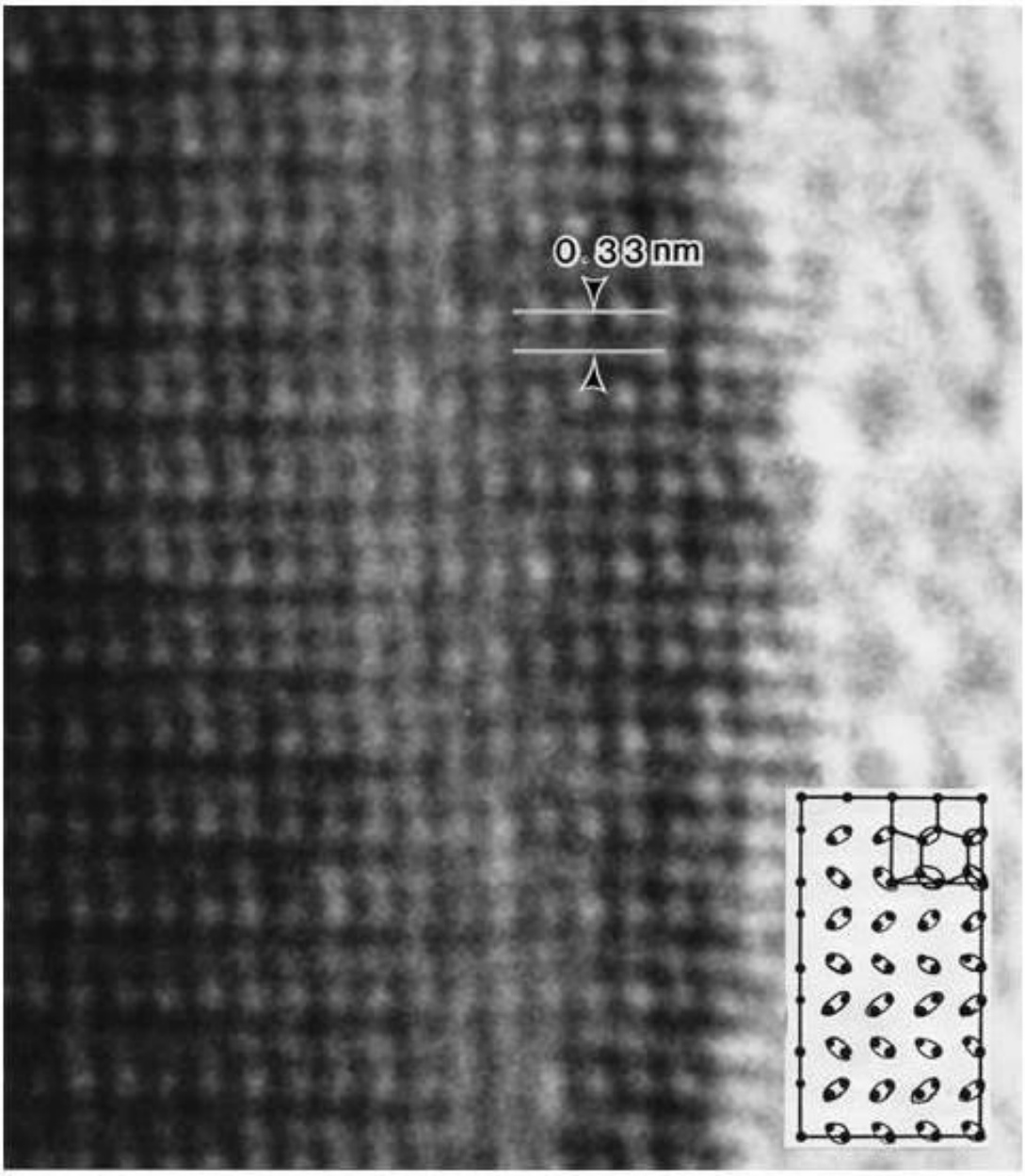

Figure 4-43: HRTEM image obtained from the whisker in the [$2\bar{1}\bar{1}0$] zone axis. A clear image from the whisker in high resolution was difficult to obtain due to its being trapped inside an amorphous carbon film support.

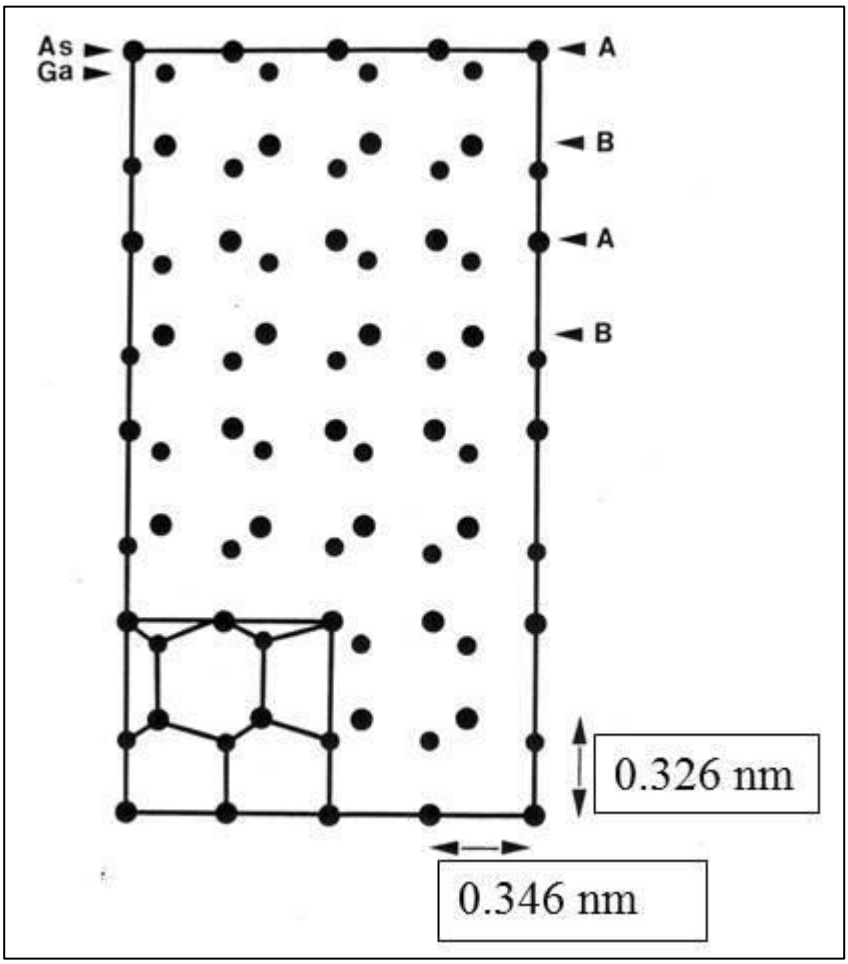

Figure 4-44: Projected structure of wurtzite phase GaAs in the [$2\bar{1}\bar{1}0$] orientation.

BF images taken from the base of the whisker captured on a Berkeley 1.5 MeV microscope are shown in Figure 4-45 and 4-46. In figure 4-45, the base already has a clear hexagonal shape, indicating that it has the wurtzite structure from the base region. There is a massive tangle of dislocations on one side of the whisker base. Even with 1.5 MeV electrons, it was difficult to penetrate through the whiskers, which were typically > 5 μm thick. Therefore, it was difficult to discern the microstructure at the base of the whiskers in figure 4-46. The corresponding diffraction pattern from the base appears to show both cubic and hexagonal phase GaAs within the first ~ 5 μm of the whiskers.

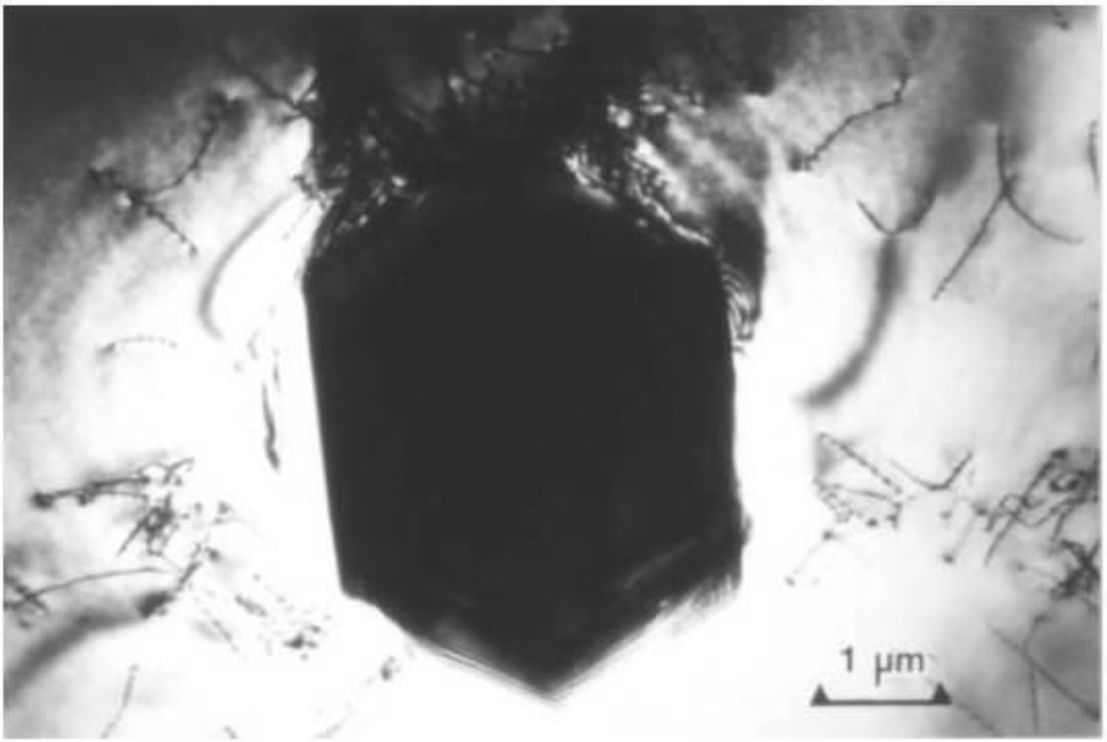

Figure 4-45: A BF HV-TEM image obtained from the base of a whisker using a Berkeley 1.5 MeV microscope.

Figure 4-46: A BF HV-TEM image at the base of a whisker showing a high density of defects at the base, and polycrystalline characteristics of the base material.

Within a relatively short period, it was discovered by the MBE system team that the thermocouple gauge for the substrate heater was miscalibrated or not functioning properly in the MBE system, so that actual substrate temperature was as much as 50-60^{o}C lower than the indicated value. This was probably not the only reason why the whisker growth started to occur in the system. As is usually the case with this type of issue, it was probably a combination of events that contributed to the sudden onset of whisker growth in the film. The initiation site for the whisker growth is clearly the oval defect, and it must have the white particles that were often seen inside the oval defects. In turn, the oval defects appear to be related to the formation of massive defect clusters in the MBE film. Some of these defect clusters can already be present in the GaAs substrate as was seen in figure 4-29. In other mechanisms, the incomplete cleaning of the surface oxide on the GaAs substrate can initiate a higher density of oval defects, which in turn can turn into whiskers if the substrate temperature is too low. There must also be a trigger that causes initial seeding of the wurtzite phase GaAs inside the oval defect. What this mechanism might be was not determined in this study. The base of the whisker contains a very high density of defects, of the order of

$10^{13}/cm^2$ and a polycrystalline phase. It may be one of these particles that begins the astoundingly fast growth of the whiskers. However, the direction of the growth of the whisker was always along the <111> direction with respect to the base GaAs. Therefore, it is not as if there is a competitive process for one of the polycrystalline phases to win out in the growth of whiskers. There is a special relationship between the <111> direction and the whisker growth. Additionally, the stop etch analysis of the growth direction shows that the growth direction of the whisker is along the $<111>_{Ga}$ direction with respect to the GaAs substrate, and this must also be something of significance in the growth mechanism for the whisker. For the VLS growth in III-V compounds, Holonyak et al. [4-42] reported that growth occurs only along the $<111>_B$ direction. Therefore, this is opposite to what is observed in the VLS mechanism.

One of the factors that might play in the initiation of whisker growth is the stress associated with the high density of dislocations and stacking faults at the vicinity of the whisker base. Normally, the stress may by relieved easily by plastic flow, which should occur at a temperature in excess of 600^oC for GaAs. Previous deformation studies on GaAs by Laister and Jenkins [4-43] showed that ductile to brittle transition temperature occurs between 550 to 600^oC in GaAs, and at higher temperatures with the addition of impurities. The fact that whisker growth is rarely observed at a substrate temperature above 600^oC indicates that some correlation exists between plastic flow or lack of it and the formation of the polycrystalline phase and growth of whiskers.

Before this work, there were several reports of whisker growth reported in MBE GaAs. It has been noted that whisker growth occurs over the "damaged" region of the substrate and it was noted that growth direction was random. Cho and Arthur [4-20] described a number of surface topographical defects, attributing the dendritic growth to faulty growth conditions such as substrate temperature, As/Ga ratio in the source beam, and the growth rate. Other surface defects described as "pyramids" and "mounds" were attributed to a residual contamination on the substrate. They noted that this latter class of defects could be largely eliminated by careful substrate preparation. The whiskers reported by Wood et al. [4-44] closely resemble the ones reported here.

Wood et al. analyzed the whiskers by energy dispersive X-ray analysis, and the chemical composition was found to be essentially stoichiometric GaAs. They attributed whisker defects to damage on the substrate surface, but the growth mechanism responsible for the whiskers was not specified. A number of other defects classified as "growth-related" have been attributed to VLS growth [4-34]. It was expected that the liquid phase necessary for the VLS growth might be molten Ga droplets, which has been ejected out of Ga source cell. The VLS growth mechanism was originally developed to explain the whisker growth in silicon, and it had been used previously to explain the growth of GaAs whiskers from vapor [4-45]. Since there was no liquid gallium observed at the tip of the whiskers, the VLS mechanism does not explain the whisker growth in this case. Additionally, a typical VLS mechanism creates smooth whiskers while in this case the surface was very rough. Much has been written about VLS growth and there are review articles and books on the subject by one of the early investigator in this field, by Wagner [4-46]. An example of a VLS whisker is shown in figure 4-47 from a work by Ihn et al. [4-47]. They grew GaAs whiskers on Si substrate using a MBE system, and using a liquid Au droplet as mediator for the whisker growth. They show a HRTEM image of the whisker having highly faulted structure, containing both cubic and hexagonal phases. As we have also seen, the growth direction is along the c-axis of the wurtzite structure. The difference is in the morphology however, they have a liquid end-cap and the surface appear much smoother. Another mechanism for whisker growth is by dislocations [4-48]. This mechanism requires the presence of screw dislocation in the substrate, which propagates through the whisker, but no such dislocation was found within the whisker.

The conclusion that can be made based on the results presented on the analysis and evidence from the MBE process is that whisker growth is initiated at lower than typically-desired MBE growth temperature for the GaAs film, below 580^{o}C. Additionally, the condition of the substrate and perhaps the effusion cells were such that it was conducive to generating a high density of oval type defects on the GaAs surface. An oval defect with the initial trigger of the formation of the white particle, which consists of a polycrystalline mixture of cubic and hexagonal GaAs is necessary

for the nucleation of whiskers. The actual growth mechanism for the whisker is not VLS or a dislocation mediated process, but rather some other mechanism, which occurs by the rapid mobility of Ga and As species on the surface that diffuse to the growing whisker. The fact that the growth direction is $<111>_A$ face of the GaAs and likely to be $<0001>_A$ direction for the wurtzite phase of the whisker may have something to do with the rapid rate of whisker growth. Stress also may play a role in the initiation of the wurtzite phase of GaAs, as the initiation site at the base of the whisker is associated with very high density of defects. Defects may also aid in a higher rate of diffusion of species into the whisker.

In recent times, it appears that oval defects are still a continuing problem in MBE growth, and the same mechanisms that were talked about in the 1980s are still mentioned in 2005, with the comment that "reason for their formation is not absolutely clear" [4-49]. Whisker growth is also a much more active area of research, with the new nanowire terminology as the catch phrase for the field. What had been a nuisance in the MBE process is now a mainstream activity for deliberately creating whiskers for new and novel device application. It is now taken for granted and well known that whisker growth in GaAs and in many other compound semiconductors, forms wurtzite structure and they have very interesting and unique electrical properties that can be exploited [4-50, 4-51, 4-52]. The actual VLS mechanism is used by providing a gold nucleation site for the VLS mechanism to function [4-53]. Some of the late breaking news recently involved the use of GaAs nanowire with wurtzite structure to function as both a light emitting diode and photoreceptor, by adjusting stress along the nanowire and thereby changing its electrical and optical properties [4-54]. It holds the promise of integrating these nanowires of GaAs into existing Si devices to act as both emitter and detector for faster transistors in the future. Use of nanowire technology is now a very active field of investigation to make use of whiskers grown with a high level of control.

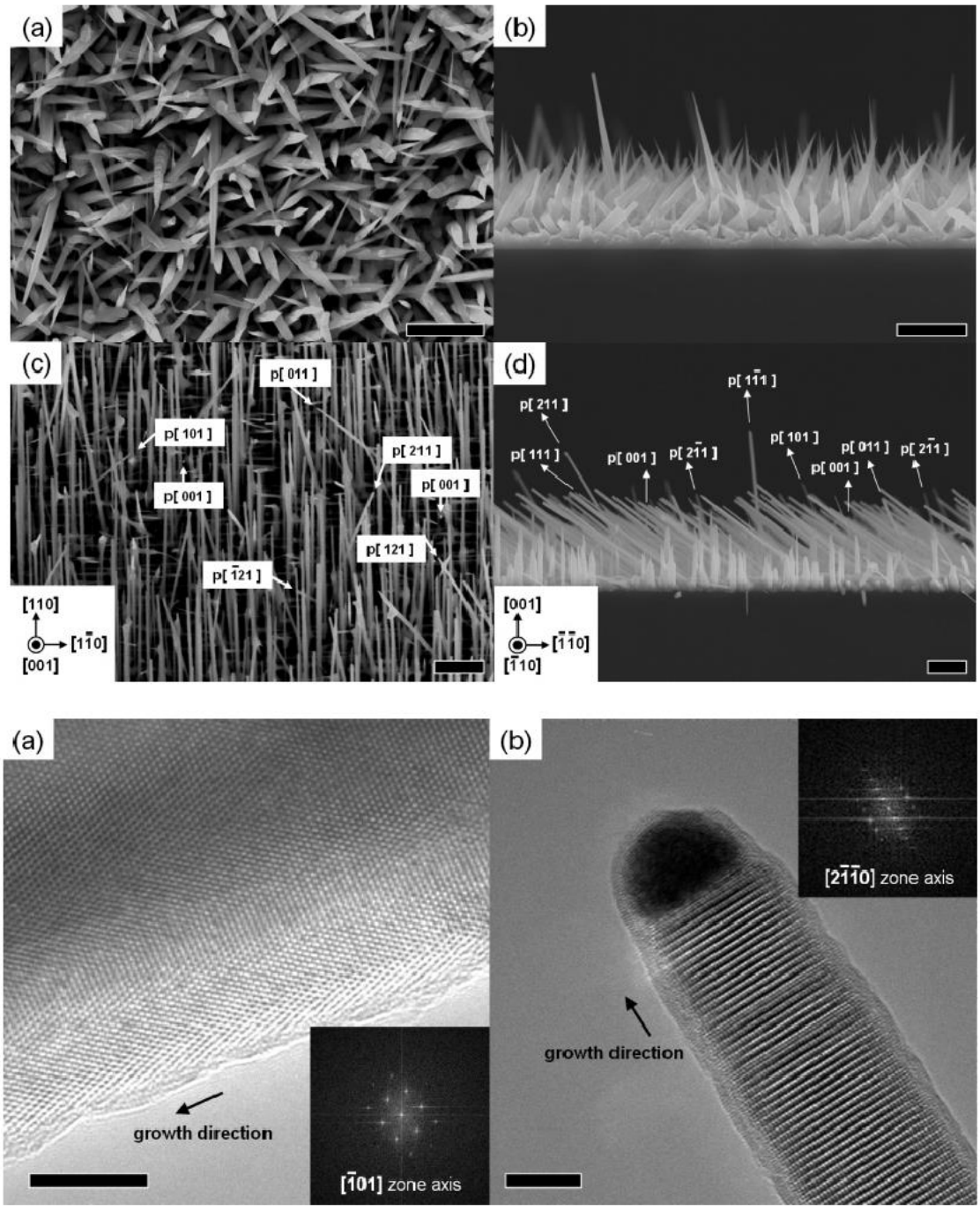

Figure 4-47: Example of whisker growth based on VLS mechanism, from Ihn et al. Ref. [4-47](2006). MBE system was used , with Si substrate and liquid Au as the mediator for the VLS growth. The structure is described as mixture of cubic sphalerite and wurtzite phase. ACS Publications, reproduced with permission.

Chapter 4 References:

[4-1] Y. Seki, H. Watanabe and J. Matsui, *Impurity effect on grown-in dislocation density of InP and GaAs crystals*, J. Appl. Phys., **49** (2), 822 (1978)

[4-2] T. Kamejima, J. Matsui, Y. Seki and H. Watanabe, *Transmission electron microscopy study of microdefects in dislocation-free GaAs and InP crystals,* J. Appl. Phys. **50** (5), 3312 (1979)

[4-3] G. T. Brown, B. Cockayne and W.R. MacEwan, *The growth of dislocation-free Ge-doped InP*, J. Crystal Growth, **51**, 369 (1981)

[4-4] P.W. Hutchinson and P.S. Dobson, *The nature of defects in n+ gallium arsenide*, Phil. Mag., **30**, 65 (1974)

[4-5] D.J. Stirland, P.D. Augustus and B.W. Straughan, *The identification of saucer-pit (S-pit) defects in GaAs*, J. Mater. Sci. **13**, 657 (1978)

[4-6] D. Laister and G.M. Jenkins, *Electrical and electron microscope studies of the annealing of tellurium-doped gallium arsenide*, Phil. Mag., **23**, 1077 (1971)

[4-7] V.D. Verner, S.K. Maksimov and D.K. Nichugovskii, *The nature of defects of crystalline structure in GaAs heavily doped with Te*, Phys. Stat. Sol. (a), **33**, 755 (1976)

[4-8] F.A. Ponce, T. Yamashita, R.H. Bube and R. Sinclair, *Imaging of defects in cadmium telluride using high resolution transmission electron microscopy*, in: Defects in Semiconductors, J. Narayan and T.Y. Tan eds. (Elsevier North Holland, NY) p 503, (1981)

[4-9] Y.Seki, J. Matsui and H. Watanabe, *Impurity effect on the growth of dislocation-free InP single-crystals*, J. Appl. Phys. **47**, 3374 (1976)

[4-10] J. P. Parsey, Y. Nanishi, L. Lagowski, and H.C. Gatos, *Bridgraan-Type Apparatus for the Study of Growth-Property Relationships*, J. Electrochem. Soc., **129**, 388 (1982)

[4-11] N. Chand, *MBE growth of high-quality GaAs*, Journal of Crystal Growth, Vol. **97**, Issue 2, 415-429, Sept (1989)

[4-12] C.T. Foxon, M.R. Boudry and B.A. Joyce, *Evaluation of surface kinetic data by the transform analysis of modulated molecular beam measurements*, Surf. Sci., **44**, 69 (1974)

[4-13] C.T. Foxon, *Molecular Beam Epitaxy,* Acta Electron., **16**, 323 (1973)

[4-14] Wikimedia commons
Creative Commons Attribution-Share Alike 3.0 Unported license.
Created by Nikhil

[4-15] J.R. Arthur, *Vapor pressures and phase equilibria in the GaAs system*, J. Phys. Chem. Solids, **28**, 2257 (1967)

[4-16] C.T. Foxon, J.A. Harvey and B.A. Joyce, *The evaporation of GaAs under equilibrium and nonequilibrium conditions using a modulated beam technique*, J. Phys. Chem. Solids, **34**, 1693 (1973)

[4-17] A.Y. Cho, *GaAs epitaxy by a molecular beam method: Observations of surface structure on the (001) face,* J. Appl. Phys. **42**, 2074 (1971)

[4-18] J. R. Arthur, *Interaction of Ga and As2 molecular beams with GaAs surfaces*, J. Appl. Phys., **39**, 4032 (1968)

[4-19] J.R. Arthur, *Surface stoichiometry and structure of GaAs*, Surf. Sci, **43**, 449 (1974)

[4-20] A.Y. Cho and J.R. Arthur, *Molecular Beam Epitaxy*, Prog. in Solid State Chem., Vol. **10**, Part 3, 157-191 (1975)

[4-21] A.Y. Cho and M.B. Panish, *Magnesium-doped GaAs and* $Al_x\ Ga_{1-x}\ As$ *by molecular beam epitaxy,* J. Appl. Phys. **43**, 5118 (1972)

[4-22] A.Y. Cho and F.K. Reinhart, *Interface and doping profile characteristics with molecular-beam epitaxy of GaAs: GaAs voltage varactor*, J. Appl. Phys. **45**, 1812 (1974)

[4-23] J. R. Arthur, *Adsorption and Desorption of* O_2 *on GaAs {111} Surfaces*, J. Appl. Phys., 3**8**, 4023 (1967)

[4-24] A.U. MacRae, *LEED Examination of Indium Phosphide and Gallium Arsenide*, J. Vac. Sci. Technol. **4**, 247 (1966)

[4-25] A.Y. Cho and I. Hayashi, *Surface structures and photoluminescence of molecular beam epitaxial films of GaAs,* Solid-State Electron. **14 (2)**, 125 (1971)

[4-26] L.L. Chang, L. Esaki, W.E. Howard, R. Ludeke and G. Schul, *Structures grown by molecular beam epitaxy*, J. Vac. Sci. Technol. **10**, 655 (1973)

[4-27] J.K. Carney, G.D. O'Clock, Jr. and L.P. Erickson, *Heterojunction devices—Doing it with GaAlAs/GaAs*, Microwaves, vol. **22**. Pp. 85-89, (Feb1982)

[4-28] G. H. Dohler, *Solid-state superlattices*, 144 Scientific American, Nov. 1983

[4-29] L. Esaki and R. Tsu, *Supperlattice and negative conductivity in semiconductors*, IBM J. Res. Dev. **14**, No.1, 61-65 (1970)

[4-30] M. Krieger, H. Sigg, N. Herres, K. Bachem and K. Köhler, *Elastic constants and Poisson ratio in the system AlAs-GaAs*, App. Phys. Lett. **66**, 682 (1995)

[4-31] P.M. Petroff, *Transmission electron microscopy of interfaces in ITI-V compound semiconductors,* J. Vac. Sci. Technol. **14** (4), 973 (1977)

[4-32] J.R. Waldrop, S.P. Kowalczyk, R.W. Grant, E.A. Kraut and D.L. Miller, *XPS measurement of GaAs-AlAs heterojunction band discontinuities—Growth sequence dependence*, J. Vac. Sci. Technol., **19** (3), 573 (1981)

[4-33] W. Krakow, *Computer Simulation of High-Resolution Electron Micrographs using Dynamical Electron Scattering*, IBM Journal of Research and Devel. Vol. **25**, Issue 1, Jan. (1981)

[4-34] R. S. Wagner and W.C. Ellis, *Vapor-liquid-solid mechanism of single-crystal growth,* Appl. Phys. Letters, **4**, 89 (1964)

[4-35] Y. G. Chai and R. Chow, *Souce and elimination of oval defects on GaAs films grown by molecular beam epitaxy*, Appl. Phys. Lett., **38**, 796 (1981)

[4-36] Y. Suzuki, M. Seiki, Y. Horikoshi and H. Okamoto, *Surface Defects on MBE-Grown GaAs*, Jap. Journ. Appl. Phys., **23**, 164 (1984)

[4-37] K. Fujiwara, K. Kanamoto, Y.N. Ohta, Y. Tokuda, T. Nakayama, *Classification and origins of GaAs oval defects grown by molecular beam epitaxy*, Journal of Crystal Growth, Vol. **80**, Issue1, pp. 104-112, Jan 1987

[4-38] N. Chand and S.N.G. Chu, *A comprehensive study and methods of elimination of oval defects in MBE-GaAs*, Journal of Crystal Growth, Vol. **104**, Issue 2, pp. 485-497, 2-July 1990

[4-39] D. W. Shaw, *Localized GaAs Etching with Acidic Hydrogen Peroxide Solutions*, J. Electrochem. Soc., Vol. **128**, Issue 4, 874-880 (1981).

[4-40] M. Baublitz, Jr., and A.L. Ruoff, *Diffraction studies of the high pressure phases of GaAs and GaP*, J. Appl. Phys., **53**(9), pp 6179-6185 (1982)

[4-41] D.E. Bradley, *Some carbon replica techniques for the electron microscopy of small specimens and fibers*, British Journal of Appl. Phys. **8**, No. 4, 150 (1957)

[4-42] N. Holonyak Jr., C.M. Wolf and J.S. Moore, *Vapor-solid growth of gallium phosphide*, Appl. Phys. Lett., **6 (4)**, 64 (1965)

[4-43] D. Laister and G.M. Jenkins, J. Materl. Science, *Deformation of single-crystal of gallium arsenide*, **8**, 1218-1232 (1973)

[4-44] C.E.C. Wood, L. Rathbun, H. Ohno and D. DeSimone, *On the origin and elimination of macroscopic defects in films*, J. Cryst. Growth, **51**, 299-303 (1981)

[4-45] R.L. Barns and W.C. Ellis, *Whisker Crystals of Gallium Arsenide and Gallium Phophide Grown by the Vapor-Liquid-Solid Mechanism*, J. Appl. Phys., **36 (7)**, 2296-2301 (1965)

[4-46] R.S. Wagner. VLS Mechanism of Crystal Growth. A.P. Levitt (Ed.), Whisker Technology, Wiley, New York, pp. 47–119 (1970)

[4-47] S-G. Ihn, J-I. Song, T-W. Kim, D-S. Leem T. Lee, S-G. Lee, E.K. Koh and K.Song, *Morphology-and orientation-controlled gallium arsenide nanowires on silicon substrates*, Nano Letters, Vol. 7, No. 1, pp. 39-44 (2007)

[4-48] G.W. Sears, *A mechanism of whisker growth*, Acta. Met **3** (4), pp 367-369 (1955)

[4-49] A. Szerling, K. Kosiel, A. Wójcik-Jedlińska, M. Płuska, and M. Bugajski, *Properties and origin of oval defects in epitaxital structures grown by molecular beam epitaxy*, Optica Applicata, Vol. XXXV, No. **3**, pp 537 - 548 (2005)

[4-50] H. G. Lee, H.C. Jeon, T. W. Kang and T. W. Kim, *Gallium arsenide crystalline nanorods grown by molecular-beam epitaxy*, Appl. Phys. Lettls., **78** (21), p 3319 (2001)

[4-51] D. Spirkoska, J. Arbiol, A. Gustafsson, S. Conesa-Boj, F. Glas, I. Zardo, M. Heigoldt, M.F. Glass, A.L. Bleloch, S. Estande, M. Kaniber, J. Rossler, F. Peiro, J.R. Morante, G. Abstreiter, L. Samuelson, and A. Fontcuberta Morral, *Structural and optical properties of high quality zinc-blende/wurtzite GaAs nanowire heterostructures*, Phy. Rev. B., **80**, 245325 (2009)

[4-52] M. Heiß, S. Conesa-Boj, J. Ren, H-H. Tseng, A. Gali, A. Rudolph, E. Uccelli, F. Peiró, J. R. Morante, D. Schuh, E. Reiger, E. Kaxiras, J. Arbiol, and A. Fontcuberta Morral, *Direct correlation of crystal structure and optical properties in wurtzite/zinc-blende GaAs nanowire heterostructure*, Phys. Rev. B., **83**, 045303 (2011)

[4-53] Z. H. Wu, X. Y. Mei, D. Kim, M. Blumin and H. E. Ruda, *Growth of Au-catalyzed ordered GaAs nanowire arrays by molecular-beam epitaxy,* Appl. Phys. Lettls, **81**, 5117 (2002)

[4-54] G. Signorello, E. Lörtscher, P.A. Khomyakov, S. Karg, D.L. Dheeraj, B. Gotsmann, H. Weman and H. Riel, *Inducing a direct-to-pseudodirect bandgap transition in wurtzite GaAs nanowires with uniaxial stress*, Nature Communications, **5**, 3655 (2013)

Chapter 5: Co-Based Thin film Magnetic Media

5.1 Magnetic Recording

Oberlin Smith was the first to describe the basic principle of magnetic recording in 1887. Valdemar Poulsen, a Danish inventor, made the first demonstration of a device using the same principle in 1898. Poulsen's device, which he called the telegraphone, consisted of a wire as a recording medium. The wire was wound around a drum, and a recording head moved along the drum on a threaded rod. It was designed as a voice recorder, and the recording drum had 100 meters of wire for a playback time of 45 seconds. In 1998, the magnetic recording community worldwide celebrated the 100 years of magnetic recording history with various events and symposiums to honor Poulsen. Papers were published and books were written to chronicle the history of magnetic recording. A detailed history of the magnetic recording technology is told in *Magnetic Recording, The First 100 Years* by Eric D. Daniel, C. Denis Mee and Mark H. Clark, which was published in 1999 [5-1].

This chapter will first describe the TEM analysis of thin film magnetic media intended for use in hard disk drives (HDD). The work was conducted from 1979 to 1984. In this period, nearly all HDDs still used oxide-coated media. The drives were very expensive and used exclusively with mainframe computers or with super minicomputers that cost hundreds of thousands of dollars. The PCs have not yet burst onto the scene. The thin film media research was in collaboration with Tu Chen at Xerox Palo Alto Research Center (Xerox PARC). Xerox PARC had already developed their famous Alto computer, and had in mind to provide large HDD storage capacity to the computer. The thin film media was the only material that could deliver such capacity.

I left Stanford in 1984 to join Tu Chen at Komag Inc., a company he founded in 1983 to commercialize the thin film media technology. Komag Inc. supplied small form factor, thin film disks to the numerous HDD start-ups that were to grow into large multi-national companies selling millions of HDDs to the PC manufacturers. The PC

revolution that ensued was supported by a dramatic reduction in the cost of storage achieved by the HDD industry, large part of which was contributed by the continuing increase in the recording density of the media.

For a period of over 20 years, Komag Inc. maintained a continuous research collaboration effort with Stanford on the analysis of thin film media. The objective was to gain better understanding of the relationship between the media microstructure and its magnetic and recording properties. The collaboration continued for an additional 5 years with Western Digital Corporation, which purchased Komag Inc. in 2007. Over this time, the collaboration provided many useful results, which benefitted our understanding of the media. This chapter will describe the evolution of the magnetic thin film media over this period, and show some of the results of the collaboration. It will be shown that some of the concepts and ideas that had started out at the time of Xerox PARC collaboration continued to play an important role in the media design, right up to the present design of the perpendicular media.

The first hard disk drive to store data and programs that was connected to a computer was IBM's Random Access Method of Accounting and Control (RAMAC), which was first introduced in 1957. Since then, the disk drives have evolved into a ubiquitous device that is used to store much of the data used in the world today. The Internet and everything that we do today in computing would be impossible without the low cost and reliable data storage that disk drives provide. In 2013, the disk drive industry represented by Seagate, Western Digital, and Toshiba produced approximately 550 million disk drives, with the data storage capacity of approximately 460 exabytes. These drives are used in every application where storage is needed, from large data farms used by companies such as Google, Yahoo, Facebook, as well as in desktop and notebook computers. This has been made possible by a significant reduction in cost for data storage and an increase in performance of disk drives over the last 57 years of its existence. The cost of data storage from the 1970s to today has been reduced by seven orders of magnitude. The recording density on the media increased by six orders magnitude over the same period. As a comparison, transistor count on a state-of-the-art microprocessor has increased by six orders of magnitude over the same period. Today,

the cost of storage has become nearly free, which allow companies such as Google and Facebook to flourish by attracting large number of users to their site with many free services that require large data storage.

Hard disk drives today use thin film media based on Co-Pt-based alloys, and 100% of the drives employ perpendicular magnetic recording technology, which started to be applied to hard disk drives in 2005. The data storage needs are growing exponentially. Many data centers now have storage capacities that are measured in many hundreds of petabytes, and it is estimated that by 2020, the amount of data stored on the planet will reach 40 zettabytes [5-2]. This is approximately five terabytes for every person in the world. The terminology for such large numbers is still not familiar in normal parlance, and they are listed in Table 5-1 below for reference.

Table 5-1: Notations for number of bytes

Megabytes	=	10^6 bytes
Gigabytes	=	10^9 bytes
Terabytes	=	10^{12} bytes
Petabytes	=	10^{15} bytes
Exabytes	=	10^{18} bytes
Zettabytes	=	10^{21} bytes
Yottabytes	=	10^{24} bytes
Zenottabytes	=	10^{27} bytes
Shilentnobytes	=	10^{30} bytes
Domegemegrottebyte	=	10^{33} bytes

In 1979, when this project on thin film magnetic media with Xerox PARC started, all hard disk drives used for data storage used oxide media composed of gamma ferric oxide ($\gamma -Fe_2O_3$). Thin film media based on metallic cobalt alloy was in the research stage at that time because it was thought to be the next generation of magnetic media that would replace the oxide media. Apple II was introduced in 1977. Mainly hobbyists and computer enthusiasts bought it, and it used 5¼-inch floppy

drives. IBM introduced its first PC in 1981, and it also came with a 5¼-inch floppy drives. The PC-XT model was the first model with a hard disk drive, and it was introduced in March 1983. The drive was made by Seagate (model ST-412) and had a capacity of 10 MB. The drive cost as much as the PC, at approximately $2000. This drive contained two 5MB disks with 5¼-inch diameter oxide media. In the late 1970s, Xerox PARC developed some of the most important computer technologies that revolutionized the computing field. They had developed the Alto computer, which was the predecessor to the Macintosh computer. Additionally, the mouse, Ethernet, laser printers, and graphical user interface (GUI) were all developed at PARC to be used together with the Alto computer. Their research into thin film magnetic media for use in computer hard disk drives was also groundbreaking technology at the time. The Alto computer used a removable 14-inch cartridge-based disk drive, made by Diablo Systems, a Xerox subsidiary. The cartridge was an industry standard format called an IBM 2315 disk cartridge, which had a capacity of 2.4 MB. It held the operating system, and many different fonts and data used in the Alto computer system.

Many of the key innovations and much of the development in hard disk drives originated at IBM because they were the original inventor of the hard disk drive, and they made successive improvements to the technology. One of the key disk drive systems that had enormous influence on the future of disk drives was the IBM 3340 drive, which was announced together with the IBM 370 mainframe computer model in 1973. IBM 3340 was also code-named Winchester and this name stuck with all subsequent disk drives, and the term "Winchester" was used synonymously with hard disk drives for a long period afterward. The reason why this disk drive is so important in the history of hard disk drive development is because it was the first to use a low mass flying head, which took off and landed on the disk surface. The head assembly was also fixed to the disk so that they operated together in a permanent fashion. The previous version used a disk pack that did not have the recording head built into it. This simple change allowed for a more simplified mechanical arrangement between the head and the disk, and contributed greatly to future miniaturization and lower cost. There was also a price to be paid because now the recording heads were flying much

closer to the disk, and constant take-off and landing of the head to the disk surface started to cause significant reliability issues with the drive. The science of tribology had to be invented and refined to solve many unique and challenging mechanical issues that developed between the head and the disk. Liquid lubricant started to be used on the disk to reduce friction and wear between the disk and the head starting with IBM 3340 disk drives.

All commercially important hard disk drives since its first introduction in 1956 with IBM 350 RAMAC until 2007 used longitudinal magnetic recording. The bits are recorded on the disk with magnetization oriented in the plane of the disk. The schematic of this arrangement is shown in Figure 5-1.

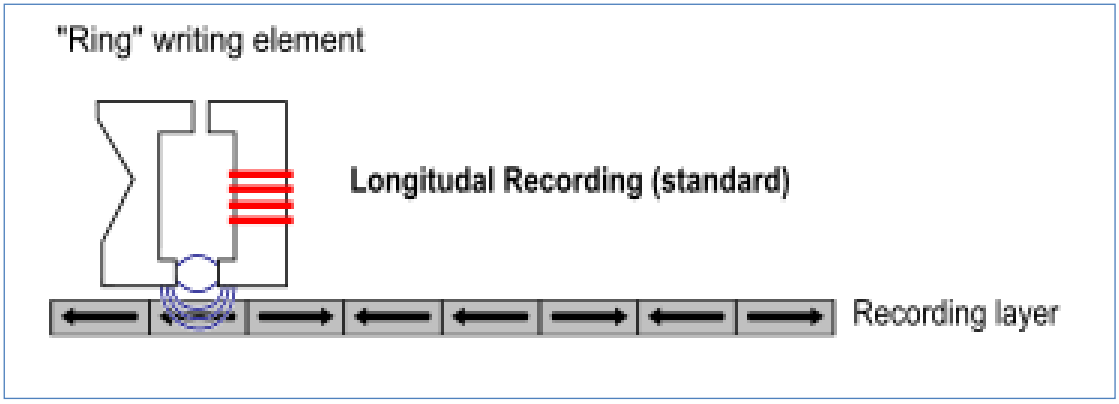

Figure 5-1: A schematic drawing illustrating the recording process for longitudinal magnetic recording.
http://commons.wikimedia.org/wiki/File:Perpendicular_Recording_Diagram.svg

Between the opposing magnetized regions along the track, there will be a demagnetizing field, and it is inherent in the recording process for the longitudinal recording process. This is an inherent disadvantage with longitudinal recording, which has always limited the packing of more transitions and, hence, bits on the media. To increase the number of transitions per unit distance, higher coercivity media is needed to prevent demagnetization fields from reducing the magnetization of the bits.

Coercivity or Hc is materials dependent and successive generation of media used different material to increase the Hc.

It is a quirk of nature that the list of materials that are ferromagnetic and suitable for magnetic recording is very limited. For the elements of importance, there are only Fe, Co and Ni to work with. Fe has been used in a form of Fe_2O_3 or ferrite (strictly speaking, it is a ferrimagnet) and various cobalt alloys are alternate choices. Ferrite particles dispersed in epoxy was developed for tape recording, and its history goes back to the 1930s in Germany where it was developed for sound recording. In the US, 3M developed the process for making acicular gamma ferric oxide and introduced a tape product using it in 1948. Coercivity was between 250 and 275 Oe, and their product became the most widely used tape material for consumer and professional applications by the early 1950s. It was quite natural that the same material came to be used for hard disk drive media and in floppy disks.

The writing and reading process in a disk drive for longitudinal media using a ring head is shown schematically in more detail in Figure 5-2. The write current (i_w) magnetizes the core material in the head near the gap, and the magnetic field spreads out. Some of the fringing or stray field near the gap reaches out and magnetizes the recording media, which can be alternated from one direction to another by changing the current direction i_w in the coil. Once the track on the disk has been written, the data can be recovered by having the track pass under the head gap again. As the magnetized region passes under the gap, the core of the head becomes magnetized. The direction of the magnetization will depend on the direction of the magnetization of the medium. The change in magnetization in the core results in a voltage across the head coil. Only the change in magnetization in the medium and, hence, in the coil, produce a voltage. This follows basic Faraday's law of $V = - d\phi/dt$ or voltage is generated if the flux changes with time. Therefore, transitions in magnetization in the media produce positive or negative voltage pulses in the head coil. The process is illustrated in Figure 5-3 for the writing and reading process.

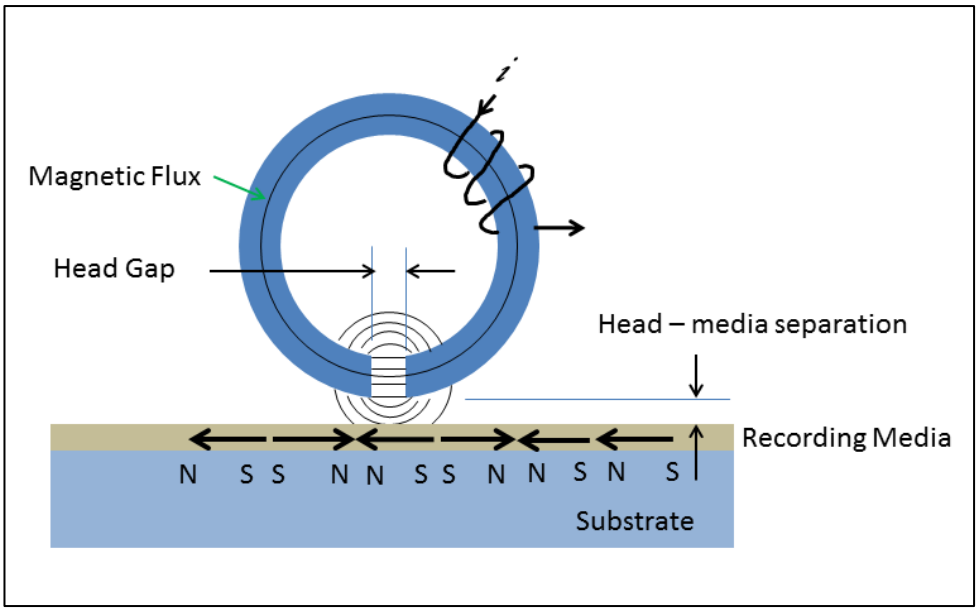

Figure 5-2: A schematic drawing illustrating the writing to and reading from the media using a ring head.

Writing and reading data to the disk was accomplished with an inductive process using wires wound around a core. Therefore, the same device was used for both writing and reading from the earliest days of magnetic recording. Because the inductive reading process depended on the speed of the change in magnetization, spinning the disk faster held some advantage as more signal was obtained. However, starting in 1990, magneto-resistive (MR) sensors started to be used for the read-back signal detection instead of using the same ring head for reading. Together with the discovery of giant magneto-resistance effect (GMR) in 1988 and its subsequent use in recording heads starting in 1997, this dramatically increased the areal density of the hard disk drive, as GMR heads were many times more sensitive to detect signal from very small bits. Additional gains were made with the introduction of tunneling magnetoresistive heads (TMR) starting in 2004.

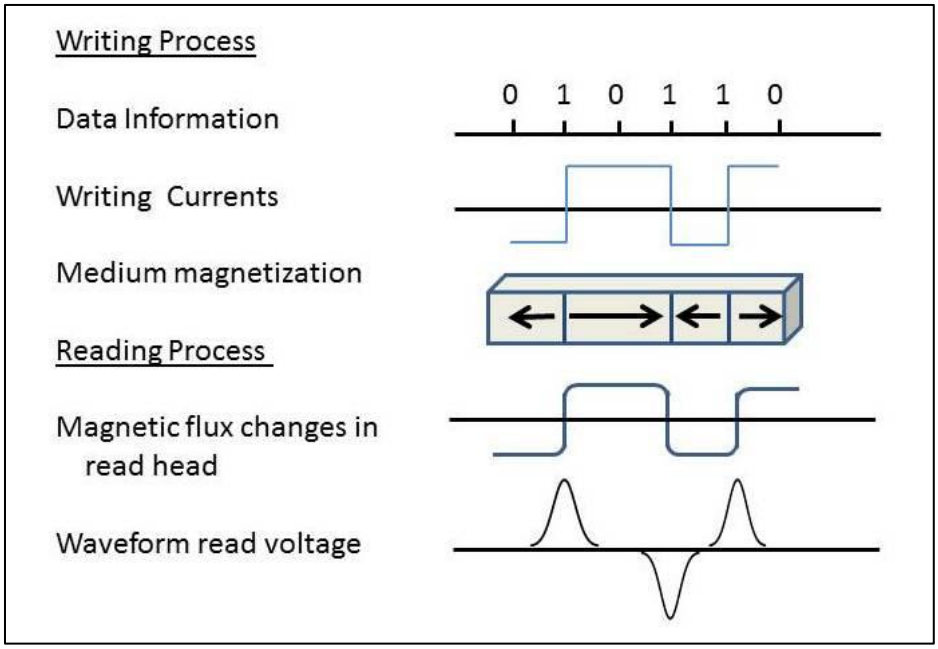

Figure 5-3: A schematic drawing illustrating the process of storing digital information on the media and the read-back process for the data.

From the above simple description of the basics of digital magnetic recording, it becomes obvious that what happens in the head field at the gap and how this field interacts with the magnetic material as it passes under the gap is of critical importance in describing the entire process. Karlqvist [5-3] formulated the general equation for the field H_x and H_y at position x, y at the gap, where x is the direction between the gap, and y away from it as shown in Figure 5-4.

$$H_x = \frac{Hg}{\pi}\left(\arctan\left(\frac{\frac{g}{2}+x}{y}\right) - \arctan\left(\frac{\frac{g}{2}-x}{y}\right)\right) \qquad \text{(Eqn. 5-1a)}$$

$$H_y = \frac{-Hg}{2\pi}\ln\left(\frac{(\frac{g}{2}+x)^2+y^2}{(\frac{g}{2}-x)^2+y^2}\right) \qquad \text{(Eqn. 5-1b)}$$

where g is the gap length and H_g is the magnetic field strength inside the head gap.

Then the output voltages $\boldsymbol{e}_x$ and $\boldsymbol{e}_y$ at time t can be derived using the principle of reciprocity. The result is given by following the equation, with also the simplification that track width $\boldsymbol{w}$ is much larger than the other dimensions in the system.

$$\boldsymbol{e}_x(\bar{x}) = - \mu_o V w \int_d^{d+\delta} dy \int_{-\infty}^{+\infty} \frac{dM_x(x-\bar{x})}{d\bar{x}} \frac{H_x(x,y)}{i} dx \qquad \text{(Eqn. 5-2a)}$$

$$\boldsymbol{e}_y(\bar{x}) = - \mu_o V w \int_d^{d+\delta} dy \int_{-\infty}^{+\infty} \frac{dM_{yx}(x-\bar{x})}{d\bar{x}} \frac{H_{xy}(x,y)}{i} dx \qquad \text{(Eqn. 5-2b)}$$

where μ_o = permeability of free space

V = velocity of the media (or head)

i = current at the head coil

d = spacing of head from the medium of thickness δ

w = track width

M_x and M_y are magnetizations

These equations form the basis of the reproduction process and are usually referred to as the reciprocity formulas [5-4].

For calculating the output voltage from transitions of finite length, it is necessary to assume that transition takes on convenient mathematical form and arc tan function is used. For transition that changes from $+M_o$ to $-M_o$ magnetization, the form is as follows:

$$M_x = \frac{2}{\pi} M_o \arctan \frac{x'}{a_x} \qquad \text{(Eqn. 5-3a)}$$

$$M_y = \frac{2}{\pi} M_o \arctan \frac{x'}{a_y} \qquad \text{(Eqn. 5-3b)}$$

where a_x and a_y are transition length parameters for longitudinal and perpendicular recording. The transition has the form as shown graphically in Figure 5-5.

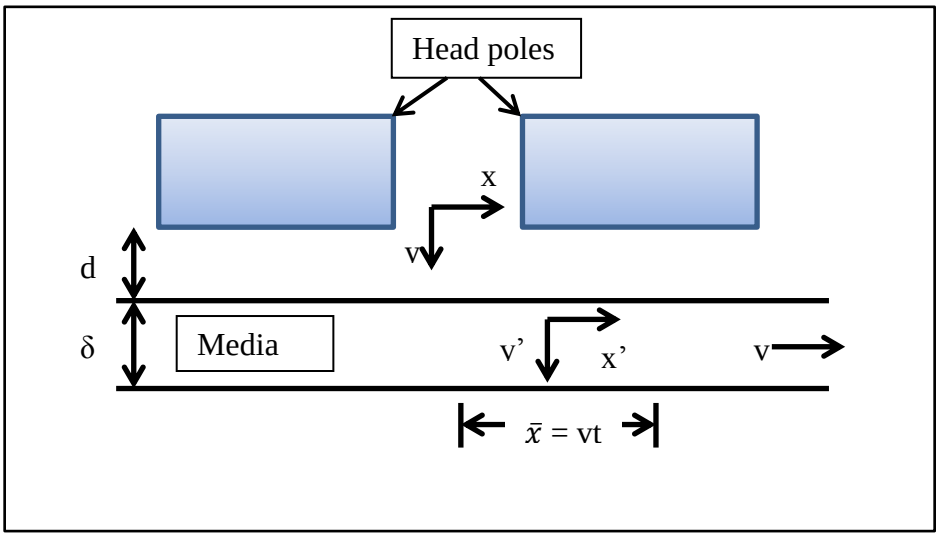

Figure 5-4: The coordinate system used for recording and playback.

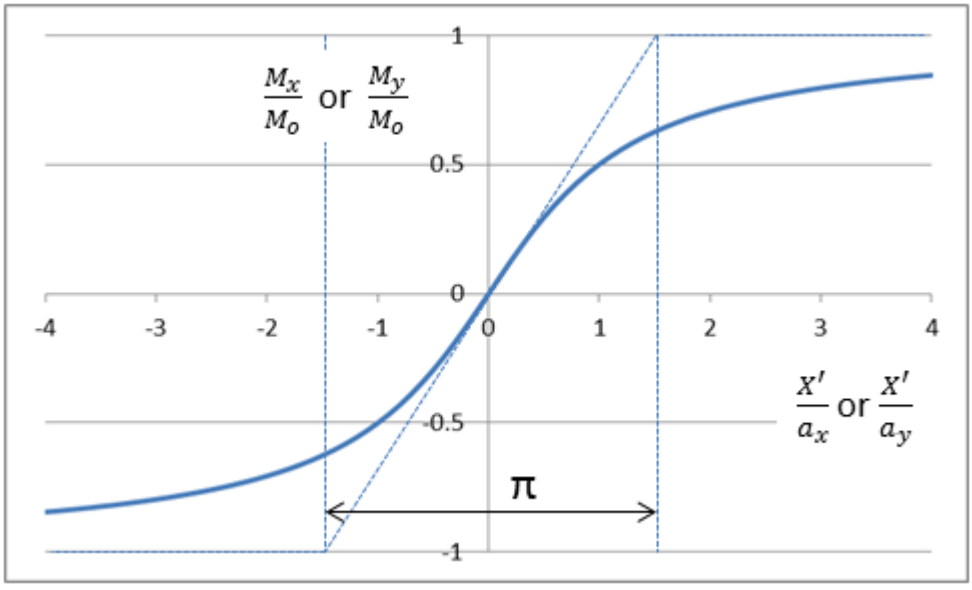

Figure 5-5: Shape of the transition in magnetic recording for arctan form for the transition. The tangent to the curve at the origin defines the transition width as πa.

One of the key parameters to come from the mathematical derivation of transition is the PW_{50}, or the pulse width at 50% of pulse amplitude, given by:

$$PW_{50} \cong \sqrt{g^2 + \frac{4}{3}(a^2 + d^2 + t^2)^{\frac{1}{2}}} \qquad \text{(Eqn. 5-4)}$$

$$a \cong Mr*t / Hc \qquad \text{(Eqn. 5-5)}$$

where g = gap length

d = head to media separation

t = media thickness

For high-density magnetic recording then, the PW_{50} can be reduced and recording density can be increased by having a small value for transition parameter "a," a small gap for the head, and reducing the head media separation and media thickness. Specifically for the "a" parameter, lower magnetization thickness product (Mr*t), and high coercivity, Hc leads to narrower transition. As for the Mr*t product, Mr itself cannot be reduced much because it is required to have enough signal from the media. Therefore, the magnetization must be maintained high enough for the signal to be detected, and physical thickness of the media should be reduced. From this perspective then, thin film media made from pure metal would have a significant advantage over ferrite particles in an epoxy binder. This is illustrated for the case of the Mr*t product for ferrite compared to several cobalt-based magnetic thin film media alloys in table 5-2. For the same value of the Mr*t product (3.5 memu/cm^2), the table lists the film thickness that would be required given the published saturation magnetization of the material, and assuming remanent magnetization (Mr) is 90% of saturation magnetization (Ms). It can be seen that thin film metallic media can be drastically thinner than oxide media for the same signal. The actual value of Ms for γ −Fe_2O_3 is

much higher, but since the particles are in an epoxy binder, only about 30% of the total media volume consists of the actual magnetic particles.

It becomes obvious the advantage that cobalt-based thin film media has over oxide media in terms of the ability to increase the areal density potential of magnetic recording. For commercial hard disk drives using $\gamma - Fe_2O_3$, the media thickness was approximately 0.7 μm, while cobalt-based media could reduce this to ~ 50 nm or 15X reduction in thickness. Other advantage was the higher coercivity potential of the thin film media. Although initially the head itself was limited for the field it could generate to switch the media, the maximum Hc capability of the $\gamma - Fe_2O_3$ was approximately 300 Oe. A 400 Oe media became possible by coating the oxide particle with a thin layer of cobalt, but further gains was not possible. However, the oxide media was the main medium used in commercially important disk drives well into mid-to late 1980s as shown in many IBM disk drives in table 5-3 and 5-4. This was obtained from the *Disk/Trend Report* for many industry firsts up to 1980 [5-5].

Table 5-2: A list of Ms, Mr, t and Mr*t products for various alloys.

Material	Ms (emu/cc)	Mr (90% of Ms) (emu/cc)	t (nm)	Mr*t (memu/cm^2)	
$\gamma - Fe_2O_3$	56	50	700	3.5	
CoP (plated)	890	800	44	3.5	
$CoRe_{7.5}$	740	666	53	3.5	
$CoCr_{22}$ *	300	270	130	3.5	*T_{sub} 300^{o}C
$CoNi_{20}$	1100	990	35	3.5	
$CoCr_{15}Ta_4$	600	540	65	3.5	
$CoNi_9Pt_{10}$	1000	900	39	3.5	
$CoNi_8Cr_6Pt_{10}$	833	750	47	3.5	

Mr*t value is arbitrarily set to 3.5 memu/cm^2 for all the media to illustrate the effect on actual film thickness (t) that would be needed for each different magnetic alloy.

* For CoCr system, the value of Ms can vary depending on the deposition temperature due to phase segregation.

Drives	Type	Year	Areal Density	Track Density	Linear Density	Capacity	# Disks	Disk Size	Comments
			Mb/in^2	tracks/inch	bits/inch				
IBM 3330	Disk Pack	1971	0.78	192	4040	100	11	14 inch	
IBM 3340	fixed *	1973	1.69	300	5636	35/75	2 or 4	14 inch	
IBM 3350	fixed	1976	3.07	478	6425	317.5	8	14 inch	
IBM 3310	fixed	1979	3.8	450	8530	64.5	6	8 inch	First fixed 8 inch
IBM 3370	fixed	1979	7.7	635	12134	571	7	14 inch	8 turn TF head
Seagate ST506	fixed	1980	1.96	255	7690	5	2	5-1/4	
IBM 3380	fixed	1981	12.2	801	15240	1260	9	14 inch	8 turn TF head
IBM 3380K	fixed	1987	35.9	2089	17200	3781	9	14 inch	31 turn TF head, all digital servo
IBM 3390-2	fixed	1989	62.6	2242	27940	3784	9	10.8 inch	31 turn film heads
	* 3340 Data module had fixed head inside the module								

Table 5-3**:** A compilation of historically important disk drives from its inception in 1956, listing some of the key parameters for the disk, track and linear density and areal densities.

Year	Name	Capacity	Disk Size/Quantity	Comments
1956	IBM 350 RAMAC	5 MB	24 inch diameter / 50 platters	First disk drive
1961	Bryant Computer 4240	90 MB	39 inch disks / 24 platters	
1962	IBM 1301 Advanced Disk File	28 MB	24 inch disks / 25 or 50 disks	
1963	IBM 1311 Low Cost File	2.68 MB	14 inch disks	First removable disk pack
1965	IBM 2310 Ramkit	1.024 MB		Single disk cartridge
1966	IBM2314 Storage Facility	29.17 MB	11 disk removale pack	First ferrite core heads
1971	IBM 3330-1 Merlin	100 MB	11 disk removale pack	First track following servo system
1973	IBM 3340 Winchester	35/70 MB	IBM 3348 removable data module	Low mass heads, lubricated disks, sealed assembly
1976	IBM 3350 Madrid	317.5 MB		Fixed disks
1979	IBM 3370 New File Project	571 MB	14 inch disks / 7 disks	First thin film heads
1980	IBM 3380 Direct Access Storage Device	2.52 GB		

Table 5-4**:** A compilation of historically important disk drives from its inception in 1956, listing some of the key parameters for the disk, track and linear density and areal densities.

5.2 Thin film Magnetic Media

Some of the key considerations that go into selection of alloys for magnetic recording are that one can obtain high Hc, have relatively high saturation magnetization, Ms, and that high degree of hexagonal crystal structure is retained with the addition of an alloying element. Cobalt metal has a very high value of M_s or saturation magnetization, and $4\pi M_s$ of 18,000 Gauss. The hexagonal close-packed structure has high uniaxial anisotropy, with Ku of $4x10^6$ ergs/cm^3 at room temperature. Other considerations of importance are that the alloy is corrosion resistant and the cost to produce it is low. For alloy selection, the equilibrium phase diagram is one of the initial guides to the selection process. The addition of an alloying element that stabilizes the hexagonal phase is important in obtaining higher Hc as the hexagonal phase has a higher magnetocrystalline anisotropy and lead to higher Hc in the media. Platinum group metal addition has the effect of enhancing the spin-orbital coupling between the atoms to enhance the anisotropy of the Co metal and, hence, raise the Hc capability of the alloy combinations. These elements are Ru, Rh, Pd, Os, Ir, and Pt. In addition, rare-earth elements are often considered as well, the most well known one is the SmCo, which has very high Hc potential. Materials that form good permanent magnets are a consideration for use as media, and they can be ranked according to the energy product (BHmax).

In the early days of thin film magnetic media, the first alloy to obtain some commercial application was CoP-plated media. This was done by electroless plating using Co-chloride and sodium hypophosphite as a reducing agent. This process can incorporate 5-6 % phosphorus into the film. The typical Hc potential of this alloy is approximately 400 to 900 Oe, with Ms of ~900 emu/cc [5-6]. It saw some of the first applications in a disk drive configuration for video replay systems. Initially, the plating process was considered lower cost than sputtering, which required an expensive vacuum system to deposit the film. Ampex's first commercial instant replay system, the HS-100 model introduced in 1967, used plated CoP disks. Considerable research was done on the CoP system and with some additional alloying elements [5-7, 5-8]. Commercialization of CoP alloy film for hard disk drives began in earnest in the 1981-

1982 timeframe that coincided with the start-up of many small form factor hard disk drive companies, which entered the market for hard disk drives for PCs and small mini-computers. Most notably, Ampex, which had very legitimate history and prowess in magnetic recording technology, began production of Alar disks [5-9], which were 5¼-inch form factor CoP electrolessly plated disks which were deposited onto an aluminum base substrate with electrolessly plated NiP coating. This disk had a CoP coating of approximately 60-80 nm with a coercivity of approximately 600 Oe. It was produced without any carbon overcoat protection and consequently had significant reliability issues in the field, and soon the company went out of business. IBM also attempted to use plated CoP film in their mainstream high-end hard disk drives such as the famed IBM 3340, but they encountered severe reliability issues and could not implement the technology and, hence, continued to use oxide media for their drives [5-3]. The continuing bad experience that they had in attempting to use thin film media in their drive kept them from embracing the new media for a long time, allowing many other smaller companies to enter the field, especially in small form factor drives.

Alternative to CoP film by electroless plating was to use all-dry sputtering technology. Many people in different organizations since the late 1960s investigated sputtered longitudinal thin film media. However, the industry was being distracted by other technologies such as magnetic bubble memory and optical recording. It took until the 1970s to realize that magnetic bubble memory was a bust. Even then, there was much more interest in perpendicular magnetic recording compared to the longitudinal media. The two shared a common deposition method, which was sputtering. Tu Chen at Xerox PARC was one of the few researchers that had been spending many years on developing longitudinal sputtered thin film media based on CoRe film [5-10], and IBM had worked on various alloys as well including CoPt alloys by Aboaf [5-11] and Yanagisawa [5-12] at NEC reported good results using CoNiPt alloys. Sputtered film technology received much more attention because of a paper by Iwasaki in Tohoku University who proposed perpendicular magnetic recording in 1977 to obtain higher recording density using CoCr film [5-13]. Perpendicular magnetic recording at the time required much thicker film compared to the longitudinal recording. Iwasaki's

CoCr film used relatively high Cr content of approximately 15-20 %. Perpendicular recording drew tremendous interest at that time, and many start-up companies attempted to commercialize the technology in the early 1980s. However, none of them succeeded. It would take another 30 years before perpendicular recording was finally adopted by the hard disk drive industry.

5.3 Co-Re Based Thin film Media

Tu Chen and his colleagues at Xerox PARC investigated Co-Re-based thin film magnetic media from 1977 to 1983. This medium was used to obtain many useful insights into thin films in general, and how the limit of magnetic recording is affected by the behavior of thin film media. The results were applicable to all other thin film media to come afterward, and they were published over several years [5-14, 15, 16, 17, and 18]. Some of the key studies are outlined here. From the point of view of the phase diagram of the Co-Re system, the existing data was limited [5-19]. The kinetics of reactions between Co and Re as well as with many other elemental additions is slow, and a long annealing time is needed to establish possible equilibrium phases. From the phase diagram, it appears that there is a good solubility of Re in Co in all composition range. The important feature of the Co-Re system is that the transformation temperature of the FCC phase to HCP is increased with Re addition in the Co-rich side of the phase diagram as shown in figure 5-6. It would suggest that the HCP phase is more stable with the Re addition. One of the critical problems with pure cobalt film is the difficulty of maintaining the hexagonal phase in a sputtered film. However, the region of interest is between 10-20 at%Re. Since another critical factor is maintaining high saturation magnetization, Ms, in the alloy. The drop in the Curie temperature is a good indicator of the drop in magnetization.

In addition to having high Hc and Ms, it is also necessary to have high hysteresis squareness for the media in order to obtain good recording performance. There are two definitions for squareness. One is defined as S = Mr/Ms or ratio of

remanence magnetization to saturation magnetization, or by S*, which was introduced by William and Comstock [5-20] as the *coercive squareness*:

$$S^* = 1 - Mr/Hc\ (dM/dH_{(H=Hc)}) \qquad \text{(Eqn. 5-6)}$$

This is the slope of the hysteresis loop at Hc, where the hysteresis loop crosses zero magnetization. S and S* are related to the transition width in magnetic recording, and ideally the values for S and S* would be 1. Additionally, squareness can be defined based on where the loop closure occurs, or based on saturation magnetization as shown in Figure 5-7.

$$S' = Mr/Mts \qquad \text{(Eqn. 5-7)}$$

CoRe films were prepared in a conventional RF diode sputtering system, using a 2-inch diameter target. Alloyed Re targets with the composition of 7.5% and 10.0% were used. The sputtering rate was controlled in the range from 0.04 to 0.30 nm/sec. by adjusting the RF power. Sputter pressure was between 5 to 100 mTorr. The substrate was a 2-inch square Corning 7059 glass plate, where half of the slide was coated with thin evaporated carbon film. This was done so that sputtered film can be easily lifted from the glass slide for TEM examination.

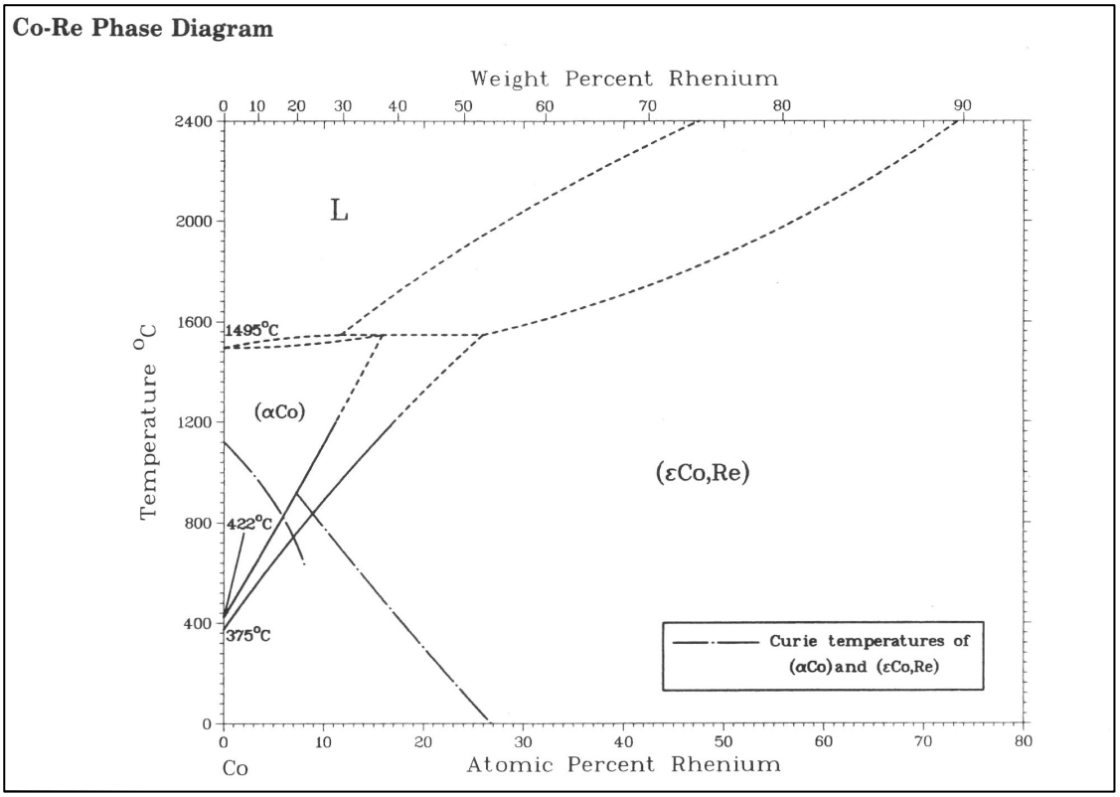

Figure 5-6: Phase diagram for Co-Re. M. Hansen, *Constitution of Binary Alloys, 2nd edition*, p. 494, (McGraw-Hill, New York, 1958) [5-19].
Reproducd with permission.

TEM specimen was prepared by dropping a few drops of collodion solution on the carbon-coated side of the slide. Collodion is a solution of pyroxylin (nitrocellulose) in ether and alcohol. When applied and dried, it forms a layer of nitrocellulose, which will exert a strong tension on the sputtered film, usually enough for the film to delaminate from the glass. Collodion film can be easily dissolved using acetone, and the delaminated film is picked up on the copper grid for TEM observation. Many films can be examined easily and rapidly using this procedure. The presence of carbon film did not affect the magnetic properties of the film, as it was verified by vibrating sample magnetometer (VSM). The substrate temperature was varied between room temperature up to 400°C. Film thickness was varied between 20 to 200 nm.

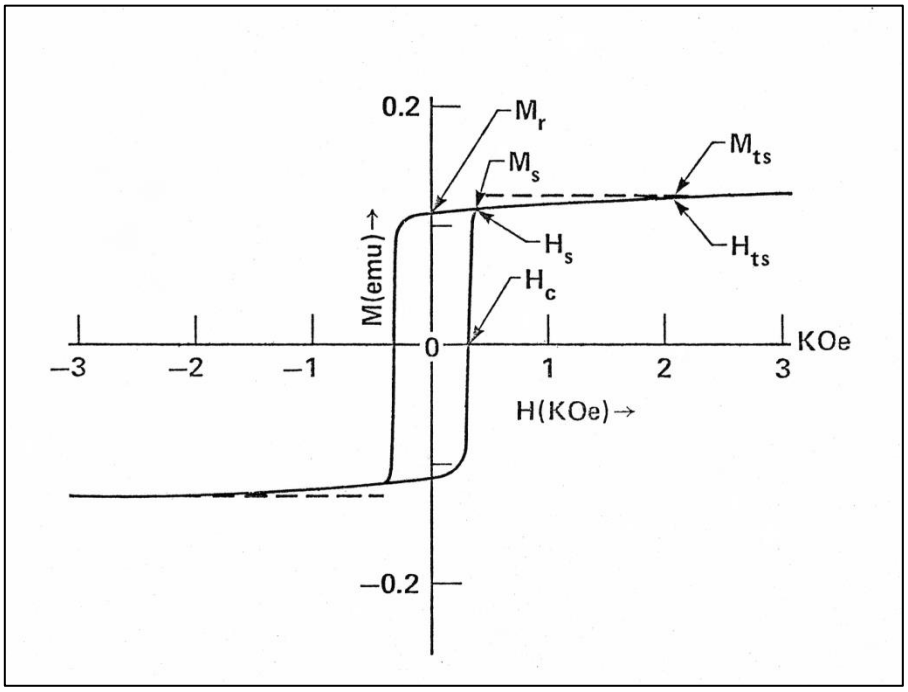

Figure 5-7: The definition of various parameters for hysteresis loop characteristics. From ref [5-16]. Copyright © 1981, IEEE, reproduced with permission.

In a previous work by Tu Chen [5-16], pure cobalt film deposited by RF diode sputtering under various conditions was analyzed. The electron diffraction pattern showed a presence of the FCC phase mixed with HCP phase, which increased with a substrate temperature above 100^{o}C. In addition, the film showed channels of voids between the grains when sputtered above 25 mTorr. As the sputtering pressure increased, the grain-to-grain separation increased, and the separation decreased above film thickness of 100 nm as crystallites started to grow together. These changes in microstructure were correlated with higher Hc with grain separation, and higher hysteresis squareness and lower Hc as grains contained more FCC phase as it was expected but also with less grain separation. This was the first instance where the correlation was made between grain isolation to hysteresis loop squareness, and to the notion that this phenomenon is related to the extent of exchange coupling between the

grains. Later on, it would be noted that higher exchange coupling between the grains (less separation) leads to higher noise in magnetic recording, hence, the importance of reducing exchange coupling to improve SNR in the film and to increase recording density [5-18]. For CoRe films, clearly, the HCP grains are more prevalent at temperatures below 300^{o}C. Hence, the addition of Re stabilizes the HCP phase. Higher HCP content in the film leads to higher Hc of approximately 600-700 Oe, and high Mr/Ms (squareness) of 80-87% and S* of 80-90%. High squareness in these films was attributed to highly interacting grains, and grain separation based on higher sputtering pressures was less pronounced than in pure cobalt films. 4πMs of 7.5% Re film was measured at ~ 9300 Gauss (Ms = 740 emu/cc). Several types of Co microstructure that were observed were categorized, and they were as follows:

Type I: All of the crystals having their c-axis oriented normal to the film plane, resembling a film having single-crystal orientation over a large area of the film. This microstructure was generally favored for higher Ar pressures, and lower substrate temperatures.

Type II: Strong preferred orientation with crystallites having their c-axis normal to the film plane, and crystallites having elongated shape. Typical narrow dimensions are 30-40 nm, and the long axis 100-200 nm. This microstructure was favored at lower Ar pressures and higher substrate temperatures.

Type III: Grains with equiaxed shape and weak preferred orientation of the grains. The grain size was 30-40 nm. This microstructure was seen as a progression from Type II structure, with lower Ar pressures and lower substrate temperatures. Hysteresis loops are quite square.

Type IV: Films deposited above 300^{o}C, containing a mixture of FCC and HCP grains. Crystallites are irregular, poorly developed, and relatively small, with grain size less than 30 nm.

An example of each type of film is shown in Figure 5-8. Images are BF TEM micrographs with respective DP in the inset.

Interesting results from these types of films were from the Lorentz microscopy of the films. Type II and III films showed in-plane ripple structure, which only appeared when the crystallites in the film had some or complete random orientation of their c-axis in the film. It was correctly deduced that the ripple is created by a change in net magnetization direction of a cluster of many randomly oriented crystallites. Therefore, the basic unit of magnetization reversal in the film is the cluster of crystallites located between the ripple. The cluster is strongly coupled magnetically with the surrounding clusters. These effects occur because the grains in the film are strongly coupled by exchange interactions. This model for magnetic behavior of CoRe films that shows in-plane ripple was used by Hughes to explain the value of Hc and squareness of a CoP-plated media. He had developed the computer model by 1978 at Xerox PARC collaborating with Tu Chen, but he did not publish his result until 1983 [5-21].

Type III media was specifically targeted for further study of its microstructure, as it had the most interesting properties for longitudinal recording, namely higher Hc and high squareness. The film contained equiaxed grains and weak preferred orientation. All of the films were sputtered at 5 mTorr using RF-diode. The sputtering target was a Co-10at%Re alloyed target with a diameter of 3 inches. Film thicknesses were all 55 $\pm$ 5 nm. The substrate temperature was varied to obtain different microstructure (at 70, 100, 150, 200 and 300^{o}C). RF input power was varied from 50, 75, and 100 watts. A Philips EM301 and EM400 TEM were used for the analysis.

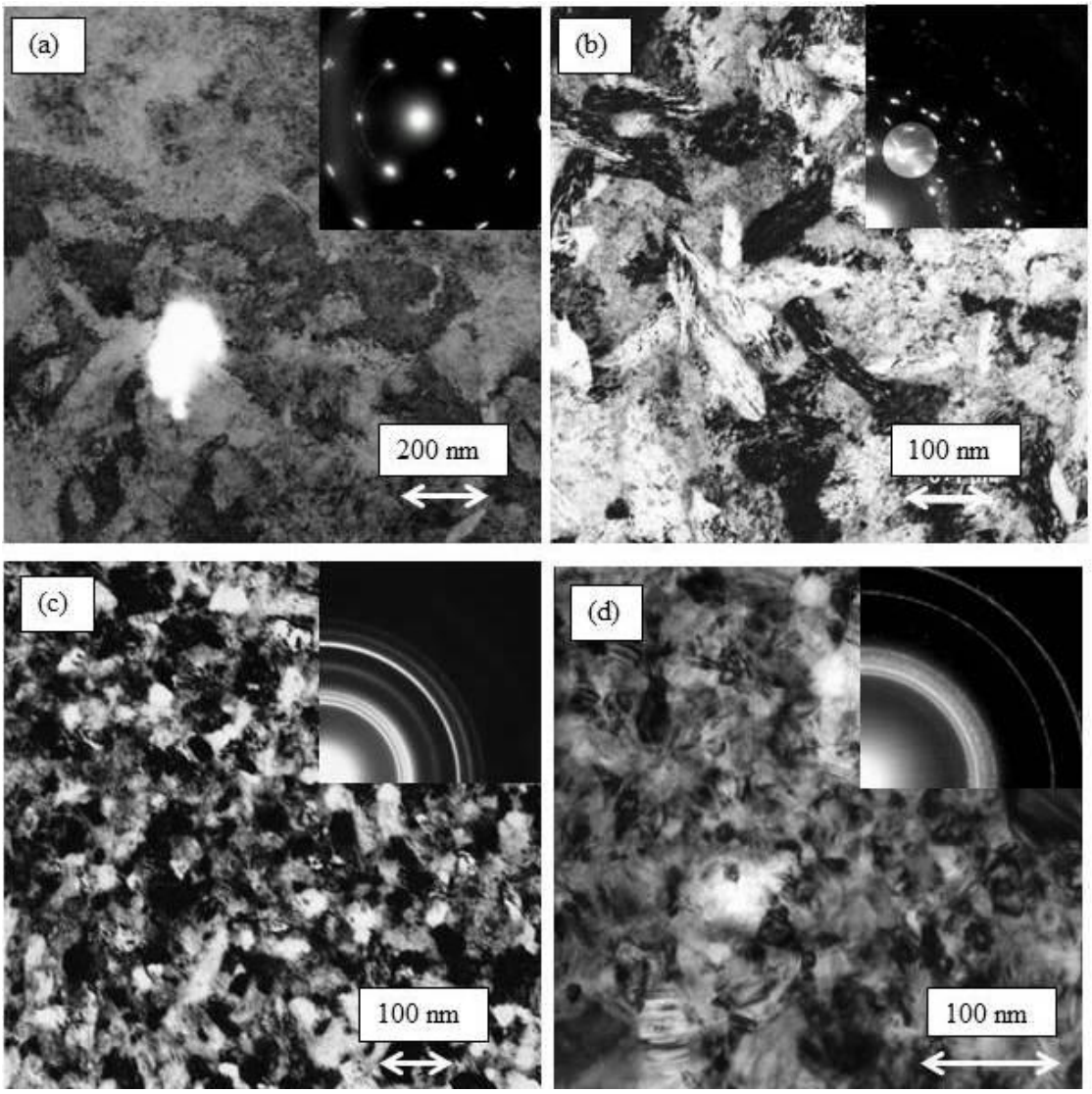

Figure 5-8: BF TEM micrographs of Type I (a), II (b) III (c) for Co10at%Re sputtered thin-film media. The white region in (a) is a hole in the media. Note the strong near-single crystal diffraction pattern obtained from the entire film. Contrast differences in the imaged area are due to different subgrain regions in the film that are slightly misoriented with each other. The diffraction pattern shown in the inset in (b) has SAD aperture, which was used in the 2½-D imaging series (not shown), (d) is Co only film, which has a mixture of some large grains and many small particles, and there is a distinct $(200)_{FCC}$ ring in the DP.

Conventional TEM diffraction analysis showed that films deposited at 300°C contain larger quantities of FCC phase in the HCP matrix. The film structure resembled the Type IV media described above. For films deposited at lower temperatures, the film contained varying amounts of FCC phase. It should be noted that only qualitative conclusions about the amount of FCC phase could be made because the diffraction lines from HCP and FCC phases overlap, as shown in Figure 5-9. Only $(200)_{FCC}$ reflection stands alone in the pattern, and the relative strength of the line indicates the amount of FCC phase present in the HCP matrix. Magnetic properties obtained from VSM measurement are shown in Table 5-5 for selective films. Hs and Ms values are obtained where the hysteresis loop closes as shown in Figure 5-7 while Hts and Mts refer to the saturation field and magnetization, respectively [5-22].

H_c (Oe)	H_s (Oe)	H_{ts} (KOe)	M_r/M_s (%)	M_r/M_{ts} (%)	Power (Watts)	Sub. Temp.(°C)
226	230	0.8	97.0	94.2	50	70
233	280	1.6	98.0	92.8	100	100
307	370	2.2	97.1	87.9	50	100
336	440	2.0	95.8	88.5	100	150
338	460	2.4	93.6	85.8	75	200
359	420	1.3	94.0	91.6	75	150
413	580	2.5	93.2	84.2	50	200
446	590	2.7	93.4	83.6	50	150

Table 5-5: VSM results and deposition conditions for Type III media. Ref [5-17].
Copyright © 1981, IEEE, reproduced with permission.

Hc vs. substrate temperature for sample series at 50, 75, and 100 RF power is shown in Figure 5-10. The increase in Hc corresponds with larger grain size that comes with higher sputter rate and temperatures. The reason for the slight drop in Hc from 150 to 200°C is potentially due to a higher amount of FCC phase in the film, although it is quantitatively difficult to show. Grain size is monotonically increasing with

substrate temperature, as it is shown in Figure 5-11. There are considerable variations in grain size within the film, and the curve is a least-square fit to the data.

Mr/Mts (squareness) is plotted against Hc in Figure 5-12, and the fit to the curve is made ignoring the two outliers, which are at 336 and 359 Oe. The reason why these two films do not fit the trend was investigated. The degree of preferred orientation was measured by taking the peak intensity between HCP(0002) and HCP($11\bar{2}0$) electron diffraction rings using a densitometer trace of the negatives.

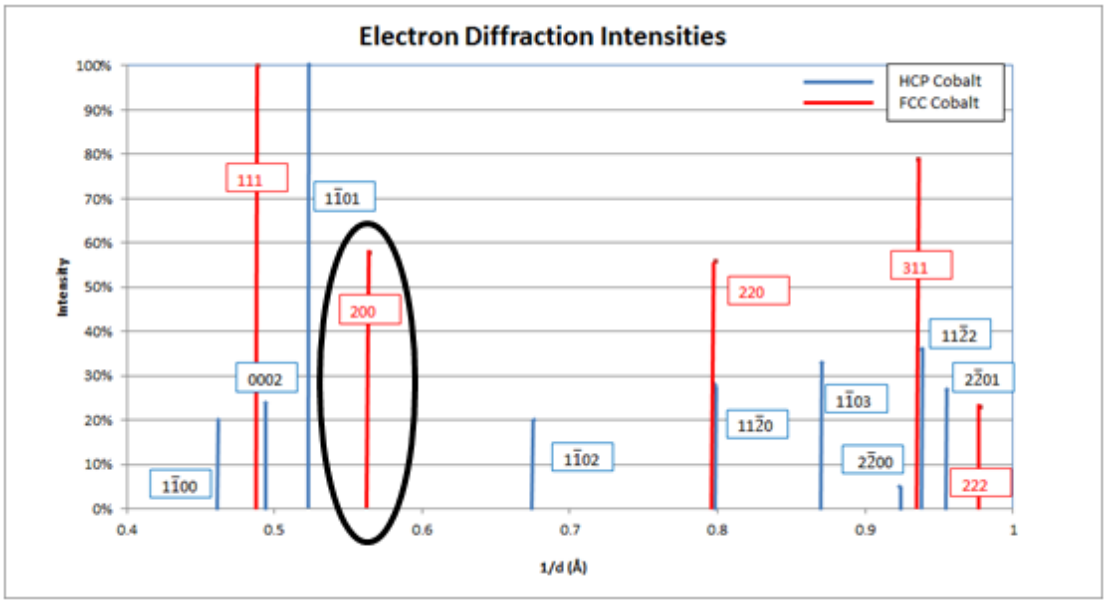

Figure 5-9: Electron diffraction pattern intensity for randomly oriented HCP and FCC phase cobalt, calculated from structure factors and multiplicities for each reflection and using scattering factors for electrons. Temperature and relativistic corrections were also put in for 120 keV electrons. It can be seen that in order to isolate the FCC reflections from the HCP, only the FCC reflection that is separated sufficiently from the HCP reflection is the $(200)_{FCC}$ reflection (circled in the figure).

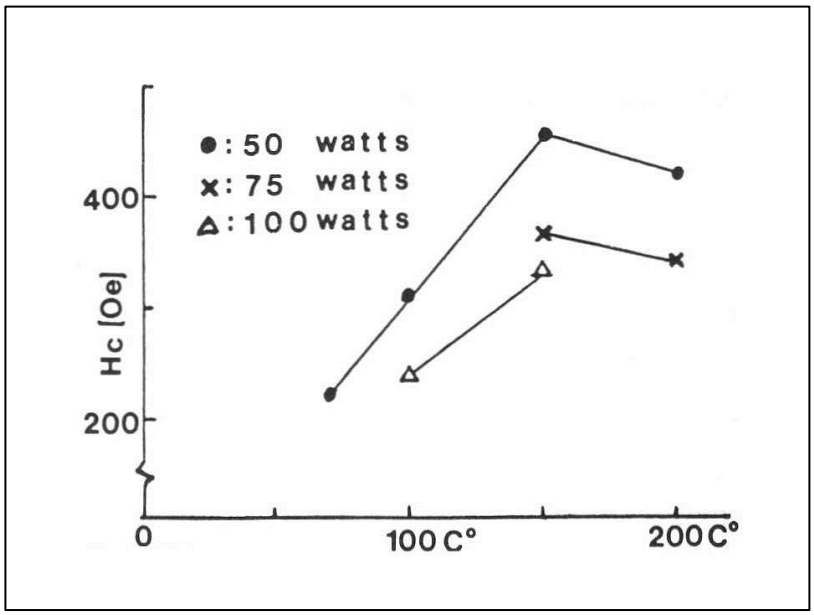

Figure 5-10: Hc vs. substrate temperature, grouped by sputter RF power.
Ref [5-17]. Copyright © 1981, IEEE, reproduced with permission.

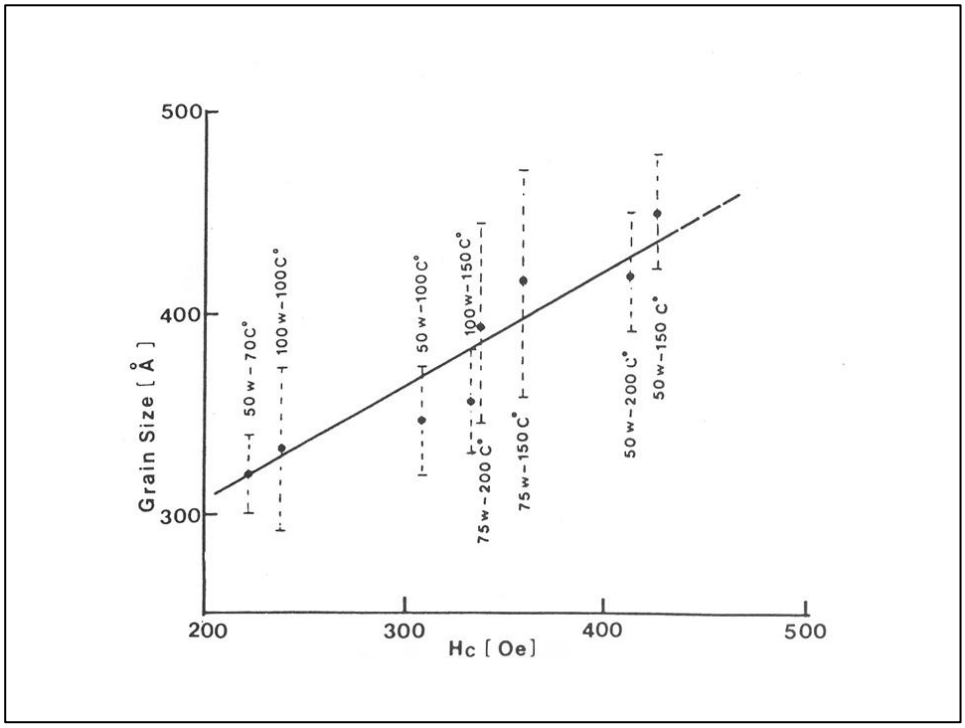

Figure 5-11: Grain size measured by TEM vs. Hc.
Ref [5-17]. Copyright © 1981, IEEE, reproduced with permission.

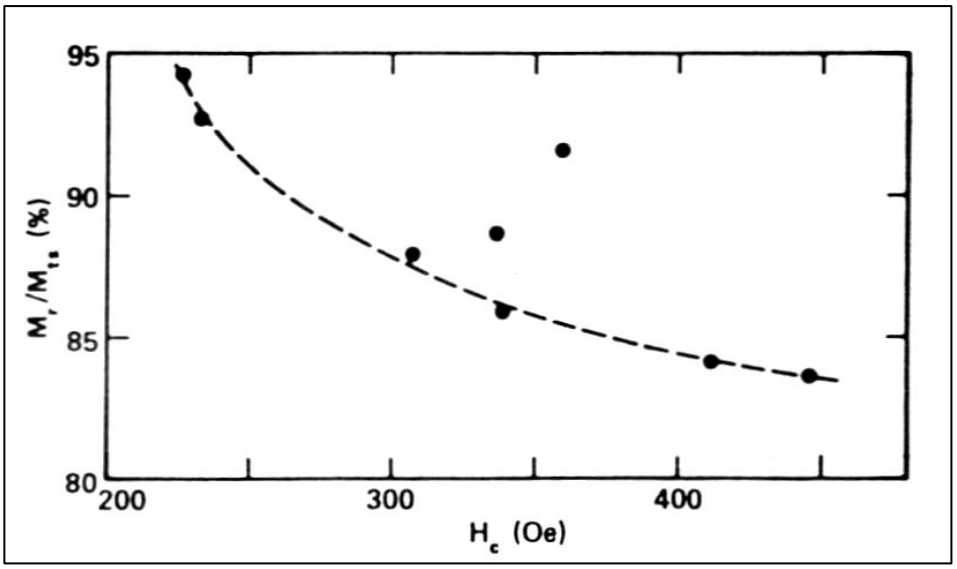

Figure 5-12: Mr/Mts vs. Hc. Two points with Hc at 336 and 359 are igonored in the curve fitting. Ref [5-17]. Copyright © 1981, IEEE. Reproduced with permission.

All of the data points from Table 5-4 is plotted in the Mr/Mts vs. $I_{(0002)}$ / $I_{(11\bar{2}0)}$ graph in Figure 5-13 and they fall along the same curve. The Hc of each film is indicated by the data point. It could be said that Hc does not track the Mr/Mts generally, but Mr/Mts or squareness is correlated well with the preferred orientation of the film. Higher values of the $I_{(0002)}/I_{(11\bar{2}0)}$ ratio are an indication of more c-axis oriented in the plane of the film in electron diffraction, in other words, the film is more horizontal, and it leads to a square hysteresis loop as expected.

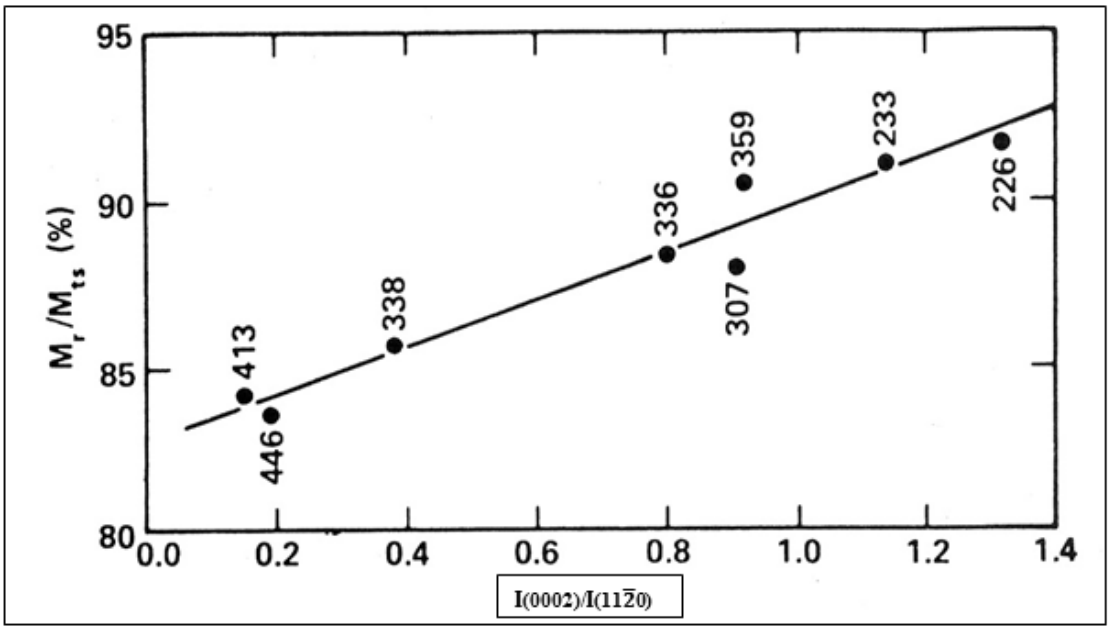

Figure 5-13: Mr/Mts plotted against HCP intensities, I(0002) / I(11$\bar{2}$0). Hc values are listed for each data point. Higher hysteresis squareness is associated with greater in-plane orientation of the c-axis (stronger (0002) intensity in electron diffraction). Ref [5-17]. Copyright © 1981, IEEE, reproduced with permission.

5.3.1 Imaging of FCC Phase in Co-10at%Re Sputtered Thin films

The optimum microstructure for longitudinal magnetic recording is a microstructure that provides a high magnetic hysteresis loop and high coercivity. To attain such a condition, it is important that the film be composed of mostly hexagonal phase cobalt. The presence of FCC phase cobalt was expected to reduce coercivity, hence, its recording density potential. Unfortunately, it is not so easy to determine the extent or even the presence of the FCC phase in the sputtered film by conventional means such as by X-ray diffraction due to closeness of some of the FCC reflections to the HCP in cobalt, and some preferred texture that often occurs in sputtered film. The stacking fault energy in cobalt is generally known to be low [5-23] at 31 M/m^{-2} at 20^{o}C. Therefore, it is expected to have a high amount of stacking faults in the grain, which

also complicates the analysis. Another complication is that grain size by design is relatively small. The quantity and the morphology of the FCC phase form an important parameter for obtaining better insight on the structure-properties relationship in the sputtered cobalt film system.

Identification of the FCC phase in Co film is difficult due to closely spaced diffraction lines for HCP and the FCC phase as shown previously in Figure 5-8. The actual situation with the electron diffraction pattern for a Co-10at%Re sputtered film containing some amount of the FCC phase is shown in Figure 5-14. The two DF images were formed by using the objective aperture shown in the DP image shown on the left. Different grains light up in the DF images since they are formed by a different set of reflections contained inside the objective aperture. The (200) reflection of FCC cobalt is still closely spaced with the other three HCP reflections nearby, namely the $(1\bar{1}00)$, (0002) and $(1\bar{1}01)$ reflections. The FCC (200) reflection is present but it is very diffuse, due to the presence of the stacking faults. Additionally, HCP $(1\bar{1}01)$, $(1\bar{1}02)$, and $(1\bar{1}03)$ are all streaked as well and very diffuse. Many bright particles that are diffracting also show striations, which are stacking faults within the grain.

It is observed that whenever (002) the FCC line is present, (hk0ℓ) lines of HCP are always broadened into a fuzzy band of diffuse intensity. The conclusion that this is due to the stacking faults on the (0001) plane of the HCP grains came indirectly from the single-crystal $(2\bar{1}\bar{1}0)$ pattern of Co-10at%Ru film shown in Figure 5-15. BF image shows stacking fault contrast running perpendicular to the streaks in the [0001] direction in the diffraction pattern. It can be seen that the distance between each stacking fault is approximately few nanometers. When the stacking fault density is very high, the distinction between the FCC and HCP phase can no longer be made. This is indicated by the fact that in some films, the fuzzy (hk0 ℓ) extends well into the FCC (002) region.

An attempt to isolate the (200) FCC reflection with a small objective aperture placed on the ring to try to isolate it is shown in Figure 5-16, together with the DF

image formed using the aperture. Some of the grains do light up, suggesting that they may be from the FCC ring, but imaging under this type of condition is difficult. It taxes the stability of the microscope and the specimen since long exposure times are needed to collect sufficient intensity using such a small aperture. The DF images show small particles that are distinct. If they are indeed coming from the (200) FCC reflections, then it can be said that the FCC phase exists as distinct particles and they are not part of the localized region within the larger hexagonal grains where local basal slips cause a localized FCC region within the HCP grains.

By comparing the two DF images in figure 5-14, in an attempt to isolate the (200)FCC ring with the objective aperture, it is possible to deduce which grains are reflecting (bright) from which reflections, hence, whether it is HCP or FCC grains, but there is some uncertainty in this determination. In the first case, the overlap of HCP and FCC reflections make unambiguous assignment impossible. In the second case, the objective aperture is simply too small in order to attempt to isolate the FCC reflection by itself. An additional technique is needed, and this is described later.

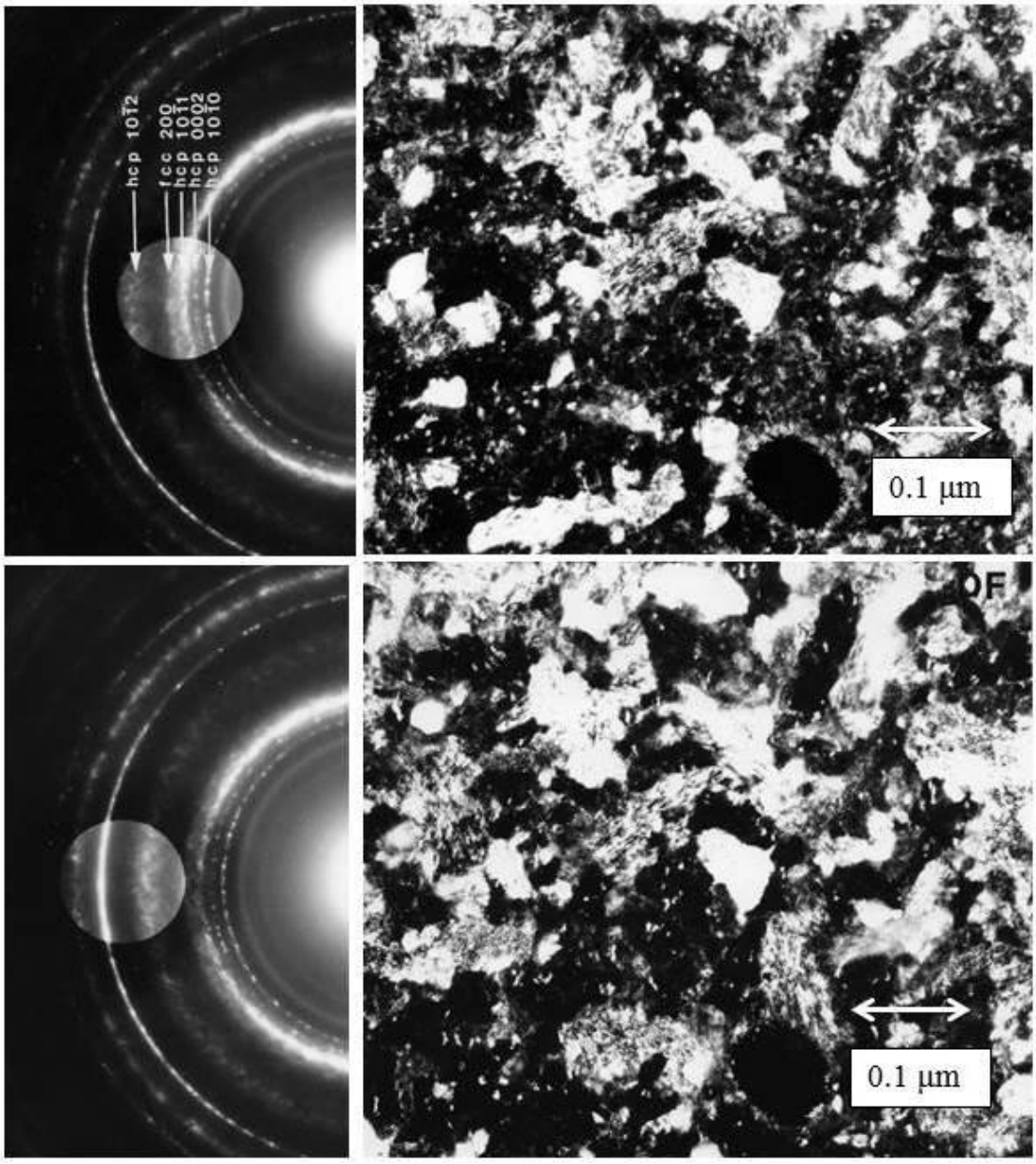

Figure 5-14: Two set of DF images taken with the objective aperture placed over the diffraction pattern as shown on the left of each DF image, for Co10at% Re sputtered film containing some amount of FCC phase. It is possible to identify some of the grains as being either FCC or HCP, but due to overlapping FCC and HCP reflections, the assignment cannot be made for certain. The dark circle at the bottom next to the micron marker is a small hole in the film. It served as a convenient marker to keep track of the grains in the images.

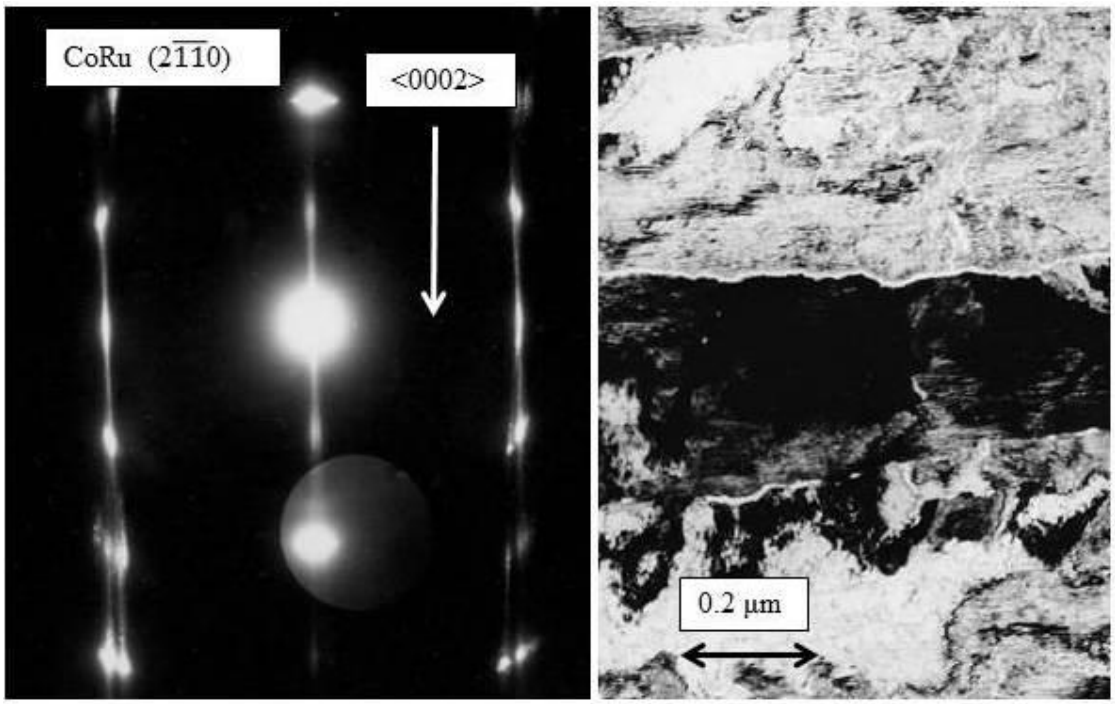

Figure 5-15: DP and BF image from Co10at%Ru film, with near single crystalline structure. The DP has been properly oriented with respect to the BF image so that h**o**rizontal striations, which are stacking faults runs along the (0001) basal plane of the cobalt structure and the streaks runs in the c-axis direction as shown in the DP. CoRu film in this image had single crystal structure that had its c-axis in the plane of the substrate, giving the DP with (2$\bar{1}\bar{1}$0) orientation. The film was quite unique in providing these growth characteristics.

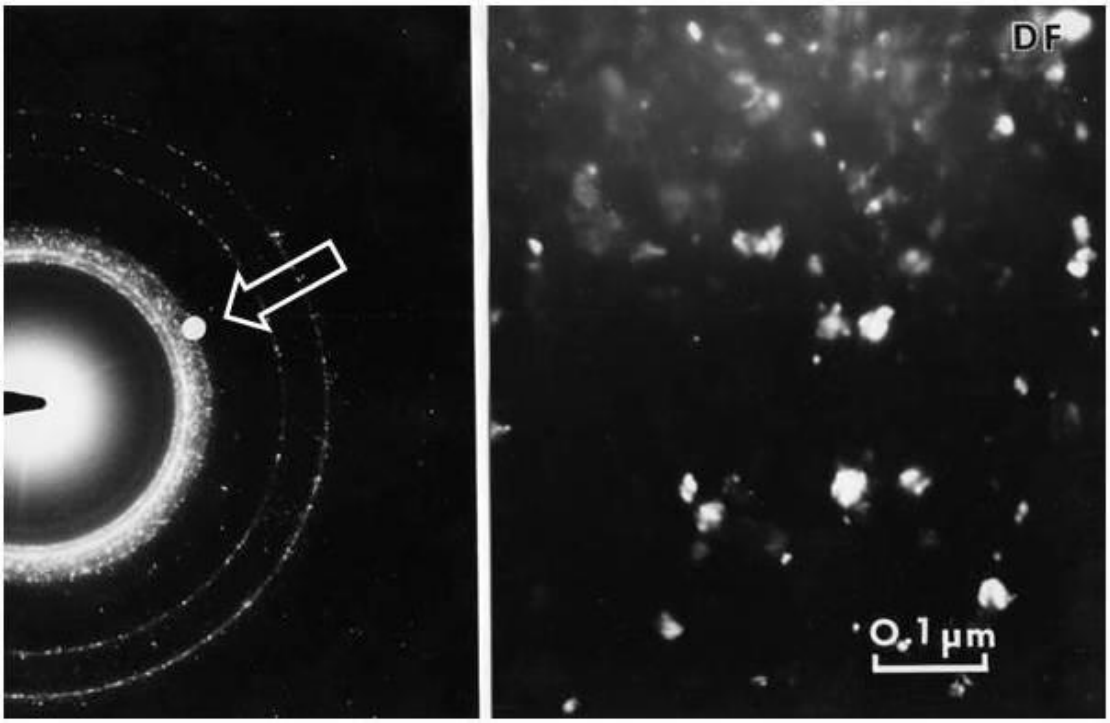

Figure 5-16: Attempt to isolate FCC(200) reflection with a small objective aperture (arrowed in the DP) in order to image only the FCC phase in Co10at%Re media. Distinctly different appearance grains did light up in the DF image, but the technique is rather difficult due to the small number of particles that will actually reflect into the small objective aperture, and the long exposure needed to obtain the image.

5.3.2 2½-D TEM Microscopy of CoRe Film

Additional TEM work, namely the 2½-D imaging analysis, was used to obtain a more detailed analysis of the microstructure. In this technique, a pair of DF images at different objective lens defocus settings is taken, using a number of diffracted beams. When the pair of micrographs is observed in a stereo viewer, after taking into account the rotation of the image with respect to the diffraction pattern, the different diffracted regions are seen at different heights according to the position of their diffraction spots

in the reciprocal space. The technique was first introduced by Bell [5-24] and practical applications described in detail by Sinclair et al. [5-25].

The 2½-D imaging method relies on the relative shift in image features with defocus, depending upon the angle α that the e-beam contributing to that image makes with respect to the microscope optic axis. This is illustrated in figure 5-17.

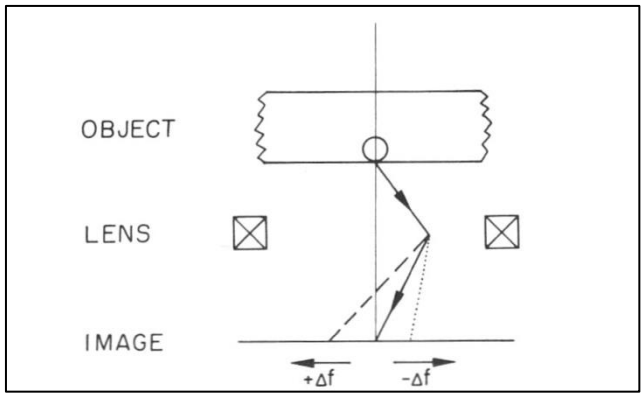

Figure 5-17: Path of the electrons with different defocus, $\pm \Delta f$. Positive defocus is with stronger objective lens current. Ref. [5-25]. Met. Trans. A, Springer Publications. Reproduced with permission.

The image shift, y is given by the following, ignoring lens aberrations.

$$y = M \, \Delta f \, \alpha \qquad \text{[Eqn. 5-8]}$$

where M = magnification

Δf = defocus from objective aperture

α = angle of the beam from the microscope optic axis.

Features giving rise to different diffraction spots are then shifted by different amounts. The relative displacement Δy_{12} is given by a differential form of eqn. 5-8:

$$\Delta y_{12} = \Delta f \, \alpha_{12} \qquad \text{[Eqn. 5-9]}$$

α_{12} is the angle between the beams. Since the diffraction angles are very small in a TEM, the above equation can be converted to reciprocal lattice vectors.

$$\Delta\bar{y}_{12} = \Delta f\, \bar{g}_{12} \qquad \text{[Eqn. 5-10]}$$

It is not obvious that displacement in the image, according to eqn. 5-9, will result in a stereoscopic effect. Figure 5-18 shows schematically how we perceive depth with two eyes, and depth perception comes about by the right and left eye seeing an object slightly differently for objects that are placed in front (the square and circle in the figure). A true 3D effect in the TEM image also can be also arranged by simply tilting the specimen and taking two images and viewing them in the stereo viewer. With appropriate magnification and tilts, what the two eyes might see can be arranged with an appropriate tilt of the specimen.

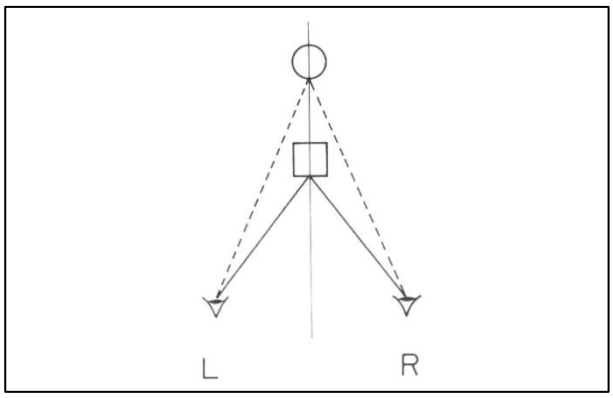

Figure 5-18: How the eye perceives depth. L and R eyes see a shift in the position of the square and circle, which is translated into perception of depth. Ref. [5-25], Met. Trans. A, Springer Publications. Reproduced with permission.

Figure 5-19 shows the situation where the relative image shift is produced by objective lens defocus. When a pair of images taken at different defocus is now imaged in a stereo viewer, the relative height of the feature now depends upon the position of its relative diffraction spots in reciprocal space, and it has no connection to its relative height in the TEM specimen. The shift in the image (for the square and the circle) now is perceived as height difference when viewed through the stereo viewer. Typical

defocus values are several microns. A pair of DF images is set up for a stereo viewer, and aligned with the diffraction pattern according to the microscope rotation calibration. Actual parallax shift can be measured using the quantitative viewer.

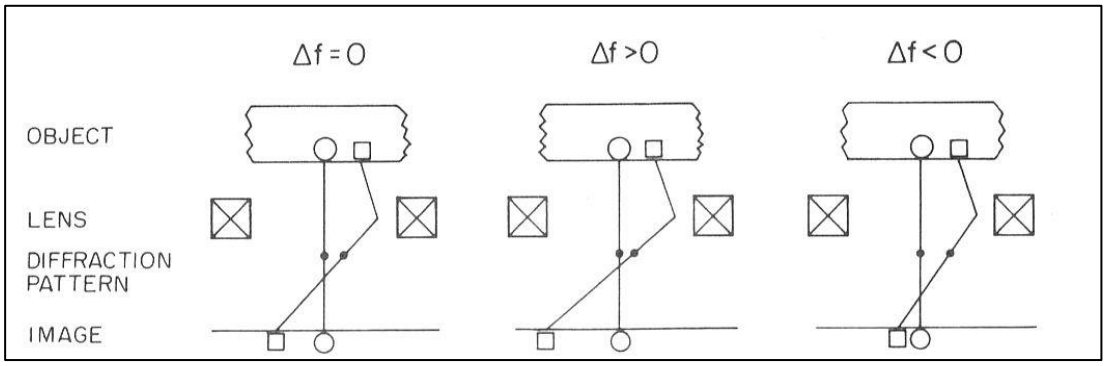

Figure 5-19: Schematic for defocus (Δf) set and the effect on the object in the specimen to the image plane (the circle and square). Ref. [5-25], Met. Trans. A, Springer Publications. Reproduced with permission.

In figure 5-20, 2½-D imaging exercise is performed on a Co10at%Re sputtered film, which has largely single-crystal-like preferred orientation, where a large area of the film shows single-crystalline diffraction pattern. This example was chosen to show how the technique works because it is a simpler example to illustrate. Closer examination reveals that the diffraction pattern contains several variants as represented by several diffraction spots. The 2½-D technique can unambiguously identify microstructural features to each diffraction spots based on stereoscopic analysis of defocus pairs. Figure 5-20 (d) is the diffraction pattern with the objective aperture used to image the DF image. It can be seen that there are several spots that are inside the objective aperture, labeled as “a” and “b”. Figure 5-20 (a) is a DF image taken at 1.1 μm underfocus, and (b and c) are taken at 1.1 μm overfocus. When DF images (a) and (b) are viewed stereoscopically, grain labeled A in (b) can come to the top, and when the DF pair (a) and (c) are viewed ([a] with left eye, [c] with right eye), the grain “B” comes to the top. This exercise then allows identification of grain “A” with diffraction spot “a” and grain “B” with diffraction spot “b.”

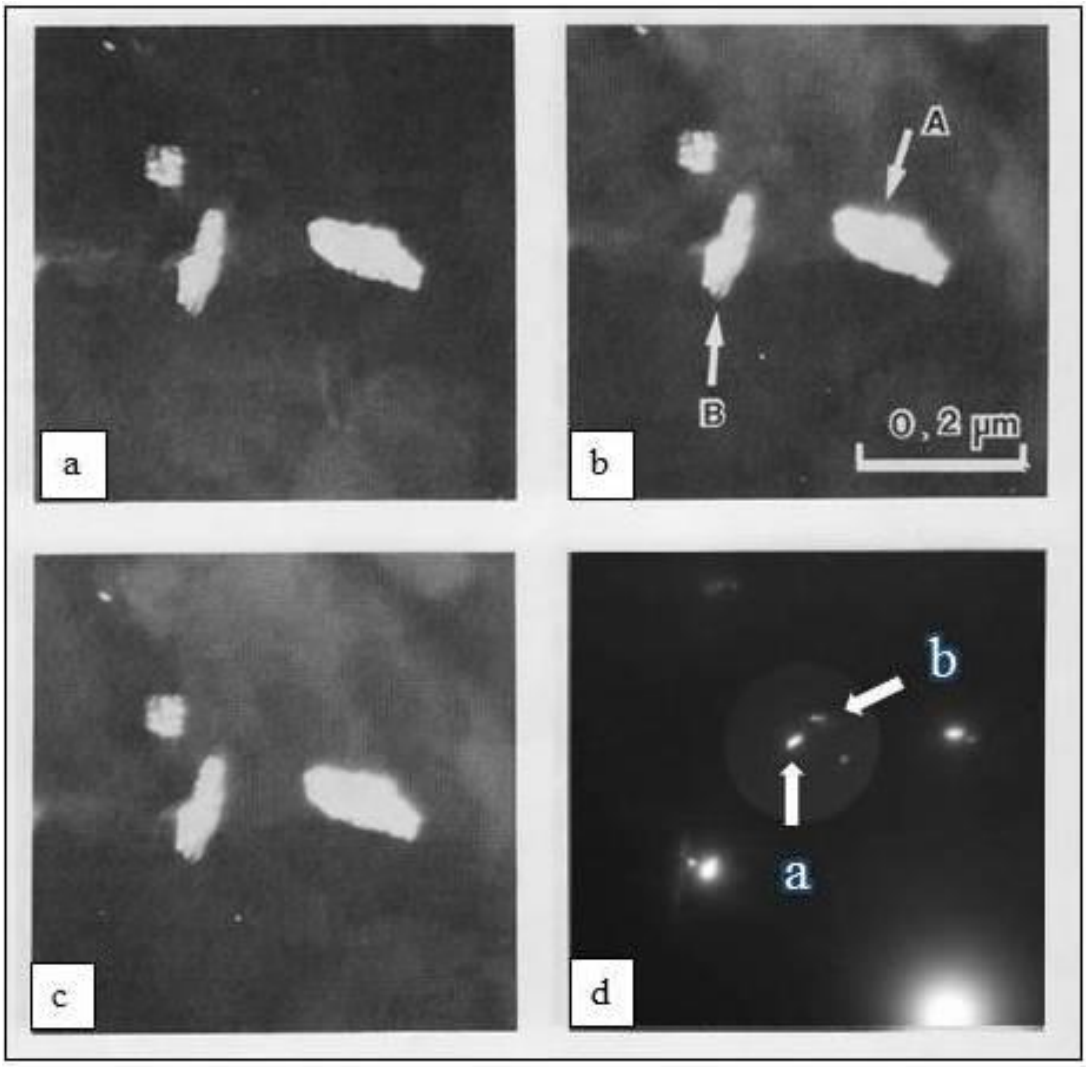

Figure 5-20: 2½-D imaging set using the objective aperture arranged in (d) to admit three diffraction spots to form the DF images. Viewing the stereoscopic image pair (a) and (b) shows that grain "A" is at the top. Viewing the pair (a) and (c) with (a) left eye and (c) right eye, the grain "B" comes to the top. This exercise can assign unambiguously that diffraction spot "a" corresponds to grain "A" and spot "b" to grain "B." Ref. [5-25]. Met. Trans. A, Springer Publications. Reproduced with permission.

Another illustrative example is with the same film, showing the single-crystalline diffraction pattern that can be seen in figure 5-21(d). The film has very strong perpendicular anisotropy, with the c-axis oriented perpendicular to the substrate

plane. There are large areas of the film that are essentially single-crystalline, an amazing situation, but the film has several variants or sub-grains that are slightly misoriented from each other. Figure 5-21 (a) and (b) are the two DF images using several of the diffracted spots taken through the objective aperture. Individual subgrain areas can be seen at a different height (with some practice) using a stereo viewer. The corresponding BF image is shown in figure 5-21 (c), and unless something like the 2½-D imaging technique is used, it is difficult to discern that there are large areas of separate subgrains that exist in the image. From the DP in Figure 5-21 (d), it can be observed that subgrains have misorientation of approximately 9^{o}. However, with more extended viewing of the stereo pairs, it can be observed that there are small grains the misorientation of which is approximately one degree or less. This detail is not easily visible by DP or by cursory examination. In addition, the grains of different orientations (bright grains in Figure 5-20, dark grains in Figure 5-21) lie in sub-grain boundaries and presumably act to hinder subgrain growth. It can be seen that with the perception of the microstructure as seen by the 2½-D imaging enhance the details that can be observed in the microstructure of complex materials.

Finally, going back to the film shown in figure 5-14, the 2½-D imaging technique was applied on selected grains in the image to attempt to identify the location in the diffraction location (inside the objective aperture) from which the image came. This is a considerably laborious task, but it is aided by a process of elimination that occurred with the conventional method as shown in figure 5-14. The map of the same region shown in the DF image is shown in figure 5-22, with the DF image from figure 5-14 on the left as a reference. The dark colored region has been unambiguously identified as coming from $(200)_{FCC}$, while the striped region remained uncertain. However, it can be seen that the FCC phase is clearly the smaller phase and exists in clusters. This microstructural analysis, together with magnetic observations based on VSM, it was possible to conclude that in this type of film with a relatively less intense $(200)_{FCC}$ ring, the FCC phase probably has relatively less influence on the overall magnetic properties of the film. They are fairly dispersed, and it appears to be inconsequential to the magnetic properties.

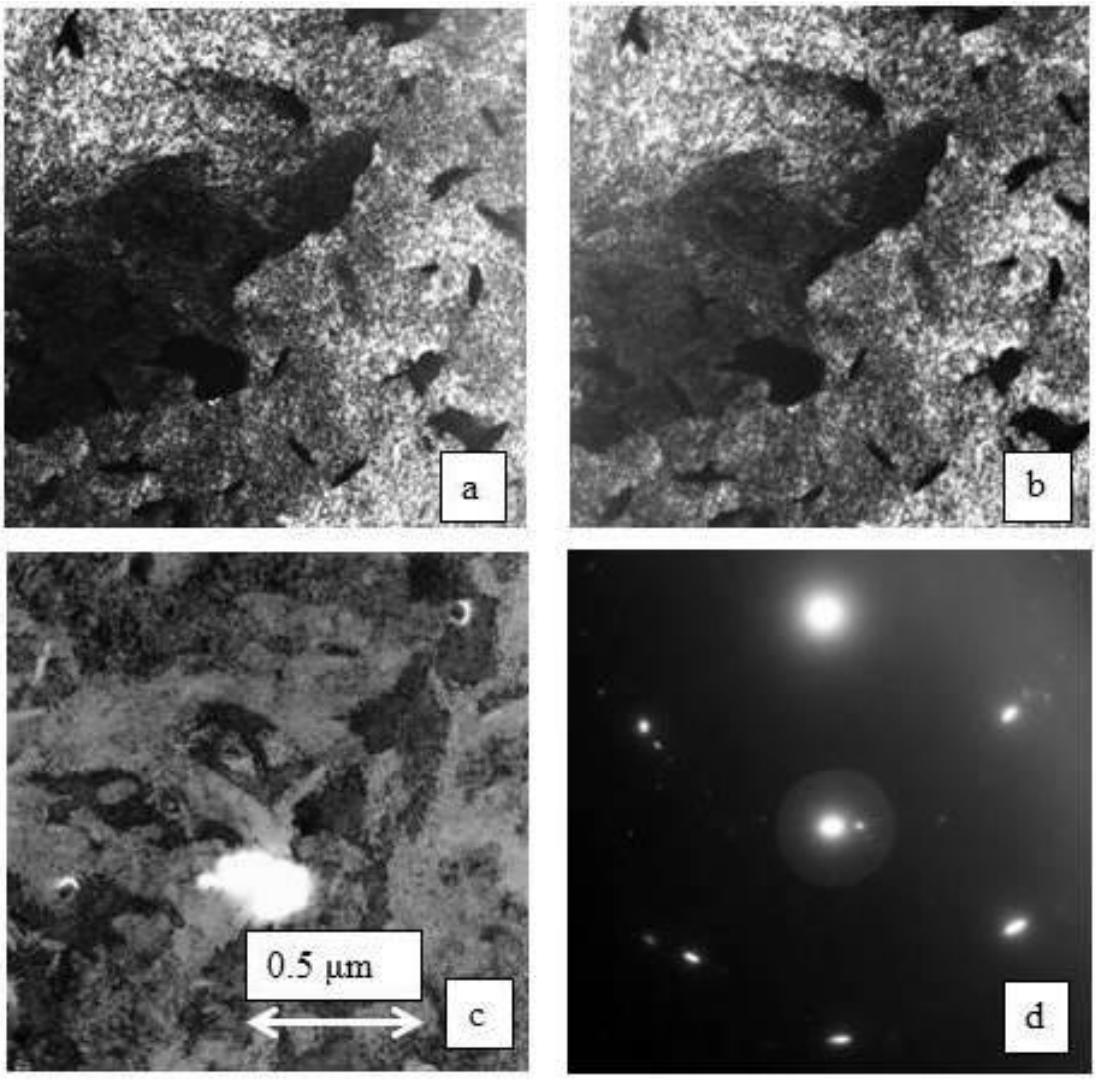

Figure 5-21: 2½-D imaging set using the diffraction pattern from (d). Co10at%Re film is largely a single crystalline film, with the c-axis perpendicular to the substrate plane. (a) and (b) are the DF stereo pair. Two distinct subgrain regions can be observed in the stereo image. The BF image is shown in (c). (d) show the diffraction pattern showing the spots used in imaging the DF with the objective aperture allowing two spots to form the image. Ref. [5-25]. Met. Trans. A, Springer Publications. Reproduced with permission.

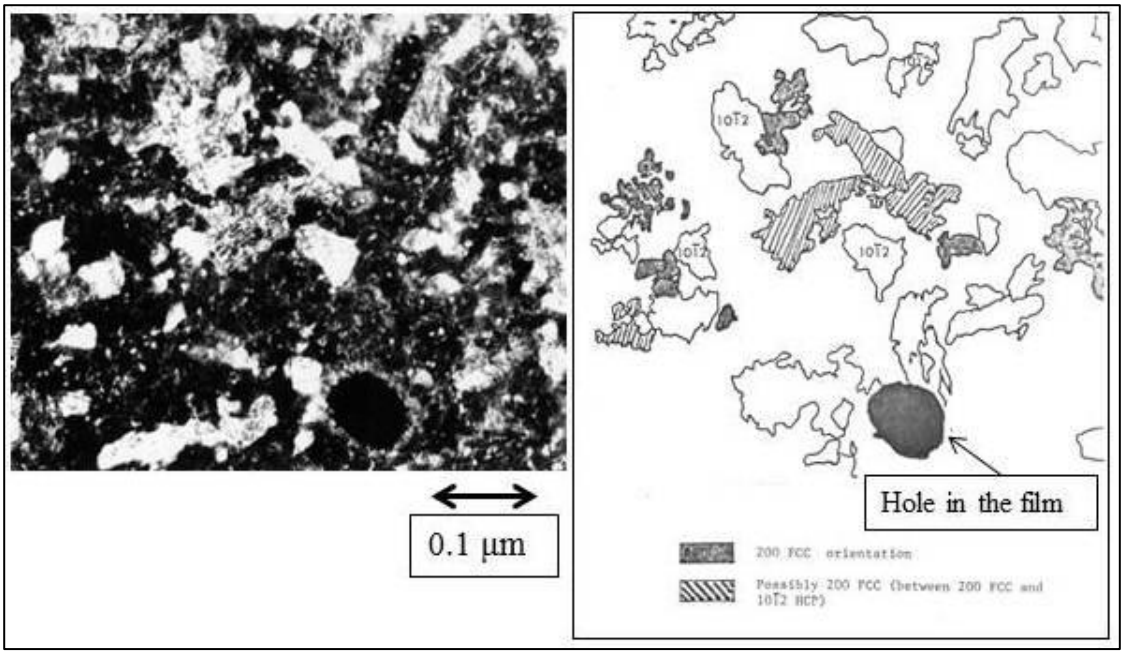

Figure 5-22: DF image of figure 5-14 with phase assignment based on 2½-D imaging technique applied to the identification of $(200)_{FCC}$ phase.

The more serious issue with cobalt alloy-based thin film media is the high density of stacking faults present in the HCP grains in the film. This will reduce the Ku (anisotropy) of the media, and reduce the Hc capability of the media. The effort to obtain a perfect grain structure that has less stacking fault will play out for many years as various sputtering processes, and alloying elements are tried to improve the crystalline perfection of the individual HCP grains in the film. A clearer picture of the high density of stacking fault present in the film is shown in figure 5-23. This film is a Type II Co10at%Re film with acicular grain structure. The DP pattern shows the outline of the objective aperture used to image the film in DF. Many grains light up as there are many reflections contained within the aperture. Arrowed reflection is $(1\bar{1}02)_{HCP}$ reflection which is streaked due to stacking faults as previously explained. A 2½-D imaging technique was used to identify the grain that the reflection belongs to, and it is arrowed in DF and BF images. The images are properly oriented with respect to the DP so that streaks in the $(1\bar{1}02)_{HCP}$ reflection run 90^o to the striations within the

arrowed grain, showing that it is positively due to the stacking faults within this particular grain.

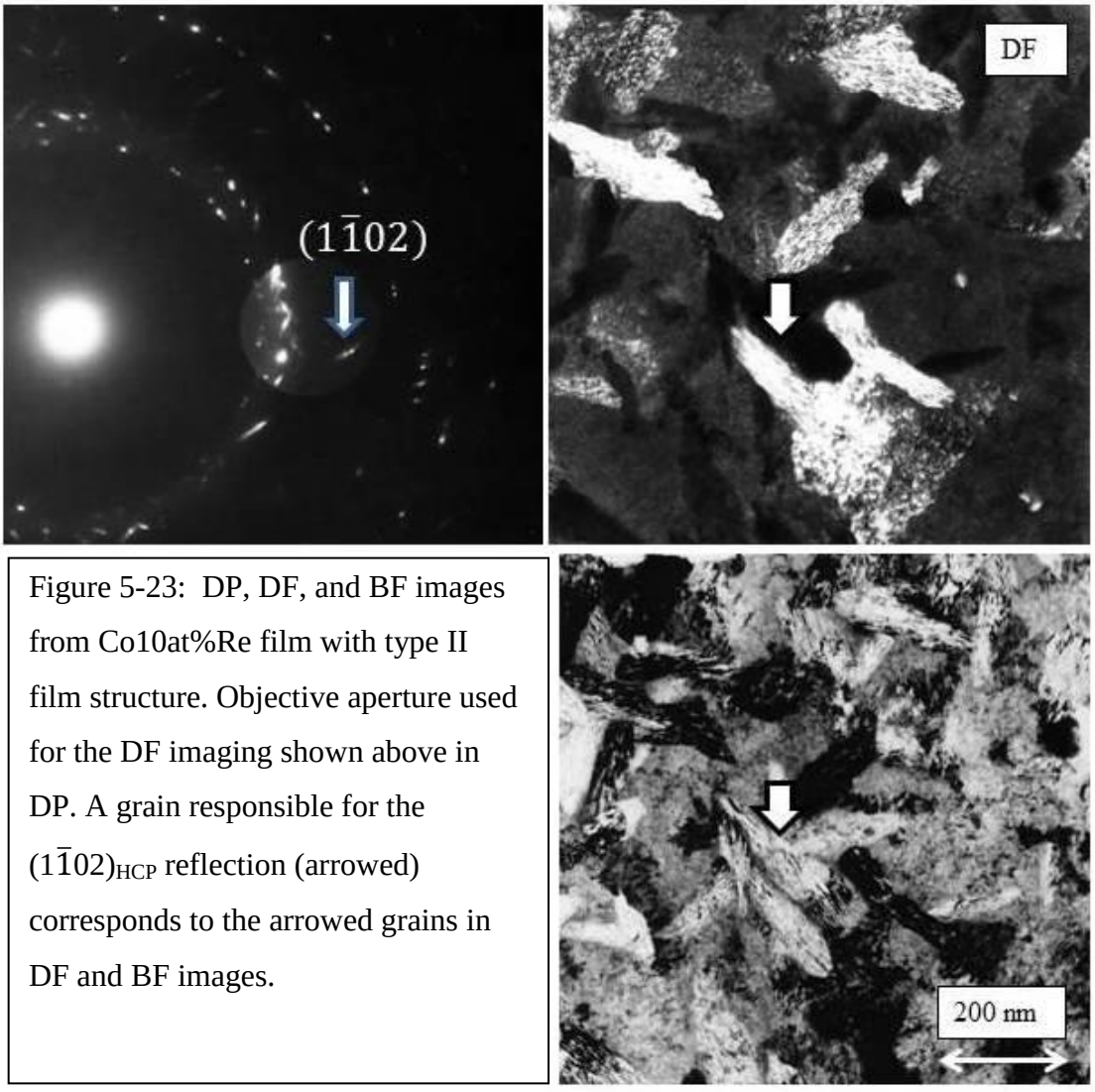

Figure 5-23: DP, DF, and BF images from Co10at%Re film with type II film structure. Objective aperture used for the DF imaging shown above in DP. A grain responsible for the $(1\bar{1}02)_{HCP}$ reflection (arrowed) corresponds to the arrowed grains in DF and BF images.

The elongated acicular grains are not desirable in thin film media because it would tend to make transitions wider and jagged. Equiaxed grains are more desirable. However, it is interesting to note that oxide media used acicular grains, which were originally developed by 3M in 1947 [5-26]. This particle media was oriented by magnets during curing along the direction of magnetic recording so that the long axis of the acicular oxide particles was oriented along the track direction. This provided

squarer hysteresis response along the recording direction for best amplitude response [5-3]. There was no way of orienting the film by the magnetic field during sputtering for thin film media; therefore, the equiaxed grain structure was more desirable.

5.4 Theory of Limits of Magnetic Recording

Based on extensive work on CoRe films using conventional and Lorentz TEM microscopy and recording measurements, Tu Chen formulated some critical theories about factors that affect magnetic recording, specifically those that relate microstructure to magnetic transitions [5-15]. Until this point in 1981, the transition length was described phenomenologically, determined primarily by the demagnetization effects associated with the transition. The magnetization within the transition was described in terms of a ramp [5-27, 28] or by arctangent model [5-29, 30, 31]. For the arctangent model and in saturation recording, the value of transition width ℓ_{min} is related to film thickness δ, coercivity Hc, and remanence Mr as:

$$\ell_{min} \approx \frac{2\pi Mr\delta}{Hc} \qquad \text{(Eqn. 5-11)}$$

when Hc/Mr < 4 π and $\delta/a << 1$, and a is the sharpness of the transition.

These models worked well enough for the oxide media. However, for thin film media, the transitions often had saw-tooth-like structures, which were much more complicated than the phenomenological description [5-32, 33]. Tu Chen constructed a TEM holder, which can apply a horizontal field across the sample to track magnetization reversal while imaging the film under Lorentz microscopy conditions. By tracking the Lorentz image through the demagnetized state, saturation, and remanence, some important observations were made regarding the state of magnetic transitions for the recorded bits in a thin film media.. The CoRe film under Lorentz

microscopy shows a ripple structure and the image is reproduced in figure 5-24. The film is in a remanence state after saturation in one direction. The direction of magnetization is indicated in the figure. The explanation of the ripple is shown in figure 5-25, which is reproduced from [5-15]. The ripples in the Lorentz images are caused by clustering of magnetization from many grains and a slight shift in magnetization direction of the clusters cause feather-like structures in the Lorentz images.

Figure 5-26 is a Lorentz image of a return-to-zero (RZ) recording pattern put on CoRe film with Hc of 220 Oe. In this figure, the distance between the transitions for the negative pulse is smaller than the positive pulse because of the partial erasure by the positive pulse. At the transition, there is a clear indication of the formation of a magnetic vortex, which is indicated by the star-like feature in the inset. A schematic of the transition is shown in figure 5-27. A set of small arrows show the direction of net magnetization across the ripple. It was concluded from the analysis that in a metallic thin film media, the maximum flux reversal that the media could support is approximately 25,000 flux reversal per inch (FRI) due to the formation of the vortex structures at the transition.

At the time that the magnetic vortex model was presented by Tu Chen in 1979 [5-15], most people assumed that this represented a fundamental limitation to increasing the recording density for the thin film media. He had mentioned the importance of taking into account the magnetic exchange interaction in the formation of the vortex structure, but did not offer any method of moderating or reduce its effect. The solution to reducing the vortex and hence improving the sharpness of the transition and increasing the bit density depended on reducing the magnetic exchange interaction between the grains. The vortex formation was the consequence of magnetostatic coupling and strong quantum mechanical exchange interactions that occur across the grain boundaries in a typical magnetic thin film media that was being made during at the time. Working with Tu Chen at Xerox PARC, Gordon Hughes actually developed a computer simulation of the switching behavior of metallic media, which included

exchange interaction, and applied the results to plated CoP media. As mentioned previously, he did not publish his results until much later in 1983 [5-21]. Even after the publication, it received little attention. It was only after several publications by Bertrum and Zhu on computer simulation of the thin film media that included the exchange in the calculation that everyone started to take more notice [5-34, 35, 36]. The key point about thin film media was its strong exchange interactions between the grains, its key weakness, which dominated its behavior in the early period of development. What had to be done to reduce exchange interaction was to physically separate the grains. They only needed to be forced apart by few nanometers because exchange forces operated over very short distances. The method Tu Chen devised initially was to use high-pressure sputtering. This was reported in 1988 by Chen and Yamashita [5-18] for the Co-10at%Re films, a few years after the process was already in use at Komag. The data is reproduced in figure 5-28. Films sputtered at relatively high pressures of 50 and 75 mtorr can isolate the grains, and the effect on the hysteresis loop is shown in the inset. Deposition parameters and VSM values for the films are listed in the table below. It should be noted that sputter pressure as listed here is higher than actual by approximately 2X. This was due to the use of pirani gauge with a defective design used at Xerox PARC, which went unnoticed for many years. The pressure reading was much higher than actual, due to the sensitivity of the filament to oxidation. The defect in the gauge was discovered at Komag and 50 and 75 mTorr listed in [5-18] are more like 25 and 38 mTorr. Switching to more reliable baratron gauges allowed this defect with the pirani gauges to be discovered.

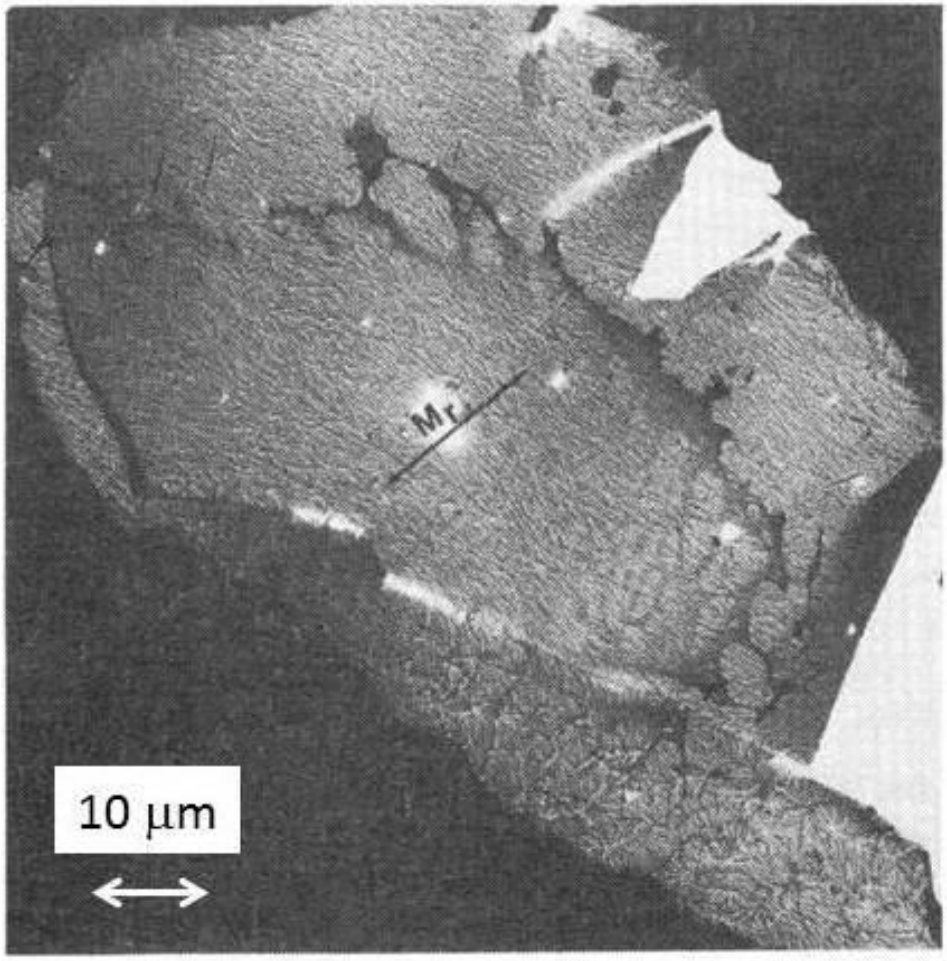

Figure 5-24: Lorentz TEM micrograph of CoRe film after saturation and release into a remanent state, with magnetization direction as indicated by the arrow. The film was saturated in-situ in the microscope while imaging the film in the Lorentz mode. The micron marker value is an approximation.

From [5-16]. Copyright © 1981, IEEE, reproduced with permission.

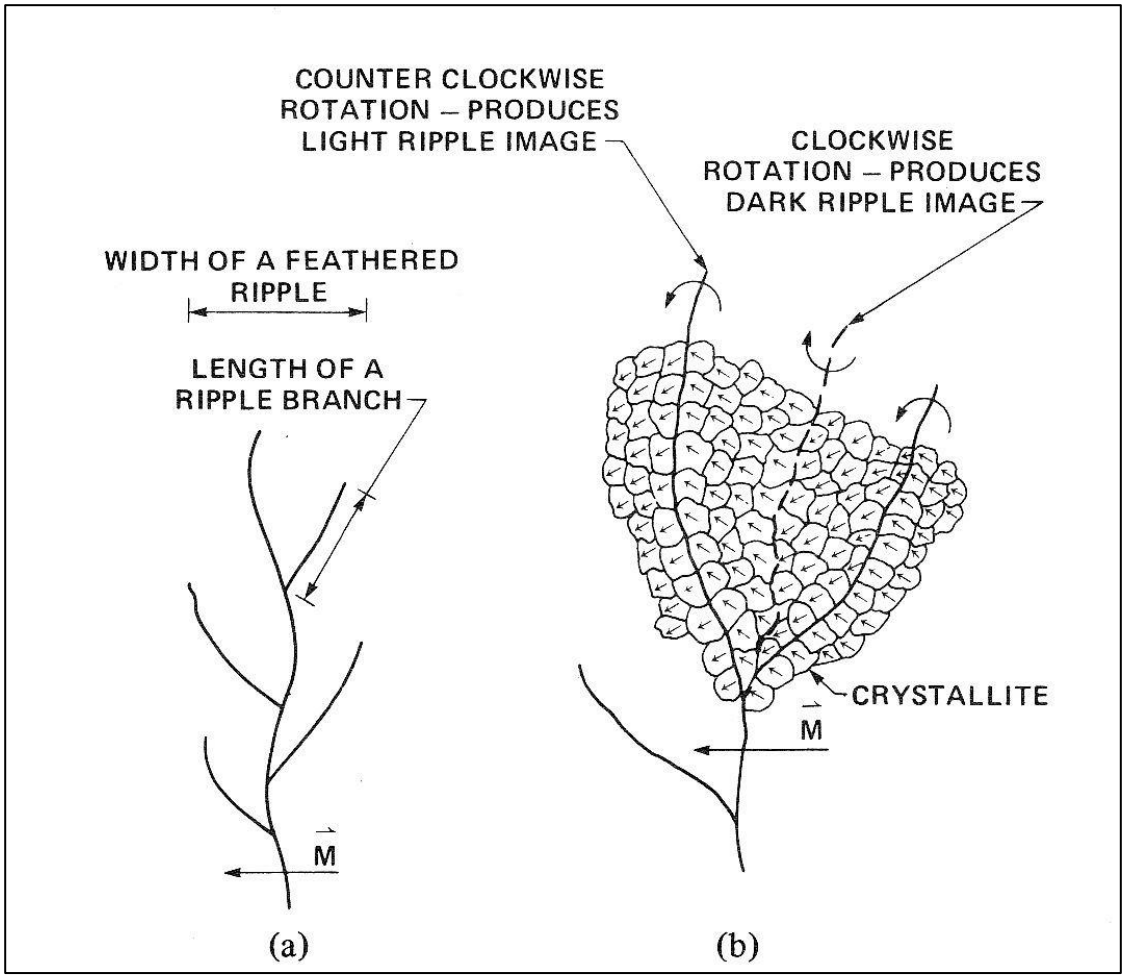

Figure 5-25: A schematic diagram of the ripple structure in Lorentz image for the CoRe thin-film media.

From [5-15]. Copyright © 1979, IEEE, reproduced with permission.

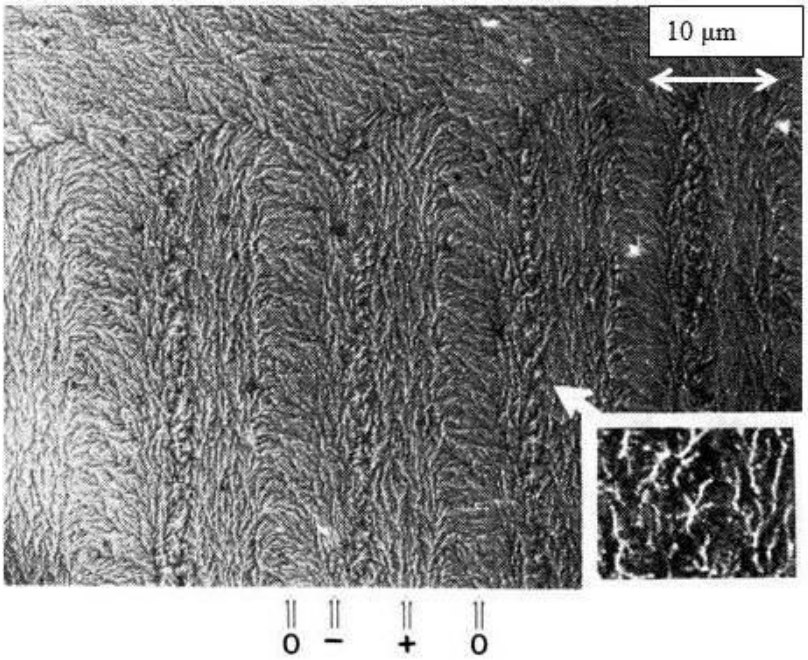

Figure 5-26: A Lorentz TEM micrograph of CoRe, Hc = 220 Oe, written with RZ pulse. From [5-16]. Copyright © 1981, IEEE, reproduced with permission.

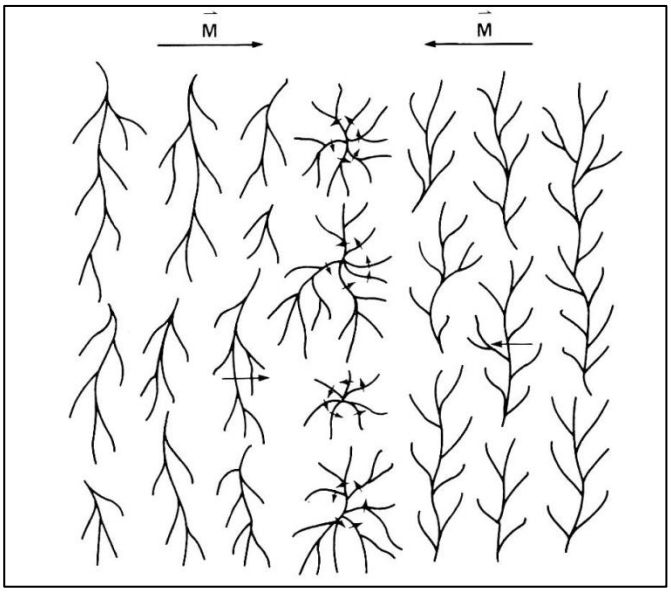

Figure 5-27: A schematic of the ripple structure as seen in Lorentz TEM micrograph. The small arrows indicate the direction of magnetization for the cluster of grains in the vortex at the transition. From [5-16]. Copyright © 1981, IEEE, reproduced with permission.

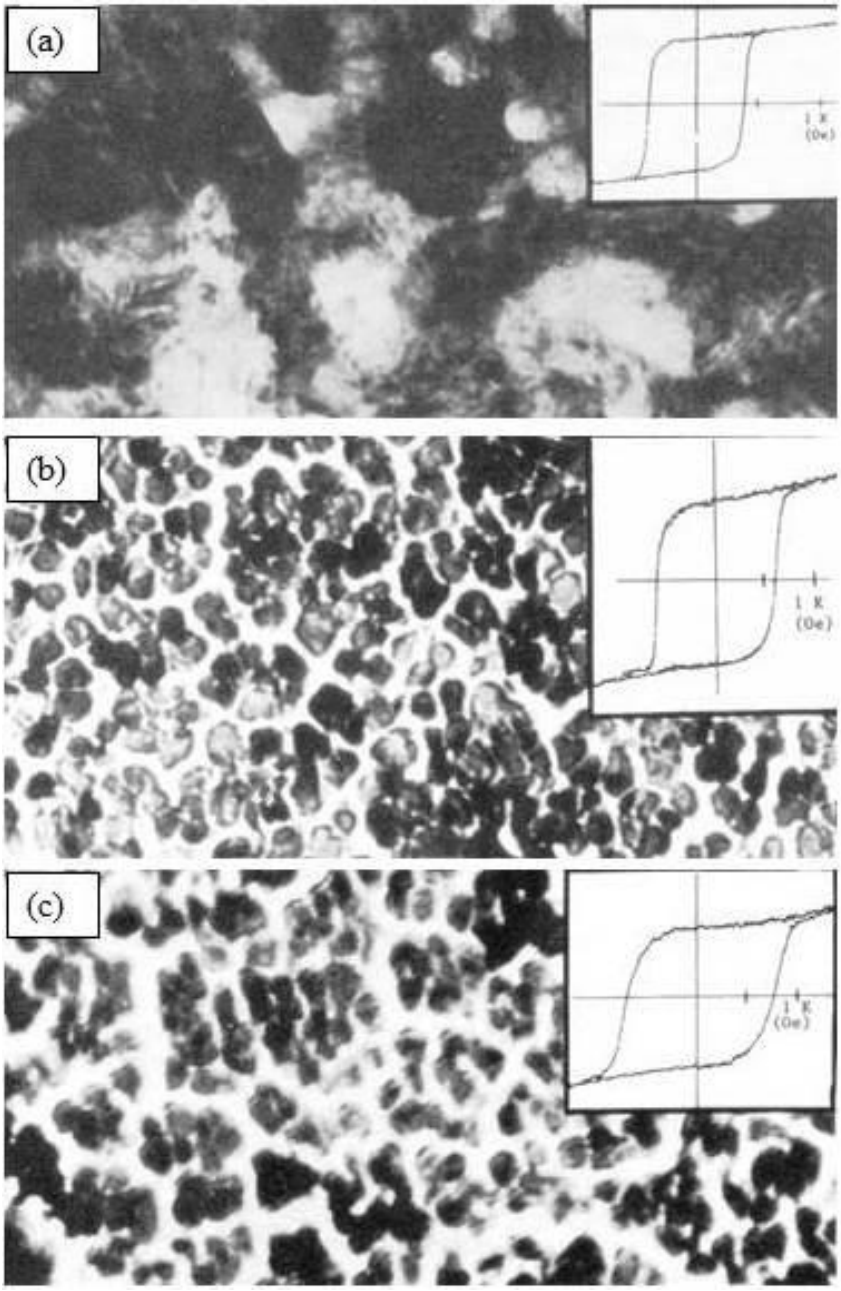

Figure 5-28: Co-10at%Re film with deposition parameters listed in the tables 5-6. Higher sputter pressure leads to greater grain isolation, lower S*, and higher Hc. This is the consequence of breaking the exchange interaction between the grains. From [5-18]. Copyright © 1988, IEEE, reproduced with permission.

Table 5-6:

The deposition conditions and measured magnetic properties of the films shown in figure 5-28. From Ref. [5-18] Copyright © 1988, IEEE, reproduced with permission.

	Substrate Temperature (°C)	Argon Pressure (mTorr)	Hc (Oe)	Mr/Ms %	S*	Grain Size (Å)
Figure 5-28 (a)	150	5	446	93.4	94.2	~ 300
Figure5-28 (b)	20	50	600	87.0	90.0	≥ 100
Figure 5-28 (c)	20	75	729	80.0	81.0	≤ 100

The history of thin film media development since 1984 would be dominated by the effort to improve the SNR of the media, to increase the areal density capability. The two are inexorably linked, and reduction in particle exchange would become the key driver for media design.

5.5 CoPt-Based Thin film Media

Many drive start-up companies entered the business from 1983 to 1984, to try to capture the market for small form factor drives for the PC market. There were three different types of media available to them. Media based on oxide (γ -Fe_2O_3) was already in use for the first PC, as it was the same media construction used in large drives such as the IBM 3380 drives. Plated CoP media was the next choice; it offered the possibility of easily doubling the capacity over the oxide media. The third choice was the sputtered thin film media based on several types of alloy systems. Hewlett-Packard was the first to produce a 5¼-inch form factor drive using sputtered thin film media, which used CoPt alloy [5-37]. Komag started with CoNiPt alloy in 1984, and others used CoNi/Cr structure. There were also perpendicular media and drive start-ups

during 1982 to1983 as well, and they used CoCr alloy for the media. CoCr and CoPt-based alloys came to dominate the longitudinal thin film media arena in relatively short time, and in this section, the CoPt alloy system will be discussed. A CoCr-based alloy will be discussed in the following section.

CoPt-based thin film media was investigated by Aboaf et al. [5-11] and by Yanagisawa et al. on CoNiPt [5-12]. CoPt with approximately 50 atomic % Pt has long been known to be very strong magnets with BH_{max} product of 76 KJ/m^3 (9.6 MGOe) [5-38]. However, $SmCo_5$ and $Nd_2Fe_{14}B$ have far stronger BHmax products now (26.5 MGOe and 50.3 MGOe, respectively) and neodymium iron boride magnets are the most widely used strong magnets in the world today. CoPt has a wide range of solid solubility in the low Pt concentration as shown in the current phase diagram in figure 5-29 by Okamoto [5-39]. Compared to the CoRe system, CoPt can achieve higher Hc. Yanagisawa investigated a wide range of CoPt binary compositions and reported highest Hc at approximately 20 atomic % Pt, of approximately 1700 Oe for the film at 350 Å thickness. Bs drops from pure Co at 17,000G down to approximately 12,000 G. With Ni addition of 10 atomic % with the composition of $Co_{80}Ni_{10}Pt_{10}$ composition, Hc of approximately 750 Oe was obtained. The key attribute sited for the CoNiPt alloy is that it is more corrosion resistant than CoPt.

One of the key disadvantages of using the CoPt alloy is that platinum is very expensive. Using a 20 atomic% platinum alloy, for example, the target will be approximately 45% platinum by weight. Since the platinum is sold by weight, the cost of platinum becomes very large and great deal of effort has to be put on reducing the consumption. For example, Hewlett-Packard developed an innovative cathode using a separate Pt target ring, which was co-sputtered with a separate pure Co-target in order to keep the utilization of the target high and keep the reclaim cost low by using a pure platinum target. NEC and Komag employed RF sputtering so that target utilization could be kept high. Komag used a composition of $Co_{83}Ni_9Pt_8$ to $Co_{81}Ni_9Pt_{12}$ to create media with Hc of 650 Oe to 1200 Oe. Initially, the magnetic alloy was sputtered directly on polished NiP/aluminum substrates, but very quickly, a process was

developed where a thin layer of RF sputtered SiO_2 coating was applied as an underlayer. The SiO_2 layer was used to clean the disk surface by means of *glow-discharge* plasma cleaning. This process helped in obtaining more uniform magnetic coating. RF sputtering of oxide material such as SiO_2 creates highly reactive oxygen radicals during sputtering, and these species can react with organic contaminants on the disk and literally burn them off the surface. This is evidenced by the rapid increase in the carbon monoxide (CO) and the CO_2 levels detected in the vacuum chamber by the residual gas analyzer (RGA) as soon as the SiO_2 target is turned on. The SiO_2 plasma also reacts with residual water vapor in the chamber, which also promotes the formation of oxygen radicals. This reaction with the water vapor also dramatically reduces the deposition rate of SiO_2.

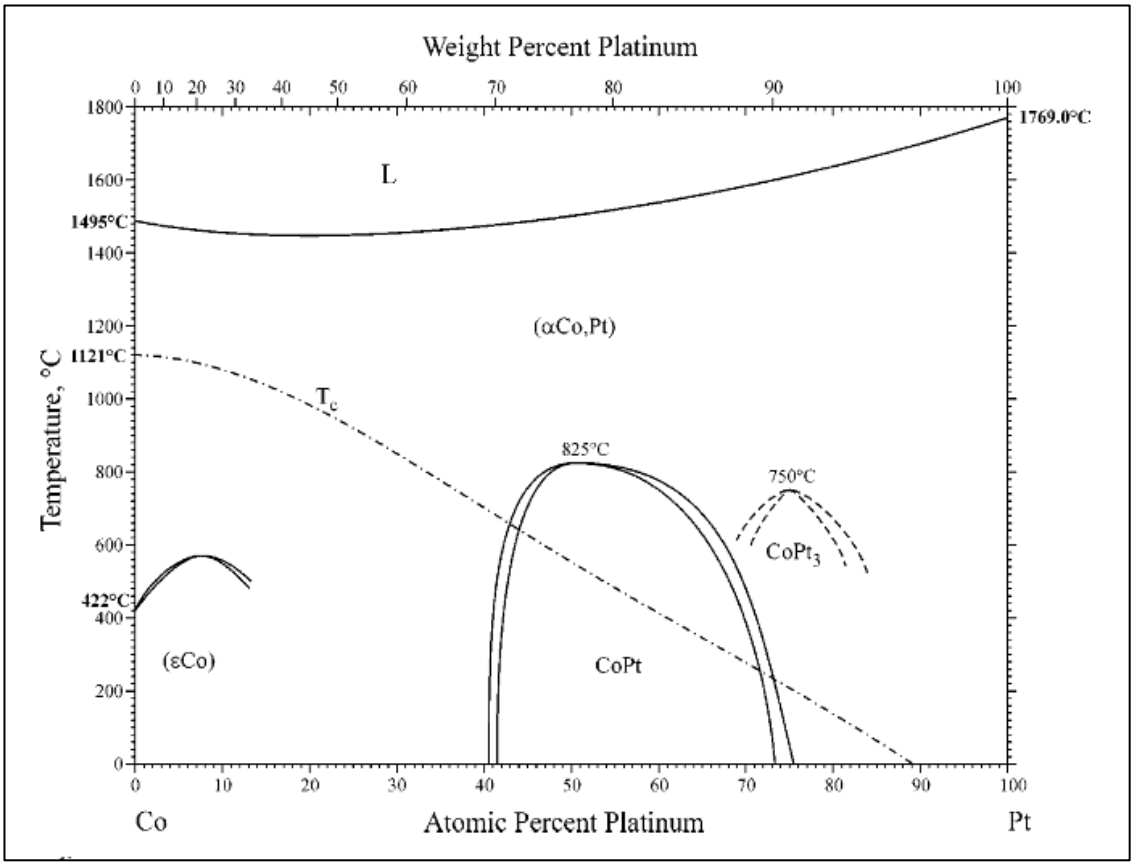

Figure 5-29: Phase diagram of Co-Pt system. From Ref. [5-39]. Reproduced with permission. Copyright © Springer 2001.

The sputtering process for the manufacture of hard disk media used an in-line sputtering tool, which consisted of multiple deposition chambers flanked on the entrance and exit side with load-lock chambers to allow panels with disks to enter and exit the vacuum system continuously. The panels were loaded with disk substrates to be coated. The panels pass-by the rectangular targets at a fixed speed to be coated with various layers of films. Therefore, this type of sputtering system is also called a *pass-by* sputtering system. The schematic of the in-line deposition tool used initially at Komag Inc. is shown in figure 5-30. Vacuum chambers in gray are separated by gate valves, and the direction of the panels in the system is indicated by arrows. The panels flow in a clockwise direction in the drawing. The system had opposing cathodes to coat both sides of the disk simultaneously and had 4 cathode pair positions. The first pair of cathodes was for deposition of the underlayer (SiO_2), a second pair for the magnetic layer, and the last two pairs for deposition of a carbon overcoat. Two pairs of cathodes were needed for the carbon cathode due to low deposition rate of graphite target used to sputter the carbon overcoat. The underlayer and magnetic layer employed RF diode deposition while the carbon layer used a DC magnetron sputtering cathode. The main chamber had a differential slit, which allowed two different pressures to be maintained between the underlayer/magnetic cathode and the carbon chambers. The slit was a set of plates placed in very close proximity to the panels so that it impeded the flow of argon gas from one side of the chamber to another.

RF sputtering required a sputter pressure of 20-30 mtorr while the DC magnetrons were most efficient in the 5-10 mTorr range. The system illustrated was manufactured by ULVAC ® Inc. The deposition rate of the magnetic layer onto the disk ranged between 400-500 Å/min, and carbon film was approximately 100-150 Å/min. There was a very low deposition rate for the SiO_2, and the thickness of the SiO_2 layer on the disk was very thin, at less than 1.0 nm. It was undetectable by a method such as Auger depth profiling. Another factor that reduced the deposition rate of SiO_2 in the in-line deposition tool was because panels in which the disks were always loaded had a fresh coating of carbon film on top of the panel surface. Together with water vapor

carried into the system by the panel, the carbon film reacted with SiO_2 so that copious amounts of CO and CO_2 were produced in the chamber. The net effect was that SiO_2 had very little deposition onto the disk. The SiO_2 coating or treatment created a square hysteresis loop, which provided good signal strength for a given magnetic film thickness. This was an economic advantage, as the target was expensive, and higher utilization was needed for the target. 650 Oe media was suitable for a 5¼-disk with approximately10 MB capacity, which equaled an approximately 10 Mb/in^2 areal density. Magnetic film thickness using $CoNi_9Pt_{10}$ alloy was ~ 70 nm, with MrT product of approximately 6 to 7 $memu/cm^2$.

The in-line sputtering tool was pumped with Roots blower pumps in the RF chamber side of the system and high capacity cryo-pumps on the DC magnetron side of the system. The base pressure was relatively poor by current standards due to the large size of the chamber, and due to many service doors needed for the system. There were also numerous feedthroughs into the system to drive the carriers through the entire system, which always presented challenges to maintaining a good vacuum in the system, even though it used ferrofluidic feedthroughs, which were rated for low leak rates. There were numerous other feedthroughs for monitoring gauges and gas inlets. Typical base pressures were in the low 10^{-6} torr.

One of the tendencies of CoNiPt alloy film was to have a strong preferred film growth direction whereby the c-axis of the hexagonal grains had their c-axis perpendicular to the film plane. Co-Re alloy film also exhibited similar tendencies as explained earlier for the various film types that were possible. This tendency for "perpendicular growth" was much more prominent as the base pressure of the sputtering system was improved over time. The perpendicular growth was very detrimental to the longitudinal magnetic recording application because such film exhibits very poor hysteresis loop squareness and rapid loss of signal amplitude for a given film thickness. Raising the thickness of the magnetic layer to compensate made things even worse as the film became even more perpendicular. X-ray diffraction analysis of the film also showed very prominent (0002) reflection as the film became

more perpendicular. Taking the cue from the base pressure effect, a process was developed for dosing the film with nitrogen gas during sputtering in the magnetic layer. This had the immediate effect of reducing the perpendicular growth, and reduction of (0002) peak in the X-ray diffraction scan. It also reduced the Hc of the film as more nitrogen was added, and hysteresis loop became squarer. The SNR of the media also improved somewhat. These effects can be explained by the introduction of more stacking faults into the HCP grains, which reduced the coercivity of the media, and reduced the tendency for the grains to develop perpendicular preferred growth. SNR improvement can be explained by a reduction in grain size. However, TEM evidence for this was not taken at that time. The effect of the nitrogen gas addition to $Co_{82}Ni_9Pt_9$ alloy is shown in figure 5-31, from reference [5-40]. Hysteresis loop with and without the nitrogen addition is shown in figure 5-32. Without the nitrogen, it can be clearly seen that in-plane loop squareness is significantly reduced. Other gasses such as water vapor and oxygen have a similar effect on coercivity and on reducing the perpendicular growth of the film. However, the nitrogen was the easiest to control and obtain a uniform effect during sputtering, as it is not very reactive compared to oxygen. Nitrogen addition also became a convenient method for controlling coercivity and many different coercivity products can be made with the same target to adjust to customer needs, as they had to optimize the media to particular recording heads that were to be used for the drive product.

Later, the effect of nitrogen addition to the media was reported with supporting TEM, SEM, and X-ray data [5-41]. Figure 5-33 shows the effect of base pressure on Hc of the CoNiPt media. It can be seen that Hc actually increases as base pressure worsens. This is due to the increase in perpendicular growth of the media with a better vacuum.

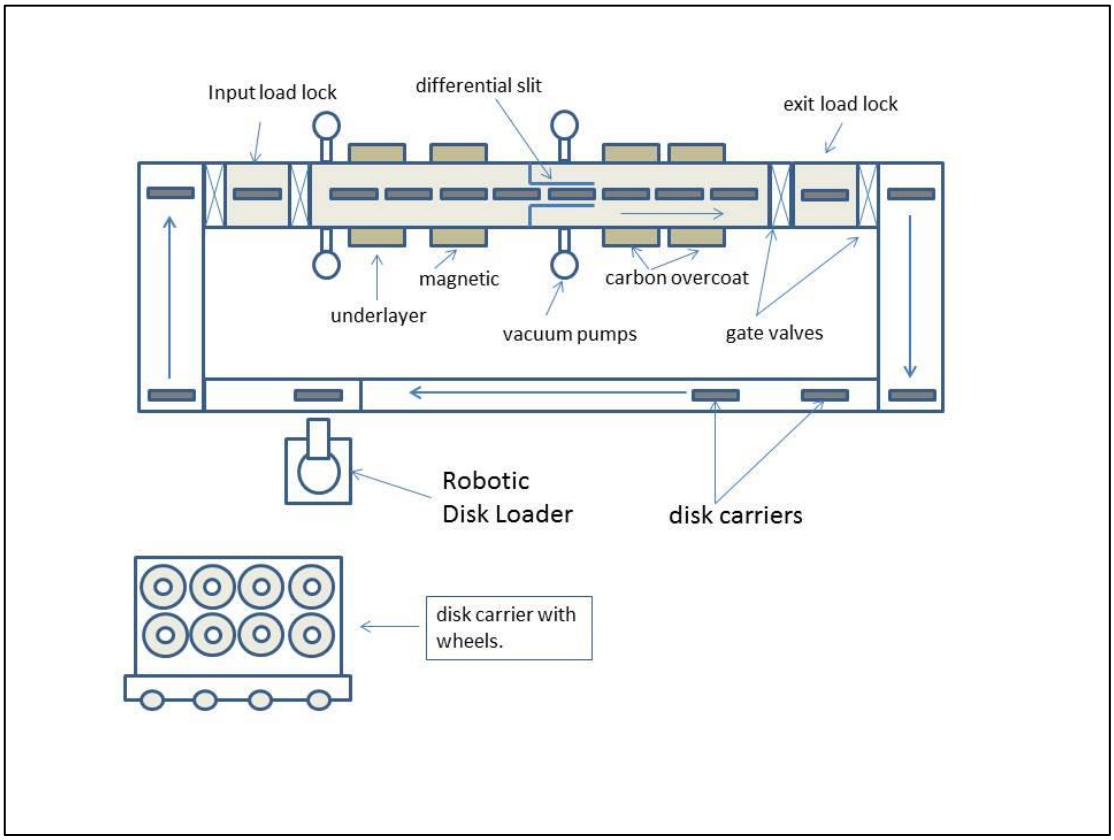

Figure 5-30: Schematic diagram of first in-line sputter tool manufactured by ULVAC ® Inc. for Komag Inc. in 1984. The shaded area represents vacuum chambers, and unshaded areas are at ambient pressure. As series of gate valves and load lock chambers allowed carriers with panels loaded with disk substrates to enter and exit the vacuum chambers continuously. The system was designed to run continuously for 2 weeks, with the throughput of 120 - 5¼-inch disks per hour.

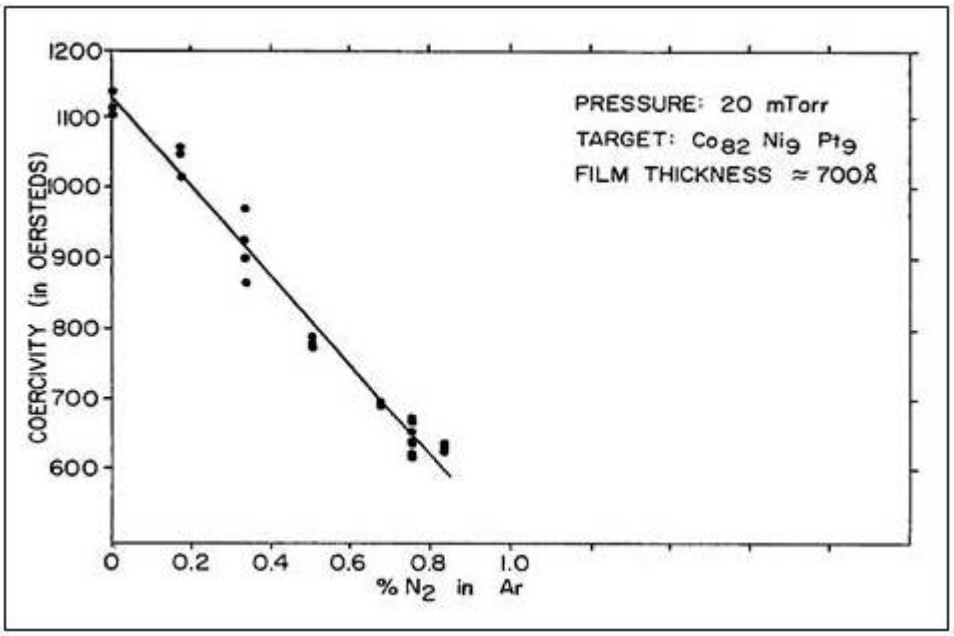

Figure 5-31: The effect on coercivity (Hc) of adding nitrogen into the CoNiPt film. From Ref. [5-40].

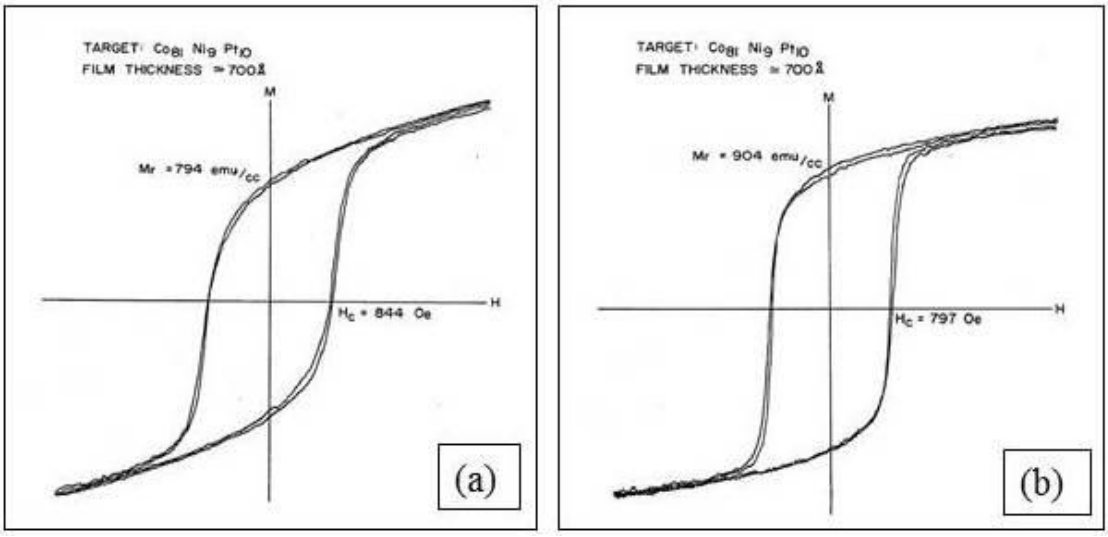

Figure 5-32: Hysteresis loop of CoNiPt film without nitrogen (a) and with nitrogen addition (b). Mr is significantly higher for (b) due to increased squarenes of the film. From Ref. [5-40].

High-resolution SEM micrographs of the films at low and high vacuum (high and low base pressure) are shown in figure 5-34. A film with worse (high) base pressure actually has worse microstructure, as the grains are broken up into smaller pieces and shows some clustering effect. Yet, the Hc of the media is much higher than with higher vacuum. The primary contributor to the base pressure effect is the residual water vapor in the system. The same effect as figure 5-33 was reproduced by deliberate and controlled injection of water vapor during sputtering.

Figure 5-35 shows the electron diffraction pattern from a $Co_{77}Ni_9Cr_4Pt_{10}$ alloy media deposited at three different nitrogen additions. The three main diffraction rings consisting of $(1\bar{1}00)$, (0002), and $(1\bar{1}01)$ reflections are shown. The diffraction pattern for 0.6% nitrogen addition shows a diffuse band (arrowed) that is at the $(1\bar{1}01)$ position. It is difficult to see this clearly in the reproduction, but the presence of the streaks is strong evidence that nitrogen addition is creating high density of stacking faults in the media grains.

Figure 5-36 shows the effect on Hc of nitrogen addition for three different alloying compositions, CoNiPt, CoNiCrPt, and CoCrPt. It can be seen that different alloys respond differently to nitrogen addition. This difference in response appears to be due to the different strength of preferred perpendicular growth for different alloy systems. The addition of Cr increase the tendency for preferred perpendicular growth, and the presence of nickel tend to reduce the effect.

Figure 5-37 shows the glancing angle X-ray diffraction trace for three different alloy systems at low base pressure without the nitrogen addition. The films were all 60 nm thick and sputtered at 30mTorr. Seeman-Bohlin glancing angle diffraction geometry was used [5-42]. Figure 5-38 shows the effect of nitrogen addition on $Co_{79}Cr_{12}Pt_{10}$ alloy by glancing angle X-ray diffraction. This alloy was chosen to illustrate the effect on the (0002) reflection as it has very strong tendencies to grow with perpendicular preferred orientation. Nitrogen additions clearly suppress the perpendicular film growth. It also can be inferred that $(1\bar{1}01)$ reflection is being

broadened, which is an indication of stacking fault formation. There is also slight lattice expansion as evidenced by the shift in (0002) reflection with nitrogen addition.

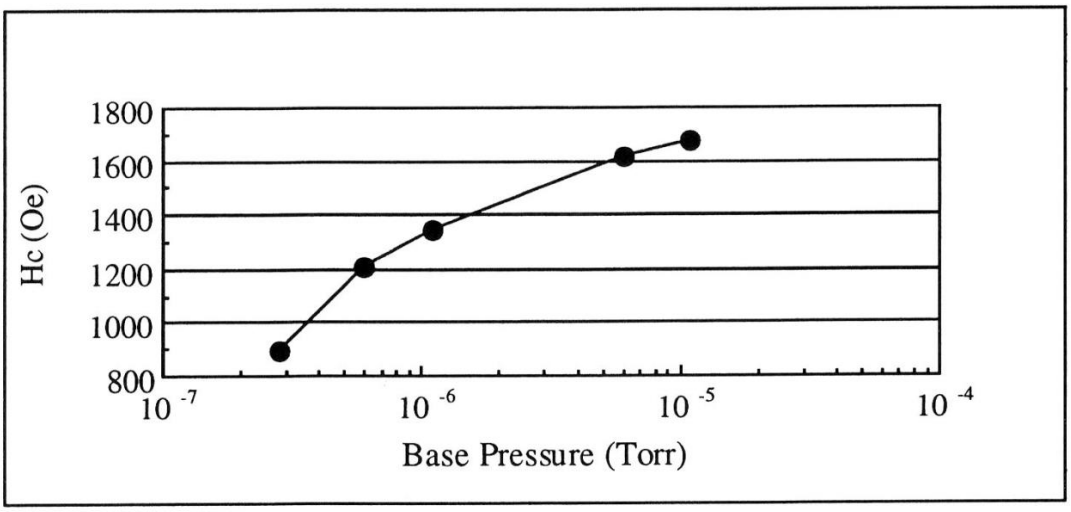

Figure 5-33: Hc vs. base pressure for CoNiPt film. Higher base pressure provides higher Hc due to increase in squareness and reduced perpendicular growth of the film.

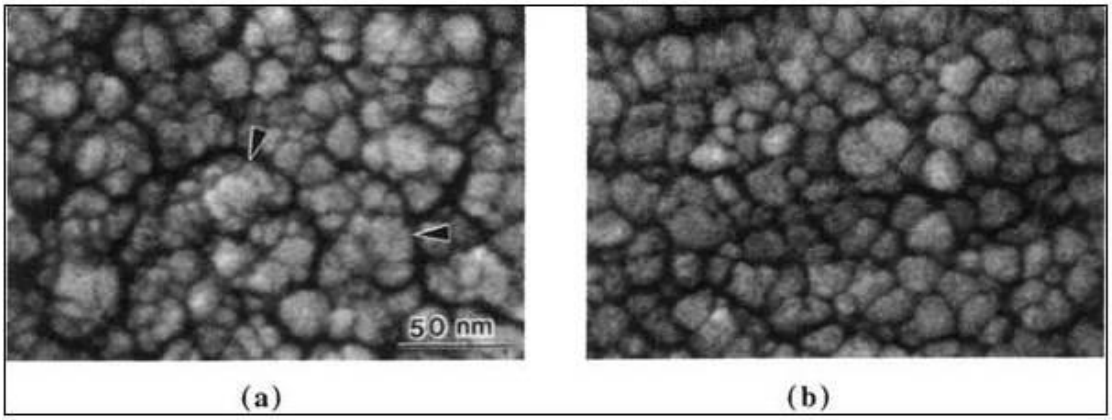

Figure 5-34: High-resolution SEM micrograph of CoNiPt film for two different base pressures: (a) 1 x 10^{-5} torr, (b) 2 x 10^{-7} torr.

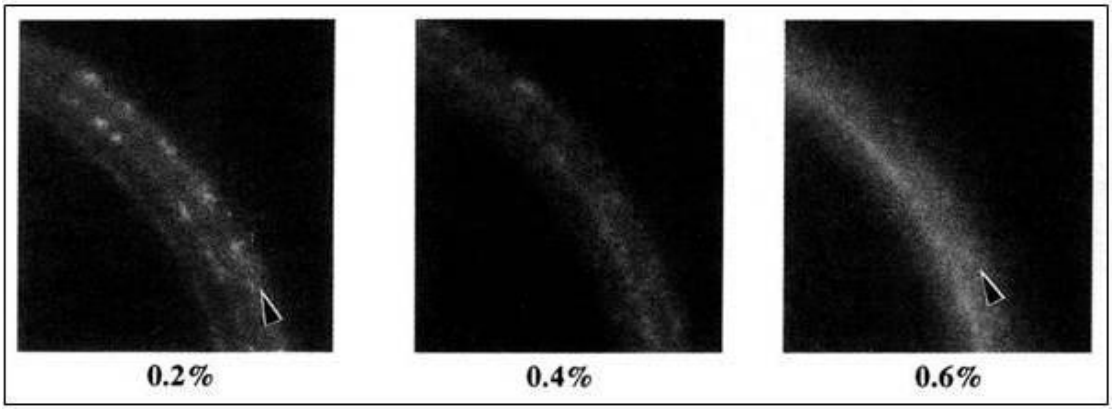

Figure 5-35: Electron diffraction pattern of $Co_{77}Ni_9Cr_4Pt_{10}$ alloy film with different nitrogen doped into the argon gas. The arrow indicates the position of $(1\bar{1}01)$ reflection.

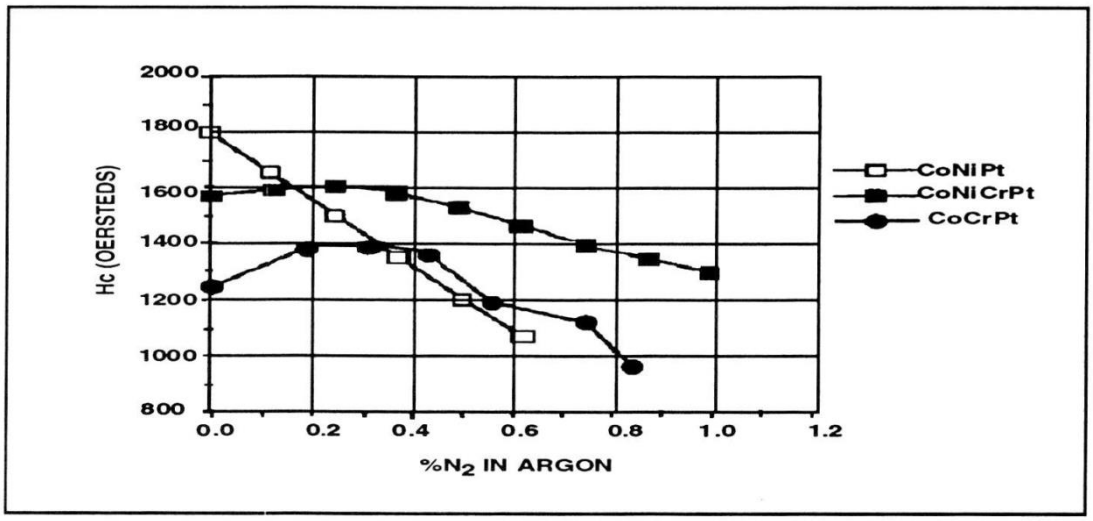

Figure 5-36: Hc vs. nitrogen addition for three different alloys, showing the difference in behavior as a function of alloy composition.

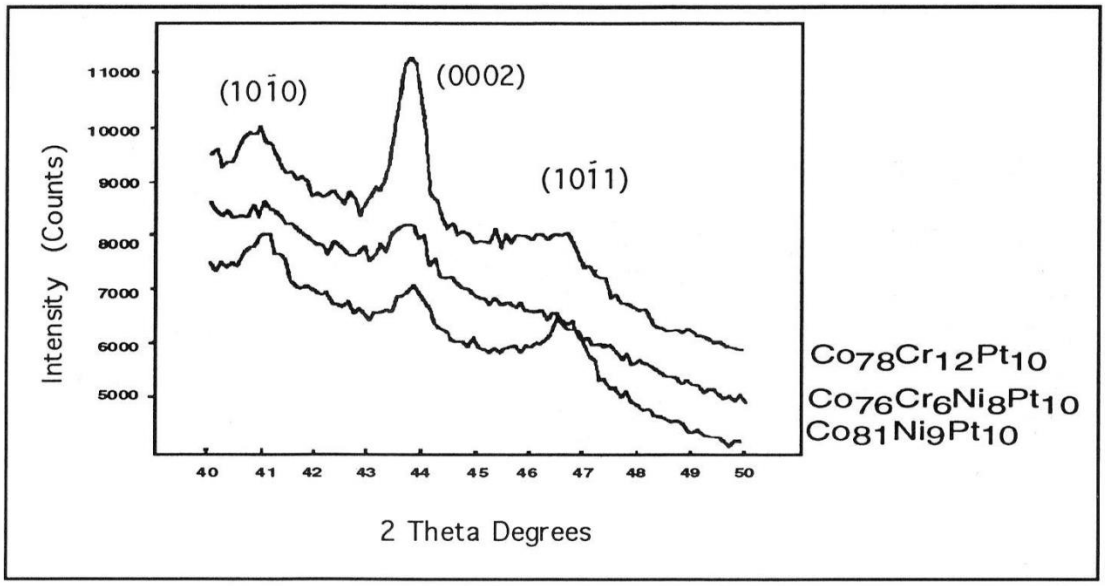

Figure 5-37: Glancing angle X-ray diffraction trace for three different alloy compositions, at low base pressure, showing the varying degree of preferred orientation. CoCrPt alloy without the Ni addition shows the greatest tendency for perpendicular growth.

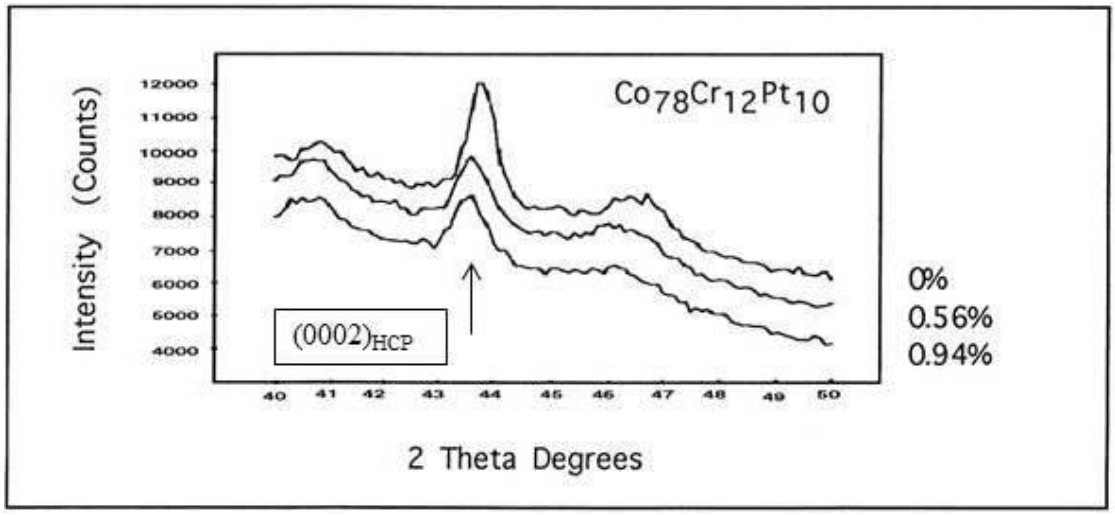

Figure 5-38: Glancing angle X-ray diffraction trace CoCrPt film with a different amount of nitrogen addition during sputtering, showing the reduction in the $(0002)_{HCP}$ reflection with higher nitrogen addition. In addition, the $(1\bar{1}01)$ reflection is reduced and broadened.

5.5.1 Sputtered Ni_xP Underlayer

By the time a 5¼ format disk required 40 MB for areal density of 40 Mb/in^2 areal density, the SNR performance of the CoNiPt film was inadequate for the density, even though the Hc of the media already had been raised to 1200 Oe or more. In fact, during this period, the thin film media generally had a noise issue compared to the oxide media, which was still being used in high-end disk drives used in large mainframe computers. The noise present in thin film media was at least 2X higher compared to the oxide media. To reduce the noise, Komag developed an underlayer consisting of sputtered Ni_xP film, which replaced the SiO_2 coating [5-43]. This underlayer served as a nucleation layer for the magnetic layer, and detailed microstructural investigation was done on the film to understand what the effect was on the growth of magnetic film and to the SNR performance of the media. Sputtering at high Ar pressure was not sufficient to obtain particle isolation as we shall see, and the nucleation process for growing the magnetic film turned out to be quite important.

The NiP coating is electrolessly plated onto an aluminum substrate to provide a hard surface on which to support the sputtered film. Plated NiP is used for a variety of applications to provide a corrosion resistant coating to various surfaces such as aluminum, copper, and steel [5-44]. In the past, an oxide media coating was directly applied to the polished aluminum surface. Oxide particles were bound in an epoxy binder, and the coating on the disk was quite thick. It was also quite soft. To support occasional landing by the recording head or intermittent contact between the head and the media, oxide media contained hard alumina particles that were mixed into the media coating. Thin film media starting with plated CoP was much thinner than oxide media, and it required the much harder surface to support the media. Electroless NiP coating was a convenient way of making the aluminum substrate much harder and durable. Ni orthophosphate was reacted with sodium hypophosphite, and some quantity of phosphorus was incorporated by the plated nickel, thereby making it amorphous and non-magnetic. The plated NiP layer filled in the defects on the aluminum surface and planarized it. The NiP surface was polished after plating to obtain a mirror finish.

Typically, the plated NiP layer contains approximately 12 wt.% P in the film. After polishing, aggressive cleaning was done on the surface to clean residual polish material and to provide a very clean surface on which to deposit the magnetic film. The CoPt alloy film sputtered directly on it usually had uniformity issues due to inconsistencies in the cleaning process used on NiP. To provide a fresh new NiP surface to the magnetic film, the NiP itself was sputtered onto the substrate. Initially, the NiP targets were manufactured from powders made from spent NiP plating solution. NiP can be precipitated out from the solution by suitable chemistry adjustment. The powder can then be consolidated to form a hot pressed target for sputtering. The typical finished thickness of electroless plated NiP for hard disk application is 10-15 μm thick.

Nickel and phosphorus form a variety of line phase compounds. Typical low phosphorus compounds include Ni_3P, Ni_5P_2, and Ni_2P [5-45]. These Ni-P compounds can be formed by sealed reaction between elemental phosphorus and nickel. A nickel phosphorus target from low phosphorus content up to Ni_2P (21.5 wt.% P) can be made by mixing various Ni_xP compounds in the appropriate amount. Trial and error was used to determine the best Ni-P composition that would provide the best magnetic performance for the CoNiPt alloy in terms of SNR, and Ni_3P composition was chosen as being the best. In addition, the ease of which the target can be fabricated was also a consideration. The target made from Ni_3P composition is crystalline with body-centered tetragonal structure. RF sputtering of this material in the range of 20 to 30 mTorr creates an amorphous film similar to the plated NiP film. However, the sputtered film has a unique nano-particle structure. TEM micrograph of the sputtered 50 nm thick Ni_3P composition film is shown in Figure 5-39, using Philips P430 EM at 300 keV, and the high-resolution SEM (HRSEM) image shown in figure 5-40 was obtained using Hitachi S900 field emission SEM operating at 10 KeV and using a heated holder [5-46]. A combination of TEM and high-resolution SEM provides a unique understanding of the structure of the Ni_3P film. SEM micrograph shows a high density of nano-sized particles, and they do not tend to grow larger with thickness as it is typical of most metal films. For ~ 40-50 nm thickness that was typically used for the NixP film, there were several layers of these sub 10 nm particles. This feature of NixP

film growth turned out to be due to the very small amount of alumina that was in the target material. The amount of alumina was between 0.5 to 1.0 wt.%. It was inadvertently introduced into the target in the process of ball milling the starting powder before hot pressing. The balls used in ball-milling were made of hard alumina, and prolonged milling was introducing a small quantity of alumina to the powder. Once this was discovered, the alumina was added into the target in a controlled fashion. RF sputtering allows a target with a variety of material inside, such as metal and oxide to be sputtered without causing problems. Apparently, a small amount of alumina, which is certain to be immiscible with Ni-P was having a significant effect on the manner in which the nano-particles were being formed. It is interesting to note here that in the oxide media the addition of alumina particles in the media to help with mechanical durability was discovered in a similar fashion when the ferrite particles were being ball-milled to obtain consistent particle size. This process introduced aluminum particles into the media, and it was noticed that the mechanical durability of the media was improved by ball milling the ferrite particles [5-3].

The comparison of magnetic media sputtered on SiO_2 vs. Ni_xP is shown in the TEM and high-resolution SEM micrographs of figure 5-41 [5-47]. The left column is CoNiPt deposited on Ni_3P, and the right column is the same alloy deposited on SiO_2. The Hc for both films is 850 Oe, S* for Ni_3P is 0.88 and 0.91 for the SiO_2 underlayer. The striking difference in the structure is seen in the BF TEM micrographs. The media sputtered on SiO_2 has a large number of grains that are clustered, with similar orientations as they are diffracting together (dark features). Alternatively, media on Ni_3P are more well-separated, and diffraction contrast is different for each grain. There is an even more striking difference in surface morphology appearance in the high-resolution SEM micrographs. The clustering of magnetic grains is reflected in more lumpy surface topography for the SiO_2 underlayer while the Ni_3P underlayer creates a uniform and smooth topography for the magnetic layer. The lines running diagonally are mechanical texture lines on the substrate, which are put there to help with tribology. The difference in the magnetic hysteresis curve between (a) and (b) is more subtle, but it is very consistent with the reduction in exchange interaction between the particles as

described previously. A slight reduction in S* is indicative of superior particle separation for the Ni_3P underlayer.

Indication of superior noise performance using the Ni_3P underlayer is shown in Figure 5-42 for a noise power spectrum of the media over 0 to 10 MHz for different writing frequencies [5-48]. SiO_2 underlayer media has much higher noise power compared to Ni_3P underlayer media. Other recording performance data such as bit shift, SNR, OW, and resolution measurements were reported, all showing superior performance for the Ni_3P underlayer media. Use of a Ni_3P underlayer provided a tremendous reduction in transition noise for the media and made it more capable of higher recording density.

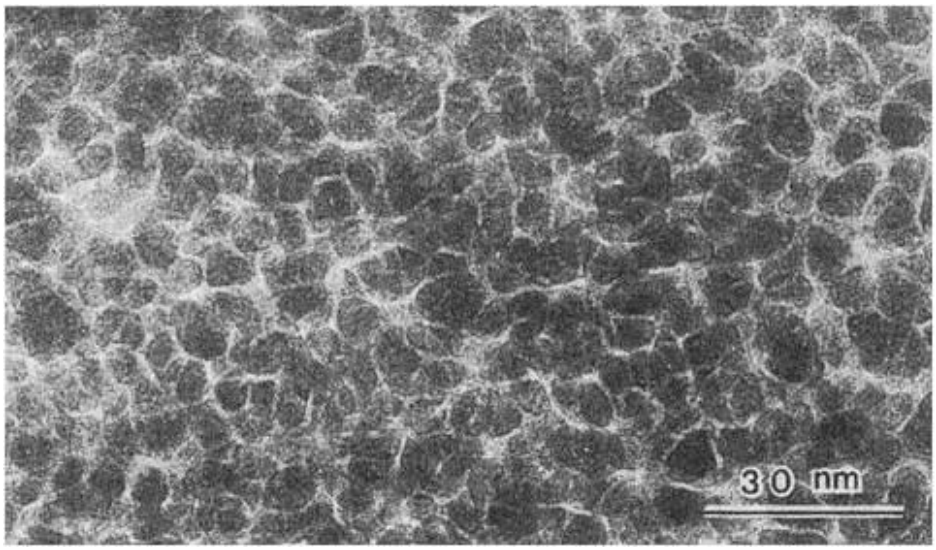

Figure 5-39: BF TEM micrograph of sputtered Ni_3P film, approximately 50 nm thick. Even though the film is amorphous based on the electron diffraction pattern, the film has a granular structure with a fibrous network of features running through the grain of the film. From Ref. [5-46]. Copyright © 1991, IEEE, reproduced with permission.

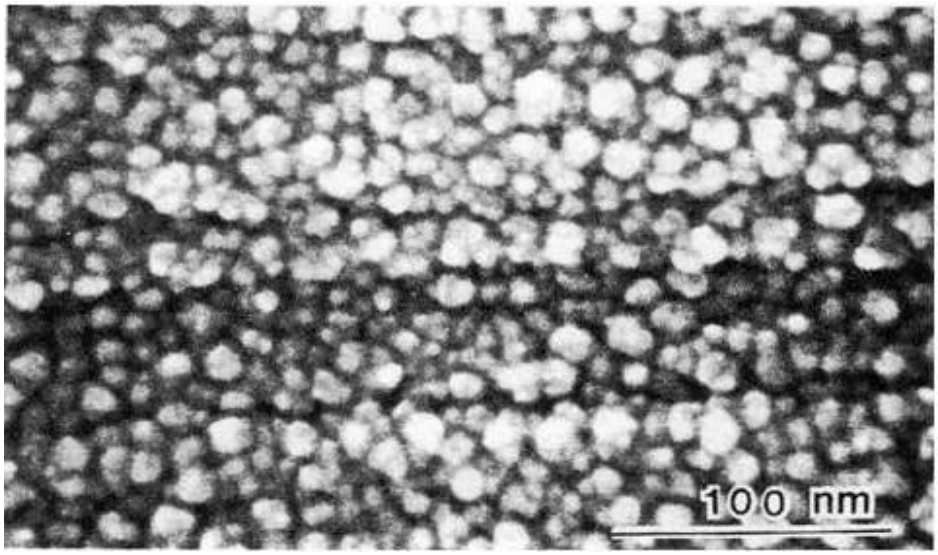

Figure 5-40: High resolution SEM micrograph of sputtered Ni_3P film, approximately 50 nm thick. The film is composed of many small particles that are less than 10 nm, which serve as nucleation sites for magnetic film that is sputtered above it. From Ref [5-46]. Copyright © 1991, IEEE, reproduced with permission.

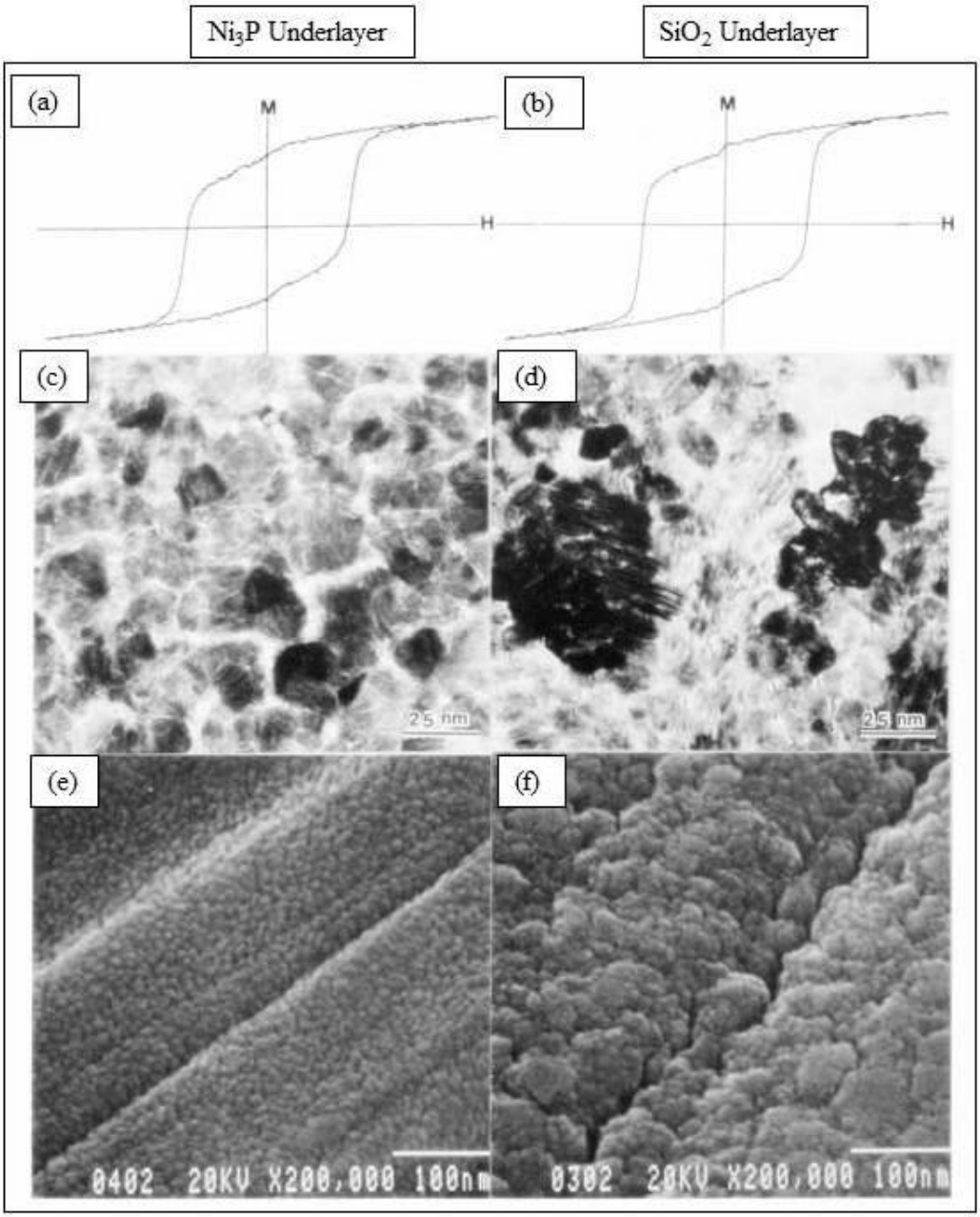

Figure 5-41: The right column (b, d, f) are for CoNiPt deposited on a SiO_2 underlayer, and the left column (a, c, e) are for the same magnetic alloy deposited on sputtered Ni_3P underlayer. The first figure is VSM hysteresis trace, the second set is BF TEM micrograph, and the third set is high-resolution SEM micrographs of the magnetic layer surface.

SiO_2 Underlayer

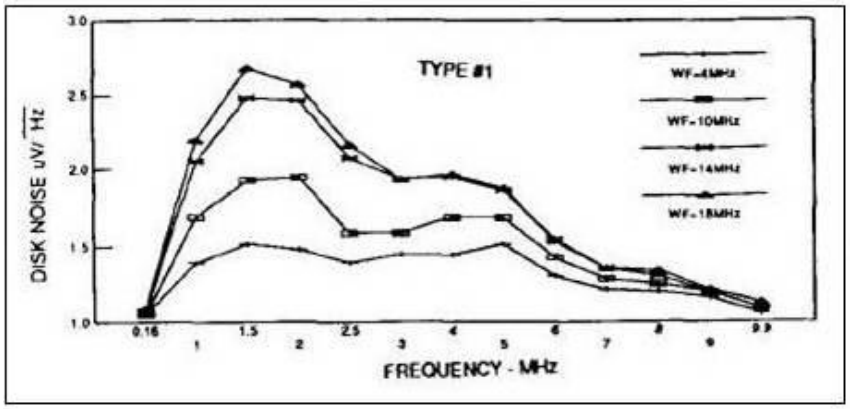

Legend
▲ - 18 MHz WF
- - 14 MHz WF
∞ - 10 MHz WF
\+ - 4 MHz WF

Ni_3P Underlayer

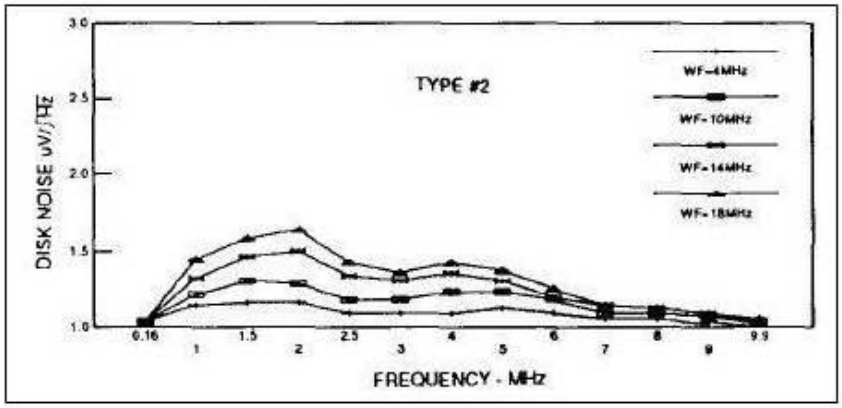

Testing conditions:

Guzik RWA 201b
Rotational speed: 3600 rpm
ID test radius: 31.8 mm
OD test radius: 62.2 mm
Pole tip length: 3 μm
High Freq. write (HF): 10M trans./sec
Low Freq. write (LF): 5M trans./sec

Test head type: Thin-film
Pole tip width: 14 μm
Gap length: 0.4 μm
Fly height: 0.175 μm

Figure 5-42: On-track noise power spectral density of CoNiPt media on SiO_2 and Ni_3P underlayers. Noise is much lower on the Ni_3P media across the entire spectrum. The power spectrum was measured using a HP 3585 spectrum analyzer; the noise was calculated as a power from 0-10 MHz minus the signal. From Ref. [5-48]. Copyright © 1988, IEEE, reproduced with permission.

5.5.2 Oxide Addition to CoNiCrPt Alloys

The original premise for the thin film media design for Komag was to employ high argon gas pressure sputtering to achieve physical separation between the grains to obtain films that were exchange decoupled. This worked to some extent, but it was quickly realized that it was not sufficient. Attention was then put on the nucleation layer, development of the NixP underlayer greatly improved the particle isolation by growing each magnetic grain more uniformly, and with separation that is more precise. This prevented crystallographic clustering of magnetic grains. Even this over time was not sufficient; an alternative method had to be developed to separate the grains. The main idea was to introduce a non-magnetic phase between the grains so that there was a more consistent and well-controlled separation of the magnetic grains. It must also be noted that it is not detrimental to the growth of the magnetic grains. Magnetic grains must be perfect in terms of crystalline structure, and retain high coercivity while reducing the grain size so that higher recording density could be achieved. Maintaining all of these requirements was difficult. One way to introduce grain isolation was to add material that is immiscible with cobalt. Initially, boron addition was tried at approximately 2 atomic %, but its effectiveness in reducing exchange coupling was rather limited. Typical composition of the alloy used was $CoNi_7Pt_{12}Ti_{1.5}Ta_{1.5}B_2$. The purpose of Ti and Ta was to attempt to improve the corrosion resistance of the alloy [5-49]. Boron has a very limited solubility in cobalt [Liao and Spears, 5-50]. Phase diagram reported by Liao and Spear is shown in figure 5-43. The system has a single eutectic with a temperature of 1102^{o}C, at the composition of 23.5 atomic% Boron is congruent with the formation of Co_2B. Solubility of boron in cobalt was determined to be less than 0.163 atomic%. In hindsight, the higher boron content is needed for segregation, and it requires heat. The process used by Komag did not use heat during sputtering, aside from normal heating that occurred during RF sputtering.

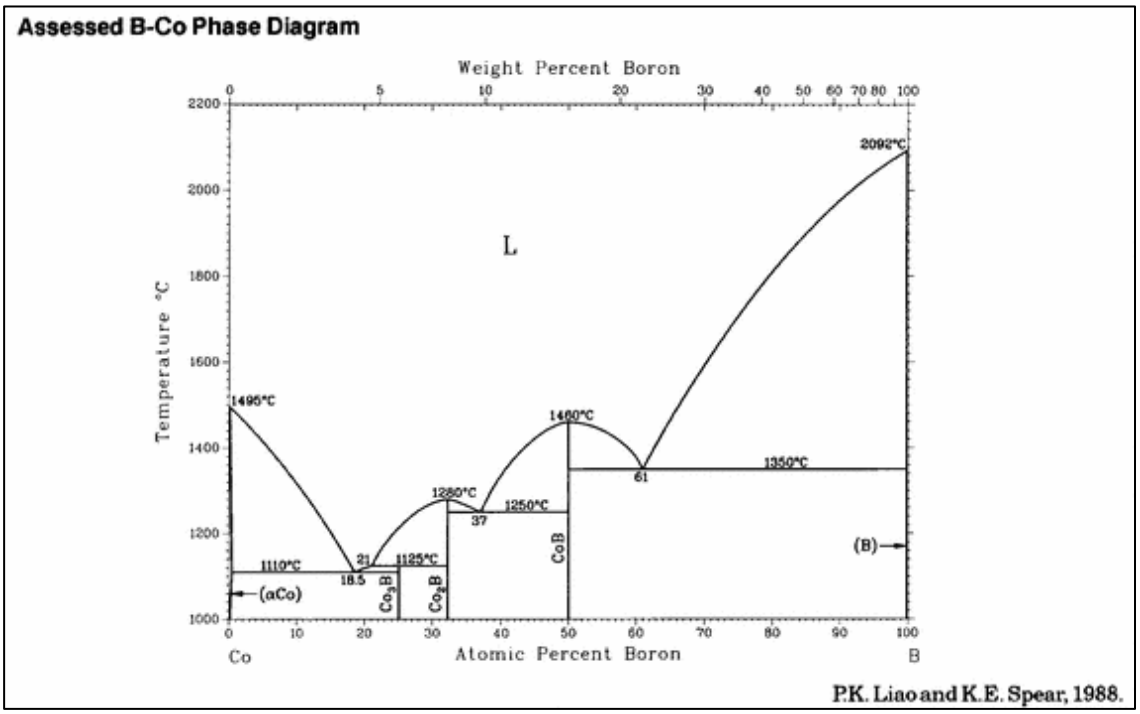

Figure 5-43: Phase diagram of Co-B system, from Liao and Spear [5-50]. Boron has very limited solubility in α-Co. Figure reproduced with permission. Copyright © Springer 2001.

The other option to force segregation in the cobalt alloy was to use reactive sputtering with oxygen or water vapor. This is to cause oxide formation, which is insoluble in cobalt. Oxygen gas showed some evidence of going to the grain boundaries in a form of oxide as seen by the effect of the media on Hc and SNR. Other workers also reported on the use of oxygen gas to modify the microstructure, thereby increasing Hc for example [Howard et al. 5-51]. In practice, however, oxygen doping proved very difficult to implement in a production tool. The reason was that oxygen was very reactive, and it would react immediately at the point of contact with the plasma at the cathode. Uniform reaction was also very difficult to achieve. For an in-line system, which Komag used with large target dimensions, introducing the gas uniformly across the length of the target was very difficult. In addition, the gas would react only at the periphery of the plasma, leaving the center of the cathode with low

concentration of oxygen. This would create a gradient in the oxygen incorporation in the media, as the panel with the disk passed by the cathode. For a static system, the issue would be that oxygen would be incorporated at the outside of the disk diameter, leaving the center of the disk with much less incorporation. Reactive oxygen sputtering had other problems if DC magnetrons were used. Oxide formation on the top of the target would *poison* the target surface, causing arcing, thereby causing defects on the disk. However, RF sputtering did not suffer from such effects. Water vapor was a more effective means of incorporating oxide into the film. Water vapor was much less reactive compared to oxygen. The gas would have more time to diffuse into the plasma and provide more uniform coverage of its effect over the disk surface. Nevertheless, considerable work went into making the gas introduction uniform. Complex gas manifolds were built to introduce the water vapor uniformly around the cathode so that uniform magnetic properties could be obtained.

Better results were obtained when oxide material was directly added into the target. A variety of oxides was tried, but one that worked well initially was CoO. With approximately 2 atomic% CoO added into the target, grain size uniformity improved, and Hc increased. The comparison was made between oxygen addition vs. CoO, and CoO was clearly superior [5-52]. Comparison of two media by HRSEM is shown in figure 5-44. Oxygen addition creates clumped and coupled granular structure while the CoO addition creates the uniform appearance. A TEM micrograph shows greater grain isolation as seen in figure 5-45. Grain size distribution was also clearly sharper as shown in figure 5-46. The effect on Hc and S* is shown in figure 5-47.

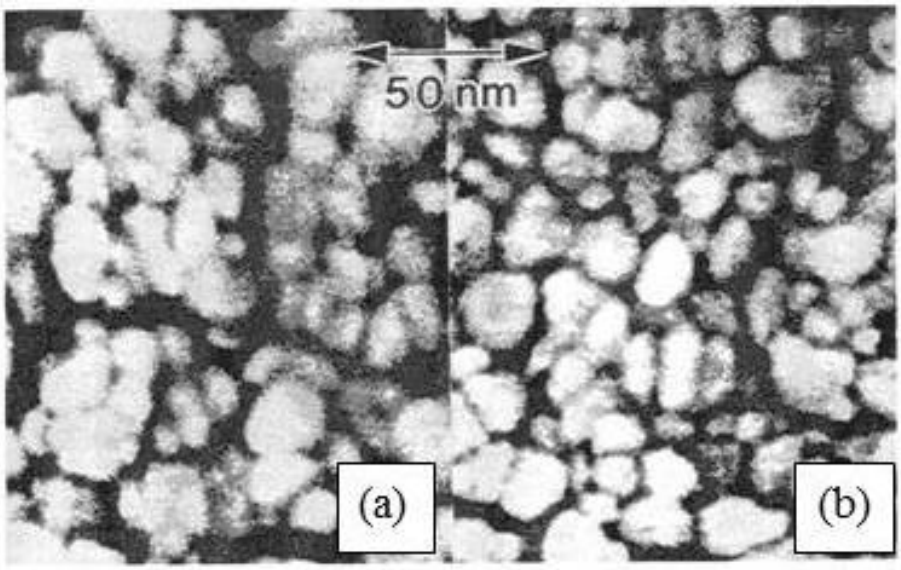

Figure 5-44: HRSEM micrograph of (a) CoNiPt with oxygen addition showing clumped grain structure. (b) CoNiPt + 2 at% CoO showing more uniform granular structure. From Ref. [5-52]. Copyright © 1994, IEEE, reproduced with permission.

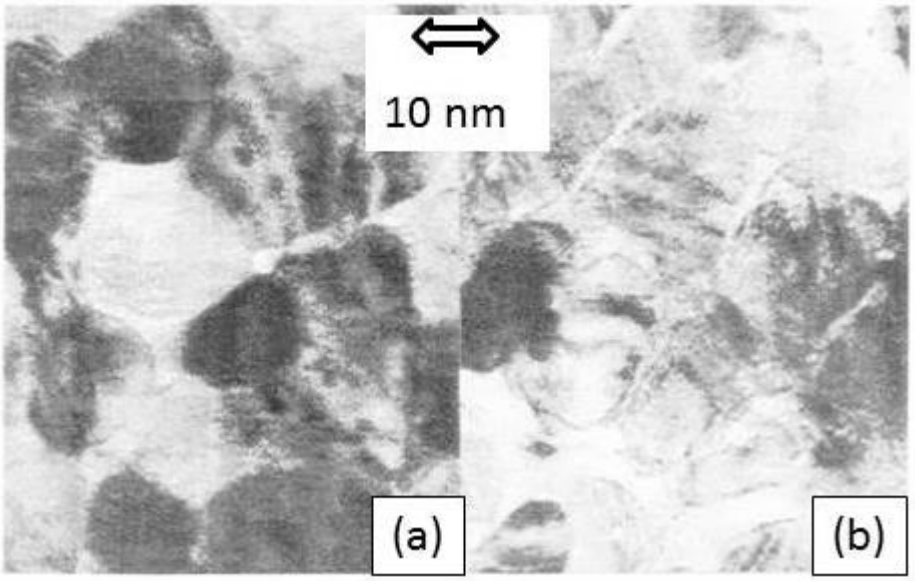

Figure 5-45: TEM micrographs of (a) CoNiPt – no oxygen and (b) CoNiPt + 2 at.% CoO. (b) shows more intergranular separation. From Ref. [5-52]. Copyright © 1994, IEEE, reproduced with permission.

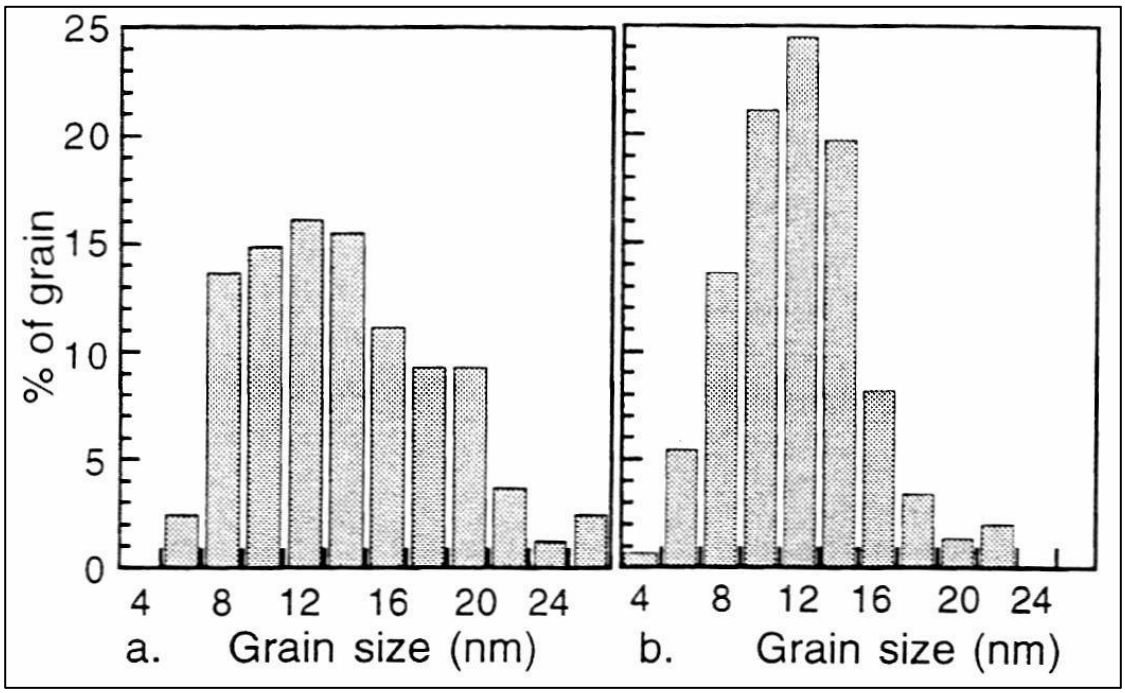

Figure 5-46: Graph of grain size distribution of (a) CoNiPt – 0.5 % oxygen and (b) CoNiPt + 2 at.% CoO. From Ref. [5-52]. Copyright © 1994, IEEE, reproduced with permission.

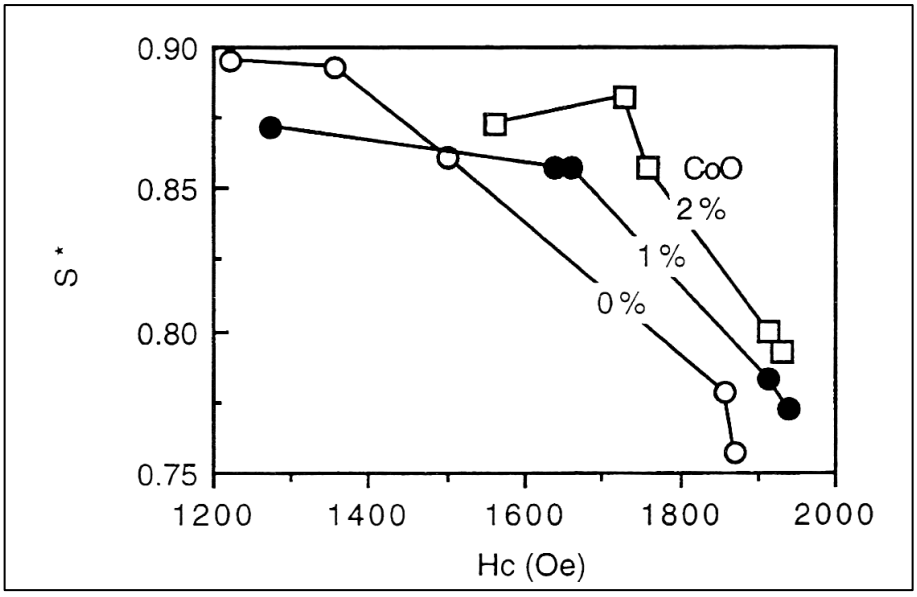

Figure 5-47: S* as function of Hc for different amount of CoO in the media. From Ref. [5-52]. Copyright © 1994, IEEE, reproduced with permission.

Oxide addition into the magnetic target was a basis for another patent [5-53]. Most oxide material has little to no solubility in the magnetic alloy material, and if done correctly, may segregate out of the magnetic grains into the grain boundary to isolate the individual grains from each other. The RF diode sputtering that was being employed provided some unique opportunities for sputtering mixed phase targets. This is because RF sputtering is capable of sputtering almost any material, metals, and insulators alike. The only concern would be that particle size in the target itself must be quite small and well distributed. The disparity in sputtering rate between metals and oxides is quite large, often by a factor of 5 to 10, so that if oxide particles were too large, it could over-heat on the target surface and spit, causing defects in the disk. However, compared to DC magnetron sputtering where conventional wisdom says that only metals can be sputtered, the RF sputtering held considerably more promise. Care must be placed in how the sputtering target is made so that different phases can be sputtered continuously without causing problems in the target or on the disk. Although many oxide materials were claimed in the patent, ones that worked well were CoO and SiO_2. Other choice included oxides of the target elements, such as Cr_2O_3 and NiO. In 1995, some examples of target compositions used in manufacturing of media included the following:

$(CoCr_{11}Pt_{13}Ta_2)_{96}\,(SiO2)_4$

$(CoNi_8Pt_{12}\,Ti_{1.5}Ta_{1.5}.B_2)_{95}\,(CoO)_5$

$(CoNi_8Pt_{12}Ti_{\,1.5}Ta_{\,1.5})_{96}\,(SiO_2)_4$

$(CoCr_{11}Pt_{13})_{94}(\,SiO_2)_6$

Considerable work went toward the fabrication of the target. The usual method of making a CoPt-based alloy target had been vacuum induction melted (VIM) targets. Additional rolling was often done to obtain near net shape and achieve some subgrain growth in the target to attempt to homogenize the target. VIM fabrication of the target had some limitations, as the cooling process from liquid could cause phase segregation in the target, and there is a potential for the compositional gradient to develop in different parts of the target or worse yet, through the thickness of the target. For the

CoNiPt target, the Pt concentration difference of 0.1 atomic % can cause an Hc change of approximately 100 Oe. Therefore, phase segregation during solidification was a big concern. For binary compositions, the existing phase diagram was a guide for alloy selection but with more than three components, the behavior of the target composition during fabrication was a guessing game. The alternative was to consider the powder metallurgy method, and hot isostatic pressing (HIP) was an attractive choice, as this method can make 100% dense casting with the enormous pressures that are used in the process. 40 Kpsi was often typical processing pressure for the HIP process. The use of powder metallurgy also meant that potentially immiscible materials could be mixed together as long as the powder was thoroughly mixed uniformly and poured into the cast. Considerable investment in equipment and expertise is involved in using the HIP process, a vendor finally was identified who acquired the right equipment, people, and expertise to process the CoPt alloy targets containing different oxide additions. Since the target dimensions used in the large in-line sputtering tool were 200 x 570 x 10 mm, the very large HIP tool was needed. Additional technology that had to be developed by the vendor was the wire-EDM or electro-discharge-machining method to slice large ingots into plates that are approximately the dimensions of the target plates. In this method, the wire saw is electrically discharged to slice slowly through a thick metal block. Considerable skill and technique are needed to operate such a tool. The vendor also had to develop powder metallurgy expertise to optimize the HIP operation in order to obtain the theoretical density and obtain fine microstructure in the finished material. The metal block that was HIP'ed was very large, enough to make several pairs of targets. Each target contained hundreds of thousands of dollars' worth of platinum. Each casting operation was a very serious affair. For alloy development work, hot press method was used to fabricate smaller targets for R&D. The typical density achieved by the hot press was in the high 80% to low 90%. It was not suitable for production use, but sufficient for development work. Inconsistencies in target density and results, combined with the possibility of defect generation, made hot pressed targets unsuitable for manufacturing.

The isotropic media based on CoPt-oxide achieved considerable refinement by the time MR (magneto-resistive) heads started to be used. The target contained multiple oxides, and fine separation was being achieved between the grain boundaries with oxide segregation. This can be seen in figure 5-48 of CoCrPtTiTa-CoO film by TEM. Cross section TEM micrograph is shown in figure 5-49.

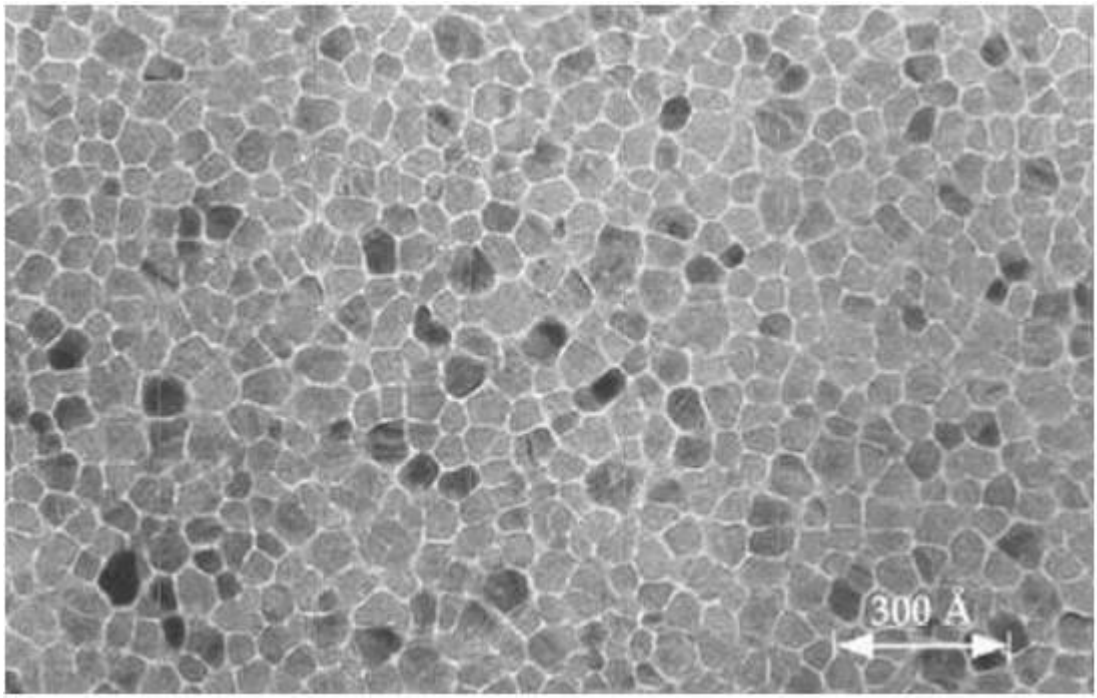

Figure 5-48: Planar BF TEM micrograph of CoCrPtTiTa-(CoO) film showing the grain boundary segregation of oxides.

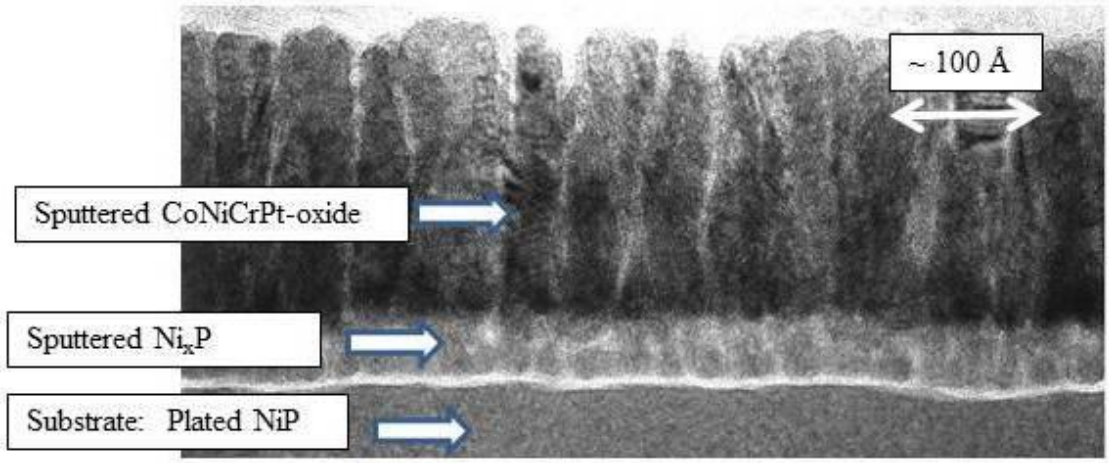

Figure 5-49: Cross section BF TEM micrograph of Komag isotropic media showing its structure.

5.6 CoCr-based Thin film Media

CoCr-based thin film media attracted interest due to its use by S. Iwasaki and his co-workers for perpendicular magnetic recording in 1977 [5-13]. In fact, Iwasaki had reported on the idea of perpendicular recording using CoCr in 1975 but it was in Japan and publication was in Japanese [5-54]. Adding Cr to Co was in order to reduce Ms, so that the requirement for perpendicular anisotropy can be maintained, which was:

$$Hk > 4\pi Ms, \quad \text{or } Ku > 2\pi Ms^2 \qquad \text{(Eqn. 5-12)}$$

where Ku = magnetocrystalline anisotropy constant

The film reported in Ref. [5-13] and [5-54] had approximately 13-15% Cr and the Ms of the alloy was 500-600 emu/cc, which is quite low for application in longitudinal recording. CoCr film was deposited on polyimide film and film thickness was 1 μm.

The hysteresis loop reported for this media is shown below in figure 5-50, from Iwasaki (1977) [5-13]. The remarkable feature of this publication is that the recording density of 30,000 BPI (bits per inch) was demonstrated, which was very high at that time.

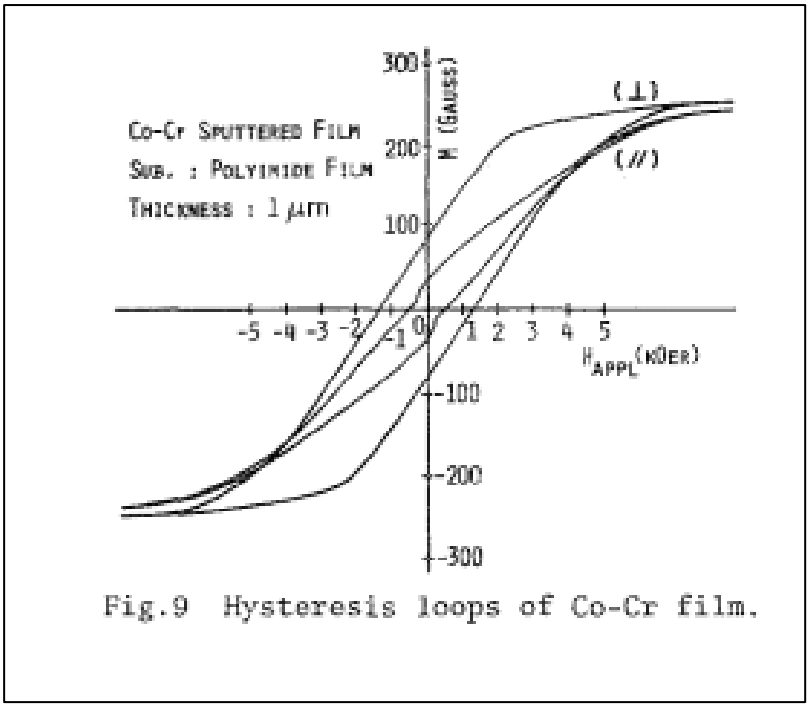

Fig.9 Hysteresis loops of Co-Cr film.

Figure 5-50: Hysteresis loop of CoCr perpendicular media, from ref [5-13].. Copyright © 1977, IEEE, reproduced by permission.

The CoCr alloy system has several reported phase diagrams that are different. The most common one is shown in figure 5-51 from Hansen [5-55]. From this phase diagram, one might expect that there is a good level of solid solubility of Cr in Co up to approximately 40% Cr. Another phase diagram that is more obscure is shown in figure 5-52. This phase diagram is shown by Moffat [5-56], which is from a Russian reference [5-57]. The phase diagram is reproduced in reference [5-58]. The reason why the phase diagrams are different is due to the sluggishness of the alloy system to reach equilibrium conditions. According to the 2nd phase diagram, an intermetallic compound, Co_3Cr can coexist with ε-Co over an extended range of compositions out to ~ 27

atomic% Cr at 300^{o}C. Because of the possible two phase field between ε-Co and Co_3Cr below 620^{o}, we proposed in 1983 that Cr concentration in the range of 13% to 25 atomic % will have a microstructure consisting of two-phase mixtures [5-58]. The Russian source reported that 16.7-20.0 atomic% Cr consist of a solid solution of hcp Co (ε-Co in the phase diagram) + Co_3Cr. We speculated that widely different results for magnetic properties being reported by different groups for CoCr might be due to a different level of phase segregation taking place in the alloy depending upon the sputtering method and deposition rates. We deposited CoCr with Cr composition of 22 atomic% at ambient temperature, 300^{o}C and at 550^{o}C. At 550^{o}C, the film had no magnetization while at ambient temperature and 300^{o}C, the film had 240 emu/cc and 300 emu/cc magnetization respectively. This result was explained in terms of the phase diagram of figure 5-52, which would indicate that at 500^{o}C, the Cr has complete solubility in ε-Co, which at this composition would not have any magnetization. However, at ambient and 300^{o}C sputtering, the film was in the two-phase field and ε-Co would have a different level of Cr content and still be magnetic. Existence for the formation of Co_3Cr was looked for in the samples prepared at different temperatures, but the evidence for them was only circumstantial. Figure 5-53 is a BF TEM micrograph of the Co22at%Cr film prepared at 550^{o}C. There is a grain boundary phase present in the image, which is filled with a different material. EDX analysis showed an elevated level of Cr compared to the surroundings, but the results were not quantitative and the TEM/EDX chemical analysis capability of the equipment at the time was not sufficient to determine the composition or chemical nature of the segregation.

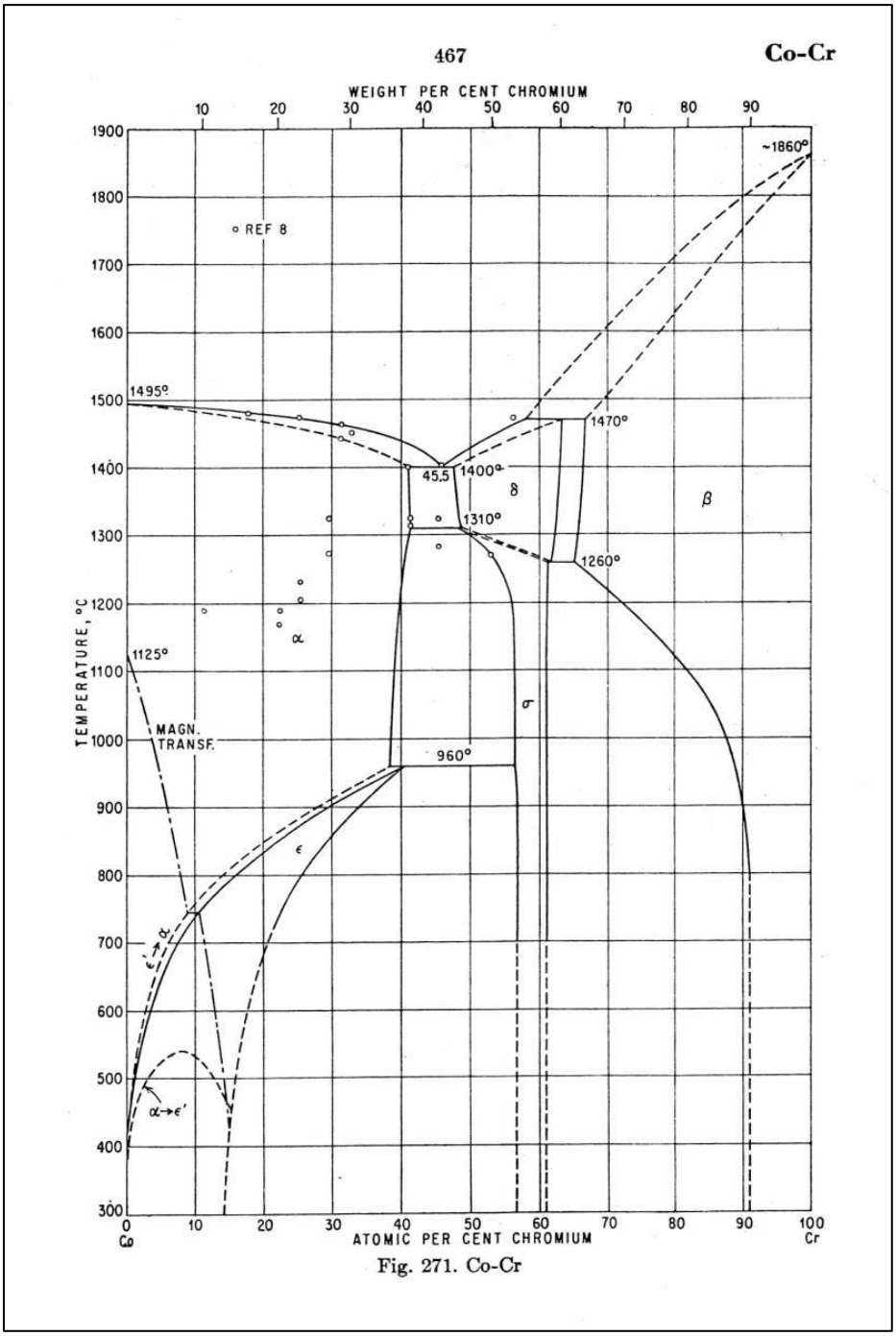

Fig. 271. Co-Cr

Figure 5-51: Phase diagram of Co-Cr system from Hansen [5-55]. α = FCC phase, ϵ = HCP phase, σ = Co_2Cr_3, β = Cr-rich BCC. Reproduced with permission. M. Hansen, Constitution of Binary Alloys, 2nd ed., pp. 467, McGraw-Hill, New York (1958)

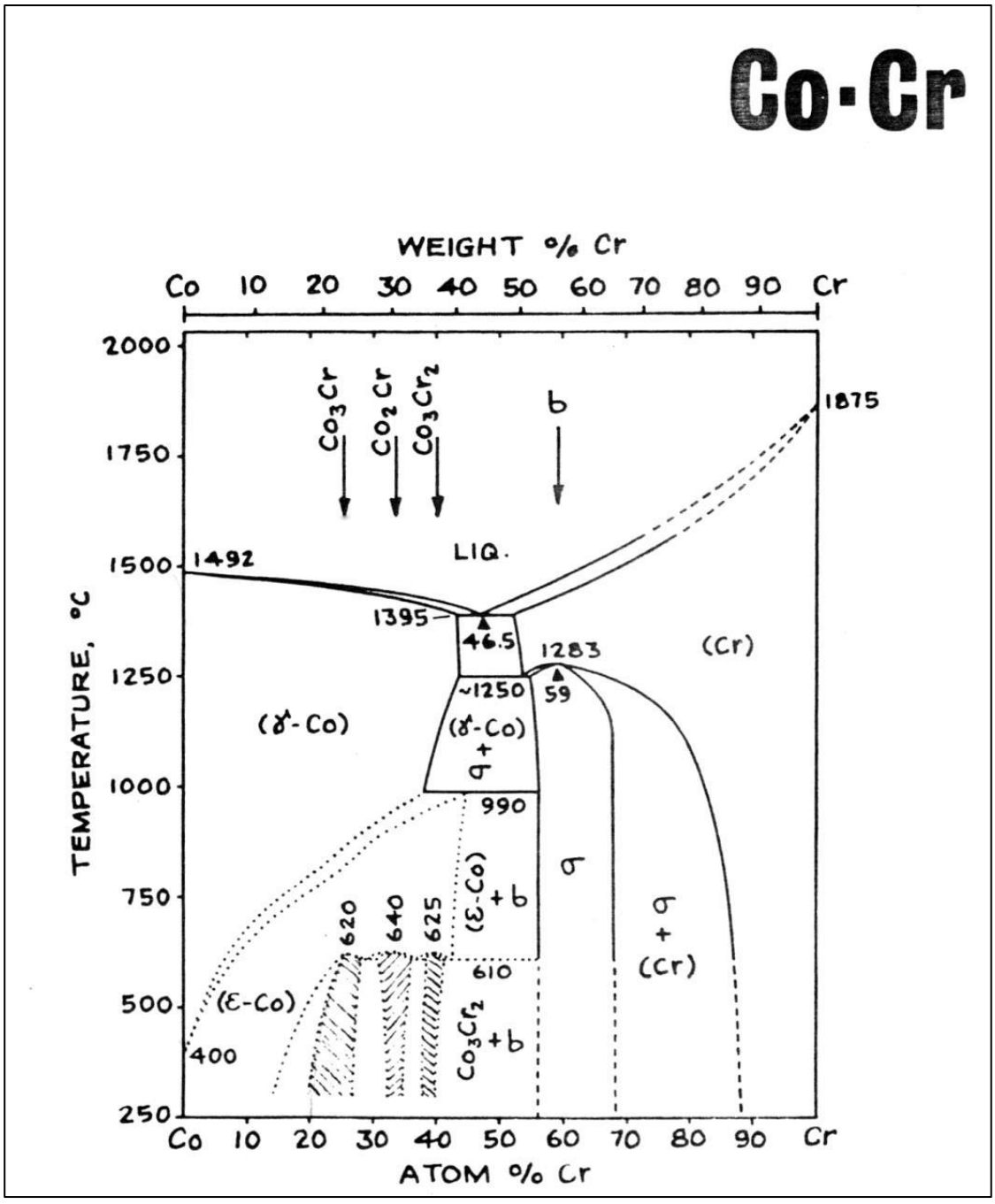

Figure 5-52: Phase diagram of Co-Cr system from Ref. [5-57, 5-58]. J. Appl. Phys. AIP Publishing, Reproduced with permission.

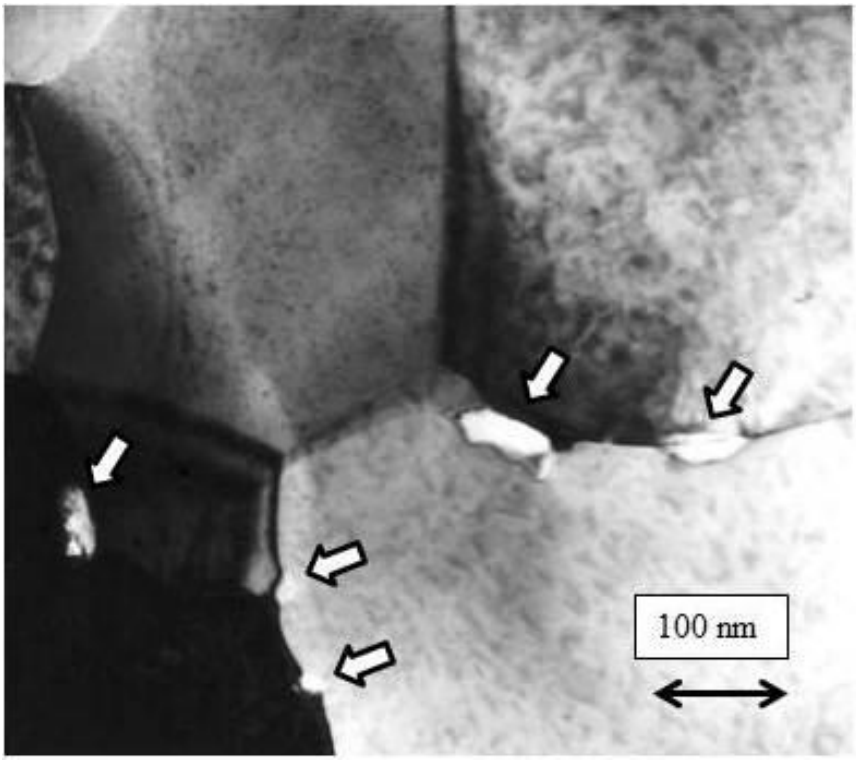

Figure 5-53: BF TEM micrograph of Co-22at%Cr perpendicular film, which was processed at substrate temperature of 550^{o}C. Arrows indicate the location of the grain boundary precipitates. EDX showed an elevated amount of Cr in these regions. From Ref. [5-58]. J. Appl. Phys. AIP Publishing, Reproduced with permission.

Later in 1987, Maeda et al noted the possibility of segregation processes in CoCr film, using chemical etching to indicate the presence of segregation [5-59]. However, what he showed was termed a *chrysanthemum* pattern inside of the individual CoCr grain. The result was more of a curiosity as it was not clear what the pattern was and what it did to the media properties. Therefore, not as much attention was put on his work. As far as a perpendicular recording application was concerned, the magnetic media community took little notice of phase segregation and media

microstructure effects in CoCr films. Much more attention was placed on whether the better perpendicular orientation is present or not, based on different seed layers, for example. Many start-up companies were funded in the early 1980s and a considerable amount of money was invested into the perpendicular recording technology in both the US and in Japan. It is estimated that in total, perhaps $1 billion dollars might have been spent on start-ups and on perpendicular recording development at major electronic firms; unfortunately, nothing came of it. By the early 1990s, perpendicular recording for hard disk drive application was all but dead. The introduction of magnetoresistive (MR) heads in early 1900s and the discovery of giant magneto resistance (GMR) and its application to the recording head greatly extended the longitudinal recording technology. The areal density increased at a rate of over 100% compound growth from 1995 to 2005 thanks to the significant increase in sensitivity that MR and GMR heads provided to the HDD industry.

5.6.1 Chromium Underlayer Media

The idea of growing cobalt film on top of chromium film began with the work by Lazzari, Melnick, and Randet in 1967 when they reported epitaxial growth of Co on Cr film, which were both evaporated [5-60]. The orientation relationship between the Cr and Co film was not stated at the time, but it was Cr (002)//Co($11\bar{2}0$). Un unexpectedly high Hc of 600 Oe was obtained at the time. Other workers, such as Maloney in 1979, followed up the work with RF sputtering of the films specifically for hard disk application [5-61]. Maloney was able to obtain Hc in the range of 300-800 Oe with a Cr underlayer thickness of 300-600 nm. Maloney did not specifically report on the structure of the film, but the high Hc that he obtained suggests that he had a good epitaxial growth of cobalt film on Cr film. Various groups worked on the sputter media process based on a Cr underlayer for several years. By 1983, three start-up media companies in the US staked their future to this process. However, the alloy that was used initially was CoNi. Several companies in Japan were also using CoNi. Two companies that began in 1983 in the US originated from IBM and they used the

Cr/CoNi process. They also added another dimension to the expitaxy between the Cr and CoNi; this was the circumferential anisotropy of the magnetic layer that was created by the circumferential mechanical texture on the disk substrate. The texture was put on the Al/NiP substrate for the purpose of reducing stiction and friction for head loading and unloading. The circumferential magnetic anisotropy effect was supposedly discovered by Atef Eltoukhy at IBM and his start-up company, Trimedia, started to use this effect and Lin Data, which also originated from IBM, attempted to use it as well. The so-called *oriented media* had a squarer hysteresis loop along the texture direction compared to the radial direction, and higher Hc along the circumferential direction of the disk, quite similar to the characteristics of the oxide disks, which had their acicular particles oriented along the recording direction using magnets during curing of the epoxy/ferrite particle solution. For the oxide media, the ferrite particles were acicular needle-like particles and the anisotropy came from the shape of the particle. When the long axes of the particles were oriented along the circumferential direction of the disk, it was much easier to magnetize along the direction of rotation of the disk and this effect is shown in figure 5-54, taken from Ref [5-3]. The oriented media hysteresis loop is shown in figure 5-55.

The nature and the source of orientation effect for CoNi/Cr on textured NiP/aluminum substrate were quite mysterious at first. No one knew where it was coming from. However, because of many years of experience using the oriented media for oxide disks, the advantages of using it seemed obvious. The epitaxial process for growing CoNi on Cr and the orientation effect using the textured substrate turned out to be much more difficult to control at first, and many companies that attempted to use this process did not have an easy time of it. Trimedia, which was probably the first to market the oriented media was sold off to Xidex, which was then sold to Hitachi Metals. Lin Data did not last long either, being sold to Nashua. The oriented media process eventually was patented by Virgle Hedgcoth [5-62], who was with Cyberdisk, another sputter thin film media start-up, which did not survive for long This patent came out some time after many companies had already started to practice it, and they had to obtain a license from Hedgecoth for the rights to use the process.

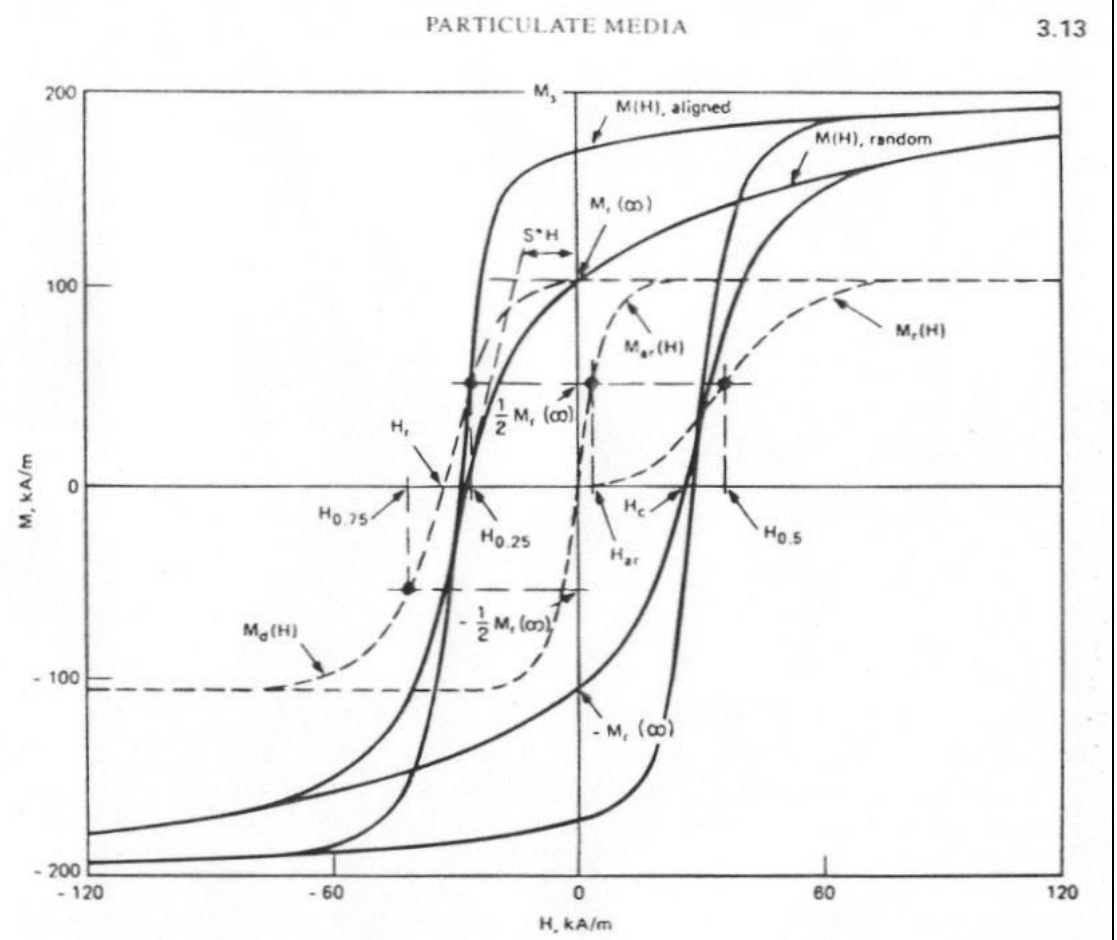

FIGURE 3.4 Magnetization $M(H)$, remanence $M_r(H)$, dc demagnetizing remanence $M_d(H)$, and anhysteretic remanence $M_{ar}(H)$ of a sample of randomly oriented γ-Fe_2O_3 particles. For the same particles, partially aligned, $M(H)$ is also included.

Figure 5-54: From *Magnetic Recording Technology, 2nd Edition* by C. Denis Mee & Eric D. Daniel. McGraw-Hill. From Ref. [5-3]. The taller hysteresis loop is for the oriented oxide media, along the track while the less square smaller loop is for random (isotropic) oxide without the magnetic field alignment during curing. Reproduced with permission.

The orientation relationship between cobalt and chromium is illustrated in Figure 5-56. The $(11\bar{2}0)$ surface of the cobalt is matched to the (001) plane of the chromium. Additionally, the c-axis of the cobalt <0001> is along the <110> direction

of the chromium lattice. This relationship that was established by Lazzari et al. [5-60] for evaporated Co on Cr film. In the plane of the film, the relationship between the Co and Cr lattice is shown in figure 5-57. Lattice mismatch in the case of pure Co and Cr is ~3% in the Cr <110> direction, slightly more at 6.4% along the alternate Cr <110> direction.

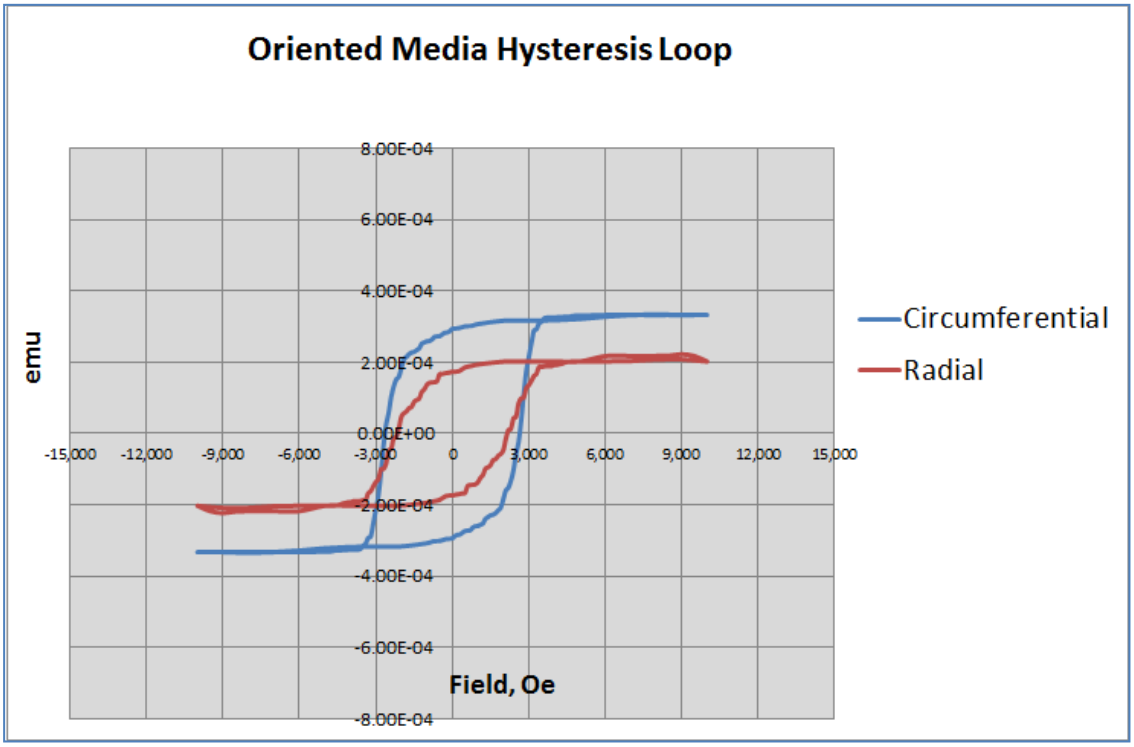

Figure 5-55: Hysteresis loop of oriented media along the texture or circumferential direction (blue) and across or radial direction to the disk (red) showing the difference in the hysteresis loop squareness.

The CoNi alloy did not last very long; it was quickly replaced by CoNiCr alloy, with the typical composition of $Co_{62.5}Ni_{30}Cr_{7.5}$. This alloy had higher Hc capability, and perhaps more corrosion resistance with the addition of Cr. Many research publications on the $Co_{80}Ni_{20}$ and CoCrNi alloy thin film came out by 1987 to 1988 [5-63, 64, 65], but there were many companies already manufacturing them. All of the Cr/CoNi or Cr/CoNiCr processes used the DC magnetron sputtering process. Initially,

the process was done either at ambient temperature or only with moderate substrate heating. Part of the reason might have been that the Al/NiP substrate that was being used at that time could not support heating much higher than 100-150^{o}C. Using higher temperature would cause the aluminum substrate to warp, or develop heat-induced defects, and the NiP plating layer could not tolerate much heating either, as it would develop very high stresses with heat and cause substrate warping. Another factor in the difficulties faced by this process was that the Cr layer and epitaxy to cobalt alloy required a good vacuum. This was difficult to achieve with the commercial sputtering tools in the early 1980s. In addition, the Cr layer had to be relatively thick, up to approximately 100 nm or more in order to obtain high enough Hc. This caused Cr grains to be relatively large in comparison to the magnetic grains, and it affected the noise performance of the media. Without a good means to break the exchange interaction between the grains, the media was limited in terms of SNR. The circumferential texture process was also difficult to produce. Initially, the tool to put circumferential texture on the disk substrate effectively did not exist.

The key breakthrough for the Cr underlayer process was the introduction of CoCrTa alloys for the magnetic layer. It is not clear who had originally come up with this alloy, which typically had a composition around $Co_{80}Cr_{15}Ta_4$. The earliest reference to this alloy appears to be with Robinson and Howard out of IBM in 1985 [5-66]. However, it is clear that this CoCrTa alloy was being developed for perpendicular recording in mind. Another report came from Fisher et al. at Seagate Magnetic in 1986 [5-67] and in 1987 [5-68], discussing the superiority of the $Co_{84}Cr_{14}Ta_2$ alloy in comparison to $Co_{84}Cr_{16}$ or $Co_{80}Ni_{20}$. Other compositions included $CoCr_{12}Ta_2$ and $CoCr_{19}W$ [5-68]. The CoCr and CoCrTa alloys were clearly developed prior to these papers for the perpendicular application. The alloy developed for perpendicular media led directly to a better longitudinal media.

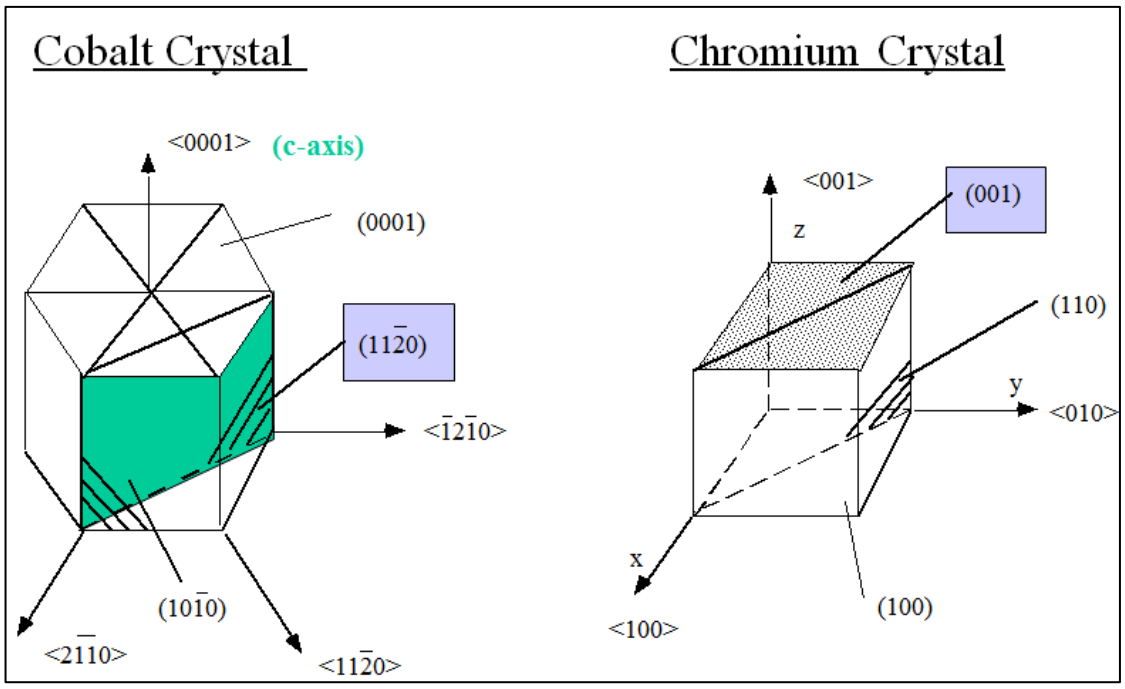

Figure 5-56: Crystal structure of Co and Cr, showing the faces that mate Co (11$\bar{2}$0) with the (001) Cr face.

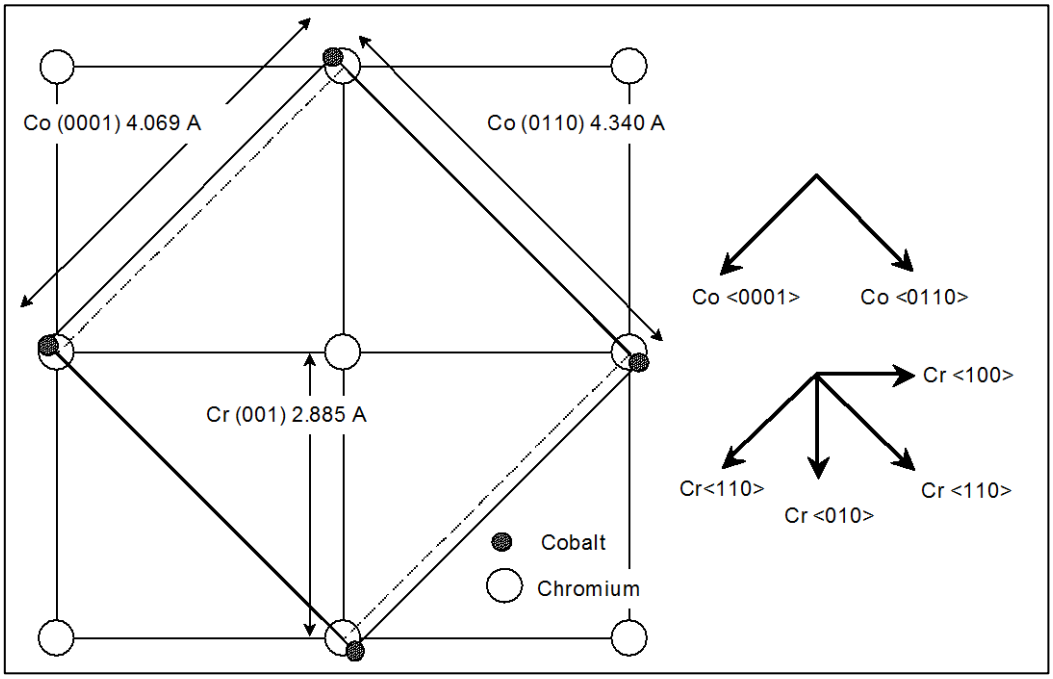

Figure 5-57: Lattice match between Co and Cr in the film plane.

IBM was clearly involved in using CoCrTa for perpendicular application, and Fisher was involved with AIM, which was a start-up company developing a perpendicular recording drive along with the media in the early 1980s. Therefore, the familiarity with the CoCr and CoCrTa alloys was already there when they began to be considered for longitudinal recording. For longitudinal application, the high Cr content used in the CoCr perpendicular application is not needed, which is to suppress Ms to keep perpendicular anisotropy. For longitudinal media, it is important to try to keep higher Ms for getting enough signals from the media, as the media thickness has to be kept as low as possible. Therefore, the Cr content for the CoCrTa alloy for the longitudinal application was scaled back to approximately 12-14 at%. There is also a folklore that says that one of the considerations was to maintain as good a corrosion resistance as possible for this alloy; the cue was taken from stainless steel which has approximately 11-12 % Cr. It is quite true that in the early period of thin film media introduction in the early 1980s, the corrosion resistance of the thin film media was a major concern. The CoP-plated media that came out prior to the sputtered thin film media was initially introduced without even a carbon overcoat, and this media suffered from very poor corrosion resistance. It also had terrible tribological performance as well, and often the two issues were considered to be related. The plated CoP gave the thin film media a bad name in the industry due to its poor corrosion performance.

The key advantage that CoCrTa alloy offered in combination with the Cr underlayer was its higher Hc capability and excellent noise properties, together with improved corrosion resistance. The microstructural analysis of CoCrTa, which might explain why it had better performance than previous CoNi and CoNiCr alloys, was not immediately forthcoming. The use of substrate heating to manipulate the properties of CoCrTa/Cr structure was not immediately obvious either. Fisher et al. reported that higher substrate temperatures reduced Hc and reported out the data to only 125^{o}C. It is more likely that they did not want to report on the effect of temperature on the media. Some substrate heating was being used on CoNi/Cr and CoCrNi/Cr, but this was mainly to increase the Cr grain size for a given film thickness, achieving higher Hc for thinner Cr. This was an important consideration because early structures required very

thick Cr thickness 100 nm or more. This necessitated frequent target changes to the sputter system and reduced machine utilization significantly. However, the heating was quite moderate to approximately 100^{o}C as Fisher had used. Another factor to CoCrTa advantage was probably because the alloy was probably easier to sputter using DC magnetron sputtering. DC magnetron sputtering requires the magnetic field to penetrate through the target to the surface. Even with very strong magnets, this was difficult to do, especially with targets that were inherently a strong magnet. Alloys such as CoPt were difficult to sputter by DC magnetron for that reason. CoCrTa in its target form was not a strong magnet, indicating that segregation taking place in the sputtered film is what causes the film to be strongly magnetic, but it is doubtful that this connection was considered at the time.

By 1990, much of the media produced had gone to the Cr underlayer process and using the orientation effect that came from the mechanical texture on the Al/NiP substrate. CoCrTa also had largely replaced the other alloys such as CoNi and CoCrNi. Other additions and composition adjustments were also being tried around the basic CoCrTa composition. The only exception was Komag, which continued to use an isotropic CoNiPt-based alloy, now with other additions to the alloy including boron and oxides. Komag also used a sputtered NixP underlayer, which was also unique. However, Komag lead a strong research effort to try to understand the fundamental nature of the CoCrTa/Cr system with collaboration with Stanford University on microstructural analysis. The key area of attention concerned the following areas:

1. Understanding the origin of the orientation effect that came from the mechanical texture and chromium underlayer.
2. Examine the grain isolation mechanism for the CoCrTa alloy, and understand its relationship to the Cr underlayer, to determine whether they are related.
3. Examine the relationship between the Cr underlayer, its structure, and grain size in relationship to the CoCrTa magnetic layer.

The purpose of these investigations was clear. The exact nature of orientation effect that came with texture and how it affected the Cr film growth was not well understood. In fact, there were significant failure modes that occurred in this process where the orientation effect was difficult to control from the texturing process itself to process issues in sputtering. It was unsure whether there was a crystallographic effect taking place in the Cr film itself or that mechanical texture imparted an effect such as magnetostriction on the magnetic layer, which was responsible for the orientation effect. Chromium film itself required further investigations because initially the chromium film had to be made very thick in order to achieve high Hc. Clearly, there were multiple grains of CoCrTa that formed on the larger base of chromium grain, and why this had to be the case needed to be understood. The objective was to make chromium grains much smaller and thinner to potentially improve the SNR of the media further, and help with the economics of sputtering. Thinner chromium would improve machine utilization and help in reducing the cost of fabrication. The third point was to understand the nature of grain boundary segregation in the CoCrTa alloy system. From previous work on this area from CoCr for perpendicular media, it was understood that some form of segregation is possible in this system. What role the Ta played, if any in the segregation process, and what material was actually in the grain boundaries that helped with the excellent SNR capability of the CoCrTa alloy, needed to be analyzed and understood.

Coming back to the role of substrate temperature on the development of the CoCrTa/Cr process, the substrate heating experiments did not show strong effects at first. It is possible that sputter system was not very well equipped to handle heating. Heating usually induce outgassing from the system, the substrate, and the substrate holders that may come out of the vacuum with each process cycle. Then, the process becomes subject to the environmental conditions inside the clean room to which the panels or carriers are exposed. In-line systems were particularly vulnerable to this type of effect, as many media manufacturers were to discover. Even the isotropic and non-chromium underlayer process that Komag had used caused significant issues in manufacturing. Very early on, Komag rigorously had to control the outside humidity of

the clean room to which the sputter panels were exposed to control the magnetic properties of the media. The chromium underlayer was much more sensitive to such factors, as it had to depend on the epitaxy between the chromium film and the magnetic layer. One critical source of outgassing was the substrate itself. The electrolessly plated NiP layer that is polished, can outgas varying amount of hydrogen depending upon the time interval between plating, polishing, and sputtering. Heating the substrate releases the gas and this had a profound effect on the epitaxy between chromium and the magnetic layer. Most media manufacturers purchased Al/NiP substrates from several vendors and the substrate undoubtedly behaved differently because each substrate vendor used slightly different plating chemistry for their process. The time interval between plating to sputter also varied. To heat substrate to ~ 200-250^{o}C, which was eventually required for CoCrTa, the NiP plated layer had to be annealed at similar temperatures for 20-30 minutes in order to outgas the NiP. This took some years to discover. Once it was realized, design and construction of the in-line continuous oven to anneal the plated disks right after plating took time to develop.

The vacuum level of the sputter system also played a role in the capability of the CoCrTa/Cr system to improve. The advent of a static single disk sputtering system in the 1990s started to improve the situation for the type of process that the CoCrTa/Cr system required. In such a system, each disk is sputtered one at a time in front of a circular target. The disk stays stationary during sputtering in a *static system*. In this manner, the disk and the target are in circular symmetry, and it is a more advantageous geometry in order to obtain circumferential magnetic orientation in the media. It was also possible to reduce the chamber size around the cathode so that a better vacuum could be maintained. In addition, the equipment vendor arranged the disk loading and unloading mechanism so that the carrier that holds the disk in the system never sees outside ambient conditions; this also reduced the chance of outgassing to only the substrate. In sputtering single disks at a time, the throughput requirement for the sputter system placed a significant burden on the mechanical system because the disks had to be moved through the system at very high speed. There were only seconds available for each sputtering station and the disk had to be moved from one chamber to another very

quickly. It took equipment vendors many years to perfect the machine capable of such mechanical motion. One notable development that should be mentioned in the context of the importance of the vacuum condition on the chromium underlayer process was the work done by Takahashi et al. at Tohoku University in collaboration with Anelva Corporation in Japan. They demonstrated that by using an *ultra-clean* vacuum condition, the chromium film thickness could be drastically reduced and still obtain high coercivity [5-69]; this pointed the way toward improving the vacuum condition in the sputter tool. Companies such as Anelva, Intevac, and Balzers created a new class of single disk static sputtering tool to take advantage of these developments to improve the deposition conditions optimized for the CoCrTa/Cr-oriented media manufacturing. Circular geometry also helped to make substrate heating more uniform as opposed to having disks loaded onto large panels. However, very high-powered and efficient heaters had to be developed, which could heat the disks from ambient to approximately 250^{o}C in a few seconds. High-powered quartz heaters and graphite heaters that could do this took some time for the equipment vendor to develop. Such rapid heating and high temperatures also caused an additional problems for the Al/NiP substrates. Aluminum substrate processing had to be adapted for such heating, and additional annealing process had to be introduced in aluminum ground substrates, similar to the situation encountered for the NiP plating. High temperatures caused stresses around intermetallic particles to pop out or form a bulge on the surface of aluminum substrates, which was reduced by high temperature anneal after the surface grounding of the aluminum substrate. Another problem that had to be solved was that NiP coating developed uneven stresses after heating, which was strong enough to warp the substrates. NiP coating can develop a surprisingly high level of internal stress after plating, of the order of hundred or two mega-Pascals [5-44]. This could be relieved by annealing the NiP in slower and more controlled fashion before sputtering. Techniques and processes also needed to be developed to control the amount of polish removal during NiP polishing so that each side of the NiP surface had the same thickness after polish to within less than a micron. A method had to be developed to precisely measure the thickness of the substrate and the NiP layer to make sure that the process stayed under control. Consequently, many issues had to be solved in order to make the most

out of the CoCrTa/Cr process, and this took many years to accomplish. Continuing improvement in the Cr underlayer also occurred, with an alloying addition to the Cr and continuing reduction in the Cr thickness so that eventually it reached a situation where one Cr grain matched one CoCrTa grain for the best-optimized noise performance.

Some of the key findings from the Komag-Stanford collaboration on oriented CoCrTa/Cr media are outlined as follows:

First, detailed TEM analysis of the preferred orientation effect in the oriented Cr/CoCrTa media was made by Nolan, Sinclair, Ranjan and Yamashita in 1992 [5-70] for the textured Al/NiP media using a Varian MDP 350 tool (predecessor tool to Intevac tool). In this work, 75nm Cr and 60 nm CoCrTa films were deposited at 225^{o}C on circumferentially textured aluminum/NiP plated substrates. Detailed analysis was made in plan view and in a cross section of the media; various TEM techniques including HRTEM and elongated probe micro-diffraction technique (EPMD) [5-71] were used to analyze the film. DF imaging of magnetic film in in plan view appears to show that the texture lines affect the local crystallography of the film. Near the texture lines, there were bright and dark stripes parallel to the texture lines and away from the texture lines, the crystallography appeared more random. The EPMD technique appears to show Co c-axis and Cr <110> axis parallel to the texture lines. However, the more careful analysis also showed less intense spots, which show the same axis perpendicular to the texture lines, which are tilted slightly out of the strong diffraction conditions. Therefore, the apparent crystallographic preferred orientation is actually coming from the local tilt of surface. The HRTEM image in cross section at the texture line also verifies that this is taking place. It was speculated that observed magnetic anisotropy comes from tilting away of the surface for Co $(11\bar{2}0)$ direction at the texture lines.

The effects of various sputtering conditions on Cr underlayer and a magnetic layer consisting of CoCrTa and CoNiCrPt alloy was made by Nolan, Sinclair, Ranjan

and Yamashita in 1993 [5-72]. In this work, an Intevac static sputter tool was used to obtain oriented Cr/magnetic layer films and the relationship between sputtering conditions and the degree of orientation in Cr and the magnetic layer, and their morphology was made. It was found that CoCrTa film had better epitaxy, and grain boundary separation compared to CoNiCrPt film, and the effect was attributed to a better lattice mismatch with Cr for CoCrTa. Higher substrate temperatures up to 250^{o}C were also used and clearly, the segregation effect in CoCrTa was evident. More detailed crystallographic analysis of the CoCrTa, CoCrPt, and CoNiCrPt deposited on Cr underlayer was reported by Nolan, Sinclair, Ranjan, and Yamashita in 1993 [5-73]. In this work, 60nm thick films of $Co_{84}Cr_{14}Ta_2$, $Co_{76}Cr_{12}Pt_{12}$, and $Co_{75}Ni_7Cr_6Pt_{12}$ alloys were deposited on a 150nm thick Cr underlayer using a Varian MDP 350 static sputtering tool. SNR measurements clearly showed the difference in noise performance between these alloys, with 33.9 dB for CoCrTa, 31.6 dB for CoCrPt and 29.3 dB for CoNiCrPt, at 20 kfci. The difference in SNR was attributed to degree of epitaxy present between the magnetic layer and the Cr layer. In addition, the CoCrTa showed the best evidence of grain boundary isolation. In these films, there were multiple cobalt grains growing on top of Cr grains, as shown in Figure 5-58 [5-74]. In this work, the $Co_{84}Cr_{12}Ta_4$ alloy was sputtered at a series of Cr thicknesses at 20, 60, and 75nm, thickness and substrate temperatures from 25^{o}C to 275^{o}C in roughly 25 to 50^{o}C increments. Samples were sputtered using an Intevac MDP 250 static sputtering tool.

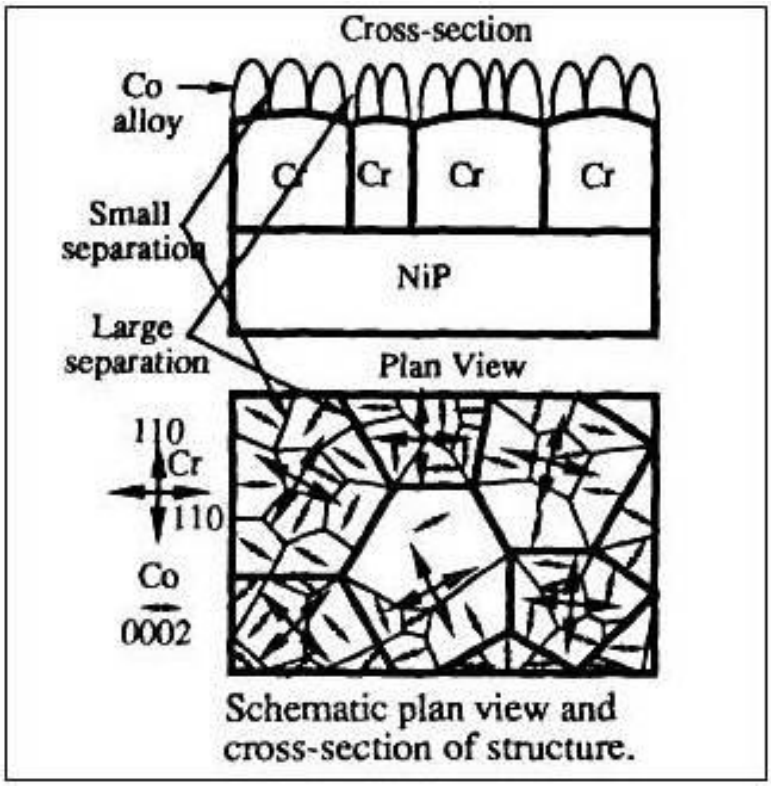

Figure 5-58: Schematic microstructure of media showing clusters of Co alloy grains (thin lines) with (0002) axes parallel to the (110) axes of the Cr grains (thick lines). From Ref. [5-74], MRS Online Proceedings Library, Cambridge University Press, reproduced with permission.

An additional microstructural and recording performance comparison for $CoCr_{12}Ta_4$/Cr media was made, this time sputtered in an in-line deposition tool, by Ranjan, Bennett, Tarnopolsky, Yamashita, Nolan, and Sincalir in 1994 [5-75]. The effect of substrate temperature on magnetic properties, recording performance, and microstructure were compared. The magnetic properties and recording performance are shown in Table 5-7. As the substrate temperature is raised to 250^{o}C, the performance of the media steadily improves. This is associated with higher Hc and a higher orientation ratio. For the recording measurement, thin film head was used, with pole and gap lengths p1/g/p2 = 3.35/0.35/3.35 μm, leading and trailing pole widths of 15 and 12 μm, respectively, and 30 turns on the inductive head. Flying height was 3.6 μ-

inches (91.44 nm) at a velocity of 7.52 m/sec. Transition noise (TN) and uniform magnetization noise (UMN) power spectral densities (PSD) were acquired using a spectrum analyzer. At each frequency, the total TN power was obtained by subtraction of the background noise and integration of the PSD. UMN raw spectra were acquired and analyzed in the frequency interval of $0.15 < f < 15$ MHz corresponding to a wave number $k = 2\pi f/\upsilon$ interval $0.12 < k < 12\ \mu m^{-1}$. UMN has been shown experimentally and theoretically to reflect magnetostatic and exchange properties of the film [5-76, 77, 78]. CL is the correlation length, which is the down-track autocorrelation function of the PSD. The UMN at lower substrate temperatures is deceiving because of low Hc. At higher substrate temperatures where high Hc is obtained, the UMN and TN are improving, and it is best at $250^{o}C$.

The grain boundary segregation effect in CoCrTa media was clearly demonstrated using nan probe energy dispersive spectroscopy (EDS) and energy filtered imaging (EFTEM) by Wittig et al. [5-79]. EDS was performed on Philips CM20ST-FEG TEM operating at 200 KeV. EFTEM imaging was done at 300 KeV using a Philips CM30T and a Gatan image filter (GIF). Using these methods and the microscopes, chemical analysis is possible with a spatial resolution of approximately 1.5 nm. Figure 5-59 shows the EFTEM chemical image for Cr and Co, showing the complementary image of Cr segregation into the grain boundary. Compositional analysis across the grain boundary is also possible in 1nm increments using this technique. Such a line scan across the grain boundary is shown in Figure 5-60. There is substantial Cr segregation at the grain boundary, but Ta remained the same. Therefore, it was speculated that Ta aids the diffusion of Cr to the grain boundaries but by itself, it is not a segregant.

T (°C)	$M_r t$ (memu/cm^2)	H_c (Oe)	S^*	ΔH (Oe)	OR, M_r	TN (arb. units)	UMN (nm)	CL (μm)	α (μm)
25	2.69	553	0.83	92	0.97	1.301	30	1.0	0.23
100	2.69	615	0.80	133	0.98	1.361	37	1.1	0.22
150	2.74	935	0.90	115	1.13	1.741	55	1.7	0.17
200	2.71	1450	0.89	200	1.43	0.755	29	1.7	0.15
225	2.68	1630	0.87	232	1.43	0.616	30	1.6	0.14
250	2.66	1773	0.84	340	1.34	0.54	22	1.6	0.13

Table 5-7: Tabulation of magnetic properties (VSM) and recording measurements for various samples sputtered at different substrate temperatures, from 25°C to 250°C. From Ref [5-75], J. Appl. Phys. AIP Publishing LLC, reproduced with permission.

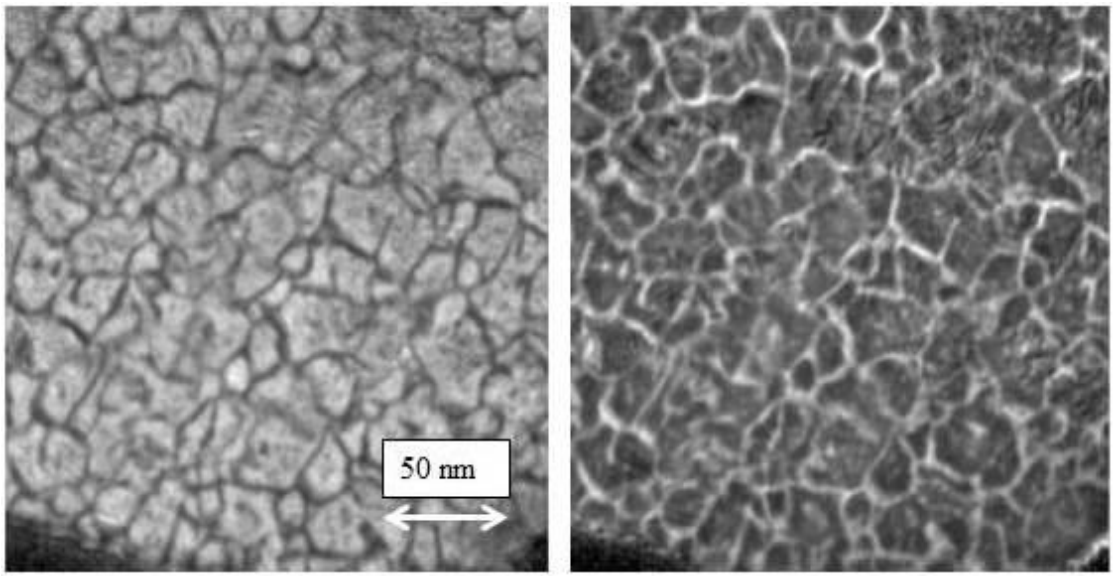

Figure 5-59: Energy filtered images of a) Co and b) Cr from $Co_{84}Cr_{12}Ta_4$ / Cr media, sputtered at 250°C substrate temperature. From Ref. [5-79] by Wittig et al., MRS Online Proceedings Library, Cambridge University Press. Reproduced with permission.

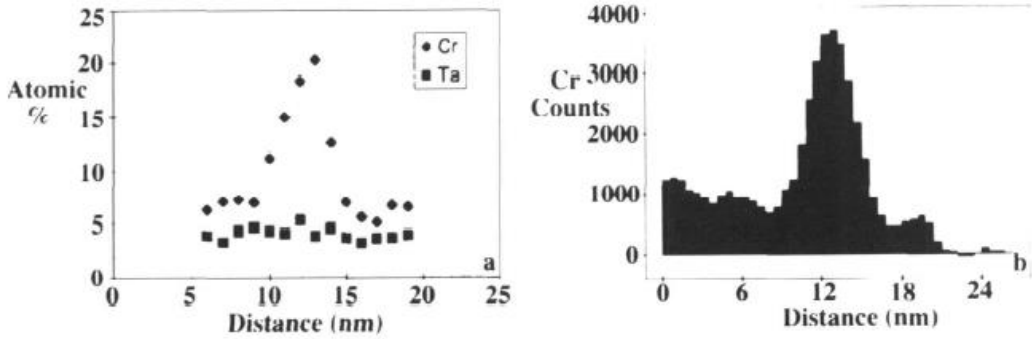

Figure 5-60: Line profiles of compositional structure by a) nanoprobe EDS and b) EFTEM, showing similar segregation to the grain boundaries. From Ref. [5-79] by Wittig et al., MRS Online Proceedings Library, Cambridge University Press, reproduced with permission. Reproduced with permission.

In conclusion, to this section on CoCrTa/Cr media, continual improvement in the media system occurred with better understanding of the source of its performance, which eventually led to this alloy system becoming the winner in the media design. Even Komag eventually had to concede, and they switched to the Cr underlayer process by 1997. By then, the knowledge gained in the alloy system also allowed the in-line system to produce a media product comparable to the static system that was beginning to dominate the industry. However, the in-line system required extensive modifications by installing significant vacuum pumping capacity and the means to pump out the panels much more thoroughly before the disks were sputtered. By the year 2000, the coercivity capability of the CoCrTa alloy had run its course, and Pt had to be added to the alloy. The addition of Pt significantly degraded the epitaxy of the alloy to the Cr underlayer. In addition, the segregation potential of the alloy was degraded. This was shown earlier in the description of Pt alloys when compared to CoCrTa. These issues were solved rapidly by the industry, as the issues were quickly understood. At Komag, the epitaxy issue was solved by introducing a thin layer of CoCrTa film deposited at a low deposition rate to help seed the epitaxy, followed by a thick CoPt-X magnetic layer [5-80]. Earlier, there were publications on double magnetic layer media consisting of a Cr/CoCrTa/CoCrPt structure, which helped to increase Hc and the orientation ratio of the CoCrPt film [5-81, 5-82]. However, in these examples, the CoCrTa first layer was a significant fraction of the total thickness, such as 1/4 or 1/8 of the total magnetic film thickness. In either case, the thickness of the CoCrTa layer was approximately 5 nm. The Komag solution used CoCrTa composition close to the CoCrTaPt top magnetic alloy, and CoCrTa was sputtered at very low rates of less than 0.1 nm/sec and film thickness was below 1.5 nm or even much thinner. Such deposition conditions and low rates combined with very low thickness for CoCrTa film were aided by improved vacuum conditions in the sputter system. Typical compositions of the alloys used were $CoCr_{16}Ta_4$ and $CoCr_{15}Ta_4Pt_5$. The substrate temperature at Cr deposition was 220^{o}C. Thicknesses were 19.5 nm for the CrV_{50} layer, CoCrTa was 0.5 nm, and the CoCrTaPt layer was 23.0 nm for MrT of approximately 0.95 memu/cm^2. The segregation problem with Pt addition in the alloy was solved by the addition of boron to the target. This was the method practiced by Komag for the

isotropic Pt alloy media for many years prior to the introduction for use in oriented media. Boron addition to the alloy allowed continuation of a vacuum induction melting (VIM) method to be used for the magnetic target. This was because the boron is in solid solution in the melt over wide composition range as seen in the Co-B phase diagram of figure 5-43. The target could be quenched quickly from the liquid phase in order to preserve the even distribution of boron inside the target.

The extent of grain isolation obtained in the early 2000 timeframe is shown in figure 5-61 for CoCrPt-B film with a boron concentration of ~10 atomic%. The film also made use of exchange coupling to increase the thermal stability of the media using the anti-ferromagnetic coupled media (AFC) concept [5-83]. In such media, a thin Ru layer is inserted between the magnetic media and two magnetic layers are antiferromagnetically coupled. This has the effect of helping with the switching of the media, even with higher Hc. This became very important in that grain size was being reduced significantly in order to improve SNR with higher recording density, and the media was starting to exhibit a superparamagnetic decay effect, where the thermal fluctuations in the media would slowly degrade the magnetization. This had started to cause enough of a concern so that the drive had to resort to re-writing the data periodically in order to refresh the data on the disk. Otherwise, the data would degrade slowly in the drive, particularly if the operating temperature of the drive was high.

Typical grain size and appearance at the end of the longitudinal media application in the mid- to latter 2000s is shown in figure 5-62. The extreme nature of the grain isolation being used during 2005 is evident. The alloy used up to ~15 atomic% boron along with Cr to isolate the grains and achieve very small grain size. The last longitudinal media achieved an areal density of over 100 Gb/in^2.

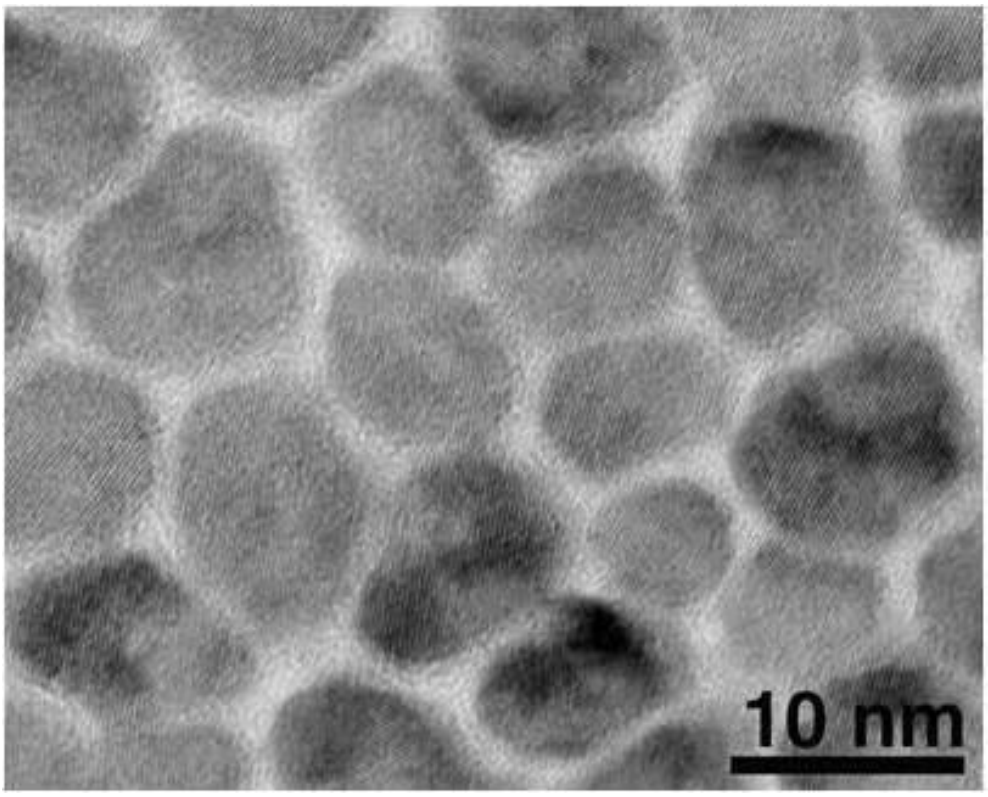

Figure 5-61: Grain boundary isolation in CoCrPt-B longitudinal media using boron as a grain boundary segregant.

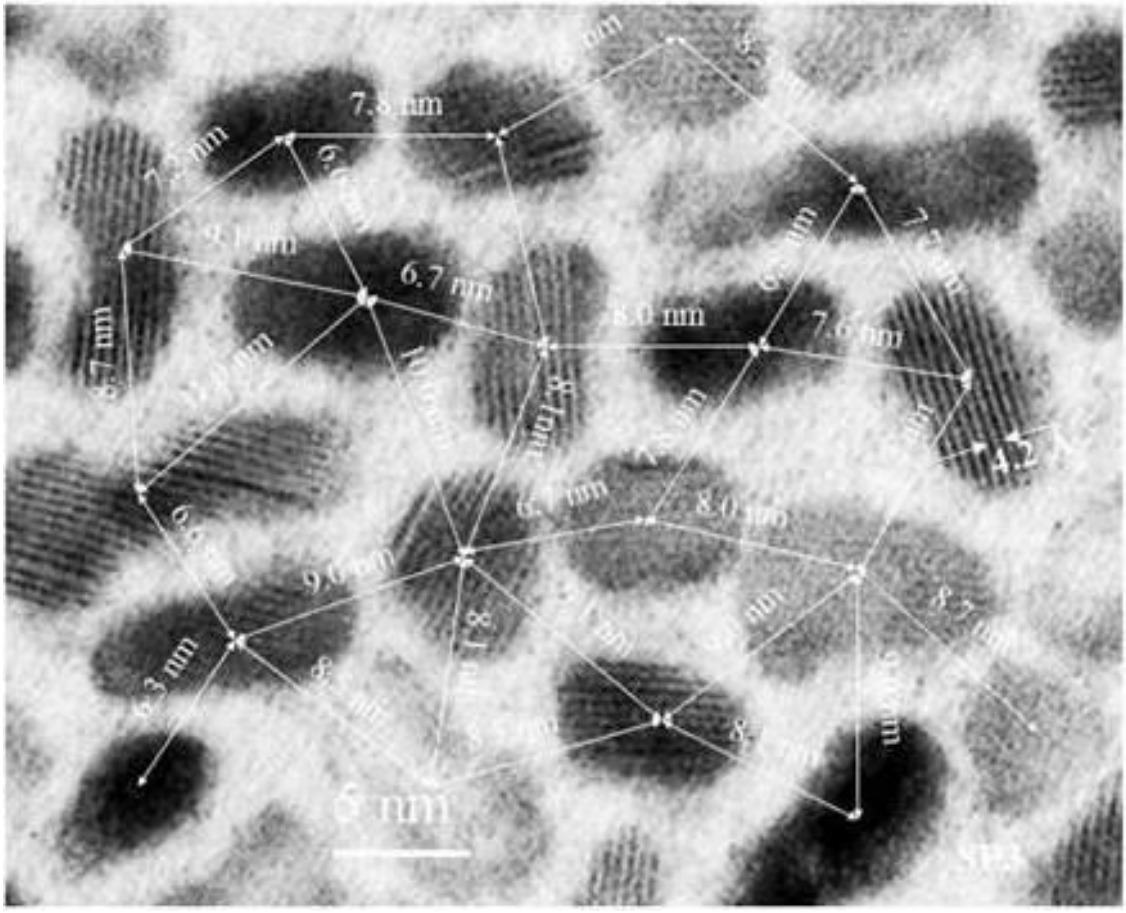

Figure 5-62: Grain boundary isolation in CoCrPt-B longitudinal media using high boron content as grain boundary segregant. Arrows indicate grain-to-grain separation distance, which can be used for the purpose of modelling. (Courtesy of Gerardo Bertero).

5.6.2 Source of Magnetic Orientation Effect in Oriented Media

The argument about whether the magnetic orientation effect was due to the crystallographic alignment of the c-axis of the magnetic layer along the circumferential direction of the texture, continued to dog the industry. The situation was complicated by the Hedgcoth patent, owner of which had staked the claim that orientation comes from a crystallographic alignment of the c-axis along the texture direction. Those companies fighting the patent had wished the effect was from something else. Whether

it was due to the litigation or not, two camps of thought emerged as to how to explain the orientation effect. One camp thought that the effect was indeed due to the crystallographic orientation of the c-axis. The second camp thought that it was due to some other phenomenon taking place, and the most likely candidate was due to stress. TEM and X-ray diffraction were the primary means to try to determine the cause, but the results remained inconclusive for a while. An excellent review article on the issue of orientation in the media was published by Johnson et al. They took the position that the orientation effect is more likely due to stress than to crystallographic orientation of the c-axis, based on several observations and arguments [5-84]. The stress argument had a strong case based on observations made on in-situ of the VSM measurement of several cobalt alloy films that were stressed during measurements [5-85]. Films in compression and in tension show a striking resemblance to the oriented media hysteresis loop as shown in Figure 5-63 for Co film. This behavior with stress is due to the negative magnetostriction coefficient for Co and for most CoCr and CoPt alloys below 20 atomic% Pt. Based on this paper then, we also proposed at that time that the orientation effect in CoCrTa/Cr film is likely due to differential stress that develops in the magnetic film. It was theorized that Cr grains develop anisotropic strain, and the effect is transmitted to the cobalt grains. It was also supported by initial HRTEM analysis, which showed random c-axis orientation in the plane of the film. Alternatively, the crystallographic orientation camp relied on X-ray diffraction data, which suggested that there was a preference for c-axis to be aligned along the texture direction. Since some of these data were collected for the purpose of supporting one side or the other in litigation preparation, business and financial considerations and interests colored people's opinions about the proper interpretation of the data that was being collected.

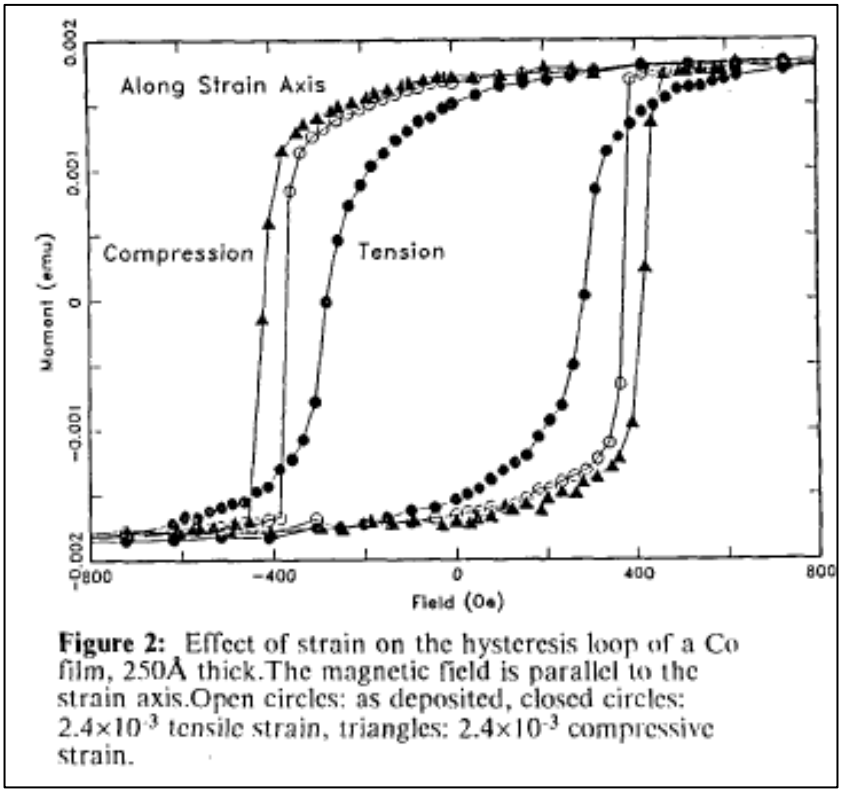

Figure 2: Effect of strain on the hysteresis loop of a Co film, 250Å thick.The magnetic field is parallel to the strain axis.Open circles: as deposited, closed circles: 2.4×10^{-3} tensile strain, triangles: 2.4×10^{-3} compressive strain.

Figure 5-63: VSM hysteresis loop for sample under compression and tension. from From Ref. [5-85], Mauri et al. .

Copyright © 1990, IEEE, Reproduced with permission

In the early 1990s, Komag was not manufacturing oriented media, but for historical reasons related to Tu Chen's personal interactions with the oriented media process in the early 1980s, Komag was firmly in the stress explanation side of the argument. Despite this situation, some of our own data showed conflicting results, where HRTEM imaging seems to show random orientation of the c-axis, but other more conventional TEM analysis, such as dark field imaging and elongated probe micro-diffraction, did show evidence for crystallographic c-axis orientation by Nolan et al. [5-70]. In this work, the evidence strongly pointed toward crystallographic orientation, at least close to the texture line. Due to the observation that, away from the texture lines, the orientation appeared to be more random or the c-axis actually oriented

perpendicular to the texture line, and it was concluded that much of the apparent c-axis orientation effects (along the texture line) was an artifact of the out-of- plane orientation of many grains along the texture lines. It was akin to the sort of effects seen when the specimen is slightly tilted, which can give the impression of the crystallographic orientation of the grains in the film.

By the mid-2000's, the timeframe when Komag had completely switched most of the production to the oriented media, opinion had switched again to lean more toward the crystallographic explanation. In addition, by this time, the patent suit issue with Hedgcoth had been largely settled as well. Continuation of more careful TEM analysis showed that there is indeed some preference for c-axis of the cobalt alloy grains to orient along the texture line, again, a stronger effect seen closer to the texture line as discovered earlier by Nolan et al. It was still difficult to quantify the results, but the tendency was clear. By this time, the mechanical texture had become so smooth and flat so that the argument based on out-of-plane orientation of the grains could no longer be made. The analysis also suggested that the Cr film also has the same tendency, which is to say that Cr <110> direction is also aligned preferentially along the texture direction. There is another set of Cr<110> direction perpendicular to the texture line with which the c-axis can also align. However, the stress in the Cr layer does play a role, and it seems to be favoring the c-axis alignment along the texture line more. The HRTEM image that shows this effect is shown in figure 5-64 showing BF and HRTEM images of the oriented media.

As mentioned earlier, the mechanical texture had become very smooth by 2005 due to the use of extremely fine diamond slurry with a particle size of only ~10 nanometers in diameter. Cross section TEM micrograph shown in figure 5-65 shows the very subtle nature of the texture; yet, the orientation effect was still quite strong. Out-of-plane effects, affecting the diffracting conditions of the grains could no longer be applied. The Cr grains were growing with some crystallographic preferred orientation as evidenced by their "square" morphology along the texture direction as seen in figure 5-66. Clear evidence of preferred crystallographic orientation for the Cr

layer was never collected, but the shape of the chromium grain was clear enough evidence. The fact that only one set of Cr <110> direction was being picked by the c-axis of the Co grains suggests that stress in the Cr film might be favoring one over the other. In conclusion, it appears as though both stress and the crystallographic contribution are responsible for the oriented media effect in the Cr/CoCrTa-X system.

It should also be mentioned in passing that the NiP substrate material itself played an important role in the orientation effect. It was only NiP that exhibited the orientation effect with texture. Texturing glass for example, does not give preferred growth for Cr film. Briefly, some other materials such as amorphous NiNb alloy were tried, and the orientation effect was not so strong (unpublished result). Additionally, the orientation effect was very sensitive to the surface property of the NiP itself. For example, the cleaning process prior to sputter could affect the orientation effect. The amount of time that the substrate sat in the air before sputtering and the subtle oxidation effect or presence of some surface contamination had a significant detrimental effect on the orientation effect. These environmental and surface effects were clearly becoming much more sensitive as the texture roughness was steadily reduced and the exact nature of this effect was never elucidated, and very little of these observations were ever published. Such issues were left undiscovered as the industry moved away from longitudinal recording using orientated media to the perpendicular recording, which did not use a texture or require orientation along the texture.

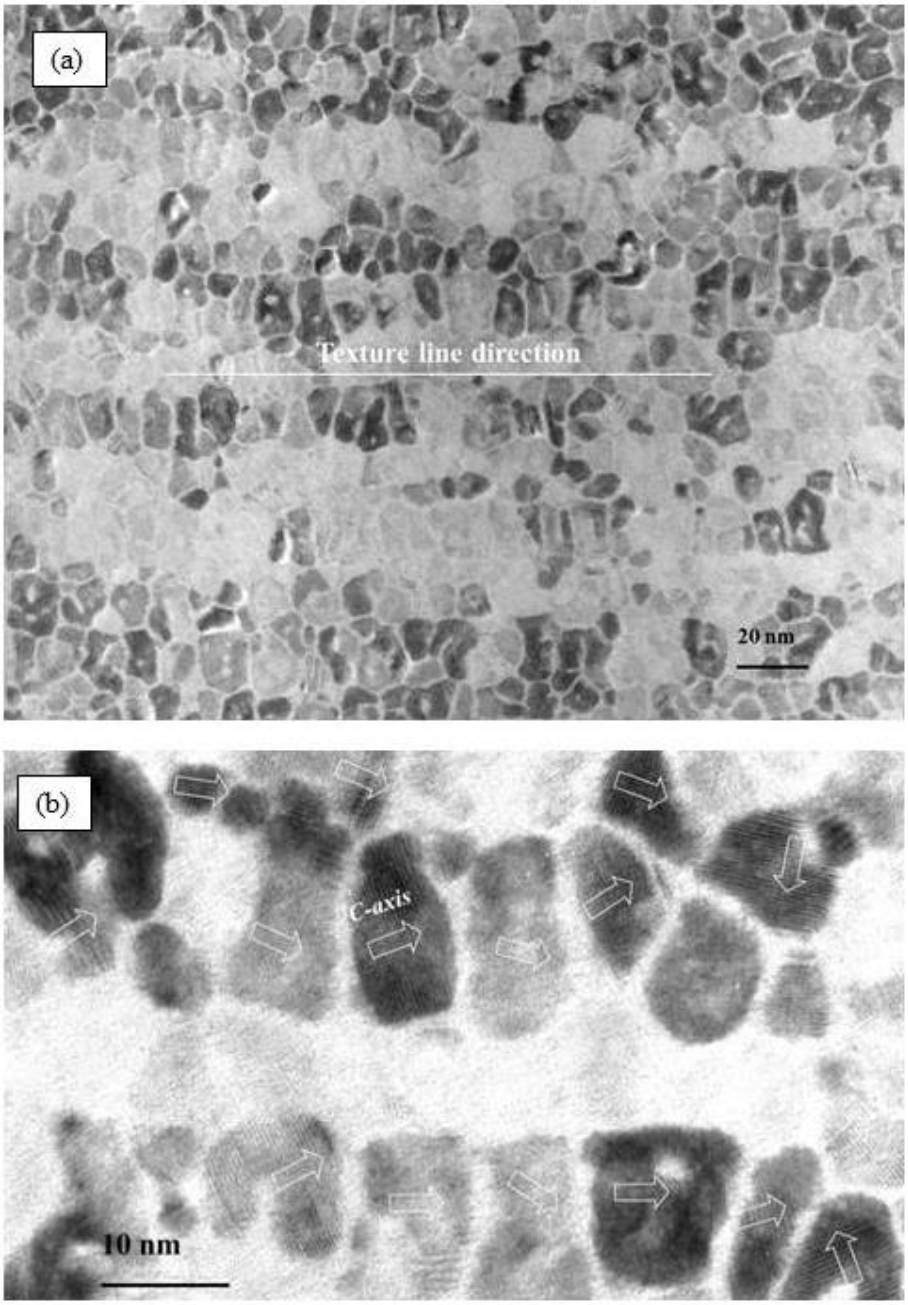

Figure 5-64: (a) is a BF image of oriented media, showing the preference for grains along the texture line to diffract together, indicating preferential alignment. (b) is an HRTEM image of cobalt grains near the texture showing the direction of the c-axis, which are pointing generally on one direction. (Unpublished results: Komag Inc.)

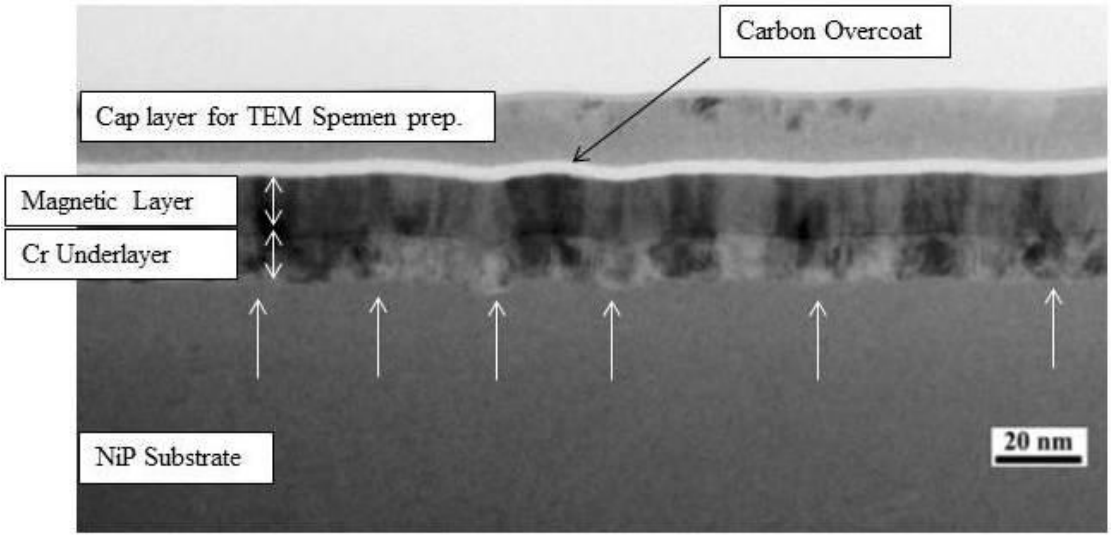

Figure 5-65: Cross section BF TEM micrograph of oriented CrX/CoCrPtTaX alloy media. Arrows indicate more obvious region of mechanical texture but other finer texture lines are not visible in cross section. Actual orientation effect seen in Cr and Co layers are on a finer scale than indicated by arrows.

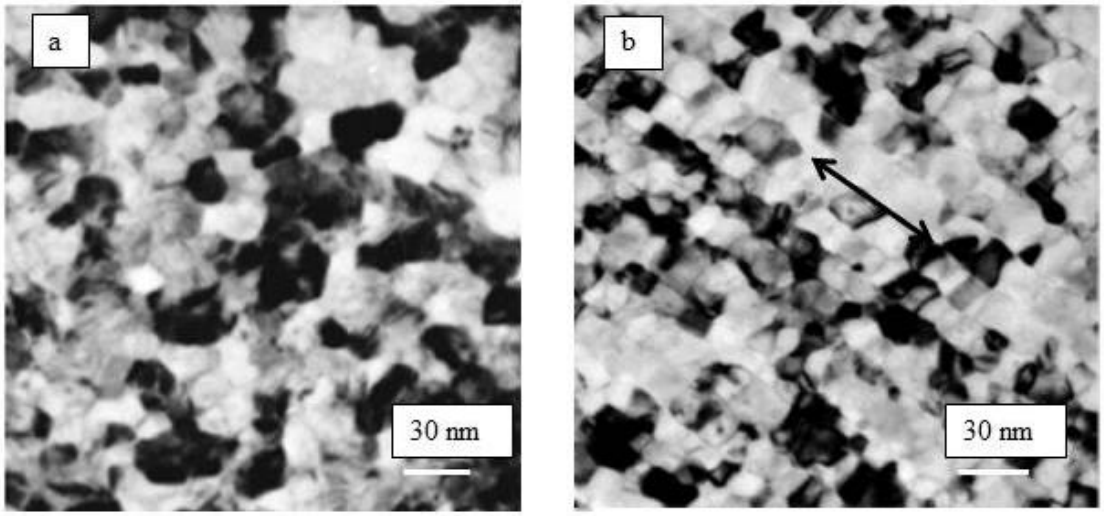

Figure 5-66: BF TEM micrographs of $CrMo_{15}$ alloy underlayer by itself, 15 nm thick. (a) is an untextured substrate where Cr grows randomly, while (b) is with mechanical texture. Note the square shape of the Cr grains. The arrow indicates the direction of the mechanical texture.

5.7 Perpendicular Media

As previously discussed in section 5.5, perpendicular magnetic recording received considerable attention initially in the early 1980s, but it was all but dead within a few years. It lay largely dormant until early 2000, a period of approximately 20 years. The reason for its resurrection was due to several factors, but the main problem was with the longitudinal media. The need for higher recording density pushed on by the introduction of MR head followed by GMR head was pushing the limit of magnetic recording. Thermal stability became a big issue as film thickness was pushed down as the great sensitivity of the GMR head allowed the benefit to be gained from thinner media. At the same time, grain size was reduced to keep up with smaller bit size in order to maintain good SNR. However, the amount of magnetic material present in the bit was approaching the superparamagnetic limit due to the reduction in total volume of material in each grain. The situation was eased for a few years by the introduction of antiferromagnetically coupled media or AFC media, where the antiferromagnetic coupling between two magnetic layers helped to stabilize the thermal stability issue [5-83]. Using the AFC media structure helped to maintain writability without having to push up the Hc in an effort to keep the thermal stability intact. The head field capability was already at the limit of the material being used in the pole of the recording head. An industry consortium that had formed over many years, the NSIC group, which met regularly every year to set the course of the industry and fund university research in magnetic recording technology decided in 2000 to propose perpendicular recording as a solution because of the limitation being faced by longitudinal recording [5-86]. Unlike the situation in the early 1980s, this time most of the industry participants in the disk drive industry were behind the decision and concerted effort was now put on developing the perpendicular magnetic recording technology. This was crucial since everyone had to be on board for such an important change to take place in the fundamental technology for magnetic recording. Considerable work was required for the head, channel, and the media to make it all happen.

The initial strategy for the media was to pick up where things were left earlier, but with the knowledge gained over the past 20 years, which was to incorporate the particle isolation scheme that was learned and applied to the longitudinal media. The longitudinal alloy that had been in use was initially tried by everyone. The difference was to use a different underlayer, which promotes perpendicular growth of the film. Material such as Ti or Ta or amorphous films generally worked well to orient the media into perpendicular orientation. There was a general tendency for the longitudinal media to develop the perpendicular growth direction, which helped. One key difference from the past CoCr experience was that the magnetic layer could now be much thinner, on the order of 100-150 nm thick compared to being over 1μm thick in the past. In this respect, the situation was considerably different from in the past because the past knowledge about obtaining perpendicular growth in the thick film was no longer relevant. The new perpendicular media must develop its perpendicular orientation much quicker while the film was still very thin. When the media is as thick as 1μm, it was easier to obtain good perpendicular growth for most of the film thickness but not at the initial 100 nm of the film.

When the longitudinal CoCrPtB alloys were turned perpendicular, a significant issue was discovered to which there was no immediate solution. This was the fact that nucleation field or Hn, which is the field at which the media saturates, was at positive field (in the first quadrant of the hysteresis loop), which was actually always the case with CoCr perpendicular films. The situation is illustrated in figure 5-67 showing the typical perpendicular hysteresis loop for conventional longitudinal media alloy composition turned into perpendicular media using the Ru underlayer. It can be seen that Hn is in the first quadrant of the hysteresis curve, or Hn is positive. This turns out to cause a significant SNR problem for high-density recording that was now being attempted for the perpendicular media. This situation arises because the anisotropy, Ku of the media is not high enough to support the magnetization perpendicular to the film. The amount of Cr and boron needed to isolate the grains in longitudinal media reduced the Ku sufficiently so that it was causing many grains to start switching when the applied field was released. Largely due to this issue, the perpendicular media failed to

beat out longitudinal media in areal density capability for a long time. There were other designs for perpendicular media involving Co/Pt multi-layers, which had a square perpendicular hysteresis loop, with large negative Hn. Superlattice structures were investigated for many years, but such structure would have been difficult to fabricate in manufacturing. Additionally there was no easy way to introduce granular separation into the superlattice structure in order to reduce exchange. Another design proposal included FePt with $L1_0$ structure, but this required an extremely high substrate temperature of over 400^{o}C to produce. This material was not ready for manufacturing, and neither were the substrates that could take such temperatures. Many researchers working on FePt grossly underestimated the ability of the industry to change the substrate material, where hundreds of millions of dollars of investments are needed to change a substrate to the entirely new material. There were other proposals such as the CGC media or coupled-granular-continuous perpendicular media [5-87], which was the combination of multi-layers with the conventional perpendicular media on top in order to provide negative Hn and AFC-like features built into the media. This structure also called for a complex sputtering chamber capable of depositing multi-layers in a production tool. A valiant attempt was made to commercialize such structure, but it turned out that recording performance was no better than a more conventional approach, which ultimately won out.

The breakthrough in media design came from the Toshiba group, which proposed a CoCrPt-oxide-based perpendicular media on top of the Ru underlayer [5-88]. The oxide magnetic media was quite similar in concept to the Komag longitudinal isotropic media. The hysteresis loop of perpendicular media based on this structure is shown in figure 5-68. Now, the Hn is in the second quadrant, with a negative value. The hysteresis loop now resembles the Co/Pt multi-layer hysteresis loop. The noise property of this oxide perpendicular media is quite good, and it is based on the isolation between grain boundaries that comes from the oxide phase. The deposition is now done at room temperature, as this alloy system actually cannot take the high temperature. Conventional substrates such as Al/NiP or glass substrates easily can be used as-is in this process.

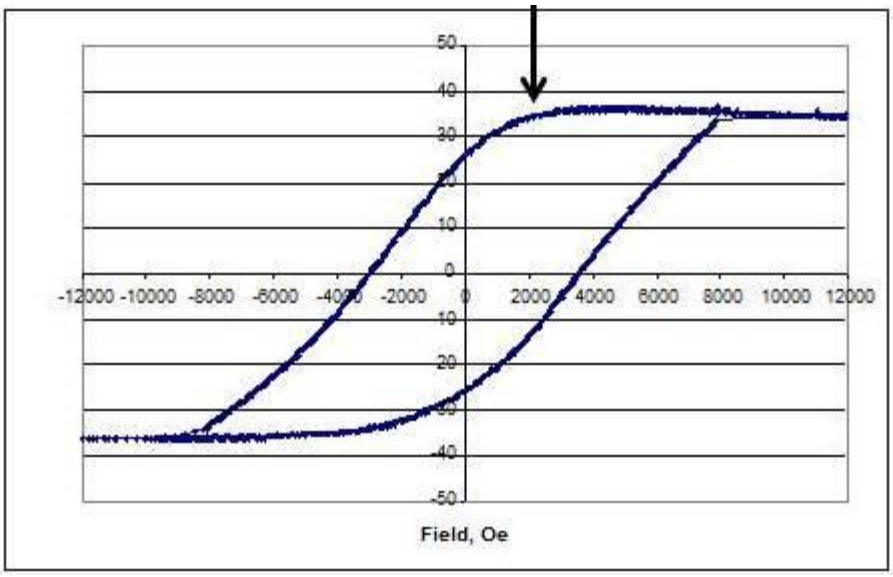

Figure 5-67: Perpendicular hysteresis loop for Ru/CoCrPtBt perependicular media, showing where the Hn, the nucleation field is positive, in the first quadrant (arrowed).

The first commercial perpendicular HDD based on this new media design was introduced by Toshiba in 2005. By 2010, nearly 100% of the magnetic thin film media used in the HDD industry was perpendicular, and 100% of the media used a CoPt-oxide-based alloy. Also, 100 % of the media made today use static sputtering systems, made by either Anelva or Intevac systems. As previously mentioned, these systems use DC magnetron cathodes. Perpendicular media use many more film layers compared to the longitudinal media. Use of soft underlayer (SUL) was difficult to sputter because the magnetic field from the cathode would be shunted. A new cathode had to be designed with extremely strong magnets. Extensive modifications in the form of additional chambers and new cathodes had to be invested in by the industry in order to be able to manufacture perpendicular media. The cost of such investment ran into hundreds of millions of dollars.

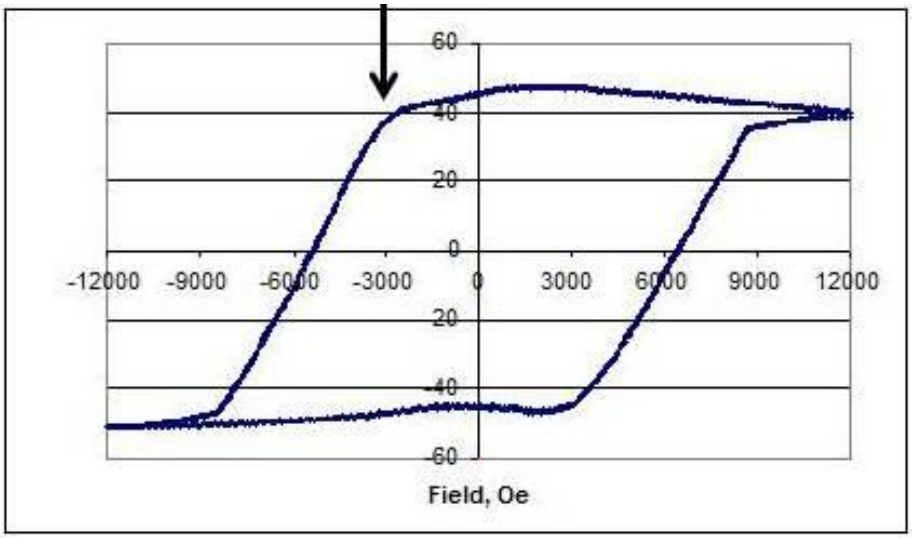

Figure 5-68: Perpendicular hysteresis loop of CoCrPt-(SiO_2) media with negative Hn nucleation field. The arrow shows the H_n in the second quadrant of the hysteresis loop.

Change to perpendicular recording also had a big impact on target manufacturing. It was no longer possible to make magnetic targets containing oxide phase by vacuum induction melting (VIM) method anymore. Therefore, the entire industry reverted or converted to the use of powder metallurgy to make the target. By this time, the hot press technology has advanced significantly so that greater press pressure could be applied toward pressing the target. Temperature control around the press has advanced as well; therefore, the expensive HIP process was no longer required. Additionally, some vendors made use of the cold HIP process to attain full theoretical density after hot pressing. The cold HIP tool could be much smaller, and they are more suited for the smaller sized circular targets that are used in static sputtering tools. The powder metallurgy technology was another difficult issue that the target vendors had to master. Since using DC magnetron was a prerequisite for obtaining the fast deposition rate needed for though-put for static tools, the target had to become capable of sputtering with DC magnetron cathodes, even with oxide phases.

Considerable effort went into making the powder mixture as fine as possible so that oxide phases could be sputtered without causing spitting, which induces a large number of defects in the disk. A large shake-out occurred in the target manufacturing industry to go from VIM to hot press and to develop the necessary powder metallurgy expertise to be able to make the CoPt-oxide targets that the industry could use.

An image from the in-plane BF TEM micrograph of a typical CoCrTaPt-(SiO_2) perpendicular media from 2003 was under development is shown in figure 5-69. The SiO_2 content in this films was approximately 10 atomic %. Later, other oxides were used. It can be seen that the appearance of the media is strikingly similar to the longitudinal isotropic media, which used oxides, as shown previously in figure 5-48. Current perpendicular media structure, as seen by cross section TEM is shown in figure 5-70, and schematic representation is shown in figure 5-71. Either glass or aluminum/NiP substrate can be used. The substrate surface is polished to the 0.1–0.2 nm level of Ra smoothness. Glass substrates are used predominantly in mobile drives with 65mm diameter glass, while 100% of the desktop drives use aluminum/NiP substrates with 95mm diameter. Special drives with several sub 95mm diameter used in servers and high-end applications use both glass and aluminum substrates. Both the magnetic layer and soft underlayer (SUL) use the thin Ru layer to form an antiferromagnetically coupled structure. The magnetic layer is for improved writability with high Hc, while, for the SUL, the exchange coupled structure is used to avoid domain formation in the film. A detailed description of each layer is listed in Table 5-8.

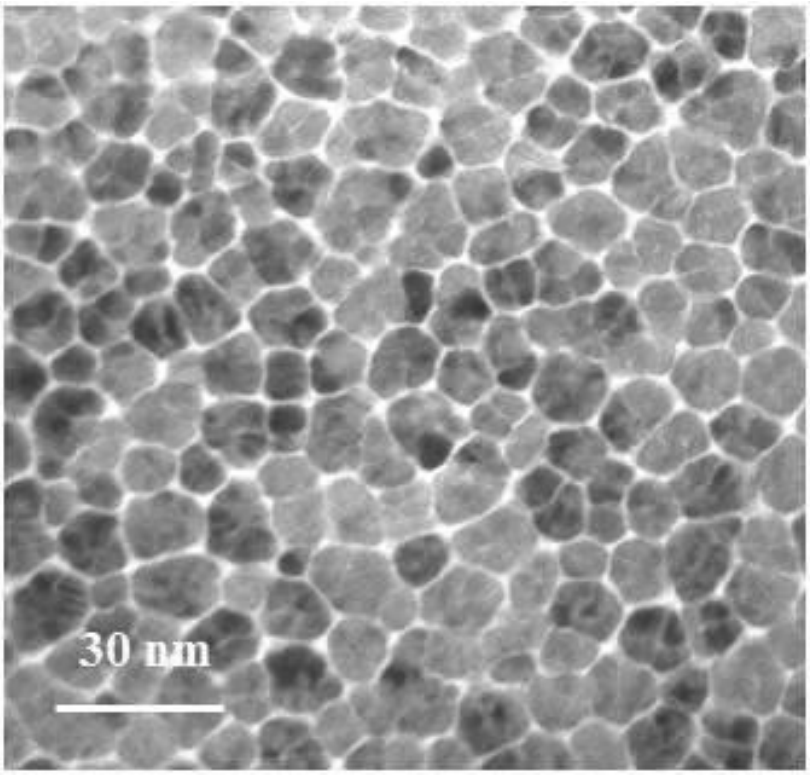

Figure 5-69: In-plane TEM micrograph of the CoCrTa-(SiO_2) perpendicular media. Film thickness ~ 16 nm. Grain to grain isolation is achieved through oxide segregation at the grain boundaries.

In 2010, the Ninth Perpendicular Magnetic Recording Conference (PMRC) was held in Sendai Japan, and in large part, the conference was to honor Professor Shun-ichi Iwasaki for the initial promotion of perpendicular magnetic recording. He had won the prestigious Japan Prize for 2010, which is bestowed by the Emperor of Japan. This was quite a turnaround for a technology that was left for dead after its initial burst of interest in the early 1980s.

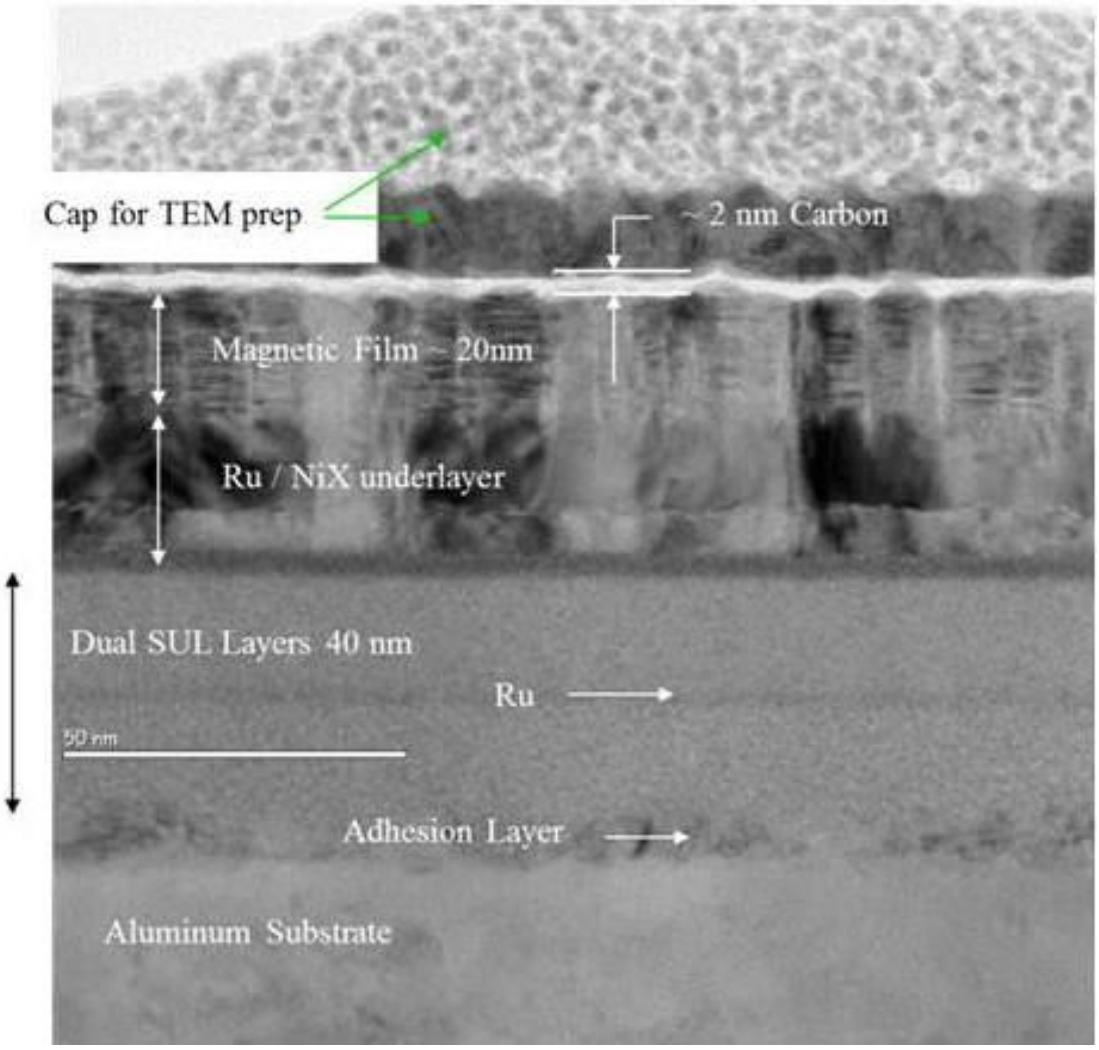

Figure 5-70: Cross section TEM micrograph of typical PMR media used in the industry, showing various layers.

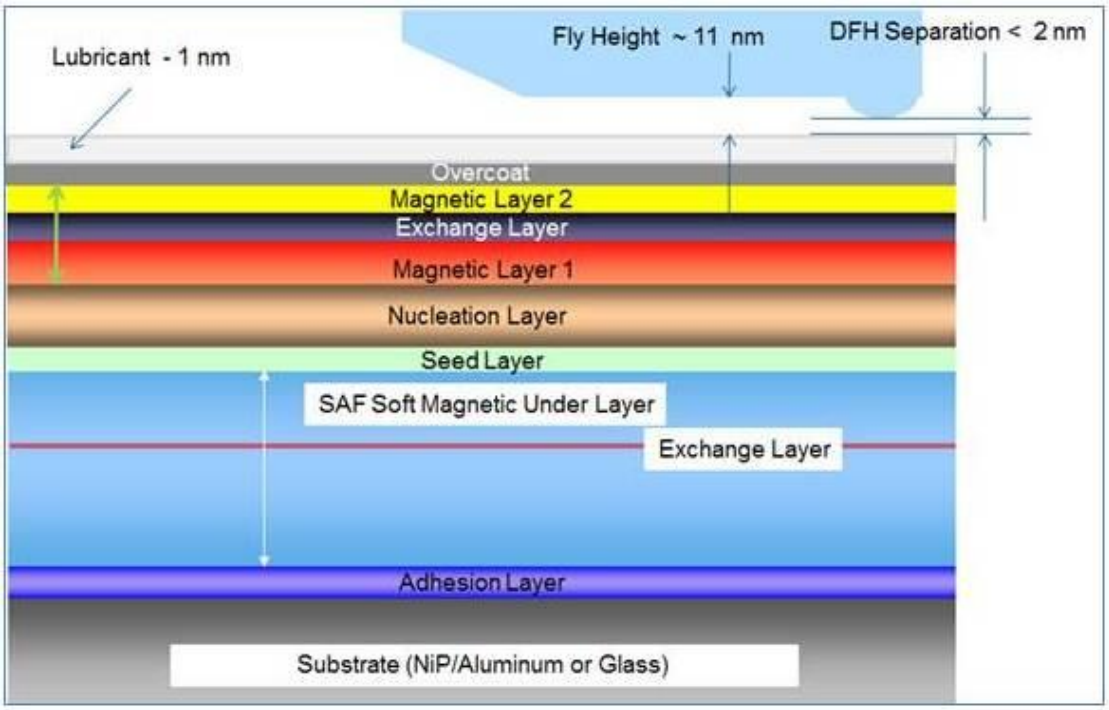

Figure 5-71: Construction of PMR media (2011 design) showing the complexity and the number of layers that are used. This type of construction was used for media up to approximately 400 Gb/in^2 areal density.

Table 5-8: List of layers used in typical perpendicular media.

Structure – from top:	Thickness
Liquid lubricant	1 nm
Overcoat: CVD carbon overcoat	2 nm
Magnetic Layer 2: Continuous CoCrTaPt-based alloy	5 nm
Exchange Layer: Ru,	0.6 nm
Magnetic Layer 1: CoCrTaPt-oxide layer,	15 nm
Nucleation Layer : Ru, NiX	30 nm
Seed Layer:	5 nm
2nd Soft Magnetic layer:	20 nm
Exchange layer: Ru	0.5 nm
1st Soft Magnetic Layer:	20 nm
Adhesion Layer:	5 nm

In summary, the magnetic thin film technology has come full circle since the early days of its start in the early 1980s. Exchange decoupling between the grains was realized as the key step in increasing the areal density capability of thin film media. Based on this concept, Komag got started and they began using isotropic CoPt-based alloys initially, and had to develop an oxide-based addition to the alloy in order to achieve greater exchange decoupling between the grains so that SNR could be improved. Associated target manufacturing involving powder metallurgy and the HIP process had to be developed by the target vendors in order to manufacture such targets. A competing process also developed around the same time using a CoCrTa-based alloy with a Cr underlayer. High-Cr content was required with additional heating to obtain segregation of Cr to the grain boundaries in order to achieve exchange decoupling. Eventually, this path proved superior and in time, 100% of the thin film media switched to using the Cr underlayer concept using a CoCrTa-based alloy. The CoCrTa alloy eventually ran out of Hc capability, and Pt began to be added. As this alloy system degraded the grain isolation, boron was added to maintain and increase the isolation. Eventually, the thermal stability limit for longitudinal recording was reached, and the industry finally had to consider the perpendicular recording. However, the CoCrTaPt-B alloys that had their origin in the CoCr alloy had too much Cr and the anisotropy available was not sufficiently high enough to obtain negative nucleation field, H_n, which was a new requirement for perpendicular recording that did not exist when areal density was low when the CoCr alloy was developed. Hence, the industry had to choose a higher anisotropy material, namely CoPt-oxide-based material very similar to the type of alloy Komag had developed for longitudinal recording. Using this alloy now in combination with the Ru underlayer, most of the key issues with noise in the perpendicular media were solved.

There is much other technology necessary in order to obtain the areal density capability that we have today in HDD, which stands at approximately 900 Gb/in^2, a far cry from the ~ 10 Mb/in^2 where the industry was when the first transition to thin film magnetic media began in early 1980s. There has been a tremendous reduction in the thickness of overcoat to protect the media, and the expertise around tribology of the system has advanced greatly. Head technology is amazingly different now with very complex structures used in detectors using tunneling MR heads and miniaturization of the head. The coding scheme used in the drive is also very different from the more primitive scheme used initially. However, the advances in the media technology have played a significant role in the continuing development of HDD technology. This is outlined in the memoir written by Tu Chen on the inception and propagation of thin film media technology [5-89].

Areal density has increased by an amazing amount over the past 30 years or so of the period covered in this chapter, from approximatley 10 Mb/in^2 at the beginning of 1984 to close to 1 Tb/in^2 today in 2014, for approximately 5 orders of increase during this time span. This is illustrated in figure 5-72 showing the areal density trend covering the entire history of the hard disk drive from its invention in 1957.

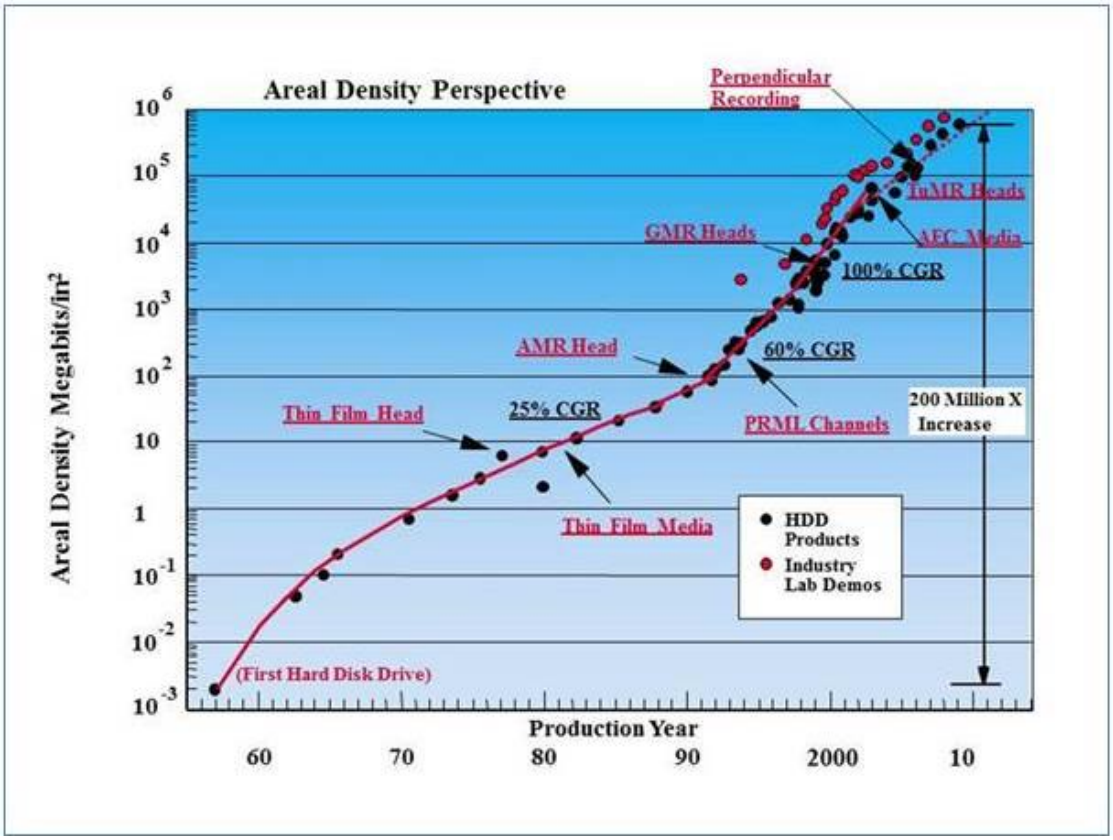

Figure 5-72: Areal density trend since the invention of HDD. This chart was created in 2010.

5.8 Thin film Stabilized Zirconia for Disk Media Overcoat

One of the critical technologies for thin film media is the use of an overcoat to protect the cobalt-based thin film from corrosion and mechanical wear due to a recording head that continually lands and takes-off from the media surface. The entire science and technology of tribology has developed over this area that involves friction and wear of the overcoat and the media beneath it. In this section, a brief description is made of the development of zirconia-based ceramic overcoats for thin film media. For this purpose, yttria-stabilized zirconia (YSZ) was used as an overcoat to protect the recording media. One of the remarkable properties of YSZ is its mechanical toughness. It is also very hard, and the ceramic knife is made using this material [5-90]. A 3 mol% yttria stabilized YSZ, for example has bending strength of 1200 MPa, and 8.5 on the Moh hardness scale (diamond having 10). The combination of toughness and hardness comes from the formation of a tetragonal phase that forms a so-called tweed pattern inside the cubic matrix of the zirconia [5-91]. The best material is made to nearly the theoretical density using the hot isostatic press (HIP) method. The purpose of using YSZ for a knife is that it is impervious to strong acid and caustic material, and never requires sharpening. It is often claimed that it does not leave any metallic taste when cutting sashimi, for example, for sushi, an important consideration for the connoisseur of sashimi and sushi.

In the period from 1983 to 1984 when thin film magnetic media had started to become commercially available, the initial product was sold without any protective overcoat over the cobalt-based thin film media. The initial product had a plated cobalt phosphorus (CoP) coating made using an electroless plating process. These initial products ran into corrosion problems and tribological issues inside the drive. In the early hard disk drives, the recording head was made to land and start-up on the disk surface every time the drive was turned on and off. Starting with IBM 3340 disk drives first introduced in 1973, the first of the so-called Winchester hard disk drives, all used this feature and it resulted in tribology becoming an important science in the development of hard disk drives. Thin film disk without the protection of an overcoat

would go on to fail in the field and caused a crisis for many disk drive start-ups that were shipping drives using the plated media [5-89]. When the thin film media made by sputtering began to be marketed in volume in the period from 1984 to 1985, the media started to be coated with sputtered carbon overcoat. The carbon film was produced by DC magnetron sputtering from a pressed graphite target. This produced an amorphous carbon film, which was called *diamond-like* carbon film, but it was a misnomer. Later, classification of various types of carbon films made by a variety of techniques put some consistency in the labeling of carbon film, and the sputtered carbon made by DC magnetrons is called a-C, for amorphous carbon film. It typically has ~ 10% "sp^3-like" bonding characteristics. Typically, even the sp^3 hybridization claim is problematic because it is based on Raman spectroscopy, and it is not, strictly speaking, a true diamond sp3 bonding that is being measured [5-92]. Nevertheless, the use of a sputtered carbon overcoat was revolutionary for use in magnetic hard disk media and sputtered thin film came to dominate the hard disk drive application within a short time. The coating together with the use of advanced lubricant made the drive reliable enough for mass consumer application. The personal computer revolution would not have happened without the cheap, and reliable hard disk drive becoming available, using the sputtered thin film media.

In the early days of its introduction, sputtered carbon overcoat was approximately 25 to 30 nm thick. It did not have any doping with any other gas aside from the use of argon gas for sputtering. With the use of liquid perfluoro poly-ether fluoro-polymer (PFPE) lubricants, the tribological performance was adequate to meet the initial requirements. However, for a newer generation of media that had to perform at higher recording density, the spacing between the recording head and the media had to be reduced, which meant that the overcoat thickness must also be reduced accordingly. At the same time, the head must also fly closer to the disk surface, which meant that the overcoat must be made more durable and wear-resistant at thinner thickness. The push for higher overall reliability also meant that corrosion resistance of the media to a variety of environmental conditions such as high temperature and humidity must improve. For a more demanding application as described for media with

higher recording density, the sputtered carbon overcoat was no longer meeting the requirements, especially with respect to corrosion protection for the media. With this issue taking place with the sputtered carbon overcoat, an attempt was then made to see whether YSZ could be sputtered to form an overcoat for thin film media. It was hoped that some of the remarkable mechanical and chemical resistance characteristics of the bulk YSZ material could be retained in thin film form.

The first order of business was to obtain a suitable target made out of YSZ material. Initially, an YSZ target made from relatively high yttria content was used at approximately 10 mole %. As it can be seen from the phase diagram in figure 5-73 [5-93], this composition would give an all-cubic phase and no benefit would result in terms of expected mechanical properties, as one would not obtain the mechanical toughness that comes from the formation of a tetragonal phase. However, the high yttria content was due to the target vendor claiming that they could not make a partially stabilized composition material. Initial sputtered film using the high yttria composition gave very promising results in terms of tribology and corrosion resistance. However, the target made by the initial vendor would not survive an extended sputtering process, which usually lasted many days of continuous operation. To sputter non-conducting material such as zirconia, RF sputtering must be employed- 13.56 MHz RF is typically used, and it complicates the sputtering greatly as it is much more difficult to employ RF sputtering compared to DC sputtering due to its complexity. One of the key detriments of RF sputtering is that the sputter rate is significantly lower compared to DC magnetron. To increase the rate as much as possible, a new type of cathode was constructed, which incorporates magnets to enhance and confine the plasma in a RF cathode, much the same way it is used in DC magnetron sputtering. Due to the very high powers involved in using RF, as much as 5-6 KW of RF power going into a target of large size, approximately 230 x 610mm, it was very difficult to cool the target. Magnetic confinement of the plasma also meant that some part of the target was heated much higher than another area. The poor thermal conductivity of zirconia also did not help. The consequence was that after less than a few hours of continued sputtering, the target would shatter into many pieces, often catastrophically. The thermal stresses from

uneven heating of the target and thermal shock associated with turning on the target and shutting it off were too high for the material to withstand. A schematic diagram of what the planar RF Magnetron Cathode looks like is illustrated in figure 5-74 with the actual cathode in operation. The cathode has two *race tracks* where the sputtering takes place on the target surface. This is arranged by the magnets placed under the target inside the cathode body. A circular purple arc signifies the presence of a magnetic field, which forms the plasma over the target surface. The photo insert shows the actual cathode in operation. Two purple race tracks are clearly visible where the sputtering is taking place. This race track region becomes extremely hot while sputtering. Underneath the target, there are large permanent magnets that provide the field for the sputtering and at the same time water cooling channels have to be provided in order to cool the target. The targets are bonded to the cathode backing plate using indium, which melts at 156^{o}C. Therefore, the back of the target has to be maintained below this temperature but on the surface of the target, the temperatures can reach very high, especially if the target is a ceramic material with poor thermal conductivity.

Realizing that it is the partially stabilized version of the YSZ composition that must be used in order to avoid the thermal shock problem with the target, another vendor was selected for proper manufacturing of the YSZ target. A similar composition used in an earlier study with the oxygen sensor was selected at approximately 4.5 mol% [5-91], and a new target was fabricated with much higher density of approximately 97-98% of theoretical density, and fabricated in such a way as to create the tetragonal phase that will provide the ultimate strength to the part. What it took was proper attention to starting powder material, thermal treatment, and length of time spent on heat treatment to obtain the desired phase composition and microstructure. The exact details were a trade secret with the vendor, therefore unknown, but the goal was clearly understood. It took an expert ceramicist with a high degree of specific experience in dealing with YSZ material to make the target material, as opposed to someone at the target manufacturer who only knew how to hot press the powder under standardized conditions, using melting temperature as the only guide.

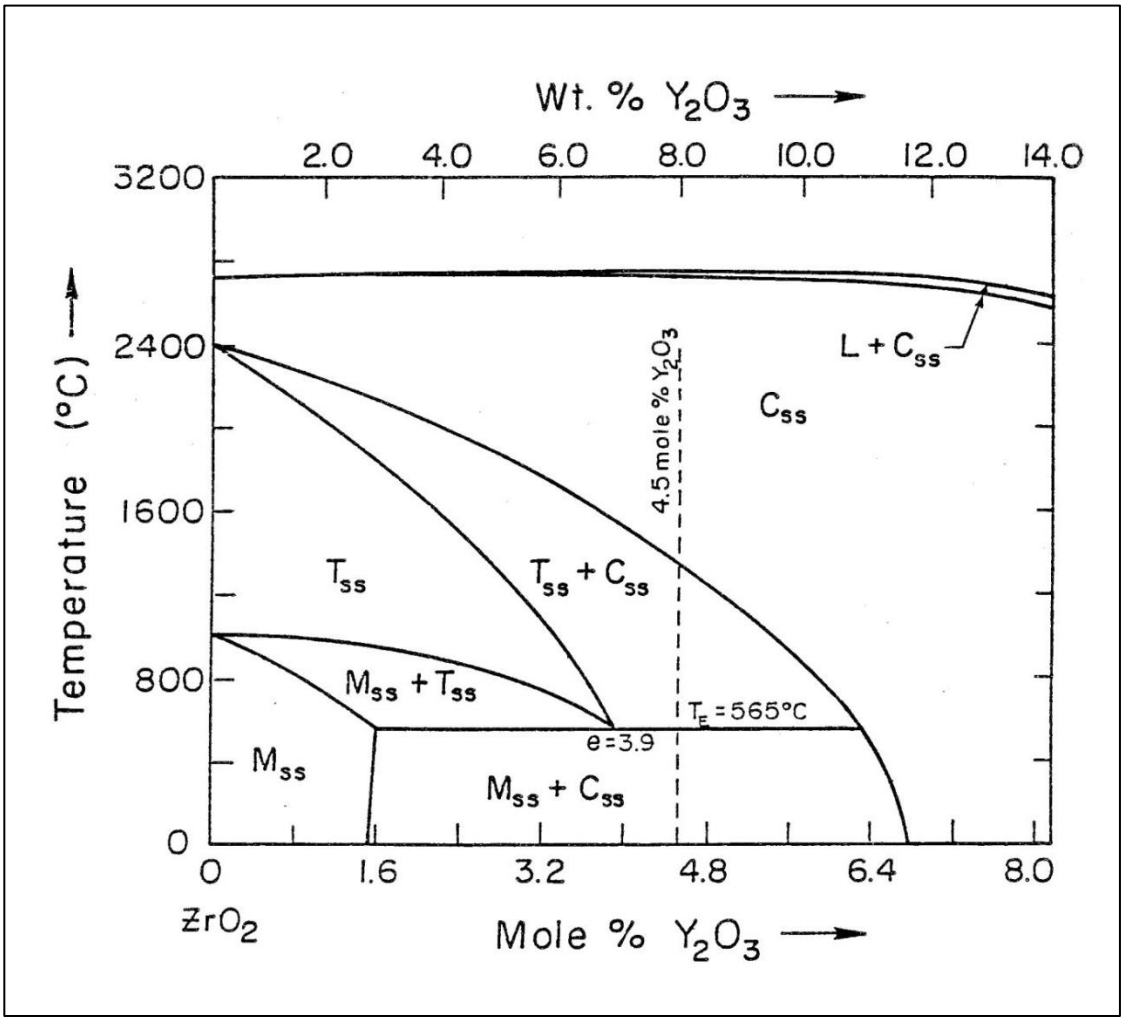

Figure 5-73: Phase diagram for the zirconia rich portion of the zirconia-yttria system by Scott [5-93]. J. Mater. Sci., Springer Publications. Reproduced with permission.

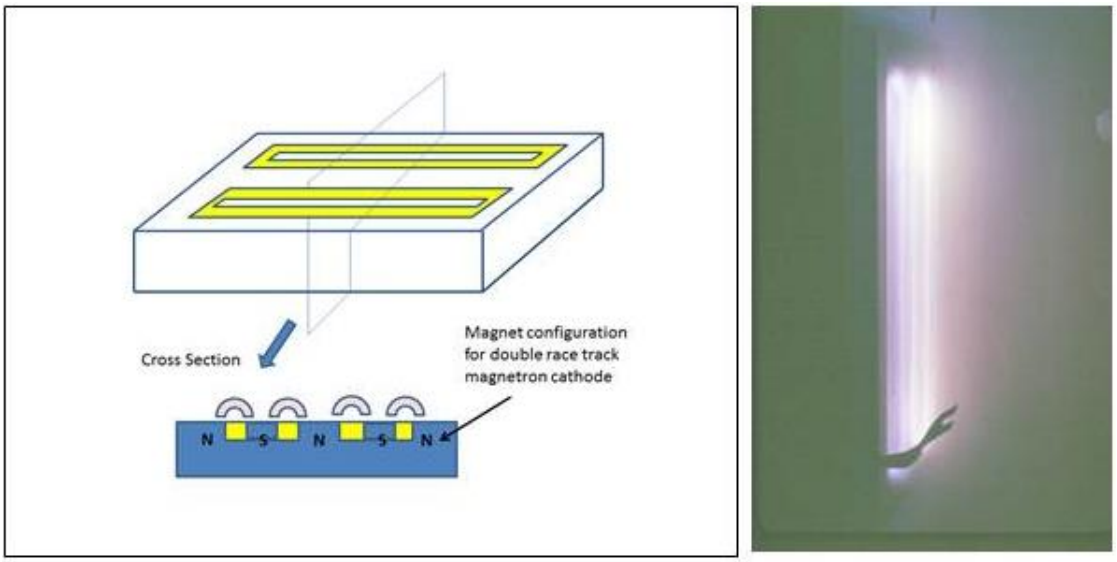

Figure 5-74: Schematic diagram of a planar RF/Magnetron cathode, and showing where the sputtering takes place on the target (yellow). Uneven geometry inherent in magnetron sputtering caused significant thermal shock problems for the target material. The photo insert shows the actual cathode in operation (the dark feature is a piece of ground wire that is not supposed to be there).

The newly fabricated material was stable in RF/Magnetron sputtering and became the manufacturing process for the film. One critical piece of expertise that we had possessed was on the selection of the starting powder for zirconia. The majority of zirconia used for sensor application has a distinct dark yellow appearance that comes from the small amount of iron that the zirconia contains. Just tens of ppm is enough to cause this color and it is due to the source of the zirconium from which the ZrO_2 is made. Fe is known to be very detrimental to the hard disk/head interface as it catalyzes the breakdown of lubricants and causes severe tribological problems. Care was taken in the selection of only the purest ZrO_2 starting material available for the target, and the finished target has a pure white appearance.

The disks from which analysis of the YSZ coating was made consisted of 5¼-inch electroless NiP coated aluminum substrate, a sputtered coating of Ni_xP ($x \sim 3$),

followed by $CoNi_9Pt_{10}$ film, followed by 20-30 nm thick sputtered YSZ coating. All three layers were sputtered by RF sputtering. The coating was done in a continuous manner in an in-line Ulvac sputtering system capable of sputtering approximately ~ 250 pcs/hour of 5¼-inch aluminum substrates. The high resolution SEM of the finished disk surface is shown in figure 5-75. A Hitachi S-900 Ultra High Resolution SEM (UH-SEM) with a special immersion objective lens capable of approximately ~ 1 nm resolution was used. It is clear from the image that the YSZ coating has a crystalline appearance, and grain size is approximately ~ 5-10 nm. Like the appearance of the coating, the line or the mound comes from the fact that the disk surface was textured. Deliberate concentric polishing marks were placed on the disk to prevent the jaw-block effect that can occur between the lubricant and the recording head if the surface of the disk is too smooth. Roughly 1 to 2 nm Ra roughness was typically put on the disk surface by this method, and the film followed this texture line contour. The SEM image to the right is a disk coated with a sputtered amorphous carbon overcoat of the same thickness for comparison. The amorphous carbon overcoat also shows a granular appearance because it transfers the underlying magnetic film microstructure to the surface.

A TEM specimen of the YSZ coating was obtained by dissolving the magnetic layer and the rest of the disk with a strong acid (conc. HCl). YSZ material was unaffected by the process and large sheets of material float to the surface, which are many millimeters in size. The sheets were picked up with a grid for TEM examination. BF TEM micrograph of the YSZ coating is shown in figure 5-76. The fine crystalline granularity of the coating is seen; the line going through the middle is the texture line. The diffraction pattern shown in figure 5-77 clearly indicates that most of the grains are cubic. There are additional faint extra rings outside of the cubic ring, which could be a monoclinic phase, but they were too faint and few to identify positively. It is clear that the sputtering process is inherently a “high temperature” process so that a high temperature cubic phase is produced. The film is *quenched* into the cubic phase before any transformation to the tetragonal phase can occur.

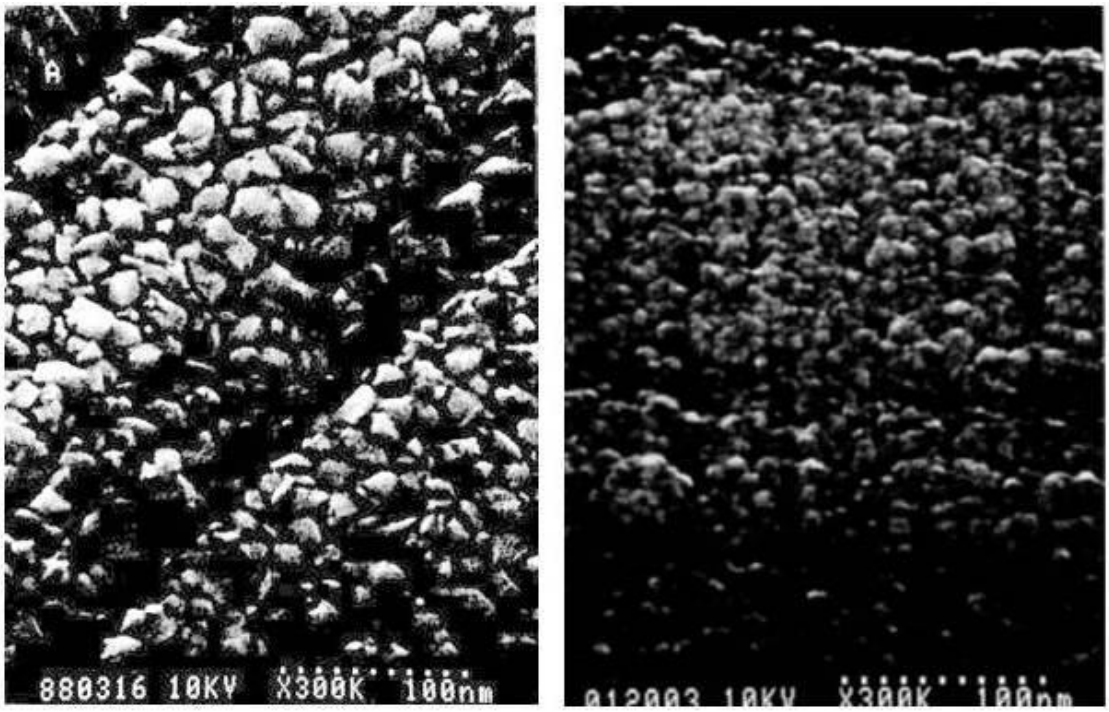

Figure 5-75: High-resolution SEM image of the YSZ coating ~ 20 nm thick (left) compared to the amorphous sputtered carbon overcoat (right). The lines are due to texture lines deliberately put on the disk. The YSZ coating is clearly crystalline in nature. Thicknesses are both 30 nm.

A contact start-stop test was performed on the disk coated with YSZ and compared with the carbon-overcoated media. A thin film head was used with a loading force of 15 grams and flying height of 12 micro-inches (0.3 μm). Disks were unlubricated in order to accelerate the wear. Contact start-stop (CSS) means that the head was repeatedly made to start (and fly) then land on the disk surface. When the disk rotation speed of 300 rpm is reached, the drive is shut down and repeated again. For a normal operation, the drive rotation speed reaches 3600 rpm. One CSS cycle for an unlubricated disk is roughly equal to 20 to 30 cycle full rpm. Figure 5-78 shows the static friction coefficient vs. number of CSS cycles for carbon-overcoated media vs. YSZ-coated media. YSZ coated media has greatly enhanced wear characteristics compared to the carbon-overcoated media. Additional tests were done with media

coated with sputtered SiO_2 and alumina (Al_2O_3). Disks coated with this material under the same testing condition failed almost immediately, within 20 cycles, often with catastrophic results (head crashes)-not shown.

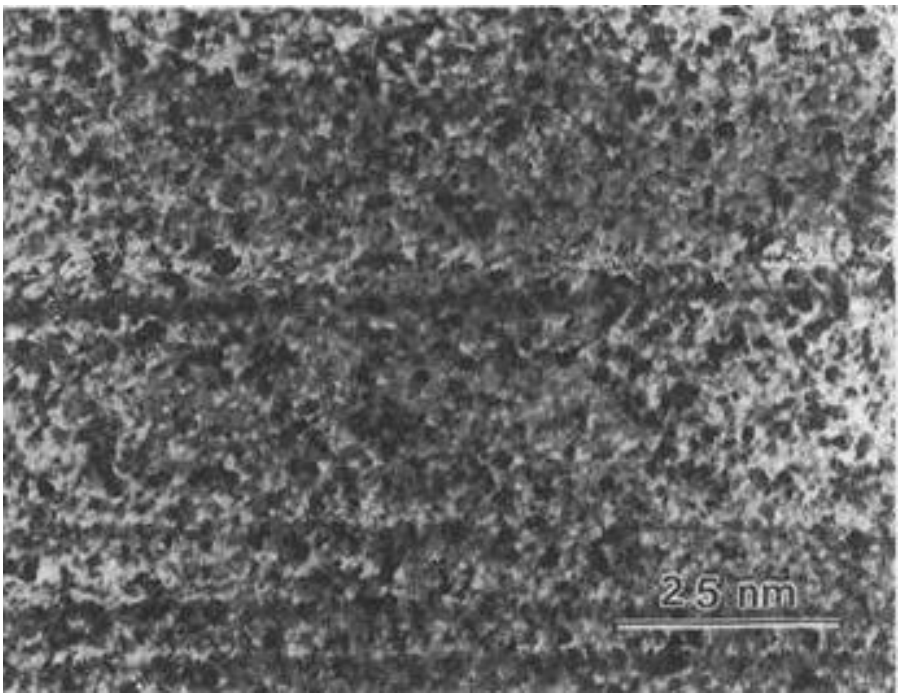

Figure 5-76: BF micrograph of YSZ coating, 30 nm thick. From Ref [5-95].
Copyright © 1988, IEEE, reproduced with permission.

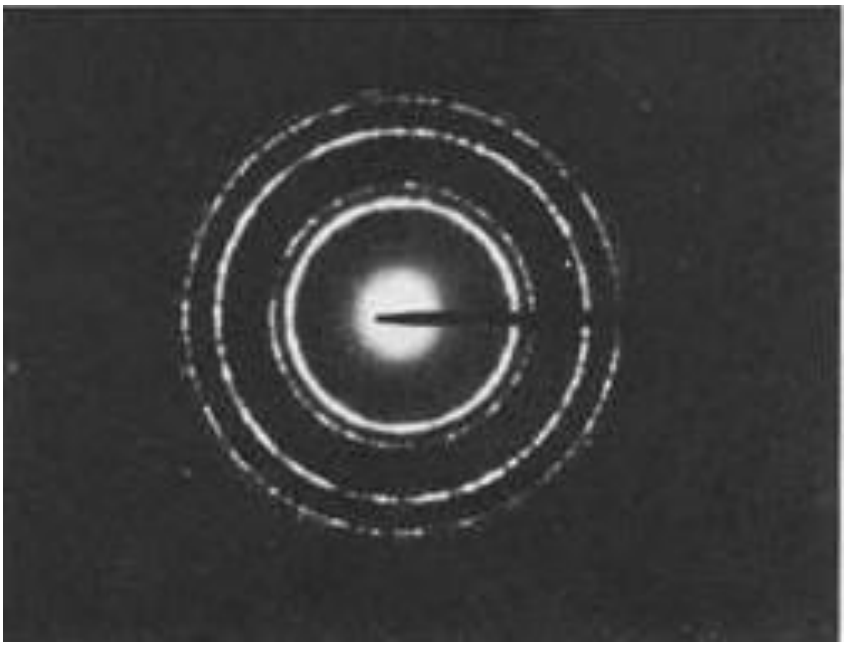

Figure 5-77: Diffraction pattern of the film from figure 5-21. The rings are for cubic phase zirconia. A few extra rings are also present, but very few and faint. From Ref [5-95].
Copyright © 1988, IEEE, reproduced with permission.

Additional wear testing was done on the media using a continuous drag test using a thin film head. Disk rotation speed was 40 rpm, with a head loading force of 15 grams. The test radius was 58mm from the center of the disk. Continuous drag testing is extremely aggressive and difficult for the media, especially when no lubricant is applied to the disk. Figure 5-79 shows the result. YSZ-coated media showed very impressive results compared to the carbon-overcoated disks. It appeared that when it comes to CSS as an overcoat and friction tests for the disk media, not having the tetragonal phase was not necessary to still obtain excellent mechanical characteristics from the YSZ coating.

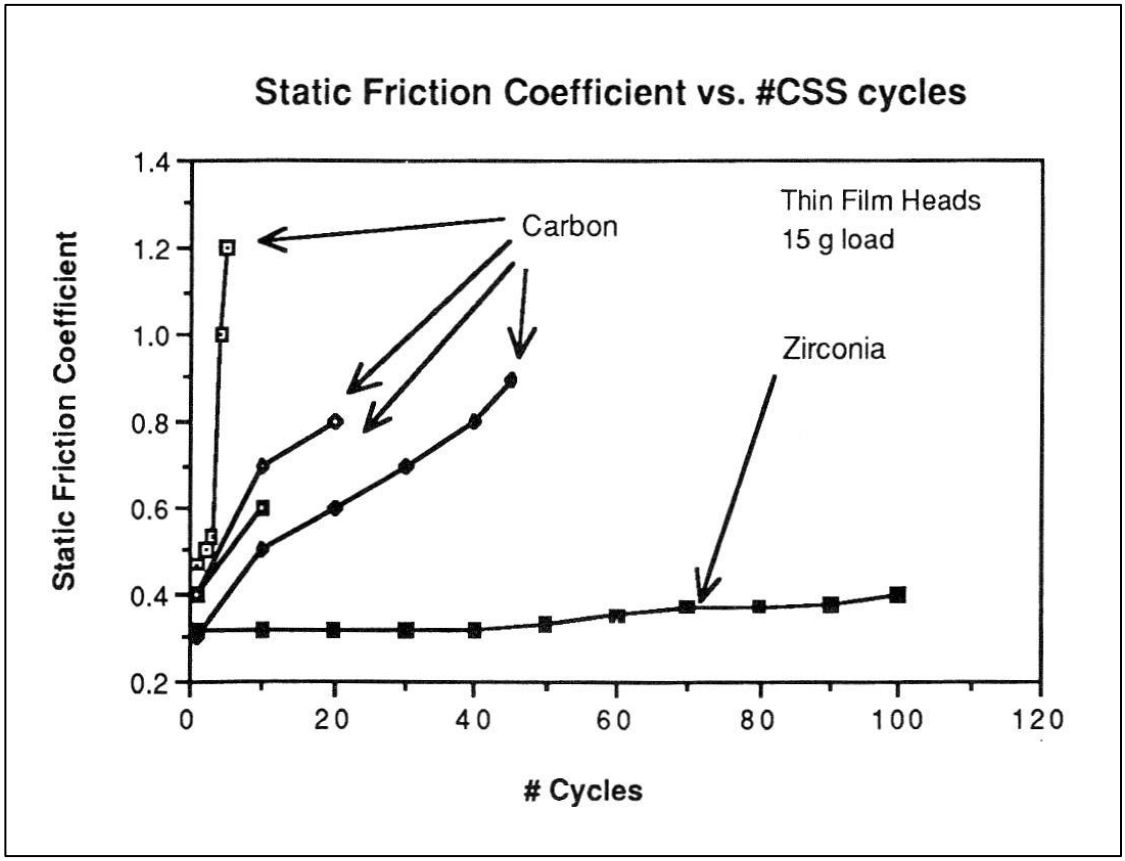

Figure 5-78: Static friction coefficient vs. number of CSS cycles for unlubricated carbon and YSZ-overcoated disk. From Ref [5-95].

Copyright © 1988, IEEE, reproduced with permission.

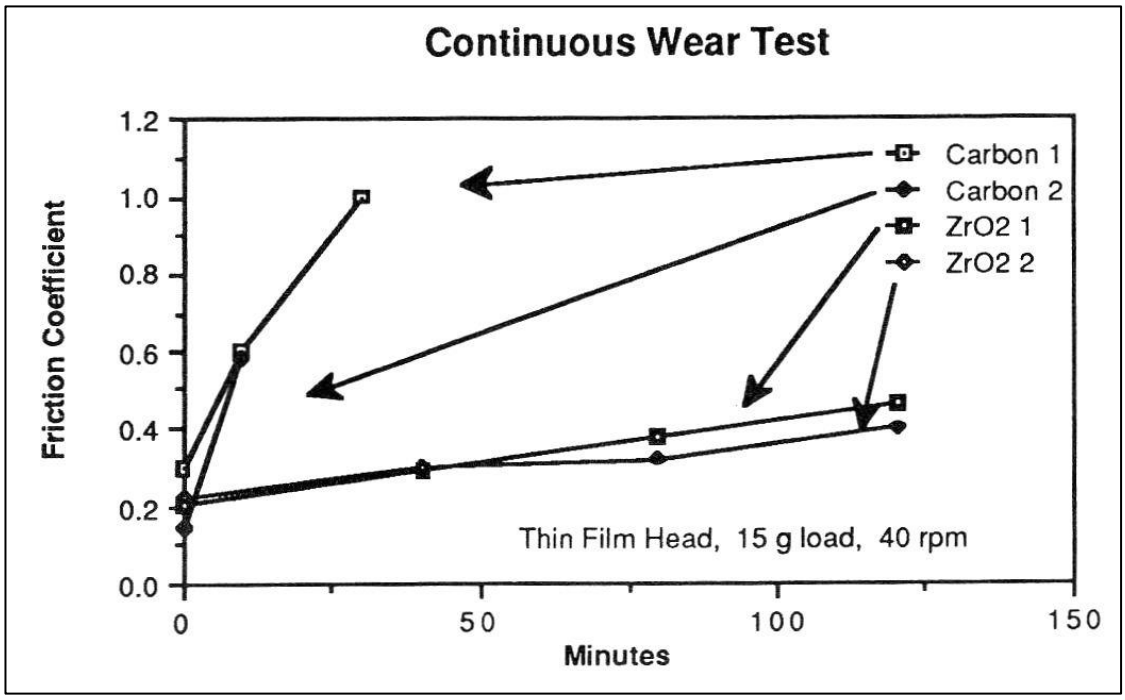

Figure 5-79: Continuous wear test on the media at 40 rpm on unlubricated carbon and YSZ-overcoated media, using thin-film head with 15 grams load.
From Ref [5-95]. Copyright © 1988, IEEE, reproduced with permission.

To test the corrosion protection capability of the YSZ overcoat, several standard tests available at the time were tried on the media. The first test involved soaking the disks in a clean room environmental chamber at 80^{o}C and 90% relative humidity for many days. After each day, the disks were burnished and tested for flyability using a 7 micro-inch (0.18μm) flying height head (glide test) followed by a test to detect magnetic defect counts. Table 5-9 summarizes the results in tabular form. A glide height test was setup to detect hard hits that protrude from of the surface and cause a signal from a piezo-electric transducer mounted on the head. When corrosion occurs, it causes CoO precipitates to form and grow on the surface of the overcoat, which protrude from of the surface. A sensitive glide head can detect it. It is a good quantitative way to look for the extent of the corrosion process taking place. When the corrosion process becomes severe enough, the glide head can crash. The magnetic test

also looks for the same event, where the corroded area causes magnetic bits not to be recorded. Four types of overcoat were tested, carbon, Al_2O_3, SiO_2 and YSZ. All of the overcoats were 30 nm in thickness.

The superior corrosion protection of the YSZ overcoat is evident. For the Al_2O_3 overcoat, the sample was kept in the chamber for 5 continuous days; therefore, it is not clear when it would have failed (before 5 days). However, it is still clearly much worse than YSZ. The corrosion mechanism in the high temperature/high humidity is that it usually occurs around small pinholes in the overcoat. Because the surface of the disk is deliberately made rough with texture for tribological reasons, it is difficult to cover the disk surface completely. YSZ coating is much more continuous and has fewwer pinholes compared to the other overcoat material. Another reason has to do with the transport of the cobalt ion species through the pinhole or through the overcoat to the disk surface. For this to occur, it is apparently necessary to have some complementary electron conduction in the overcoat. For carbon overcoat, for example, the electrical resistivity of the overcoat is relatively low, and such a carbon film performs poorly in all corrosion tests. YSZ has very high resistivity compared to all the other films in the list. Much later in time when the carbon overcoat was prepared with hydrogen doping, the film became much more electrically resistive and at the same time became much better for corrosion protection. A typical corrosion site at the initial stages is shown in figure 5-80, showing the characteristic CoO whiskers that form around a pinhole on the disk surface. When this process is extended greatly, the entire disk surface turns blue, as indicated in the table for carbon overcoat after 5 days of the test.

Table 5-9 **Corrosion Test at 80oC, 90% rel. Humidity**

# Days tested	Criteria:	Cabon	Al_2O_3	SiO_2	YSZ
1	Visual	Ok	NA	Δ	ok
	Magnetic	Ok	NA	Fail	ok
	Glide Height	Ok	NA	Fail	ok
2	Visual	Δ	NA	Δ	ok
	Magnetic	Increase	NA	Fail	ok
	Glide Height	Fail	NA	Fail	ok
3	Visual	Δ	NA	Δ	ok
	Magnetic	Fail	NA	Fail	ok
	Glide Height	Fail	NA	Fail	ok
5	Visual	All blue	Δ		ok
	Magnetic	Fail	Fail		ok
	Glide Height	Fail	Fail		ok
7	Visual				ok
	Magnetic				slight increase
	Glide Height				ok

Criteria		
	Glide Test	7 micro-inches (0.18 µm)
	Magnetic test	< 10 defects at 68% clipe level, 1400 tracks/inch
	Δ	some corrosion pits
	OK	pass test criteria
	NA	data not available

Table 5-9: Corrosion test results for various overcoats, thickness ~ 30 nm.
From Ref [5-95]. Copyright © 1988, IEEE, reproduced with permission.

Additional data to compare the carbon overcoat against the YSZ overcoat was taken at more gentle corrosion testing conditions of 75^{o}C and 80% relative humidity. Disks were scanned for magnetic defects, and the number was counted to provide more quantitative results. This is shown in figure 5-81. Again, the YSZ overcoat is considerably superior to the carbon overcoat for protecting the media.

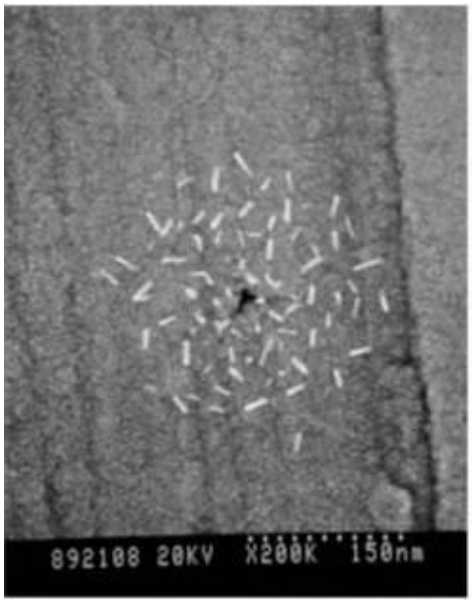

Figure 5-80: Corrosion product (CoO) forming on the surface of the disk after the high temperature/high humidity exposure (carbon overcoat ~ 30 nm). Texture lines and voids in the films are often a source of incomplete coverage by the overcoat.

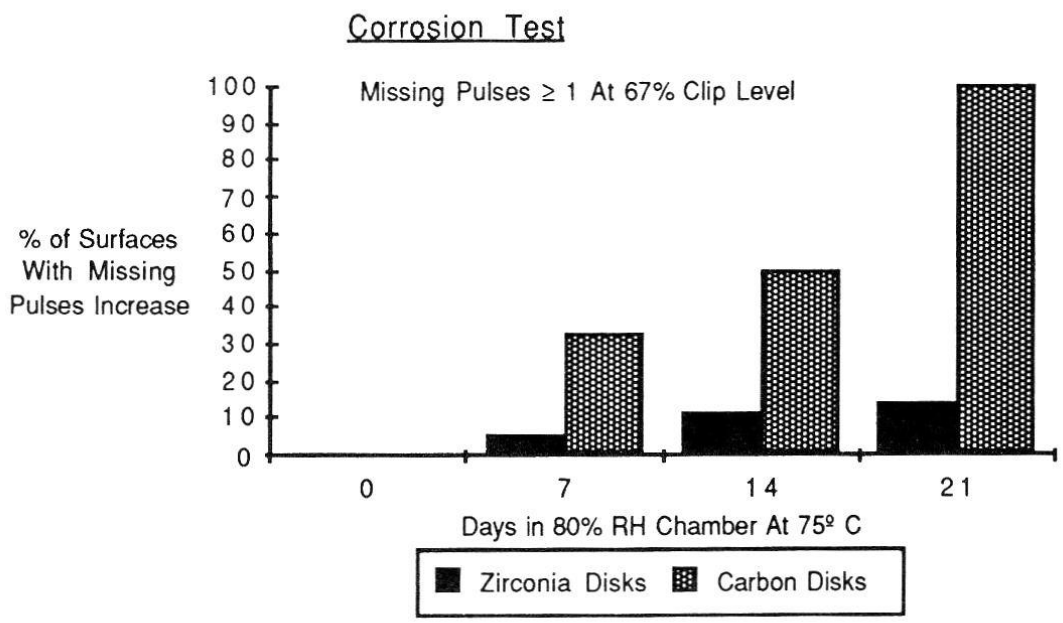

Figure 5-81: More gentle corrosion test at 75°C and 80% relative humidity to compare the performance of YSZ overcoat against the carbon overcoat. Disks were certified (magnetic testing) and the increase in defects due to corrosion was counted over 21 days of exposure. From Ref [5-95]. Copyright © 1988, IEEE, reproduced with permission.

With the polar lubricant, z-dol [5-94] that had been in use at the time, the YSZ overcoat worked very well in terms of CSS testing. YSZ-coated media easily surpassed 100,000 CSS cycles, which typically took weeks of testing. The carbon overcoated disk could only reach approximately 50,000 CSS cycle on average, and the friction coefficient for each start-up increased from approximately 0.2 to 0.6 after the test. Alternatively, the YSZ overcoat maintained very low friction coefficient for a long time. Such data is shown in figure 5-82. One data point went out to nearly 120,000 cycles, and the friction coefficient was still 0.2. The good result was attributed to the fact that the z-dol lubricant has an –OH end group on the molecule, and it seems to have a strong affinity for the YSZ overcoat surface. The presence of a polar surface on the YSZ appears to retain the lubricant molecule on its surface much better than for the carbon overcoat.

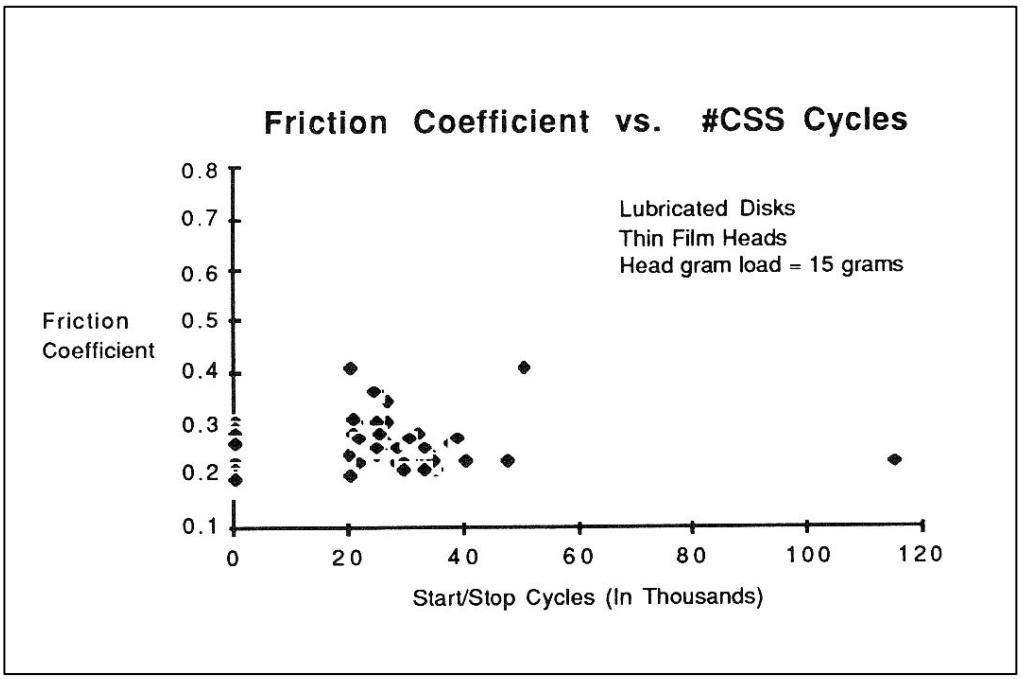

Figure 5-82: Results of drive level contact start stop (CSS) test on lubricated YSZ overcoat with z-dol lubricant showing friction coefficient vs. number of CSS cycles. A thin-film head with a 15-grams load was used for the test. From Ref [5-95]. Copyright © 1988, IEEE, reproduced with permission.

With these results, many millions of disk media were produced for commercial sale using the YSZ overcoat. Results of this work were published in 1988 [5-95], and patents were obtained for the invention [5-96, 5-97].

The fact that sputtered YSZ forms a pure cubic phase film from the partially stabilized composition suggests that, for this material, there is still sufficient mobility in the atoms to form crystalline material, but it is still a highly non-equilibrium process. The cubic phase is essentially frozen-in, and the kinetics of the process prevents any formation of the tetragonal phase. For thin film application such as in use for overcoat, it was actually detrimental to have a crystalline phase material, as the overcoat thickness must be reduced in order to improve the spacing loss between the head and the media. Much more fine-grained or amorphous phase material would be more desirable if it could still provide the desirable mechanical corrosion protection. The SiO_2 and Al_2O_3 films shown in table 5-8 were also sputtered by RF magnetron process and these form completely amorphous films. However, they performed very poorly in terms of mechanical and corrosion protection. Therefore, there is more to these properties with respect to being amorphous, but it was interesting to consider what happens to YSZ film if it can be made much more fine-grained or amorphous in order to see what becomes of their mechanical and corrosion protection properties.

Amorphous YSZ film was created by the addition of Al_2O_3 into the target. According to the literature, ZrO_2 and Al_2O_3 are practically immiscible with each other. A more recent phase diagram for the ZrO_2–Al_2O_3 system was published in 1997, which illustrates this point [5-98]. This phase diagram is reproduced in figure 5-83. Mutual insolubility of the ZrO_2 and Al_2O_3 was an important consideration for target manufacturing. For this mixture, the stabilized YSZ powder was mixed with Al_2O_3 powders, and the reaction between them would have been unfavorable. The YSZ phase was providing excellent mechanical strength to the target, namely, the thermal shock. Just enough Al_2O_3 needed to be added so that the effect can be felt in the sputtered film, but not in the target itself.

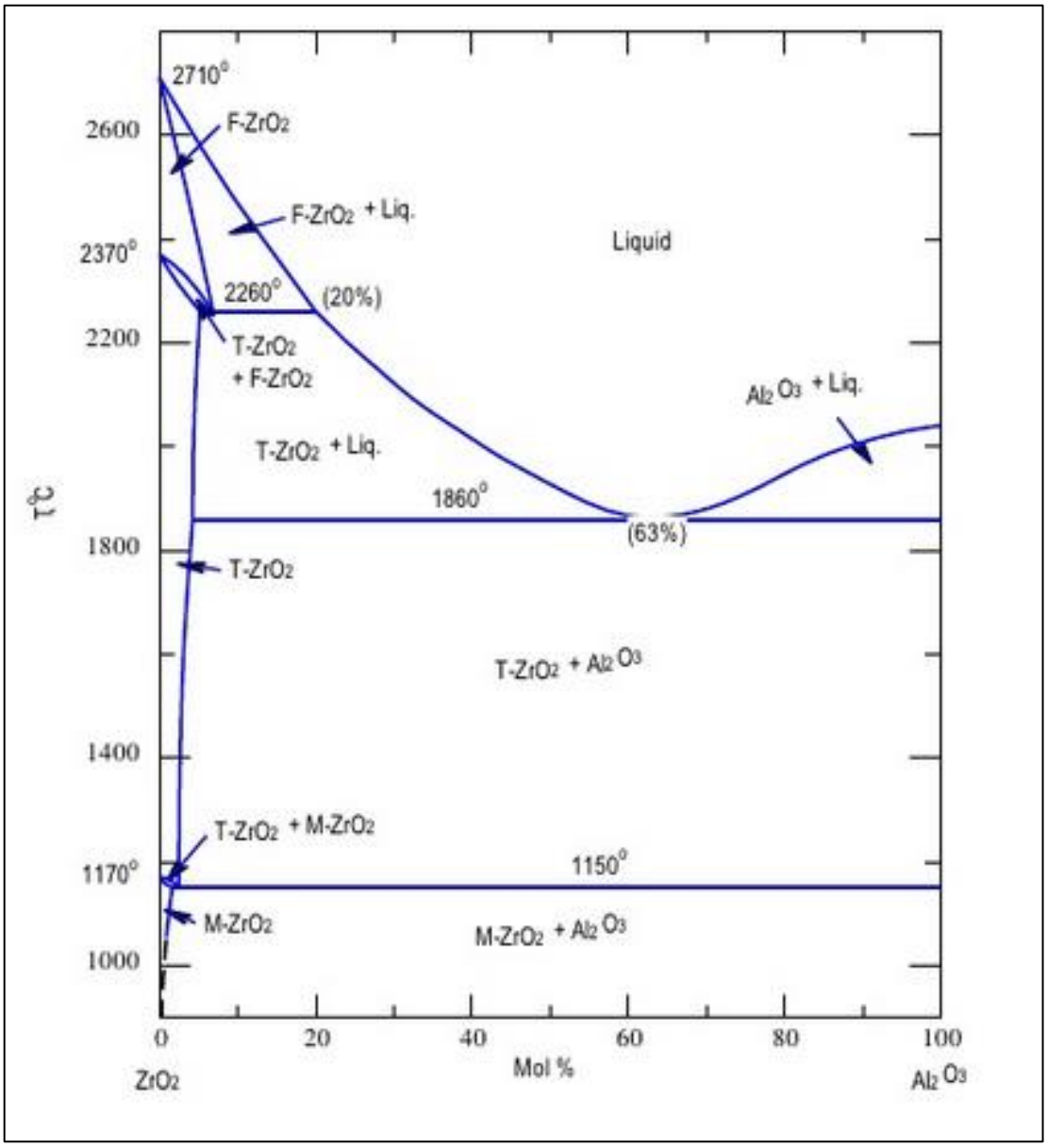

Figure 5-83: ZrO_2–Al_2O_3 phase diagram from ref [5-98] by Lakiza and Lopato, showing the low solubility of alumina in zirconia. J. Am. Ceram. Soc., John Wiley and Sons, reproduced with permission.

A 10 mol% alumina addition into the YSZ target was sufficient to create the completely amorphous film. This is shown in figure 5-84, showing the BF TEM image and the corresponding diffraction pattern. The BF TEM image shows the more

featureless film, and any contrast that is present comes from the film following the contours of the crystalline magnetic film underneath. Being amorphous, the film has the ability to follow the disk surface better and shows much more uniform coverage of the disk surface.

The mechanical properties of the various compositions of YSZ with Al_2O_3 where the amorphous film is formed did not perform as well as polycrystalline YSZ. However, their corrosion protection capability was superior to YSZ or to Al_2O_3 by itself. YSZ + 10 mol% Al_2O_3 was successfully applied to magneto-optics (MO) disks where corrosion protection properties were paramount. MO disk used a Tb-Fe-Co alloy for their strong magneto-optic Kerr effect, and this material was extremely sensitive to oxidation. During target fabrication of this material, for example, the machine surfacing had to be done under oil so that material did not oxidize (actually burn) during machining. MO disks do not require CSS, as is the case with hard disk media, because the read-write operation is done with a laser. However, there is some heating of the material. Therefore, the protective material must withstand the laser heating, and at the same time, the material must have some anti-reflective characteristics that can be tuned. YSZ+ Al_2O_3 served such requirements very well, and it was used successfully in a commercial product. The 5¼-inch MO disk using the YSZ+ Al_2O_3 coating is shown below in figure 5-85. This media made over 25 years ago still functioned perfectly when tested recently in a now antiquated MO drive attached to an equally antiquated Mac computer of that era. The zirconia coating had been doing its job for all these years.

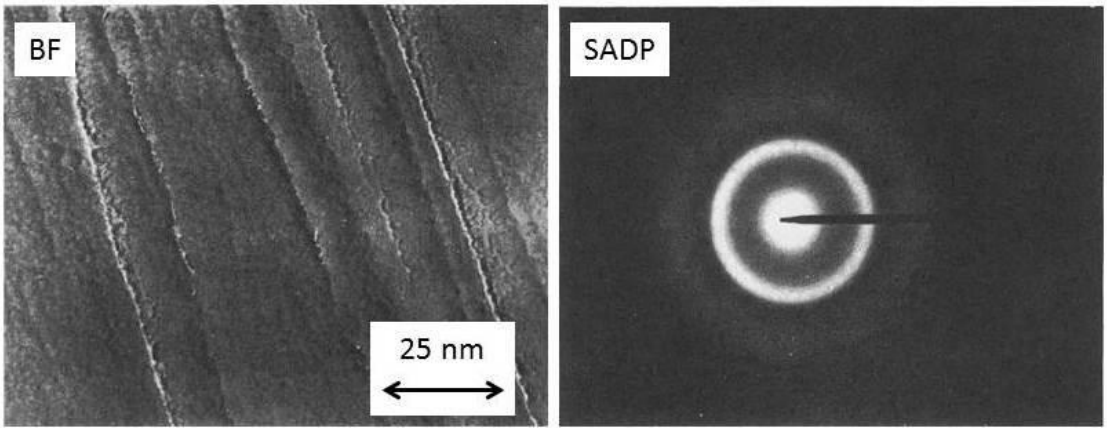

Figure 5-84: BF and diffraction pattern of YSZ + 10 mol% Al_2O_3. The film becomes amorphous with the addition of Al_2O_3. From Ref.[5-59].
Copyright © 1988, IEEE, reproduced with permission.

Figure 5-85: Magneto Optic disk cartridge manufactured by Komag Inc. in 1988 time frame. The disk holds ~ 500 MB, and use Tb-Fe-Co alloy for its magnetic layer. It is sandwiched above and below with several hundred Å thick layer of YSZ + Al_2O_3 coating to serve as anti-reflective coating and corrosion protection layer against the plastic polycarbonate disk and air.

Chapter 5 References:

[5-1] Eric D. Daniel, C. Denis Mee, Mark H. Clark, Magnetic Recording, The First 100 Years, IEEE Press (1999)

[5-2] http://www.latimes.com/business/technology/la-fi-tn-sony-185-tb-cassette-tape-storage-record-20140505-story.html

[5-3] C. Denis Mee and Eric D. Daniel editors, Magnetic Recording Technology, 2nd edition, IEEE press and McGraw-Hill (1995)

[5-4] N. Smith, *Reciprocity Principles for Magnetic Recording*, IEEE Trans. Magn. MAG-**23**, No. 4, pp. 1995-2002 (July 1987)

[5-5] James N. Porter, *Disk/Trend Report, A Historical Perspective of the Disk Drive Industry*, Presented at THIC Meeting at Sony Auditorium (April 19-20, 2005)

[5-6] Electroless Plating: Fundamentals and Applications, Glenn O. Mallory, Juan B. Hajdu, editors, Chapter 18, Electroless Cobalt and Cobalt Alloys, W.H. Safranek, American Electroplaters and Surface Finishers Society, William Andrew Publishing (1990)

[5-7] J.S. Judge, J.R. Morrison, and D.E. Speliotis
Very High Coercivity Chemically Deposited Co-Ni Films,
Journal of Applied Physics, Vol. **36**, Issue 3, pp. 948-949 (March 1965)

[5-8] D.E. Speliotis, J.R. Morrison and J.S. Judge,
A Correlation Between Magnetic Properties and Recording Behavior in Metallic Chemically Deposited Surfaces,
IEEE Transactions on Magnetics, Vol. MAG-**1**, No. 4, pp. 348-352 (Dec. 1965)

[5-9] H.N. Bertrum and L.D. Fielder, *Amplitude and bit shift spectra comparisons in thin metallic media*, IEEE Trans. Magn. Mag-**19**, No. 5, pp. 1605-1607 (Sept 1983)

[5-10] T. Chen and G.B. Charlan, *High coercivity and high hysteresis loop squareness of sputtered Co-Re thin film*, J. Appl. Phys., **50**, 4385 (1979)

[5-11] J. Aboaf, S. Herd and E. Klokholm,
Magnetic properties and structure of cobalt-platinum thin films,
IEEE Transactions on Magnetics, Vol. **19**, Issue 4, pp. 1514-1519 (July 1983)

[5-12] M. Yanagisawa, N. Shiota, H. Yamaguchi and Y. Suganuma, *Corrosion-resisting Co-Pt thin film medium for high density recording*, IEEE Transactions on Magnetics, Vol. **19**, issue 5, pp. 1638-1640 (Sept. 1983)

[5-13] S. Iwasaki and Y. Nakamura *An analysis of the magnetization mode for high density magnetic recording*, IEEE Transactions on Magnetics, MAG-**13**, No. 5, pp. 1272-1277 (Sept. 1977)

[5-14] T. Chen, D.A. Rogowski and R.M. White, J. Appl. Phys., Vol **49** (3), pp. 1816-1818 (1977)

[5-15] T. Chen and R.M. Martin, *The Physical Limit of High Density Recording in Metallic Magnetic Thin film Media*, Presented at the 1979 INTERMAG Conference in New York City, IEEE Transactions on Magnetics, MAG-**15**, No. 6, pp. 1444-1446 (Nov. 1979)

[5-16] T. Chen, *The Micromagnetic Properties of High-Coercivity Metallic Thin films and their Effects on the Limit of Packing Density in Digital Recording*, IEEE. Trans. Magn., MAG-**17**, pp 1181-1191 (1981)

[5-17] T. Chen, T. Yamashita and R. Sinclair, *The Effect of Orientation, Grain size and Polymorphism on magnetic properties of sputtered Co-Re thin film media*, IEEE Trans. Mag., MAG-**17**, No.6, pp. 3187- 3189 (November 1981)

[5-18] T. Chen and T. Yamashita, *Physical Origin of Limits in the Performance of Thin film Longitudinal Recording Media*, IEEE Trans. Magn. Vol. **24**, No. 6, pp. 2700-2705 (1988)

[5-19] M. Hansen, Constitution of Binary Alloys, 2nd edition, (McGraw-Hill, New York), pp. 494 (1958)

[5-20] M.L. Williams and R.L. Comstock, *An Analytical Model of the Write Process in Digital Magnetic Recording*, AIP Conf. Proc. **5**, 738 (1971)

[5-21] G. F. Hughes, *Magnetization reversal in cobalt-phosphorus films*, J. Appl. Phys., **54**, 5306 (1983)

[5-22] T. Chen, *The micromagnetic properties of high coercivity metallic thin films and their effects on the limit of packing density in digital recording*, IEEE Trans. Mag., Vol MAG-**17**, pp 1181-1191 (1981)

[5-23] W. Betteridge, COBALT and its Alloys, John Wiley & Sons, 1982.

[5-24] W.L.Bell, J. Appl. Phys., *2^1/2D Electron Microscopy: Through-Focus Dark-Field Image Shifts*, Vol. **47**, p. 1676 (1976)

[5-25] R. Sinclair, G.M.Michael and T. Yamashita, *Metallurgical Applications of the 2½ D TEM Technique*, Metallurgical Trans. A, Vol. **12A**, pp.1503-1512 (August 1981)

[5-26] Steven Schoenherr, The History of Magnetic Recording, Univ. of San Diego, Audio Engineering Society (Nov. 5, 2002) http://www.aes.org/aeshc/docs/recording.technology.history/magnetic4.html

[5-27] D.F. Speliotis and J.R. Morrison, *A Theoretical analysis of saturation magnetic recording*, IBM J. Res. Develop., Vol. **10**, pp. 233-243 (1966)

[5-28] A. Aharoni, *Theory of NRZ recording*, IEEE Trans. Magn., Vol. MAG-**2**, pp100-109 (1966)

[5-29] R. I. Potter, *Analysis of saturation magnetic recording based on Arctangent magnetization transitions*, J. Appl. Phys., Vol. **41**, pp. 1647-1651 (1970)

[5-30] P. I. Bonyhard, A.V. Davies and B.K. Middleton, *A theory of digital magnetic recording on metallic films*, IEEE Trans. Magn., Vol. MAG-**2**, pp. 1-5 (1966)

[5-31] N. Curland and D.E. Speliotis, *Transition region in recorded magnetization pattern*, J. Appl. Phys., Vol. **41**, pp. 1099-1101 (1970)

[5-32] J. Daval and D. Randet, *Electron microscopy on high coercive-force Co-Cr composite films*, IEEE Trans. Magn., Vol. MAG-**6**, pp 768-773 (1970)

[5-33] D.D. Dressler and J.H. Judy, *A Study of digitally recorded transitions in thin magnetic films*, IEEE Trans. Magn., Vol. MAG-**10**, pp. 674-677 (1974)

[5-34] J.G. Zhu and H.N. Bertrum, *Micromagnetic Studies of Thin Metallic Films*, J. Appl. Phys., **63**, 3248 (1988)

[5-35] J.G. Zhu and H.N. Bertrum , *Magnetization reversals and domain structures in thin film recording media*, J. Appl. Phys., **69**, 6084 (1991)

[5-36] J.G. Zhu and H.N. Bertrum , *Magnetization structures in thin film recording media*, IEEE Trans. Magn. MAG-**27**, 3533 (1991)

[5-37] Hewlett-Packard Journal, November 1985

[5-38] *Platinum Alloy Permanent Magnets*, Platinum Metals Rev., **1** (3) pp. 84-86 (1957)

[5-39] H. Okamoto, *Co-Pt (Cobalt-Platinum)*, J. Phase Equilibria, Vol. 22, Issue 5, pp 591 (2001)

[5-40] US Patent, 4,749, 459, Tsutomu T. Yamashita, Ching-Cheng Shir and Tu Chen, *Method for manufacturing of thin film magnetic media* (June 7, 1988)

[5-41] T. Yamashita, R. Ranjan, L.H. Chan, M.Lu, C.A. Ross, J. Chang and G. Tarnopolsky, *The Effect of Microstructure on the Magnetic Properties of Thin film Magnetic Media*, Mat. Res. Soc. Symp. Proc. Vol. **343**, pp 285-296 (1994)

[5-42] P.A. Flinn and G.A. Waychunas, *A new X-ray diffractometer design for thin film texture, strain and phase characterization*, J. Vac. Sci. Technol. B6, pp 1749-1755 (1988)

[5-43] US Patent 4, 786, 564, Tu Chen and Tsutomu T. Yamashita, *Method for manufacturing a magnetic disk having reduced bit shift, minimized noise, increased resolution and uniform magnetic characteristics, and the resulting disk* (Nov. 22, 1988)

[5-44] R.N. Duncan, *Electroless Nickel: Alternative to Chromium Coatings, Metal Progress*, pp. 31-36 (June 1985)

[5-45] H. Okamoto, *Ni-P (Nickel-Phosphorus)*, J. Phase Equilibria and Diffusion, Vol. 31, No. 2, p. 200 (1990)

[5-46] T. Yamashita, L.H. Chan, T. Fujiwara and Tu Chen, *Sputtered NixP Underlayer for CoPt-Based Thin film Magnetic Media*, IEEE Trans. Mag., Vol. **27**, No.6, pp. 4727 – 4729 (Nov. 1991)

[5-47] L.Chan, T. Yamashita and R. Sinclair, *Transmission Electron Microscopy and High-Resolution Scanning Electron Microscopy of Co-Ni-Pt Thin film Magnetic Recording Media*, Proceedings of the 47th Annual Meeting of the Electron Microscopy Society of America, G.W. Bailey, Ed., (1989)

[5-48] S. Miura, T. Yamashita, G. Ching and T. Chen, *Noise and bit jitter performance of CoNiPt thin film longitudinal recording media and its effect on recording performance*, IEEE Trans. Magn., Vol. **24**, No. 6, pp. 2718 – 2720 (November 1988)

[5-49] US Patent 5,631,094, Rajiv Y. Ranjan, Tu Chen, Tsutomu T. Yamashita and John K.-J. Chen, *Magnetic alloy for improved corrosion resistance and magnetic performance*, (May 20, 1997)

[5-50] P.K. Liao and K.E. Spear, *The B-Co (Boron-Cobalt) System*, Bulletin of Alloy Phase Diagrams, Vol. **9**, Issue 4, pp 452-257 (Aug. 1988)

[5-51] J.K. Howard, R.G. Simmons and T. Yogi, *Low noise thin film metal alloy magnetic recording disk*, US Patent 5,066,552 (1991)

[5-52] R. Ranjan, M. Lu, T. Yamashita and T. Chen, *Effect of Cobalt Oxide Addition on Co-Pt Media*, IEEE Trans. Mag., Vol. **30**, No. 5, pp. 3942-3944 (1994)

[5-53] T. Chen, R. Y. Ranjan, T. T. Yamashita, M. Lu, K. Kadokura, J. K. Chen and T. J. Yuen, *Magnetic Alloy and Method for manufacturing same*, US Patent 5,658,659 (August 19, 1997)

[5-54] S. Iwasaki and H. Yamazaki; Co-Cr sputtered films with perpendicular magnetic anisotropy," 7th Ann. Conf. on Magnetics, Japan, 4pA-7, (in Japanese) (1975)

[5-55] M. Hansen, Constitution of Binary Alloys, 2nd ed., pp. 467, McGraw-Hill, New York (1958)

[5-56] W.G. Moffatt, The Handbook of Binary Phase Diagrams, General Electric Company (1978)

[5-57] A.T. Gregor'ev, E. Yü-p'u, and E.M. Sokolovskaya, *Solid-State Transformations in the Cobalt-rich Region of the Chromium-Cobalt System*, Russian J. Inorgan. Chem., Vol. **6**, No. 7, pp. 827-930 (July, 1961)

[5-58] T. Chen, G.B. Charlan and T. Yamashita, *A comparison of the uniaxial anisotropy in sputtered Co-Re and Co-Cr perpendicular recording media*, J.Appl. Phys., Vol. **54**, No. 9, pp. 5103-5111 (1983)

[5-59] Y. Maeda and M. Asahi, *Segregated microstructure in sputtered Co-Cr film revealed by wet-etching*, J. Appl. Phys., **61**, 1972 (1987)

[5-60] J. P. Lazzari, I. Melnick and D. Randet, *Thin Evaporated Films with High Coercive Force*, IEEE Trans. Mag, Vol. MAG-**3**, No., 3, pp. 205-207 (September 1967)

[5-61] W.T. Maloney, *RF-Sputtered Chromium-Cobalt Films for High-Density Longitudinal Magnetic Recording*, IEEE Trans. Mag Vol. MAG-**15**, No., 6, pp. 1546-1548 (1979)

[5-62] Virgle L. Hedgcoth, Magnetic recording disk and sputtering process and apparatus for producing the same, US patent 4,735,840 (April 5, 1988)

[5-63] L. Herte and A. Lang, *Effect of ion bombardment during deposition on magnetic film properties*, J. Vac. Sci. Technol., Vol. **18**, Issue 2, pp. 153-155 (1981)

[5-64] H. Yamaguchi and M. Yanagisawa, *Magnetic Properties and Structures of sputtered CoNi/Cr Films*, IEEE Trans., Magn., Vol. MAG-**22**, No. 576-578 (1986)

[5-65] T. Yamada, N. Tani, M. Ishikawa, Y. Ota, K. Nakamura and A. Itoh, *CoNiCr/Cr Sputtered Thin film Disks*, IEEE Trans., Magn., Vol. MAG-**21**, No. 5, pp. 1429-1431 (1985)

[5-66] C.J. Robinson and J.K. Howard, *Microstructure and Magnetic Properties of CoCrTa films*, 1985 MRS Fall Meeting, Vol. 54 (1985)

[5-67] R. Fisher, J. Allan, and J. Pressesky, *Magnetic properties and longitudinal recording performance of corrosion-resistant alloy films*, *IEEE Transactions on Magnetics*, Vol. **22**, Issue 5, pp. 352-354 (Sept 1986)

[5-68] J. Allan, and R. Fisher, *A Comparison of the Magnetic and Recording Properties of Sputtered Ternary Alloys for High Density Applications*, IEEE Transactions on Magnetics, Vol. MAG-**23**, No. 1, pp. 122-124, (Jan. 1987)

[5-69] M. Takahashi, A. Kikuchi and S. Kawakita, *The Ultra Clean Sputtering Process and High-Density Magnetic Recording Media*, IEEE Trans. Magn. Vol. **33**, No. 5, pp. 2938 – 2943 (Sept. 1997).

[5-70] T.P. Nolan, R. Sinclair, R. Ranjan and T. Yamashita, *Microstructure and crystallography of textured CoCrTa/Cr recording media*, Ultramicroscopy, **47**, pp. 437-446 (1992)

[5-71] M.A. Parker, K.E. Johnson, C. Hwang and A. Bermea, Proc. 49th Annual EMSA Meeting, Eds. G.W. Bailey and E.L. Hall (San Francisco Press, San Francisco), pp 762 (1991)

[5-72] T.P. Nolan, R. Sinclair, R. Ranjan and T. Yamashita, *Transmission Electron Microscopic Analysis of Microstructural Features in Magnetic Recording Media*, IEEE Trans. Magn. Vol. **29**, No.1, pp. 292-299 (Jan. 1993)

[5-73] T.P. Nolan, R. Sinclair, R. Ranjan and T. Yamashita, *Effect of microstructural features on media noise in longitudinal recording media*, J. Appl. Phys. **73**, (10), pp. 5566 – 5568 (15 May, 1993)

[5-74] T.P. Nolan, R. Sinclair, R. Ranjan, T. Yamashita, G. Tarnopolsky and W. Bennett, *Correlation of Structure and Properties in Thin film Magnetic Media,* Mat. Res. Soc. Symp. Proc. Vol. **343**, pp. 297-302, Materials Research Society (1994)

[5-75] R. Ranjan, W.R. Bennett, G.J. Tarnopolsky, T. Yamashita, T.P. Nolan and R. Sinclair, *Noise properties and microstructure of oriented CoCrTa/Cr media*, J. Appl. Phys. **75** (10), pp. 6144 – 6146, 15 (May 1994)

[5-76] G.J. Tarnopolsky, H.N. Bertrum and L.T. Tran, *Magnetization fluctuations and characteristic lengths for sputtered CoP/Cr thin film media*, J. Appl. Phys. **69**, 4730 (1991)

[5-77] H.N. Bertrum and R. Arias, *Fast thermal reversal of magnetic particles*, J. Appl. Phys. **71**, 5151 (1992)

[5-78] J.-G Zhu and H.N. Bertrum, *Magnetization reversal and domain structures in thin film recording media*, J. Appl. Phys. **69**, 4709 (1991)

[5-79] J. E. Wittig, T.P. Nolan, R. Sinclair and J. Bentley, *Chromium Distribution in CoCrTa/Cr Longitudinal Recording Media*, Mat. Res. Soc. Symp. Proc. Vol. **517**, pp. 211-216, Materials Research Society (1998)

[5-80] US Patent 6,500,567 B1, Gerardo Bertero, Charles Changqing Chen, Tu Chen, Tsutomu Yamashita, Makoto Imakawa, and Michinobu Suekane, *Ultra-thin nucleation layer for magnetic thin film media and the method for manufacturing the same* (Dec. 31, 2002)

[5-81] P. Glije, J.M. Sivertsen and J.H. Judy, *Advanced Multilayer Thin films for Ultra-High Density Magnetic Recording Media*, IEEE Trans. Magn. Vol. **30**, No. 6, pp. 3957-3959 (1994)

[5-82] L. L. Z. Fang and D. N. Lambeth, *New High Coercivity Cobalt Alloy Thin film Medium Structure for Longitudinal Recording*, Appl. Phys. Letters, **65** (24), pp. 3137 (Dec 12, 1994)

[5-83] E. E. Fullerton, D.T. Margulies, M.E. Schabes, M. Carey, G. Gurney, A. Moser, M. Best, G. Zeitzer, K. Rubin, H. Rosen and M. Doerner, *Antiferromagnetically coupled magnetic media layers for thermally stable high-density recording*, Appl. Phys. Lett. **77**, 3806 (2000)

[5-84] K.E. Johnson, M. Mirzamaani and M. F. Doerner, *In-Plane Anisotropy in Thin film Media: Physical Origins of Orientation Ratio (Invited)*, IEEE Trans. Magn. Vol. **31**, No. 6, pp 2721-2727 (November 1995)

[5-85] D. Mauri, V.S. Speriosu, T. Yogi, G. Castillo and D.T. Peterson, Magnetoelastic Properties of Very Thin Co-Alloy Films, IEEE Tran. Magn. Vol. **26**, No. 5, pp. 1584-1586 (September 1990)

[5-86] R. Wood, *The Feasibility of Magnetic Recording at 1 Tbit per Square Inch*, IEEE Trans. Mag. Vol. **36,** no. 1, pp. 36-42 (Jan. 2000)

[5-87] Y. Sonobe, D. Weller, Y. Ikeda, K. Takano, M.E. Schabes, G. Zeltzer, H. Do, B.K. Yen, and M.E. Best, *Coupled granular/continuous medium for thermally stable perpendicular magnetic recording*, Journal of Magnetism and Magnetic Materials, Vol. **235**, Issue 1-3, pp. 424-428 (October 2001)

[5-88] A. Takeo, S. Oikawa, T. Hikosaka, and Y. Tanaka, *A new design to suppress recording demagnetization for perpendicular recording*, IEEE Transactions on Magnetics, Vol. **36**, No. 5, pp. 2378-2380 (Sept. 2000)

[5-89] Tu Chen, The Evolution of Thin film Magnetic Media and Its Contribution to the Recent Growth in Information Technology, My Personal Experiences In Founding Komag Inc., May 2014 electronic publication at Computer History Museum of Mt. View, California, http://www.computerhistory.org/collections/catalog/102718661

[5-90] http://en.wikipedia.org/wiki/Ceramic_knife

[5-91] Ph.D. Thesis, F. K. Moghadam, *Electrical and Microstructural Characterization of Stabilized Zirconia Solid Electrolytes*, Stanford University (May 1981)

[5-92] J. Robertson, Diamond-like amorphous carbon, Materials Science and Engineering: R: Reports, Vol. **37**, Issues 4-6, pp. 129-281 (May 2002)

[5-93] H.G. Scott, *Phase relationships in zirconia-yttria system*, J. Mater. Sci. **10** [9], 1527 (1975)

[5-94] Fomblin Z-Dol, Trademark of Ausimont Inc, Sold by Solvay Solexis

[5-95] T. Yamashita, G.L. Chen, J. Shir and T. Chen *Sputtered ZrO_2 Overcoat with Superior Corrosion Protection and Mechanical Performance in Thin film Rigid Disk Application*, IEEE Trans. Magn. Vol. **24**, No. 6 (Nov. 1988)

[5-96] US Patent 4,929,500, *Corrosion resistant magnetic disk*, Tsutomu T. Yamashita, Ching-Cheng Shir, and Tu Chen

[5-97] US Patent 4,898,774, *Corrosion and wear resistant magnetic disk*, Tsutomu T. Yamashita, Ching-Cheng Shir, Tu Chen and Ga-Lane Chen

[5-98] S.N. Lakiza and L.M. Lopato, *Stable and metastable phase relations in the system alumina-zirconia-yttria*, J. Am. Ceram. Soc., **80**, [4], 893-902 (1997)

In reference to IEEE copyrighted material that is used with permission in this thesis, the IEEE does not endorse any of Stanford University products or services. Internal or personal use of this material is permitted. If interested in reprinting/republishing IEEE copyrighted material for advertising or promotional purposes or for creating new collective works for resale or redistribution, please go to http://www.ieee.org/publications_standards/publications/rights/rights_link.html to learn how to obtain a license from RightsLink.

Chapter 6: Summary and Future Work

6.1 Summary of Work Presented in this Thesis

6.1.1 HRTEM Technique

The HRTEM technique was investigated and applied to the CdTe [011] specimen to try to obtain the highest resolution possible from a Philips EM400 microscope operating at 120 keV and with C_s of 1.1mm. Microscope operating conditions were carefully adjusted and measured where possible, and experimental images were compared with computational models based on both Bloch wave formulation and multi-slice formulation to elucidate the microscope and specimen conditions where atomic resolution might be possible. It was concluded that under a very limited set of conditions, images that resolve Cd and Te species are possible with the microscope, but the images are obtained beyond the conventional Scherzer resolving power of the microscope, therefore, subject to significant difficulties in interpretation due to the complex interaction of diffracted beams and microscope parameters.

More practical application of the HRTEM method at approximately the Scherzer resolution of 0.3 nm was used to study a variety of problems that are amenable to the use of the technique, such as analyzing lattice defects in CdTe, CdS, and GaAs. Additionally, semiconductor interfaces of CdS/CdTe and MBE GaAs structures were studied to determine the structural details of the interfaces as a function of various processing parameters such as substrate treatments and film growth methods. For this task, conventional TEM methods and other materials characterization tools such as X-ray diffraction, X-ray topography, and EDX were used. By using proper microscope settings at the Scherzer resolution or by use of virtual aperture set by the beam divergence, the images thus obtained consisted of image spots that represent a pair of atoms, for example Cd-Te, Cd-S or Ga-As, which can change from white atoms or black atoms depending upon the microscope defocus and specimen thickness. In addition, by limiting the analysis to only the thin part of the specimen, the images are

easier to interpret in a straightforward manner. The image can be directly related to the actual atomic structure as long as one does not attempt to interpret the images beyond the resolution limit of the microscope.

One of the significant results of this work is the use of a video camera to record rapidly evolving events at high resolution in the microscope in-situ. TEM parameters were optimized for video imaging, and digital image processing was done in order to enhance the SNR and contrast of the images. Some of the unique phenomena observed in real time include surface reconfiguration, dislocation motion, and dislocation reactions. These results were obtained for the first time using TEM equipped with a video camera. Our results sparked interest in pursuing similar results with other materials and contributed to the effort to improve the video capability for use in the TEM. Today, the video camera is an indispensable tool for TEM and it has replaced the use of negatives to obtain images. In-situ imaging of dynamic events in TEM has become a commonplace activity with various add-on features built into the TEM such as the environmental chamber and the use of heating and cooling holders as well as holders designed to apply current and voltages to the specimen. Online real-time image processing is also possible with the video images with sophisticated software and high-powered computers that process the images in real time.

Another area of contribution that this work has made is in the area of specimen preparation. With the cooperation and help from many individuals and in particular from Hewlett-Packard, the techniques that were used here for the preparation of a cross section sample have become much more widespread and in common use as our work was published, and the techniques that we employed were disseminated. The dimpler tool, in particular, has become an indispensable tool in most TEM facilities in the world.

Finally, the latest technology with aberration-corrected TEM was used to image CdTe again in [011] projection. Using the Titan 80-300 model TEM operating at 300 kV with the CEOS aberration correction lens system, the 0.162 nm separations between the Cd and Te position were resolved using the NCSI imaging technique.

Images with this resolution were only seen at the extremely thin part of the specimen. Image simulation was used to compare the experimental images with the simulation. Only partial correlation was made, and much more work is necessary to tune the simulation to match to the experimental images.

6.1.2 Defects in CdTe and CdS

Various dislocation types were studied by HRTEM technique on CdTe. Additional work was done on CdS, but this was more limited compared to the work on CdTe. Defects observed by HRTEM were characterized, and their defect types were determined through careful analysis of the images. Even though many of the defects seen in CdTe were undoubtedly introduced inadvertently by ion-milling used in TEM specimen preparation, it was useful to see the dislocations and their reactions at near atomic resolution using the HRTEM technique. Being able to see the actual dislocation structures and their motion and reactions taking place in real time provided additional insights about them as opposed to seeing them only through the theoretical models and reaction equations.

6.1.3 CdS/CdTe Heterojunction Solar Cells

CdS/CdTe heterojunction interfaces were characterized by conventional and HRTEM for cells that had been electrically characterized. Some insights were obtained for the structural relationship between the CdS film deposited by e-beam evaporation and CVD methods with the CdTe substrate surface. Considerable differences were observed in CdS morphology and even its crystalline type, depending upon the surface treatment used on CdTe and its crystalline orientation. For example, a cubic CdS film can form on freshly cleaved {110} CdTe and has very poor junction performance due to its high resistivity. CdTe surface can become very clean after hydrogen annealing at moderate temperatures, and it can stay clean even after some air exposure. This

characteristic of CdTe probably allows good film growth of hexagonal phase CdS to the CdTe surface, thereby providing good junction performance. HRTEM analysis allowed direct imaging of several different types of epitaxy that occur between CdS and CdTe. When the surface was left with residue from bromine-methanol treatment or oxidation, the CdS film grew poorly, and HRTEM showed evidence of interfacial compounds that compromised the junction performance, and CdS formed a polycrystalline film. Despite the wide differences in the quality of CdS films, the difference in junction performance was not so large between them so that CdS/CdTe junction system appears to be robust and flexible for creating useful solar cell structure. Successful commercial use of the CdS/CdTe heterojunction solar cells suggests that this robustness in being able to form good junctions with low-cost processing is a key factor in its success.

The following papers were published on the topic of HRTEM imaging of CdTe and CdTe heterojunctions.

(Refereed)

1. "Atomic Motion on the Surface of a Cadmium Telluride Single-crystal", R. Sinclair, T. Yamashita and F.A. Ponce, Nature, **290**, pp. 386-388 (1981).

2. "High-Resolution Lattice Imaging of Cadmium Telluride", T. Yamashita, F.A. Ponce, P. Pirouz and R. Sinclair, Philos. Mag., **A45**, pp. 693-711 (1982).

3. "Dynamic Observation of Defect Annealing in CdTe at Lattice Resolution", R. Sinclair, F.A. Ponce, T. Yamashita, D.J. Smith, R.A. Camps, L.A. Freeman, S.J. Erasmus, W.C. Nixon, K.C.A. Smith and C.J.D. Catto, Nature, **298**, pp. 127-131 (1982).

4. "Cadmium Telluride Films and Solar Cells" R.H. Bube, A. Fahrenbruch, R. Sinclair, T.C. Anthony, C. Fortmann, W. Huber, C-T. Lee, T. Thorpe and T. Yamashita, IEEE Trans. Electron Devices, **ED-31**, pp. 528-538 (1984).

(Non-refereed)

1. "High-Resolution Imaging of Cadmium Telluride", R. Sinclair, F. Ponce, T. Yamashita and P. Pirouz, *Proc.7th European Congress on Electron Microscopy*, pp. 312-313 (1980).

2. "Structure Imaging of Defects in Cadmium Telluride", F. Ponce, T. Yamashita and R. Sinclair, 38th Proc. EMSA, pp. 320-321 (1980).

3. "Imaging of Defects in Cadmium Telluride Using High-Resolution Transmission Electron Microscopy", F.A. Ponce, T. Yamashita, R.H. Bube and R. Sinclair, in *Defects in Semiconductors*, eds. J. Narayan and T.Y. Tan, (1981).

4. "High-Resolution Transmission Electron Microscopy of Semiconductor Materials", R. Sinclair, F.A. Ponce, J.C. Bravman, T. Yamashita and P. Pirouz, *Proc. of the 2nd Conference on Microscopy of Semiconducting Materials*, Oxford, England, pp. 147-152 (1981).

5. "High-Resolution Imaging of Semiconductor Interfaces", R. Sinclair, F.A. Ponce, T. Yamashita and J.C. Bravman, 39th Proc. EMSA, pp. 124-127 (1981).

6. "Dynamic Observation of Atomic-Level Events in Cadmium Telluride by High-Resolution TEM", T. Yamashita and R. Sinclair, in *Defects in Semiconductors*, eds. J.W. Corbett and S. Mahajan, (Elsevier North-Holland), pp. 295-299 (1982).

7. "High-Resolution Electron Microscopy II-VI Compound Semiconductors", R. Sinclair, F.A. Ponce, T. Yamashita and David J. Smith, Inst. Phys. Conference Series 67, pp. 103-108 (1983)

8. "High-Voltage High-Resolution Electron Microscopy of Compound Semiconductors", R. Sinclair, F.A. Ponce, T. Yamashita and David J. Smith, *Proc. 7th Int'l Conference on High Voltage Electron Microscopy*, LBL Report #16031, pp. 31-34 (1983).

9. "Lattice Imaging of CdS/CdTe Solar Cell Interface", T. Yamashita, J.G. Werthen, R.H. Bube and R. Sinclair, 41st Proc. EMSA, ed. G.W. Bailey, San Francisco Press, San Francisco, pp. 124-125 (1983).

10. "Observation of Dislocation Reactions in CdTe at Lattice Resolution", T. Yamashita and R. Sinclair, 41st Proc. EMSA, pp. 112-113 (1983)

11. "A Mechanical grinding machine for the preparation of TEM specimens", T. Yamashita, EMSA Bulletin **10**, 66 (1980).

12. “High resolution imaging of semiconductor interfaces”, R. Sinclari, F.A. Ponce, T. Yamashita and J.C. Bravman, Norelco Reporter, Vol. 29, Issue 1EM, pp. 22-23 (1982)

13. “Atomic motion on the surface of a cadmium telluride single-crystal”, R. Sinclair, T. Yamashita and F.A. Ponce, Norelco Reporter, Vol. 29, Issue 1EM, pp. 19-21 (1982)

14. “High resolution lattice imaging of the CdS/CdTe interface (solar cells)”, T. Yamashita, J.G. Werthen, R. Sinclari and R.H. Bube, Conference record of the sixteenth IEEE Photovoltaic Specialists Conference – San Diego, CA, USA, 1982, pp. 1433-4

6.1.4 Defects in MBE-GaAs

MBE GaAs grown on LEC GaAs crystals is the basis of a variety of important devices that are in widespread use today. HRTEM and other conventional materials science analytical techniques, including conventional TEM methods, were used to obtain useful insight about the types of defects that are present in the LEC GaAs material itself and in the MBE film. In particular, the oval defects, which have been the bane of MBE films for a long time, were characterized in terms of their crystallography, morphology, and structure. They appear to have their origin in the dislocation tangles that exist in the LEC GaAs substrate itself, and some other external factors that occur during MBE GaAs growth. They contain a seed material that forms inside the oval defects, which appears to consist of hexagonal phase GaAs, which, under some growth conditions, can lead to rapid whisker growth. When the whisker growth initiates, they grow extremely rapidly, and it was discovered that they have hexagonal wurtzite crystal structure. They grow with a specific crystallographic relationship to the substrate, along the $\{111\}_A$ or the gallium direction with respect to the GaAs substrate. These whiskers were nuisance, which was to be avoided during the time of this study, but today the whiskers themselves are deliberately grown to make interesting devices out of them and have become a subject of intense research activities.

6.1.5 Co-based Thin film Magnetic Media

Evolution of thin film magnetic media from its inception in the research level investigation at Xerox PARC with CoRe alloys to commercial application in the form of CoPt-based alloy is outlined and explained. The importance of grain isolation and its effect on the noise performance of the media through exchange decoupling is explained in detail, and how this single factor played the most significant role in the astounding areal density increase achieved by the HDD industry as a whole. The initial grain isolation scheme involved the use of physical isolation through sputtering at high argon pressure. This evolved to the use of various nucleation layers to isolate the grains, and use of chromium and oxides to segregate into the grain boundaries. Development of a CoCr-based alloy, which relied on chromium segregation into the grain boundaries, is described in detail. Oxide segregation developed at Komag is also described in detail, and how such concepts were based on the use and understanding of phase diagrams for cobalt and its alloys. Today's perpendicular media, which is used in 100% of the media used in the hard disk drives manufactured today, uses oxide-based isolation in the cobalt alloys. How this came to be is outlined in a historical fashion based on some of the key development in the evolution of thin film media. Work that was done on understanding of chrome segregation in CoCr-based alloy in this work has greatly contributed to the improvements that were made on this alloy system and extended the longitudinal media for a long time.

As an addendum, the excellent mechanical property of stabilized zirconia was used to form a sputtered thin film version of the zirconia as use for a protective overcoat on thin film magnetic media with excellent results. Obtaining the proper microstructure with yttria-stabilized zirconia was an important consideration for the target material, which encounters significant thermal shock during sputtering. The resulting sputtered film consisted mainly of a high-temperature cubic phase with only a hint of the presence of the tetragonal phase. The grain size of the sputtered films was very small on the order of several nanometers. Therefore, it was not possible to elucidate whether the individual grains contained a tetragonal phase as in the bulk material. However, the sputtered film had excellent mechanical properties against

repeated landing and rubbing of its surface by the recording head. It also had excellent protection against corrosion so that it protected the sensitive magnetic thin film. A zirconia phase diagram with respect to other oxide additions was used to develop a thin- film composition based on zirconia with alumina, in order to obtain an amorphous structure in the sputtered film. This occurs because when an immiscible system is sputtered, it often results in the amorphous film. Zirconia with 10% alumina was used to create protective coating for a magneto-optic recording disk, which performed very well in protecting the very sensitive TbFeCo alloys that are used in the recording material for the magneto-optic application.

The following publications include the work described in this thesis.

(Refereed)

1. "Metallurgical Applications of the 2 1/2 D TEM Technique", R. Sinclair, G.M. Michal and T. Yamashita, Met. Trans., **12A**, pp. 1503-1512 (1981).

2. "The Effect of Orientation, Grain Size and Polymorphism on Magnetic Properties of Sputtered Co-Re Thin Film Media", T. Chen, T. Yamashita and R. Sinclair, IEEE Trans. Magn., **MAG-17**, pp. 3187-3189 (1981).

3. "Microstructure and Crystallography of Textured CoCrTa/Cr Sputtered Thin Film Media for Longitudinal Recording", T.P. Nolan, R. Sinclair, R. Ranjan and T. Yamashita, Ultramicroscopy, **47**, pp. 437-446 (1992).

4. "Transmission Electron Microscopic Analysis of Microstructural Features in Magnetic Recording Media", T.P. Nolan, R. Sinclair, R. Ranjan and T. Yamashita, IEEE Trans. Magn., **29**, pp. 292-299 (1993).

5. "Crystallographic Orientation of Textured CoCrTa/Cr Recording Media", T.P. Nolan, R. Sinclair, R. Ranjan and T. Yamashita, J. Appl. Phys., **73**, pp. 5117-5124 (1993).

6. "Effect of Microstructural Features on Media Noise in Longitudinal Recording Media", T.P. Nolan, R. Sinclair, R. Ranjan and T. Yamashita, J. Appl. Phys., **73**, pp. 5566-5568 (1993).

7. "Noise Properties and Microstructure of Oriented CoCrTa/Cr Media", R. Ranjan, W. R. Bennett, G.J. Tarnopolsky, T. Yamashita, T.P. Nolan and R. Sinclair, J. Appl. Phys., **75**, pp. 6144-6146 (1994).

8. "Lorentz Transmission Electron Microscopy Study of Micromagnetic Structures in Real Computer Hard Disks," K. Tang, M. R. Visokay, R. Sinclair, C. Ross, R. Ranjan and T. Yamashita, IEEE Trans. Magn., **32**, pp. 4130-4132 (1996).

9. "Magnetic Clusters, Intergranular Exchange Interaction and Their Microstructural Basis in Thin Film Longitudinal Media", K. Tang, M.E. Schabes, C.A. Ross, L. He, R. Ranjan, T. Yamashita and R. Sinclair, IEEE Trans. Magn., **33**, pp. 4074-4076 (1997).

10. "Chromium Segregation in CoCrTa/Cr and CoCrPt/Cr Thin Films for Longitudinal Recording Media", J.E. Wittig, T.P. Nolan, C.A. Ross, M.E. Schabes, K. Tang, R. Sinclair, and J. Bentley, IEEE Trans. Magn., **34**, pp. 1564-1566 (1998).

11. Tu Chen and T. Yamashita, *Physical Origin of Limits in the Performance of Thin film Longitudinal Recording Media*, IEEE Trans. Magn. Vol. **24**, No. 6, pp. 2700-2705 (1988)

12. T. Yamashita, R. Ranjan, L.H. Chan, M.Lu, C.A. Ross, J. Chang and G. Tarnopolsky, *The Effect of Microstructure on the Magnetic Properties of Thin Film Magnetic Media*, Mat. Res. Soc. Symp. Proc. Vol. **343**, pp 285-296 (1994)

13. T. Yamashita, L.H. Chan, T. Fujiwara and Tu Chen, *Sputtered NixP Underlayer for CoPt-Based Thin Film Magnetic Media*, IEEE Trans. Mag., Vol. **27**, No.6, pp. 4727 – 4729 (Nov. 1991)

14. S. Miura, T. Yamashita, G. Ching and T. Chen, *Noise and bit jitter performance of CoNiPt thin film longitudinal recording media and its effect on recording performance*, IEEE Trans. Magn., Vol. **24**, No. 6, pp. 2718 – 2720 (November 1988)

15. R. Ranjan, M. Lu, T. Yamashita and T. Chen, *Effect of Cobalt Oxide Addition on Co-Pt Media*, IEEE Trans. Mag., Vol. **30**, No. 5, pp. 3942-3944 (1994)

16. Tu Chen, G.B. Charlan and Tom Yamashita, *A comparison of the uniaxial anisotropy in sputtered Co-Re and Co-Cr perpendicular recording media*, J.Appl. Phys., Vol. **54**, No. 9, pp. 5103-5111 (1983)

17. T.P. Nolan, R. Sinclair, R. Ranjan and T. Yamashita, *Transmission Electron Microscopic Analysis of Microstructural Features in Magnetic Recording Media*, IEEE Trans. Magn. Vol. **29**, No.1, pp. 292-299 (Jan. 1993)

(Non-refereed)

1. "Transmission Electron Microscopy and High-Resolution Scanning Electron Microscopy of Co-Ni-Pt Thin Film Magnetic Recording Media", L. Chan, T. Yamashita and R. Sinclair, 47th Proc. EMSA, pp. 570-571 (1989).

2. "Correlation of Microstructural and Magnetic Properties of Longitudinal Recording Media Using TEM", T.P. Nolan, R. Sinclair, T. Yamashita and R. Ranjan, 51st Proc. MSA, pp. 1016-1017 (1993).

3. "Correlation of Structure and Properties in Thin film Magnetic Media", T.P. Nolan, R. Sinclair, T. Yamashita, R. Ranjan, G. Tarnopolsky and W. Bennett, Mat. Res. Soc. Symp. Proc., **343**, pp. 297-302 (1994).

4. "Correlation of Micro-structural, Micro-chemical and Micro-magnetic Properties of Longitudinal Recording Media Using CM20 FEG Lorentz TEM", T.P. Nolan, R. Sinclair, T. Yamashita and R. Ranjan, 52nd Proc. MSA, pp. 892-893 (1994).

The following refereed papers were published on stabilized zirconia.

1. "Transmission Electron Microscopy of Annealed ZrO_2+8Mol%Sc_2O_3", F.K. Moghadam, T. Yamashita, R. Sinclair and D.A. Stevenson, J. Am. Ceram. Soc., **66**, pp. 213-217 (1983).

2. "Characterization of the current-blackening phenomena in Scandia stabilized zirconia using transmission electron microscopy", F.K. Moghadam, T. Yamashita and D.A. Stevenson, J. Mater. Sci., 18, p 2255-2259 (1983).

3. "Sputtered ZrO_2 Overcoat with Superior Corrosion Protection and Mechanical Performance in Thin Film Rigid Disk Application", T. Yamashita, G.L. Chen, J. Shir and T. Chen, IEEE Trans. Magn. Vol. **24**, No. 6 (Nov. 1988)

6.2 Advances Since These Studies

6.2.1 HRTEM Technique

The HRTEM technique has advanced greatly since the work outlined in this thesis, which was done in the early 1980s, the development of the aberration-free lens being the most significant. Now, the C_s of the microscope can be adjusted from a small negative to a positive value to obtain the image contrast that is desired for the material being imaged. The point resolution of the microscope is sufficient to image most material at atomic resolution, including light atoms such as carbon and oxygen. Single atoms now can be imaged with much ease compared to the past, such as individual carbon atoms in a graphene sheet. Also important is the use of a very bright and highly coherent field emission source for the beam and obtaining a very narrow energy spread of 0.14 eV. This provides a very high resolution for chemical analysis using EELS. Other advances are in the area of convenience and ease of use for the TEM, which include video imaging and digital image processing that allows rapid collection of data and on-the-fly image analysis such as FFT and correction of image astigmatism to a high degree. An aberration corrector is useful at all operational voltages, and this has been a boon to the study of biological specimens and low Z element imaging where beam damage is a big issue. The ability to obtain high-resolution images with very low C_s at even 80 kV means that biological specimens can be imaged with atomic resolution, which was impossible to do before.

The EELS technique also has advanced significantly through the improvement in the tool and reduction in the energy spread from the TEM. Energy filtered images are possible so that atomic species can be identified in the specimen to near atomic resolution. Combined with HRTEM, this makes the current generation of aberration corrected TEM one of the most capable tools for material analysis. This combined with the ability to conduct in-situ reactions within the specimen with the environmental chamber has greatly expanded the type of investigation that can be studied inside TEM. All of these capabilities come with a price tag. Even a standard well-equipped analytical TEM costs well over $2M and high-performance C_s corrected TEM can run

upwards of $8M. Therefore, efficient use of the microscope time has become very important as well, and various convenience features to make this possible have become a standard feature of modern microscopes.

Specimen preparation also has advanced greatly from the 1980s by the advent of FIB tools to select and prepare TEM specimens. These tools are also quite expensive and require an expert user. Nevertheless, FIB tool has revolutionized the TEM analysis field due to its versatility. It has become an indispensable tool for failure analysis and analytical TEM since specific defects can be analyzed very quickly by obtaining TEM specimens directly from the region of interest in plain view and in cross section from a working part. It is now widely used, in the semiconductor field and in the hard disk drive field as well, to examine small defects and determine their source. It is not unusual for TEM in such a facility to operate continuously to monitor and conduct the failure analysis function in corporate failure analysis labs around the world. With a typical price tag of over $2M for the FIB tool, the specimen preparation cannot be said to have become easier, just more expensive but more assured. However, many of the conventional techniques for preparing TEM specimens outlined in this thesis are still in widespread use.

6.2.2 Defects in CdTe and CdS

There have not been a great number of studies about defects in CdTe and CdS since the 1980s because these materials are used in only very specialized applications. Infrared detectors and solar cell applications probably constitute the biggest use of these materials. In a solar cell, the CdS/CdTe junction is used by a single company; therefore, there are only a limited number of researchers studying this material from a fundamental perspective. Various regulations and safety protocols necessary to deal with CdTe also make a study of this material difficult even in larger institutions. Significant infrastructure is necessary to deal with waste handling when dealing with and processing CdTe.

6.2.3 CdS/CdTe Heterojunction Solar Cells

CdS/CdTe heterojunction cells have gotten a significant boost in successfully commercialization since their adoption by First Solar. Consequently, there are a number of institutions around the world that continue to study this structure. However, compared to silicon and other materials such as organic solar cells, the number of researchers working on a CdTe system are relatively few. Much of the attention is focused on creating new type of junctions, which are lower cost and based on cheaper and less toxic materials. Key work on CdS/CdTe revolves around the thin film version of the heterojunction and understanding the relationship between the junction performance and some material properties or processing conditions. A typical thin film solar cell consists of polycrystalline CdTe and CdS. Typical TEM analysis is made more difficult by the complexity of such a structure. The performance of these cells depends on the various post-deposition treatments, and current work seems to be directed toward trying to understand what the treatment does to the microstructure and the junction performance. Much of the effect is in the CdTe absorber layer, and this is where probably more work may be useful. Not much has been detailed about what happens at CdTe grain boundaries and at the CdS/CdTe interface because of post-processing.

6.2.4 Defects in MBE-GaAs

Oval defects were continuing problems in MBE GaAs for at least 10-20 years subsequent to this work, and there have been claims of it being solved several times, only to resurface again. I have not seen the type of analysis that should be done given the capability of today's microscope and specimen preparation method using FIB that easily could be applied to solve the oval defects once and for all. Perhaps the industrial labs have solved it, and such activities are not carried out by academia. The dollar amount of the business using MBE GaAs is probably small compared to other industries, such as silicon device manufacturer or HDD manufacturer. Therefore, the full capability of the modern TEM facility may not have been applied to this problem yet.

6.2.5 GaAs Whiskers

It was with some surprise to learn that GaAs whiskers have become a mainstream activity for many researchers in recent times. There was a great deal of interest in trying to make use of the whiskers for devices; because of this, much attention seems to be going to the fabrication process. IBM's announcement of GaAs whiskers to use as LEDs and photoreceptors is one example, where it was considered a major breakthrough for the device using this material [4-54]. Nevertheless, the characterization of the whisker itself and detailed description of the nucleation and growth process still seems to be lacking. There is an opportunity to contribute in this area by bringing to bear the full capability of the analytical TEM on this problem.

6.2.6 Co-based Thin Film Magnetic Media

Since 2010, the HDD industry has converted all of the recording technology to perpendicular recording, and 100% of the media in use today employ oxide segregations in the main magnetic media, which use CoPt-based alloys. The oxide phase typically consists of SiO_2, CoO, Ta_2O_3, TiO_2, and a few others. All of them work in the same way to isolate the magnetic layer grains to obtain the best exchange decoupling between the grains. The areal density growth (CAGR) or compound annual growth rate for recording density has slowed to less than 10% as initial gains from perpendicular recording have now been exhausted and not much more can be gained from the media technology. At the same time, the competition in the industry has also been reduced through acquisitions and exit from the industry by other players, so that there are only three HDD manufacturers left in the industry; Seagate, Western Digital, and Toshiba. There are an equally small number of independent component manufacturers left, namely, Showa Denko and Fuji Electric in the media and only TDK in recording heads. Toshiba uses captive vendors, Showa and TDK to manufacture all of their head and media while Seagate and Western Digital manufactures most of their own components. In such an environment, research on recording media technology is

only being made at these few companies or at small number of institutions that are connected to, or receiving funding from, these companies.

A key area of interest now for both industry and academia for the recording media has shifted to heat-assisted media that use $L1_0$ structure FePt alloys on a MgO underlayer. Recording mode is still perpendicular, and the same rules developed in longitudinal and current perpendicular media still apply, namely, that grains must be isolated, and FePt grains must be small and well oriented with perpendicular anisotropy. Oxide addition to the sputtering target is used to obtain grain isolation. FePt is deposited at relatively high temperatures, and there are many technical and practical difficulties with the process that have been difficult to solve. MgO underlayer to setup the perpendicular growth of FePt has not worked well, forming large grains that are much larger than FePt grains, and the deposition rate required to obtain good performance is much too slow for manufacturing. FePt also does not form well-isolated and uniform grains. High-temperature processing also poses additional difficulties with substrates and sputtering tools. Probably most of the industry research attention on media is focused on FePt and its alloys to come up with a viable system that can replace the current magnetic recording media. Heat-assisted magnetic recording technology has additional challenges. The recording head must carry a laser to heat the disk while recording; the design and engineering needed to channel the laser onto the media surface is challenging indeed. The situation is actually much more difficult than when the industry converted from oxide media to thin film media. At least during that period, the same head could be adapted for use in both types of media. Three key areas of technology involved in HDD (i.e., media, tribology, and head) must all be worked on together this time in order to convert to the heat-assisted magnetic recording technology, all adding to become an unprecedented level of challenge for the entire industry. Much work is still needed for the underlayer, magnetic film, and on the resulting tribology of the media to work with the laser heating. Conventional TEM and HRTEM methods, including EELS spectroscopy and EELS-based chemical mapping of the media, are being used to investigate the structure of the media, and relate them back to the processing conditions used to make them. This is a very active area of

research for industrial laboratories in the field and in universities getting funding from the industry and industry consortium.

6.3 Future Work

6.3.1 HRTEM Technique

The focus of the HRTEM technique is no longer about obtaining higher and higher resolution because of the introduction of aberration corrected lens. Resolution is achievable at the atomic level. Therefore, the attention is much more focused on the application of the technique to ever more challenging problems on difficult materials, such as low Z material and organic specimens. A new capability to map chemicals and chemical structure of the material at near atomic resolution has opened up many new avenues of research into old issues that could not be analyzed previously. The ability to also conduct in-situ reactions with the specimen in an environmental chamber also allow very interesting observations of chemical reactions as they occur. Modern TEMs have become very versatile and indispensable tools for many fields of study. Obtaining the ultimate resolution capability of the TEM for organic compounds and carbon materials such as graphene and its derivative structures remain a very active area of investigation. Such materials have many interesting future applications in electronic and materials applications, which will require considerable innovations in processing and formulation to commercialize them. This will require close collaboration with TEM and processing sciences to understand how these materials behave. Very few other tools offer the versatility of the modern HRTEM tool for the study of these nanostructured materials.

6.3.2 Defects in CdTe and CdS

As mentioned earlier, CdTe and CdS materials by themselves are not receiving much attention in scientific studies. The main interest for them comes from the

application side, which uses these materials in infrared detectors and in solar cells. Fundamental studies in lattice defects in CdTe and CdS may be of interest in relating the findings as prototypical defects in these types of semiconductor materials since it is easy to introduce many defects into these materials, as evidenced from this thesis. Hence, it may be the case that both materials, particularly the CdTe, are good candidate materials to study various defect atmospheres in terms of structure and the chemistry between them using tools such as EELS and aberration-corrected HRTEM. Point defects, for example, such as vacancies, interstitials, and dopants may be interesting to look at if enough of them can be introduced into the material to have a chance of catching them. The use of low kV imaging may be important, as CdTe is easy to damage by e-beam. Use of environmental cells for reaction and heating stages may provide interesting findings of the detailed behavior of various defects in these materials that can be related to more commercially interesting materials such as silicon and GaAs.

6.3.3 CdS/CdTe Heterojunction Solar Cells

CdS/CdTe heterojunction cells are interesting as a viable solar cell structure through the success of First Solar in successfully commercializing them as a low-cost alternative to silicon-based solar cells. The challenge to them as the leading technology for thin film-based solar cells comes from CIGS (i.e., copper indium gallium selenide), which was prevalent for a while but not as less so now. First Solar continues to be the preeminent supplier of thin film-based solar cells. The only concern for this technology is the issue of toxicity with CdTe and many countries such as Japan are not in favor of using this cell structure for the commercial, residential application. Nevertheless, so far, First Solar has addressed such concerns and continues to have success in selling their products, but most, if not all, of them for large commercial installations. A number of laboratories in the world continue to work on CdS/CdTe heterojunction cells, and there will be an opportunity to improve upon the design of the solar cell. First Solar themselves continue to invest heavily in improving the efficiency of the cell and make

a periodic announcement on improvement in efficiency, but there are very few details about how they are achieving the improvements. Some of the interesting topics are in the $CdCl_2$ heat-treatment process where little is known for certain about why this process improves the performance of the cell so greatly. The junction continues to be an important area of study, and a more detailed microstructural understanding of the interface should surely net some benefit. Better understanding of the CdTe film itself as to what occurs in these materials after each process step should be interesting as well. Carrier type and mobility, and point defect types are just some of the questions that remain largely unanswered about the material. Relating what can be observed at this interface with modern high-performance TEM and relating them to the experimental processing conditions should net a better understanding, which aids in further gains in efficiency. One of the topics that were not covered in this work, which is also very important in solar efficiency, is the exact nature of the interface between the materials and their front and back contacts. Forming good ohmic contacts to CdTe has always represented challenges, and there is considerable trial and error involved in obtaining good contacts and a detailed understanding of what actually occurs are solely lacking. Study of this interface between the contact and CdTe has been a difficult and messy affair, as I have also discovered. It did not lend itself to useful TEM analysis at that time because of the limitation of the TEM tool at the time. Modern TEM with high-performance chemical analysis capabilities would surely help in improving the analysis considerably.

6.3.4 Defects in MBE-GaAs

MBE GaAs has a much smaller market compared to silicon in terms of the dollar value of the business, but it is in a technically very important market that demands some of the highest performance in the electro-optic field. As such, devices gain more importance over time over more traditional silicon-based technologies; the improvements that are necessary in the GaAs defect level will surely become more important. Being a compound semiconductor, GaAs causes more complications in the

formation of defects and how they behave electrically and optically in devices. As mentioned in Chapter 4, LEC GaAs continues to have a much higher level of defects compared to silicon, and the defect was speculated to have "As" atmosphere around them for example. Such effects associated with microdefects would be an excellent choice of study for properly equipped HRTEM with sensitive chemical analytical capabilities. Apparently, after claims of being solved so many times, the oval defects continue to exist in MBE-GaAs. It should be solved once and for all by the proper application of FIB cross sectioning and analytical TEM to determine the exact nature of their growth and their structure to obtain the most up-to-date understanding of the evolution of this defect. This should help in obtaining the solution to eradicating this defect once and for all.

6.3.5 GaAs Whiskers

Even as it is claimed that it is now well understood that GaAs whiskers have a hexagonal structure in the literature, the detailed analysis of how they form and the resulting structure appear to be lacking. Numbers of techniques are employed to excite whisker growth and some involve actual VLS growth mechanisms while others do not. However, the whiskers are treated as being rather similar, which is probably not the case at all. Comparison of the whiskers made by different techniques will likely provide more insight into the growth mechanism and how it affects the detailed structure of the whiskers. As some investigators are clever and skilled in manipulating these whiskers into devices, their interest will surely grow as they begin to see differences in their electrical properties depending upon how the whiskers were grown. Conducting electrical measurements on the whiskers in-situ in the microscope combined with HRTEM and conventional TEM method analysis will provide some interesting discoveries about the whiskers in the future.

6.3.6 Co-based Thin Film Magnetic Media

In the hard disk drive industry, much of the advanced thin film media research has migrated to the investigation of $L1_0$-FePt-based film for heat-assisted magnetic recording. The current perpendicular magnetic recording using CoPt-oxide-based media has basically run out of further significant improvements; consequently, the areal density compound annualized growth rate (CAGR) of the media and the drive have slowed to single digits. FePt also has added an oxide phase, which must segregate at the grain boundaries to separate the FePt particles. It is very difficult to obtain high-quality FePt grains and it is probably due to the kinetics of forming the $L1_0$ crystal structure. The formation of this phase is sluggish, as evidenced by the requirement for high-temperature processing and the significantly slower deposition rate that is required for its formation. Improving this situation is going to be the make or break challenge for the viability of this media. Additional challenges are in the area of epitaxy and growth over the MgO film surface, which act as a seed for the perpendicular growth of the FePt grains. The situation with MgO is analogous to the situation that existed with Cr underlayers for CoCr-based alloys in the early days of its use. Just as Cr grains were forced to be thick, and the grains were very large, MgO is in the same situation and something must happen with this underlayer in terms of becoming a viable base for the FePt media. A new invention is probably required. More detailed understanding of MgO and how it works with the FePt grains would be a good start in either improving its behavior or moving on to something else that might work better.

CoPt-based film may receive a resurgence in interest if STT-MRAM technology makes inroads into its use as a memory device in various applications. The structure using this technology is amenable to further reduction in cell size, as it uses spin torque effect in forming the basic unit of the memory cell. It is exquisitely sensitive and has the added benefit of being non-volatile. The exact nature of some of the difficulties involved in the stability of the STT-RAM devices is not yet well understood. If it is something to do with the material choice itself, then there will be an

opportunity to contribute to the success of this device if a solution can be found on improving the stability of this device.